Université de Montréal

Développement et caractérisation de dérivés dipyrrométhène pour des applications dans le domaine du photovoltaïque

par
André Yvon-Bessette

Département de chimie
Faculté des arts et des sciences

Thèse présentée à la Faculté des études supérieures et postdoctorales
en vue de l'obtention du grade de
Philosophiae doctor (Ph.D.) en chimie

Septembre 2015

Résumé

Ce projet de recherche mené en collaboration industrielle avec St-Jean Photochimie Inc. / PCAS Canada vise le développement et la caractérisation de dérivés dipyrrométhène pour des applications dans le domaine du photovoltaïque. La quête du récoltage des photons se situant dans le proche-infrarouge a été au centre des modifications structurales explorées afin d'augmenter l'efficacité de conversion des cellules solaires de type organique et à pigments photosensibles. Trois familles de composés intégrant le motif dipyrrométhène ont été synthétisées et caractérisées du point de vue spectroscopique, électrochimique, structural ainsi que par modélisation moléculaire afin d'établir des relations structures-propriétés.

La première famille comporte six azadipyrrométhènes au potentiel de coordination tétradentate sur des centres métalliques. Le développement d'une nouvelle voie synthétique asymétrique combinée à l'utilisation d'une voie symétrique classique ont permis d'obtenir l'ensemble des combinaisons de substituants possibles sur les aryles proximaux incluant les noyaux 2-hydroxyphényle, 2-méthoxyphényle et 2-pyridyle. La modulation du maximum d'absorption dans le rouge a pu être faite entre 598 et 619 nm. De même, la présence de groupements méthoxyle ou hydroxyle augmente l'absorption dans le violet (~410 nm) tel que démontré par modélisation. La caractérisation électrochimique a montré que les dérivés tétradentates étaient en général moins stables aux processus redox que leur contre-parti bidentate.

La deuxième famille comporte dix dérivés BODIPY fusionnés de façon asymétrique en position [*b*]. L'aryle proximal a été modifié de façon systématique afin de mieux comprendre l'impact des substituents riches en électron et de la fusion de cycles aromatiques. De plus, ces dérivés ont été mis en relation avec une vaste série de composés analogues. Les résultats empiriques ont montré que les propriétés optoélectroniques de la plateforme sont régies par le degré de communication électronique entre l'aryle proximal, le pyrrole sur lequel il est attaché et le noyau

indolique adjacent à ce dernier. Les maximums d'absorption dans le rouge sont modulables entre 547 et 628 nm et la fluorescence des composés se situe dans le proche-infrarouge. L'un des composé s'est révélé souhaitable pour une utilisation en photovoltaïque ainsi qu'à titre de sonde à pH.

La troisième famille comporte cinq complexes neutres de Ru^{II} basés sur des polypyridines et portant un ligand azadipyrrométhène cyclométalé. Les composés ont montré une forte absorption de photons dans la région de 600 à 800 nm (rouge à proche-infrarouge) et qui a pu être étendue au-delà de 1100 nm dans le cas des dérivés portant un ligand terpyridine. L'analyse des propriétés optoélectroniques de façon empirique et théorique a montré un impact significatif de la cyclométalation et ouvert la voie pour leur étude en tant que photosensibilisateurs en OPV et en DSSC. La capacité d'un des complexes à photo-injecter un électron dans la bande de conduction du semi-conducteur TiO_2 a été démontré en collaboration avec le groupe du Pr Gerald J. Meyer à University of North Carolina at Chapel Hill, premier pas vers une utilisation dans les cellules solaires à pigments photosensibles. La stabilité des complexes en solution s'est toutefois avérée problématique et des pistes de solutions sont suggérées basées sur les connaissances acquises dans le cadre de cette thèse.

Mots-clés : Dipyrrométhène; Azadipyrrométhène; BODIPY; Aza-BODIPY; Proche-infrarouge; Conversion d'énergie solaire; Photovoltaïque; Cellule solaire organique; Cellule solaire à pigments photosensibles; Sonde à pH; Chimie de coordination; Bore; Ruthénium; Cuivre; Rhénium; Complexes neutres de Ru^{II}; Cyclométalation; Électrochimie; Photophysique; Structures rayons X; Modélisation moléculaire.

Abstract

This research project carried out in industrial collaboration with Saint-Jean Photochemicals Inc. / PCAS Canada aims at the development and characterization of dipyrromethene derivatives for photovoltaic applications. The quest for harvesting near-infrared photons was the central focus and various structural modifications were explored to improve the power conversion efficiency of organic and dye-sensitized solar cells (OPV and DSSC, respectively). Three families of chromophores which embedded a dipyrromethene motif were synthesized and characterized through spectroscopy, electrochemistry, X-ray diffraction and computationnal modelization in order to establish their structure-properties relationship.

The first family includes six azadipyrromethenes with potential for tetradentate coordination on metallic centers. The development of a new asymmetric synthetic route together with the classical symmetric one allowed access to all possible combinations of derivatives including 2-hydroxyphenyl, 2-methoxyphenyl and 2-pyridyl substituents in the proximal position of the dipyrromethene. Modulation of the absorption maxima in the red ranged between 598 and 619 nm. Also, having methoxy or hydroxy substituents provided an increase of the violet absorption (~410 nm) as established by modelization. Electrochemical characterization showed that the tetradentate azadipyrromethenes were generally less stable towards redox processes as compared to their bidentate counter-parts.

The second family includes ten asymmetric benzo[*b*]-fused BODIPYs where the proximal aryl was systematically modified in order to assess the impact of electron-rich substituents and fused aromatic cycles. The derivatives were further compared to a wide series of related BODIPYs. Empirical results showed the optoelectronic properties are dictated by the extend of electronic communication between the proximal aryl, the pyrrol to which it is attached and the adjacent indolic moiety. Absorption maxima in the red were modulated between 547 nm and 628 nm and the fluorescence was in the near-

infrared. One compound proved to be a potential candidate for photovoltaic and pH probe applications.

The third family includes five neutral Ru^{II} polypyridine complexes bearing a cyclometalated azadipyrromethene ligand. The compounds exhibit strong light absorption in the 600 – 800 nm range (red to near-infrared) that tails beyond 1100 nm in the terpyridine-based adducts. Analysis of the optoelectronic properties showed a significant impact of this novel cyclometalation strategy for dipyrromethene derivatives and paved the way for further incorporation of the resulting complexes as photosensitizers in OPV and DSSC. In collaboration with the group of Pr Gerald J. Meyer at the University of North Carolina at Chapel Hill, the capacity of one compound to photo-inject its electron into the conduction band of the TiO_2 semiconductor was established, a first step towards their use in dye-sensitized solar cells. The structural instability in solution of the complexes hindered their full potential for photovoltaic applications and suggestions to improve them are proposed based on the knowledge acquired in the course of this thesis.

Keywords : Dipyrromethene; Azadipyrromethene; BODIPY; Aza-BODIPY; Near-infrared; Solar energy conversion; Photovoltaic; Organic photovoltaic (OPV); Dye-Sensitized Solar Cells (DSSC); pH probe; Coordination chemistry; Bore; Ruthenium; Copper; Rhenium; Neutral Ru^{II} complexes; Cyclometalation; Electrochemistry; Photophysic; X-ray structures; Computationnal modelization.

Table des Matières

Liste des Tableaux

Liste des Figures

Liste des Schémas

Liste des abréviations

A	Accepteur
Abs	Absorbance
ADPM	Azadipyrrométhène
Aza-BODIPY	Chélate BF_2^+ d'un azadipyrrométhène
BHJSC	*Bulk-heterojunctions Solar Cells*
BODIPY	Chélate BF_2^+ d'un dipyrrométhène
br	*Broad*
calcd	*Calculated*
C_{XX}	Dérivé fullerène contenant XX carbones
CV	Voltammétrie cyclique
Δ	Chaleur
δ	Déplacement chimique
d	Doublet
d	Orbitales *d*
D	Donneur
D - A	Donneur-Accepteur
DCM	Dichlorométhane
DFT	*Density-Functional Theory*
DPM	Dipyrrométhène
DPV	*Differential pulse voltammetry*
DSSC	*Dye-Sensitized Solar Cells*; Cellules solaires à pigments photosensibles
E	Énergie
e^-	électron

E_d	Différence d'énergie entre les LUMO du D et de l'A
E_g	Séparation de bandes (*Band-Gap Energy*)
eq	Équivalents
ESI	*Electronic supporting informations*
ETA	*Extremely Thin Absorber*
eT	*Energy transfer*
fac	Facial
FF	*Fill Factor*
GmbH	Société à responsabilité limitée allemande
h+	Trou positif
HOMO	*Highest Occupied Molecular Orbital*
HR-ESIMS	*High-Resolution Electro Spray Ionization Mass Spectrometry*
HRMS	*High-Resolution Mass Spectrometry*
hν	Irradiation lumineuse
IR	Infrarouge
ITO	*Indium Tin Oxyde*
J	Constante de couplage
J_{sc}	Densité de courant du petit circuit (*Short-circuit current density*)
J_{mp}	Courant de la cellule solaire
J_L	Courant généré par la lumière
J-V	Courbe courant-voltage
λ_{ab}	Longueur d'onde de l'absorption
λ_{max}	Longueur d'onde de l'absorption maximale
L	Ligands
LC	Chromatographie liquide (*Liquid chromatography*)

L_D	Distance de diffusion de l'exciton
LX	Ligand bidentate de type neutre (L) et anionique (X)
LUMO	*Lowest Unoccupied Molecular Orbital*
M	Métal
MSD	Détecteur par spectroscopie de masse (*Mass spectroscopy detector*)
m/*z*	Masse sur charge
n	Semi-conducteur de type négatif
n	Normal / linéaire
η	Efficacité de conversion solaire (*power-conversion efficiency*; PCE)
NA	Non disponible (*Non-available*)
NIR	Proche infrarouge (*Near-Infrared*)
NMR	Résonance magnétique nucléaire
OAc	Acétate
OPV	*Organic Photovoltaic Devices*
Ox	Oxydation
p	Semi-conducteur de type positif
p	para-
PCBM	[6,6]-phenyl-C61-butyric acid methyl ester
PCE	*Power Conversion Efficiency*
PEDOT:PSS	Poly(3,4-ethylene-dioxythiophene):poly(styrenesulfonate)
PHJSC	*Planar-Heterojunctions Solar Cells*
P_{in}	Puissance à l'entrée
P_{out}	Puissance à la sortie
ppm	Parties par million
PSII	Photosystème II

q	Quadruplet
Red	Réduction
RMN	Résonance magnétique nucléaire
rpm	Révolutions par minute
r.t.	Température ambiante (*Room temperature*)
s	Singulet ou seconde
SCE	Électrode au calomel saturée de KCl
t	Triplet
TBAP	Tetrabutylammonium hexafluorophosphate
THF	Tétrahydrofurane
TOF	Temps de vol (*Time of flight*)
TW	Térawatt
UV	Ultraviolet
vis	Visible
V_B	Gain en voltage généré à l'intérieur de la cellule solaire
V_{OC}	Voltage du circuit ouvert (*Open-circuit voltage*)
V_{MP}	Voltage de la cellule solaire
$V_{built\text{-}in}$	Built-in Potential

À Anne-Catherine Bédard,
You are my everything

« Science is not only a disciple of reason but,
also, one of romance and passion. »
- Stephen Hawking (1942 –)

« Most people say that it is the intellect which makes a great scientist.
They are wrong : it is character. »
- Albert Einstein (1879 – 1955)

Remerciements

Tout d'abord, je souhaite sincèrement remercier les organismes subventionnaires suivants d'avoir rendu possible la réalisation de mes travaux de Ph.D. industriel avec la compagnie Saint-Jean Photochimie Inc. (SJPC) / PCAS Canada :

- Fonds québécois de la recherche sur la nature et les technologies (FQRNT)
- Conseil de recherches en sciences naturelles et génie (CRSNG)
- Mitacs
- Hydro-Québec
- Université de Montréal (Bourses FESP – Chimie)

Mes remerciements vont aussi au Pr Garry S. Hanan pour m'avoir accueilli dans son groupe de recherche et avoir cru dès le début de cette aventure à la possibilité d'une collaboration fructueuse avec un partenaire industriel comme SJPC. Sans son appui et sa grande flexibilité, il apparaît clair à mes yeux que d'intéressantes découvertes scientifiques ainsi qu'un encadrement hors du commun et enrichissant n'auraient pu s'offrir à moi.

Je souhaite également remercier du plus profond de mon cœur toute l'équipe de chez SJPC de m'avoir supporté et conseillé dans les diverses phases de recherche de mon doctorat. Plus particulièrement, je souhaite exprimer toute ma gratitude à mon directeur de recherche, le Dr Denis Désilets, pour la confiance indéfectible dont il a fait preuve à mon égard ainsi que son support constant face aux différents obstacles qui se sont présentés en cours de route. Il a aussi toute mon admiration pour le courage dont il

a fait preuve suite à la maladie qui l'a accablé au cours des deux dernières années. Il est à mes yeux le meilleur patron, mentor et professeur dont j'aurais pu rêver. Le support quotidien de Francis Bélanger durant ma M.Sc. ainsi que la première année de mon Ph.D. a contribué à faire de moi un meilleur chimiste de synthèse et à mieux saisir le monde de la recherche industrielle. Je me dois également de faire une mention toute spéciale à cinq collègues et amis qui m'ont aidé d'une multitude de façons au fil des années : Khalil Feghali, Sylvain Boucher, Ian Marcotte, Vincent Lemieux et Simon H. Drouin. Un autre collègue des premiers jours chez SJPC, maintenant converti au monde de la gestion, est devenu un ami proche en la personne de Martin Giguère. Finalement, cette belle expérience industrielle n'aurait pu être rendue possible sans le support de membres clés de l'organisation. Le Dr Philippe Hugelé, Directeur Général, a fait preuve d'une grande ouverture d'esprit et de souplesse face aux contraintes particulières d'un stagiaire en co-direction. De même, Mme Caroline Renaud, Directrice des Ressources Humaines, a démontré à de multiples reprises à quel point elle a à cœur le développement des jeunes professionnels. Merci à vous tous pour la belle atmosphère de camaraderie qui fait de SJPC un endroit si extraordinaire où œuvrer!

Je voudrais aussi souligner l'aide précieuse des membres du groupe Hanan que j'ai eu la chance de côtoyer et qui m'ont aidé dans mon exploration de la recherche académique. Plus particulièrement : Mihaela Cibian, le Dr Daniel Chartrand, Baptiste Laramée-Milette, la Dr Elodie Rousset, Thomas Auvray, Mathieu Leblanc, la Dr Marie-Pierre Santoni, le Dr Amlan K. Pal, la Dr Janaina G. Ferrera ainsi que le Pr Samik Nag.

De plus, j'ai eu le plaisir de superviser Andrew O'Connor dans le cadre de deux stages. Sa rencontre fût un réel plaisir et un enrichissement personnel à plusieurs égards.

L'aide de Marie-Christine Tang, Karine Venne et Alexandra Furtos du service de spectroscopie de masse ainsi que de Cédric Malveau, Antoine Hamel et Sylvie Bilodeau de celui de RMN a aussi été vivement appréciée.

À titre plus personnel, je tiens à remercier mon père, Gilles Bessette, pour tous les efforts et sacrifices qu'il a fait pour me permettre d'être la personne épanouie que je suis aujourd'hui. Notre vision de la vie est souvent diamétralement opposé, mais je sais au fond de moi qu'il a toujours voulu mon bonheur, et ce, même dans les moments plus éprouvants. Ma grand-maman Jacqueline Roy a aussi été une source d'inspiration depuis mon plus jeune âge. Elle m'a enseigné à observer et apprécier l'équilibre qui prévaut dans la Nature, tant du point de vue environnemental qu'humain. J'ai aussi l'immense privilège d'avoir été mentoré depuis mes études post-secondaires par une famille d'exception : Geneviève & Louis Béland, Élisabeth, Marianne et Laurent. Je manque de mots pour décrire tout le respect, la reconnaissance et l'amour que j'éprouve pour chancun d'entre vous.

Un immense merci à ma femme Anne-Catherine Bédard qui partage mes plus grandes aspirations et qui me donne foi à un avenir rempli de bonheur. Son support au cours de ce Ph.D. a été au-delà de mes attentes et je lui serais toujours reconnaissant de sa patience d'ange à mon égard. J'ai déjà hâte à la suite de notre aventure familiale, qui nous mènera d'abord à Boston et puis de par le monde! Taimetaime ma belle Chérie!

Finalement, notre fidèle compagne Vic est sans doute l'épagneule française la plus connaissante de l'Histoire de la Chimie. Elle a survécu à la rédaction de deux thèses de Ph.D. dans la même année, et ce, toujours avec la même joie de vivre qui la caractérise !

Chapitre 1 : Introduction[†]

1.1 – La quête des photons dans le proche-infrarouge

La lumière constitue la source ultime d'énergie et d'information accessible aux organismes vivants sur Terre.[1] La capacité à utiliser cette source afin de contrôler et sonder divers processus tant physiques que biologiques est donc au cœur de l'activité scientifique. Les photons du proche-infrarouge (*near-infrared; NIR*) constituent une cible particulièrement de choix pour les scientifiques du 21^{e} siècle. Situés dans la région du spectre électromagnétique comprise entre 700 et 2000 nm,[2] ils offrent des avantages indéniables pour des applications tant en science des matériaux que de la vie.

À la base, environ 50% de toute l'intensité lumineuse du Soleil qui nous parvient se trouve dans l'infrarouge.[2] Il n'est donc pas surprenant de constater que les bactéries, algues et plantes aient évoluées pour permettre au photosystème II (PSII) d'absorber un maximum de photons entre 550 et 800 nm (Figure 1.1), à la limite du rouge et au début du NIR.[3] Sans doute parmi les plus belles enzymes que la Nature ait concoctée, le PSII est un hétérodimère (D1 et D2) auto-assemblé et capable de se regénérer qui permet le photo-récoltage de l'énergie solaire et son utilisation subséquente dans la séparation de l'eau en H_2 et O_2 (Figure 1.2). L'antenne est composée de chromophores organiques (***β*-carotène**) et organométalliques (**chlorophylle *a***) attachés de façon covalente à une

---

[†] Certains segments de l'introduction font l'objet d'une inspiration libre d'éléments récemment publiés en français dans mon mémoire de M.Sc. (*Développement de nouveaux matériaux organométalliques pour des applications dans le domaine de la conversion d'énergie solaire*; **2012**) et en anglais dans une revue de la littérature : A. Bessette and G. S. Hanan, *Chemical Society Reviews*, **2014**, 43, 3342 – 3405.

structure de protéines contenant des transporteurs d'électrons (phéophytines et plastoquinones) ainsi que d'autres co-facteurs nécessaires à son bon fonctionnement.[4] Cette structure est capable de s'adapter lors de la photo-excitation des chromophores pour maximiser l'efficacité des transferts énergétiques et électroniques vers le centre de réaction métallique à base de Mn_4Ca qui catalyse la conversion de deux molécules d'eau en O_2 et $4H^+$.[5] Encore plus impressionnant, le PSII semble avoir atteint un stade de quasi-perfection évolutive, étant peu altéré entre sa version dans les cyanobactéries procaryotes et celles retrouvées dans les algues et plantes eukaryotes.[6] La compréhension des processus impliqués dans la photosynthèse naturelle continue d'être une source de recherche intensive et d'inspiration pour le design de systèmes artificiels où la fonction de photo-récoltage sera répliquée de façon simplifiée.[5]

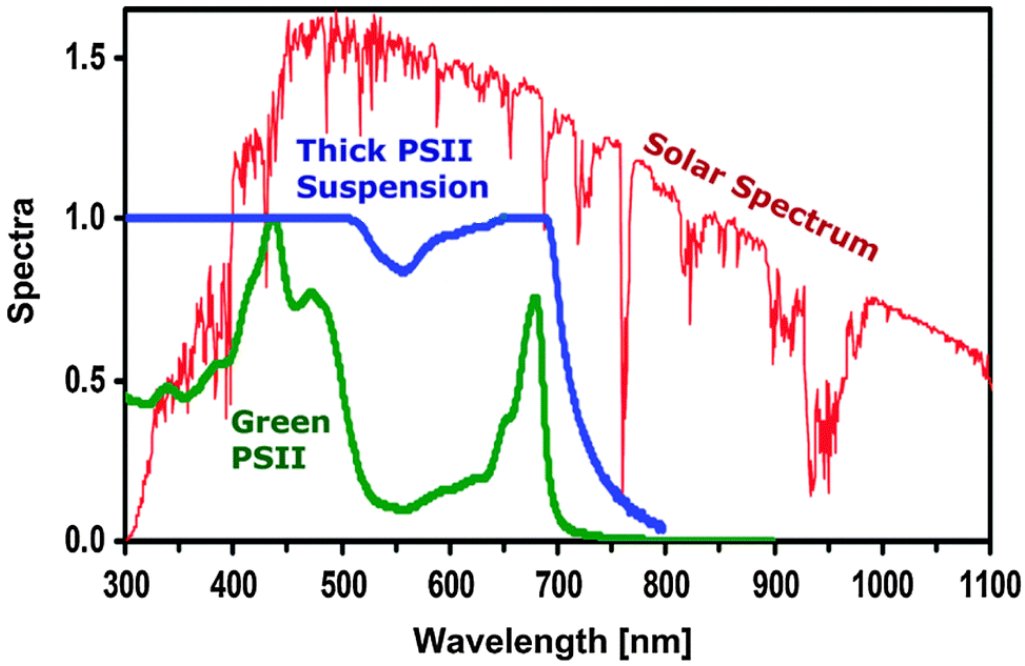

Figure 1.1 – Spectre solaire et absorption du PSII des plantes.[3]

(Reprinted with permission from *ref 3*. © 2009 American Chemical Society)

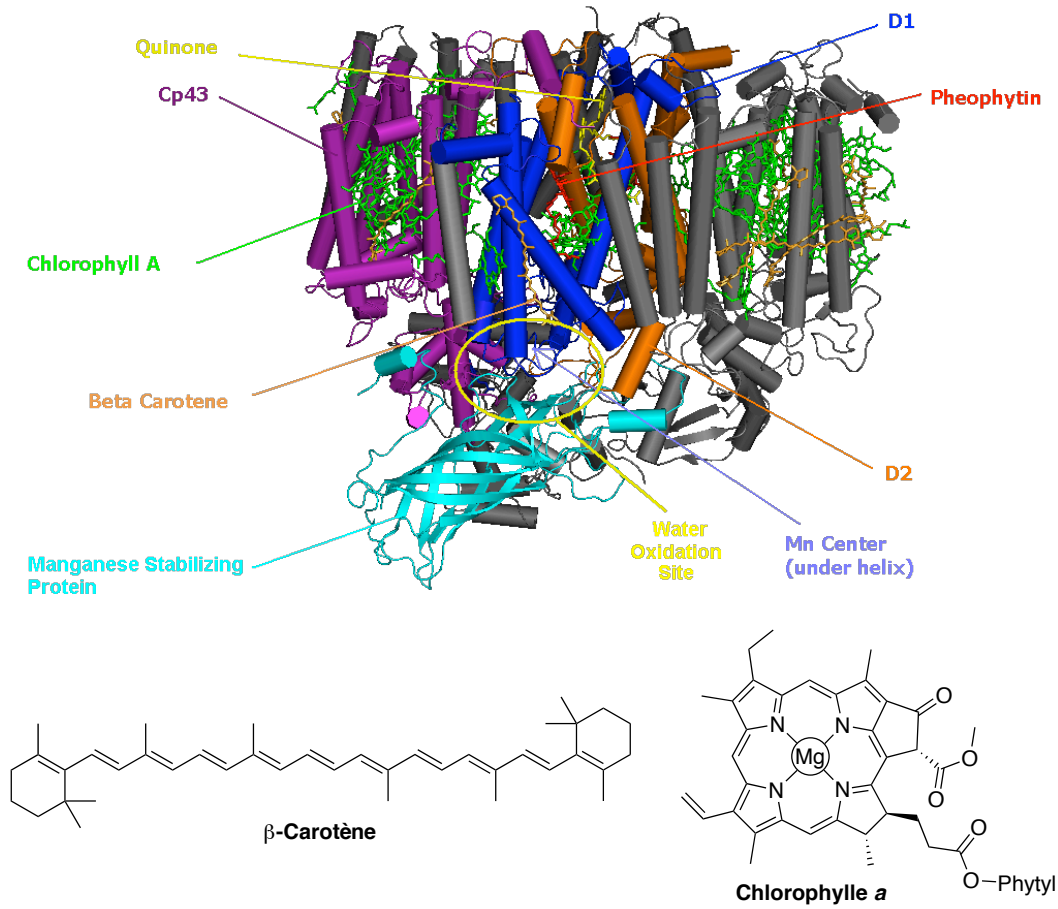

Figure 1.2 – Structures du PSII et des chromophores ***β*-carotène** et **chlorophyl *a***.[7,8] (Reprinted with permission from *ref 8*. © 2005 Nature Publishing Group.)

Du point de vue des matériaux, l'absorption des photons dans le NIR de façon directe ou *via* la conversion ascendante de photons (*photon upconversion*) permet notamment d'améliorer le rendement des dispositifs photovoltaïques en récoltant une plus grande portion du flux solaire atteignant la Terre.[9,10] La conversion ascendante des photons du proche-infrarouge est aussi utilisée en science des matériaux pour l'enregistrement haute-capacité de données, l'intégration dans des dispositifs d'affichage, la détection chimique, la photocatalyse et même pour empêcher la contre-façon.[10,11]

Du point de vue biomédical, la capacité de travailler avec les photons de base énergie du NIR permet de détecter efficacement le signal lumineux à travers la peau. Cette dernière absorbe à plus haute énergie dans le spectre visible et génère une auto-fluorescence due aux biomolécules s'y trouvant.[12] L'utilisation du NIR permet aussi de limiter les photo-dommages infligés aux tissus biologiques étudiés. Le développement de sondes fluorescentes dans le NIR a ainsi permis de monitorer la production, la localisation et le transport de biomolécules d'intérêt, et ce, directement dans leur environnement et de façon non-invasive. Elles permettent aussi la détection, le suivi de l'évolution et le traitement des maladies *in vivo*, tout en fournissant des indications sur l'efficacité des médicaments.[12-16]

Tributaire d'une expertise synthétique principalement acquise dans le domaine des colorants pour le textile lors de la révolution industrielle et dans les arts graphiques au 20^{e} siècle, les chimistes d'aujourd'hui ont entrepris une quête de l'utilisation des photons situés dans le proche-infrarouge en se basant sur la modulation des propriétés optoélectroniques de chromophores et fluorophores dévelopés naguère.[17] De nombreuses stratégies pour y parvenir existent et une série d'entre elles ont été explorées dans le cadre de cette thèse. Notamment, les propriétés de dérivés dipyrrométhène ont été ajustées par l'extension des systèmes électroniques π-conjugués, l'emploi de groupements fonctionnels à richesse électronique variable, la génération d'un effet donneur-accepteur (*Push-Pull*; D – A), la coordination de divers métaux de transition ainsi que l'ajustement du mode de coordination des ligands. Ces stratégies seront mises en contexte dans les sections à venir de l'introduction et discutées en détails dans les chapitres subséquents. L'application potentielle dans le domaine du photovoltaïque des

composés obtenus a été le fil conducteur de ces travaux. La section suivante permettra de mieux comprendre l'évolution des enjeux qui est survenu durant le cours de mes études doctorales ainsi que les exigences spécifiques s'y rattachant.

1.2 – Le domaine du photovoltaïque

1.2.1 – Contexte général

L'effet photovoltaïque consiste à la génération d'un courant électrique à l'intérieur d'une cellule lorsqu'un matériau semi-conducteur est irradié par un faisceau lumineux. Lors de l'absorption des photons par le matériau semi-conducteur, des électrons de la bande de valence du semi-conducteur sont promus vers sa bande de conduction. Les paires électron-trou obtenus peuvent alors génèrer une tension électrique à la jonction de deux matériaux dans le circuit et ainsi accomplir un travail électrique utile.[18] Les physiciens français Antoine Becquerel et son fils Alexandre-Edmond furent les premiers à observer cet effet et à le présenter devant l'Académie des sciences en 1839, sans toutefois bien en comprendre la provenance.[19] Il s'agit en fait d'une manifestation spécifique d'un autre effet plus général, celui photoélectrique, qui a été étudié par le physicien allemand Heinrich Rudolf Hertz en 1887.[20] L'effet photoélectrique consiste de son côté en l'émission d'électrons par un matériau lorsqu'il est exposé à la lumière ou à un rayonnement électromagnétique de fréquence suffisamment élevée. L'expérience type de cet effet consiste à éclairer une plaque métallique qui émet des électrons en retour. En 1905, le physicien allemand Albert Einstein expliqua pour la première fois la loi de l'effet photovoltaïque en utilisant les concepts de photons et de quantum d'énergie nécessaires à la promotion des électrons de la bande de valence à celle de conduction. Cette découverte lui valut son prix Nobel de physique en 1921.[21]

Pour déterminer l'efficacité de conversion solaire (power-conversion efficiency; PCE; η) d'une cellule photovoltaïque, les courbes de Courant-Voltage (J-V) dans le noir et sous illumination solaire sont utilisées comme méthode de caractérisation directe. Les paramètres essentiels déterminant la performance de la cellule solaire sont représentés dans la Figure 1.3 (J_{SC} = short-circuit current density; FF = fill factor; V_{mp} et J_{mp} sont le voltage et le courant, respectivement, auquel le pouvoir à la sortie du dispositif atteint son maximum; J_L est le courant généré par la lumière).[22,23] Ainsi, l'équation de η est définie comme le ratio du pouvoir maximum à la sortie (P_{out}) sur celui à l'entrée (P_{in}).

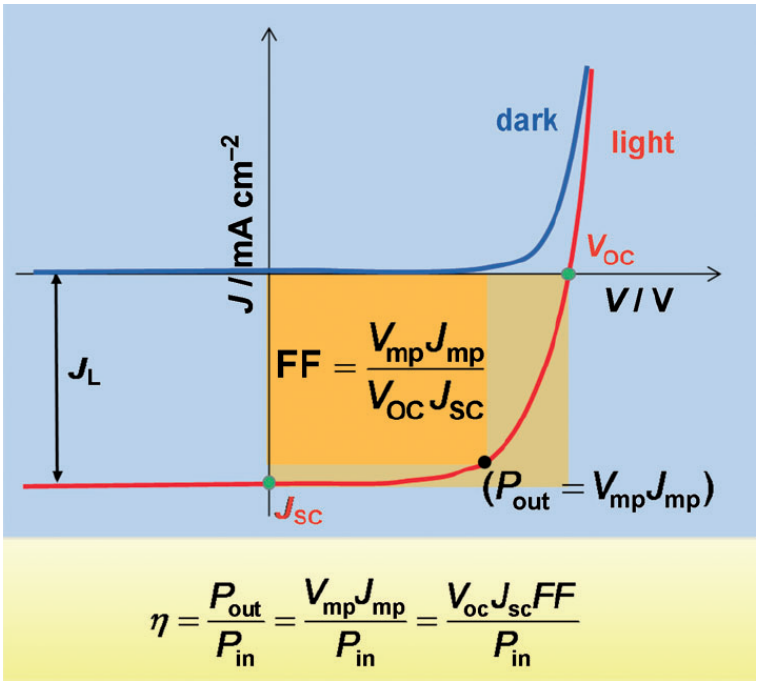

Figure 1.3 – Courbes de Courant-Voltage (J-V) caractérisant les cellules solaires.[22]

(Reprinted with permission from *ref 22.* © 2012 John Wiley and Sons)

Les dispositifs solaires de première et deuxième générations basées sur une jonction simple dans l'état solide présentent des rendements intéressants de conversion solaire. En effet, les dispositifs de première génération à base de Si cristallin oscillent autour de 25% de conversion, alors que ceux de deuxième génération à base de couche mince de GaAs atteignent 28,8 %.[24] La deuxième génération s'avère très près de la limite thermodynamique théorique d'efficacité de 31 % pour les dispositifs à jonction simple. Cette limite, connu sous le nom de Shockley-Queisser, peut être surpassée en utilisant des systèmes multijonctions pour viser des efficacités avoisinant les 95 % du cycle de Carnot.[25] Les panneaux solaires multijonctions, faisant parti de la troisième génération, frôlent un PCE de 40 % en combinant plusieurs semi-conducteurs ayant des énergies de séparation des bandes (*energy band-gap*; E_g) complémentaires pour l'absorption simultanée de différentes portions du spectre solaire. Des rendements de conversion dépassant les 45 % peuvent aussi être obtenus en ajoutant des concentrateurs de lumière à l'architecture des panneaux solaires multijonctions.[24,26] Cependant, de nombreux désavantages sont associés avec les différents types de cellules photovoltaïque décrits jusqu'à présent. Leur processus de fabrication est hautement énergivore et requiert des installations spécialisées afin d'obtenir des matériaux semi-conducteurs d'une très grande pureté.[27] Leur incapacité à récolter efficacement l'énergie solaire lors des journées nuageuses ou lorsque la lumière a une incidence indirecte sont d'autres problèmes non-négligeables pour leur intégration dans des réseaux de production électrique à grand déploiement.[28] L'ajout de concentrateurs optiques et de dispositifs pour traquer le mouvement du soleil en cours de journée fait aussi gonfler la facture tant à l'achat que pour l'entretient subséquent.[28,29] L'impact environnemental à long terme des cellules contenant des métaux lourds tels l'arsenic et le cadmium

constitue un autre élément critique à considérer.[30] Finalement, la rigidité inhérente de ces panneaux solaires les limite à des applications statiques, par exemple sur les toitures de maison, dans des fermes solaire ou encore sur les satellites et autres stations spatiales.[27]

Afin de réduire les coûts associés à la production de l'énergie photovoltaïque et pour le rendre compétitif face aux énergies de source fossile ou nucléaire, le Département de l'Énergie (DOE) des États-Unis a lancé en 2010 le programme « SunShot ».[31] Doté d'un budget oscillant entre 270 et 290 millions de dollars US par année, ce programme finance à la fois la recherche fondamentale et le déploiement des technologies à grande échelle afin de réduire de 75% le coût par kWh d'ici 2020. Le programme américain est actuellement parmi les plus vigoureux à l'échelle mondiale pour cette source d'énergie et devrait leur permettre de rattraper les capacités de production photovoltaïque de l'Allemagne, de l'Espagne et du Japon qui la financent aussi activement.[32]

Face aux changements climatiques et à une volonté politique de trouver des sources d'énergie renouvelables, le domaine du photovoltaïque évolue rapidement et une riche variété de technologies compétitionnent pour émerger. Parmi les principales nouvelles générations de cellules, mentionnons : les cellules photoélectrochimiques basées sur des jonctions nanocristallines ou des réseaux interpénétrants (*interpenetrating networks*); les cellules tandems pour le clivage d'eau par la lumière visible; les cellules à base de points quantiques (*Quantum Dots*); les cellules hétérojonctions solides sensibilisées par des colorants (*Dye-Sensitized Solar Cells*; DSSC) et celles de type absorbant extrêmement mince (ETA); les jonctions molles ainsi que les cellules solaires

organiques (*Organic Photovoltaic*; OPV). La recherche dans le domaine est passablement active et certaines de ces nouvelles technologies se retrouvent déjà à l'échelle commerciale.

Au début de mes études doctorales en 2012, les deux types de cellules photovoltaïques « émergentes » qui occupaient l'avant-scène étaient le OPV et la DSSC (Figure 1.4). Depuis, un nouveau type de cellule dont l'absorbant est basé sur des structures cristallines pérovskites hybrides organique/inorganique a fait son apparation et vole la vedette avec une efficacité de conversion qui a franchi la barre des 20 % en 2015.[33-35] Initialement basée sur une architecture similaire à la DSSC, la cellule de pérovskite évolue rapidement et les nouvelles versions sont significativement altérées. Cette technologie est vouée à un bel avenir, notamment avec une première commercialisation envisageable dès 2017.[36] Cependant, les chercheurs devront en comprendre les propriétées électroniques fondamentales et surmonter les problèmes d'instabilité des modules. En fait, la dégradation hâtive au contact de l'humidité et plus généralement la solubilité dans l'eau de ces matériaux à base d'halure de plomb ou d'étain soulève une inquiétude environnementale significative. De leur côté, les cellules de type OPV et DSSC ont une efficacité de conversion maximale de l'ordre de 11,0 % et 11,9 %, respectivement, ce qui est plus faible que les principales technologies photovoltaïques exploitées à grande échelle.[24] En contre partie, elles offrent plusieurs avantages les rendant particulièrement attrayantes face à la compétition :

1. Flexibilité de la cellule permettant de l'incorporer virtuellement n'importe où.
2. Intégrable dans le design architectural ou les textiles.

3. Faible poids du module.
4. Efficacité accrue par temps nuageux et sous lumière diffuse.
5. Faible coût de production et retour sur l'énergie mis dans la fabrication < 0,5 ans (*vs.* ~2,5 ans pour Si cristallin).[37-40]
6. Faible quantité de produits hasardeux pour l'environnement.
7. Vaste modulation des propriétés optoélectroniques accessible via le design rationnel des chromophores.

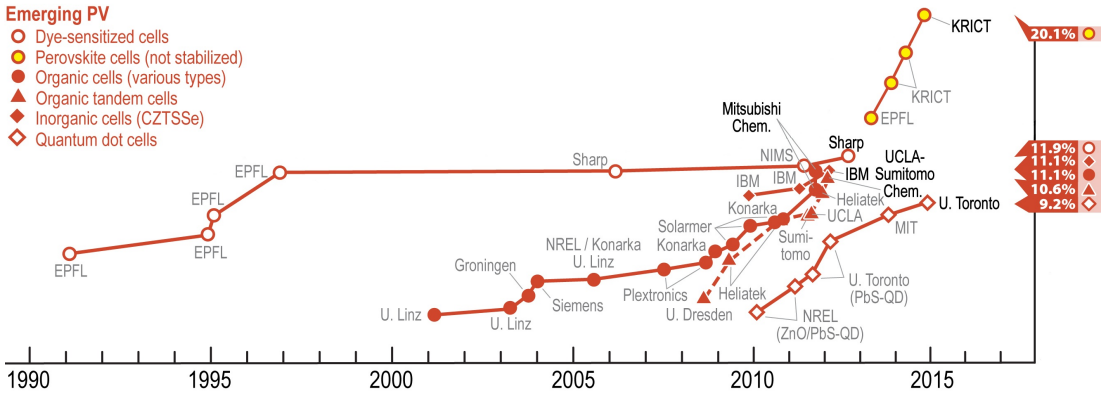

Figure 1.4 – Croissance de l'efficacité de conversion solaire (PCE) des cellules photovoltaïque émergentes au fil des années.[41]

Grâce à l'expertise combinée du groupe de recherche du Pr Garry S. Hanan dans le domaine du photo-récoltage d'énergie et de la compagnie St-Jean Photochimie Inc. (SJPC; devenu PCAS Canada en 2015) dans les domaines de l'électronique imprimée et des colorants, nous avons donc entrepris de développer de nouveaux dérivés dipyrrométhène pour leur application en OPV et en DSSC.

1.2.2 – Principe de fonctionnement d'une cellule solaire organique (OPV)

Le schéma d'une cellule solaire organique hétérojonction typique est présenté à la Figure 1.5.[9] Cette cellule de 3ème génération consiste en deux semi-conducteurs, l'un de type « n » et l'autre de type « p », qui sont déposés entre une cathode d'aluminium et une anode transparente d'oxyde d'indium-étain (ITO). Le contact entre les deux semi-conducteurs peut se faire de façon planaire, lorsqu'ils sont déposés sur le substrat par couches succesives, ou bien sous la forme d'un réseau interpénétrant (*bulk heterojunction solar cells*; BHJSC) dont la surface de contact interfaciale est grandement augmentée et favorise ainsi la séparation des charges. De plus, une couche de PEDOT:PSS est intercalée entre l'anode et la couche d'hétérojonctions pour augmenter la qualité de la surface de contact et des transferts de charge qui se déroulent à cette interface. Le matériau de type « n » est généralement constitué de dérivés de fullerène car ces derniers offrent une LUMO base en énergie qui agit comme un accepteur (A) d'électron (e^-) et transporte efficacement la charge négative vers la cathode. Cependant, un sujet d'actualité dans le domaine est le remplacement de ces dérivés fullerènes par des polymères, des petites molécules organiques ou encore des complexes organométalliques afin d'obtenir une meilleur modulation des propriétés optoélectroniques, i.e. la capacité d'absorber des photons supplémentaires grâce à l'accepteur et un meilleur agencement des niveaux électroniques avec le donneur (D).[42-48] De son côté, la couche photoactive de type « p » est celle qui agit comme donneur d'électron, et donc comme un transporteur de trous positifs (h^+). Cette couche peut être basée sur de petites molécules dans le cas des hétérojonctions planes ou bien sur des polymères formant des nanodomaines avec les dérivés de fullerène dans le cas des

BHJSC. Il s'agit de la composante principale à avoir été optimisée depuis l'avènement du OPV et celle sur laquelle les efforts ont été concentrés dans le cadre de cette thèse. À titre de référence, notons que deux polymères donneurs ont été particulièrement étudiés en BHJSC, soit le poly(3-hexylthiophène) (**P3HT**) ainsi que le **PCDTBT** (Figure 1.5).[49] Le **P3HT** présente une absorption allant jusqu'à environ 600 nm et offre une PCE avoisinant les 3% combiné au **PCBM**. De son côté le **PCDTBT** développé par le groupe du Pr Mario Leclerc absorbe jusqu'à environ 650 nm et atteint un maximum d'efficacité de 7,5% lorsque mélangé avec le PC70BM comme accepteur.[50] Bien que plusieurs facteurs affectent la performance globale d'une cellule solaire, notons tout de même que le PCE est plus que doublé entre ces deux polymères en étendant le profil d'absorption de 50 nm vers le rouge.

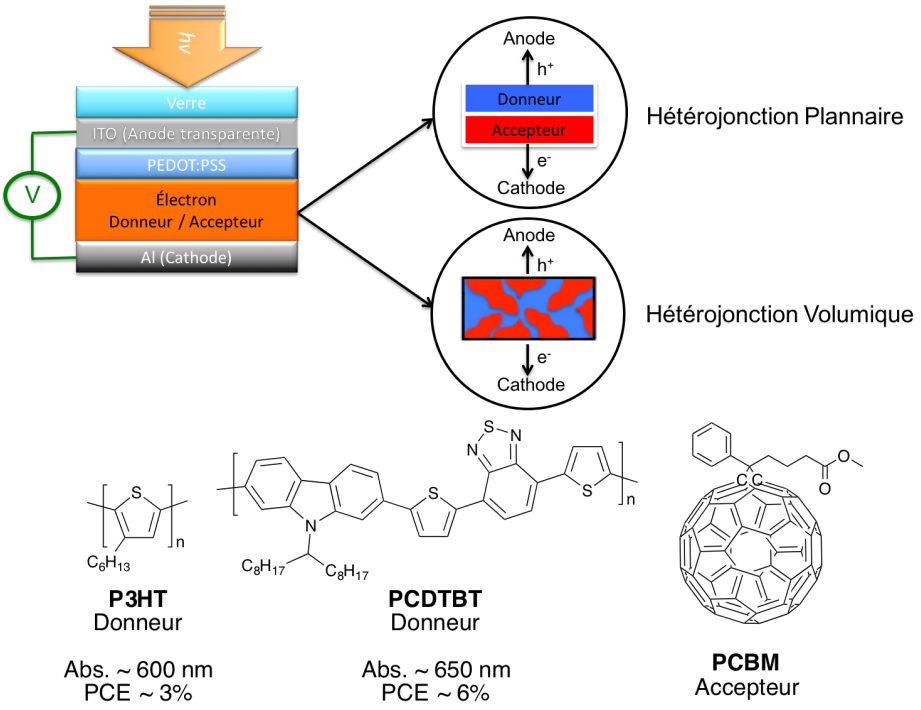

Figure 1.5 – Représentation schématique d'une cellule solaire organique de type hétérojonction plane et BHJSC ainsi que des matériaux de référence.[9]
(Adapted from Ref. 9 with permission from The Royal Society of Chemistry)

Le mécanisme de fonctionnement des cellules solaires de type D – A hétérojonctions survient en quatre temps.[51] Premièrement, il y a une photoexcitation dans le matériel donneur qui mène à la création de la paire électron-trou, aussi appelé exciton. Dans un deuxième temps, l'exciton diffuse vers l'interface de l'hétérojonction D – A. Si la distance à parcourir est supérieure à la distance de diffusion maximale (max L_D), il y aura une recombinaison de la paire électron-trou annihilant tout autre processus subséquents. De là vient l'importance d'avoir une bonne surface de contact entre le donneur et l'accepteur (*vide supra*). Toutefois, la formation d'un réseau nanoscopique D – A interpénétrant de qualité en BHJSC est très difficile à contrôler et encore plus à prévoir *a priori* de l'assemblage de la cellule. La morphologie fait donc parti des aspects de recherche clés à optimiser afin d'augmenter la PCE.[52] La troisième étape du mécanisme consiste en la dissociation de l'exciton à l'interface D – A. En fait, cette étape est le passage de l'électron de la LUMO du donneur vers celle de l'accepteur. De son côté, le trou réintègre la HOMO du donneur. Finalement, la quatrième étape consiste au transport des charges générées à l'étape précédente vers leur électrode respective. Dans l'ensemble, ce mécanisme mène à la génération par la lumière d'un courant électrique pouvant être converti en travail électrique utile.

La Figure 1.6 présente les énergies relatives des orbitales HOMO et LUMO pour le donneur et l'accepteur ainsi que les principaux paramètres y étant associés.[9] L'énergie de séparation des bandes (*energy band-gap*; E_g) correspond à l'énergie lumineuse requise pour exciter un électron de la HOMO vers la LUMO du donneur. Le principal défi lors de l'optimisation du donneur réside donc dans la rédution du E_g afin de pouvoir utiliser les photons (*hv*) de plus faible énergie du NIR.[9,53] Les principales stratégies pour

y arriver seront décrites à la section 1.4.2. En outre, il est aussi important de favoriser des matériaux donneurs possédant une bonne mobilité des trous générés lors de la photoexcitation afin que la cellule sépare les charges efficacement.[54] Le gain en voltage généré à l'intérieur de la cellule (V_B) est linéairement dépendant du voltage du circuit ouvert (open-circuit voltage; V_{OC}). La différence d'énergie entre la LUMO du donneur et celle de l'accepteur (E_d) est la force motrice pour le transfert d'électron et doit être d'environ 0,3 – 0,4 eV pour assurer une bonne dissociation de l'exciton en une paire de charges à l'interface D-A.[55] Dans le cas de l'accepteur PCBM, le niveau de la LUMO est estimé à -4,3 eV par rapport au vide et le donneur optimal doit donc posséder une LUMO autour de -4,0 eV.[56] Il est aussi possible d'ajouter un additif dans les dispositifs de type BHJSC qui consiste en un chromophore agissant comme photosensibilisateur additionnel capable de donné des électrons.[57] Cet additif tend à augmenter à la fois le rendement de conversion énergétique de la cellule solaire et la panchromaticité de l'absorption solaire vers la région du NIR. Il s'agit d'un concept relativement nouveau dans l'évolution du OPV et certaines des molécules discutées dans cette thèse ont le potentiel d'être utilisé à titre d'additif.

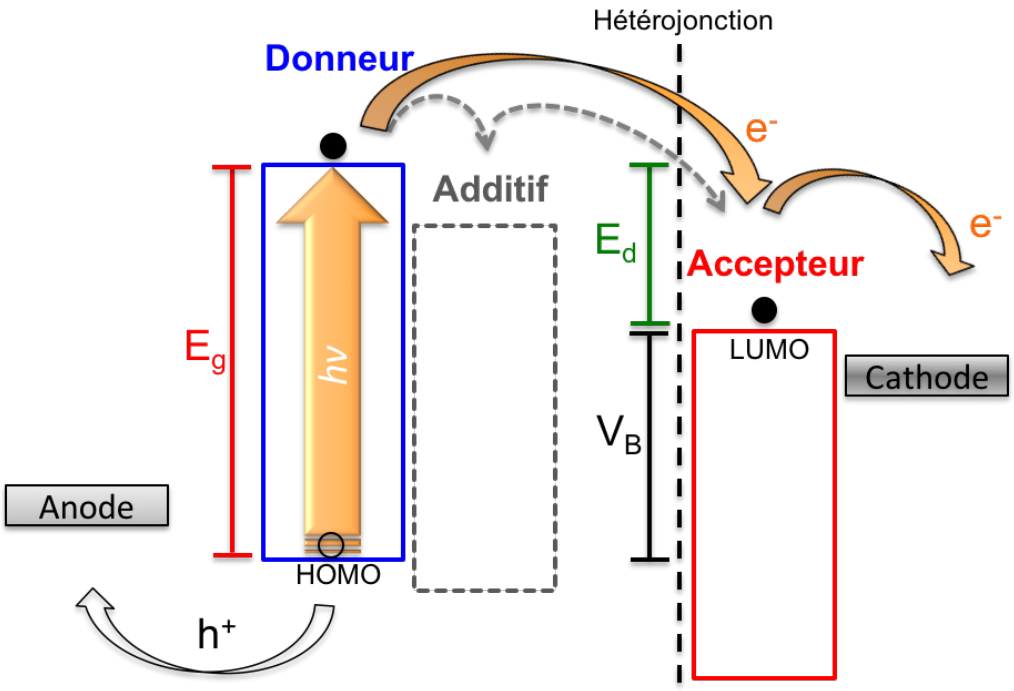

Figure 1.6 – Principe de fonctionnement d'une cellule solaire organique (OPV).[9]

(Adapted from Ref. 9 with permission from The Royal Society of Chemistry)

1.2.3 – Principe de fonctionnement d'une cellule solaire à pigments photosensibles (DSSC)

Les cellules solaires à pigments photosensibles font partie de la catégorie des hétérojonctions de troisième génération (Figure 1.7). Il s'agit de cellules électrochimiques dont la photoanode est typiquement basée sur une couche transparente de dioxyde de titane (TiO_2) mésoporique, le semi-conducteur sur lequel sont greffés les pigments photosensibles, et qui est en contact direct avec un electrolyte (liquide, gel ou solide) permettant le transfert des charges avec la contre-électrode (*e.g.* Pt).[58] La couche mésoporique de TiO_2 a une épaisseur d'environ 10 micromètres et une porosité de l'ordre de 50 – 60%. Elle est en fait le résultat de la fusion de multiples nanoparticules de 10 – 30 nm de diamètre, ce qui offre une surface de contact optimale pour le transfert des charges à l'interface avec l'électrolyte (hétérojonction). La couche mésoporique est déposée sur un substrat transparent (verre ou platisque flexible) enduit d'une couche d'oxyde d'étain dopée au fluore (FTO) agissant comme transporteur de charge. Les pigments servant à photoinjecter un électron dans la bande de conduction du semi-conducteur (*vide infra*) sont généralement des complexes de ruthénium ou des dérivés de porphyrines, mais peuvent aussi être de nature purement organique comme dans le cas des BODIPYs.[59-63] Comparativement au donneur en OPV, ils possèdent la particularité d'un groupement chimique permettant l'interaction avec la surface du TiO_2. Le groupement acide carboxylique (-COOH) est un standard dans le domaine pour l'adsorption, mais d'autres groupements tels le sulfonate ($-SO_3^-$), les silanes [$-SiX_3$ ou $-Si(OX)_3$], le phosphonate [$-PO(OH)_2$], l'hydroxamate (-CO-NH-OH), la pyridine et la 1,2-tropolone ($C_7H_6O_2$; 2-hydroxy-2,4,6-cycloheptatrién-1-one) sont aussi utilisés.[64-66] L'important demeure toutefois d'avoir un groupement d'attache suffisament fort pour

éviter que le chromophore se désorbe et entraine une perte d'efficacité de la cellule due à un effet de filtre, à la dégradation des pigments ou la diminution de la performance de la contre-électrode.[58] L'électrolyte de choix a historiquement été le couple redox de I^- / I_3^- ,[67,68] mais d'autres médiums font l'objet de recherche active afin d'obtenir un meilleur agencement des niveaux énergétiques avec les milliers de photosensibilisateurs investigués depuis la découverte séminale de O'Regan et Grätzel en 1991.[69,70] Finalement, l'optimisation des performances passe aussi par le remplacement de la contre-électrode de platine ou encore de la photoanode de TiO_2 par d'autres semi-conducteurs tel l'oxyde de zinc (ZnO).[71]

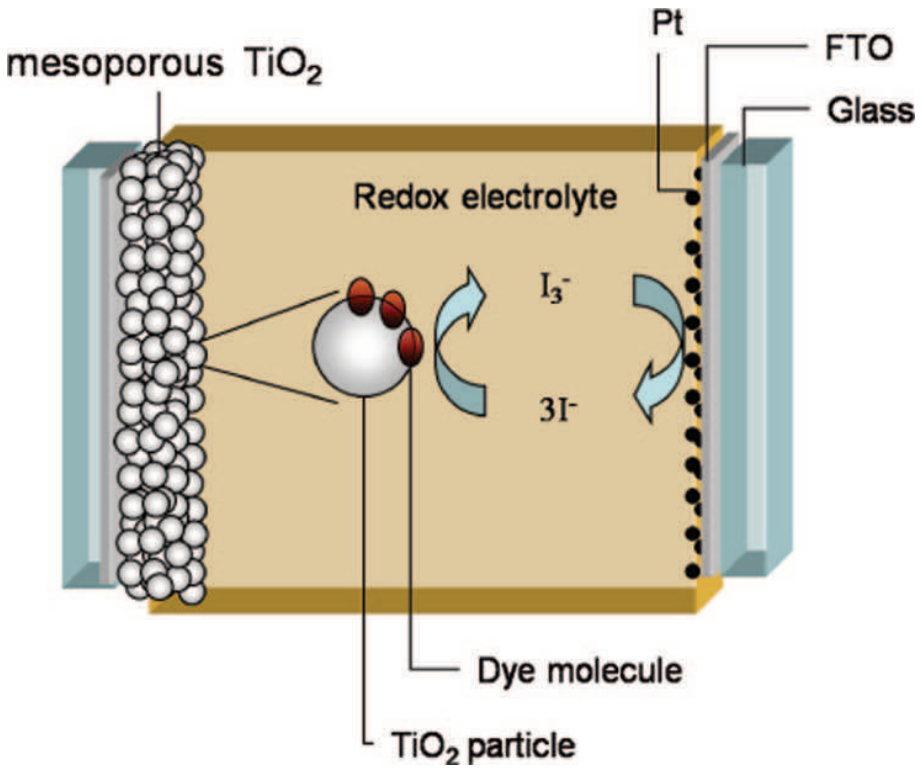

Figure 1.7 – Représentation schématique d'une cellule solaire à pigments photosensibles.[58]

(Reprinted with permission from *ref 58*. © 2010 American Chemical Society)

Les principaux transferts électroniques impliqués en DSSC sont schématisés et numérotés dans la Figure 1.8.[58] Initialement, un photon promeut un électron du photosensibilisateur de son état de repos (*ground-state* ; S) vers son état excité (S*) (numéroté 0). À ce stade, deux transferts électroniques distincts peuvent survenir : la désactivation de l'état excité vers l'état de repos par divers processus intramoléculaires (1), ce qui est contre-productif, ou l'injection de l'électron dans la bande de conduction du TiO_2 (2) amorçant le cycle catalytique de production de courant. Ce deuxième processus a marqué l'avènement de la DSSC lorsque le groupe de recherche du Pr Michael Grätzel a montré que divers complexes de ruthéniums à base de ligands polypyridines et thiocyanates ont la capacité de photo-injecter un électron de façon ultra-rapide (de l'ordre du femtoseconde ; $x10^{-15}$ seconde) dans la bande de conduction du semi-conducteur auquel ils sont greffés. Pour que la cellule fonctionne de façon efficace, le processus de photo-injection doit être favorisé par rapport à la désactivation de l'état excité. Le photosensibilisateur doit donc posséder un temps de vie dans l'état excité (*excited state lifetime*) suffisament long pour permettre la photo-injection. Pour les principaux complexes de ruthénium utilisés en DSSC, ce temps de vie est de l'ordre de 20 – 60 ns ($x10^{-9}$ s).[72] Des études de cinétique réalisées par Durrant *et al.* ont cependant montrées que la photo-injection peut se faire beaucoup plus lentement dans une cellule DSSC complète, demi-vie de l'ordre de 150 ps ($x10^{-12}$ s), ce qui met le processus en compétion cinétique avec la désactivation.[73] Une fois le photosensibilisateur oxydé, le donneur du médiateur rédox (I^-) le réduit (3) dans un temps de l'ordre de la microseconde ($x10^{-6}$ s). En parralèle, l'électron qui a été photo-injecté dans la bande de conduction du TiO_2 migre à travers le film mésoporeux (4) dans une échelle temporelle du miliseconde ($x10^{-3}$ s) en sautant d'une nanoparticule à l'autre. Par contre, deux

processus recombinatifs peuvent empêcher l'électron de circuler adéquatement dans le circuit, soit celui avec le chromophore oxidé (5) ou avec l'accepteur I_3^- du couple redox (6). Dans le cas de la recombinaison avec le chromophore, l'échelle de temps varie sur plusieurs ordres de grandeur allant du microseconde à la miliseconde en fonction de la concentration des électrons dans le semi-conducteur et donc implicitement de l'intensité lumineuse qui frappe la cellule. De son côté, la recombinaison avec l'accepteur est considéré comme le temps de vie de l'électron et s'avère très long dans les système à base du couple redox I^- / I_3^- ($x10^{-3}$ s). Cet aspect explique la prédominance de ce médiateur comparativement à tous les autres qui ont été investigués. Finalement, le dernier transfert électronique permettant de compléter le cycle dans le circuit électrique est la réduction de l'électron accepteur (I_3^-) à la contre-électrode. Ainsi, un parcours idéal implique que l'électron photo-injecté dans le semi-conducteur à partir du chromophore irradié parcours la couche mésoporeuse, circule dans le circuit externe et revient pour réduire le médiateur rédox ayant lui-même regénéré le photosensibilisateur oxydé.

Parmi les principaux photosensibilisateurs utilisés, les complexes de Ru^{II} **N3** et **N719** basés sur des bpy ainsi le **Black Dye** basé sur un motif tpy sont devenus des standards dans l'industrie en raison de leur PCE dépassant 10% (Figure 1.9).[30] Leur décomposition à long terme due à la photo-éjection des ligands thiocyanate a cependant incité l'évaluation d'alternatives. L'actuel détenteur du record de photoconversion est le composé **SM315** basé sur une porphyrine de zinc neutre.[74] Il intègre un effet *Push-Pull* entre le noyau aryle amine riche en électron et celui benzothiadiazole qui les accepte. Ces concepts ont inspirés le design des chromophores ADPM présentés au Chapitre 4.

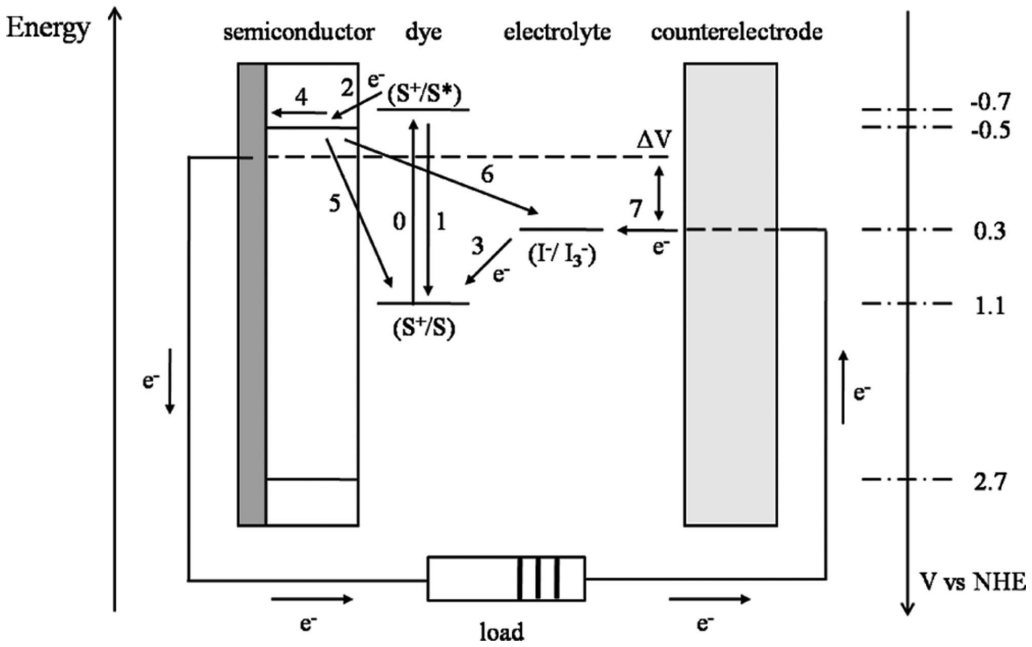

Figure 1.8 – Principe de fonctionnement d'une cellule solaire à pigments photosensibles.[58]

(Reprinted with permission from *ref 58*. © 2010 American Chemical Society)

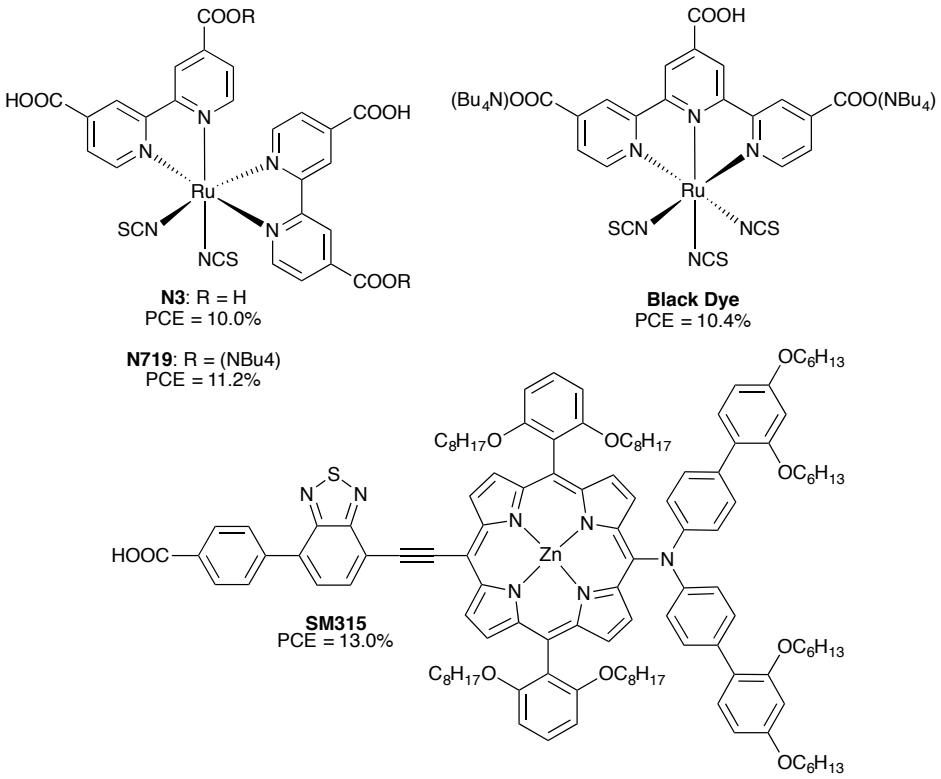

Figure 1.9 – Principaux photosensibilisateurs étudiés en DSSC avec un PCE > 10%.[30,75]

1.3 – Les dérivés dipyrrométhène

1.3.1 – Contexte général

La structure chimique des dipyrrométhènes (DPM) et des aza-dipyrrométhènes (ADPM) en fait de proches parents des porphyrinoïdes (Figure 1.10).[9] En effet, ces chromophores cyanine hautement absorbants représentent respectivement des demi-porphyrines et demi-phtalocyanines. Bien que les porphyrinoïdes constituent la famille de choix utilisée par la Nature, notamment dans le PSII et dans l'hémoglobine, ils demeurent un défi synthétique de taille pour les chimistes en raison de l'étape de macrocyclisation à faible rendement. Leur utilisation en chimie des matériaux est assurément très significative, mais le coût de production doit être tenu en compte pour la commercialisation des applications en découlant.[13,76,77] De plus, leur structure de tétrapyrrole macrocyclique hautement conjugué offre une faible solubilité ainsi qu'une flexibilité limitée en ce qui a trait à la coordination de métaux de transition (ligand tétradentate planaire de type dianionique; X_2L_2).[78]

En comparaison, les dérivés dipyrrométhène sont des ligands bidentate de type monoanionique (XL) pourvus de propriétés photophysique similiares au porphyrinoïdes. Le remplacement du carbone *meso* des DPM par l'azote dans les ADPM permet un déplacement bathochrome de l'absorption intéressant du point de vue du photo-récoltage d'énergie. Les BODIPYs et Aza-BODIPYs résultant de la coordination d'un cation BF_2 ont fait l'objet d'une attention particulière en raison de leur absorptivité modulable, leur fluorescence impressionnante et leur grande photostabilitée qui permet de les intégrer dans de nombreuses applications en sciences de la vie et en chimie des matériaux.[79-85]

Ces avantages sont le fruit de la rigidification du coeur dipyrrole par la présence du BF_2 et peuvent aussi être atteint par la coordination de centres métalliques. La versatilité synthétique de la plateforme DPM permet de moduler les propriétés optoélectroniques d'une multitude de façons, notamment avec des réactions spécifiquement associées aux différentes positions et à la modification de leur mode de coordination (*vide infra*).[9,81,86] La Figure 1.11 résume cette versatilité pour le coeur BODIPY, bien que la plupart de ces réactions soient aussi accesssibles avec les autres dérivés DPM. Le lecteur trouvera une discussion plus poussée de la multitude de possibilités qu'offre la plateforme dipyrrométhène au fil des pages de cette thèse ainsi que dans les références citées.

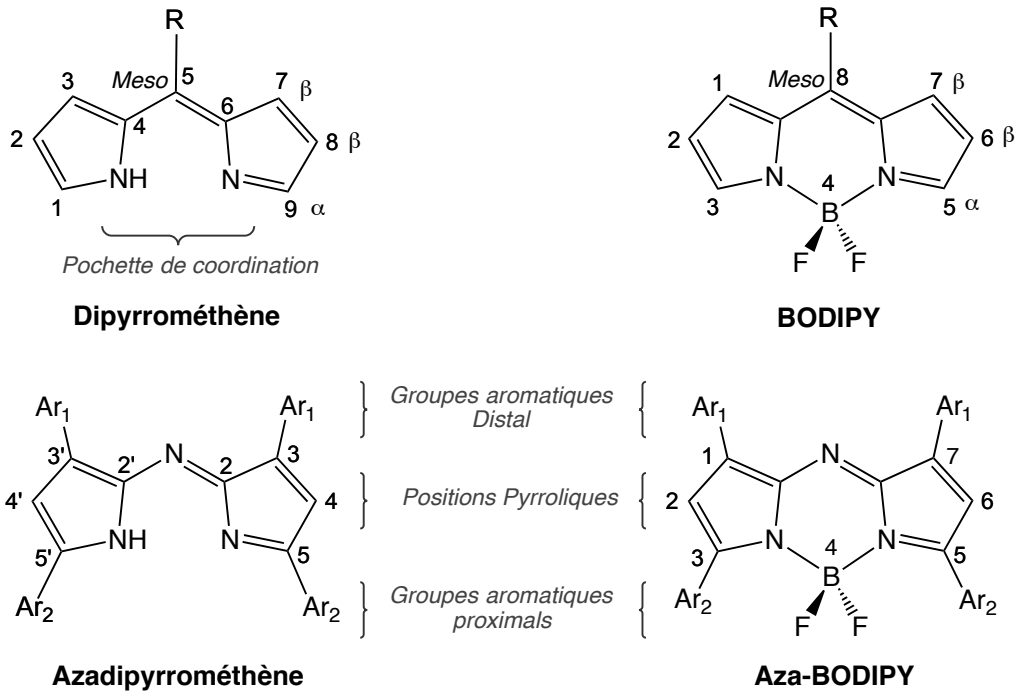

Figure 1.10 – Structure du cœur des dipyrrométhènes et des aza-dipyrrométhènes. (Adapted from Ref. 9 with permission from The Royal Society of Chemistry)

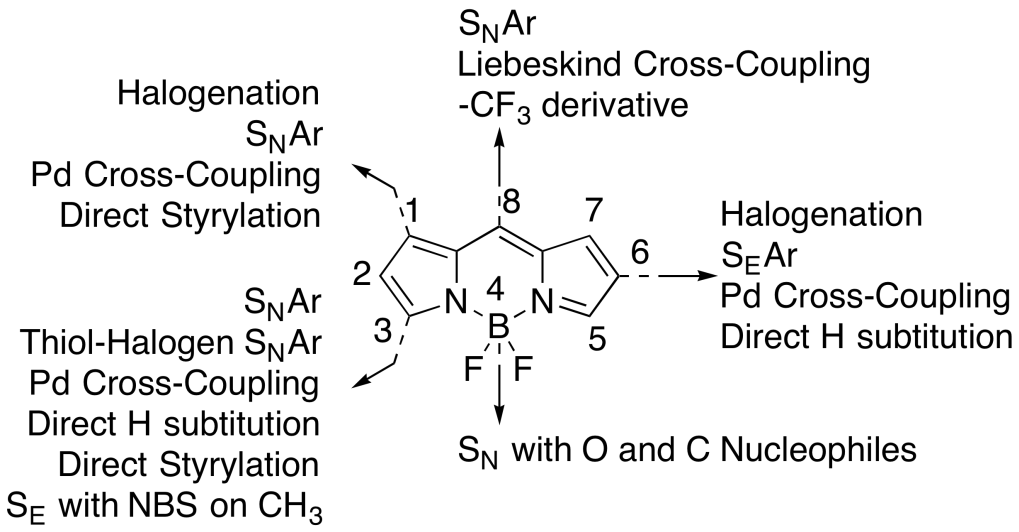

Figure 1.11 – Versatilité synthétique des BODIPYs.[9]

(Reproduced from Ref. 9 with permission from The Royal Society of Chemistry)

1.3.2 – Exemples pertinents d'utilisation en photo-récoltage d'énergie

L'intégration de dérivés dipyrrométhène pour diverses applications en photo-récoltage d'énergie est un sujet de recherche soutenu au cours des dernières années. Nous avons d'ailleurs publié une revue de la littérature en 2014 sur leur design, synthèse et propriétés photophysiques visant à stimuler leur utilisation en OPV.[9] D'autres articles ont fait de même pour la DSSC et les antennes moléculaires.[63,80,87,88] Loin de se vouloir exhaustive, la section qui suit contient un bref survol de certains systèmes d'intérêt conçus de façon rationnelle pour leur utilisation dans une application donnée. Elle exemplifie aussi la versatilité synthétique accessible qui a été discutée dans la section précédente.

Dans un contexte biomimétique du PSII des plantes, Pistolis *et al.* ont rapporté l'auto-assemblage d'une antenne moléculaire hexagonale discrète dont les coins sont constitués de six BODIPYs (vert) positionnés de façon perpendiculaire aux douze complexes de Pt^{II} (rose) formant les arêtes [représentation schématique 3D à la Figure 1.12 (i)].[89] Cet assemblage multi-chromophorique de type D – A est retenu ensemble par des espaceurs 4,4'-bpy agissant comme donneur. L'antenne a une absorption maximale à 513 nm et présente un processus émissif à 533 nm (Φ_F = 0,88; τ = 6,34 ns) qui n'est pas désactivé malgré la présence des centres métalliques. En fait, les auteurs ont pu démontrer que les BODIPYs y sont espacés et orientés de façon quasi-parfaite pour permettre leur communication via un mécanisme de Förster (FRET), i.e. transfert énergétique à travers l'espace entre les chromophores due à des interactions de résonance de leurs dipôles. Le système constitue donc un exemple éloquent de concentrateur solaire.

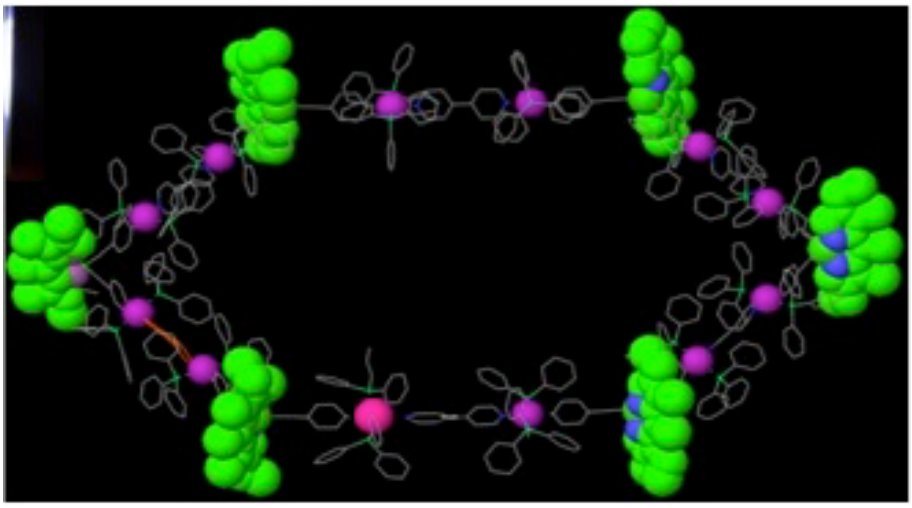

(i) [89]

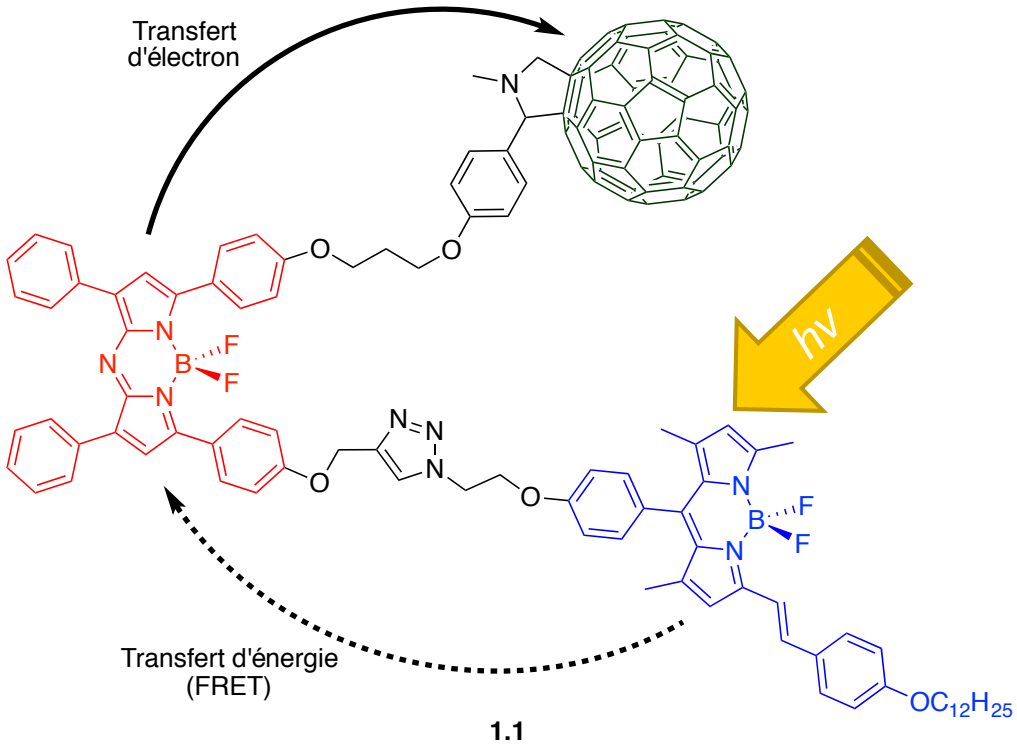

(ii) [90]

Figure 1.12 – Étude des transferts énergétiques dans des systèmes moléculaires basés sur (i) une antenne moléculaire hexagonale auto-assemblée BODIPYs – complexes de Pt^{II} et (ii) une polyade BODIPY – Aza-BODIPY – Fullerène.

(Reproduced from Ref. 89 with permission from The Royal Society of Chemistry)

Un second exemple d'antenne moléculaire est présenté à la Figure 1.12 (ii).[90] Un BODIPY à la conjuguaison électronique étendue par un styryl en proximal a été lié par chimie clic via sa position *meso* à l'un des phényles proximaux d'un Aza-BODIPY. L'ensemble moléculaire est complété par un dérivé fullerène attaché au second phényle proximal de l'Aza-BODIPY. La triade moléculaire **1.1** est électroniquement découplée en raison des espaceurs alkyl les unissant, ce qui permet d'observer sous irradiation lumineuse un transfert énergétique de type Förster du BODIPY vers l'Aza-BODIPY suivi d'un transfert électronique de ce dernier vers l'accepteur fullerène. Cet effet d'entonnoir moléculaire permet une mimique des événements se déroulant dans le PSII. Il constitue aussi une preuve de l'intérêt des dérivés dipyrrométhène en tant que matériaux donneurs en OPV, où les fullerènes sont utilisés comme accepteurs d'électrons.

L'idée d'une photosynthèse artificielle capable de séparer l'eau en ses constituants O_2 et H_2 est un objectif critique afin d'accéder à une économie libre des énergies fossiles.[91-93] Des exemples de feuilles artificielles ont d'ailleurs été rapportés et suscitent l'attention de la communauté scientifique, sans toutefois être en mesure d'offrir à la fois efficacité, robustesse et faible coût de production.[94,95] Le côté réductif du processus, la photo-production de d'hydrogène moléculaire, permet d'emmagasiner de l'énergie solaire sous forme chimique et de la réutiliser ultérieurement pour une combustion propre libérant l'eau comme seul produit. De façon analogue à la DSSC, le processus de réduction de l'eau en H_2 dans une cellule photochimique requiert un photosensibilisateur greffé aux nano-particules de TiO_2 qui soit capable de générer une paire électron-trou et de photo-injecter l'électron dans la bande de conduction du semi-

conducteur. Afin d'augmenter l'efficacité des chromophores à transfert de charge effectuant cette tâche, le groupe de recherche du Pr Richard Eisenberg a récemment ajouté un colorant organique BODIPY de façon covalente à une série de complexes de Pt^{II} diimine dithyolate.[96] D'entre tous, la dyade moléculaire **1.2** présentée à la Figure 1.13 a démontré une excellente capacité à photo-produire de l'H_2 durant une période d'irradiation prolongée (~ 40 000 cycles catalytiques relatif au photosensibilisateur en 12 jours). L'utilisation de dyades organique / inorganique a permis d'augmenter l'activité des systèmes étudiés sous la lumière verte (530 nm) comparativement aux composantes prises séparément, validant ainsi cette approche synthétique en photosynthèse artificielle.

Figure 1.13 – Dyade BODIPY – Pt^{II} diimine dithyolate incorporée dans un système catalytique pour la photo-production d'hydrogène moléculaire.[96]

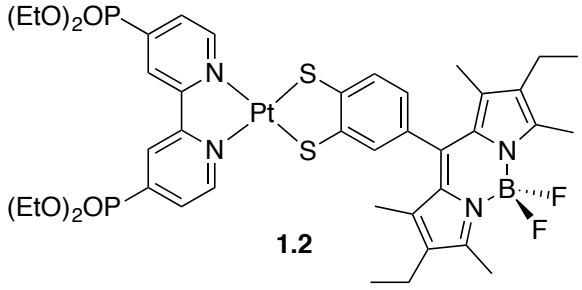

1.2

Grâce à la grande versatilité synthétique et à la modularité des propriétés optoélectroniques des dérivés dipyrrométhène, ces derniers ont été employés en OPV à la fois à titre de matériaux donneurs et accepteurs.[9] La Figure 1.14 présente l'intégration du motif DPM à l'intérieur de donneurs organiques et polymériques ainsi que dans un complexe organométallique utilisé en tant qu'accepteur non-fullerène. Le dérivé BODIPY **1.3** utilisé comme donneur par Ziessel *et al.* en 2012 constitue la petite molécule conjuguée avec la meilleure efficacité de conversion solaire en OPV rapportée à ce jour de la famille des dipyrrométhènes.[97] Un PCE de 4,7% est obtenu lorsque la molécule est assemblée en cellule de type BHJSC dans un ratio 1 : 0.5 BODIPY / PCBM. Son efficacité est grandement redevable à son absorption panchromatique qui atteint un maximum à 780 nm et s'étire passé 850 nm en film solide. Pour y parvenir, la conjuguaison a été étendue par condensation de Knovenagel entre un dérivé tétraméthyles BODIPY et un aldéhyde installé sur le fragment bis-thiophène correspondant. Le co-polymère **1.4** contenant une unité BODIPY conjuguée à un thiophène via des liaisons triples a été préparé par le groupe de Fréchet en 2010.[98] Les 2,0% d'efficacité de conversion constituaient à l'époque l'un des meilleurs résultats pour un matériel donneur basé sur un colorant, notamment due à un bon alignement de la LUMO avec celle du PCBM ainsi qu'une HOMO basse en énergie offrant un large V_{OC} de 0,8 V. Par contre, les auteurs notaient le besoin d'améliorer la morphologie des films obtenus en BHJSC et de poursuivre les ajustements structuraux afin de tirer le plein potentiel des polymères à base de BODIPYs. Le dérivé symétrique **1.5** fusionné aux positions [*a*] et portant des groupements hexyl-thiophène est un cas particulièrement intéressant dans la mesure où il est l'un des rare exemple de dérivé dipyrrométhène à avoir été utilisé en tant qu'additif. En ajoutant seulement 5% en poids de ce BODIPY à

une cellule BHJSC basé sur le **P3HT** comme donneur principal, le groupe de Kubo a été en mesure d'augmenter le PCE de 3,7% à 4,3%.[57] Cette efficacité acrue est le résultat des photons supplémentaires absorbés par l'additif dans la région du proche infrarouge, i.e. entre 700 et 800 nm. Finalement, la coordination de deux ligands azadipyrrométhène sur un centre métallique a permis au groupe de la Pr Sauvé de proposer de nouveaux accepteurs non-fullerène pour le OPV.[44,99-101] D'entre tous les dérivés explorés, le complexe homoleptique de Zn^{II} **1.6** s'est avéré le plus intéressant avec un PCE atteignant 4,1% lorsque combiné avec le **P3HT** comme donneur dans un ratio de 1 : 0,7 D / A.[44] Deux aspects clés pour l'utilisation de molécules en tant que semi-conducteur de type « n » sont une grande affinitée électronique ainsi qu'une faible énergie de réorganisation.[100] Les complexes homoleptiques à base d'ADPM possèdent ces deux propriétés, tout comme les dérivés fullerènes, en plus d'offir une absorption de photons accrue dans le rouge et le NIR qui peut contribuer à de meilleures performances photovoltaïques. L'une des limitations actuelle pour l'utilisation de ces dérivés ADPM en tant qu'accepteur « universel » réside toutefois dans le fait que la majorité des matériaux donneurs ont été optimisés avec les niveaux énergétiques du PCBM comme précepte de départ. Il est donc à souhaiter que d'autres donneurs seront développés dans un avenir proche avec les paramètres de cette nouvelle classe d'accepteurs.

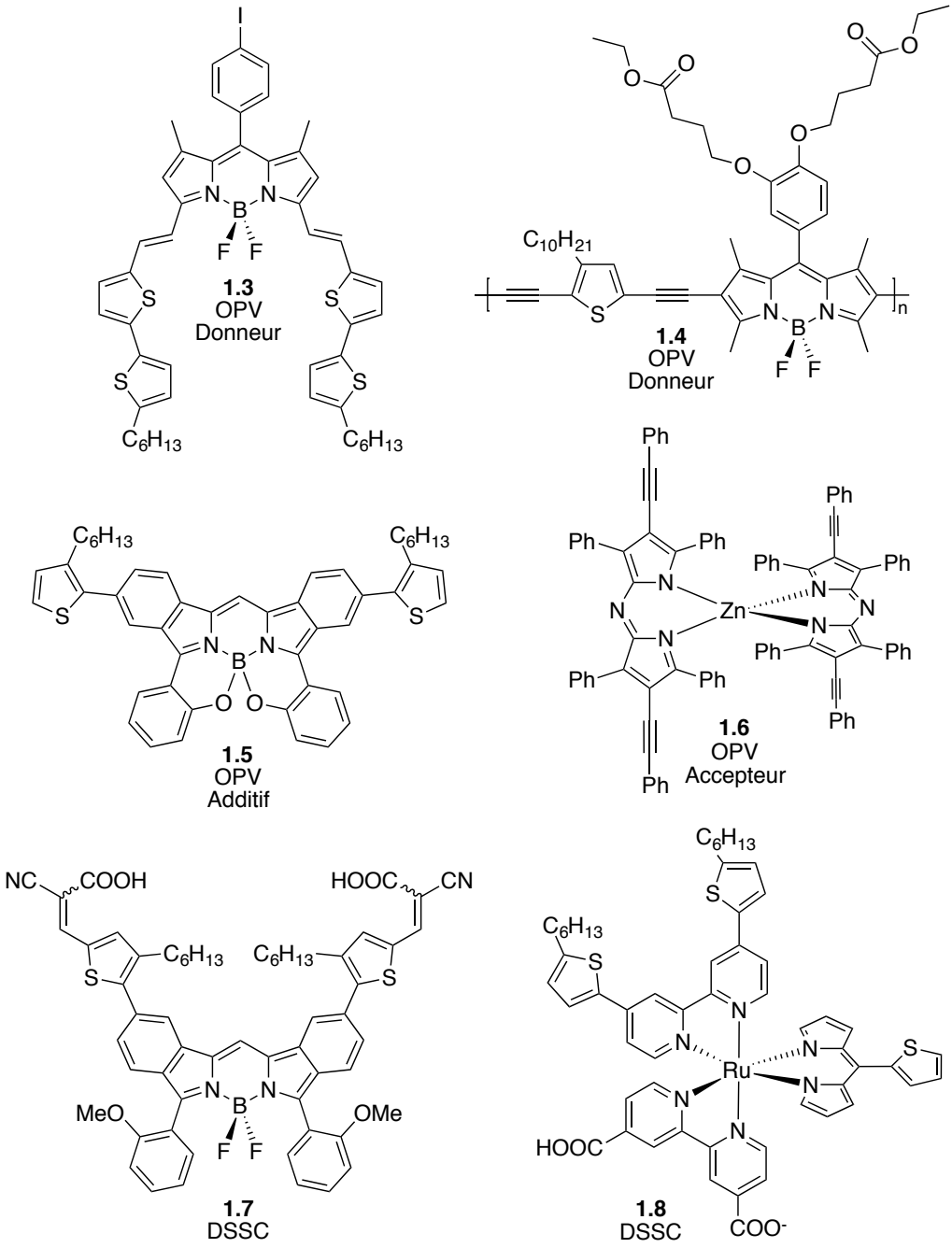

Figure 1.14 – Dérivés dipyrrométhène utilisés en OPV et DSSC.[44,57,97,98,102,103]

Finalement, deux exemples de dérivés DPM appliqués en DSSC sont aussi représentés à la Figure 1.14. Le BODIPY symétrique **1.7** est fusionné aux positions [*a*] et équipé de motifs hexyl-thiophènes qui sont substitués avec des groupements cyanovinyls électron-attracteurs servant aussi pour l'ancrage à la surface du TiO_2.[103] Ce chromophore hautement conjugué absorbe au maximum à 660 nm (ε = 1,09 x 10^5 M^{-1} cm^{-1}) et offre un PCE de 6,06%. Il s'agit de la plus haute valeur obtenue pour un dérivé BODIPY en DSSC et a été accompli sans la présence de groupements électron-donneurs puissants tels les tri-arylamines qui sont couramment employés dans le domaine afin de générer un effet D-A. Le complexe de Ru^{II} tri-hétéroleptique zwitterionique **1.8** est celui qui présente la plus haute efficacité de conversion en DSSC pour un complexe organométallique munit d'un ligand DPM. Son PCE de 3,4% a été obtenu en combinant les propriétés optoélectroniques intéressantes du DPM, i.e. bande d'absorption complémentaire à la MLCT des ruthenium polypyridines et haute absorptivité molaire, avec celles des deux ligands bipyridines jouant chacun un rôle spécifique. Un ligand 2,2'-bpy portant des hexyl-thiophènes permet de déstabiliser l'état excité pour favoriser la photo-injection alors que l'autre porte les groupements d'acide carboxylique pour l'ancrage du photosensibilisateur au semi-conducteur. Bien que les systèmes de Ru^{II} à base de DPM commencent à susciter de l'intérêt, ils demeurent pour le moment encore nettement en deçà des résultats de PCE obtenus avec les dérivés porphyrines ou encore avec les complexes de ruthénium portant les ligands isothiocyanate (-NCS) qu'ils espèrent remplacer.[102,104-108]

1.4 – Mise en contexte des travaux de Ph.D.

1.4.1 – Résultats photovoltaïque préliminaires et leur incidence sur l'orientation initiale de la recherche

Dans le cadre de mes études de M.Sc. en collaboration entre le Pr Hanan et la compagnie St-Jean-Photochimie Inc., nous avons étudié la relation structure-propriétés dans la série de dérivés ADPM **1.9** – **1.20** (Figure 1.15).[109] Bien que les dérivés basés sur le ligand tétra-phényles ADPM **1.9** avaient préalablement été rapportés, nous avons étendu la comparaison avec ceux basés sur le ligand électron-riche tétra-*p*-méthoxy-phényles ADPM **1.10** afin de mieux comprendre l'effet de la coordination de centres métaliques dans l'état d'oxydation II (cobalt, nickel, cuivre, zinc) ainsi que du B^{III} sur les propriétés optoélectroniques des complexes obtenus. Le but sous-jacent de cette recherche était aussi de cerner le potentiel des dérivés ADPM pour leur intégration en cellules solaires de type OPV.

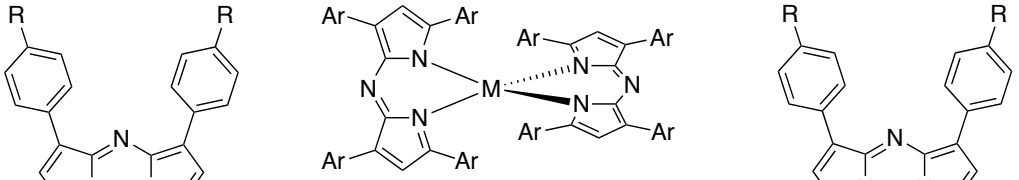

1.9 R = H
1.10 R = OMe

1.11 M = Co^{II}; Ar = Ph
1.12 M = Co^{II}; Ar = *p*-OMe-Ph
1.13 M = Ni^{II}; Ar = Ph
1.14 M = Ni^{II}; Ar = *p*-OMe-Ph
1.15 M = Cu^{II}; Ar = Ph
1.16 M = Cu^{II}; Ar = *p*-OMe-Ph
1.17 M = Zn^{II}; Ar = Ph
1.18 M = Zn^{II}; Ar = *p*-OMe-Ph

1.19 R = H
1.20 R = OMe

Figure 1.15 – Dérivés ADPM investigués dans le cadre de ma M.Sc.[109]

Les niveaux énergétiques des orbitales moléculaires frontières HOMO et LUMO tels qu'obtenus par électrochimie dans le dichlorométhane pour la série sont présentés à la Figure 1.16 ainsi que le niveau de la LUMO de l'accepteur PCBM à -4,3 eV (rouge). L'analyse de ces résultats a révélé que le ligand ADPM **1.10** et les complexes homoleptiques correspondants de Co^{II} (**1.12**), de Ni^{II} (**1.14**) et de Zn^{II} (**1.18**) offraient un niveau de la LUMO supérieur par ~ 0,3 eV ou plus à celui de la LUMO du PCBM. Ce premier élément suggérait donc que leur intégration en OPV à titre de matériel donneur pourrait être envisageable, particulièrement compte tenu des faibles E_g (1,60 – 1,68 eV).

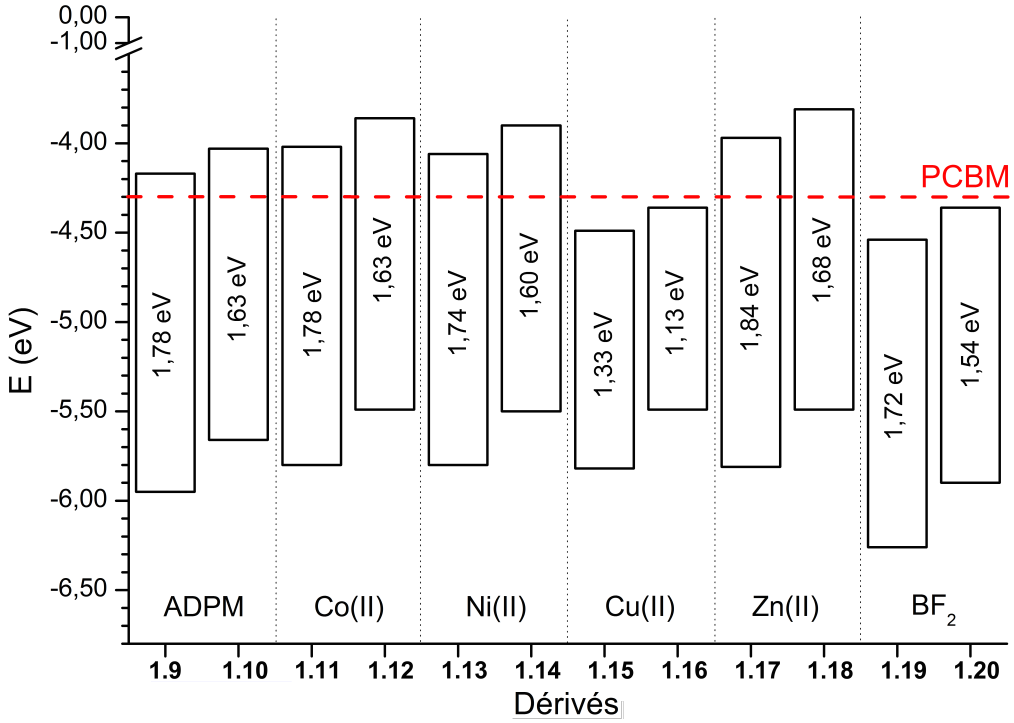

Figure 1.16 – Niveaux énergétiques des composés **1.9** – **1.20** obtenus par électrochimie.[109]

(Reprinted with permission from *ref 109*. © 2012 American Chemical Society)

Le deuxième élément clé à considérer avec les complexes homoleptiques obtenus était l'amplification et l'élargissement des bandes d'absorption tant dans le visible que vers le NIR comparativement à leur ligand ADPM correspondant. La Figure 1.17 présente un comparatif en solution dans le dichlorométhane entre l'ADPM **1.10**, son complexe homoleptique de Zn^{II} **1.18** et son dérivé Aza-BODIPY **1.20** qui illustre cette situation. Il est intéressant de noter que l'aborption du complexe de Zn^{II} s'étend jusqu'à 800 nm, soit 50 nm plus loin dans le proche-infrarouge que l'Aza-BODIPY.

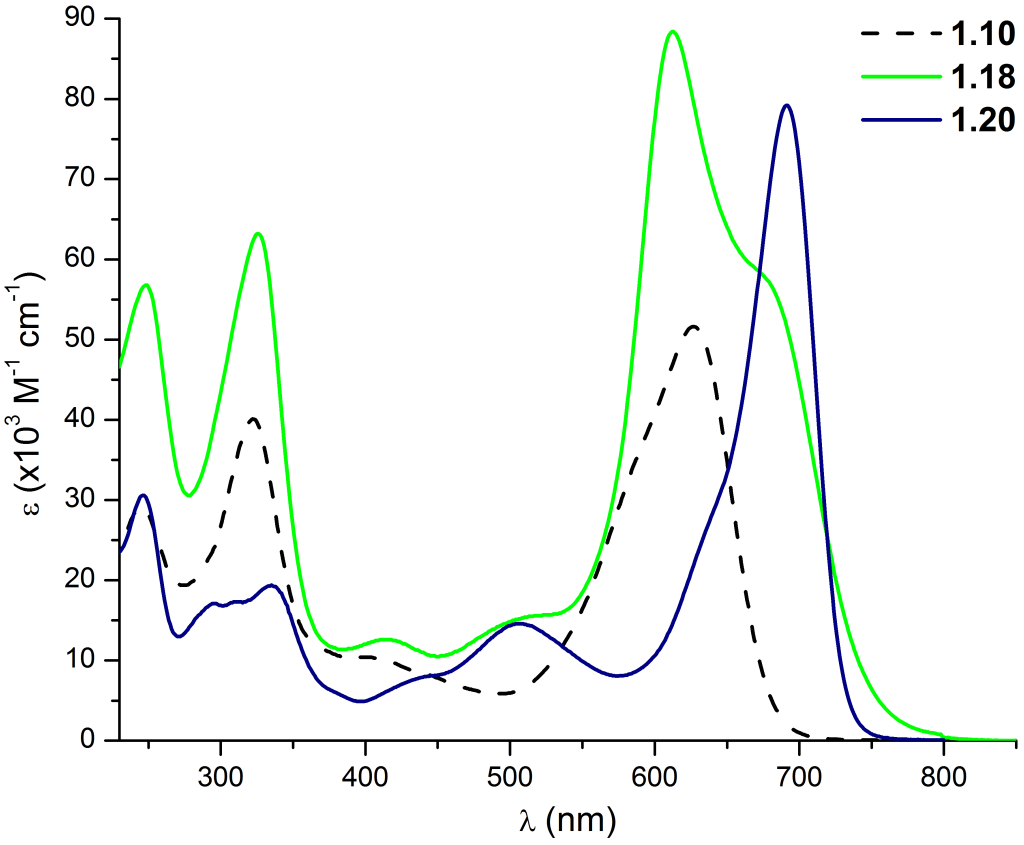

Figure 1.17 – Comparaison des propriétés optiques des dérivés ADPM **1.10**, **1.18** et **1.20**.[109]

Ces résultats très prometteurs nous ont incités à collaborer avec la Pr Geneviève Sauvé et son étudiant Chunlai Wang afin de déterminer le potentiel des composés **1.10**, **1.12**, **1.14** et **1.18** en tant qu'éléments photo-actifs dans des cellules solaires de type OPV (Table 1.I).[110] Dans un premier temps, ils ont testé les composés à titre de matériel donneur en combinaison avec le **PCBM** comme accepteur dans un ratio de 1 : 1. Leurs résultats ont montré que les quatres dérivés offraient un rendement de conversion inférieur à 1%, allant de 0,03 % pour le complexe de cobalt **1.12** à 0,23 % pour l'ADPM **1.10**. Le meilleur complexe a été celui de zinc (**1.18**) à 0,14%, alors que celui de nickel (**1.14**) à 0,06% était à peine plus haut que celui de cobalt. Face à ces résultats, le meilleur complexe homoleptique à base de zinc a été testé en tant qu'additif avec le **P3HT** comme co-donneur et le **PCBM** comme accepteur (ratio de 1 : 1 : 2, respectivement). Malheureusement, l'ajout de **1.18** a fait chuter la performance de la cellule de plus de la moitié comparativement à celle de référence à 1 : 1 **P3HT** / **PCBM** (PCE = 1,30 *vs.* 2,70%). Finalement, les composés ont aussi été testés comme accepteurs pour le **P3HT** dans un ratio 1 : 1. Aucune efficacité n'a été obtenue pour les cellules contenant les complexes de cobalt et de nickel, alors que celui de zinc a atteint 0,03%. L'ADPM **1.10** a quant à lui atteint une conversion négligeable (<0,01%). Globalement, ces performances photovoltaïques non-optimisées nous ont permis de tirer quelques conclusions intéressantes :

1. La morphologie des films obtenus était généralement mauvaise, et plus particulièrement dans le cas des complexes homoleptiques dont la structure tridimensionnelle a pu nuire. La structure plannaire de l'ADPM

1.10 semblerait donc plus souhaitable pour le développement de donneurs.

2. Le complexe homoleptique ayant le mieux performé tant à titre de donneur, d'additif ou même d'accepteur en OPV a été celui à base de Zn^{II}. Cette observation soutient l'idée que les centres métalliques dont les orbitales *d* ne sont pas saturée (e.g. d^7 pour Co^{II} et d^8 pour Ni^{II}) nuisent au transfert électronique entre le donneur et l'accepteur de la couche photoactive en raison de leur contribution électronique aux orbitales frontières du complexe.[100] Elle corrobore aussi ce qui a été observé dans le cadre d'autres études menées par la Pr Sauvé utilisant des complexes homoleptiques à base d'ADPM comme potentiels accepteurs.[44,101] Dans le cas du complexe de Zn^{II} possédant une couche *d* complète à 10 électrons, le métal sert en fait de point d'ancrage pour permettre la communication entre les deux ligands par interactions $\pi - \pi$ et la rigidification de la structure, sans toutefois interférer au point de vue des orbitales moléculaires frontières.

3. L'utilisation d'une trop grande quantitée d'additif peut être nuisible au PCE (ratio 1 : 1 entre les co-donneurs), particulièrement si celui-ci s'avère un relativement bon accepteur pour l'autre donneur avec lequel il est utilisé.

Fort de ces informations préliminaires, nous avons choisi d'investiguer différentes stratégies de modulation des propriétées optoélectroniques afin que la deuxième génération de dérivés obtenue présente à la fois des niveaux électroniques

souhaitables pour la photoinjection (OPV et / ou DSSC), une morphologie adéquate en OPV ainsi qu'une absorption panchromatique s'étendant jusque dans le NIR.

Table 1.I – Résultats des tests photovoltaïques en cellule OPV pour les dérivés ADPM **1.10**, **1.12**, **1.14** et **1.18**.[111]

Dispositif	Ratio	Recuit	V_{OC} (V)	J_{SC} (mA cm^{-2})	FF	PCE (%)
Donneur						
1.10 : PCBM	1:1	Non	0,43	1,61	0,36	0,23
1.12 : PCBM	1:1	Non	0,25	0,35	0,33	0,03
1.14 : PCBM	1:1	Non	0,31	0,57	0,33	0,06
1.18 : PCBM	1:1	Non	0,26	1,68	0,33	0,14
Additif						
1.18 : P3HT : PCBM	1:1:2	120°C / 0,5 h	4,60	0,51	0,55	1,30
P3HT : PCBM	1:1	120°C / 0,5 h	8,26	0,56	0,59	2,70
Accepteur						
P3HT : PCBM	1:1	Non	0,62	7,56	0,63	2,93
P3HT : **1.10**	1:1	Non	0,17	0,08	0,25	<0,01
P3HT : **1.12**	1:1	Non	---	---	---	---
P3HT : **1.14**	1:1	Non	---	---	---	---
P3HT : **1.18**	1:1	120°C / 0,5 h	0,32	0,27	0,28	0,03
P3HT : **1.18**	1:1	Non	0,24	0,35	0,32	0,03

1.4.2 – Les stratégies de modulation des propriétés optoélectroniques vers le proche-infrarouge

Plusieurs stratégies ont été utilisées pour moduler les propriétés des dérivés dipyrrométhène vers le proche-infrarouge au fil du temps. À la base, le simple remplacement du carbone *meso* sur le DPM pour un azote dans l'ADPM permet un déplacement bathochrome d'environ 50 nm.[109,112] En outre, l'utilisation de l'effet donneur – accepteur (*Push – Pull*) à l'intérieur d'une molécule conjuguée est un effet largement utilisé pour obtenir un E_g réduit.[113] La Figure 1.18 démontre cet effet lorsque les orbitales moléculaires de ces deux sous-unitées sont combinées. Le complexe **SM315** et le copolymère **PCDTBT** constituent deux exemples concrets de l'utilisation du motif D – A en photovoltaïque (Figures 1.9 et 1.5, respectivement). Le simple ajout de groupements riches en électrons permet aussi d'obtenir un déplacement bathochrome, tel que celui de 43 nm observé dans le dichlorométhane entre l'Aza-BODIPY tétraphényles **1.19** et son analogue tétra-*p*-méthoxy-phényles **1.20** (λ_{max} = 648 et 691 nm, respectivement).[109]

L'extension du système électronique π-conjugué est une autre stratégie permettant d'absorber les photons à plus base énergie. La figure 1.19 montre l'effet théorique engendrée par la fusion d'un cycle aromatique sur les positions [*a*] et [*b*] du cœur BODIPY.[9,114] Le mode de fusion en position [*b*] s'avère particulièrement intéressant du point de vue du développement de nouveaux chromophores absorbants dans le NIR pour le photovoltaïque en raison de la faible augmentation du niveau de la HOMO (+0,15 eV *vs.* BODIPY) par rapport à la diminution significative de la LUMO

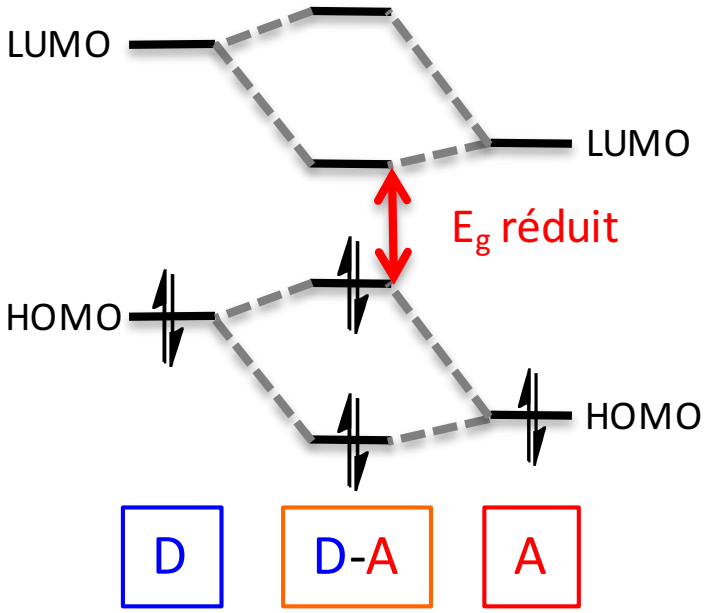

Figure 1.18 – Représention schématique de l'effet donneur – accepteur (*Push – Pull*) sur les orbitales moléculaires.

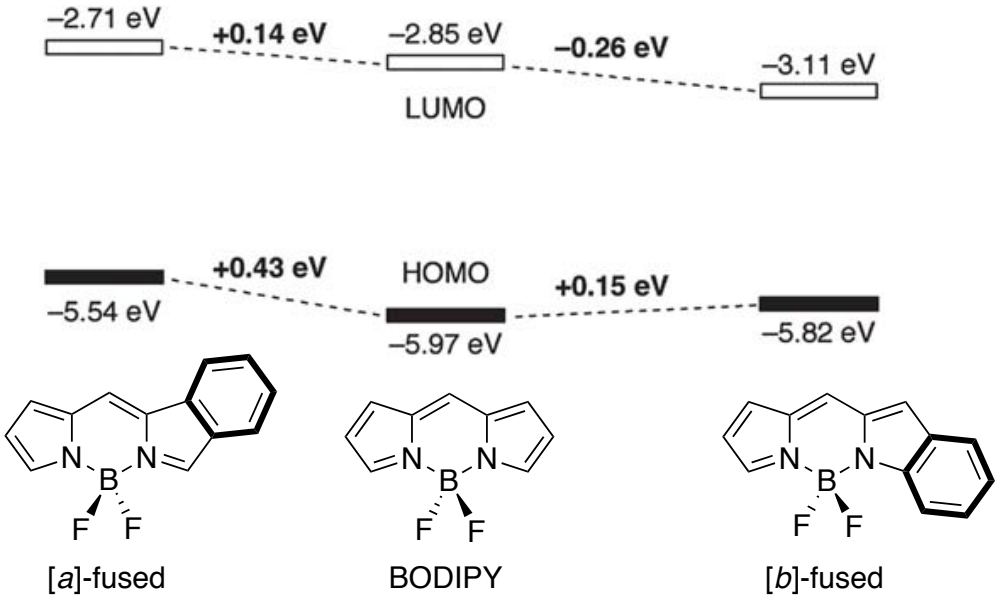

Figure 1.19 – Effet théorique des modes de fusion sur le cœur BODIPY.[114]
(Adapted from Ref. 114 with permission from The Royal Society of Chemistry)

(-0,26 eV). Cet effet combiné sur les orbitales frontières devrait *a priori* permettre le maintient d'un large V_{OC} une fois intégré en cellule solaire, tout en permettant de réduire le E_g du donneur afin de récolter les photons de plus faible énergie (*vide supra*). Pour cette raison, nous avons ainsi choisi d'explorer cette modification structurale des DPM plus en détails (voir Chapitre 3).

Finalement, la plateforme DPM présente la possibilité de moduler aisément le mode de coordination pour passer de bidentate à tridentate ou tétradentate en fonction de la structure du ligand et du cation utilisé (B^{III} ou métal de transition).[9,86-88,115-117] L'idée générale derrière l'utilisation de la coordination comme stratégie pour atteindre le NIR réside dans le fait que le cation force une meilleure planarité entre les deux fragments pyrrole, ce qui favorise la délocalisation des électrons π dans le système conjugué. Dans le cas des ligands DPM polydentates, l'ajout d'autres sites coordonnants permet d'étendre encore plus cette conjuguaison à travers les différentes parties du système. Par exemple, la chélation des 2-oxy-phényles proximaux sur le bore dans le composé **1.5** rigidifie la structure et permet une absorption jusqu'à 733 nm dans le THF.[57] En comparaison, l'analogue **1.7** portant des 2-méthoxyphényles proximaux non-chélatés n'atteint que 660 nm dans le même solvant, et ce, malgré le motif *Push-Pull* généré avec les groupements cyanovinyles présents dans la molécule.[103] Le choix du centre métallique affecte quant à lui les propriétés photophysique (e.g. iridium ou bore pour des composés hautement fluorescents) et électronique (voir Figure 1.13), ce qui permet une modulation accrue pour des applications précises.

1.6 – Bibliographie

1. Broichhagen, J.; Frank, J. A.; Trauner, D. *Acc. Chem. Res.* **2015**, *48*, 1947.
2. Zeng, L.; Jiao, C.; Huang, X.; Huang, K.-W.; Chin, W.-S.; Wu, J. *Org. Lett.* **2011**, *13*, 6026.
3. Dau, H.; Zaharieva, I. *Acc. Chem. Res.* **2009**, *42*, 1861.
4. Guskov, A.; Kern, J.; Gabdulkhakov, A.; Broser, M.; Zouni, A.; Saenger, W. *Nat. Struct. Mol. Biol.* **2009**, *16*, 334.
5. Scholes, G. D.; Fleming, G. R.; Olaya-Castro, A.; van Grondelle, R. *Nat. Chem.* **2011**, *3*, 763.
6. Nickelsen, J.; Rengstl, B. *Annual Review of Plant Biology* **2013**, *64*, 609.
7. Image du PSII d'une cyanobactérie préparée par Curtis Neveu sur Pymol à partir de la structure cristallographique PDB 2AXT. Reproduite sous la license de documentation libre GNU.
8. Loll, B.; Kern, J.; Saenger, W.; Zouni, A.; Biesiadka, J. *Nature* **2005**, *438*, 1040.
9. Bessette, A.; Hanan, G. S. *Chem. Soc. Rev.* **2014**, *43*, 3342.
10. Tsang, M.-K.; Bai, G.; Hao, J. *Chem. Soc. Rev.* **2015**, *44*, 1585.
11. Zhou, J.; Liu, Q.; Feng, W.; Sun, Y.; Li, F. *Chem. Rev.* **2015**, *115*, 395.
12. Yuan, L.; Lin, W.; Zheng, K.; He, L.; Huang, W. *Chem. Soc. Rev.* **2013**, *42*, 622.
13. Xu, H.; Chen, R.; Sun, Q.; Lai, W.; Su, Q.; Huang, W.; Liu, X. *Chem. Soc. Rev.* **2014**.
14. Yao, J.; Yang, M.; Duan, Y. *Chem. Rev.* **2014**, *114*, 6130.
15. Guo, Z.; Park, S.; Yoon, J.; Shin, I. *Chem. Soc. Rev.* **2014**, *43*, 16.
16. Heffern, M. C.; Matosziuk, L. M.; Meade, T. J. *Chem. Rev.* **2014**, *114*, 4496.
17. Kanetkar, V. *Reson.* **2010**, *15*, 794.
18. Hains, A. W.; Liang, Z.; Woodhouse, M. A.; Gregg, B. A. *Chem. Rev.* **2010**.
19. Becquerel, A. E. *C. R. Acad. Sci.* **1839**, *9*, 561.
20. Hertz, H. R. *Ann. Phys. (Berlin)* **1887**, *33*, 983.
21. *"The Nobel Prize in Physics 1921"* Nobelprize.org, http://www.nobelprize.org/nobel_prizes/physics/laureates/1921/, 04/17/2012
22. Mishra, A.; Bäuerle, P. *Angew. Chem., Int. Ed.* **2012**, *51*, 2020.
23. Il est à noter que la nomenclature des paramètres pour la caractérisation des cellules solaires provient du domaine de la physique et non de la chimie. Cela entraîne des disparités, notamment concernant le courant où le "J" est utilisé en physique plutôt que le "I" conventionnel en chimie. Se référer à la liste des abréviations.
24. Green, M. A.; Emery, K.; Hishikawa, Y.; Warta, W.; Dunlop, E. D. *Prog. Photovolt: Res. Appl.* **2015**, *23*, 805.
25. Green, M. A. *Third Generation Photovoltaics: Advanced Solar Energy Conversion*; Springer-Verlag Berlin Heidelberg, 2003.
26. Buljan, M.; Mendes-Lopes, J.; Benítez, P.; Miñano, J. C. *J. Photon. Energy.* **2014**, *4*, 040995.
27. Gratzel, M. *Nature* **2001**, *414*, 338.
28. Curtright, A. E.; Apt, J. *Prog. Photovolt: Res. Appl.* **2008**, *16*, 241.
29. Drury, E.; Lopez, A.; Denholm, P.; Margolis, R. *Prog. Photovolt: Res. Appl.* **2014**, *22*, 1302.

30. Bomben, P. G.; Robson, K. C. D.; Koivisto, B. D.; Berlinguette, C. P. *Coord. Chem. Rev.* **2012**, *256*, 1438.
31. Heber, J. *Nat. Mater.* **2012**, *11*, 178.
32. Price, S.; Margolis, R. *2008 Solar Technologies Market Report*, NREL, 2010.
33. Green, M. A.; Bein, T. *Nat. Mater.* **2015**, *14*, 559.
34. Stranks, S. D.; Snaith, H. J. *Nat. Nanotechnol.* **2015**, *10*, 391.
35. Boix, P. P.; Nonomura, K.; Mathews, N.; Mhaisalkar, S. G. *Mater. Today* **2014**, *17*, 16.
36. Peplow, M. *ACS Central Science* **2015**, *1*, 159.
37. Darling, S. B.; You, F. *RSC Adv.* **2013**, *3*, 17633.
38. Lizin, S.; Van Passel, S.; De Schepper, E.; Maes, W.; Lutsen, L.; Manca, J.; Vanderzande, D. *Energy Environ. Sci.* **2013**, *6*, 3136.
39. Hug, H.; Bader, M.; Mair, P.; Glatzel, T. *Applied Energy* **2014**, *115*, 216.
40. Parisi, M. L.; Maranghi, S.; Basosi, R. *Renewable and Sustainable Energy Reviews* **2014**, *39*, 124.
41. Image adaptée de "Best Research-Cell Efficiencies" produit par le National Renewable Energy Laboratory (NREL). http://www.nrel.gov/ncpv/images/efficiency_chart.jpg, consulté le 9 septembre 2015.
42. Zhao, J.; Li, Y.; Lin, H.; Liu, Y.; Jiang, K.; Mu, C.; Ma, T.; Lin Lai, J. Y.; Hu, H.; Yu, D.; Yan, H. *Energy Environ. Sci.* **2015**, *8*, 520.
43. Sun, D.; Meng, D.; Cai, Y.; Fan, B.; Li, Y.; Jiang, W.; Huo, L.; Sun, Y.; Wang, Z. *J. Am. Chem. Soc.* **2015**, ASAP.
44. Senevirathna, W.; Liao, J.-y.; Mao, Z.; Gu, J.; Porter, M.; Wang, C.; Fernando, R.; Sauve, G. *J. Mater. Chem. A* **2015**, *3*, 4203.
45. McAfee, S. M.; Topple, J. M.; Hill, I. G.; Welch, G. C. *J. Mater. Chem. A* **2015**, *3*, 16393.
46. Cnops, K.; Zango, G.; Genoe, J.; Heremans, P.; Martinez-Diaz, M. V.; Torres, T.; Cheyns, D. *J. Am. Chem. Soc.* **2015**, *137*, 8991.
47. Poe, A. M.; Della Pelle, A. M.; Subrahmanyam, A. V.; White, W.; Wantz, G.; Thayumanavan, S. *Chem. Commun.* **2014**, *50*, 2913.
48. Cnops, K.; Rand, B. P.; Cheyns, D.; Verreet, B.; Empl, M. A.; Heremans, P. *Nat. Commun.* **2014**, *5*, 3406.
49. Gendron, D.; Leclerc, M. *Energy Environ. Sci.* **2011**, *4*, 1225.
50. Beaupre, S.; Leclerc, M. *J. Mater. Chem. A* **2013**, *1*, 11097.
51. Cheng, Y.-J.; Yang, S.-H.; Hsu, C.-S. *Chem. Rev.* **2009**, *109*, 5868.
52. Dang, M. T.; Wuest, J. D. *Chem. Soc. Rev.* **2013**, *42*, 9105.
53. Dou, L.; Liu, Y.; Hong, Z.; Li, G.; Yang, Y. *Chem. Rev.* **2015**.
54. Saeki, A.; Koizumi, Y.; Aida, T.; Seki, S. *Acc. Chem. Res.* **2012**.
55. Scharber, M. C.; Mühlbacher, D.; Koppe, M.; Denk, P.; Waldauf, C.; Heeger, A. J.; Brabec, C. J. *Adv. Mater.* **2006**, *18*, 789.
56. Différentes valeurs pour le niveau énergétique de la LUMO du PCBM par rapport au vide sont rapportées dans la littérature. La valeur de -4.3 eV utilisée provient de: Blouin *et al.*, *J. Am. Chem. Soc.* **2008**, *130*, 732.
57. Kubo, Y.; Watanabe, K.; Nishiyabu, R.; Hata, R.; Murakami, A.; Shoda, T.; Ota, H. *Org. Lett.* **2011**, *13*, 4574.

58. Hagfeldt, A.; Boschloo, G.; Sun, L.; Kloo, L.; Pettersson, H. *Chem. Rev.* **2010**, *110*, 6595.
59. Grätzel, M. *Acc. Chem. Res.* **2009**, *42*, 1788.
60. Milot, R. L.; Schmuttenmaer, C. A. *Acc. Chem. Res.* **2015**, *48*, 1423.
61. Jakubikova, E.; Bowman, D. N. *Acc. Chem. Res.* **2015**, *48*, 1441.
62. Lee, C.-P.; Lin, R. Y.-Y.; Lin, L.-Y.; Li, C.-T.; Chu, T.-C.; Sun, S.-S.; Lin, J. T.; Ho, K.-C. *RSC Adv.* **2015**, *5*, 23810.
63. Singh, S. P.; Gayathri, T. *Eur. J. Org. Chem.* **2014**, *2014*, 4689.
64. Zhang, L.; Cole, J. M. *ACS Appl. Mater. Interfaces* **2015**, *7*, 3427.
65. Brewster, T. P.; Konezny, S. J.; Sheehan, S. W.; Martini, L. A.; Schmuttenmaer, C. A.; Batista, V. S.; Crabtree, R. H. *Inorg. Chem.* **2013**, *52*, 6752.
66. Higashino, T.; Fujimori, Y.; Sugiura, K.; Tsuji, Y.; Ito, S.; Imahori, H. *Angew. Chem., Int. Ed.* **2015**, *54*, 9052.
67. O'Regan, B.; Gratzel, M. *Nature* **1991**, *353*, 737.
68. Boschloo, G.; Hagfeldt, A. *Acc. Chem. Res.* **2009**, *42*, 1819.
69. Wu, J.; Lan, Z.; Lin, J.; Huang, M.; Huang, Y.; Fan, L.; Luo, G. *Chem. Rev.* **2015**, *115*, 2136.
70. Bella, F.; Gerbaldi, C.; Barolo, C.; Gratzel, M. *Chem. Soc. Rev.* **2015**, *44*, 3431.
71. Ye, M.; Wen, X.; Wang, M.; Iocozzia, J.; Zhang, N.; Lin, C.; Lin, Z. *Mater. Today* **2015**, *18*, 155.
72. Hagfeldt, A.; Grätzel, M. *Acc. Chem. Res.* **2000**, *33*, 269.
73. Koops, S. E.; O'Regan, B. C.; Barnes, P. R. F.; Durrant, J. R. *J. Am. Chem. Soc.* **2009**, *131*, 4808.
74. Mathew, S.; Yella, A.; Gao, P.; Humphry-Baker, R.; CurchodBasile, F. E.; Ashari-Astani, N.; Tavernelli, I.; Rothlisberger, U.; Nazeeruddin, M. K.; Grätzel, M. *Nat. Chem.* **2014**, *6*, 242.
75. Higashino, T.; Imahori, H. *Dalton Trans.* **2015**, *44*, 448.
76. Auwarter, W.; Ecija, D.; Klappenberger, F.; Barth, J. V. *Nat Chem* **2015**, *7*, 105.
77. Radivojevic, I.; Varotto, A.; Farley, C.; Drain, C. M. *Energy Environ. Sci.* **2010**, *3*, 1897.
78. Fukuzumi, S.; Honda, T.; Kojima, T. *Coord. Chem. Rev.* **2012**, *256*, 2488.
79. Ulrich, G.; Ziessel, R.; Harriman, A. *Angew. Chem., Int. Ed.* **2008**, *47*, 1184.
80. Ziessel, R.; Harriman, A. *Chem. Commun.* **2011**, *47*, 611.
81. Loudet, A.; Burgess, K. *Chem. Rev.* **2007**, *107*, 4891.
82. Boens, N.; Leen, V.; Dehaen, W. *Chem. Soc. Rev.* **2012**, *41*, 1130.
83. Kamkaew, A.; Lim, S. H.; Lee, H. B.; Kiew, L. V.; Chung, L. Y.; Burgess, K. *Chem. Soc. Rev.* **2013**, *42*, 77.
84. Kowada, T.; Maeda, H.; Kikuchi, K. *Chem. Soc. Rev.* **2015**, *44*, 4953.
85. Lu, H.; Mack, J.; Yang, Y.; Shen, Z. *Chem. Soc. Rev.* **2014**, *43*, 4778.
86. Wood, T. E.; Thompson, A. *Chem. Rev.* **2007**, *107*, 1831.
87. Baudron, S. A. *Dalton Trans.* **2013**, *42*, 7498.
88. Sakamoto, R.; Iwashima, T.; Tsuchiya, M.; Toyoda, R.; Matsuoka, R.; Kogel, J. F.; Kusaka, S.; Hoshiko, K.; Yagi, T.; Nagayama, T.; Nishihara, H. *J. Mater. Chem. A* **2015**, *3*, 15357.
89. Pistolis, G.; Kaloudi Chantzea, A.; Karakostas, N.; Pitterl, F.; Raptopoulou, C.; Glezos, N. *Chem. Commun.* **2012**, *48*, 12213.

90. Shi, W.-J.; El-Khouly, M. E.; Ohkubo, K.; Fukuzumi, S.; Ng, D. K. P. *Chem. Eur. J.* **2013**, *19*, 11332.
91. House, R. L.; Iha, N. Y. M.; Coppo, R. L.; Alibabaei, L.; Sherman, B. D.; Kang, P.; Brennaman, M. K.; Hoertz, P. G.; Meyer, T. J. *J. Photochem. Photobiol. C*.
92. Kärkäs, M. D.; Verho, O.; Johnston, E. V.; Åkermark, B. *Chem. Rev.* **2014**, *114*, 11863.
93. Alibabaei, L.; Sherman, B. D.; Norris, M. R.; Brennaman, M. K.; Meyer, T. J. *PNAS* **2015**, *112*, 5899.
94. Marshall, J. *Nature* **2014**, *510*, 22.
95. Nocera, D. G. *Acc. Chem. Res.* **2012**, *45*, 767.
96. Zheng, B.; Sabatini, R. P.; Fu, W.-F.; Eum, M.-S.; Brennessel, W. W.; Wang, L.; McCamant, D. W.; Eisenberg, R. *PNAS* **2015**, *112*, E3987.
97. Bura, T.; Leclerc, N.; Fall, S.; Lévêque, P.; Heiser, T.; Retailleau, P.; Rihn, S.; Mirloup, A.; Ziessel, R. *J. Am. Chem. Soc.* **2012**, *134*, 17404.
98. Kim, B.; Ma, B.; Donuru, V. R.; Liu, H.; Frechet, J. M. J. *Chem. Commun.* **2010**, *46*, 4148.
99. Daddario, C. M.; Han, Q.; Zeller, M.; Sauvé, G. *Eur. J. Inorg. Chem.* **2015**, n/a.
100. Senevirathna, W.; Daddario, C. M.; Sauvé, G. *J. Phys. Chem. Lett.* **2014**, *5*, 935.
101. Senevirathna, W.; Sauvé, G. *J. Mater. Chem. C* **2013**, *1*, 6684.
102. Li, G.; Hu, K.; Robson, K. C. D.; Gorelsky, S. I.; Meyer, G. J.; Berlinguette, C. P.; Shatruk, M. *Chem. Eur. J.* **2015**, *21*, 2173.
103. Kubo, Y.; Eguchi, D.; Matsumoto, A.; Nishiyabu, R.; Yakushiji, H.; Shigaki, K.; Kaneko, M. *J. Mater. Chem. A* **2014**, *2*, 5204.
104. Swetha, T.; Niveditha, S.; Bhanuprakash, K.; Singh, S. P. *Electrochim. Acta* **2015**, *153*, 343.
105. Li, G.; Yella, A.; Brown, D. G.; Gorelsky, S. I.; Nazeeruddin, M. K.; Grätzel, M.; Berlinguette, C. P.; Shatruk, M. *Inorg. Chem.* **2014**, *53*, 5417.
106. Li, G.; Hu, K.; Yi, C.; Knappenberger, K. L.; Meyer, G. J.; Gorelsky, S. I.; Shatruk, M. *J. Phys. Chem. C* **2013**, *117*, 17399.
107. Li, G.; Ray, L.; Glass, E. N.; Kovnir, K.; Khoroshutin, A.; Gorelsky, S. I.; Shatruk, M. *Inorg. Chem.* **2012**, *51*, 1614.
108. Li, G.; Bomben, P. G.; Robson, K. C. D.; Gorelsky, S. I.; Berlinguette, C. P.; Shatruk, M. *Chem. Commun.* **2012**, *48*, 8790.
109. Bessette, A.; Ferreira, J. G.; Giguère, M.; Bélanger, F.; Désilets, D.; Hanan, G. S. *Inorg. Chem.* **2012**, *51*, 12132.
110. Travaux effectués par Chunlai Wang du groupe de la Pr Geneviève Sauvé à la Case Western Reserve University (USA). Architecture de la cellule solaire de type inverse. Dépôt des films à partir d'une solution dans le dichlorobenzène. Résultats non-publiés.
111. Travaux effectués par Chunlai Wang du groupe de recherche de la Pr Geneviève Sauvé à la Case Western Reserve University (USA). Architecture de la cellule solaire de type inverse. Dépôt des films à partir d'une solution dans le dichlorobenzène. Résultats non-publiés.
112. Guy, R.; Jones, R. *Aust. J. Chem.* **1966**, *19*, 1871.
113. Bures, F. *RSC Adv.* **2014**, *4*, 58826.
114. Wakamiya, A.; Murakami, T.; Yamaguchi, S. *Chem. Sci.* **2013**, *4*, 1002.

115. Beziau, A.; Baudron, S. A.; Rasoloarison, D.; Hosseini, M. W. *CrystEngComm* **2014**, *16*, 4973.
116. Béziau, A.; Baudron, S. A.; Rogez, G.; Hosseini, M. W. *Inorg. Chem.* **2015**, *54*, 2032.
117. Chang, T. M.; Sinharay, S.; Astashkin, A. V.; Tomat, E. *Inorg. Chem.* **2014**, *53*, 7518.

Chapitre 2 : Introducing Asymmetry in Tetradentate Azadipyrromethene Chromophores: A Systematic Study of the Impact on Electronic and Photophysical Properties

André Bessette[1,2], Mihaela Cibian[1], Francis Bélanger[2], Denis Désilets[2] and Garry S. Hanan[1] *.

[1] Département de Chimie, Université de Montréal, Pavillon J.-A. Bombardier, 5155 Decelles Avenue, Montréal, Québec, H3T-2B1, Canada

[2] Saint-Jean Photochemicals Inc., 725 Trotter street, Saint-Jean-sur-Richelieu, Québec, J3B 8J8, Canada.

Physical Chemistry Chemical Physics, **2014**, *16*, 22207-22221.

Contribution des auteurs:

- André Bessette : synthèse et charactérisation; électrochimie, photophysique, modélisation moléculaire et rédaction de l'article.
- Mihaela Cibian: cristallographie rayons-X
- Francis Bélanger: superviseur en industrie
- Denis Désilets: Co-directeur en industrie
- Garry S. Hanan: Co-directeur académique

Lien permanent vers l'article (DOI) : 10.1039/C4CP02629B

2.1 – Abstract

As analogues of the porphyrinoid and dipyrromethene families of dye, azadipyrromethene (ADPM) derivatives exhibit exciting photophysical properties. Their high absorbance (**ε** up to 100 000 $M^{-1}cm^{-1}$) in the yellow-to-red region and the strong NIR luminescence encountered in boron-chelated Aza-BODIPY analogues are especially interesting in the context of light-harvesting and life science applications. In the present study, we endeavored a comparative study of symmetric and asymmetric tetradentate ADPM derivatives **1** – **6** versus the reference bidentate motifs of **7** and **8** in order to gain insights on their structure – property relationship. This is of interest since the tetradentate motif opens the way for extended π-conjugation through metal-mediated planarization, in a bio-mimicry fashion of metalloporphyrinoids, and is known to induce a bathochromic shift toward the NIR. A new straightforward synthetic approach is used to access asymmetric derivatives **4** – **6** that avoids the tedious heterocycle formation of nitroso-pyrrole intermediates. In addition, photophysic, electrochemistry, computational modelization (DFT and TD-DFT) and X-ray structural characterization of ADPMs are used to better understand the potential of these new chromophores.

2.2 – Keywords

Azadipyrromethene; Panchromatic dyes; Tetradentate ligand design; Asymmetric synthesis; Heterocyclic synthesis; Photophysic; Electrochemistry; Computational modelization; DFT; TD-DFT; X-ray Structures.

2.3 – Introduction

Azadipyrromethene (ADPM) is a class of deep blue organic chromophores discovered by Rogers[1-3] in the 1940's currently attracting renewed interest for its far-red to near-infrared (NIR) optical properties advantageously similar to dipyrromethene (DPM) and porphyrinoid (*e.g.* naturally-encountered Chlorophyll *a* chromophores) (Figure 2.1).[4,5] ADPM and DPM present the synthetic benefit of avoiding the low-yield macrocyclization step and difficult purification associated with porphyrinoids, while maintaining an intense absorption band (ε up to 100 000 $M^{-1}cm^{-1}$) in the yellow-to-red part of the spectrum. They also offer abundant leverage possibilities in order to fine-tune their properties by substituent modification and greater versatility of metal coordination geometries as compared to the rigid square-planar geometry encountered in tetrapyrrole macrocycles. The main advantage of ADPM over DPM resides in the intrinsic bathochromic shift in the absorption band (about 50 nm) provided by substitution to a nitrogen bridge at the *meso*- position of the DPM core. All these advantages coupled with the strong NIR emission in corresponding BF_2-chelates of DPM and ADPM, known in literature as BODIPY and Aza-BODIPY respectively, have led to a wide range of applications, including: fluorescent indicators and sensors;[6-9] fluorescence imaging agents;[10, 11] photosensitizers for photodynamic therapy;[12-14] advanced luminescent and light-active material component;[15-19] nonlinear optic;[20] light-harvesting antennae[21-28] and photovoltaic devices.[4, 29-34] With these multiple applications and their imperative need for further fine-tuning of optical and electrochemical properties, one field in which ADPM is actively used is coordination chemistry, where the metallic center opens up many new exciting opportunities.[31, 35-45]

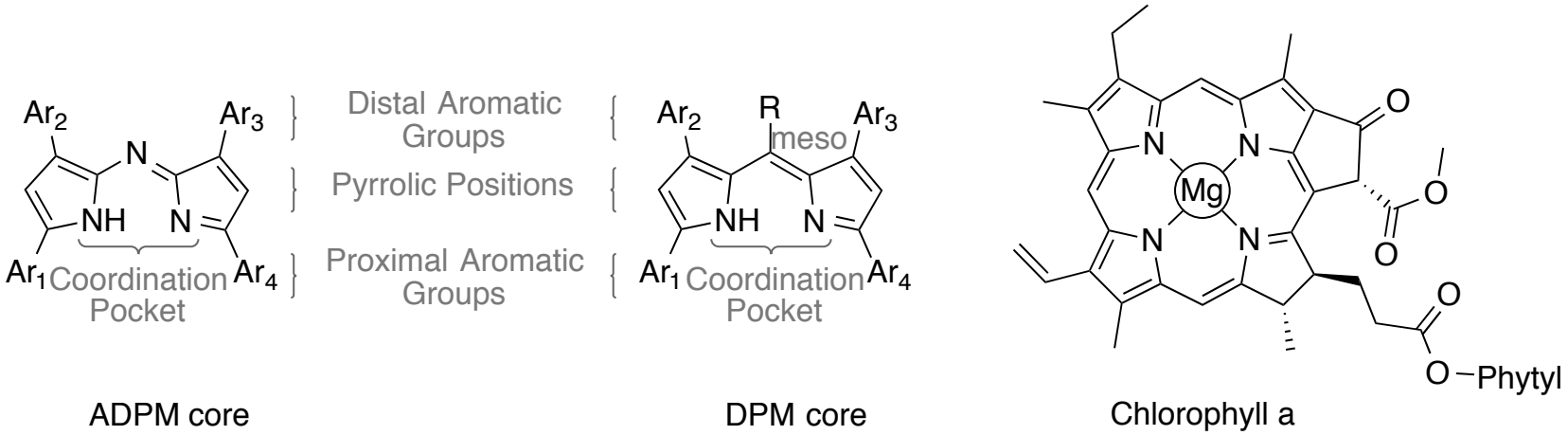

Figure 2.1 – Azadipyrromethene (ADPM) and dipyrromethene (DPM) cores along with Chlorophyll *a* porphyrin.

In this context, we are interested in the design of new ADPM that would coordinate metallic centers in a tetradentate fashion, red-shifting even further the NIR properties by extension of the conjugation. The concept of restricting the possible conformations of ADPM to induce a bathochromic shift in the spectral absorption and emission has already been demonstrated, either by ring constrain / fusion[46-48] or B-O chelation.[49] Toward this goal, metal-mediated planarization effects still need to be explored in a similar fashion as the bio-mimicry of metalloporphyrinoids and natural bilin-type chlorophyll catabolite metal complexes.[50-54] Applications other than light-harvesting and photovoltaic can further be envisioned for such derivatives, such as catalytic and biomedical ones.[55-58]

In order to achieve these organometallic structures, new symmetric and asymmetric tetradentate ADPM containing additional heterocycles or heteroatoms on the proximal aryl groups needs to be developed (refer to Figure 2.1). While thiophene and pyridine rings have already been used as replacement for phenyls,[8, 59] their incorporation into a tetradentate motif was not optimal since the thiophenes lead to an overly wide bite angle for metallic coordination and the pyridines were reported only at the distal positions. In light of a recent mechanistic studies on the formation of tetraphenyl ADPM **7** using ^{15}N-labeling method reported by O'Shea *et al.*,[60] we endeavored to investigate symmetric tetradentate ADPM **1** – **3** and their corresponding asymmetric analogues **4** – **6** (Figure 2.2). While asymmetric tetraaryl ADPMs were already accessible by condensation of 2,4-diaryl-5-nitroso-pyrroles with 2,4-diarylpyrroles,[46, 61] we report herein a more straightforward synthesis that avoids tedious heterocycle formation of nitroso-pyrrole intermediates.[62] Our approach simply react the 2,4-diarylpyrrole with the

easily accessible corresponding nitro-ketone precursor common to all ADPM dye formation. In addition to the new synthetic route proposed, a comparative study of the symmetric and asymmetric ADPM **1** – **8** including photophysic, electrochemistry, computational modelization (DFT and TD-DFT) and X-ray structural data analysis (for compounds **1**, **3** – **5** and **8**) will be presented in order to establish the trends and impact of the various accessible proximal aryl substitutions.

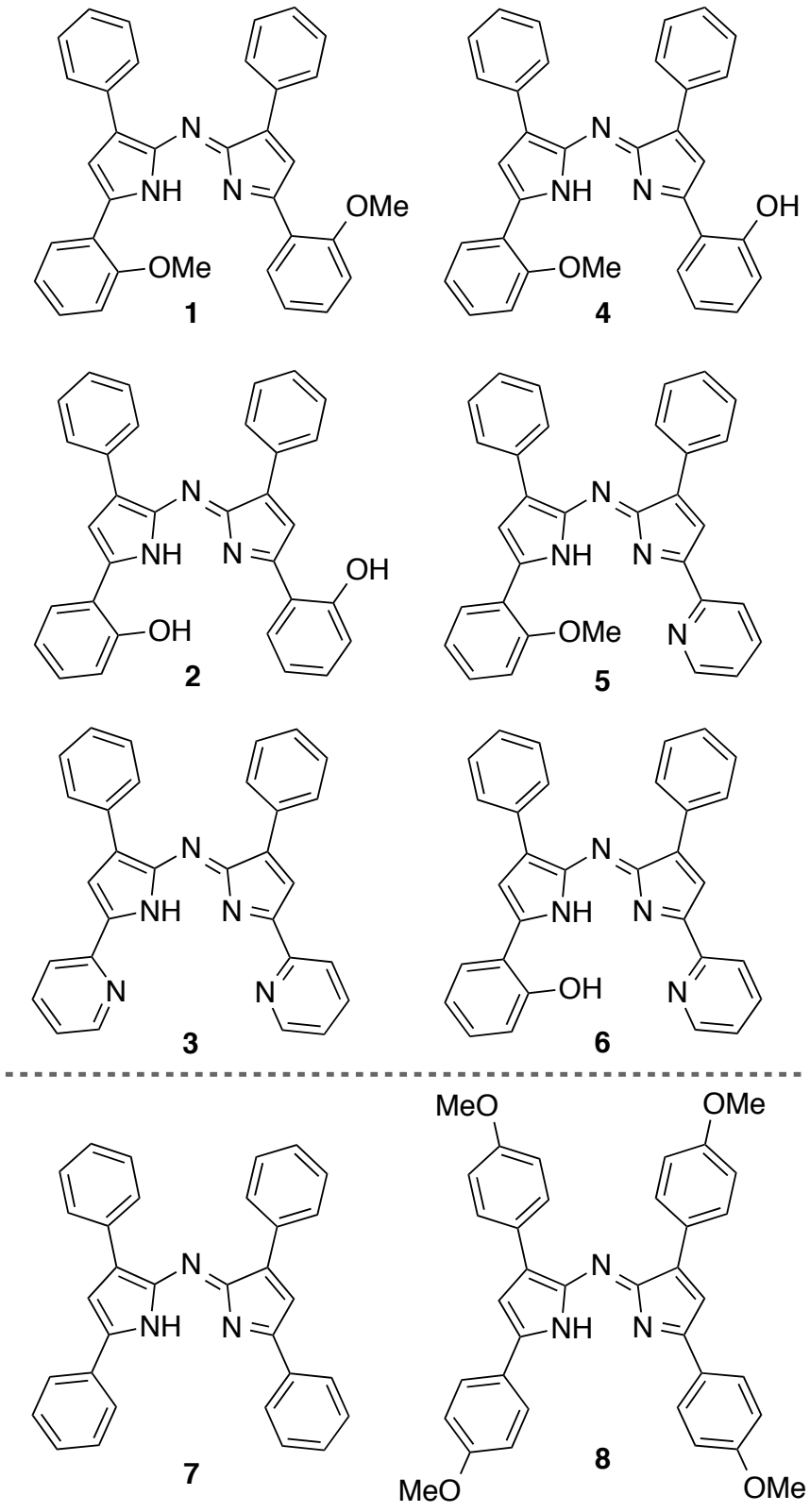

Figure 2.2 – ADPM compounds investigated herein.

2.4 – Experimental Section

2.4.1 – Materials and Instrumentation

Literature procedures were used for the synthesis of compounds **1**, **2**, **7**, **10**, **11** and 3-phenyl-1-(pyridin-2-yl)prop-2-en-1-one.[14, 46, 49, 63, 64] ADPM **8** was obtained from Saint-Jean Photochemicals Inc. (sjpc.com) and used as received. Reagents and solvents were obtained commercially and used without further purification. Reactions were carried out under ambient atmosphere. Solvents were removed under reduced pressure using a rotary evaporator unless otherwise stated.

Nuclear magnetic resonance (NMR) spectra were recorded in $CDCl_3$ at room temperature (r.t.) on a Bruker AV400 spectrometer at 400 MHz for ^{1}H NMR and at 100 MHz for ^{13}C NMR, unless otherwise stated. 125 MHz ^{13}C NMR of ADPM **4** was recorded on a Bruker Avance 500 spectrometer, while 175 MHz ^{13}C NMR of ADPM **5** and **6** were obtained on a Bruker Avance 700. Chemical shifts are reported in part per million (ppm) relative to residual solvent protons (7.26 ppm for chloroform-d) and the carbon resonance of the solvent (77.16 ppm for chloroform-d). High-Resolution Electro Spray Ionization Mass Spectrometry (HR-ESIMS) was performed on a Liquid Chromatography / Mass Spectrometry with a Time of Flight detector (LC/MS TOF) from Agilent. Absorption spectra were measured in CH_2Cl_2 (DCM) at concentrations obeying Beer-Lambert's law at r.t. on a Cary 500i UV-vis-NIR Spectrophotometer. The absence of fluorescence for the series of ADPM investigated herein was assessed on a Cary Eclipse Fluorescence Spectrophotometer. Full details on crystal structure

determination and refinement data for compounds **1**, **3**, **4** and **5** are provided in Supporting Information (SI).

Electrochemical measurements were carried out in argon-purged CH_2Cl_2 at room temperature with a BAS CV50W multipurpose potentiostat. The working electrode used was a glassy carbon electrode for every compound. The counter electrode was a Pt wire, and the pseudo-reference electrode was a silver wire. The reference was set using an internal 1 mM ferrocene/ferrocenium sample at 0.46 V vs SCE in CH_2Cl_2. The concentration of the compounds was about 1 mM. Tetrabutylammonium hexafluorophosphate (TBAP) was used as supporting electrolyte and its concentration was 0.10 M. Cyclic voltammograms (CV) were obtained at scan rates of 50, 100, 200, and 500 mV/s. For reversible processes, half-wave potentials (vs. SCE) from CV were used. To establish the potential of irreversible processes, differential pulse voltammetry (DPV) experiments were performed with a step rate of 4 mV, a pulse height of 50 mV, and a frequency of 5 Hz. Criteria for reversibility were the separation of 60 mV between cathodic and anodic peaks, the close to unity ratio of the intensities of the cathodic and anodic currents, and the constancy of the peak potential on changing scan rate.

Experimental uncertainties are as follows: absorption maxima, ±2 nm; molar absorption coefficient, 10%; redox potentials, ± 10 mV.

2.4.2 – Computational Methods

Computational modelization of ADPM **1** – **8** was achieved following the general procedure depicted by Jacquemin and coworkers for Aza-BODIPYs.[65] All calculations were performed with the Gaussian 09 software (G09).[66] Geometry optimizations, frequency calculations and molecular orbital (MO) calculations were performed by DFT method using the PBE0[67 - 69] / 6-311G(2d,p) basis set using the Polarization Continuum Model (PCM)[70] of dichloromethane. Crystallographic coordinates were used as starting points for geometry optimizations when available. When no crystallographic data were available for a given compound, modification of a similar derivative was used. Tight convergence criteria and no symmetry constraints were imposed during the optimization process. Only positive frequencies were found for the optimized structures. The absorption spectra were calculated by TD-DFT from optimized structures, using the BMK[71] / 6-311+G(2d,p) level of theory with the PCM of dichloromethane. MOs were visualized (isovalue = 0.02) with GaussView 3 software.[72] GaussSum 6.5 was employed to extract from TD-DFT results the absorption energies and oscillator strengths, while molecular orbital energies were obtained from DFT.[73] Chemissian 3.3 program was used to represent MO's energy levels (Figure 2.5), experimental vs calculated optical absorption spectrum (refer to SI) and determine the electronic distribution (in %) of the various parts of the ADPM chromophore (refer to SI).[74]

2.4.3 – Synthetic Methods

Azadipyrromethene **3**

4-nitro-3-phenyl-1-(pyridin-2-yl)butan-1-one **9** (1.00 g, 3.70 mmol) was dissolved in EtOH (3 mL) and ammonium acetate (10.2 g, 130 mmol) was added and the reaction mixture was refluxed for 12 h. The reaction mixture was evaporated to dryness, dissolved in CH_2Cl_2 and washed with water (3x). The organic phase was evaporated and the purple residue was purified by silica gel chromatography (1 : 1 THF / heptane). The product crystallized as thin dark purple needles suitable for X-ray structural analysis on the sides of the collection tubes, while decomposition in solution occurs. Yield = 9 mg (1 %). ^{1}H NMR ($CDCl_3$, 400 MHz) δ/ppm: 7.26 (br. s., 1 H), 7.30 - 7.54 (m, 10 H), 7.81 - 7.90 (m, 2 H), 8.09 (d, J=7.3 Hz, 3 H), 8.22 (br. s., 2 H), 8.77 (d, J=4.0 Hz, 2 H), 12.79 (br. s., 1 H). Mass Spec (m/z); MS calcd for $C_{30}H_{21}N_5$: $[(M+H)^+]$ 452.18697, found: 452.18572.

Azadipyrromethene **4**

A suspension of 2-(2-methoxyphenyl)-4-phenyl-1H-pyrrole **10** (409 mg, 1.64 mmol) and 1-(2-hydroxyphenyl)-4-nitro-3-phenylbutan-1-one **11** (444 mg, 1.64 mmol) in EtOH (5 mL) was heated to 50 °C under magnetic stirring. Upon solubilization, ammonium acetate (4.52 g, 57.3 mmol) was added and the reaction mixture was refluxed for 24 h. The crude mixture was cooled down, evaporated to dryness, dissolved in CH_2Cl_2 and washed with water (3x). The organic phase was evaporated and the dark-purple residue was purified by silica gel chromatography (15 : 85 AcOEt / heptane). Recrystallization in hot heptane and in vacuo drying afforded dark purple needles

suitable for X-ray structural analysis. Yield = 368 mg (45 %). ^{1}H NMR ($CDCl_3$, 400 MHz) δ/ppm: 4.04 (s, 3 H), 7.03 (t, J=7.6 Hz, 1 H), 7.06 - 7.17 (m, 4 H), 7.32 - 7.47 (m, 8 H), 7.48 (s, 1 H), 7.79 - 7.90 (m, 2H), 7.98 - 8.07 (m, 4 H), 11.41 (br. s., 1 H), 12.55 (s, 1 H). ^{13}C NMR ($CDCl_3$, 125 MHz) δ/ppm: 169.7, 160.6, 157.2, 148.3, 139.4, 136.4, 135.9, 134.0, 133.2, 133.1, 130.2, 129.6, 129.2, 128.9, 128.6, 128.2 (2C), 128.1, 127.7, 127.6, 121.3, 121.1, 119.6, 118.1, 117.3, 117.2, 111.9, 109.9, 56.6. Mass Spec (m/z); HR-ESIMS calcd for $C_{33}H_{25}N_3O_2$: [$(M+H)^+$] 496.20195, found: 496.20238. Elemental Analysis: calcd: C = 79.98 %, H = 5.08 %, N = 8,48 %; found: C = 79.83 %, H = 5.00 %, N = 8.43 %.

Azadipyrromethene **5**

2-(2-methoxyphenyl)-4-phenyl-1H-pyrrole **10** (300 mg, 1.20 mmol) and 4-nitro-3-phenyl-1-(pyridin-2-yl)butan-1-one **9** (325 mg, 1.20 mmol) were dissolved in EtOH (5 mL). Ammonium acetate (590 mg, 7.44 mmol) was added and the reaction mixture was refluxed for 12h. The reaction mixture was evaporated to dryness, dissolved in CH_2Cl_2 and washed with water (3x). The organic phase was evaporated and the dark-blue residue was purified by silica gel chromatography (25 : 75 AcOEt / heptane). The dark-purple powder obtained was recrystallized with DCM and heptane to afford purple/gold-shinning cubic crystals suitable for X-ray structural analysis. Yield = 115 mg (40 %).^{1}H NMR ($CDCl_3$, 400 MHz) δ/ppm: 4.05 (s, 3 H), 7.09 (d, J=8.4 Hz, 1 H), 7.16 (t, J=7.4 Hz, 1 H), 7.31 - 7.44 (m, 9 H), 7.44 - 7.50 (m, 1 H), 7.61(s, 1 H), 7.82 - 7.89 (m, 1 H), 7.93 - 8.07 (m, 4 H), 8.12 - 8.24 (m, 1 H), 8.76 (d, J=4.8 Hz, 1 H), 12.63 (br. s., 1 H). ^{13}C NMR ($CDCl_3$, 175 MHz) δ/ppm: 158.0, 157.7, 151.8, 151.4, 151.1, 149.9, 146.7,

143.3, 140.8, 136.3, 134.0, 133.8, 131.3, 129.4, 129.2, 129.1, 128.19, 128.17, 127.83, 127.77, 123.7, 121.5, 121.4, 120.5, 116.9, 116.4, 112.2, 56.2. Mass Spec (m/z); HR-ESIMS calcd for $C_{32}H_{25}N_4O$: $[(M+H)^+]$ 481.20229, found: 481.20252. Elemental Analysis: calcd: C = 79.98 %, H = 5.03 %, N = 11.66 %; found: C = 79.95 %, H = 5.04 %, N = 11.75 %.

Azadipyrromethene **6**

A suspension of 2-(4-phenyl-1H-pyrrol-2-yl)phenol **12** (839 mg, 3.57 mmol) and 4-nitro-3-phenyl-1-(pyridin-2-yl)butan-1-one **9** (964 mg, 3.57 mmol) in EtOH (10 mL) was heated to 50°C under magnetic stirring. Upon solubilization, ammonium acetate (9.82 g, 125 mmol) was added and the reaction mixture was refluxed for 12h. The crude mixture was evaporated to dryness, dissolved in CH_2Cl_2 and washed with water (3x). The organic phase was evaporated and the dark-purple residue was purified by silica gel chromatography (25 : 75 AcOEt / heptane). Vacuum drying afforded a dark-purple powder. Yield = 712 mg (43 %). ^{1}H NMR ($CDCl_3$, 400 MHz) δ/ppm: 7.03 (t, J=7.5 Hz, 1 H), 7.10 - 7.21 (m, 2 H), 7.24 (br. s., 1 H), 7.31 - 7.38 (m, 1 H), 7.38 - 7.50 (m, 6 H), 7.53(s, 1 H), 7.71 - 7.79 (m, 2 H), 7.82 (d, J=7.7 Hz, 1 H), 8.02 (t, J=7.0 Hz, 4 H), 8.76 (d, J=4.4 Hz, 1 H), 11.19 (br. s., 1 H), 12.54 (br. s., 1 H). ^{13}C NMR ($CDCl_3$, 175 MHz) δ/ppm: 134.4, 134.2, 134.00, 133.99, 132.6, 130.9, 130.80, 130.77, 130.4, 129.9, 129.3, 129.0, 128.9, 128.7, 128.27, 128.25, 128.1, 127.9, 127.8, 127.7, 127.5, 127.4, 127.3, 122.7, 119.7, 118.0, 117.9. Mass Spec (m/z); HR-ESIMS calcd for $C_{31}H_{22}N_4O$: $[(M+H)^+]$ 467.18664, found: 467.18724. Elemental Analysis: calcd for $C_{31}H_{22}N_4O \bullet 0.5$

H_2O: C = 78.30 %, H = 4.87 %, N = 11.78 %; found: C = 78.27 %, H = 4.47 %, N = 11.98 %.

4-nitro-3-phenyl-1-(pyridin-2-yl)butan-1-one **9**

3-phenyl-1-(pyridin-2-yl)prop-2-en-1-one (10.0 g, 47.8 mmol) and nitromethane (27.25 mL, 478 mmol) were dissolved in EtOH (150 mL). KOH powder (0.54 g, 9.56 mmol) was added under magnetic stirring and the reaction mixture was heated at 60 °C for 3 h. The crude was concentrated in vacuo and purified by silica gel chromatography (2 : 8 AcOEt / heptane). Vacuum drying afforded dark yellow oil. Yield = 10.8 g (84 %). Characterization matched previously reported literature.[32]

2-(4-phenyl-1H-pyrrol-2-yl)phenol **12**

To a flamed-dried flask equipped with a magnetic stirrer, 2-(2-methoxyphenyl)-4-phenyl-1H-pyrrole **10** (1.40 g, 5.62 mmol) was dissolved in anhydrous CH_2Cl_2 (200 mL). The reaction mixture was then degassed and kept under an inert atmosphere (N_2) at 0 °C. A solution of 1M BBr_3 in CH_2Cl_2 (28.1 mL, 28.1 mmol) was added dropwise and the reaction mixture was stirred at 0 °C for 15 min. The reaction mixture was than warmed to r.t. and stirred for another 24 h (or upon completion by TLC). The reaction was cooled back to 0 °C and quenched by slow addition of water. The organic and aqueous phases were separated and the latter was further dried with anhydrous Na_2SO_4, filtered and concentrated in vacuo. The crude oil was purified by silica gel chromatography (2 : 8 AcOEt / Heptane). Vacuum drying afforded dark yellow oil.

Yield = 839 mg (64 %). This light and air sensitive product was brought to the next step without further characterization.

2.5 – Results and Discussion

2.5.1 – Design Strategy

Our study began by the synthesis of symmetric tetra-aryl ADPM derivatives based on the known reaction of 4-nitro-1,3-diarylbutan-1-ones with an ammonium source in ethanol.[60] The tetradentate ADPM **1** with methoxy- and **2** with hydroxyl-groups were synthetized according to the procedures reported by O'Shea *et al.*[49, 63] In the case of ADPM **3** bearing 2-pyridyl proximal substituents, we adapted the synthesis of the corresponding ADPM with 2-pyridyl substituents installed in distal positions reported by Akkaya and coworkers.[8] Nitro-ketone derivative **9** was reacted in the presence of an excess of NH_4OAc (Scheme 2.1) to lead to the expected tetradentate chromophore in poor yield (1 %). Although the reaction proceeded smoothly to give the desired product (by TLC analysis), the amount of recovered ADPM after purification on silica gel column was very small.[76] We postulate the degradation of the product during purification arises from the increased reactivity of the adjacent carbons of the N-bridge due to the conjugated electron-poor pyridine substituents. Luckily, we found X-ray quality crystals of ADPM **3** forming upon slow evaporation on the walls of the collected fractions that confirmed the accessibility of this tetradentate motif (refer to X-ray section, Figure 2.7). Based on previous work, we believe further complexation of a metal ion should allow for an overall stabilization avoiding such decomposition.[35]

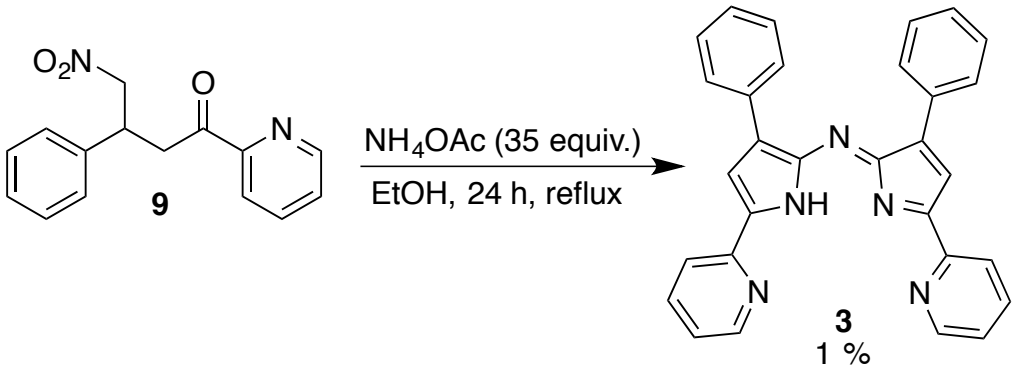

Scheme 2.1 – Synthesis of the symmetric ADPM **3**.

With symmetric tetradentate ADPM **1** – **3** in hand, we undertook the preparation of the more challenging asymmetric derivatives **4** – **6** in a combinatorial fashion. Our retrosynthetic analysis was based on the mechanistic insights provided lately by O'Shea and coworkers.[60] We envisioned that asymmetric tetraaryl ADPM could be obtained by reacting 2,4-diarylpyrrole with the corresponding nitro-ketone precursor common to the formation of all symmetric ADPM dyes. This new synthesis would avoid the tedious formation of nitroso-pyrrole intermediates[62] and open a straightforward route to asymmetric ADPMs. Indeed, one could envision obtaining a mixture of both symmetric products being obtained in addition to the desired asymmetric one. Keeping this challenge in mind, we were pleased to observe the selective formation of asymmetric ADPM **4** – **6** using our novel strategy (Scheme 2.2). Reaction conditions derived from the symmetric ADPM synthesis yielded the adduct **4** in a satisfactory 45% yield through the reaction for one day of 2-(2-methoxyphenyl)-4-phenyl-1*H*-pyrrole **10** with 1-(2-hydroxyphenyl)-4-nitro-3-phenylbutan-1-one **11** in the presence of ammonium acetate into ethanolic solution.[77] Using the same procedure, the 2,4-diarylpyrrole **10** was used with nitroketone **9** to access in 40% yield the ADPM **5** with a 2-methoxyphenyl and a 2-

pyridyl as the proximal substituents. To obtain the 2-hydroxyphenyl / 2-pyridyl substituted ADPM **6**, a deprotection strategy of **10** using BBr_3 reagent to provide the intermediate 2-(4-phenyl-1*H*-pyrrol-2-yl)phenol **12** was used. This sensitive intermediate was quickly reacted after purification on silica column with 2-pyridyl nitroketone **9** to provide the desired chromophore in 43% yield. It is noteworthy that our approach is the only one that gives access to this ADPM derivative. In fact, the 2-(4-phenyl-1*H*-pyrrol-2-yl)pyridine that would be needed in O'Shea's nitroso-pyrrole route is difficult to access since pyrrolic formation of the latter from nitroketone **9** was not possible. Similarly, the direct pyrrolic formation from the corresponding nitroketone **11** failed in our hands to yield **12**. Overall, the synthetic methodology presented herein to reach asymmetric tetradentate ADPMs present yields comparable to their corresponding symmetric derivatives in a forthright synthetic approach.

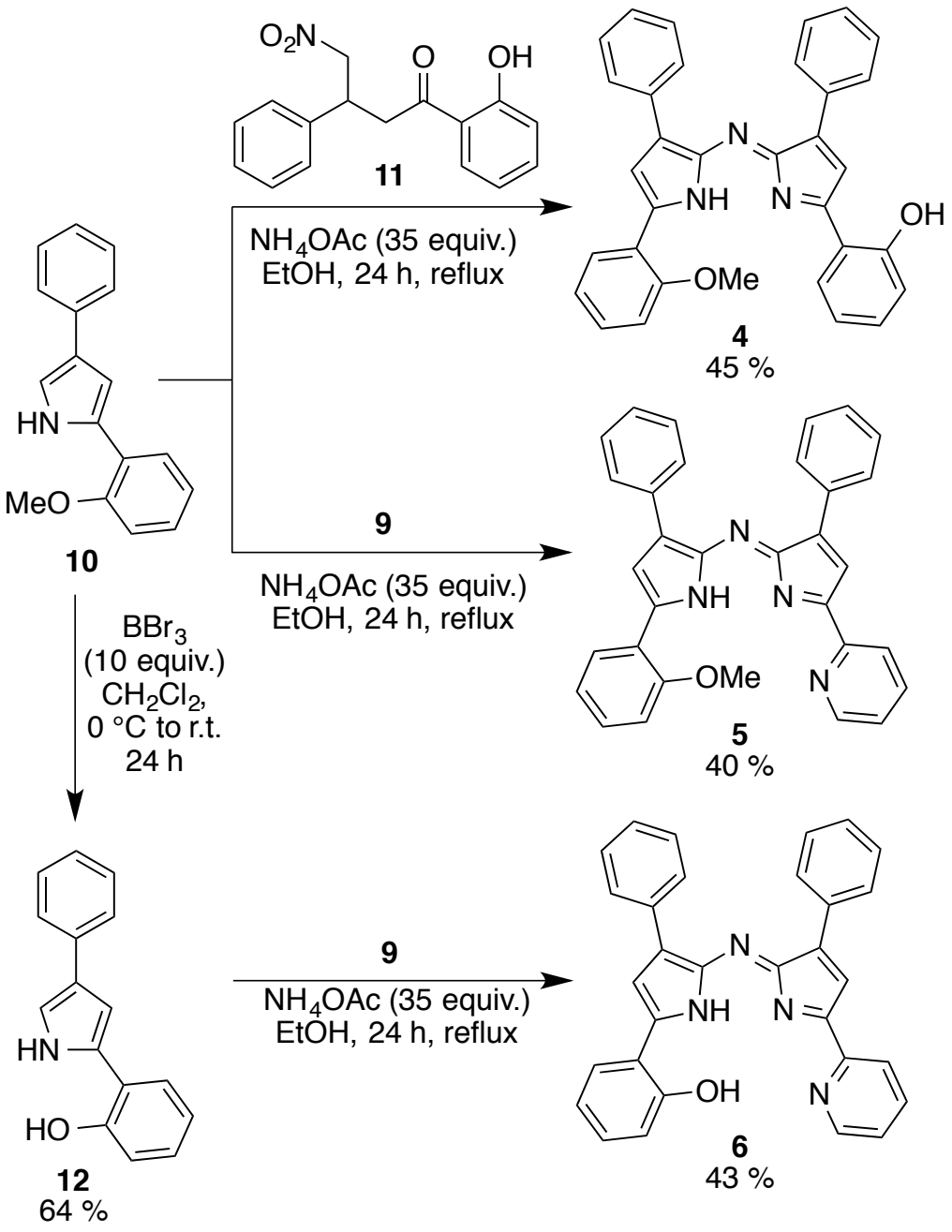

Scheme 2.2 – Synthesis of asymmetric ADPM derivatives **4** – **6**.

2.5.2 – Spectroscopic Properties

The most attractive feature of azadipyrromethenes is their intense and broad absorption band found in the green to red part of the visible spectrum, leading to a purple / deep blue pigment. As mentioned previously, absorption at such low energy is of great interest for multiple applications and fine control on the exact wavelength of the maxima is therefore highly desirable. Spectroscopic properties in dichloromethane solution of tetradentate ADPMs **1** – **6** were recorded and are summarized in Table 2.I. No fluorescence was observed for the series. Further comparisons were made to related bidentate motif ADPM derivatives **7** and the more electron-rich **8**, previously reported bearing four *p*-methoxyphenyl substituents.[35]

Table 2.I – Compiled UV / vis absorption data for ADPM derivatives **1** – **8** in CH_2Cl_2 and corresponding TD-DFT calculated absorption band for $\lambda_{max\ red}$

	Absorption [a] [b]				**Abs band** [c]
	$\lambda_{max\ near\text{-}UV}$, **nm**	$\lambda_{max\ violet}$, **nm**	$\lambda_{shoulder}$, **nm**	$\lambda_{max\ red}$, **nm**	$\lambda_{max\ red\ Theo}$, **nm**
1	299 (34)	407 (6.8)	---	605 (47)	553 (0.834)
2	307 (26)	415 (6.0)	577 (21)	615 (39)	560 (0.834)
3	307 (30)	---	558 (28)	590 (39)	547 (0.877)
4	307 (35)	417 (8.3)	576 (28)	619 (52)	571 (0.861)
5	298 (30)	417 (3.9)	567 (24)	602 (33)	566 (0.830)
6	308 (36)	418 (6.9)	561 (28)	598 (43)	564 (0.850)
7	302 (41)	---	---	596 (46)	551 (0.885)
8	322 (40)	414 (10)	---	627 (52)	587 (0.889)

[a] Acquisition at 293K. [b] Extinction coefficient given in parenthesis (ε , $x10^3$ $M^{-1}cm^{-1}$). [c] TD-BMK/6-311+G(2d,p); PCM = CH_2Cl_2. Oscillator strength given in parenthesis. Full assignation of the absorption bands available in SI (Tables S.2 – S.9)

For the symmetric tetradentate derivatives **1** – **3** (Figure 2.3a), ADPM **2** ($\lambda_{max\ red}$ = 615 nm) bearing *ortho*-hydroxyphenyl substituents in proximal position exhibits the highest bathochromic shift (+19 nm) compared to the reference ADPM **7** ($\lambda_{max\ red}$ = 596 nm). In contrast, ADPM **1** ($\lambda_{max\ red}$ = 605 nm) with methoxy groups presents a bathochromic shift of +9 nm. These red shifts in the absorption maxima for ADPM **1** and **2** result from the contributions of electron-donors moieties, in a similar fashion to the +31 nm shift observed in the analogous ADPM **8**. Purely based on an analysis of the Hammett parameter, the biggest red shift arising from hydroxyl groups in ADPM **2** compared to methoxy groups in ADPM **1** (+19 nm vs +9 nm, respectively) is consistent with their relative electron-donating behavior (σ = -0.37 for -OH vs σ = -0.27 for -OMe).[78] In addition, the intramolecular H-bonds in dichloromethane solutions of ADPM **1** and **2** contribute to improve the overall conjugation throughout the molecules, thus leading to lower energy light absorption. This argument was first observed in the X-ray structure of ADPM **1** (see X-ray section; Figure 2.7), which was subsequently supported for both ADPM **1** and **2** by computational modelization with application of the Polarity Continuum Model (PCM) of dichloromethane (see Computational Modelization section). On the other hand, the electron deficient 2-pyridyl moieties in ADPM **3** ($\lambda_{max\ red}$ = 590 nm) provide a hypsochromic shift of -6 nm compared to ADPM **7**, also in accordance with the Hammett parameter argument (σ = 0.17 for 2-pyridyl moiety).[78] Interestingly, appearance of a small additional absorption band in the violet / blue at (~ 410 nm, ε = ~ 6 x 10^3 $M^{-1}cm^{-1}$) is noticeable for the two first tetradentate derivatives **1** and **2**, a behavior also found in the *p*-methoxy substituted ADPM **8**. As will be discussed in more details in the Computational Modelization section, TD-DFT calculations

identified this absorption band as an electronic transition from the methoxy or hydroxyl groups toward the ADPM core. Overall, the symmetric tetradentate ADPM derivatives **1** – **3** reveal that a modulation of up to 25 nm is achievable ranging from the electron-poor ADPM **3** to the electron-richest ADPM **2**, which also takes advantage of intramolecular hydrogen bonding in the latter.

Asymmetric tetradentate derivatives **4** – **6** (Figure 2.3b) present an advantageous combination of the properties observed in their symmetric counterparts. For instance, in the case of ADPM **4** the intramolecular H-bonds are acting in a synergetic manner to push the absorption up to 619 nm (+23 nm compared to ADPM **7**) (see X-ray section; Figure 2.8). Similarly, the extinction coefficient significantly increases as compared to the reference (ε = 52 x 10^3 for **4** vs 46 x 10^3 $M^{-1}cm^{-1}$ for **7**). Remarkably, this synergy leads to planarization of the ADPM chromophore and a bathochromically-shifted intense absorption that gives good insight on the metal ion coordination effect. The integration of a 2-pyridyl moiety in ADPM **5** ($\lambda_{max\ red}$ = 602 nm) and **6** ($\lambda_{max\ red}$ = 598 nm) provides smaller bathochromic shifts of +6 and +2 nm, respectively. A decrease in extinction coefficients was also observed for **5** and **6** (ε = 33 x 10^3 $M^{-1}cm^{-1}$ and 43 x 10^3 $M^{-1}cm^{-1}$, respectively). These observations are in line with less electron-donating systems and still provide a red shift due to the methoxy or hydroxyl substituent. The additional absorption band at ~410 nm seen in symmetric ADPM **1**, **2** and **8** was also noticeable in asymmetrical adducts **4** and **6** bearing the hydroxyl substituent. In contrast, ADPM **5** with the methoxy substituent present a relatively smaller band similar to reference **7**.

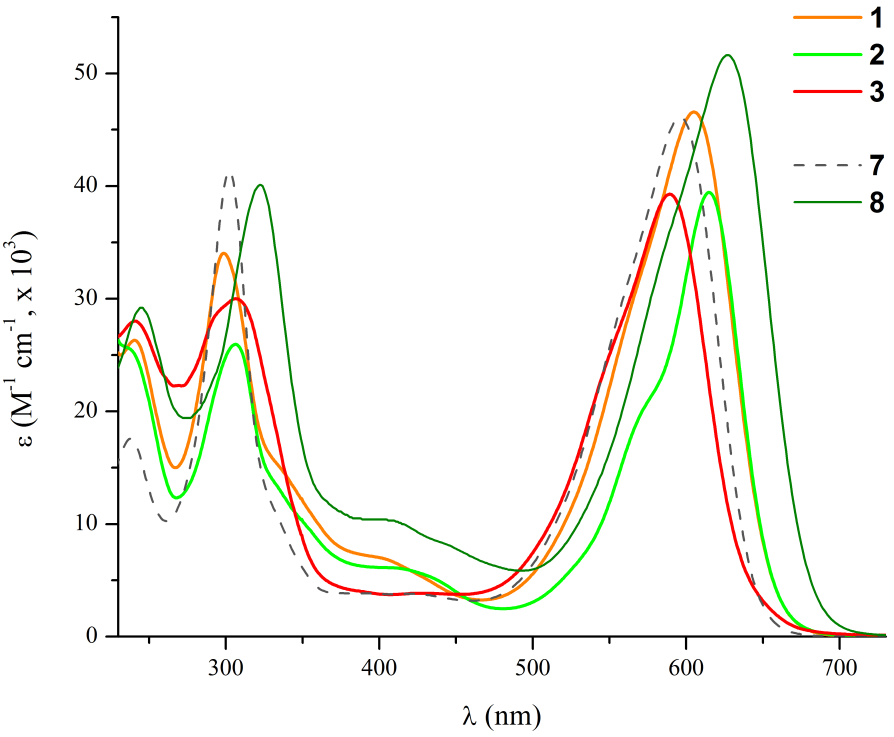

a)

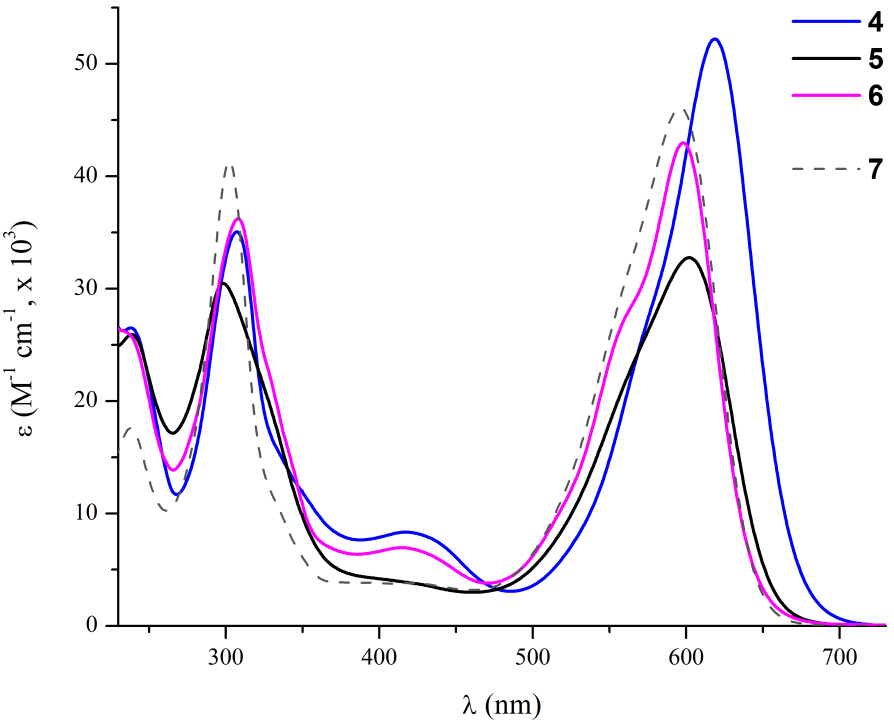

b)

Figure 2.3 – Absorption spectra in DCM of: *a)* symmetric ADPM derivatives **1** – **3**, **7** and **8** *b)* asymmetric **4** – **6**.

2.5.3 – Electrochemistry

The gathering of information concerning the energy levels of tetradentate ADPM chromophores **1** – **6** and their potential metallic complexes is essential for further integration in various photoactive materials. While optical properties such as absorption and emission can indicate the energy difference between the HOMO and LUMO, only electrochemistry is able to further provide their exact energy level in the ground state. This is especially relevant for a fine-tuning of the properties in given applications. For instance, a mismatch between the LUMO levels of the donor and the acceptor molecules in dye-sensitized solar cells (DSSC) or organic photovoltaic (OPV) devices would not allow efficient electron transfer upon photoexcitation.[4, 79-81] Similarly, a high-lying HOMO level might oxidize air-exposed photovoltaic devices or fluorescent sensors in biological environments.[6, 82] Applications in photocatalysis and electrogenerated chemiluminescence also need insights provided by electrochemistry.[17, 83] In this study, the effect of tetradentate motif in ADPM **1** – **6** was compared by cyclic and differential pulse voltammetry techniques (CV and DPV, respectively) to corresponding bidentate derivatives **7** and **8** (Table 2.2 and SI). These empirical techniques afforded critical information concerning electronic processes and exact energies associated with their HOMO / LUMO states that can further be rationalized with the computational modelization study made (Table 2.3 and Figure 2.4).

Table 2.II – Electrochemical data for ADPM derivatives **1** – **8** in CH_2Cl_2.

	$E_{1/2}$(Ox) [a]			$E_{1/2}$(Red) [a]		
1[b]	1.38[c]	1.06[c]	0.92[c]	-0.78 (123)	-1.40 (149)	---
2	---	1.33[c]	0.75[c]	-0.60[c]	-0.86[c]	-1.05[c, d]
3	1.16[c, e]	1.04[c]	0.66[c]	-0.72 (156)	-0.87[c]	-1.32[c, f]
4	1.29[c, g]	1.14[c]	0.88[c]	-0.78[c]	-1.22 (140)	-1.68
5	---	1.20[c]	0.94[c]	-0.82 (146)	-1.32 (109)	-1.44
6	1.26[c]	1.00[c]	0.83[c]	-0.72[c]	-1.12 (141)	-1.59
7	---	1.36	1.01 (91)	-0.78 (72)	-1.45 (16)	---
8	1.30[c]	1.10[c]	0.71 (61)	-0.92 (106)	-1.52 (193)	---

a) Potentials are in volts vs SCE for CH_2Cl_2deaerated solutions, 0.1 M of TBAP, recorded at 25 ± 1 °C at a sweep rate of 50 mV/s. The difference between cathodic and anodic peak potentials (mV) is given in parentheses. b) Interactions between compound **1** and ferrocene internal reference was observed. Values are reported without correction. Ferrocene value was measured before and after analysis of the compound to assess there was no drifting of the electrode. c) Irreversible. Determined by differential pulse voltammetry (DPV). d) Additional irreversible oxidation observed at -1.60 V. e) Additional irreversible oxidation observed at 1.36 V. f) Two additional irreversible reductions observed at -1.77 and -1.84 V. g) Additional irreversible oxidation was observed at 1.41 V.

Table 2.III – HOMO / LUMO levels (in eV) as determined by electrochemistry in CH_2Cl_2 and theoretical calculation along with corresponding ΔE for ADPM derivatives **1** – **8**.

	HOMO Redox	**LUMO Redox**	ΔE_{Redox} [a]	**HOMO Theo** [b]	**LUMO Theo** [b]	ΔE_{Theo} [a]	ΔE_{Opt} [d]
1	-5.87	-4.16	1.71	-5.45	-2.88	2.57	1.86
2	-5.70	-4.35	1.35	-5.67	-3.13	2.54	1.88
3	-5.61	-4.22	1.39	-5.74	-3.15	2.59	1.93
4	-5.82	-4.16	1.66	-5.52	-3.03	2.49	1.85
5	-5.89	-4.13	1.76	-5.58	-3.06	2.52	1.89
6	-5.77	-4.23	1.54	-5.59	-3.06	2.53	1.92
7	-5.95 [c]	-4.17 [c]	1.78	-5.62	-3.05	2.57	1.92
8	-5.66 [c]	-4.03 [c]	1.63	-5.23	-2.81	2.42	1.82

a) Energetic difference (ΔE, in eV) between the HOMO and the LUMO. b) Obtained by theoretical calculation (r-pbe0 / 6-311g(2d,p)) using the CPCM = CH_2Cl_2 polarizable conductor calculation model. c) Obtained from previous work.[34] d) ΔE qualitatively obtained from the red end of the Gaussian peak of the $\lambda_{max\ red}$ in DCM solution and converted in eV using the formula $E = hc / \lambda$.

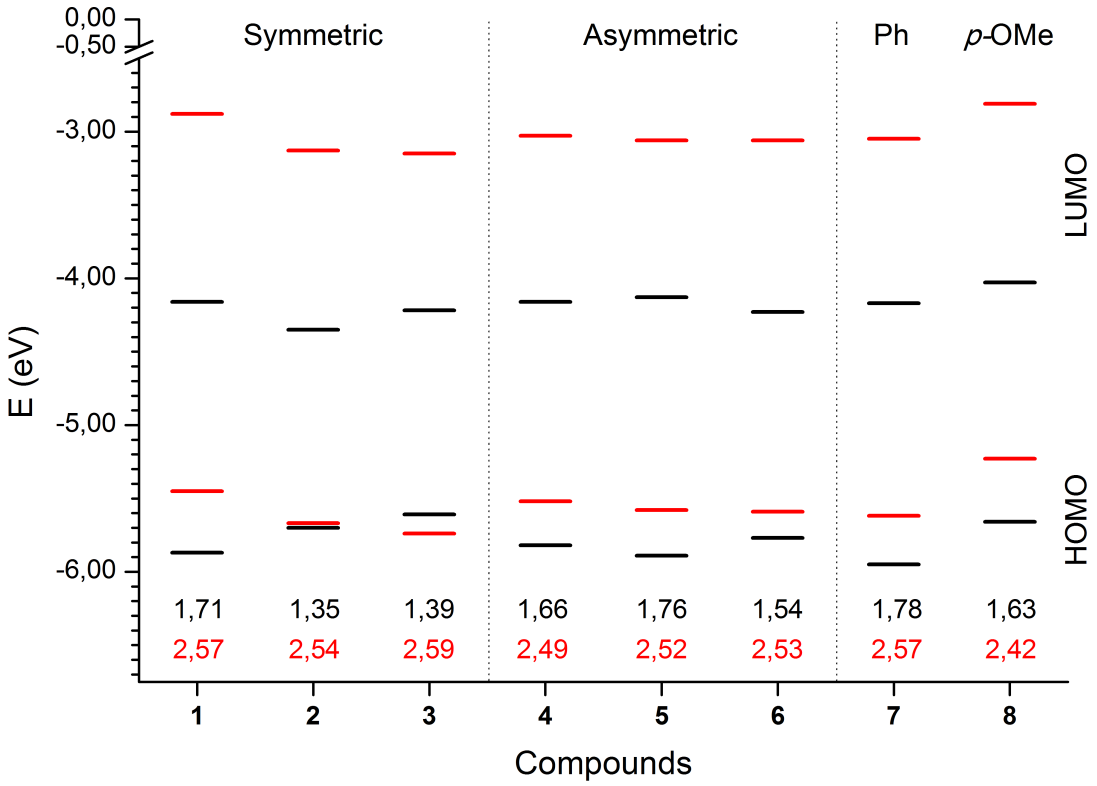

Figure 2.4 – Representation of HOMO / LUMO energy levels (in eV) of ADPM derivatives **1** – **8** as obtained by electrochemistry (black) and DFT calculations (red) along with their associated band-gaps (ΔE in eV; bottom values).

An overview of the electrochemical data for tetradentate ADPMs **1** – **6** (Table 2.2) suggests a relatively lower stability to oxidation in dichloromethane solution compared to the reference tetraphenyl ADPM **7**. It can be observed that both the first and second oxidation processes are irreversible plus at lower potential in all tetradentate derivatives when compared to the reference, where «pseudoreversible» one-electron processes occur at 1.01 (91) and 1.36 (137) V (mV) vs SCE. In fact, the first oxidation range from 0.66 V for the symmetric ADPM **3** up to 0.94 V for asymmetric ADPM **5** and the second oxidation from 1.00 V for asymmetric derivative **6** up to 1.33 V in the case of the symmetric **2**. In addition, decomposition still appears when a third process is

implied (ADPM **1** [1.38 V], **3** [1.16 V], **4** [1.29 V] and **6** [1.26 V]). As a comparison, the electron-rich *para*-methoxyphenyl ADPM **8** showed a pseudoreversible first oxidation at 0.71 (61) V (mV), while instability arises for the second and third ones [1.10 and 1.30 V, respectively]. Irreversible redox processes encountered in substituted ADPM derivatives might be the result of secondary reactions arising in their oxidized forms and are of concern for integration as light-harvesting or life science system components since they are more likely to decompose over time in such environment.[6, 79, 84, 85] It is noteworthy that previous work has shown that further coordination of ADPM chromophores onto various metallic centers (e.g. Co^{II}, Ni^{II}, Zn^{II} and Ir^{III}) or the metalloid borane tends to stabilize oxidation processes, therefore improving their potential for such applications.[29, 31, 35, 43, 45]

The situation is slightly different for reduction processes, where ADPM **1** and **5** that bear at least one methoxy group can stabilize in pseudoreversible fashion electrons added. Two processes are observed for ADPM **1** [-0.78 (123) and -1.40 (149) V (mV)] and three in the case of **5** [-0.82 (146), -1.32 (109) and -1.44 (122) V (mV)]. These derivatives behave similarly to the reference **7** [-0.78 (72) and -1.45 (16) V (mV)] and the corresponding tetra-methoxy ADPM **8** [-0.92 (106) and -1.52 (193) V (mV)]. The hydroxyl-substituted ADPM **2** presents three irreversible reductions [-0.60, -0.86 and -1.05 V], while ADPM **3** bearing electron-poor 2-pyridyl proximal substituents has a first pseudoreversible reduction at -0.72 (156) V (mV) and two other ones that are irreversibles at -0.87 and -1.32 V. On the contrary, ADPMs **4** and **6** both present a first reduction that is irreversible, while their second and third ones are pseudoreversibles [-0.78, -1.22 (140) and -1.68 (135) V (mV) for **4**; -0.72, -1.12 (141) and -1.59 (132) for **6**].

From these findings, it appears that derivatives bearing a proximal hydroxyl substituent (ADPM **2**, **4** and **6**) tend to have an irreversible first reduction process. On the other hand, reduction processes implying the methoxy and / or 2-pyridyl moieties present a reversible character. In addition, the presence of two *ortho*-methoxyphenyl groups in proximal positions encountered in ADPM **1** led to easier reductions processes than in the corresponding tetra-methoxy derivative **8**, as can be expected by less electron density present in the former case. Further insights on the molecular orbitals (MOs) implied in the various redox processes can be obtained by analysis of the electron density map provided by computational modelization, which will be discussed in the corresponding section.

Once converted in eV, the potentials of HOMO and LUMO obtained (Table 2.3) are relevant for a better understanding of the structure – property relationship uniting ADPM **1** – **8** and fine-tuning their incorporation in many applications. The HOMO level increases in the series of symmetric ADPMs **1** to **3** (Figure 2.4). This behavior seems counterintuitive based solely on the Hammett parameter analysis made before, since the latter, which bears 2-pyridyl proximal rings, should be the hardest to oxidize in the triad. This theoretical assumption is further supported by computational modelization (Figure 2.4). However, the instability of ADPM **3** observed during the synthesis tends to explain the empirical results obtained by electrochemistry. In the case of ADPM **1** and **2**, the expected trend is respected between the two since the presence of two electron-rich hydroxyl groups in **2** lead to an oxidation potential that is +0.17 eV more positive as compared to **1** (-5.70 vs -5.87 eV, respectively). Still, the bidentate ADPM **8** bearing four electron-rich –OMe groups remains the easiest to oxidize at -5.66 eV while the

tetraphenyl reference compound **7** is the hardest of the series at -5.95 eV. On their side, the asymmetric derivatives **4** to **6** exhibit interesting synergetic effects, with their HOMO levels staying within the range observed for their symmetric counterparts. ADPM **4** with one methoxy and one hydroxyl substituent groups have an HOMO located at -5.82 eV, in between the one of ADPM **1** and **2**. ADPM **5** with an *ortho*-methoxy group and a 2-pyridyl moiety is slightly harder to oxidize with a HOMO at -5.89 eV. While **4** should theoretically present the easiest oxidation of the asymmetric derivatives series due to the presence of two electron-donor substituents, it is ADPM **6** with the hydroxyl group and a 2-pyridyl moiety that happens to be with a HOMO at -5.77 eV. This odd behavior might be attributable to similar oxidation instability as it was observed for ADPM **3**.

Even though the first reduction potential obtained doesn't formally refer to the calculated LUMO energy level of a molecule, it still represents the ability of a molecule to stabilize a negative charge and therefore provides a first approximation of the LUMO's tendency in a series. One observation that can be made from the first reduction process in the series is that *ortho*-methoxy substituents in proximal position appears to have little effect on the LUMO position (-4.16 eV for ADPM **1** and **4**; -4.13 eV for ADPM **5**) as compared to the reference compound **7** (-4.17 eV). This observation suggests the reduction is happening far apart from the proximal moiety when a methoxy substituent is present. This is especially true when considering that ADPM **8** bearing *p*-methoxy groups (including two on the distal rings) was the harder to reduce at -4.03 eV. The presence of 2-pyridyl moieties makes the reduction process easier as can be expected from an electron-poor moiety, with empirical LUMO lying at -4.22 eV for

ADPM **3** and -4.23 eV for ADPM **6**. Finally, the relatively easy reduction at -4.35 eV encountered in ADPM **2** appears to result from instability of the dye since an irreversible peak was observed (Figures I.S14 and I.S15). As mentioned previously, introduction of a hydroxyl substituent led to such irreversibility for tetradentate derivatives **4** and **6** as well.

The combination of substituent effects on the HOMO and LUMO of tetradentate derivatives led to redox band-gaps (ΔE_{Redox}) ranging from 1.35 eV for symmetric ADPM **2** up to 1.76 eV for asymmetric ADPM **5**. Thus, a fine-tuning of up to 0.41 eV can therefore be achieved in the tetradentate ADPM series presented herein. As compared, a smaller variation of 0.15 eV was observed between the reference compound **7** (1.78 eV) and the electron-rich ADPM **8** equipped of four *p*-methoxy substituents (1.63 eV). Overall, electrochemistry revealed that an accurate control on the energy levels could be achieved through careful selection of the substituents nature, position and combination in ADPM derivatives.

2.5.4 – Computational Modelization

2.5.4.1 – DFT analysis

Computational modelization is a highly valuable tool to provide theoretical information at the molecular scale on relative energy levels, electronic distribution in molecular orbitals (MOs), absorption transitions and many other important physical properties such as electron transport within a family of derivatives.[86-88] Great insights have been provided lately for applications in OPV, DSSC and more broadly speaking for molecular design of organic chromophores with specific UV-vis to NIR absorption and emission properties.[89-96] Fortunately, systematic computational modelization and benchmarks have already been achieved for BF_2-chelated BODIPY and Aza-BODIPY derivatives in order to establish a general and validated procedure.[65, 97, 98]

DFT results obtained for the ADPM series investigated herein revealed interesting information on their relative HOMO / LUMO energy levels (Figure 2.4; Figure I.S24 of SI) and associated electron distribution (Figures 2.5 and 2.6; Table I.S1 of SI). The theoretical band gap ($\Delta E_{\text{Theo DFT}}$) ranges from 2.42 to 2.59 eV (Table 2.3), however, these values are considerably overvalued compared to empirical electrochemistry results (ΔE_{Redox} = 1.35 – 1.78 eV) rendering them difficult to compare directly. As mentioned previously, this is mainly due to the first reduction process probed by electrochemistry being different from the LUMO energy level calculated by DFT and to the instability observed in the tetradentate ADPM series. It is worth noting that the overall match is better when comparing $\Delta E_{\text{Theo DFT}}$ with optical band-gaps (ΔE_{Opt} = 1.82 – 1.96 eV) (Table 2.3), which are in line with the stability of the dyes observed by photophysical characterization.

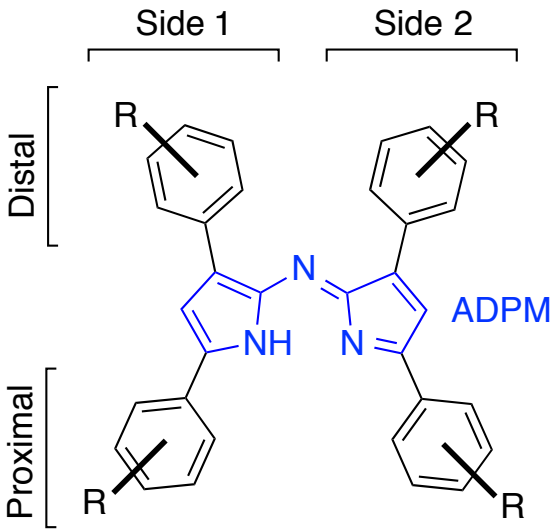

Figure 2.5 – Division of ADPM chromophore for computational modelization analysis

For reference compound **7**, the HOMO calculated at -5.62 eV is mainly centered on the dipyrrolic moiety (ADPM; 66 % of the electronic distribution) and to a lesser extent on the two proximal phenyls (13 % for proximal aryl 1 and 9 % for proximal aryl 2). The LUMO evaluated at -3.05 eV has less ADPM character (63 %), and therefore, transfers less of its electronic density toward proximal aryl 2 (from 9% in the HOMO up to 14%). Similarly, the three other phenyl groups have each 1% less to contribute to this reorganization. The effect of bearing four *para*-methoxyphenyl substituents in ADPM **8** appears to be a marked increase of +0.39 eV for HOMO level (-5.23 eV) and a +0.24 eV change for the LUMO (-2.81 eV), which corresponds to the relative trends observed by electrochemistry (+ 0.29 eV and + 0.14 eV, respectively; Table 2.3). In this latter symmetric derivative, the electron density of the HOMO is clearly decreased from the ADPM moiety (54 %) as compared to reference **7**, as a result of the four electron-rich substituents' contribution. On the other hand, the LUMO appears to be similarly divided on the substituents, with a small diminution of 2% on the ADPM moiety (61 %)

compared to the reference. From these insights, it appears that the first oxidation process observed by electrochemistry for **7** and **8** is most probably based on the ADPM moiety, and it is more affected by the proximal substituents than the distal ones. This last observation is truly stimulating as it provides an additional argument for the exploration of the tetradentate motif as a mean to shift the absorption of ADPMs toward the NIR. The first reduction process should accommodate an additional electron on the distal substituents since the electron density is at the lowest on these positions (about 6% in both derivatives). Another interesting observation to be made is that the HOMO's electronic distribution in both derivatives tends to avoid the bridging nitrogen of the dipyrrolic moiety, dividing the π-system of the chromophore into two sides each including a pyrrole with its proximal and distal aromatic substituents. Instead, it appears the LUMO have a restored delocalization throughout the ADPM moiety, even though the overall electronic distribution tends to be more equilibrated with the transfer of density toward the peripheral substituents. These observations are in line with the modelization results obtained for similar Aza-BODIPYs systems. For example, Russo *et al.* looked at derivatives bearing four phenyls and *para*-methoxyphenyl substituents in proximal or distal positions.[99] They found a similar behavior of electronic distribution in their symmetric derivatives. The group of Jacquemin obtained results consistent with those of Russo when comparing the frontier orbitals of an Aza-BODIPY bearing para-dimethylaminophenyl electron-donating substituents linked through an alkyne on the proximal phenyls.[65] Kobayashi *et al.* also made a direct comparison by computational modelization between a benzo-fused ADPM derivative and its BF_2-chelated counterpart that revealed a high similarity in the electronic distribution between corresponding HOMOs and LUMOs.[100] This latter example demonstrates the utility of comparing

ADPM frontier orbitals with their Aza-BODIPY derivatives and also supports the validity of using a similar computational approach. Finally, the computational results reported lately by Sauvé and coworkers at a lower level of theory for the reference ADPM **7** (PBE0/6-31G(d,p) in gas phase, i.e. no PCM; HOMO = -4.63 eV; LUMO = -3.29 eV; $\Delta E_{\text{Theo DFT}}$ = 1.33 eV)[101] reveals that the computational procedure used herein provides a better fit of about 1 eV for the HOMO (-5.62 eV calculated; -5.95 eV empirical).[102]

A visual overview of the symmetric tetradentate ADPM **1** – **3** (Figure 2.6) reveals very similar electronic distribution as compared to symmetric references **7** and **8**, where the ADPM moiety and the proximal aryls concentrate most of the density. This is further supported by the values of electronic distribution reported in Table I.S1 (SI). The presence of two *ortho*-methoxyphenyl substituents in ADPM **1** provides a HOMO resting at -5.45 eV, in between the two bidentate references. The electronic distribution analysis proved that the density is again transferred from the ADPM moiety (62%) to the proximal substituents (17% for proximal 1 and 11% for proximal 2) as compared to **7**. Essentially, the effect of *ortho*-methoxy substituents on the proximal positions of **1** appears to be similar to the one encountered for the *para*-methoxyphenyl in ADPM **8** (17% for proximal 1 and 12% for proximal 2), while the distal phenyls have a similar density to reference **7**. The theoretical LUMO lying at -2.88 eV is also in accordance with the two ADPMs of reference. The only difference is found in the electronic distribution, where the ADPM moiety of **1** (66 %; +3 % vs ADPM **7**) is affected by the presence of methoxy substituents in an opposite fashion than that observed for **8** (61 %; -2 % vs **7**). In fact, this increased of density on the central moiety in ADPM **1** comes

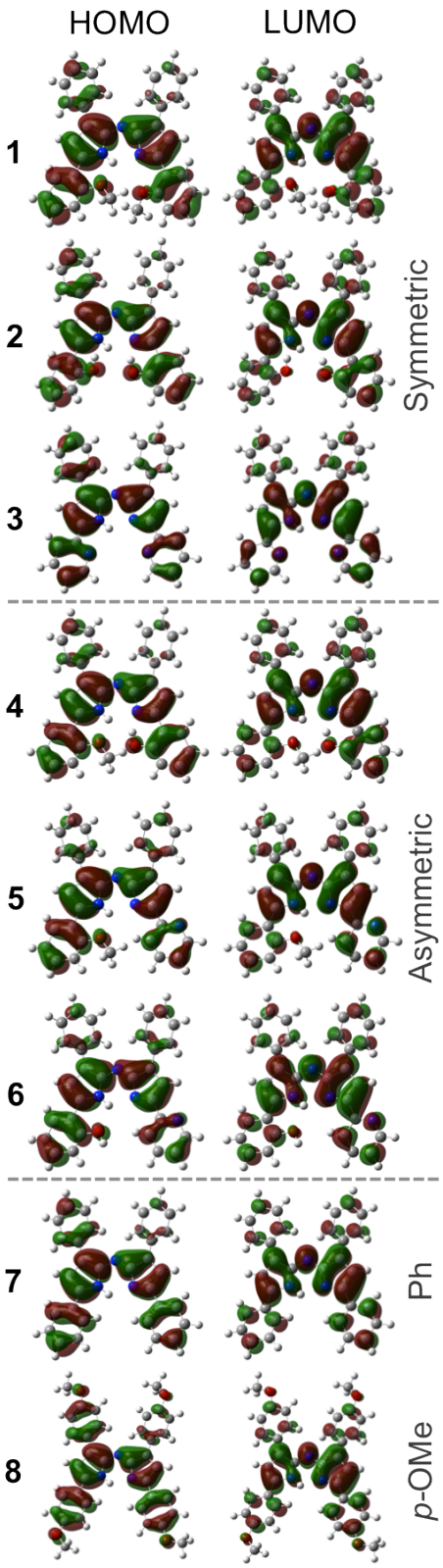

Figure 2.6 – Representation of HOMO and LUMO of ADPM derivatives **1** – **8** as obtained by DFT computational modelization (Isovalue = 0.02)

from the diminution found on the proximal aryl 1 substituent (8 %) as compared to reference **7** (12 %), a situation not observed in the *para*-substituted **8** (12 %).

ADPM **2** bearing *ortho*-hydroxyl groups present a calculated HOMO at -5.67 eV, lower than its methoxy counterpart ADPM **1**. This finding is in direct opposition with the Hammett parameter analysis and the electrochemical trend observed, where the first oxidation was 0.17 eV less positive (refer to Table 2.3). In fact, variations of electronic distribution on the ADPM moiety as compared to reference **7** between the tetradentate ADPM **1** (62%; -4 % vs **7**) and **2** (59%; -7 % vs **7**) is consistent with what should be expected from their relative electron-donating ability. However, the principal difference that explains this trend seems to be a better repartition between the two proximal groups in ADPM **2** (15 % for proximal aryl 1 and 16 % for proximal aryl 2). For instance, ADPM **1** had a distribution of 17% on proximal 1 and 11% on proximal 2, while reference **7** was at 13% and 9%, respectively. The LUMO at -3.13 eV present an electronic distribution very similar to ADPM **1**, even though it should lie at higher energy due to the electron-rich character of hydroxyl substituents.

As for symmetric tetradentate ADPM **3**, the observed trends are reversed due to the presence of electron-poor 2-pyridyl moieties. The theoretical HOMO, lying at -5.74 eV, is the lower of the symmetric derivatives as can be expected. The composition of this MO has an enriched electron density on the ADPM moiety (68 %; +2 % vs **7**) while the proximal substituents both decreased by 1% compared to the tetraphenyl reference. In the same vein, the LUMO at -3.15 eV is the easier to reduce. The electronic distribution of that MO is mainly centered on the ADPM moiety (70 %; +7 % vs **7**), with a lower density on both proximal 2-pyridyl moieties (7 and 11 %, respectively; -5 and -

3% vs **7**). From this last observation, it can be proposed with confidence that the first reduction process observed empirically should imply the pyridine rings.

With the analysis of symmetric derivatives in hand, the asymmetry encountered in tetradentate ADPM **4** – **6** ought to reveal interesting features, such as which substituent tends to affect a given frontier MO more. A look at the MO shapes in those derivatives appears to follow the general trends observed previously (Figure 2.6), i.e., a HOMO divided in two with no conjugation on the bridge of the ADPM moiety, while the LUMO restores the bridging conjugation. The tetradentate ADPM **4** bearing the two electron-donor groups studied herein has a calculated HOMO lying at -5.52 eV, in between its two corresponding symmetric derivatives **1** (-5.45 eV) and **2** (-5.67 eV) albeit being closer to the former. This is of interest since Hammett parameter analysis would suggest a higher character arising from the hydroxyl substituent to influence the first oxidation. Interestingly, one can rationalize that the methoxy group is attached to the "dominant" side 1, where the electronic density is concentrated and tends to be better delocalized throughout as opposed to side 2. This can be expressed by the fact proximal aryl 1 position is holding 17% of the density, the exact same amount found in ADPM **1**, while the hydroxyl group on proximal aryl 2 is at 14% and the ADPM moiety as a whole at 60%. Therefore, it can be considered that the *ortho*-methoxy substituent is dictating the nature of the HOMO. This is in good agreement with the empirical value obtained where the HOMO was at -5.82 eV, closer to the methoxy derivative **1** (-5.87 eV) than the hydroxyl derivative **2** (-5.70 eV). For the LUMO calculated at -3.03 eV, the situation appears to be reversed since it lies closer to the hydroxyl symmetric counterpart **2** (-3.13 eV) than the methoxy derivative **1** (-2.88 eV). However, it is difficult to draw any clear

trend from the electronic distribution since it is very similar for the two symmetric derivatives. Similarly, the electrochemical data reveals a first reduction for ADPM **4** at the exact same levels as **1** (-4.16 eV) that should indicate a methoxy-based LUMO, but the irreversibility of the process as encountered in all the hydroxyl derivatives recluses the MO assignment. When introducing a 2-pyridyl moiety in the system (ADPM **5** and **6**), calculated data tend to demonstrate that electronic distribution is mainly affected by this substituent, i.e., the effect of a methoxy or hydroxyl substituent is virtually equivalent. For instance, the calculated HOMO of ADPM **5** is lying at -5.58 eV, close to the -5.59 eV of ADPM **6**. Likewise, the LUMO of both adducts is at -3.06 eV and the exact same electronic distribution is found (ADPM moiety at 67%, proximal aryl 1 bearing the electron-rich substituent at 8% and proximal aryl 2 bearing the pyridyl at 11%). In this situation, calculations appear to be offset when compared to the electrochemical data, but the instability observed in solution again makes it difficult to draw direct conclusions other than the 2-pyridyl substituents having a dominant effect on frontier MOs.

Globally, the DFT modelization of tetradentate ADPM derivatives show that factors other than the classical Hammett parameter might be necessary to fully rationalize trends encountered in the series. Therefore, one still needs to consider insights provided by computational modelization, electrochemistry and structural analysis in order to have a complete representation of a given class of ADPMs and to further fine-tune their properties in a logical manner.

2.5.4.1 – TD-DFT analysis

A systematic TD-DFT analysis of ADPM chromophores is reported here for the first time using TD-BMK/6-311+G(2d,p). Calculated optical absorption bands, oscillator strengths (osc. strengths) and orbitals implied in the excitation for derivatives **1** – **8** are summarized in Tables I.S2 – I.S9 of SI. Assignment of the transition origin was further made based on this latter information in order to assess the effect of the various substituents studied herein. Figures I.S25 – I.S32 (see SI) present a superposition of the experimental spectrum obtained in dichloromethane solution and the calculated bands. At first glance, there is a very good correlation between the calculated transitions and empirical observations, which is very promising for *in silico* investigations of potential new ADPMs before their actual synthesis. The relative order of the $\lambda_{max\ red\ Theo}$ for the compounds fully respect the trend observed by UV-vis spectroscopy. A theoretical range of 547 nm for the electron-poor ADPM **3** up to 587 nm for the electron-rich ADPM **8** is found, which tends to underestimate the empirical results ($\lambda_{max\ red}$ ranging from 590 for **3** up to 627 nm for **8**, Table 2.1). This offset may vary between 34 and 55 nm from the experimental results, depending on the substituents involved and the shape of the absorption spectrum. Slight shifts obtained for the transition energies calculated by TD-DFT can be attributed to the use of a simple solvent model, i.e. no corrections beyond linear-response, and the use of vertical transition that neglect the vibronic effects.[103] The methodology outlined herein is based on the work of Jacquemin *et al.*, who previously benchmarked his work for $-BF_2^+$ chelated aza-BODIPYs.[65]

Looking more specifically at tetraphenyl reference **7**, the calculated transition at 551 nm (osc. strength = 0.885) corresponds to the observed $\lambda_{max\ red}$ = 590 nm, a

difference of -39 nm. As can be expected, this excitation is evaluated to be at 99% a HOMO to LUMO (H -> L) transition where the electronic density on the side 1 of the chromophore is transferred toward the side 2 and the ADPM moiety (refer to Figure 5). In comparison, ADPM **8** has a calculated transition at 587 nm (0.889) that corresponds to $\lambda_{max\ red}$ = 627 nm, a difference of -40 nm that is similar to what was observed for **7**. This 99% H -> L transition takes the density of three peripheral *p*-methoxyphenyl substituents toward the distal 2 substituent and ADPM moiety.

The analysis of tetradentate ADPM **1** – **6** show the H -> L transition to be characteristic of every $\lambda_{max\ red}$ transition observed (99 %), as expected. Based on this unambiguous behavior throughout the series and our main interest toward $\lambda_{max\ red}$ from a light-harvesting point of view, we used a simple MO analysis method rather than the difference density plot or the more advanced concept of natural transition orbitals (NTO).[104, 105] While these two last analysis methods can help represents transitions when a high degree of orbital mixing is obtained from the TD-DFT calculations,[103] no such mixing was found herein and the MO analysis method therefore appears faster and equally satisfactory to represent the $\lambda_{max\ red}$ transitions. The symmetric derivatives **1** and **2,** having electron density transferred from the conjugated side 1 toward the ADPM moiety, differ from the electron-poor 2-pyridyl derivative **3,** where the transfer is additionally delocalized over the rest of side 2. Interestingly, TD-DFT results are in good agreement with the Hammett parameter trend as the calculated transition of hydroxyl-substituted **2** at 560 nm (0.834) shows a plus 9 nm difference compared to reference **7**, while methoxy bearing ADPM **1** transition found at 553 nm (0.834) is only plus 2 nm. Similarly, ADPM **3** with electron-withdrawing substituents is calculated at

547 nm (0.877), a minus 4 nm hypsochromic difference. When asymmetry is introduced, both substituents contribute to the $\lambda_{max\ red\ Theo}$. ADPM **4** has a calculated transition at 571 nm (0.861). This is a +20 nm difference compared to **7** arising from a synergetic effect of the methoxy and hydroxyl proximal substituents, i.e. the difference is twice as high as the sum of their individual contributions found previously in symmetric derivatives. This behavior might be attributable to a push-pull effect, especially when looking at the introduction of the electron-withdrawing 2-pyridyl moiety in ADPM **5** and **6**. In these latter derivatives, the donor substituent involved transfers the electronic density toward the side bearing the 2-pyridyl group in addition to the ADPM moiety. In this way, the calculated difference still stands at plus 15 nm for adduct **5** and plus 13 nm for **6**.

The observed $\lambda_{max\ violet}$ prominent in compounds bearing methoxy or hydroxyl substituents, including *para*-substituted ADPM **8**, attracted our attention since it represents an efficient way to improve the overall panchromaticity of ADPM chromophores for light-harvesting applications. Maxima of this new absorption band range between 407 nm for **1** and 418 nm for **6**, with extinction coefficients (ε) evaluated at 3.9 – 10 x 10^3 $M^{-1}cm^{-1}$ for the series. The systematic assignation of the excitation calculated by TD-DFT to their corresponding observed absorption band was used to unravel origin of this band (Tables I.S2 – I.S9). First looking at the reference, tetraphenyl ADPM **7** present more or less a plateau in the 370 – 430 nm spectrum region, with an ε ~ 3.75 x 10^{-3} $M^{-1}cm^{-1}$. Two calculated transitions are found in this range at 372 nm (osc. strength = 0.190) and 428 nm (0.059) to explain the non-zero absorption. They are, respectively, H-2 -> L (97%) and H-1 -> L (96%) excitations taking the electronic density from the distal 1 and 2 phenyls toward their proximal

counterparts and the ADPM moiety. Careful analysis of the data revealed the apparition of $\lambda_{max\ violet}$ in ADPMs **1**, **2**, **4** – **6** and **8** is attributable in each case to a significant increase in the oscillator strength of at least one of these two transitions (up to 249% compared to **7**). In addition, a new transition is found in all these derivatives implying electronic transfer from the peripheral substituents toward the ADPM moiety upon photoexcitation. On the other hand, the ADPM **3** with 2-pyridyl proximal substituents with no observed $\lambda_{max\ violet}$ have only two calculated transitions at 381 nm (0.164) and 441 nm (0.064). These transitions are bathochromically shifted compared to reference **7**, as can be expected from the electron-withdrawing effect, but with similar intensity of oscillator strengths (86% and 108% of the reference value, respectively).

2.5.5 – X-Ray Diffraction

Crystals suitable for X-ray diffraction studies were obtained for compounds **1**, **3**, **4** and **5**.[106] Solid-state structure and refinement data are presented in figures 7 – 8 and SI. All the four compounds crystallized in the monoclinic crystal system, space groups: $P2_1/n$, $P2_1$, Pc, and $P2_1/c$, respectively (Table I.S10). For ADPM **3**, only isotropic refinement of the structure was performed due to poor crystal quality and only the connectivity of the atoms is discussed herein (Figure 2.7 bottom; see SI for more details). However, the identity of this last compound was further confirmed by mass spectrometry performed on the same crystal sample (see experimental section 2.4).

For compounds **1**, **4** and **5**, an analysis of bond lengths in the ADPM unit (Table I.S11) confirms the conjugated nature of this moiety, as found for similar compounds.[35, 49] In addition, the observed planarity of the central pyrrolic rings is another common feature of the ADPM derivatives.[35, 37] The tilt angle between the planes of the central pyrrolic rings is 1.3(1)° in ADPM **8** bearing *para*- substituents on the aryl rings.[35] In comparison, compounds **1**, **4**, and **5** all featuring *ortho*- substituted proximal aryl rings present slight deviations from planarity of the pyrrolic rings, with values for corresponding tilt angles of 10.9(1)°, 8.0(1)°, and 9.8(1)°, respectively (Table I.S11).

Conventional H-bonding and weak H-bonding (intramolecular and intermolecular), together with π – π and π – H-D (D = C(sp2), N, O) interactions can be identified as packing forces in the three structures. The intramolecular H-bonding patterns in **1**, **4**, and **5** are represented in figures 7 and 8. The analysis of the corresponding numeric values (Table I.S12) show conventional and weak H-bonds.[107] A

3-center bifurcated H-bonding pattern (N1—H1···O1 and N1—H1···N3) is observed for each of the three structures.[108]

The orientation of aryl rings with respect to the ADPM moiety is dictated by the steric tension induced in the substitution pattern, as well as attractive and repulsive intramolecular and intermolecular H-bonding and π – π interactions. Values of the tilt angles between the plane of the ADPM moiety and the plane of the aryl rings are shown in the SI (Table I.S11). As a general observation, the proximal aryl rings are less tilted with respect to the ADPM plane than the distal ones for the three structures (with one exception: Ar_1 and Ar_2 in compound **1** – see Figure 1 for the nomenclature). The position of the *ortho* substituents on the proximal aryl rings is endo (Ar_1) / exo (Ar_4) in case of **1** and **5**, and becomes endo (Ar_1) / endo (Ar_4) for compound **4**, most probably due to the extended H-bonding pattern specific to **4** (Figures 2.8 and I.S33). The 'opening' angles of the ADPM moiety (i.e. C1-N2-C17, N1-C1-N2 and N2-C17-N3) are higher in this last compound, as can be expected from the more sterically hindered conformation (Table I.S11).

Compound **4** crystallized with four molecules in the asymmetric unit showing similar conformations, bond lengths and angles. The proximal aryl substituents and the ADPM moiety are very close to planarity, with values for the tilt angles between the corresponding planes ranging between 1.2(1) – 4.2(1)°. The only notable difference among the four molecules is observed at the level of distal aryl rings, which present different orientations maximizing the π – H-C(sp^2) intermolecular interactions between two adjacent molecules (Figure S.33).

The enhanced rigidity obtained by the specific intramolecular H-bonding pattern, the global planarity in the molecule and the stronger $\pi - \pi$ and π – H-C(sp^2) interactions can all be related to the photophysical properties of the system. For example, red-shifted maxima and higher molar absorptivity observed in the absorption properties of compound **4** (see Spectroscopic Properties section) are indicative that these specific interactions can be partially maintained in solution.

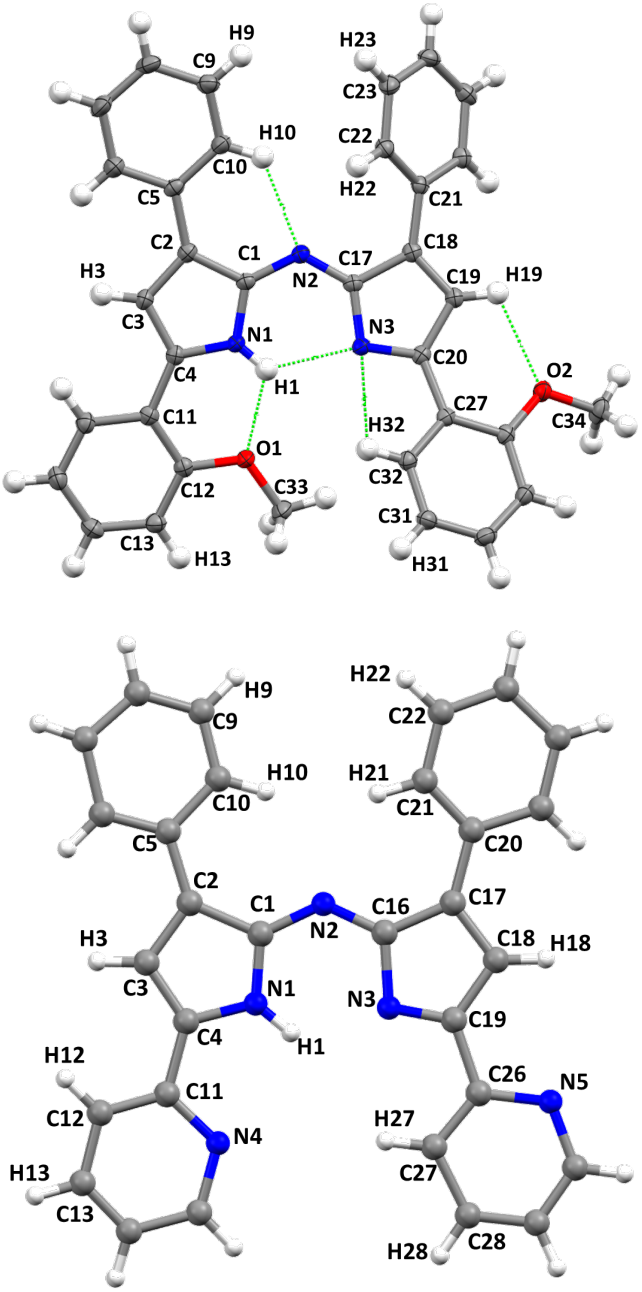

Figure 2.7 – Solid-state structures of symmetric ADPM **1** (top; ellipsoids shown at 50% probability level; intramolecular H-bonds represented in green) and ADPM **3** (bottom; isotropic model).

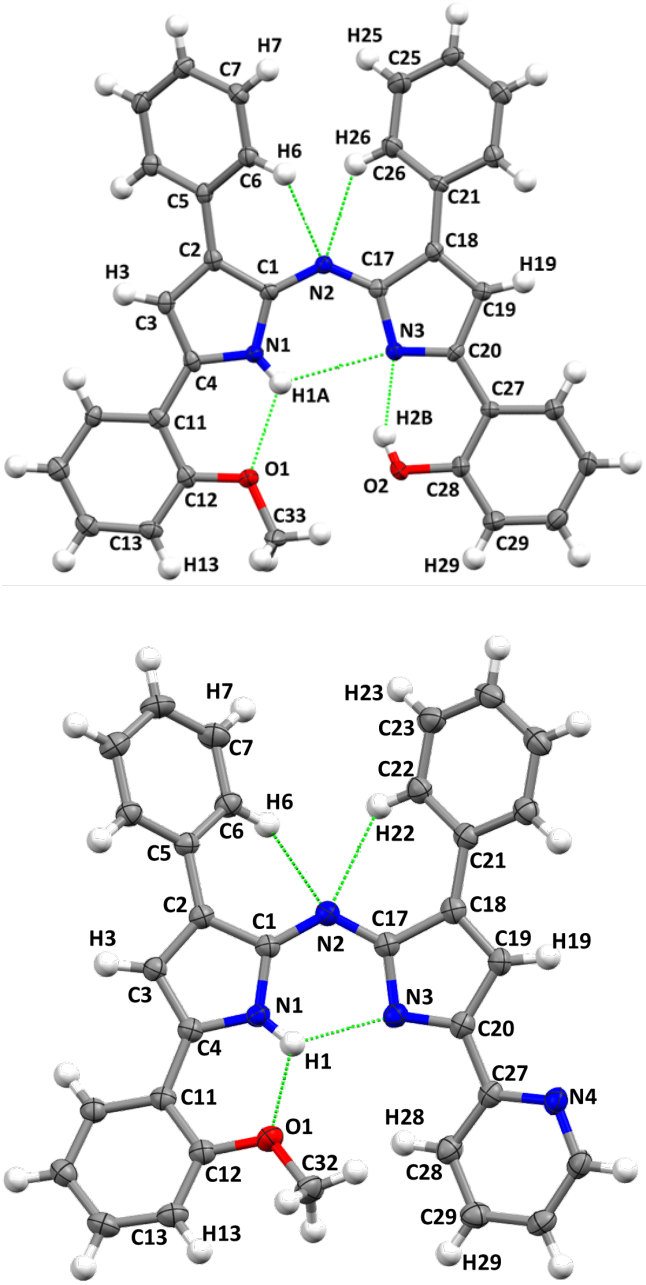

Figure 2.8 – Solid-state structures of asymmetric ADPM **4** (top; only one of the four molecules in the asymmetric unit is presented) and ADPM **5** (bottom; ellipsoids shown at 50% probability level; intramolecular H-bonds represented in green).

2.6 – Conclusions

In conclusion, the systematic study of symmetric and asymmetric tetradentate ADPM chromophores **1** – **6** was achieved and compared with reference bidentate compounds **7** and **8** in order to gain information on their structure – property relationship. Four of the derivatives have never been reported before and symmetric ADPM **3** represent the first example of 2-pyridyl moieties installed in the proximal position. This comparative investigation was made possible through a new straightforward synthetic approach to access asymmetric derivatives **4 – 6** that avoid the tedious heterocycle formation of nitroso-pyrrole intermediates. Tetradentate ADPMs were studied by UV-vis spectroscopy, revealing the possibility of fine-tuning the absorption maxima from 598 up to 619 nm in the red part of the spectrum and to improve harvesting of violet light (~410 nm) through variation of the proximal substituents combination, although no emission was observed. Further characterization was made by electrochemistry in order to obtain the energy levels of the chromophores, which is crucial for their integration into various photoactive materials. The experimental data showed a tendency for degradation upon redox processes in solution, which might be addressed by coordination of the ligands to metal ions as was previously reported. X-Ray structural analysis was made on previously reported ADPM **1** and newly synthetized ADPM **3 – 5** and these structural data were used for computational modelization of the series. DFT theoretical calculations at the PBE0 / 6-311G(2d,p) level provided information on the factors affecting frontier molecular orbitals and energy levels observed empirically. The TD-DFT protocol used for the first time on ADPM chromophores, TD-BMK/6-311+G(2d,p) (PCM = CH_2Cl_2), was able to establish a good

correlation with the observed absorption spectrum and explained the improved absorption of violet light. These compounds are especially of interest since the tetradentate motifs developed herein allow for a bio-mimicry of metalloporphyrinoids, without the demanding synthesis of the macrocycles. Noteworthy, the π-conjugation extension made possible through metal-mediated planarization should induce bathochromic shift toward the NIR, a critical region for light-harvesting applications. In addition, the coordination mode ranging from XL_3 to X_3L possible with tetradentate ADPM **1** – **6** offers an unsurpassed versatility. From there, multiple applications can be envisioned, varying from light-harvesting / photoactive materials to catalysts, sensors and even beyond.

2.7 – Acknowledgements

GSH thanks the Natural Sciences and Engineering Research Council of Canada, the Centre for Self-Assembled Chemical Structures (CSACS), the Centre in Green Chemistry and Catalysis (CGCC) and the Université de Montréal (UdeM) for financial support. AB is thankful of NSERC, FQRNT and Saint-Jean Photochemicals Inc. (sjpc.com) for funding through a BMP-Innovation grant and to UdeM for an excellence grant. An acknowledgment goes to Compute Canada / Calcul Canada for access through their national supercomputing platform at University of Manitoba's Grex infrastructure supported by Westgrid. AB is grateful to Anne-Catherine Bédard and Daniel Chartrand for useful scientific discussions. The authors are also appreciative to the NMR, Mass Spectroscopy and X-ray laboratories of UdeM plus Prof. Christian Reber for access to his UV/vis instrument.

2.8 – Associated content

Supporting Information

NMR and HR-ESIMS data for newly synthesized ADPM **3** – **6**; cyclic and differential pulse voltammograms for ADPM **1** – **6**; DFT and TD-DFT computational modelization data for ADPM **1** – **8**; crystal data and details of the structure determination for **1**, **3**, **4** and **5** (CCDC Numbers 1005388 – 1005391) along with packing diagram of **4**.

2.9 – Bibliography

1. Rogers, M. A. T. *Nature* **1943**, *151*, 504.
2. Rogers, M. A. T. *J. Chem. Soc.* **1943**, 590.
3. Rogers, M. A. T.; (Imperial Chemical Industries Ltd.). US, 1945.
4. Bessette, A.; Hanan, G. S. *Chem. Soc. Rev.* **2014**, *43*, 3342.
5. Loudet, A.; Burgess, K. *Chem. Rev.* **2007**, *107*, 4891.
6. Boens, N.; Leen, V.; Dehaen, W. *Chem. Soc. Rev.* **2012**, *41*, 1130.
7. Gawley, R. E.; Mao, H.; Haque, M. M.; Thorne, J. B.; Pharr, J. S. *J. Org. Chem.* **2007**, *72*, 2187.
8. Coskun, A.; Yilmaz, M. D.; Akkaya, E. U. *Org. Lett.* **2007**, *9*, 607.
9. Jokic, T.; Borisov, S. M.; Saf, R.; Nielsen, D. A.; Kühl, M.; Klimant, I. *Anal. Chem.* **2012**, *84*, 6723.
10. Yuan, L.; Lin, W.; Zheng, K.; He, L.; Huang, W. *Chem. Soc. Rev.* **2013**, *42*, 622.
11. Collado, D.; Vida, Y.; Najera, F.; Perez-Inestrosa, E. *RSC Adv.* **2014**, *4*, 2306.
12. Awuah, S. G.; You, Y. *RSC Adv.* **2012**, *2*, 11169.
13. Batat, P.; Cantuel, M.; Jonusauskas, G.; Scarpantonio, L.; Palma, A.; O'Shea, D. F.; McClenaghan, N. D. *J. Phys. Chem. A* **2011**, *115*, 14034
14. Gorman, A.; Killoran, J.; O'Shea, C.; Kenna, T.; Gallagher, W. M.; O'Shea, D. F. *J. Am. Chem. Soc.* **2004**, *126*, 10619.
15. Tanaka, K.; Chujo, Y. *Macromol. Rapid Commun.* **2012**, *33*, 1235.
16. Benstead, M.; Mehl, G. H.; Boyle, R. W. *Tetrahedron* **2011**, *67*, 3573.
17. Nepomnyashchii, A. B.; Bard, A. J. *Acc. Chem. Res.* **2012**, *45*, 1844.
18. Ma, X.; Mao, X.; Zhang, S.; Huang, X.; Cheng, Y.; Zhu, C. *Polym. Chem.* **2013**, *4*, 520.
19. Ma, X.; Jiang, X.; Zhang, S.; Huang, X.; Cheng, Y.; Zhu, C. *Polym. Chem.* **2013**, *4*, 4396.
20. Tekin, S.; Küçüköz, B.; Yılmaz, H.; Sevinç, G.; Hayvalı, M.; Gul Yaglioglu, H.; Elmali, A. *J. Photochem. Photobiol., A* **2013**, *256*, 23.
21. Ziessel, R.; Harriman, A. *Chem. Commun.* **2011**, *47*, 611.
22. Ziessel, R.; Ulrich, G.; Haefele, A.; Harriman, A. *J. Am. Chem. Soc.* **2013**, *135*, 11330.
23. Lee, C. Y.; Farha, O. K.; Hong, B. J.; Sarjeant, A. A.; Nguyen, S. T.; Hupp, J. T. *J. Am. Chem. Soc.* **2011**, *133*, 15858.
24. Shi, W.-J.; El-Khouly, M. E.; Ohkubo, K.; Fukuzumi, S.; Ng, D. K. P. *Chem. Eur. J.* **2013**, *19*, 11332.
25. D'Souza, F.; Amin, A. N.; El-Khouly, M. E.; Subbaiyan, N. K.; Zandler, M. E.; Fukuzumi, S. *J. Am. Chem. Soc.* **2012**, *134*, 654.
26. Yuan, M.; Yin, X.; Zheng, H.; Ouyang, C.; Zuo, Z.; Liu, H.; Li, Y. *Chem. Asian J.* **2009**, *4*, 707.
27. Amin, A. N.; El-Khouly, M. E.; Subbaiyan, N. K.; Zandler, M. E.; Fukuzumi, S.; D'Souza, F. *Chem. Commun.* **2012**, *48*, 206.
28. Gobeze, H. B.; Bandi, V.; D'Souza, F. *Phys. Chem. Chem. Phys.* **2014**, *16*, 18720.
29. Senevirathna, W.; Sauvé, G. *J. Mater. Chem. C* **2013**, *1*, 6684.

30. Mueller, T.; Gresser, R.; Leo, K.; Riede, M. *Sol. Energy Mater. Sol. Cells* **2012**, *99*, 176.
31. Gao, L.; Tang, S.; Zhu, L.; Sauvé, G. *Macromolecules* **2012**, *45*, 7404.
32. Gao, L.; Senevirathna, W.; Sauvé, G. v. *Org. Lett.* **2011**, *13*, 5354.
33. Leblebici, S. Y.; Chen, T. L.; Olalde-Velasco, P.; Yang, W.; Ma, B. *ACS Appl. Mater. Interfaces* **2013**, *5*, 10105.
34. Khan, T. K.; Sheokand, P.; Agarwal, N. *Eur. J. Org. Chem.* **2014**, 1416.
35. Bessette, A.; Ferreira, J. G.; Giguère, M.; Bélanger, F.; Désilets, D.; Hanan, G. S. *Inorg. Chem.* **2012**, *51*, 12132.
36. Sakamoto, R.; Kusaka, S.; Kitagawa, Y.; Kishida, M.-a.; Hayashi, M.; Takara, Y.; Tsuchiya, M.; Kakinuma, J.; Takeda, T.; Hirata, K.; Ogino, T.; Kawahara, K.; Yagi, T.; Ikehira, S.; Nakamura, T.; Isomura, M.; Toyama, M.; Ichikawa, S.; Okumura, M.; Nishihara, H. *Dalton Trans.* **2012**, *41*, 14035.
37. Palma, A.; Gallagher, J. F.; Mueller-Bunz, H.; Wolowska, J.; McInnes, E. J. L.; O'Shea, D. F. *Dalton Trans.* **2009**, 273.
38. Teets, T. S.; Partyka, D. V.; Updegraff, J. B.; Gray, T. G. *Inorg. Chem.* **2008**, *47*, 2338.
39. Deligonul, N.; Gray, T. G. *Inorg. Chem.* **2013**, *52*, 13048.
40. Gao, L.; Deligonul, N.; Gray, T. G. *Inorg. Chem.* **2012**, *51*, 7682.
41. Teets, T. S.; Updegraff, J. B., III; Esswein, A. J.; Gray, T. G. *Inorg. Chem.* **2009**, *48*, 8134.
42. Partyka, D. V.; Deligonul, N.; Washington, M. P.; Gray, T. G. *Organometallics* **2009**, *28*, 5837.
43. Deligonul, N.; Browne, A. R.; Golen, J. A.; Rheingold, A. L.; Gray, T. G. *Organometallics* **2014**, *33*, 637.
44. Berhe, S. A.; Rodriguez, M. T.; Park, E.; Nesterov, V. N.; Pan, H.; Youngblood, W. J. *Inorg. Chem.* **2014**, *53*, 2346.
45. McLean, T. M.; Telfer, S. G.; Elliott, A. B. S.; Gordon, K. C.; Lein, M.; Waterland, M. R. *Dalton Trans.* **2014**, *43*, 17746.
46. Zhao, W.; Carreira, E. M. *Chem. - Eur. J.* **2006**, *12*, 7254.
47. Zhao, W.; Carreira, E. M. *Angew. Chem., Int. Ed.* **2005**, *44*, 1677.
48. Wu, Y.; Cheng, C.; Jiao, L.; Yu, C.; Wang, S.; Wei, Y.; Mu, X.; Hao, E. *Org. Lett.* **2014**, *16*, 748.
49. Loudet, A.; Bandichhor, R.; Burgess, K.; Palma, A.; McDonnell, S. O.; Hall, M. J.; O'Shea, D. F. *Org. Lett.* **2008**, *10*, 4771.
50. Scholes, G. D.; Fleming, G. R.; Olaya-Castro, A.; van Grondelle, R. *Nat. Chem.* **2011**, *3*, 763.
51. Hill, J. P.; D'Souza, F.; Ariga, K. In *Supramolecular Chemistry*; John Wiley & Sons, Ltd: 2012.
52. Fukuzumi, S.; Honda, T.; Kojima, T. *Coord. Chem. Rev.* **2012**, *256*, 2488.
53. Nemykin, V. N.; Galloni, P.; Floris, B.; Vecchi, A. *J. Porphyrins Phthalocyanines* **2013**, *17*, 165.
54. Li, C.; Ulrich, M.; Liu, X.; Wurst, K.; Muller, T.; Krautler, B. *Chem. Sci.* **2014**, *5*, 3388.
55. Hennessy, E. T.; Betley, T. A. *Science* **2013**, *340*, 591.
56. Prier, C. K.; Rankic, D. A.; MacMillan, D. W. C. *Chem. Rev.* **2013**, *113*, 5322.
57. Whiteoak, C. J.; Salassa, G.; Kleij, A. W. *Chem. Soc. Rev.* **2012**, *41*, 622.

58. Rausaria, S.; Kamadulski, A.; Rath, N. P.; Bryant, L.; Chen, Z.; Salvemini, D.; Neumann, W. L. *J. Am. Chem. Soc.* **2011**, *133*, 4200.
59. Zhang, X.; Yu, H.; Xiao, Y. *J. Org. Chem.* **2012**, *77*, 669.
60. Grossi, M.; Palma, A.; McDonnell, S. O.; Hall, M. J.; Rai, D. K.; Muldoon, J.; O'Shea, D. F. *J. Org. Chem.* **2012**, *77*, 9304.
61. Hall, M. J.; McDonnell, S. O.; Killoran, J.; O'Shea, D. F. *J. Org. Chem.* **2005**, *70*, 5571.
62. In *Comprehensive Heterocyclic Chemistry*; Bird, C. W., Cheeseman, G. W. H., Eds.; Pergamon: Oxford, 1984; Vol. 4, p 209.
63. Loudet, A.; Bandichhor, R.; Wu, L.; Burgess, K. *Tetrahedron* **2008**, *64*, 3642.
64. Buryakovskaya, E. G.; Tsukerman, S. V.; Lavrushkin, V. F. *Russ. J. Phys. Chem.* **1969**, *43*, 477.
65. Le Guennic, B.; Maury, O.; Jacquemin, D. *Phys. Chem. Chem. Phys.* **2012**, *14*, 157.
66. Frisch, M. J.; Trucks, G. W.; Schlegel, H. B.; Scuseria, G. E.; Robb, M. A.; Cheeseman, J. R.; Scalmani, G.; Barone, V.; Mennucci, B.; Petersson, G. A.; Nakatsuji, H.; Caricato, M.; Li, X.; Hratchian, H. P.; Izmaylov, A. F.; Bloino, J.; Zheng, G.; Sonnenberg, J. L.; Hada, M.; Ehara, M.; Toyota, K.; Fukuda, R.; Hasegawa, J.; Ishida, M.; Nakajima, T.; Honda, Y.; Kitao, O.; Nakai, H.; Vreven, T.; J. A. Montgomery, J.; Peralta, J. E.; Ogliaro, F.; Bearpark, M.; Heyd, J. J.; Brothers, E.; Kudin, K. N.; Staroverov, V. N.; Kobayashi, R.; Normand, J.; Raghavachari, K.; Rendell, A.; Burant, J. C.; Iyengar, S. S.; Tomasi, J.; Cossi, M.; Rega, N.; Millam, J. M.; Klene, M.; Knox, J. E.; Cross, J. B.; Bakken, V.; Adamo, C.; Jaramillo, J.; Gomperts, R.; Stratmann, R. E.; Yazyev, O.; Austin, A. J.; Cammi, R.; Pomelli, C.; Ochterski, J. W.; Martin, R. L.; Morokuma, K.; Zakrzewski, V. G.; Voth, G. A.; Salvador, P.; Dannenberg, J. J.; Dapprich, S.; Daniels, A. D.; Farkas, Ö.; Foresman, J. B.; Ortiz, J. V.; Cioslowski, J.; Fox, D. J.; Gaussian Inc.: Wallingford CT 2009.
67. Perdew, J. P.; Burke, K.; Ernzerhof, M. *Phys. Rev. Lett.* **1996**, *77*, 3865.
68. Perdew, J. P.; Burke, K.; Ernzerhof, M. *Phys. Rev. Lett.* **1997**, *78*, 1396.
69. Adamo, C.; Barone, V. *J. Chem. Phys.* **1999**, *110*, 6158.
70. Tomasi, J.; Mennucci, B.; Cammi, R. *Chem. Rev.* **2005**, *105*, 2999.
71. Boese, A. D.; Martin, J. M. L. *J. Chem. Phys.* **2004**, *121*, 3405.
72. Dennington, R.; Keith, T.; Millam, J.; Eppinnett, K.; Hovell, W. L.; Gilliland, R.; Semichem Inc.: Shawnee Mission KS, 2003.
73. O'Boyle, N. M.; Tenderholt, A. L.; Langner, K. M. *J. Comp. Chem.* **2008**, *29*, 839.
74. Chemissian, a computer program to analyze and visualize quantum-chemical calculations, by L. Skripnikov. For the current version, see www.chemissian.com
75. Blay, G.; Incerti, C.; Muñoz, M. C.; Pedro, J. R. *Eur. J. Org. Chem.* **2013**, 1696.
76. Removal of the solvent at 30°C in vacuo led to the discoloration of the solution, i.e. degradation of the chromophore.
77. To note, it was mandatory to solubilize both partner in warm EtOH before adding the ammonium source, otherwise, the undesired formation of the symmetric ADPM 2 resulting from the nitroketone partner was observed to a greater extend.
78. Hansch, C.; Leo, A.; Taft, R. W. *Chem. Rev.* **1991**, *91*, 165.
79. Mishra, A.; Bäuerle, P. *Angew. Chem., Int. Ed.* **2012**, *51*, 2020.

80. Li, Y. *Acc. Chem. Res.* **2012**, *45*, 723.
81. Kolemen, S.; Bozdemir, O. A.; Cakmak, Y.; Barin, G.; Erten-Ela, S.; Marszalek, M.; Yum, J.-H.; Zakeeruddin, S. M.; Nazeeruddin, M. K.; Grätzel, M.; Akkaya, E. U. *Chem. Sci.* **2011**, *2*, 949.
82. Blouin, N.; Michaud, A.; Gendron, D.; Wakim, S.; Blair, E.; Neagu-Plesu, R.; Belletête, M.; Durocher, G.; Tao, Y.; Leclerc, M. *J. Am. Chem. Soc.* **2008**, *130*, 732.
83. Li, W.; Li, L.; Xiao, H.; Qi, R.; Huang, Y.; Xie, Z.; Jing, X.; Zhang, H. *RSC Adv.* **2013**, *3*, 13417.
84. Gendron, D.; Leclerc, M. *Energy Environ. Sci.* **2011**, *4*, 1225.
85. Son, H. J.; Carsten, B.; Jung, I. H.; Yu, L. *Energy Environ. Sci.* **2012**, *5*, 8158.
86. Zhao, Y.; Truhlar, D. G. *Acc. Chem. Res.* **2008**, *41*, 157.
87. Geerlings, P.; Fias, S.; Boisdenghien, Z.; De Proft, F. *Chem. Soc. Rev.* **2014**, *43*, 4989.
88. Yoshizawa, K. *Acc. Chem. Res.* **2012**, *45*, 1612.
89. Hachmann, J.; Olivares-Amaya, R.; Jinich, A.; Appleton, A. L.; Blood-Forsythe, M. A.; Seress, L. R.; Roman-Salgado, C.; Trepte, K.; Atahan-Evrenk, S.; Er, S.; Shrestha, S.; Mondal, R.; Sokolov, A.; Bao, Z.; Aspuru-Guzik, A. *Energy Environ. Sci.* **2014**, *7*, 698.
90. Pastore, M.; Fantacci, S.; De Angelis, F. *J. Phys. Chem. C* **2013**, *117*, 3685.
91. Preat, J.; Jacquemin, D.; Perpete, E. A. *Energy Environ. Sci.* **2010**, *3*, 891.
92. Liu, X.; Xu, Z.; Cole, J. M. *J. Phys. Chem. C* **2013**, *117*, 16584.
93. Jacquemin, D.; Planchat, A.; Adamo, C.; Mennucci, B. *J. Chem. Theo. Comp.* **2012**, *8*, 2359.
94. Qi, D.; Jiang, J. *J. Phys. Chem. A* **2011**, *115*, 13811.
95. Fabian, J. *Dyes Pigm.* **2010**, *84*, 36.
96. Jacquemin, D.; Perpète, E. A.; Ciofini, I.; Adamo, C. *Acc. Chem. Res.* **2009**, *42*, 326.
97. Chibani, S.; Le Guennic, B.; Charaf-Eddin, A.; Laurent, A. D.; Jacquemin, D. *Chem. Sci.* **2013**, *4*, 1950.
98. Chibani, S.; Le Guennic, B.; Charaf-Eddin, A.; Maury, O.; Andraud, C.; Jacquemin, D. *J. Chem. Theo. Comp.* **2012**, *8*, 3303.
99. Quartarolo, A. D.; Russo, N.; Sicilia, E. *Chem. - Eur. J.* **2006**, *12*, 6797.
100. Lu, H.; Shimizu, S.; Mack, J.; Shen, Z.; Kobayashi, N. *Chem. Asian J.* **2011**, *6*, 1026.
101. Senevirathna, W.; Daddario, C. M.; Sauvé, G. *J. Phys. Chem. Lett.* **2014**, *5*, 935.
102. Indeed, one has to keep in mind that formal evaluation of redox properties in solution by computational modelization generally demand, in addition to the geometry optimization of the ground state molecule under a polarization continuum, a look at oxidized and reduced forms in order to account for molecular and solvent reorganization energies. While such a highly demanding procedure tends to be more accurate, the ratter simple DFT procedure PBE0/6-311G(2d,p) with PCM depicted here appears to be a highly valuable tool in order to establish a qualitative structure-property relationship in a series of ADPMs at much lower computational cost. For more details, refer to: (a) Davis *et al.*, *J Phys. Chem. A* **2010**, *114*, 12299; (b) Lynch *et al.*, *J. Org. Chem.* **2012**, *77*, 6423; (c) Mendez-Hernandez *et al.*, *J. Mol. Model.* **2013**, *19*, 2845.

103. Adamo, C.; Jacquemin, D. *Chem. Soc. Rev.* **2013**, *42*, 845.
104. Plasser, F.; Wormit, M.; Dreuw, A. *J. Chem. Phys.* **2014**, *141*, 024106.
105. Plasser, F.; Bäppler, S. A.; Wormit, M.; Dreuw, A. *J. Chem. Phys.* **2014**, *141*, 024107.
106. CCDC 1005388-1005391 contains the supplementary crystallographic data for this paper. These data can be obtained free of charge via www.ccdc.cam.ac.uk/data_request/cif, or by emailing data_request@ccdc.cam.ac.uk, or by contacting The Cambridge Crystallographic Data Centre, 12, Union Road, Cambridge CB2 1EZ, UK; fax: +44 1223 336033.
107. Desiraju, G. R.; Steiner, T. *The Weak Hydrogen Bond: In Structural Chemistry and Biology*; Oxford University Press, **1999**.
108. Jeffrey, G.; Saenger, W. In *Hydrogen Bonding in Biological Structures*; Springer Berlin Heidelberg: **1991**, p 15.

Chapitre 3 : Non-symmetric benzo[*b*]-fused BODIPYs as a versatile fluorophore platform reaching the NIR: A systematic study of the underlying structure–property relationship

André Bessette[1,2], Thomas Auvray[1], Denis Désilets[2] and Garry S. Hanan[1] *.

[1] Département de Chimie, Université de Montréal, Pavillon J.-A. Bombardier, 5155 Decelles Avenue, Montréal, Québec, H3T-2B1, Canada

[2] Saint-Jean Photochemicals Inc., 725 Trotter street, Saint-Jean-sur-Richelieu, Québec, J3B 8J8, Canada.

Accepté avec révisions mineures le 29 novembre 2015 par *Dalton Transactions*
Identification du manuscrit : DT-ART-11-2015-004444

Contribution des auteurs:

- André Bessette : synthèse et charactérisation; électrochimie, photophysique, modélisation moléculaire et rédaction de l'article.
- Thomas Auvray: cristallographie rayons-X
- Denis Désilets: Co-directeur en industrie
- Garry S. Hanan: Co-directeur académique

3.1 – Abstract

Ten newly synthesized non-symmetric benzo[*b*]-fused BODIPYs are compared with an extended series of nine related families (23 compounds) to gain insights into their structure–property relationship. The insertion of a fused indole moiety in the dipyrromethene core and variation of various substituents on the proximal aryl, including fused aromatic groups, lead to pronounced changes in the properties of compounds **1** – **10**. By taking advantage of this versatile synthetic platform that allows facile substituent modifications and extension of the π-conjugated system, significant bathochromic shifts in the absorption (λ_{max} = 511 – 597 nm) and emission (601 – 757 nm) bands are achieved. Although the oxidation potentials of the compounds varies considerably through the series (+1.28 – +1.65 V) due to the significant contribution of the aryl function to the HOMO, the reduction remains much more consistent (-0.61 to -0.79 V) as the LUMO resides primarily on the dipyrromethene core with little aryl contribution as calculated by DFT. For example, installation of a dimethylamine substituent in the para position of the aryl group leads to dramatic modification of the optoelectronic properties of the absorption (597 nm) and emission (757 nm) maxima. The full electrochemical, photophysical and computational analyses of the compounds and the structural characterization of compounds **1**, **5**, **8**, and **9** are further used to rationalize the potential of this powerful platform.

3.2 – Keywords

benzo[*b*]-fused BODIPYs; Panchromatic dyes; NIR emission; Non-symmetric synthesis; π-conjugated materials; Structure-property relationships; Photophysic; Electrochemistry; Computational modelization; DFT; TD-DFT; X-Ray structures.

3.3 – Introduction

BODIPYs have proved to be highly versatile fluorescent dyes owing to their remarkable photophysical properties including intense absorption in the red, bright fluorescence, photochemical and thermal stabilities along with inertness towards pH and fluctuations in polarity.[1,2] The 4,4-difluoro-4-bora-3a,4a-diaza-*s*-indacene skeleton on which it is based has been the focus of intense research in the last decades in order to modulate the optoelectronic properties so as to extend its range of action towards the deep-red and near-infrared (NIR) (refer to Figure 3.1 for nomenclature).[3-5] Great benefits come with harnessing the lower energy part of the visible / NIR spectrum, such as more efficient photovoltaic materials and improved sensibility in biological applications where the body absorbs most of the high-energy visible photons.[6-9] BODIPYs were hence integrated in an abundance of useful applications such as fluorescence imaging,[8-12] cancer photodynamic therapy,[13-15] metal-free photocatalysis,[16-19] electrochemiluminescence,[20] OLEDs and laser dyes;[21] transistors,[22] artificial light-harvesting antenna,[23-25] hydrogen production,[26,27] organic photovoltaic (OPV) and dye-sensitized solar cells (DSSC);[3, 28-31] all of which require the ability to fine-tune their properties. Multiple structural modifications at the periphery and at the boron atom were studied, thanks to the rich chemistry accessible on all the positions of the core.[1, 3, 5, 32] Besides, replacing the *meso* carbon atom on the skeleton by a nitrogen atom affords the closely related family of aza-BODIPYs with red-shifted optical properties. The BF_2 chelate itself can also be replaced to use the dipyrromethene (DPM) and aza-dipyrromethene (ADPM) cores as ligands for various metals.[3, 33-35] The design of non-symmetric derivatives is another efficient way to significantly alter the optoelectronic

properties, notably by generating a push-pull effect that reduces the HOMO-LUMO gap (ΔE).[36-41] Recently, much attention was devoted to extending the π-conjugated system of BODIPYs through ring-fusing strategies, with a selection of relevant examples illustrated in Figure 3.1. Among them, the benzannulation of one pyrrole at the [*b*] bound proved to be an interesting avenue to obtain a narrower ΔE as compared to the same type of fusing at the [*a*] bound. In fact, Wakamiya *et al.* showed that the non-symmetric benzo[*b*]-fused skeleton can be regarded as a combination of the electron-donating (EDG) pyrrole and the electron-withdrawing (EWG) azafulvalene moieties that generates a push-pull effect within the BODIPY core.[42] The enhanced azafulvalene character in this type of fused system decreases the LUMO while maintaining a moderate increase of the HOMO, a combination of effects that is highly suitable for the design of air-stable NIR dyes. In our ongoing efforts to harvest the NIR photons for energy conversion applications,[43-47] we were attracted by the obvious advantages of the benzo[*b*]-fused BODIPY (BbF) platform and made the hypothesis that combining the push-pull effect obtained through non-symmetry of the core with various electron-rich proximal aryl groups directly connected on the EDG pyrrole moiety would allow significant modulation of the optoelectronic properties. Non-symmetric BbF **1** – **10** were prepared based on a versatile synthetic methodology allowing easy substituent modifications and extension of the π-conjugated system (Scheme 3.1). A critical analysis was undertaken to ascertain the effect of the fusion mode within the BbF series and across an extensive series of 23 derivatives from 9 different BODIPY families (Figure 3.1). The structure-property relationship was established through electrochemistry, spectroscopy, computational modelization and the X-ray structural characterization of key BbF derivatives **1**, **5**, **8** and **9.**

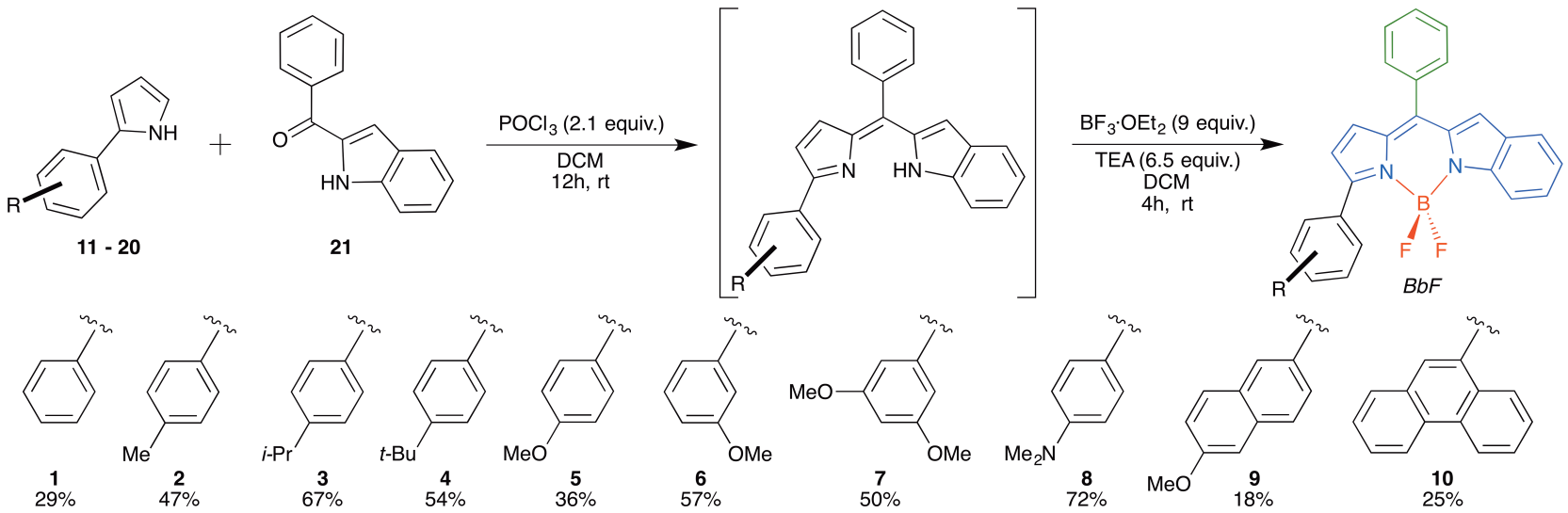

Scheme 3.1 – Synthesis of non-symmetric benzo[b]-fused BODIPYs (BbF) **1** – **10**.

Yields over two steps; refer to ESI for specific conditions of BbF **8**.† Fragmentation colour code for analysis: Blue = benzo[b]-fused DPM core, Green = meso-phenyl, Red = BF2 chelate, Black = proximal aryl substituent.

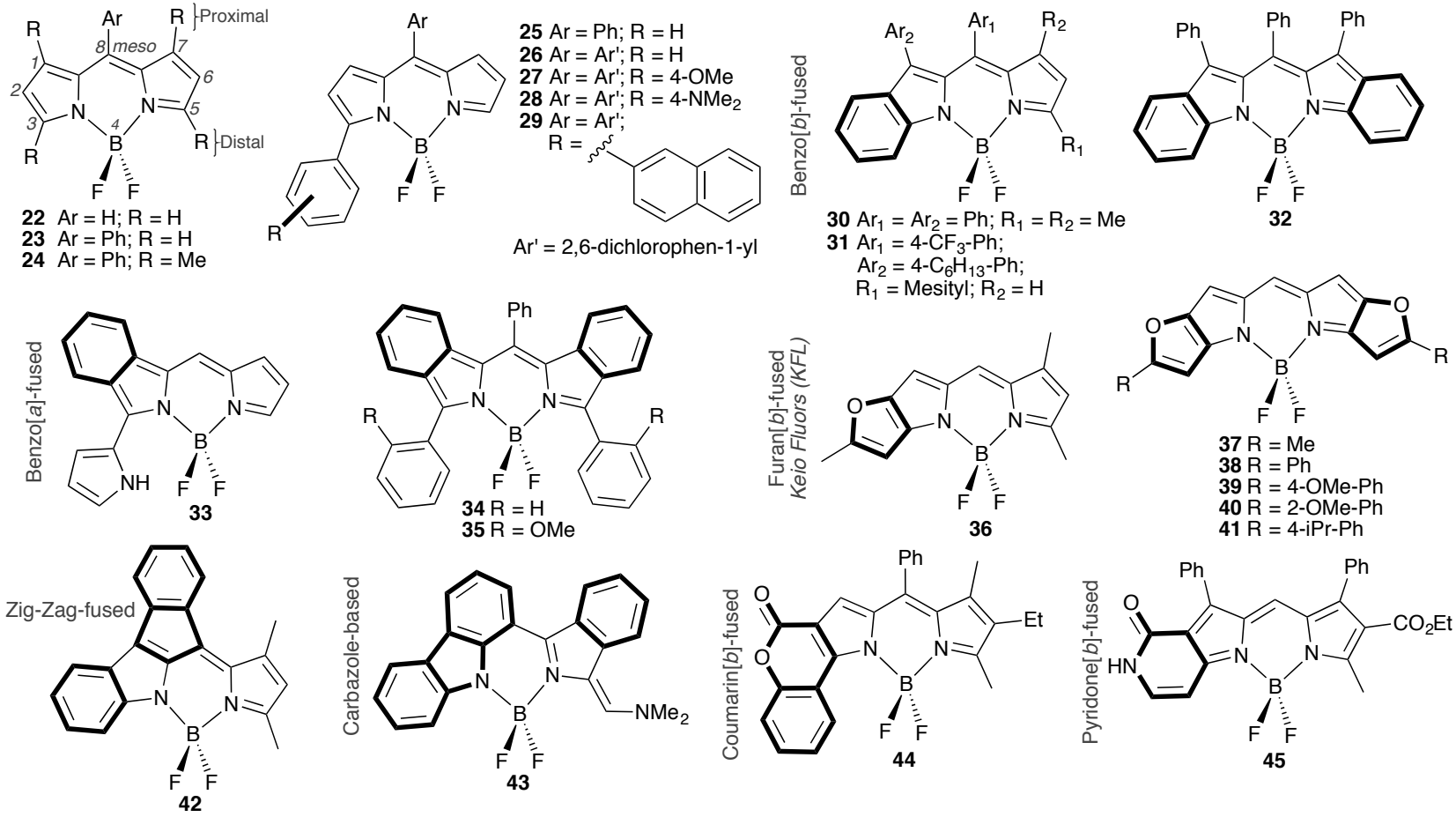

Figure 3.1 – Related BODIPYs of interest discussed herein.

Refer to Table II.S1 of ESI for a compilation of the optoelectronic properties previously reported in literature.†

3.4 – Results and Discussion

3.4.1 – Taking Advantage of a Versatile Synthetic Platform

Inspired by two recent studies looking at the impact of the fusion mode in benzene-fused BODIPYs,[42, 48] we undertook to synthetize the series of ten non-symmetric benzo[*b*]-fused BODIPYs **1** – **10** where the proximal aryl substituent is systematically altered with electron-rich substituents (Scheme 3.1 and Synthetic Methods of ESI†). The main objective is to gain insights into the range of optoelectronic tuning achievable through proximal aryl substitution in order to reach the NIR spectral region and suitable energy levels in both photovoltaic and life sciences applications.[3, 5, 8, 49] Therefore, our two-steps synthetic methodology was based on the initial reaction of the corresponding aryl-pyrrole **11** – **20** with (1*H*-indol-2-yl)(phenyl)methanone **21** in presence of 2.1 equivalents of phosphoryl chloride in CH_2Cl_2 at room temperature. The benzo[*b*]-fused dipyrromethene intermediates thus formed were isolated as crude products, followed by the coordination of the BF_2 chelate upon reaction with a large excess of boron trifluoride diethyl etherate and triethylamine (TEA). The yields over two-steps obtained varied from a modest 18% in the case of 6-methoxynaphthalen-2-yl substituted BbF **9** up to 67% for BbF **3** bearing a *p*-^{i}Pr-phenyl. In the specific case of BbF **8**, it was observed that the first step of the methodology should also include 1.1 equivalent of TEA in order to keep the dimethylamine group deprotonated during the synthesis and was followed by air exposure to insure complete oxidation to the dipyrromethene intermediate (refer to ESI†). In this manner, the overall yield reached 72%. Crystals suitable for X-ray diffraction analysis were obtained for BbF derivatives

1, **5**, **8** and **9**, which displayed extended conjugation throughout the benzo[*b*]-fused DPM core, partial conjugation with the proximal aryl substituents and almost no conjugation at all with the *meso* phenyl in the solid state (Figure 3.7 and corresponding X-ray section). Of note, both pyrrolic and indolic fragments on which the synthetic platform is based provide a rich chemistry where all the positions, including the *meso*- one, can easily be modified either separately or all at once to fit specific application requirements.[3, 32, 50-54] Overall, this synthetic approach is tolerant to substitution of the proximal aryl with different alkyl chains (**1** – **4**), electron-donating groups in *para* (**5** and **8**) or electron-withdrawing groups in *meta* (**6** and **7**) along with implementation of extended π-conjugated systems (**9** and **10**).[55]

3.4.2 – Electrochemical Properties

Insights from electrochemistry are essential to establish if ground state energy levels and overall stability of BODIPYs **1** – **10** are suitable for use in the previously mentioned applications. For example, efficient electron transfer upon photoexcitation in OPV and DSSC require a proper match between the LUMO levels of both the donor (D) and acceptor (A).[6, 56] Equally, the HOMO level must imperatively lie below the air oxidation threshold in order to avoid accelerated degradation of fluorescent sensors and photovoltaic devices.[57, 58] The electrochemical properties of the benzo-[*b*]-fused BODIPY series **1** – **10** were investigated by differential-pulsed voltammetry (DPV) and cyclic voltammetry (CV) techniques in CH_2Cl_2 (Table 3.I and ESI†; DPV redox potentials are given in the text unless otherwise noted) and were compared to previously reported electrochemical data found for some related derivatives (Figure 3.1 and Table

II.S1†). Combined with the computational modelization studies made by DFT (Table 3.II; Figures 3.2 and 3.4), these two techniques provide critical information regarding the HOMO / LUMO energy levels and the stability of electronic processes.

Table 3.I – Electrochemical data for BbF **1** – **10**.

	$\mathbf{E_{Ox}}$ [a]	$\mathbf{E_{Red}}$ [a]
1	1.55, 1.45, 1.33	-0.67 (-0.68 [126])[b], -1.57, -1.78
2	1.65, 1.55, 1.36	-0.64 (-0.66 [163])[b], -1.54, -1.62
3	1.61, 1.52, 1.33	-0.68 (-0.67 [145])[b], -1.53, -1.60
4	1.48, 1.44, 1.27	-0.61 (-0.64 [150])[b], -1.49, -1.53
5	1.54, 1.46, 1.31	-0.64 (-0.70 [164])[b], -1.49, -1.52
6	1.54, 1.39, 1.28	-0.67 (-0.62 [160])[b], -1.58, -1.67
7	1.39	-0.65 (-0.61 [155])[b], -1.54, -1.58
8	1.68, 1.50, 1.40, 0.88	-0.79 (-0.78 [179])[b], -1.57, -1.64
9	1.50, 1.40, 1.26	-0.65 (-0.64 [109])[b], -1.51, -1.55
10	1.65, 1.58, 1.40	-0.64 (-0.64 [141])[b], -1.52, -1.58

[a] Determined by DPV. Potentials are in volts *vs*. SCE for CH_2Cl_2 deaerated solutions, 0.1 M of TBAP, recorded at 25 ± 1 °C at a sweep rate of 50 mV/s. Irreversible process unless otherwise stated. [b] Pseudo-reversible process. Half-wave potential determined by CV given in parentheses with the difference between cathodic and anodic peak potentials (mV) in brackets.

The electrochemical data in Table 3.1 and associated cyclic voltammograms presented in the ESI (Figures II.S42 – II.S61†) show that the BbF series present irreversible oxidation processes along with a first reversible reduction followed by two closely separated irreversible processes. In the case of reference adduct **1** bearing an unsubstituted proximal phenyl, three irreversible oxidations are found at 1.33, 1.45 and

1.55 V *vs.* SCE. DFT calculations suggest that the first oxidation is more likely to happen on the delocalized π-system including the benzo[*b*]-fused DPM core and the proximal phenyl, with almost no contribution from either the *meso*-phenyl or the BF_2 fragments (Figure 3.4). On the reduction side, the first reversible process at -0.67 V (see Table 3.II) is followed by two distinct irreversible processes at -1.57 and -1.78 V. The calculated LUMO, a first approximation of the most likely fragments to receive an electron, suggests that it involves mainly the DPM core and its *meso*-phenyl with a decreased contribution from the proximal aryl group. These observations are in line with the calculations of Wakamiya *et al.* where the HOMO was associated with the electron-rich pyrrole fragment while the LUMO mainly involved the electron-poor indole with an increased azafulvalene character.[42]

Interestingly, the fully unsubstituted BODIPY **22** presents only two irreversible processes, at 1.61 V for its oxidation and -0.73 V for its reduction, while the *meso*-phenyl substituted **23** irreversibly oxidizes at slightly higher potential (1.65 V) and has a first reversible reduction also at -0.73 V followed by an irreversible one at -1.71 V (Table II.S1†).[59, 60] Thus, the *meso*-phenyl moiety found both in benzo[*b*]-fused BODIPY **1** and unfused derivative **23** contributes to the reversibility of the first reduction process, and an additional irreversible reduction each at -1.78 and -1.71 V, respectively. This finding is also in accordance with the DFT calculations (*vide supra*). On the other hand, the presence of blocking groups on the 1,3,5,7 positions of the BODIPY core, such as the methyl in adduct **24**, allow for a reversible first oxidation process (1.51 V).[48] The absence of such blocking groups on the distal side of the BbF **1** – **10** series, therefore, appears to be in part responsible for the irreversible first oxidation

that is observed. Another important element to consider is how the replacement of the pyrrole by an indole moiety in fused systems affects the overall stability towards oxidation. The electrochemical data of closely related derivatives indicates that the [*b*]-fused indole moiety itself might give rise to the instability since fully capped derivatives **30** (non-symmetric; 1.57 V) and **32** (symmetric; 1.66 V) both have an irreversible first oxidation, just as uncapped derivative **31** (1.51 V) does.[42, 48] In contrast, fully substituted symmetric benzo[*a*]-fused **34** and **35** present reversible first oxidations at much less positive oxidation potentials (0.83 and 0.78V, respectively).[61] Of note, a fully-fused BODIPY, dimerized through the [*b*] bound based on the structure of **31**, was found to offer reversibility of the first oxidation process even though it was uncapped on the pyrrole fragments,[42] thus paving the way towards stable benzo[*b*]-fused system.

An interesting difference on the redox properties is observed upon substitution with various alkyl chains at the *para* position of the proximal aryl. With respect to reference BbF **1**, introduction of a methyl group in adduct **2** changes the first oxidation potentials by +30 mV (1.36V) and the second and third by +100 mV (1.55 and 1.65 V). All three reductions are easier to access by the same ~30 mV amount (-0.64, -1.54 and -1.62 V). Isopropyl substituted BbF **3** oxidizes at the same potential as compound **1** (1.33 V) and is complemented with stabilized second and third oxidation processes (1.52 and 1.61 V). Similarly, the first reduction is almost identical at -0.68 V to that of **1** with slightly less negative second and third processes (-1.53 and 1.60 V, respectively). In contrast, all three oxidation processes of ^{t}Bu derivative **4** are destabilized (1.27, 1.44 and 1.48 V) due to stronger electron donation, while the reduction ones are significantly less negative (-0.61, -1.49 and -1.53 V) relative to BbF **1**. The increase in the oxidation

potentials within the BbF **2** – **4** series is not in full agreement with the Hammett parameter trend expected (Me: σ_p = -0.17; ^{i}Pr: σ_p = -0.15; ^{t}Bu: σ_p = -0.20),[62] as **3** displays a more difficult oxidation than **2**. However, the bulky and electron-rich ^{t}Bu derivative **4** is markedly affected as compared to the smaller alkyl groups of **2** and **3**. The reduction potentials of BbF **2** and **3** are similar to the reference **1**, pointing towards little influence of proximal aryl groups in the energy of the LUMO. There also exists a mismatch of the redox potentials of the BbF **2** – **4** series relative to **1** that might find its source in a poor electronic delocalization between the proximal phenyl and the benzo[*b*]-fused DPM core. DFT calculations with PCM of CH_2Cl_2 support this assumption by the presence of two partial nodes on the *meta* carbons of the proximal phenyl in the HOMO of **1** and a higher dihedral angle between the two fragments (φ = 34.74° for **1** *vs.* 33.03° for **2**, 33.46° for **3** and 33.07° for **4**). Another important point to consider is that extended conjugation in BbF **2** – **4** causes a notable decrease and alteration of the dipole moments *vs.* **1** (refer to Figure 3.4) that hamper redox processes due to reduced polarizability within the molecules. Thus, it appears the choice of alkyl chains on the proximal aryl isn't as innocent as one would *a priori* expect from an electrochemical perspective since the *para* substitution seems to favour better delocalization within the π-conjugated system.

Incorporation of a stronger electron-donating group like *p*-methoxy (σ_p = -0.27) leads to BbF **5** being only slightly easier to oxidize (1.31, 1.46 and 1.54 V) compared with reference **1**, but less than in the case of ^{t}Bu substituted **4**. In a similar fashion to compounds **2** – **4**, reduction processes of **5** are also easier to access by DPV (-0.64, -1.49 and -1.52 V) compared to **1** even though cyclic voltammetry seems to indicate a more

difficult first reduction (-0.70 V [164 mV]). These results are rather surprising since significantly better π-electron delocalization throughout the whole system in BbF **5** was found both by X-ray structural data and theoretical calculations. In fact, the dihedral angle between the proximal aryl and the pyrrole was smaller [$\varphi_{C12\text{-}C13\text{-}C14\text{-}C15}$ of -18.9(4) / +11.6(3)° *vs.* -34.6(2)° for **1** by X-ray; 30.95° *vs.* 34.74° for **1** and 33.03 for **4** by DFT] in addition to the smaller tilt angle between the planes of the pyrrole and the benzo[b]-fused pyrrole [10.3(1) *vs.* 15.3(1)° for **1** by X-ray]. Furthermore, a higher dipole moment was calculated (7.26 D *vs.* 5.96 D for **4** and 6.39 D for **1**) that should affect the redox potentials as well. A possible explanation lies in the strong H-bonding regime observed in BbF **5** that may alter the reorganizational energy needed to stabilize charges during redox processes. In the case of BbF **8** bearing the strongest electron-donating group of the series, the dimethylamine substituent (σ_p = -0.83), the first oxidation is much easier to access at 0.88 V. A comparison with its closest analogue, *N,N*-dimethylaniline (0.80 V), suggests that the facile oxidation is due to the substituent itself.[63] The facile oxidation of the dimethylaminophenyl group also has implications for in the emission spectroscopy as discussed later. The first reduction of **8** is more difficult (-0.79 V) *vs.* BbF **1**, as can be expected. This result combines effects of the strong electron donation of dimethylamine with the most planar π-conjugated system of the series (tilt angle between pyrrole and benzo [*b*]-fused pyrrole planes of 4.2(1)° by X-ray and 7.5° by DFT; $\varphi_{C12\text{-}C13\text{-}C14\text{-}C15}$ = -27.7(2)° by X-ray and 24.75° calculated). A much stronger and quasi-perpendicular dipole moment (7.68 D) relative to **1** is also found. The presence of such an electron-rich group and improved conjugation allow the system to tolerate a total of four oxidized states within the CH_2Cl_2 potential window (0.88, 1.40, 1.50 and

1.68 V) related to both the dimethylamine itself and the dipyrromethene core. In addition to the first reduction, BbF **8** has two other processes at -1.57 and -1.64 V.

Introducing a methoxy substituent at the *meta* position of the aryl is expected to make it an electron-withdrawing group by induction (σ_m = +0.12) and should result in more positive oxidations and less negative reductions if the proximal aryl and the benzo[*b*]-fused DPM core are fully conjugated. Less positive oxidation processes are instead observed for BbF **6** (1.28, 1.39 and 1.54 V) bearing one *meta*-methoxy group as compared to **1**. Actually, the ease of oxidation provided by the *meta*-methoxy is even greater than for the *para*-methoxy substituted BbF **5** regarding the first and second oxidations. The first two reductions (-0.67 and -1.58 V) are nearly equivalent to what was observed for **1**, whilst the third one at -1.67 V is less negative by 0.11 V. All three reductive processes are, however, more negative than in the case of **5**, against what would be expected. Adding a second methoxy substituent in *meta* position leads BbF **7** to exhibit a significantly stabilized oxidative process at 1.39 V, as expected from computational studies, and is a 0.11 V positive shift compared to BbF **6** and 0.06 V from **1**. The origin of the oxidative processes might be altered as described previously for **8** since **7** only has a single oxidation compared to three for **5** and **6** and the value at 1.39 V match the second oxidative process of **6**. The reduction processes for BbF **7** (-0.65, -1.54 and -1.58 V) are easier to access than for **1** and **6**. Therefore, it appears the peculiar behaviour of BbF **6** and **7** relative to the reference **1** and closely related **5** cannot be described by the sole electron donating / withdrawing propensity of the substituent. The logic behind rather resides in a combined effect with three other factors previously exposed, i.e. a weaker communication through the π-conjugated system (φ = 35.24° with

one node on meta carbon for **6**; φ = 36.10° with two nodes for **7**) allied with the alteration of dipole moments (5.42 and 4.91 D, respectively) and potentially weaker H-bonding relative to BbF **5** as described in the X-ray section.

Extension of the π-electron conjugation path by fusion of cycles on the proximal aryl promises interesting effects since a complex system is at play, with inter-correlated factors dictating the experimental properties. BbF **9** combines both a 2-naphtyl unit and an electron-rich 6-methoxy substituent equivalent to the *para*-substitution of a single phenyl through mesomerism. In principle, this should provide redox processes that are easier to access as compared to reference **1**. Indeed, the results are as expected, with easier oxidations (1.26, 1.40 and 1.50 V) and reductions (-0.65, -1.51 and -1.55 V). Full expression of the substituent effect occurs due to the small calculated dihedral angle of 31.72° that promotes delocalization of the π-electrons combined with the largest dipolar moment of the series (7.73 D). However, this is not the case with BbF **10** for which the large calculated dihedral angle of 55.46° caused by steric hindrance almost completely inhibits the communication between the 9-phenanthrene moiety and the benzo[*b*]-fused DPM core. A slight orbital overlap between the two fragments still persists in the HOMO that maintains a minimal electronic connection as can be appreciated in Figure 3.5. The dipole vector is mainly translated compared to **1**, with a slightly shorter modulus (6.16 *vs.* 6.39 D, respectively). Altogether, oxidations processes are found at more positive potentials (1.40, 1.58 and 1.65 V) compared to **1**, whereas reductions become even easier (-0.64, -1.52, -1.58 V).

Conversion of the first oxidation and reduction potentials obtained by electrochemistry into eV is relevant in order to establish the energy level of the HOMO

and LUMO frontier molecular orbitals and to evaluate if the benzo[*b*]-fused BODIPYs reported herein meet the specific requirements for multiple applications (*vide supra*; Table 3.II and Figure 3.2). A common requirement in all types of applications is to present a HOMO below the oxidation threshold established at -5.27 eV,[58] which is the case for the whole BbF series. Results indicate that the HOMO is in the range of -6.34 for **7** and **10** up to -5.82 eV for **8**, therefore, they are air stable. For photovoltaic applications, exact positions of the LUMO and the excited state oxidation potentials (E_{Ox}*) are required to ensure proper electronic transfers between the acceptor and the donor components of the studied system.[64] It was found that LUMO levels are in the range of -4.34 eV for **4** up to -4.15 eV for **8**, with E_{Ox}* between -4.30 eV for **7** and **10** up to -4.05 eV for **8**. These values suggest that all derivatives in the BbF series present the possibility to be integrated into photovoltaic devices since both their LUMOs and E_{Ox}*, or at least the latter, are lying slightly above the LUMO of the main acceptor used in OPV [fullerene-based $PC_{60}BM$ (between -3.91 and -4.3 eV)][65] or of the TiO_2 conduction band (-4.2 eV)[66] used in DSSC. Interestingly, further fine-tuning can be achieved in OPV through careful selection of alternative acceptor materials that would provide the optimal driving force of about 0.3 eV suitable for good exciton dissociation into a pair of charges at the D – A interface.[67-75] Of all derivatives, BbF **8** bearing the NMe_2 group appears to be the best candidate for photovoltaic based on the highest lying LUMO / E_{Ox}* and the smallest ΔE_{Ox} (1.67 eV) / ΔE_{Opt} (1.77 eV) that allow for harvesting of low energy photons.[3]

Table 3.II – HOMO / LUMO levels (in eV) as determined by electrochemistry and theoretical calculations along with corresponding ΔE and estimated excited state oxidation potential (E_{ox}*) for BbF **1** – **10**.[a]

	HOMO redox	**LUMO redox**	**ΔE_{Ox}**	**E_{Ox}***	**HOMO theo**	**LUMO theo**	**ΔE_{Theo}**
1	-6.27	-4.28	1.99	-4.20	-6.13	-3.23	2.90
2	-6.31	-4.31	2.00	-4.26	-6.07	-3.20	2.87
3	-6.28	-4.27	2.01	-4.23	-6.07	-3.20	2.87
4	-6.22	-4.34	1.88	-4.16	-6.07	-3.20	2.87
5	-6.25	-4.31	1.95	-4.22	-5.94	-3.14	2.80
6	-6.22	-4.28	1.94	-4.16	-6.13	-3.22	2.91
7	-6.34	-4.30	2.04	-4.30	-6.12	-3.21	2.91
8	-5.82	-4.15	1.67	-4.05	-5.51	-3.00	2.51
9	-6.20	-4.29	1.91	-4.23	-5.86	-3.19	2.67
10	-6.34	-4.31	2.03	-4.30	-6.07	-3.22	2.85

[a] Energy difference (ΔE, in eV) between the HOMO and the LUMO using corresponding method. Theoretical calculations using r-PBE0/6-311g(2d,p) DFT method with PCM = CH_2Cl_2. Estimated excited state oxidation potential calculated using: E_{ox}* = E_{Ox} + ΔE_{Opt}.

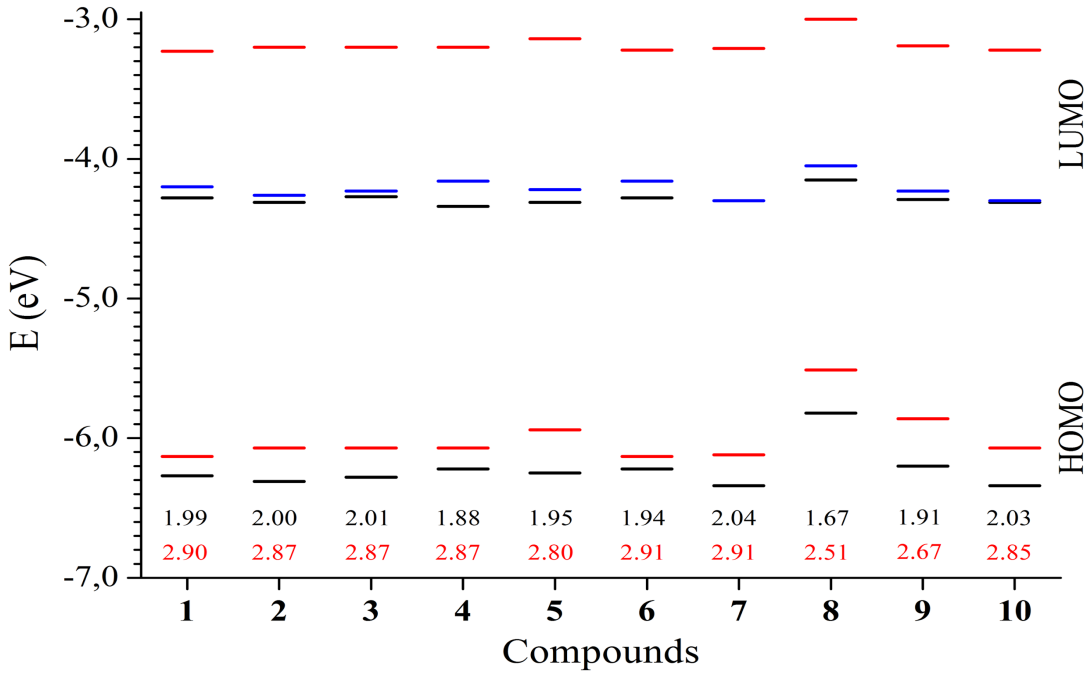

Figure 3.2 – Energy levels of BbF **1** – **10** (electrochemistry in black, DFT calculations in red and corresponding ΔE at the bottom ; estimated excited E_{ox}* in blue).

3.4.3 – Red Absorption and NIR Emission Properties

Spectroscopic data for the series are summarized in Table 3.III and Figure 3.3, while individual spectra can be found in the ESI (Figures II.S25 – II.S41†). Overview of the photophysical properties of the BbF series in CH_2Cl_2 solution reveals a strong absorption of red light (λ_{red} = 547 – 626 nm; extinction coefficients (ε) = 36 – 57 x 10^3 M^{-1} cm^{-1}) complemented mainly by four other absorption bands of lower intensity, along with a relatively weak fluorescence (Φ_F = <0.01 – 0.11) spanning the deep-red to NIR parts of the electromagnetic spectrum (λ_{Em} = 606 – 757 nm; broad emissions from *ca.* 560 up to 875 nm). Such tuneable properties are highly desirable for various applications (*vide supra*) and the series will be further analyzed by TD-DFT in the computational modelization section and herein relative to previously reported BODIPYs (refer to

Figure 3.1 and Table II.S1†; in CH_2Cl_2 unless otherwise stated) in order to gain a better understanding of the impact of fusion modes and substitution on the rings.

Looking first at absorption spectroscopy, reference BbF **1** presents its lowest energy band at 553 nm (ε = 52 x 10^3 M^{-1} cm^{-1}) in dichloromethane that is bathochromically shifted by +49 nm *vs.* both the basic BODIPY core **22** (λ_{red} = 504 nm; ε = 14 x 10^3 M^{-1} cm^{-1}) and *meso*-phenyl substituted **23** (λ_{red} = 504 nm; ε = 58 x 10^3 M^{-1} cm^{-1}) measured in chloroform.[59] The solvatochromic effect on the λ_{red} between CH_2Cl_2 and $CHCl_3$ appears to be relatively negligible since **23** in DCM is at 500 nm (ε = 33 x 10^3 M^{-1} cm^{-1}), but the decrease in solvent polarity tends to diminish the extinction coefficient.[76] Therefore, the benzo[*b*]-fused chromophore **1** with a rigidified structure presents significantly improved photophysical properties compared to related BODIPYs **22** and **23**. This +49 nm bathochromic shift is also of the same magnitude to what can be observe by altering the *meso* carbon with a nitrogen atom in azadipyrromethene (ADPM) and Aza-BODIPY.[35, 39] When methyl groups are installed at the proximal and distal positions of the BODIPY core in **24** (λ_{red} =501 nm; ε = 87 x 10^3 M^{-1} cm^{-1}), only a +1 nm shift is observed *vs.* **23**.[77]

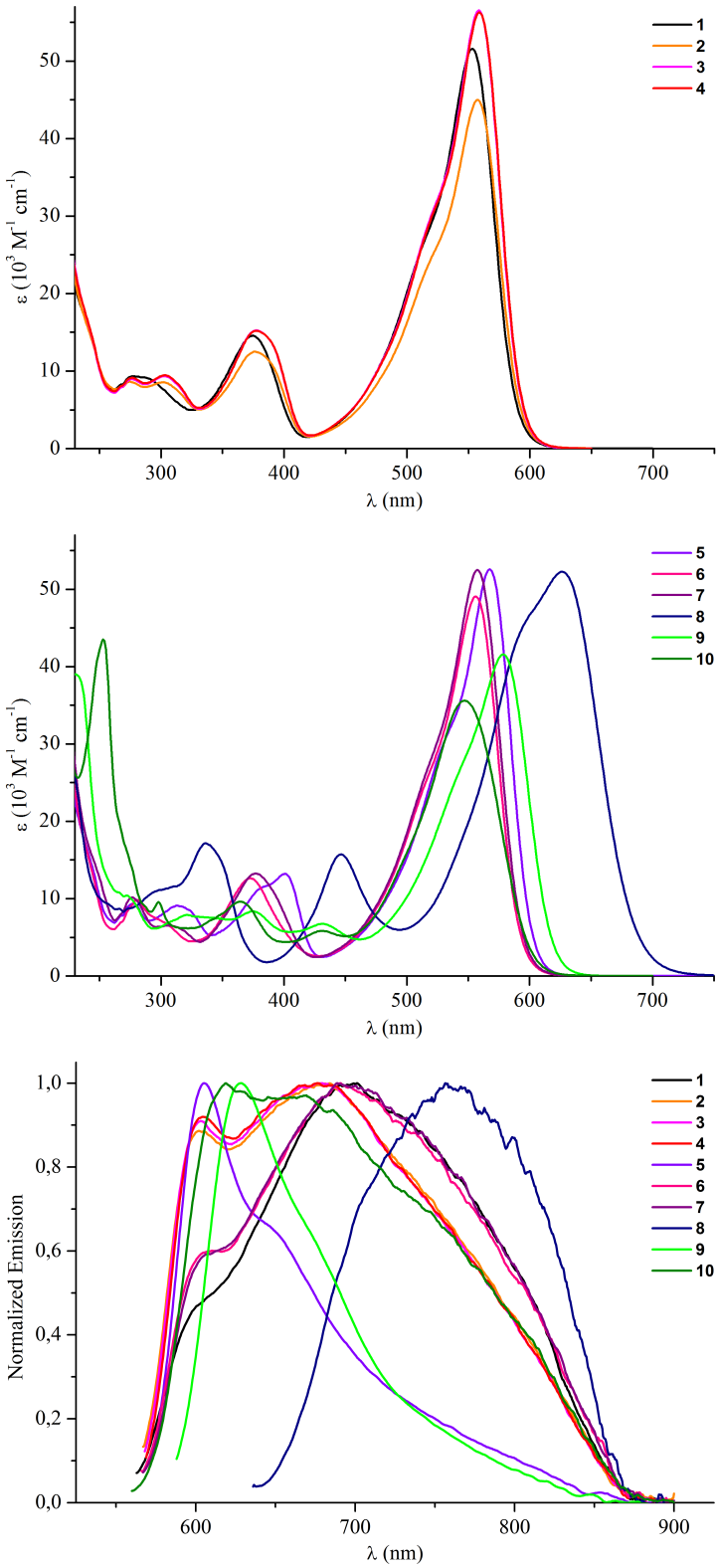

Figure 3.3 – UV/vis absorption spectra of BbF **1** – **4** (top) and **5** – **10** (middle) and their normalized emission profiles (bottom) in CH_2Cl_2 solution.

Table 3.III – HOMO / LUMO levels (in eV) as determined by electrochemistry and theoretical calculations along with corresponding ΔE and estimated excited state oxidation potential (E_{ox}*) for BbF **1** – **10**.[a]

	Absorption [a]							**Emission** [b]					
	λ_{UV}	$\lambda_{near\ UV}$	λ_{violet}	$\lambda_{sh\ orange}$	λ_{red}	ΔE_{Opt} (eV)	$\lambda_{red\ theo}$ [c]	λ_{Em}	FWHM	Δ_{Stoke} (cm^{-1})	Φ_F	τ (ns)	k_r / k_{nr} (10^9 s^{-1})
1	277 (9.3)	287 (9.2)	374 (15)	517 (28)	553 (52)	2.07	479 (0.939)	701	205	3818	< 0.01	0.48	0.02 / 2.1
[d]	274 (7.6)	282 (7.6)	373 (12)	513 (24)	545 (39)	2.10	---	734	256	4725	< 0.01	0.17	0.06 / 5.8
2	275 (8.6)	302 (8.6)	377 (12)	521 (25)	557 (45)	2.05	484 (0.987)	684	207	3333	0.02	0.59	0.03 / 1.7
3	276 (9.0)	303 (9.3)	378 (15)	523 (31)	558 (57)	2.05	484 (1.01)	679	207	3193	0.02	0.58	0.03 / 1.7
4	277 (9.1)	303 (9.5)	378 (15)	525 (32)	559 (56)	2.06	485 (1.01)	677	204	3118	0.01	0.56	0.02 / 1.8
5	278 (9.4)	314 (9.1)	401 (13)	537 (33)	567 (53)	2.03	495 (1.05)	606	88	1135	0.05	0.78	0.06 / 1.2
[d]	276 (10)	311 (9.7)	397 (14)	531 (37)	559 (54)	2.06	---	601	115	1250	< 0.01	0.22	0.05 / 4.5
6	281 (9.8)	303 (6.9)	373 (13)	520 (27)	556 (49)	2.06	479 (0.946)	691	222	3514	0.01	0.50	0.02 / 2.0
7	277 (10)	307 (6.5)	377 (13)	522 (29)	557 (52)	2.04	477 (0.942)	689	216	3439	0.01	0.50	0.02 / 2.0
8	301 (11)	336 (17)	446 (16)	597 (46)	626 (52)	1.77	542 (1.18)	757	149	2764	< 0.01	< 0.1	---
[d]	311 (13)	336 (20)	444 (16)	595 (53)	615 (57)	1.78	---	---	---	---	----	---	---
[e]	---	283 (16)	379 (15)	522 (29)	555 (54)	2.07	---	---	---	---	---	---	---
[f]	---	282 (17)	400 (16)	518 (36)	550 (60)	2.03	---	---	---	---	---	---	---
9	272 (10)	321 (7.9)[g]	431 (6.7)	548 (28)	578 (42)	1.97	511 (1.20)	628	87	1377	0.11	0.85	0.13 / 1.0
[d]	268 (11)	319 (7.5)[h]	426 (6.4)	536 (25)	569 (37)	2.03	---	632	116	1752	0.01	0.22	0.05 / 4.5
10	273 (16)	298 (9.5)[g]	431 (5.8)	511 (20)	547 (36)	2.04	491 (0.901)	619	196	2127	< 0.01	0.39	0.03 / 2.5
[d]	284 (10)	296 (11)[h]	426 (6.4)	502 (23)	536 (40)	2.10	---	592	230	1765	< 0.01	< 0.1	---

[a] Acquired at 25 ± 1 °C in CH_2Cl_2, otherwise stated. λ in nm. Extinction coefficients are given in parentheses (ε, x10^3 $M^{-1}cm^{-1}$). Shoulder = sh. ΔE_{Opt} qualitatively obtained from the red end of the Gaussian peak of λ_{red} (in nm) and converted into eV using $E = hc / \lambda$. [b] Emission maximum (λ_{Em}) obtained by excitation at corresponding λ_{red}. Full width at half-maximum (FWHM) in nm. Fluorescence quantum yields (Φ_F) obtained on a calibrated integration sphere. Fluorescence lifetime (τ) upon excitation by a pulsed laser at 405 nm (Standard deviation ≤ 0.02 ns). Radiative (k_r) and non-radiative (k_{nr}) rate constants were calculated using: $k_r = \Phi_F / \tau$ and $k_{nr} = (1-\Phi_F) / \tau$. [c] TD-BMK/6-311+G(2d,p); PCM = CH_2Cl_2. Oscillator strength given in parenthesis. Full assignation of the absorption bands available in the ESI. [d] In acetonitrile. [e] In CH_2Cl_2 with an excess of $HClO_4$. [f] In acetonitrile with an excess of $HClO_4$. [g] Another absorption band observed at 375 nm (ε = 8.3x10^3 $M^{-1}cm^{-1}$) for **9** and at 365 nm (ε = 9.6x10^3 $M^{-1}cm^{-1}$) for **10**. [h] Another absorption band observed at 373 nm (ε = 8.3x10^3 $M^{-1}cm^{-1}$) for **9** and at 364 nm (ε = 11x10^3 $M^{-1}cm^{-1}$) for **10**.

The closest family of non-symmetric dyes without the benzo[*b*]-fused moiety is the series **25** – **29** that was studied by the groups of Boens and Dehaen in acetonitrile (ACN).[78, 79] It will be discussed later in this section compared to their corresponding BbF in ACN, but it can already be noted that implementation of the benzo[*b*]-fused moiety provide an intrinsic red-shift of +22 nm (545 nm for **1** *vs.* 522 nm for **25**). Relative to closely related non-symmetric benzo[*b*]-fused derivatives **30** (λ_{red} = 512 nm; ε = 42 x 10^3 M^{-1} cm^{-1}) and **31** (λ_{red} = 539 nm in THF; ε = 54 x 10^3 M^{-1} cm^{-1}),[42, 48] it can be outlined that the presence of the unhindered proximal phenyl in BbF **1** contributes more significantly to reduce the HOMO-LUMO gap than does a methyl or a sterically crowded mesityl, both of which diminish the conjugation. Similarly, aryls installed on their indole moiety appear to have less effect on the resulting λ_{red} than the proximal phenyl does in **1**. These two last observations further support our initial hypothesis that the proximal aryl can provide significant leverage for modulation of the optoelectronic properties. Adding a second benzo[*b*]-fused moiety and two phenyls on the free indolic positions in symmetric derivative **32** further extends the π-conjugated system and allows the λ_{red} to be shifted by +15 nm, up to 568 nm, but at the price of a decreased extinction coefficient (42 x 10^3 M^{-1} cm^{-1}).[48] Fusing the benzene at the [*a*] bound in non-symmetric derivative **33** provide a λ_{red} at 570 nm, but present the major drawback of a free pyrrole in proximal position prone to unwanted side-reactions or degradation, especially in biological environment.[80] More stable symmetric benzo[*a*]-fused derivative **34** present interesting photophysical properties (λ_{red} = 631 nm; ε = 102 x 10^3 M^{-1} cm^{-1}) while **35** substituted with two proximal *ortho*-methoxy phenyls shows an hypsochromic shift of -14 nm due to the steric hindrance with the fused aromatic groups (λ_{red} = 617 nm; ε = 108

x 10^3 M^{-1} cm^{-1}).[61] Nevertheless, non-symmetric BbF **1** is more red-shifted than other [*b*]-fused moieties such as furan-based Keio Fluor **36** (542 nm in $CHCl_3$; ε = 140 x 10^3 M^{-1} cm^{-1}) and coumarin-based **44** (516 nm; ε = 36 x 10^3 M^{-1} cm^{-1}).[81, 82] Pyridone-[*b*]-fused **45** reaches out to 578 nm (ε = 105 x 10^3 M^{-1} cm^{-1}),[83] but a push-pull motif between the electron-rich pyridone moiety on one side and the electron-poor ester on the other makes it difficult to assess clearly if the higher bathochromic shift observed *vs.* **1** is solely due to the fusion mode. Adding a zig-zag fusion to the benzo[*b*]-fused moiety in **42** leads to a -35 nm hypsochromic shift of the maxima of absorption (518 nm; ε = 56 x 10^3 M^{-1} cm^{-1}) *vs.* the BbF of reference combined with a broad tailing towards the NIR centered at *ca.* 770 nm.[48] Interestingly, a combination of benzo[*a*]-fused and imbricated carbazole moiety in BODIPY derivative **43** (482 nm; ε = ~55 x 10^3 M^{-1} cm^{-1}) absorbs at shorter wavelength in the red than the reference BbF **1**.[84] This is unexpected as each of the underlying modes of ring fusion taken separately point towards an increased bathochromic shift, i.e. symmetric benzo[*a*]-fused **34** absorbs further than its benzo[*b*]-fused counterpart **32** and zig-zag-fused **42** gives a tailing in the NIR. Overall, it appears not all the modes of ring fusion are equivalent and their interplay might provide counterintuitive effects on the photophysical properties.

As it was previously exposed with electrochemistry, the various substituents used in the BbF series provide a mean to considerably modulate their properties. The effect of the various alkyl chains in *para* position of the proximal aryl allows a tuning by +4 – 6 nm of the λ_{red} compared to BbF **1**; with **2** at 557 nm (Me; ε = 45 x 10^3 M^{-1} cm^{-1}), **3** at 558 nm (^{i}Pr; ε = 57 x 10^3 M^{-1} cm^{-1}) and **4** at 559 nm (^{t}Bu; ε = 56 x 10^3 M^{-1} cm^{-1}). This bathochromic trend is in line with the sequence of electron-donating alkyl groups and

extended conjugation discussed earlier, albeit within experimental error. BbF **5** bearing the proximal *p*-OMe-Ph exhibits red shift of +14 nm *vs.* reference **1**, with λ_{red} at 567 nm (ε = 53 x 10^3 M^{-1} cm^{-1}). Interestingly, substitution in *meta* position with one methoxy group in **6** (λ_{red} = 556 nm; ε = 49 x 10^3 M^{-1} cm^{-1}) or two in **7** (λ_{red} = 557 nm; ε = 52 x 10^3 M^{-1} cm^{-1}) doesn't provide the expected hypsochromic shift, rather moving the maxima of absorption respectively to +3 and +4 nm *vs.* **1**. The bathochromic shift observed for these EWG by induction is still much smaller than in the case of BbF **5** with electron-donation of the methoxy directly in the π-conjugated system. Again in the case of the photophysical properties, it appears the peculiar behaviour of BbF **6** and **7** relative to the reference **1** and closely related **5** cannot be described by the sole electron donating / withdrawing propensity of the substituent and must take into account the three other factors previously exposed in the electrochemistry section (extend of communication through the π-conjugated system; alteration of the dipole moment; strength of the H-bonding). As can be expected by structural characterization of BbF **8**, the presence of the strongly coupled EDG dimethylamine in *para* position leads to a significant +73 nm red-shift (λ_{red} = 626 nm; ε = 52 x 10^3 M^{-1} cm^{-1}) which suggests a charge-transfer transition from the dimethylamine to the dipyrromethene core. Such a shift in the optical properties makes this BbF derivative highly suitable for photovoltaic applications.[3] Addition of an excess of $HClO_4$ in the UV cuvette instantly protonated the substituent ($NHMe_2^+$), leading to a drastic -71 nm hypsochromic shift of the λ_{red} (555 nm; ε = 54 x 10^3 M^{-1} cm^{-1}) (Figure II.S36†) leaving the intrinsic absorption profile of the dipyrromethene core, supporting the assignment of this charge-transfer transition. The overall absorption profile also closely matches that of reference BbF **1**, proving retained

structural integrity of the dye and its potential use as pH-sensitive probe. Extension of the π-conjugated system in 6-methoxynaphthalen-2-yl substituted BbF **9** (λ_{red} = 578 nm; $\varepsilon = 42 \times 10^3$ M^{-1} cm^{-1}) provides a +25 nm red-shift *vs.* **1**, which is an intermediate effect between the *p*-OMe-Ph BbF **5** and the *p*-NMe_2-Ph BbF **8**. Further extension of π-conjugated system with the 9-phenanthrene moiety leads to the only hypsochromic shift of the series, by 6 nm, clearly attributable to the poor communication between this sterically crowded substituent and the BODIPY core (*vide supra*). Finally, a comparative overview of variously substituted Keio Fluors (KFL) **36** – **41** studied in $CHCl_3$ provide interesting information that can be extended to the BbF series.[81, 85] Going from the non-symmetric KFL **36** (λ_{red} = 542 nm) to the symmetric **37** (λ_{red} = 579 nm) gives a +37 nm bathochromic shift, which is as important as increasing the conjugation with additional phenyls in the symmetric KFL **38** (λ_{red} = 652 nm; +73 nm red-shift / *ca.* 36.5 nm per Ph). This trend is in accordance with the +11 nm shift obtained for BbF **9** *vs.* **5** (+25 nm *vs.* **1**), which disfavours the idea of replacing the proximal aryl in the series by alkyl chains for efficient absorption of deep-red light. Within the symmetric KFL derivatives, it is interesting to note that *para*-^{i}Pr-phenyls in **41** (λ_{red} = 662 nm) provide a bathochromic shift of +10 nm compared to **38** while *ortho*-OMe-phenyls give +19 nm in **40** (λ_{red} = 671 nm) and *para*-OMe-phenyls +21 nm in **39** (λ_{red} = 673 nm). When comparing the bathochromic effect per aryl obtained in KFL *vs.* their BbF counterparts, it is exactly the same for ^{i}Pr-Ph (+5 nm) and slightly less important for *ortho* / *para* substituted KFL's (+9.5 / 10.5 nm) than in BbF **5** (+14 nm). This suggests that rational fine-tuning can be achieved when designing new BODIPYs, given that the substituents used will affect the conjugation pathways in a similar fashion.

As mentioned previously, a few derivatives of the BbF series were further studied in ACN solvent (Figures II.S25, II.S27, II.S32, II.S37, II.S39 and II.S41†) in order to establish a better correlation with the unfused non-symmetric derivatives **25** – **29**.[78, 79] The direct comparison in ACN of BbF **1** and derivative **25** that are both equipped with a phenyl at the *meso* position shows that a red-shift of +22 nm is obtained by benzo[*b*]-fusion (λ_{red} = 545 and 523 nm, respectively). This shift also needs to be related to the +9 nm shift of **1** *vs.* BODIPY **26** bearing a sterically hindered and electron-poor *meso*-2,6-dichlorophen-1-yl moiety (λ_{red} = 536 nm). Since derivatives **27** – **29** also have this last moiety, the reduction of 13 nm in the bathochromic shift of **26** *vs.* **25** needs to be kept in mind. From there, it can be seen that BbF **5** (λ_{red} = 559 nm) has only a shift of +5 nm *vs.* the unfused derivative **27** (λ_{red} = 552 nm) (+14 nm *vs.* **1)**. For BbF **8** (λ_{red} = 615 nm), a shift of +7 nm *vs.* **28** (λ_{red} = 608 nm) is obtained (+70 nm *vs.* **1**). Hence, it can be noted from these comparisons implying BbFs **1**, **5** and **8** that substitution at the *para* position of the proximal aryl has less effect on the benzo[*b*]-fused system relative to the same substitution on the unfused pyrrole of compounds **27** – **29**. Interestingly, the authors behind the study of unfused systems also tested the addition of $HClO_4$ in excess to a methanolic solution of **28** and observed a similar blue-shift behaviour (-73 nm) from 608 nm back to 535 nm.[78] As it is insoluble in methanol, BbF **8** was further tested in ACN and protonation of the dimethyl group provided a smaller hypsochromic shift of -65 nm, from 615 nm back to 550 nm. Non-symmetric derivative **29** (λ_{red} = 547 nm) allows a better evaluation of the sole effect of extending the π-conjugated system with a 2-naphthalen moiety. A red-shift of +11 nm is found compared to its proximal phenyl counterpart **26**, while BbF **9** (λ_{red} = 569 nm) reaches +24 nm *vs.* BbF **1**. Thus, addition

of the methoxy group in **9** should provide a red-shift of about +13 nm compared to a related BbF bearing a simple naphthalene, which is consistent with the +14 nm shift obtained for BbF **5** *vs.* **1**. Even though the exact unfused counterpart was not available, we looked at BbF **10** (λ_{red} = 569 nm) to further probe if the more polar ACN medium would promote a better communication between the sterically hindering phenanthrene moiety and the adjacent pyrrole. A blue-shift of -9 nm compared to **1** is found in ACN, which is higher than the -6 nm obtained in DCM and indicate an overall destabilization. This investigation of the five BbF in ACN also ascertained that a moderate solvatochromic effect occurs when switching from the less polar DCM, with blue-shifted values between -8 nm for derivatives **1** and **5** up to -11 nm for **8** and **10**. BbF **9** presented an intermediate shift at -9 nm. As a gauge, these values are about two-to-three times more appreciable than the -4 nm blue-shift encountered in the simpler BODIPY **24**.[86]

Emission properties of the non-symmetric benzo[*b*]-fused platform reported herein are highly promising due to the broad fluorescence in the NIR region (*vide supra*; Figure 3.3 bottom; Table 3.III) and large Stoke shifts (up to 3818 cm^{-1} in CH_2Cl_2 / 4725 cm^{-1} in ACN for BbF **1**). As it is expected from the free rotating *meso*-phenyl offering a major deactivation pathway of the excited state,[87] the quantum yields (Φ_F) obtained are rather low (BbF **1**, **8** and **10** below 0.01 and highest values reaching 0.05 for **5** and 0.11 for **9** in CH_2Cl_2 solution). For BbF **8**, this nearly non-fluorescent behaviour is expected due to low energy of the emission and potential quenching of the excited state by the dimethylamino group, as shown for compound **28**.[78] Indeed, apart from complex **8**, all of the complexes display both higher and lower energy emission bands assigned to the

typical fluorescence of BODIPYs and to charge-transfer bands, respectively (Figure 3.4). The latter assignment is suggested by the broad nature of the emission bands between 684-757 nm and their strong dependence on solvent polarity. The emission is almost fully quenched in polar ACN solvent for the five BbF studied. The lifetimes are also very short in both solvents (τ < 1 ns throughout the series) and leads to high non-radiative rate constants (k_{nr} = 1.0 - 2.5 x 10^9 s^{-1} in DCM). However, this low Φ_F can easily be overcome by incorporating stoppers to the phenyl rotation either on the BODIPY core, *e.g.* **23** (Φ_F = 0.03) *vs.* 1,3,5,7-tetramethyl substituted **24** (Φ_F = 0.67) in DCM,[76, 77] or directly on the *meso* substituent, *e.g.* unfused derivative **25** (Φ_F = 0.02) enlightens by substitution with the *meso*-2,6-dichlorophen-1-yl of **26** (Φ_F = 0.88) in ACN.[78, 79] This assumption is even further supported by other unfused derivatives **27** (Φ_F = 0.85) and **29** (Φ_F = 0.77) bearing similar proximal substituents encountered in the BbF series and the versatile synthetic platform on which the latter is based (*vide supra*). Along this line, non-symmetric benzo[*b*]-fused **30** equipped with both a phenyl and a methyl as blocking groups increased Φ_F up to 0.10 even though no proximal aryl group was installed.[48]

3.4.4 – Computational Modelization Insights

Multiple parameters need to be considered when choosing a computational modelization method in order to find a good equilibrium between highly accurate results and the computational cost.[88-91] In the specific field of BODIPYs dyes and their related Aza-BODIPYs, significant efforts have been made recently by Jacquemin and coworkers to reach a good compromise.[92-95] Still, many different DFT protocols can be found within the field in order to predict or rationalize their optoelectronic properties.[42, 48, 84, 96-98] Based on our previous work with ADPM derivatives using a method developed by Jacquemin *et al.* for Aza-BODIPYs, we decided to use the TD-DFT // DFT protocol PCM-TD-BMK/6-311+G(2d,p) // PCM-PBE0/6-311G(2d,p) with the Polarization Continuum Model (PCM) of CH_2Cl_2 in order to gain insights on the molecular orbitals and structural properties of the BbF series by DFT along with the optical transitions involved by TD-DFT (refer to Computational Methods of ESI†).[39, 95] While this protocol presents inherent limitations due to the vertical approximation, it already proved to rapidly reach semi-quantitative estimates of the λ_{max} and to be flexible towards important structural changes (Aza-BODIPY *vs.* ADPM; various type of aryls in proximal and distal positions). The opportunity to further test this protocol by expending it to BODIPYs, comparing the DFT structural optimization with crystallographic data and assessing the ability of TD-DFT to predict the relative order of λ_{max} within the BbF series thus became appealing.

As mentioned in the electrochemical section, structural information is essential to rationalize experimental results. The first step to ascertain the validity of the PCM-PBE0/6-311G(2d,p) DFT method was to start the calculations from the crystallographic

data obtained for the reference BbF **1** and to optimize it. The second step was to construct from these data other BbF of the series and compared their optimized structures with available crystallographic data for BbF **5**, **8** and **9** (Tables II.S23 and II.S24†). The result was a good matching of bond lengths *vs.* the X-ray data in atoms not directly implied in a structural modification, supporting that an appropriate DFT method was used. Planarization of the DPM core was calculated in all cases, which is generally offset from X-ray results. However, the method was still able to distinguish the better delocalization encountered in BbF **8**. Obviously, one also needs to consider the single molecule environment of theoretical calculations as opposed to the intermolecular forces taking place in the crystal packing in order to explain up to a certain extent the structural differences found. The main drawback of this method appears to be its inability to properly estimate the relative order in the strength of intramolecular H-bonding between the hydrogen on the *ortho* carbon of the proximal aryl and one of the fluoride atoms on the nearby BF_2 chelate (Tables II.S25 and II.S28†). Actually, the computation established that this H-bonding should theoretically be the strongest in BbF **8** where the *p*-NMe_2 is expected to provide the best conjugation with the pyrrole moiety to which it is attached. X-Ray crystal structure showed that this H-bonding is in fact less important than for *p*-OMe substituted BbF **5**, since two different H-bonds were possible in this specific derivative. As optimization explores the energy continuum around the starting geometry in order to find a well of stability, such a special case found in **5** couldn't be predicted by any computational methods. Therefore, the benchmarking of the DFT method used appears satisfactory for the BbF series investigated herein.

The frontier molecular orbitals are depicted in Figure 3.4 and the electronic distribution on the different fragments is given in Table II.S2 and Figure II.S62 of ESI†. Results show the HOMO is mainly located on the benzo[*b*]-fused DPM core and the proximal aryl, with almost no electronic density on the *meso*-phenyl or the BF_2 chelate. The contribution of the *para* substituents on the proximal aryl increases with the strength of the EDG; 10% for reference **1**, 15% for alkyl substituted **2** – **4**, 28% for methoxy substituted **5** and 58% for **8** bearing the dimethylamine group. Introducing one or two methoxy groups in *meta*-positions leads to 13% in **6** and 12% in **7**, respectively, as anticipated from the EWG by an induction effect. Extending the π-conjugated system in **9** leads to 50% of electronic density being found on the 6-methoxynaphthalen-2-yl moiety. Only 34% of density is observed in **10** as expected from the bulky phenanthren-9-yl moiety which decreases communication with the adjacent pyrrole (*vide supra*). The empty LUMO presents an electronic redistribution mainly from the DPM core and proximal aryl towards the *meso*-phenyl and BF_2 chelate according to the same trend described in detail for the HOMO upon variation of the substituent. Therefore, calculations suggest that the indole moiety keeps its EWG character throughout the series as the electron-richness of the pyrrole is tuned by the proximal phenyl, reinforcing the idea of a push-pull effect within the BODIPY core.

The dipole moment was found to be of great importance in the factors governing the electrochemical properties (*vide supra*). Calculations indicate that three key parameters are interplaying to modify the overall polarity of the molecule: i) the nature of the proximal substituent; ii) the degree of communication between the proximal aryl and the adjacent pyrrole; iii) the degree of communication within the benzo[*b*]-fused

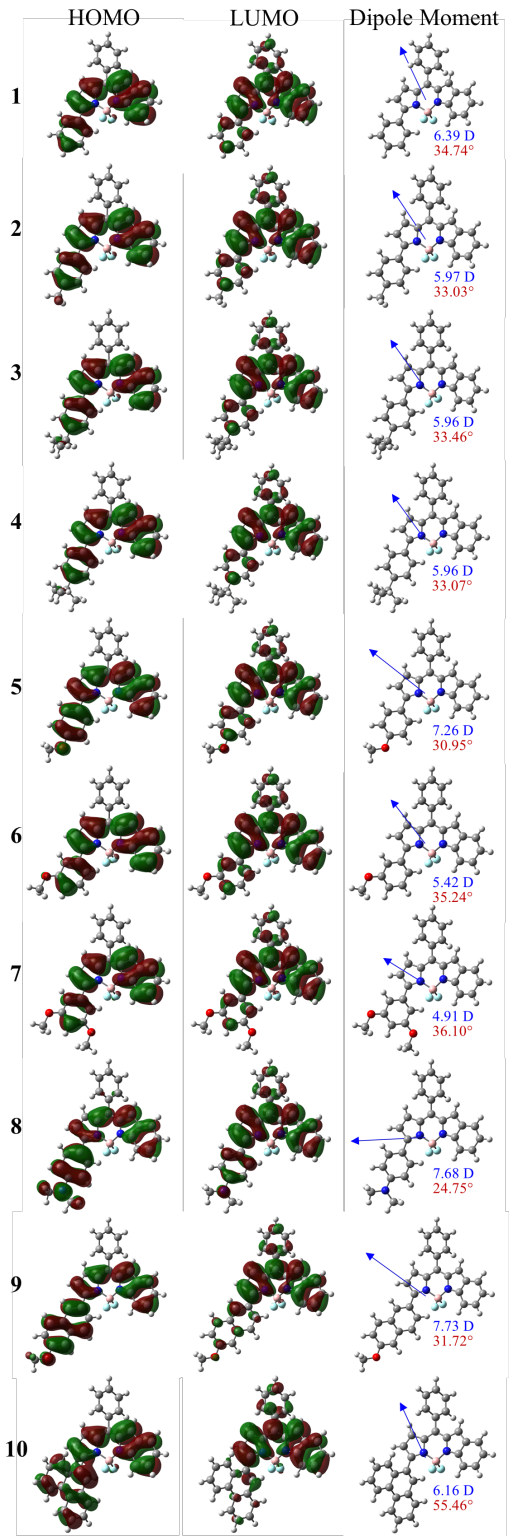

Figure 3.4 – HOMO / LUMO (isovalue = 0.02), dipole moment vector (blue; modulus given in Debye) and dihedral angle (red; φ) between the proximal aryl and the DPM core of BbF **1** – **10** as obtained by DFT.

BODIPY core. Such information is thus critical to bear in mind when designing new dyes with specific electronic properties.

When comparing the energy levels obtained by computation *vs.* experimental ones (Figure 3.2 and Table 3.III), a few discrepancies are found. First, the DFT method tends to underestimate the variation in alkyl substituents on the HOMO and LUMO. Second, theoretical results for BbF **5** are offset since computation alone cannot account for the strong H-bonding regime providing two different molecular configurations and overriding the *para*-substitution trend effect. Third, the induction effect of the *meta*-methoxy substituted BbF **6** and **7** is poorly accounted for as compared to reference **1**. Still, a significant difference is correctly predicted for the HOMO between **7** and *para* substituted Bbf **5**. Fourth, DFT predicts a similar planarization of the benzo[*b*]-fused BODIPY core throughout the series with a tilt angle between planes of the pyrrole and the benzo[b]-fused pyrrole in the range of 8.6 – 8.9°, an exception being that of BbF **8** at 7.5° (Tables II.S23 and II.S24†). This planarization was found to be much more variable in the available X-ray data (Table II.S27†), ranging from 4.2° in **5** up to 15.3° in **1**. This difference suggests that in some cases computational analyses overestimate the overall communication of π-electrons between the different molecule's components and, therefore, the impact of the proximal aryl. Fortunately, the method was able to properly identify the more pronounced planarization effect of the *p*-NMe_2-Ph on the benzo[*b*]-fused BODIPY core in BbF **8**. It also provided a very good match with empirical results in the BbF **8** – **10** series, showing its reliability when strong EDG are used or when the conjugation between the proximal aryl and adjacent pyrrole is sterically hindered. Altogether, care must be taken in the analysis of computational results when so many

parameters are interplaying. This is especially important if the method is to be use *a priori* of the synthesis.

A complete analysis by TD-DFT of optical transitions for the BbF series in CH_2Cl_2 is provided in Figure 3.5, Table 3.3 and in the ESI† (Figures II.S63 – II.S72; Tables II.S3 – II.S22). The trend in $\lambda_{red\ theo}$ calculated is generally in excellent agreement with the empirical order. The method accounts for a red-shift of +5 – 6 nm in alkyls substituted derivatives **2** – **4** compared to reference BbF **1**, which was found to be of +4 – 6 nm for λ_{red}. Similarly, the calculated shift of +16 nm for BbF **5** is close to the empiric +14 nm. Inductive effect of the *meta*-methoxy groups is taken into account by the TD-DFT with a -2 nm hypsochromic shift for **7** and no shift for **6**, but empiric values were slightly red-shifted by +4 and +3 nm, respectively, compared to BbF **1**. Remarkably, the biggest calculated shift in the series was for BbF **8** (+63 nm), in accordance with the biggest one measured (+73 nm). The relative order of *p*-methoxyphenyl substituted **5** (+16 nm vs. **1**), 6-methoxynaphthalen-2-yl **9** (+32 nm; +25 nm observed) and *p*-dimethylaminephenyl **8** (+63 nm) was also properly modeled. The only major difference obtained was the predicted bathochromic shift of +12 nm for BbF **10** that was in fact found to be an hypsochromic one (-6 nm). Therefore, the PCM-TD-BMK/6-311+G(2d,p) protocol used provides reliable semi-quantitative trend with *para*-substitution and extended π-conjugated system where the steric hindrance is not too important.

The calculated transitions obtained by TD-DFT and Natural Transition Orbitals (NTO) analysis can help assign the observed absorption band in the BbF series.[99] The reference BbF **1** has a strong T1 transition (osc. strength = 0.939) corresponding to the

λ_{red} at 553 nm which involves the HOMO -> LUMO orbitals at 99% (Figure 3.5 and Table II.S3). This T1 transition is constant throughout the whole BbF series **1** – **10**, with almost no orbital mixing encountered. Therefore, their λ_{red} can be illustrated by looking at the variation of electronic density between the HOMO and the LUMO in Figure 3.4. The shoulder in the orange part of the spectrum for **1** ($\lambda_{sh\ orange}$ = 517 nm) corresponds to the weak T2 transition (osc. strength = 0.015) where the electronic density upon excitation is mainly taken from the indole moiety towards the whole benzo[*b*]-fused BODIPY core and the proximal phenyl (HOMO-1 -> LUMO at 98%). At higher energy, λ_{violet} at 374 nm is attributable to a combination of T3 – T6 with mixed orbitals contributions from the proximal phenyl, the adjacent pyrrole and the *meso*-phenyl that are all heading to the LUMO upon photoexcitation. The absorption band $\lambda_{near\ UV}$ at 287 nm is another combination of transitions leading to the LUMO. In this case, T7 transfers density mainly from the proximal phenyl, the adjacent pyrrole and the *meso*-phenyl while T8 does it from the indole moiety. Beyond that point, highly energetic transitions in the UV region start to reach higher unoccupied orbitals such as in T9 (HOMO -> LUMO+1 at 84%) and T10 (HOMO -> LUMO+2 at 84%). These two last calculated transitions account for the λ_{UV} at 277 nm. An almost identical assignation as the reference **1** can be made for alkyl substituted BbF **2** – **4**, which is in accordance with the observed absorption spectrum at the top of Figure 3.3. The only significant difference regards the better definition of $\lambda_{near\ UV}$ at *ca.* 300 nm, which is due to the electron-donating properties of the alkyls providing a slight red-shift. *Para*-methoxyphenyl substituted BbF **5** has an apparent splitting of the λ_{violet} at 401 nm and *ca.* 380 nm. This is simply due to the increased oscillator strength of T4 (0.031 vs. 0.025 in **1**). Except this

feature, the general absorption profile is very similar to previously discussed BbF **1** – **4**. Spectra of BbF **6** and **7** are alike, with a higher λ_{UV} absorption band *vs.* $\lambda_{near\ UV}$ that arises from the increased contribution of the *meta*-substituents in T9 and T10 associate with λ_{UV}. BbF **8** is of interest since $\lambda_{near\ UV}$ drastically increases compared to reference **1** in addition to the expected red-shift of absorption maxima due to the strong EDG. This last band involves calculated transitions T4 – T6 where the proximal aryl, the adjacent pyrrole and the *meso*-phenyl all transfer their electronic density towards the LUMO. The general effect of extending the π-conjugated system of the proximal aryl in BbF **9** and **10** is a broadening of the absorption bands in the visible part of the spectrum (*ca.* 280 to 450 nm). For BbF **9**, the most significant impact of the extension is seen in T3, corresponding to λ_{violet}, and T4 associated with the new band at 375 nm. In BbF **10**, the impact is on transitions T3 – T5, with T3 corresponding to λ_{violet} plus T4 and T5 associated with the new band observed at 365 nm.

Overall, the semi-quantitative TD-DFT // DFT protocol used to rationalize the empirical results of electrochemistry and spectroscopy provided essential insights. Still, a critical analysis of the calculations compared to experimental measurements showed that the complex interplay of structural factors in the BbF series is hardly accounted *in silico* and precautions should be taken if modelization is to be made ahead of the synthesis.

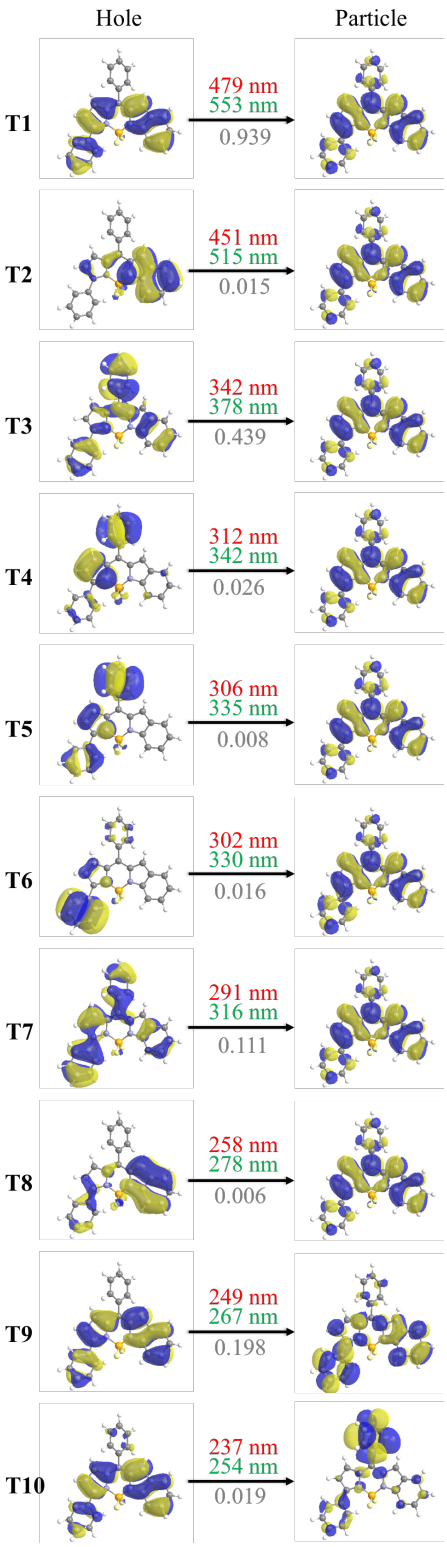

Figure 3.5 – NTO analysis for absorption transitions T1 – T10 of reference BbF **1.**

(red = calculated; green = corrected; grey = oscillator strength).

Refer to ESI for a complete analysis of the series.†

3.4.5 – X-Ray Diffraction

Crystals suitable for X-ray diffraction studies were obtained for a good variety of substituents on the proximal aryl including the reference BbF **1** and *para*-substituted derivatives **5** equipped with a methoxy, **8** with a dimethylamine and **9** with the extended π-conjugated system of 6-methoxynaphthalen-2-yl (Figure 3.6 and Tables II.S26 – II.S28†). Compounds **1**, **8** and **9** crystallized in the orthorhombic crystal system (Pbca, $P2_12_12_1$ and $Pna2_1$ space groups, respectively) while **5** crystallized in the $P2_1/c$ space group (Table II.S26†). The latter structure required additional refinement operations in order to model the disordered *p*-OMe-Ph moiety due to intramolecular hydrogen-bonding with both fluoride atoms acting as acceptors for a C-H donor in *ortho*-position of the proximal aryl group. Thus, two positions coexist for this substituent in a 53 : 47 ratio. While H-bonds were observed in all four complexes, only one hydrogen bond to a single fluoride atom was observed for **1**, **8** and **9** leading to no such disorder (Figure 3.6 and Table II.S28†). According to the requirements of donor-acceptor distance and donor-H-acceptor angles for strong H-bonding (D···A = 2.5 – 3.2 Å / D-H···A = 130 – 180°),[100] it was found that all four compounds fall within this regime. However, only BbF **5** is within the expected range for strong H-bonds regarding H-acceptor distances (H···A = 1.5 – 2.2 Å), with values of 2.080(1) and 1.933(1) Å for the two disordered positions. BbF **8** is slightly longer [2.227(1) Å] to be considered in the strong regime, while a larger deviation is observed for reference **1** and **9** [2.352(1) and 2.351(1) Å, respectively]. Investigation of the core structure shows that the introduction of the benzo[*b*]-fused pyrrole favours the resonance form with the benzene being aromatic and nonaromatic azafulvene substructures (as depicted in Scheme 3.1) over a quinoidal

structure of the indole moiety, at least in the solid-state. Supporting this, C1-N1 is longer than C13-N2 [1.372(2) – 1.378(2) *vs.* 1.347(2) – 1.359(2) Å] and C8-C9 is longer than C9-C10 [1.425(2) – 1.432(2) *vs.* 1.381(2) – 1.384(3) Å] in all four compounds (Table III.S27†). A similar observation was reported by Wakamiya *et al.* for the non-symmetric benzo[*b*]-fused BODIPY **31** (Figure 3.1) and further calculations suggested the quinoid form also contributes to some extent to the resonance equilibrium.[42] The tilt angle between the pyrrole ring and its benzo[*b*]-fused pyrrole counterpart also helps understand the extent of conjugation within the DPM core itself. The bottom of Figure 6 shows that this angle is much smaller in the case of BbF **8** [4.2(1)°] than for **9** [9.9(1)°], **5** [10.3(1)°] or the reference **1** [15.3(1)°]. Thus, the electron delocalization efficiency follows the same trend with **8** having the most conjugated core and **1** the least.

No other significant variation (within 3σ) on bond lengths or angles was found except in the case of BbF **8** for which the C13-C14 bond connecting the proximal aryl substituent to the pyrrole ring is shorter than in other BbF derivatives [1.452(2) *vs.* 1.466(2) – 1.470(2) Å], indicating some double-bond character and an increased communication between the π-electrons of the two fragments. This was also supported by the shorter C17-N3 distance [1.358(2) Å] as compared to *N,N*-dimethylaniline [1.385(4) Å].[101] The dihedral angle between the proximal aryl and the pyrrole ring (C12-C13-C14-C15) in **5** exhibits the smallest angles [-18.4(4) and +11.6(3)° for the two disordered positions] as compared to **8** [-27.7(2)°], **1** [-34.6(2)] and **9** [+39.5(3)°] in increasing order. This trend is consistent with the short intramolecular H-bonding distance in the solid-state, i.e., compound **5** displays the shortest H-to-F distance consistent with a strong C-H to F hydrogen bond, and therefore, the lowest tilt angle of

the solid-state structures. The tilt angles between the *meso*-phenyl and the DPM moiety display less deviation, with absolute values between 47.4(1)° for **9** and 52.2(1)° for **8**. Interestingly, BbF **9** crystallized with both the proximal aryl and *meso*-phenyl in opposite directions as compared to related derivatives.

Together, these structural results revealed a significant interplay in the degree of communication between the proximal aryl, the pyrrole to which it is attached and the adjacent indole moiety which is in agreement with electrochemical, photophysical and theoretical data previously discussed.

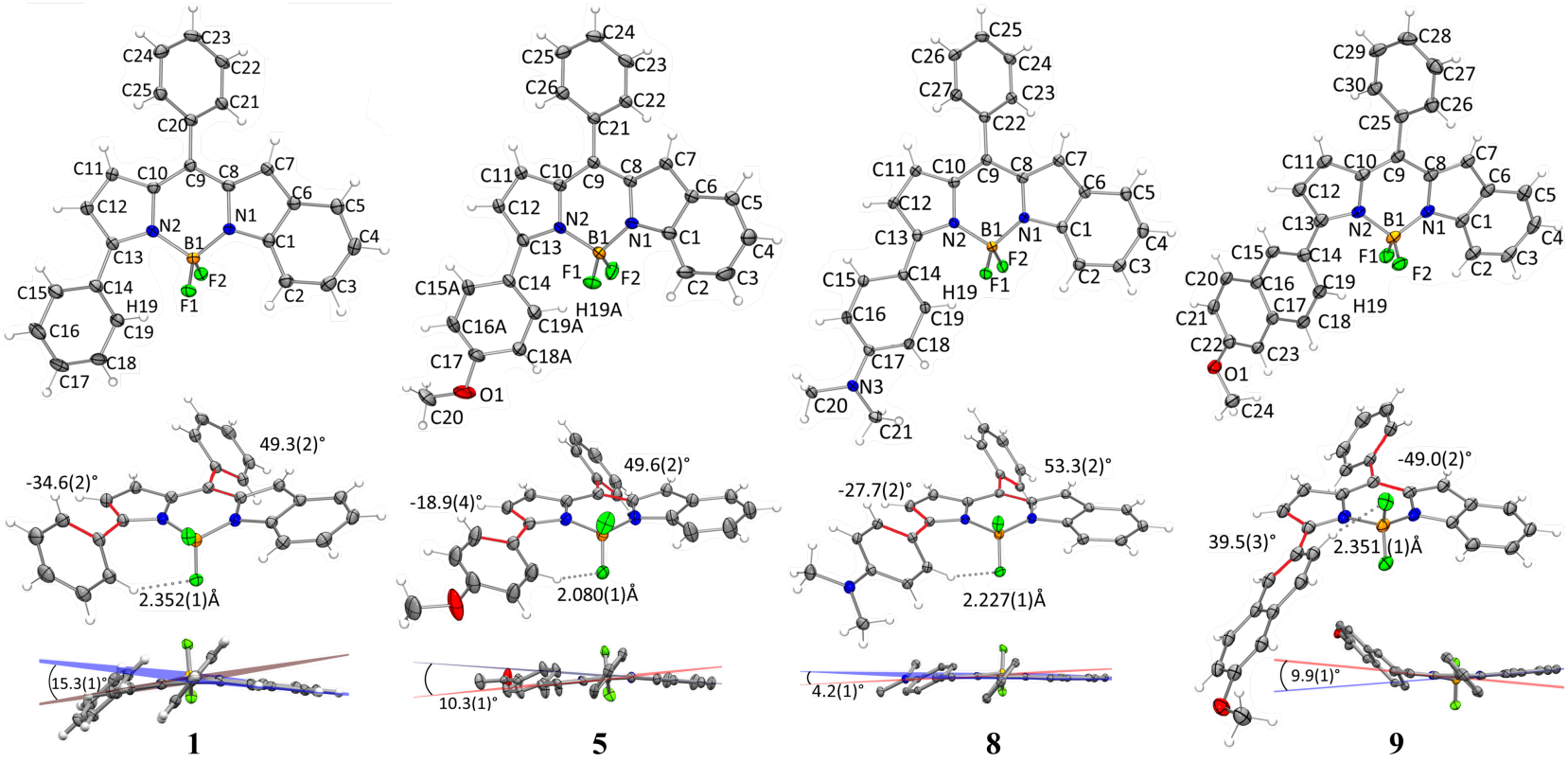

Figure 3.6 – Solid-state structures of BbF **1** (R_1 = 4.88 %), **5** (5.04 %)**, 8** (2.77 %) and **9** (3.04 %).

[Ellipsoids shown at 50 % probability level; intramolecular H-bonds represented in dot grey; dihedral angles defined in red, angle between pyrrole and indole planes (bottom)]

3.5 – Conclusion

In summary, a novel family of ten non-symmetric benzo[*b*]-fused BODIPYs bearing various proximal aryls was prepared according to a versatile synthetic method. A critical analysis compared the optoelectronic properties obtained within the BbF series and across an extensive series of 23 derivatives from 9 different BODIPY families. Such an exercise provides a better overview of the impact of various fusion modes and π-system modifications available for BODIPYs and may provide guidelines for the design of new fluorophores specifically tailored for the plethora of applications where these compounds are now applied. Along this line, the non-symmetric BbF platform reported herein was discussed regarding the requirements for photovoltaic component and molecular probes. Adduct **8** was shown to be especially interesting for both type of applications. X-Ray structural characterization and computational modelization were further used to gain insights on the properties observed by electrochemistry and spectroscopy. In order to assess the validity of the computational protocol used and to evaluate its potential as a reference, it was compared to the structural data obtained by crystallography and other experimental measurements. Overall, the BbF platform proves to be a powerful one as it offers considerable leverage for efficient fine-tuning of optoelectronic properties and applications as efficient deep-red absorbers and NIR fluorophores.

3.6 – Associated Content

Supporting Information

† Electronic Supplementary Information (ESI; Annexe II) available: Experimental section including materials, instrumentation and synthetic methods; NMR; MS; electrochemical and spectroscopic details; computational methods and results; crystallographic data for BbF **1**, **5**, **8** and **9** (CCDC 1418610 – 1418613).

3.6 – Acknowledgements

GSH thanks the Natural Sciences and Engineering Research Council of Canada, the Centre for Self-Assembled Chemical Structures (CSACS), the Centre in Green Chemistry and Catalysis (CGCC) and the Université de Montréal for financial support. AB is obliged to NSERC, FQRNT and PCAS Canada for a BMP-Innovation grant; MITACS for an Accelerate grant and to Hydro-Québec for an excellence grant. Compute Canada is thanked for access to their national supercomputing platform as are Prof. Dmitrii F. Perepichka and Dr M. Rajeswara Rao for access and support in the use of their integrating sphere. AB is grateful to Dr Anne-Catherine Bédard for useful scientific discussions.

3.7 – Bibliography

1. A. Loudet and K. Burgess, *Chem. Rev.*, 2007, **107**, 4891-4932.
2. R. Ziessel, G. Ulrich and A. Harriman, *New J. Chem.*, 2007, **31**, 496-501.
3. A. Bessette and G. S. Hanan, *Chem. Soc. Rev.*, 2014, **43**, 3342-3405.
4. G. Ulrich, R. Ziessel and A. Harriman, *Angew. Chem., Int. Ed.*, 2008, **47**, 1184-1201.
5. H. Lu, J. Mack, Y. Yang and Z. Shen, *Chem. Soc. Rev.*, 2014, **43**, 4778-4823.
6. A. Mishra and P. Bäuerle, *Angew. Chem., Int. Ed.*, 2012, **51**, 2020-2067.
7. S. K. Balasingam, M. Lee, K. Man Gu and Y. Jun, *Chem. Commun.*, 2013, **49**, 1471-1487.
8. T. Kowada, H. Maeda and K. Kikuchi, *Chem. Soc. Rev.*, 2015, **44**, 4953-4972.
9. L. Yuan, W. Lin, K. Zheng, L. He and W. Huang, *Chem. Soc. Rev.*, 2013, **42**, 622-661.
10. D. Su, J. Oh, S.-C. Lee, J. M. Lim, S. Sahu, X. Yu, D. Kim and Y.-T. Chang, *Chem. Sci.*, 2014, **5**, 4812-4818.
11. T. Papalia, G. Siracusano, I. Colao, A. Barattucci, M. C. Aversa, S. Serroni, G. Zappalà, S. Campagna, M. T. Sciortino, F. Puntoriero and P. Bonaccorsi, *Dyes Pigm.*, 2014, **110**, 67-71.
12. T. Papalia, R. Lappano, A. Barattucci, A. Pisano, G. Bruno, M. F. Santolla, S. Campagna, P. De Marco, F. Puntoriero, E. M. De Francesco, C. Rosano, M. Maggiolini and P. Bonaccorsi, *Org. Biomol. Chem.*, 2015, **13**, 10437-10441.
13. A. Kamkaew, S. H. Lim, H. B. Lee, L. V. Kiew, L. Y. Chung and K. Burgess, *Chem. Soc. Rev.*, 2013, **42**, 77-88.
14. C. Zhang, J. Zhao, S. Wu, Z. Wang, W. Wu, J. Ma, S. Guo and L. Huang, *J. Am. Chem. Soc.*, 2013, **135**, 10566-10578.
15. Y. Yang, Q. Guo, H. Chen, Z. Zhou, Z. Guo and Z. Shen, *Chem. Commun.*, 2013, **49**, 3940-3942.
16. S. Guo, L. Ma, J. Zhao, B. Kucukoz, A. Karatay, M. Hayvali, H. G. Yaglioglu and A. Elmali, *Chem. Sci.*, 2014, **5**, 489-500.
17. X.-F. Zhang and X. Yang, *J. Phys. Chem. B*, 2013, **117**, 5533-5539.
18. X.-F. Zhang and X. Yang, *J. Phys. Chem. B*, 2013, **117**, 9050-9055.
19. W. Li, L. Li, H. Xiao, R. Qi, Y. Huang, Z. Xie, X. Jing and H. Zhang, *RSC Adv.*, 2013, **3**, 13417-13421.
20. A. B. Nepomnyashchii and A. J. Bard, *Acc. Chem. Res.*, 2012, **45**, 1844-1853.
21. D. Frath, J. Massue, G. Ulrich and R. Ziessel, *Angew. Chem., Int. Ed.*, 2014, **53**, 2290-2310.
22. S. Debnath, S. Singh, A. Bedi, K. Krishnamoorthy and S. S. Zade, *J. Phys. Chem. C*, 2015, **119**, 15859-15867.
23. R. Ziessel, G. Ulrich, A. Haefele and A. Harriman, *J. Am. Chem. Soc.*, 2013, **135**, 11330-11344.

24. J. Iehl, J.-F. Nierengarten, A. Harriman, T. Bura and R. Ziessel, *J. Am. Chem. Soc.*, 2012, **134**, 988-998.
25. R. Ziessel and A. Harriman, *Chem. Commun.*, 2011, **47**, 611-631.
26. B. Zheng, R. P. Sabatini, W.-F. Fu, M.-S. Eum, W. W. Brennessel, L. Wang, D. W. McCamant and R. Eisenberg, *PNAS*, 2015, **112**, E3987-E3996.
27. L. Dura, J. Ahrens, M.-M. Pohl, S. Höfler, M. Bröring and T. Beweries, *Chem. Eur. J.*, 2015, **21**, 13549-13552.
28. A. M. Poe, A. M. Della Pelle, A. V. Subrahmanyam, W. White, G. Wantz and S. Thayumanavan, *Chem. Commun.*, 2014, **50**, 2913-2915.
29. Y. Kubo, D. Eguchi, A. Matsumoto, R. Nishiyabu, H. Yakushiji, K. Shigaki and M. Kaneko, *J. Mater. Chem. A*, 2014, **2**, 5204-5211.
30. S. Kolemen, O. A. Bozdemir, Y. Cakmak, G. Barin, S. Erten-Ela, M. Marszalek, J.-H. Yum, S. M. Zakeeruddin, M. K. Nazeeruddin, M. Grätzel and E. U. Akkaya, *Chem. Sci.*, 2011, **2**, 949-954.
31. S. P. Singh and T. Gayathri, *Eur. J. Org. Chem.*, 2014, **2014**, 4689-4707.
32. V. Lakshmi, M. Rajeswara Rao and M. Ravikanth, *Org. Biomol. Chem.*, 2015, **13**, 2501-2517.
33. T. E. Wood and A. Thompson, *Chem. Rev.*, 2007, **107**, 1831-1861.
34. M. Cibian, A. Bessette, A. O'Connor, J. G. Ferreira and G. S. Hanan, *Acta Crystallogr., Sect. C*, 2015, **71**, 122-127.
35. A. Bessette, J. G. Ferreira, M. Giguère, F. Bélanger, D. Désilets and G. S. Hanan, *Inorg. Chem.*, 2012, **51**, 12132-12141.
36. Y. V. Zatsikha, E. Maligaspe, A. A. Purchel, N. O. Didukh, Y. Wang, Y. P. Kovtun, D. A. Blank and V. N. Nemykin, *Inorg. Chem.*, 2015, **54**, 7915-7928.
37. I. García-Moreno, L. Wang, A. Costela, J. Bañuelos, I. López Arbeloa and Y. Xiao, *ChemPhysChem*, 2012, **13**, 3923-3931.
38. L. Jiao, C. Yu, M. Liu, Y. Wu, K. Cong, T. Meng, Y. Wang and E. Hao, *J. Org. Chem.*, 2010, **75**, 6035-6038.
39. A. Bessette, M. Cibian, F. Belanger, D. Desilets and G. S. Hanan, *Phys. Chem. Chem. Phys.*, 2014, **16**, 22207-22221.
40. H. Liu, H. Lu, Z. Zhou, S. Shimizu, Z. Li, N. Kobayashi and Z. Shen, *Chem. Commun.*, 2015, **51**, 1713-1716.
41. S. Shimizu , A. Murayama, T. Haruyama, T. Iino, S. Mori, H. Furuta and N. Kobayashi *Chem. Eur. J.*, 2015, **21**, 12996-13003.
42. A. Wakamiya, T. Murakami and S. Yamaguchi, *Chem. Sci.*, 2013, **4**, 1002-1007.
43. E. Rousset, D. Chartrand, I. Ciofini, V. Marvaud and G. S. Hanan, *Chem. Commun.*, 2015, **51**, 9261-9264.
44. M.-P. Santoni, A. K. Pal, G. S. Hanan, M.-C. Tang, A. Furtos and B. Hasenknopf, *Dalton Trans.*, 2014, **43**, 6990-6993.
45. A. K. Pal, S. Serroni, N. Zaccheroni, S. Campagna and G. S. Hanan, *Chem. Sci.*, 2014, **5**, 4800-4811.
46. A. K. Pal, N. Zaccheroni, S. Campagna and G. S. Hanan, *Chem. Commun.*, 2014, **50**, 6846-6849.

47. A. K. Pal and G. S. Hanan, *Chem. Soc. Rev.*, 2014, **43**, 6184-6197.
48. Y. Ni, W. Zeng, K.-W. Huang and J. Wu, *Chem. Commun.*, 2013, **49**, 1217-1219.
49. Y. Ni and J. Wu, *Org. Biomol. Chem.*, 2014, **12**, 3774-3791.
50. M. Verdoes, U. Hillaert, B. I. Florea, M. Sae-Heng, M. D. P. Risseeuw, D. V. Filippov, G. A. van der Marel and H. S. Overkleeft, *Bioorg. Med. Chem. Lett.*, 2007, **17**, 6169-6171.
51. R. D. Rieth, N. P. Mankad, E. Calimano and J. P. Sadighi, *Org. Lett.*, 2004, **6**, 3981-3983.
52. W.-C. Gao, S. Jiang, R.-L. Wang and C. Zhang, *Chem. Commun.*, 2013, **49**, 4890-4892.
53. G. R. Humphrey and J. T. Kuethe, *Chem. Rev.*, 2006, **106**, 2875-2911.
54. N. Kaewchangwat, R. Sukato, V. Vchirawongkwin, T. Vilaivan, M. Sukwattanasinitt and S. Wacharasindhu, *Green Chemistry*, 2015, **17**, 460-465.
55. Preparation of para-nitro-phenyl substituted electron-poor BbF was not attainable in our hands using the described synthetic methodology.
56. Y. Li, *Acc. Chem. Res.*, 2012, **45**, 723–733.
57. N. Boens, V. Leen and W. Dehaen, *Chem. Soc. Rev.*, 2012, **41**, 1130-1172.
58. N. Blouin, A. Michaud, D. Gendron, S. Wakim, E. Blair, R. Neagu-Plesu, M. Belletête, G. Durocher, Y. Tao and M. Leclerc, *J. Am. Chem. Soc.*, 2008, **130**, 732-742.
59. V. Lakshmi, M. Shaikh and M. Ravikanth, *J. Fluoresc.*, 2013, **23**, 519-525.
60. V. J. Richards, A. L. Gower, J. E. H. B. Smith, E. S. Davies, D. Lahaye, A. G. Slater, W. Lewis, A. J. Blake, N. R. Champness and D. L. Kays, *Chem. Commun.*, 2012, **48**, 1751-1753.
61. Y. Tomimori, T. Okujima, T. Yano, S. Mori, N. Ono, H. Yamada and H. Uno, *Tetrahedron*, 2011, **67**, 3187-3193.
62. C. Hansch, A. Leo and R. W. Taft, *Chem. Rev.*, 1991, **91**, 165-195.
63. H. Svith, H. Jensen, J. Almstedt, P. Andersson, T. Lundbäck, K. Daasbjerg and M. Jonsson, *J. Phys. Chem. A*, 2004, **108**, 4805-4811.
64. While the ground state electrochemistry of isolated molecules does not provide the formal E_{Ox}*****, adding the ΔEOpt to the HOMO level provide a good first approximation based on the Rehm-Weller equation with no added work function term.
65. Various values are reported in literature regarding the exact LUMO level of the PCBM vs vacuum. The value of -3.91 eV is from: He *et al.*, *Phys. Chem. Chem. Phys.*, 2011, **13**, 1970-1983. The value of -4.3 eV is from: Blouin *et al.*, *J. Am. Chem. Soc.* 2008, **130**, 732-742.
66. A. Hagfeldt, G. Boschloo, L. Sun, L. Kloo and H. Pettersson, *Chem. Rev.*, 2010, **110**, 6595-6663.
67. S. M. McAfee, J. M. Topple, I. G. Hill and G. C. Welch, *J. Mater. Chem. A*, 2015, **3**, 16393-16408.
68. K. Cnops, G. Zango, J. Genoe, P. Heremans, M. V. Martinez-Diaz, T. Torres and D. Cheyns, *J. Am. Chem. Soc.*, 2015, **137**, 8991-8997.

69. D. Sun, D. Meng, Y. Cai, B. Fan, Y. Li, W. Jiang, L. Huo, Y. Sun and Z. Wang, *J. Am. Chem. Soc.*, 2015, **137**, 11156-11162.
70. W. Senevirathna, J.-y. Liao, Z. Mao, J. Gu, M. Porter, C. Wang, R. Fernando and G. Sauve, *J. Mater. Chem. A*, 2015, **3**, 4203-4214.
71. J. Zhao, Y. Li, H. Lin, Y. Liu, K. Jiang, C. Mu, T. Ma, J. Y. Lin Lai, H. Hu, D. Yu and H. Yan, *Energy Environ. Sci.*, 2015, **8**, 520-525.
72. Y. Lin and X. Zhan, *Materials Horizons*, 2014, **1**, 470-488.
73. K. Cnops, B. P. Rand, D. Cheyns, B. Verreet, M. A. Empl and P. Heremans, *Nat. Commun.*, 2014, **5**, 3406.
74. P. Sonar, J. P. Fong Lim and K. L. Chan, *Energy Environ. Sci.*, 2011, **4**, 1558-1574.
75. M. C. Scharber, D. Mühlbacher, M. Koppe, P. Denk, C. Waldauf, A. J. Heeger and C. J. Brabec, *Adv. Mater.*, 2006, **18**, 789-794.
76. C. Yu, L. Jiao, H. Yin, J. Zhou, W. Pang, Y. Wu, Z. Wang, G. Yang and E. Hao, *Eur. J. Org. Chem.*, 2011, **2011**, 5460-5468.
77. L. Wang, Y. Zhang and Y. Xiao, *RSC Adv.*, 2013, **3**, 2203-2206.
78. B. Verbelen, S. Boodts, J. Hofkens, N. Boens and W. Dehaen, *Angew. Chem., Int. Ed.*, 2015, **54**, 4612-4616.
79. L. Wang, B. Verbelen, C. Tonnele, D. Beljonne, R. Lazzaroni, V. Leen, W. Dehaen and N. Boens, *Photochem. Photobiol. Sci.*, 2013, **12**, 835-847.
80. C. Yu, Y. Xu, L. Jiao, J. Zhou, Z. Wang and E. Hao, *Chem. Eur. J.*, 2012, **18**, 6437-6442.
81. K. Umezawa, A. Matsui, Y. Nakamura, D. Citterio and K. Suzuki, *Chem. Eur. J.*, 2009, **15**, 1096-1106.
82. A. Y. Bochkov, I. O. Akchurin, O. A. Dyachenko and V. F. Traven, *Chem. Commun.*, 2013, **49**, 11653-11655.
83. Y. V. Zatsikha, V. P. Yakubovskyi, M. P. Shandura, I. Y. Dubey and Y. P. Kovtun, *Tetrahedron*, 2013, **69**, 2233-2238.
84. C. Maeda, T. Todaka and T. Ema, *Org. Lett.*, 2015, **17**, 3090-3093.
85. K. Umezawa, Y. Nakamura, H. Makino, D. Citterio and K. Suzuki, *J. Am. Chem. Soc.*, 2008, **130**, 1550-1551.
86. K. Guzow, K. Kornowska and W. Wiczk, *Tetrahedron Lett.*, 2009, **50**, 2908-2910.
87. H. L. Kee, C. Kirmaier, L. Yu, P. Thamyongkit, W. J. Youngblood, M. E. Calder, L. Ramos, B. C. Noll, D. F. Bocian, W. R. Scheidt, R. R. Birge, J. S. Lindsey and D. Holten, *J. Phys. Chem. B*, 2005, **109**, 20433-20443.
88. P. Geerlings, S. Fias, Z. Boisdenghien and F. De Proft, *Chem. Soc. Rev.*, 2014, **43**, 4989-5008.
89. C. Adamo and D. Jacquemin, *Chem. Soc. Rev.*, 2013, **42**, 845-856.
90. D. Jacquemin, E. A. Perpète, I. Ciofini and C. Adamo, *Acc. Chem. Res.*, 2009, **42**, 326-334.
91. B. Le Guennic and D. Jacquemin, *Acc. Chem. Res.*, 2015, **48**, 530-537.
92. S. Chibani, B. Le Guennic, A. Charaf-Eddin, A. D. Laurent and D. Jacquemin, *Chem. Sci.*, 2013, **4**, 1950-1963.

93. D. Jacquemin, A. Planchat, C. Adamo and B. Mennucci, *J. Chem. Theo. Comp.*, 2012, **8**, 2359-2372.
94. S. Chibani, A. D. Laurent, B. Le Guennic and D. Jacquemin, *J. Chem. Theo. Comp.*, 2014, **10**, 4574-4582.
95. B. Le Guennic, O. Maury and D. Jacquemin, *Phys. Chem. Chem. Phys.*, 2012, **14**, 157-164.
96. Y. Chen, J. Zhao, H. Guo and L. Xie, *J. Org. Chem.*, 2012, **77**, 2192-2206.
97. S. Mukherjee and P. Thilagar, *RSC Adv.*, 2015, **5**, 2706-2714.
98. L. Zhang, L.-Y. Zou, J.-F. Guo, D. Wang and A.-M. Ren, *New J. Chem.*, **2015**, ASAP.
99. R. L. Martin, *The Journal of Chemical Physics*, 2003, **118**, 4775-4777.
100. G. R. Desiraju and T. Steiner, *The Weak Hydrogen Bond: In Structural Chemistry and Biology*, Oxford University Press, New York, 2001.
101. T. Dahl, *Acta Crystallogr., Sect. C*, 1985, 41, 931-933.

Chapitre 4 : Azadipyrromethene Cyclometalation on Neutral Ru^{II} Complexes: Photosensitizers with Extended Near-Infrared Absorption for Solar Energy Conversion Applications

André Bessette,[a, b] Mihaela Cibian,[a] Janaina G. Ferreira,[a] Brian DiMarco,[c] Francis Bélanger,[b] Denis Désilets,[b] Gerald J. Meyer,*[c] and Garry S. Hanan*[a]

[a] Département de Chimie, Université de Montréal, Pavillon J.-A. Bombardier, 5155 Decelles Avenue, Montréal, Québec, H3T-2B1, Canada

[b] Saint-Jean Photochemicals Inc., 725 Trotter street, Saint-Jean-sur-Richelieu, Québec, J3B 8J8, Canada.

[c] Departments of Chemistry and Materials Science & Engineering, The University of North Carolina at Chapel Hill, Chapel Hill, North Carolina, 27599-3290, USA.

Soumis le 30 septembre 2015 à *Chemical Science*
Identification du manuscrit : SC-EDG-09-2015-003713

Contribution des auteurs:

- André Bessette : synthèse et charactérisation; électrochimie, photophysique, modélisation moléculaire et rédaction de l'article.
- Mihaela Cibian et Janaina G. Ferreira: cristallographie rayons-X
- Brian DiMarco et Gerald J. Meyer: Tests de photoinjection
- Francis Bélanger: superviseur en industrie
- Denis Désilets et Garry S. Hanan: Co-directeurs

4.1 – Abstract

In the on-going quest to harvest near-infrared (NIR) photons for energy conversion applications, a novel family of neutral ruthenium (II) sensitizers has been developed by cyclometalation of an azadipyrromethene chromophore. These rare examples of neutral ruthenium complexes based on polypyridine ligands exhibit an impressive panchromaticity achieved by the cyclometalation strategy, with strong light absorption in the 600 – 800 nm range that tails beyond 1100 nm in the terpyridine-based adducts. Evaluation of the potential for Dye-Sensitized Solar Cells (DSSC) and Organic Photovoltaic (OPV) applications is made through rationalization of the structure-property relationship by spectroscopic, electrochemical, X-ray structural and computational modelization investigations. Spectroscopic evidence for photo-induced charge injection into the conduction band of TiO_2 is also provided.

4.2 – Keywords

Neutral Ru^{II} complexes; Azadipyrromethene; Cyclometalation; Panchromatic dyes; NIR absorption; Photovoltaic; Dye-sensitized solar cells (DSSC); Organic Photovoltaic (OPV); π-conjugated materials; Structure-property relationships; Photophysic; Electrochemistry; Photoinjection; Computational modelization; DFT; TD-DFT; X-Ray structures.

4.3 – Introduction

A world powered exclusively by renewable sources is an attainable goal over the course of the 21st century and constitutes one of the main challenges for humankind.[1,2] To reach such an ambitious ideal, solar energy represents one of the most meaningful alternatives to consider in order to finally replace fossil fuels as our principal energy source. Nature's photosynthetic systems found in plants and microorganisms symbolize an unlimited source of inspiration for the scientific community working on solar energy conversion, continuously revealing crucial secrets.[3,4] From Dye-Sensitized Solar Cells (DSSCs) to artificial leaves, the optoelectronic devices developed so far have all integrated elements, functions or principles observed in photosystem II (PSII).[5,6] Among the best example of ideas gleaned from nature, the use of push-pull neutral metalloporphyrins co-sensitized with organic chromophores has led to power conversion efficiencies (PCE) of over 13% in DSSCs due to greater panchromaticity.[7-9] Significant PCE improvements have also been achieved in Organic Photovoltaic (OPV) devices by extending the absorption of photons toward the near-infrared (NIR) spectral region.[10-13] The quest for materials that absorb in the NIR resides in the fact that *ca.* 50% of the total solar radiation intensity hitting Earth's surface is in the range of 700 to 2000 nm, with core part of the flux centered between 600 to 800 nm.[10,14] It is, therefore, not surprising that PSII efficiently absorbs light up to about 800 nm.[15]

Among the best chromophores to reach the red-to-NIR spectral regions are azadipyrromethenes (ADPMs), a family of dye structurally related to dipyrromethene (DPM) and porphyrinoids.[16] The advantages that ADPM has over the DPM and porphyrinoids are both synthetic and electronic. ADPM doesn't require the tedious and

low yielding macrocyclic formation step of the porphyrinoids and it has an intrinsic bathochromic shift of about 50 nm as compared to DPM. Their high absorbance in the yellow-to-red part of the spectrum and strong NIR luminescence encountered in BF_2-chelated Aza-BODIPY analogues are appealing in the context of designing new light-harvesting materials.[17-23] This is especially true as they provide a flexible coordinating motif to further fine-tune their properties with various metallic centers.[24-31] Lately, DPM- and ADPM-based materials have found application as photosensitizers in DSSC and OPV applications where they have provided significant improvements of panchromaticity and PCE.[16,32-37]

Herein, we report the development of a novel family of organometallic sensitizers based for the very first time on the cyclometalation of an ADPM chromophore to form neutral ruthenium (II) complexes (Scheme 4.1). The resulting photosensitizers present an impressive panchromaticity, with strong light absorption in the 600 – 800 nm range which even reaches beyond 1100 nm in the case of terpyridine-based adducts. Evaluation of their solar energy conversion potential for DSSC and OPV applications is made possible through a systematic investigation of spectroscopic, electrochemical and X-ray structural properties. Computational modelization also provides strong support in order to assess the effect of various structural modifications implemented in the series. Further testing in solar cells points toward efficient charge photoinjection in DSSC and unprecedented NIR light absorption for a ruthenium-based photosensitizer,[38-47] even when compared to related complexes bearing the DPM moiety.[48-53]

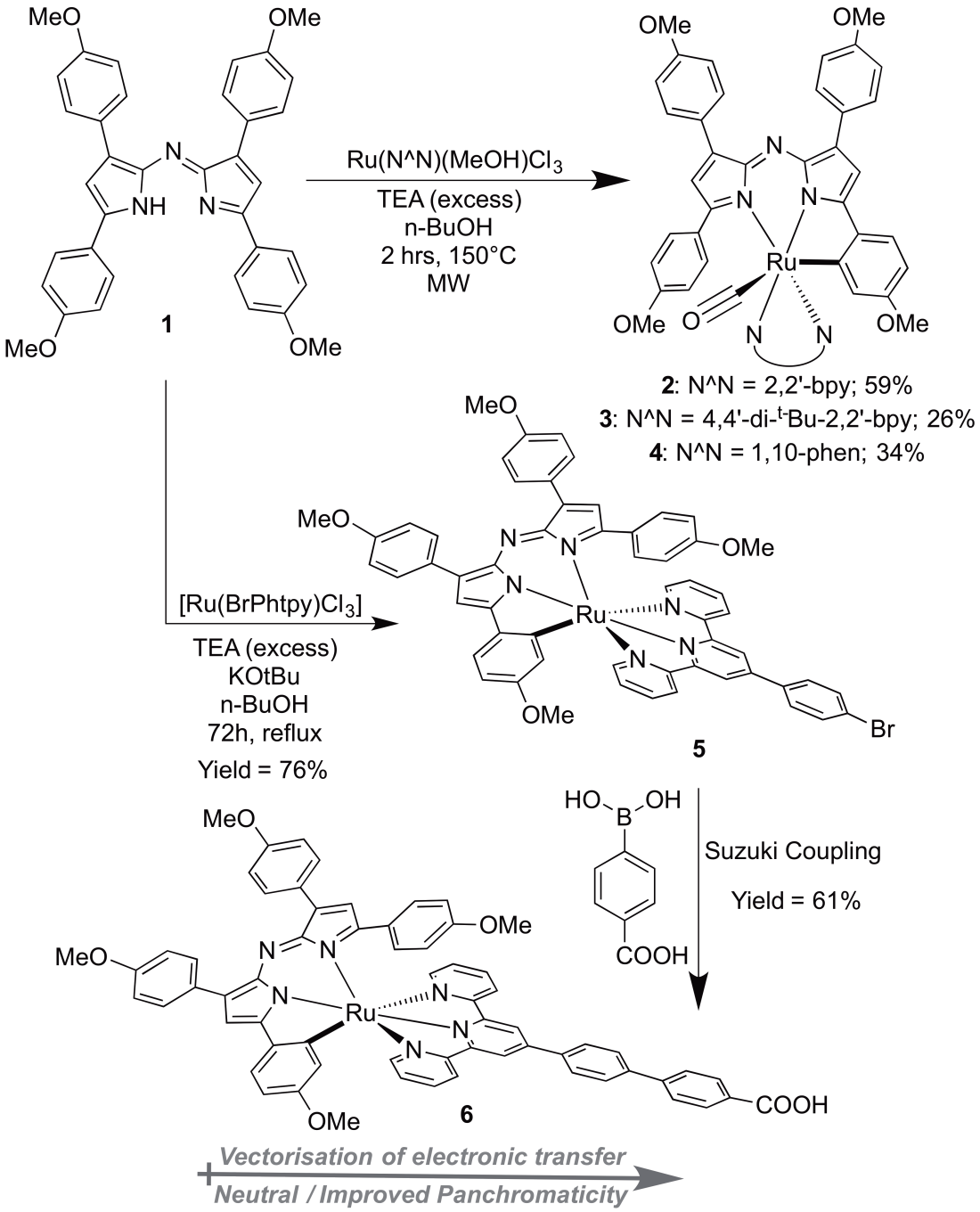

Scheme 4.1 – Synthesis of cyclometalated ADPM neutral Ru(II) sensitizers **2** – **6**.

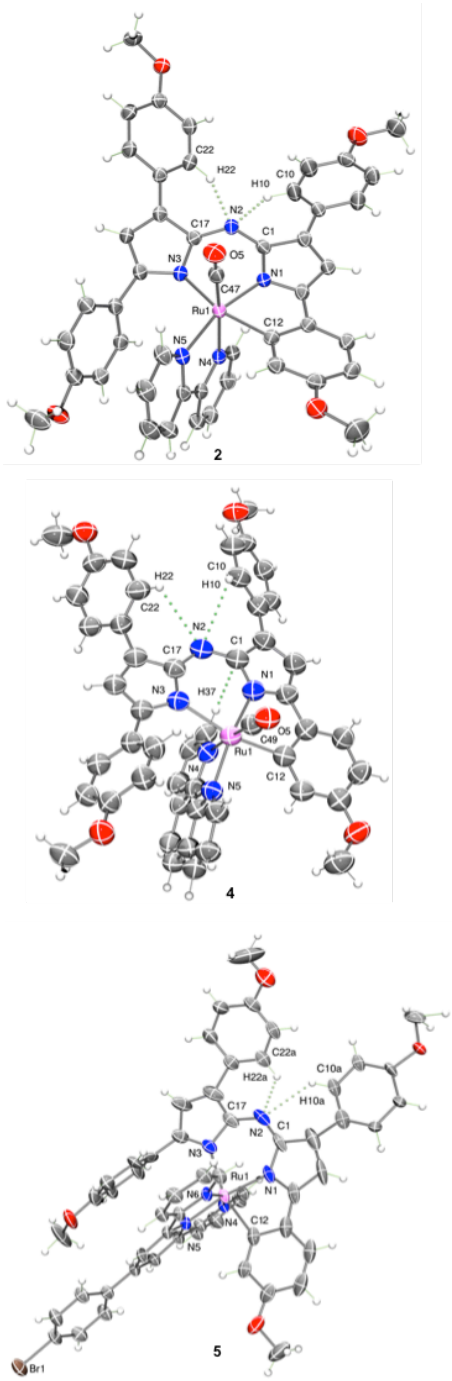

Figure 4.1 – Solid-state structures of ADPM sensitizers **2** (ellipsoids shown at 50% probability level; co-crystallized solvent omitted for clarity; intramolecular H-bonds represented in green), **4** (ellipsoids shown at 30% probability level; only one of the two molecules in the asymmetric unit presented; minor-disorder component omitted for clarity) and **5** (ellipsoids drawn at 50% probability level; co-crystallized solvent and minor-disorder components omitted for clarity).

4.4 – Results and Discussion

4.4.1 – Rational Design of Cyclometalated ADPM Photosensitizers

To fully take advantage of ADPM's intrinsic photophysical and electronic properties for solar energy conversion applications, we undertook the cyclometalation of **1** on a Ru^{II} metallic center to generate neutral sensitizers **2** – **6** (Scheme 4.1). As verified by X-ray structural data (Figure 4.1), this cyclometalation strategy causes the planarization of an aryl group adjacent to the two coordinating pyrrolic cycles. The resulting tridentate ADPM motif with a X_2L type of coordination provides better electron delocalization throughout the conjugated π-system and promotes absorption in the NIR due to a HOMO-LUMO band-gap (ΔE).[16] In addition, the presence of two σ-donating bonds on the metal from deprotonation of one pyrrole and one phenyl ring destabilize the ruthenium t_{2g} orbital significantly.[41] Our cyclometalation strategy presents similar advantages to NCS- free derivatives and the modular synthesis obtained in other cycloruthenated sensitizers, while outperforming their photophysical properties due to the ADPM core.[42-45] This is also the case as compared to closely related bidentate DPM ruthenium complexes.[49-53] The choice of ADPM **1** bearing electron-rich *p*-methoxy substituents on phenyl rings was both intended to tune the energy level of the resulting sensitizer and provide, upon photoexcitation, a vectorization of electronic transfer toward the acceptor unit, e.g. titanium dioxide in DSSC or PCBM in OPV applications.[7,10,54] In addition, ancillary ligands of the ruthenium dication constitute other important levers to tune the energy levels of the sensitizers (carbonyl and bpy / ^{t}-Bu-bpy / phen for **2** – **4**, respectively; terpyridine derivatives 4'-4-bromophenyl-2,2':6',2"-terpyridine [tpy-Ph-Br] for **5** and 4'-([2,2':6',2"-terpyridin]-4'-yl)-[1,1'-

biphenyl]-4-carboxylic acid [tpy-Ph_2-COOH] for **6**). Carbonyl ligands are known to stabilize ruthenium complexes and they could be directly formed by oxidation of the methanol ligand present in the Ru(N^N)(MeOH)Cl_3 starting materials.[55] While compound **7** bearing the carboxylic acid anchoring groups (Figure 4.2) was unattainable in our hands due to decomposition during purification, we were able to isolate compound **6** for integration into DSSCs. The series of derivatives obtain herein is also among the rare examples of neutral ruthenium complexes bearing polypyridine ligands (N^N or N^N^N), which are quickly gaining attention for photosensitization.[56-60] Finally, our design of neutral sensitizers was envisioned to favour electron injection as compared to commercially available cationic ruthenium sensitizers such as bpy-based **N3** and **N719** or tpy-based **Black Dye**.[7,9,61] Altogether, we believe cyclometalation of ADPM in neutral Ru(II) sensitizers mimics light-harvesting metalloporphyrinoids such as Chlorophyll *a*, while offering a simpler synthetic methodology that increases its potential for direct applications.

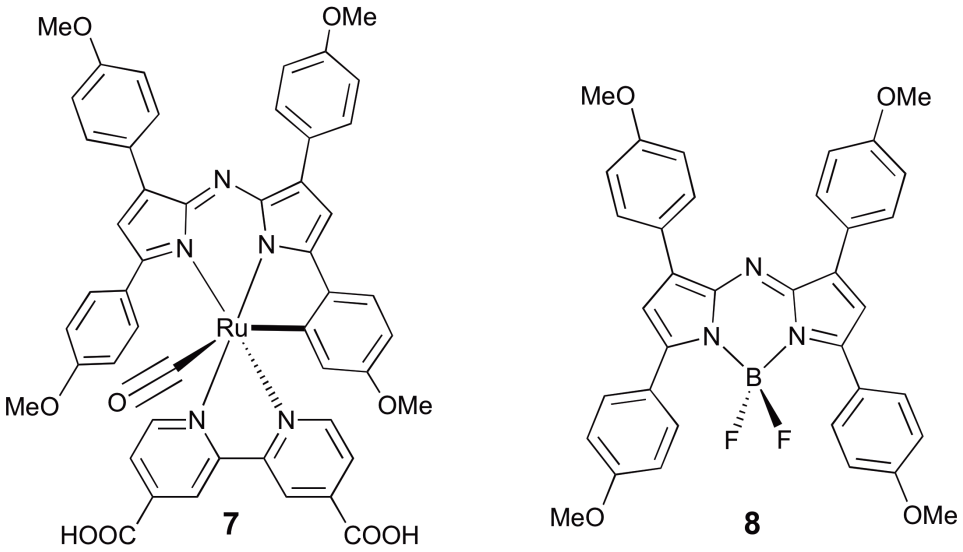

Figure 4.2 – Attempted sensitizer **7** and corresponding Aza-BODIPY **8**.

4.4.2 – X-Ray Diffraction

Crystals suitable for X-ray diffraction studies were obtained for compounds **2**, **4**, and **5** (Figure 4.1). They crystallized in the space groups *I-4*, $P2_1/c$, and *P-1*, respectively (Table III.S15). All three complexes display distorted octahedral geometry at the Ru^{II} center. They highlight the ADPM moiety coordinated in meridional fashion, acting as a tridentate ligand, by cyclometallation of one of the proximal aryl groups. In both adducts **2** and **4**, the coordination sphere around the metal center is completed by an axial carbonyl ligand, and by one bpy and phen ligands, respectively. In compound **5**, the tpy-Ph-Br ligand occupies the second meridional position. Selected bond lengths and angles are compared in Table III.S16. In all three compounds, the Ru-N_{ADPM} bond lengths are within normal ranges for Ru-N bonds in Ru^{II} polypyridyl complexes.[62-64] The Ru-$N1_{ADPM}$ bond lengths [2.022(8) – 2.055(5) Å] *trans* to $N_{bpy\ /\ phen}$ (N5) in **2** and **4**, and *trans* to N'_{phtpy} (N5) in **5**, are shorter than the Ru-$N3_{ADPM}$ analogues, *trans* to C_{cyclo} (C12) [2.192(6) – 2.222(3) Å]. The bond lengths Ru-$N4_{bpy\ /\ phen}$ (axial, *trans* to C_{CO} in **2** and **4**), and Ru-$N4_{phtpy}$ (axial, in **5**) are longer than the Ru-$N5_{bpy\ /\ phen/\ tpy\text{-}Ph\text{-}Br}$ (equatorial, *trans* to $N1_{ADPM}$) ones. In all three complexes, the Ru-C_{cyclo} bonds are longer than those in cationic Ru^{II} complexes with cyclometallated bpy [2.046(8) Å – UBUTUG][65] and tpy [1.99(1) Å – UDOHUQ].[66] The Ru-$C12_{cyclo}$ bonds are similar in **2** [2.071(3) Å] and **4** [2.069(10) Å], and are comparable with those in neutral Ru^{II} complexes with cyclometallated bpy ligands [2.063(5) Å – VAKMAX].[67] However, they are slightly longer in **5** [2.102(3) Å] most probably due to steric reasons: the tpy-Ph-Br ligand forces further away the cyclometallated proximal aryl group of the ADPM moiety *vs.* the bpy / phen ligands. In **2** and **4**, the bond lengths around the Ru^{II} center are comparable with

those found in other complexes with similar coordination environment (QUBZAO)[68] and neutral charge (EJOHUG)[69] (Table III.S17). The Ru-C_{CO} and the C—O bond lengths in **2** and **4** are identical within 3σ, with the average values being 1.823(12) Å and 1.158(13) Å, respectively; however the latter are significantly longer than in free CO (1.128 Å)[70] as a result of back-donation from the ruthenium in the carbonyl ligand π*-orbitals. In addition, the Ru-C_{CO} and the C—O bond lengths in **2** and **4** are shorter than those found in the pentacoordinated neutral Ru-carbonyl complex of N_4-macrocyclic ligands, suggesting a lower degree of back-donation in the latter [e.g. BAMKUW – Ru-C_{CO} 1.87(1) Å and C—O 1.10(1) Å],[71] while being in the same range as those reported for the neutral hexacoordinated Ru-carbonyl complexes with pentadentate flexible macrocyclic ligands [e. g. CAHWIR – Ru-C_{CO} = 1.833(5) Å and C-O = 1.156(7) Å].[72] In **5**, Ru-N_{phtpy} bonds are similar with those found in neutral Ru^{II} complexes with tpy ligands [e.q. ALOMEU – 2.044(4); 1.947(4); 2.037(4)].[73] The origin of the distortion from regular octahedron in the three compounds is the small bite angle of the ADPM, phen, bpy, and tpy-Ph-Br ligands. The bite angle of the ADPM ligand coordinated in the tridentate cyclometallated chelate is 161.6(1)° in **2**, 164.1(4)° in **4**, and 160.2(2)° in **5**, values that are slightly higher than those found for the corresponding angles of tpy ligands [e.q. 157.8(1)° in $Ru(tpy\text{-}Ph)_2^{2+}$],[64] but significantly lower than the ideal 180° value. In addition, a lower N_{ADPM}-Ru-$N_{tpy\text{-}Ph\text{-}br}$ angle in **5** (168.7(2)°) as compared with the *trans* N-Ru-N angle in $Ru(tpy\text{-}Ph)_2^{2+}$ [179.1(2)°], results in the larger deviation from the perfect octahedral geometry observed in **5** *vs.* **2** and **4**. The bite angle of the bpy ligand in **2** [76.9(1)°] is lower than the corresponding bite angle in $Ru(bpy)_3^{2+}$ [78.6(2)°],[63] while the bite angles of phen in **4** and and tpy-Ph-Br in **5** [79.1(3)° and 158.2(2)°] are similar with those reported for $Ru(phen)_3^{2+}$ and $Ru(tpy\text{-}Ph)_2^{2+}$ [80.2(7)°)

and 157.8(1)°].[62,64] The bite angle of the *N,N'*-ADPM ligand in **2**, **4**, and **5** are 82.1(1)°, 85.1(3)°, and 82.3(2). The higher value in **4** is the effect of differences in packing interactions (*vide infra*), resulting in the non-cyclometallated ADPM proximal aryl being twisted away from the phen moiety. This fact, together with the bigger bite angle of phen *vs.* bpy, results in **4** being closer to octahedral geometry than **2**, which has effects on the optoelectronic properties of the complexes as observed by Hammarström and Johansson.[74] The analysis of the differences in conformation of ADPM ligands in **2**, **4** and **5** *vs.* the free ligand,[25] other metallic mono-ADPM[26,75,76] and homoleptic ADPM complexes[25,77] was undertaken. The periplanar angles of the aryl rings and the plane of the ADPM backbone are reported in Table III.S16. The most important feature in this respect is the effect of the cyclometallation, resulting in the extended planarization of the ADPM ligand from the pyrollic backbone to the proximal cyclometallated aryl ring. As a consequence, the 'canting' of the metal-chelate ring, observed in other metallic complexes of ADPM ligands[25,26,75-77] is eliminated. The presence in the structures of an additional N^N or N^N^N ligand capable of forming π–π interactions with the non-cyclometallated proximal aryl ring of the ADPM moiety offers the premises for a second general feature within these complexes, as clearly identified in **2** and **5** (Figures 4.1, III.S36, III.S39 and III.S40). Additional discussion regarding packing features of **2**, **4** and **5** can be found in the ESI (Annexe III).

4.4.3 – Panchromatic Absorption Properties

Investigation of the photophysical properties of photosensitizers **2** – **6** as compared to ADPM **1** and its corresponding Aza-BODIPY **8** (Figure 4.2) revealed a strong potential for NIR photon absorption combined with an unsurpassed panchromaticity for ruthenium-based chromophores (Figure 4.3 and Table 4.I).[38-43,46,47,49-52] The overall effect of ADPM cyclometalation for all the compounds studied consists in a decrease of extinction coefficient (ε) joined by a broadening of absorption bands both toward the visible and NIR spectral regions. Combined with corresponding ancillary ligands, a synergy in the absorption profile is obtained which allows light to be harvested steadily throughout the visible spectrum. Free ligand **1** presents a sharp absorption maximum in the red at 627 nm ($\lambda_{max\ red;}$ ε = 52 x 10^3 M^{-1} cm^{-1}) with a tail up to 700 nm in dichloromethane. For Ru^{II} complex **2,** this value is red-shifted to 660 nm (ε = 17 x 10^3 M^{-1} cm^{-1}) with an almost equally high band as a shoulder at 719 nm ($\lambda_{shoulder\ red}$; ε = 15 x 10^3 M^{-1} cm^{-1}) that tails past 850 nm. This bpy-based sensitizer also presents a shoulder in the green at 550 nm ($\lambda_{shoulder\ green}$; ε = 15 x 10^3 M^{-1} cm^{-1}) and another maximum of absorption in the purple at 436 nm ($\lambda_{max\ purple}$; ε = 15 x 10^3 M^{-1} cm^{-1}). Closely related N^N derivatives **3** and **4** present similar spectral features, with $\lambda_{max\ red}$ at 654 and 659 nm (ε = 15 x 10^3 M^{-1} cm^{-1}), respectively, with shoulders in the red at 712 (ε = 16 x 10^3 M^{-1} cm^{-1}) and 702 nm (ε = 17 x 10^3 M^{-1} cm^{-1}) tailing toward the NIR. Panchromaticity is also preserved for **3** and **4** with $\lambda_{shoulder\ green}$ at 552 and 544 nm (ε = 15 x 10^3 M^{-1} cm^{-1}), respectively, along with $\lambda_{max\ purple}$ at 439 and 437 nm (ε = 15 x 10^3 M^{-1} cm^{-1}). In the case of tpy-based derivatives **5** and **6**, the absorption profile is slightly different and presents a tailing band out beyond 1100 nm. The absorption maxima is

hypsochromically shifted in the orange at 610 (ε = 22 x 10^3 M^{-1} cm^{-1}) and 600 nm (ε = 16 x 10^3 M^{-1} cm^{-1}), respectively, but the shoulder of the absorption band reaches 752 (ε = 5.6 x 10^3 M^{-1} cm^{-1}) and 753 nm (ε = 5.4 x 10^3 M^{-1} cm^{-1}) in the NIR region. Photosensitizer **5** exhibits a sharp shoulder in the green at 536 nm (ε = 14 x 10^3 M^{-1} cm^{-1}) and a maximum in the purple at 423 nm (ε = 16 x 10^3 M^{-1} cm^{-1}). Features in that portion of the spectrum are smoothed out in the case of **6**, with a discrete shoulder in the green at 538 nm (ε = 13 x 10^3 M^{-1} cm^{-1}) and $\lambda_{max\ purple}$ at 422 nm (ε = 13 x 10^3 M^{-1} cm^{-1}). In comparison, the BF_2-chelation in Aza-BODIPY **8** leads to a shift of the maxima to 691 nm (ε = 79 x 10^3 M^{-1} cm^{-1}) with a tailing limited to about 750 nm. Of interest, a B,O-chelated BODIPY derivative used as additive in a P3HT OPV solar cell was reported to have a maxima reaching 747 nm (ε = 148 x 10^3 M^{-1} cm^{-1}) tailing up to 800 nm.[78] A variety of ruthenium complexes used for DSSC also constitute valuable benchmarks. Classic **N3** dye (λ_{max} = 530 nm in MeCN; ε = 13 x 10^3 M^{-1} cm^{-}1; tail up to *ca.* 750 nm)[52] and **Black Dye** (λ_{max} = 605 nm in DMF / MeOH [4:1 v/v]; ε = 8.7 x 10^3 M^{-1} cm^{-1}; tail up to *ca.* 850 nm)[79] both exhibit significantly lower extinction coefficients and panchromaticity than related N^N sensitizers **2** – **4** and tpy-based **5** and **6**, respectively. This is also the case compared with closely related ruthenium thienyl-DPM complexes where the best bpy-based derivative have a λ_{max} = 540 nm (ε 19 x 10^3 M^{-1} cm^{-1}) tailing up to *ca.* 750 nm and tpy-based derivative reach a λ_{max} of 750 nm (ε = 2.7 x 10^3 M^{-1} cm^{-1}) tailing to *ca.* 950 nm.[50,51] Therefore, it appears that cyclometalation of the ADPM moiety with a ruthenium dication provides outstanding spectral features ranging all the way from the visible up to the NIR spectral regions. A more detailed investigation of implied transitions by TD-DFT will be discussed in the computational section.

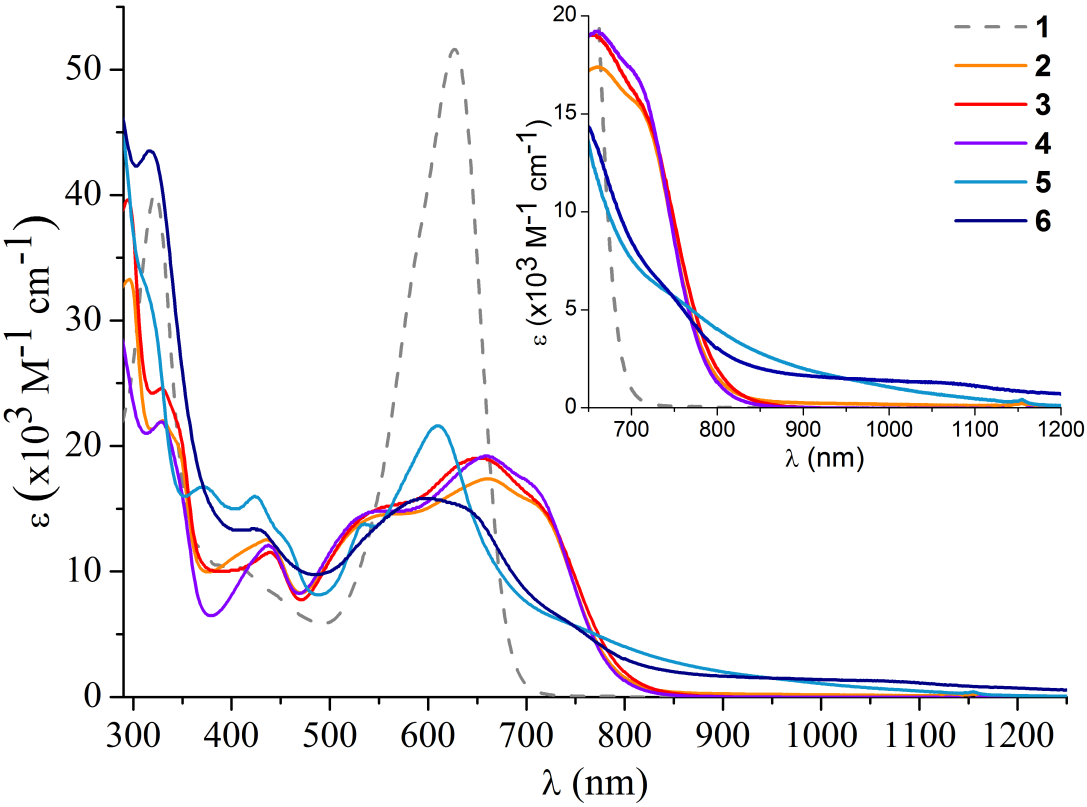

Figure 4.3 – UV/vis absorption spectra of ADPM ligand **1** and cyclometalated complexes **2** – **6**. Inset: absorption in the NIR region.

Table 4.I – Photophysical data for ADPM ligand **1**, cyclometalated complexes **2** – **6** and Aza-BODIPY **8**.[a]

Entry	$\lambda_{max\ purple}$ (nm)	$\lambda_{shoulder\ green}$ (nm)	$\lambda_{max\ red}$ (nm)	$\lambda_{shoulder\ red}$ (nm)	ΔE_{Opt} (eV)
1[b]	414 (10)	---	627 (52)	---	1.81
2	436 (13)	550 (15)	660 (17)	712 (15)	1.40
3	439 (12)	552 (15)	654 (19)	712 (16)	1.39
4	437 (12)	544 (15)	659 (19)	702 (17)	1.41
5	423 (16)	536 (14)	610 (22)	752 (5.6)	1.10
6[c]	422 (13)	538 (13)	600 (16)	753 (5.4)	1.06
8[b]	440 (8)	---	691 (79)	---	1.71

[a] Extinction coefficient are given in parentheses (ε, x10^3 $M^{-1}cm^{-1}$). In CH_2Cl_2 unless otherwise stated. Aquisition at 293K. ΔE_{Opt} qualitatively obtained from the red end of the Gaussian peak of $\lambda_{shoulder\ red}$ and converted in eV using formula E = hc/λ. [b] Values from literature.[25] [c] In MeOH for entire line.

4.4.4 – Electrochemical Properties

To determine if new sensitizers are efficient photoactive materials in DSSC and OPV applications, their exact energy levels need to be assessed and their overall stability must be well understood. For instance, in DSSC applications, a high-lying HOMO level of a given sensitizer might lead to difficulties for the redox mediator (e.g. I^- / I_3^- couple at -5.0 eV)[80] to reduce it after photoinjection of an electron into TiO_2 or to rapid deterioration of the photovoltaic device upon exposition to air (oxidation threshold at -5.27 eV).[42,81-83] A mismatch between the E_{Ox}^* level of the sensitizer and the corresponding acceptor, e.g. fullerene-based PCBM (between -3.91 and -4.3 eV)[84] in OPV or the TiO_2 conduction band in DSSC (~ -4.2 eV),[5, 85] would hinder electron transfer upon photoexcitation.[10,16,54] Based on the Rehm-Weller equation for intermolecular electron transfer reaction and accounting for the photoexcited nature of the reductant species in photovoltaic devices, the excited state oxidation potential (E_{ox}*) must lie above the acceptor electronic level, particularly in coordination complexes which exhibit rapid intersystem crossing to a lower-lying triplet state.[5,86] To this end, standard OPV and DSSC requirements are depicted in Figure 4.4 along with the HOMO / LUMO and E_{Ox}* levels as obtained both by electrochemistry (black), computational modelization (red) and absorption spectra (blue) for photosensitizers **2** – **6**. Additional solar conversion application in the quickly growing field of photocatalysis also requires insights from electrochemistry in order to efficiently achieve new light-mediated organic transformations.[87-89] Therefore, the electrochemical properties observed experimentally by cyclic and differential pulse voltammetry techniques (CV and DPV, respectively) for the series are discussed herein in detail and will be further rationalized by computational

modelization results. Such a systematic analysis is intended to better understand how the structural changes within the series fine-tune the energy levels and alter the stability of the complexes to redox processes.

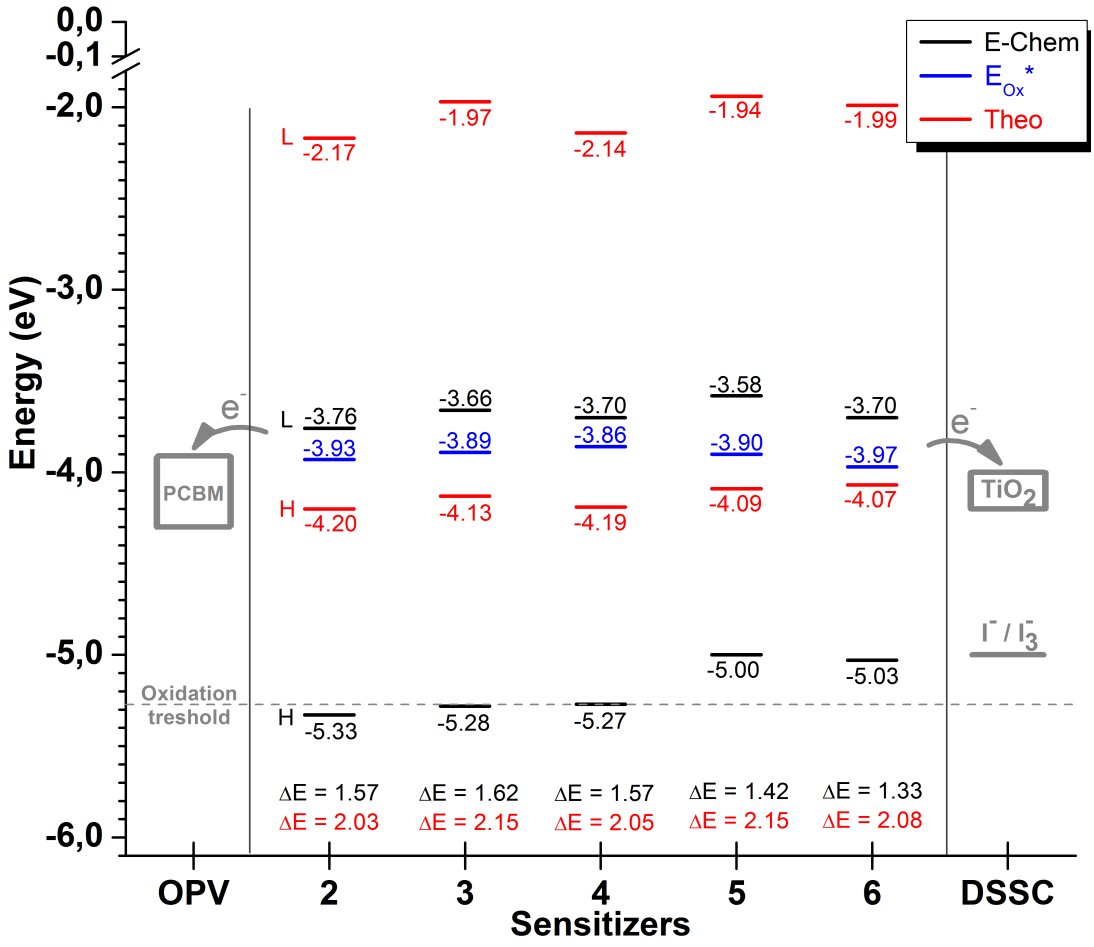

Figure 4.4 – Energy levels of ADPM sensitizers **2** – **6** *vs.* standard OPV (left) and DSSC (right) requirements.

(electrochemistry in black, estimated excited state oxidation potential [$E_{Ox}^* = E_{Ox} + \Delta E_{Opt}$] in blue and DFT calculations in red)

(refer to text and notes thereof)

An overview of the electrochemical data (Table 4.II) of ruthenium photosensitizers **2** – **4** bearing bidendate N^N and carbonyl ligands shows the presence of four oxidation processes, the first two of which are irreversible followed by two "pseudoreversible" ones. In addition, two reduction processes can be observed, the first being pseudoreversible and followed by a second irreversible one. In contrast, the free ADPM ligand **1** presents only three oxidation processes, where the first one is reversible at 0.71 (61) V (mV) vs SCE and the two others are irreversible (1.10 and 1.30 V, respectively), along with two pseudoreversible reductions (-0.92 (106) and -1.52 (193) V, respectively). The corresponding Aza-BODIPY **8** behaves in a similar fashion to **1**, except that its first oxidation at 0.95 V is irreversible and a general increase of the oxidation potentials is due to the electron-withdrawing BF_2 chelate (1.34 and 1.52 V, respectively). The two pseudoreversible reduction processes are also at lower potentials of -0.58 (107) and -1.37 (92) V owing to the poorer electron density in the molecule. Interestingly, the conjunction of a Ru^{II} cation with the presence of N^N and carbonyl ligands appears to significantly destabilize the energy levels of complexes obtained as compared to the free ADPM ligand and exemplified by the first oxidation ranging between 0.32 and 0.39 V for **4** and **2**, respectively, with an intermediate value at 0.34 V for **3**. DFT calculations revealed that the HOMO in the **2** – **4** series resides mainly on the ADPM and cyclometalated moieties (*vide infra*), which explain the relative order observed in the oxidation processes. Since the carbonyl ligand is constant in the three derivatives, N^N ligands therefore dictate the order of oxidation potentials. The increasing ease of oxidation follows the growth of electron density encountered in the bpy / ^{t}Bu-bpy / phen series. Similarly, the irreversible second oxidation is in the 0.43 – 0.48 V range (**4** and **2**, respectively), with an intermediate value at 0.46 V for **3**. The

third pseudoreversible process standing at 0.79 V in all three compounds is ligand-based. In fact, it closely matches the first pseudoreversible oxidation of ADPM **1** at 0.71 V that was found to be centered on the azadipyrromethene core with additional contribution from the proximal aryls.[24] The slight shift to more positive potential as compared to the free ligand is due to the presence of the electron withdrawing Ru^{II} cation. The pseudoreversible fourth oxidation at 0.91 (176) for **2**, 0.95 (102) for **3** and 0.93 (204) V in the case of **4** is attributable to the metal centered $Ru^{III/II}$ process, in agreement with other closely related neutral Ru^{II} complexes bearing both cyclometalated and carbonyl ligands.[90] The first pseudoreversible reduction process stands at -1.19 (124) V for **2,** -1.28 (157) V for **3** and -1.25 (167) for **4**. Both the calculated LUMO obtained by DFT (*vide infra*) and related Ru^{II} diimine complexes suggest this process is occurring on the N^N moiety rather than the ADPM one.[91] The second irreversible reduction process follows at -1.82, -1.93 and -1.89 V, respectively, most likely localized on the ADPM ligand based on DFT insights (Table III.S2†). The terpyridine-based photosensitizers **5** and **6** present a first oxidation at 0.06 (87) and 0.08 V, respectively, This is about 0.30 V more easily oxidized as compared to related bidentate N^N derivatives **2** – **4**, 0.55 V *vs.* cyclometalated $Ru(tpy)(N^N^C)^{1+}$ [0.61 (60) V in ACN; N^N^C(H) = 6-phenyl-2,2'-bipyridine] and 1.25 V *vs.* $Ru(tpy)_2^{2+}$ [1.31 (60) V in ACN], a logical trend based on the extended π-conjugated system of tridentate derivatives and global charge of the complexes.[92] Theoretical calculations of van Koten *et al.* on the two last complexes showed a significant decrease of the Mulliken population on the ruthenium center of the HOMO when changing one L_3 type tpy ligand for a XL_2 type N^N^C (0.68 vs. 0.50 electron on the d_{xy} orbital, respectively), which is in line with our own calculations indicating that the X_2L cyclometalated ADPM ligand further decrease

to only 10% the electron density on the metal (Table III.S2†). Therefore, this first oxidation for the two neutral complexes reported herein is best described as a ligand-based process with 88% of the electronic density on the ADPM core plus the cyclometalated aryl. Compound **5** has two extra pseudoreversible oxidation processes at 0.66 (50) and 1.30 (153) V. DFT suggests the former reversible one should be the $Ru^{III/II}$ process with a 42% electronic density on the metal (Table III.S2†). In the case of adduct **6**, data acquired in more polar DMF for improved solubility reveals three additional irreversible oxidation processes at 0.50, 0.94 and 1.31 V. The first pseudoreversible reduction processes at -1.37 (101) V in photosensitizer **5** is localized on the tpy-Ph-Br, as expected for a cyclometalated complex and also supported by DFT (Table III.S2†).[92] [93] Another irreversible process follows at -1.87 V. After its conversion to **6**, the first reduction is at -1.25 V along with three other ones at -1.79, -2.04 and -2.35 V.[94]

Table 4.II – Electrochemical data for ADPM ligand **1**, cyclometalated complexes **2** – **6** and Aza-BODIPY **8**.

Entry	$E_{1/2}$(Ox) [a]	$E_{1/2}$(Red) [a]
1[f]	1.30[b], 1.10[b], 0.71 (61)	-0.92 (106), -1.52 (193)
2	0.95 (102), 0.79 (88), 0.48[b], 0.39[b]	-1.19 (124), -1.82[b]
3	0.91 (176), 0.79 (127), 0.46[b], 0.34[b]	-1.28 (157), -1.93[b]
4	0.93 (204), 0.79 (103), 0.43[b], 0.32[b]	-1.25 (167), -1.89[b]
5[c]	1.30 (153), 0.66 (54), 0.06 (87)	-1.37 (101), -1.87[b]
6[d]	1.31[b], 0.94[b], 0.50[b], 0.08[b]	-1.25[b], -1.79[b][e]
8[f]	1.52[b], 1.34[b], 0.95[b]	-0.58 (107), -1.37 (92)

[a] Potentials in volts vs SCE for CH_2Cl_2 deaerated solutions (otherwise stated); 0.1 M in TBAP; recorded at 25 ± 1 °C; sweep rate of 50 mV/s. Difference between cathodic and anodic peak potentials (mV) given in parentheses. [b] Irreversible. Determined by DPV. [c] Two reduction peaks associated with decomposition were observed by DPV at -0.54 and -0.70 V. [d] In DMF deaerated solution. Poorly soluble [e] Two additional irreversible reductions were observed at -2.04 and -2.35 V. [f] From previous work.[25]

The HOMO and LUMO levels expressed in eV (Figure 4.4 and Table III.S1†) are relevant in order to better understand the structure–property relationship that units photosensitizers **2** – **6** and to fine-tune their incorporation into DSSCs and OPV devices. As mentioned above, the rising energy of the HOMO that is mainly based on the ADPM ligand for the series **2** – **4** (-5.33, -5.28 and -5,27 eV vs vacuum, respectively) is consistent with the electron density contribution trend in the N^N ligands. On the other hand, the first reduction potential determined by electrochemistry and associated to the LUMO exhibits an increase between **2** (-3.76 eV) and **3** (-3.66 eV), while that of adduct **4** stands in between at -3.70 eV. Based on DFT results (*vide infra*), the LUMO lies mainly on the N^N ligand (*ca.* 90%) with a small contribution made by the metal center (*ca.* 5%) for **2** and **3**, which explains the relative order of energy levels since bpy should be a better acceptor than the electron-rich ^{t}-Bu-bpy. The situation is slightly different in the case of **4** as the orbital appears to be almost entirely based on the phenanthroline moiety (99% of the electronic density, Table III.S2†), with no contribution made by the metal center. Therefore, the latter dication might be better considered as an electron-withdrawing group coordinated to the phen, with no contributing electron density, which explains the lowest LUMO level observed. The resulting electrochemical band gaps (ΔE_{Redox}) obtained are of 1.57 eV for both **2** and **4** up to 1.62 eV for **3**. It is important to note that while ground state electrochemistry of isolated molecules reported here do not provide the formal E_{Ox}* needed for a complete picture in actual photovoltaic devices, an estimation was made by adding the ΔE_{Opt} to the first oxidation potential (Figure 4.4 and Table III.S1†) to give an Eox* for potential photoinjection from the singlet state. Results indicate E_{Ox}* levels of the series range from -3.86 to -3.97 eV and are above the requirements of the two solar conversion applications mentioned above. In addition, the

low reorganizational energy upon photoexcitation usually associated with polypyridyl ruthenium complexes should lead to a E_{Ox}* similar to the measured reduction potential.[95] Promisingly, the three ADPM cyclometalated adducts based on a N^N and carbonyl ligands exhibit HOMO levels slightly below the oxidation threshold, low band gaps along with LUMO / E_{Ox}* levels that are over the LUMO energy level of the PCBM acceptor and the energy level of the conduction band of TiO_2. With such energy levels features, this new class of neutral Ru^{II} sensitizer bearing a cyclometalated ADPM appears to be suited for applications in OPV and DSSC if efficient singlet-state photoinjection occurs. To note, an optimal driving force of about 0.2 – 0.3 eV is suitable for efficient electron transfers toward the acceptor unit.[5,16,47] Tpy-based sensitizers **5** and **6** present a significantly destabilized HOMO level about 0.3 eV higher at -5.00 and -5.03 eV, respectively. In addition to the extended π-conjugated system of these tridentate derivatives discussed previously, this phenomenon is also attributable to the removal of the carbonyl ligand that accepts back-donation into its π* orbitals from the metal center. A better appreciation of such a structural modification can be obtain by comparing the values of the classic $Ru(tpy)_2^{2+}$ at -6.26 eV or $Ru(dgpy)(Ph\text{-}tpy)^{2+}$ and $Ru(dgpy)(Ph\text{-}dpt)^{2+}$ bearing a strong *sigma*-donating ligand 2,6-diguanidylpyridine (dgpy) at -5.45 eV.[96,97] It can be observed that the presence of the N^N^C dianionic ADPM cyclometalated ligand shifts the oxidation potential compared to these respective complexes by *ca.* 1.25 and 0.45 eV. Unfortunately, the drastic shift also lead to its air-sensitive nature as observed during the synthesis of **5** and upon long-term air exposition of **6** in solution (*vide supra*). The LUMO level of adduct **5** is the highest of the series at -3.58 eV, while extension of the conjugation on tpy moiety achieved in sensitizer **6**

stabilizes it by 120 mV at -3.70 eV. From the E_{Ox}* energy level at -3.97 eV of sensitizer **6**, which is slightly higher than for **Black Dye** (LUMO = -4.00 eV),[41] the former adduct bearing a carboxylic acid anchoring group should provide a suitable driving force for the photoinjection in the TiO_2 conduction band.

4.4.5 – Computational Modelization Insights

DFT methods provide useful insights for OPV and DSSC applications through careful analysis of the relative energy levels in a given series of photosensitizers, electronic distribution of their frontier molecular orbitals (MOs) and calculated dipole moment.[98-102] Based on the simple and accurate approach of Méndez-Hernández *et al.* for the correlation of experimental redox potentials and DFT-calculated HOMO / LUMO energies,[103] we endeavoured to use a joint theoretical-experimental approach to gain a better understanding of electrochemical trends and provide guidelines for further developments of related cyclometalated sensitizers. Theoretical energy levels obtained using the B3LYP / 6-31G* (C, H, O, N) and LanL2DZ (Ru) level of theory are depicted in Figure 4.4 and summarized in Table III.S1†.

A quick visual overview of frontier molecular orbitals represented in Figure 5 shows that the HOMO is mainly centered on the ADPM ligand, including the cyclometalated moiety, and partially on the ruthenium dication in all the series of sensitizers **2** – **6**. On the other hand, the LUMO primarily resides on the N^N or tpy ancillary ligand along with the metallic center in all cases except for sensitizer **5** where an additional small contribution to this empty orbital can be found on the ADPM moiety. Photosensitizer **6**, which bears the carboxylic acid anchoring group for DSSC, clearly

exhibits a LUMO delocalized throughout the whole tpy-based ligand as compared to **5** where only the tpy core close to the metal is involved. Further support of this HOMO / LUMO analysis can be found in ESI, where a definition of the various moieties present in the photosensitizers (Figure III.S30†) along with a detailed analysis of the electronic contribution (Table III.S2†) are presented.

The computational results are of great interest since they suggest an important vectorization of the electronic transfer from the electron-rich cyclometalated ADPM ligand toward the pyridine-based counter-ligands and support the rational design of this new family (*vide supra*). This behaviour suitable for the development of efficient OPV and DSSC sensitizers is further reinforced by calculated dipole moment vectors represented in Figure 5 (blue arrows) pointing in each case from the Ru(II) metallic center toward the N^N or tpy-based ligand. The vector modulus obtained are of 4.88 and 4.94 Debye for **5** and **6**, respectively, and in the range of 8.41 – 9.95 Debye for N^N based sensitizers. Such an increase of the modulus value in the latter cases is attributed to the electron-accepting carbonyl ligand that helps reduce the electron density of the metallic center.

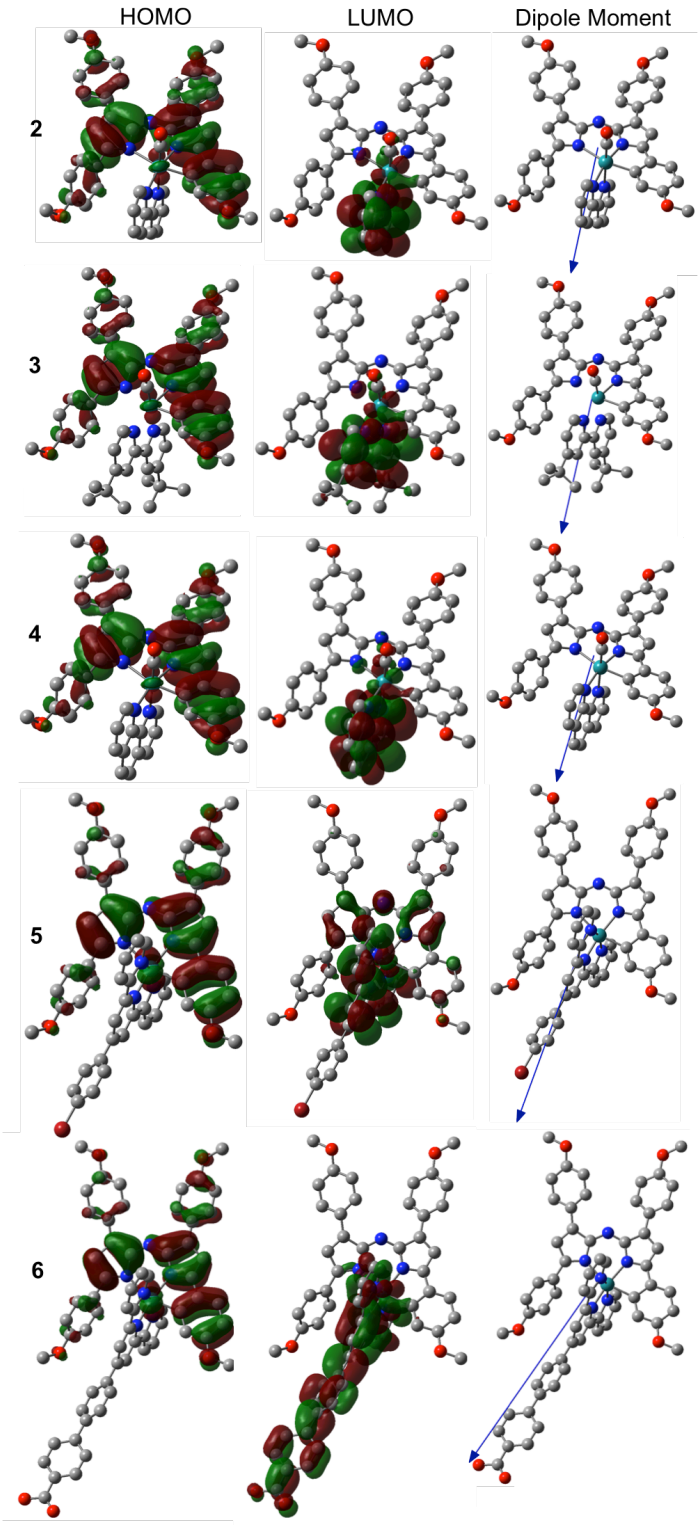

Figure 4.5 – HOMO / LUMO and dipole moment vector of ADPM sensitizers **2** – **6** as calculated by DFT.

(Isovalue = 0.02; hydrogen atoms are omitted for clarity; dipole moment x 3 for **5** and **6**)

Regarding the relative position of theoretical HOMO / LUMO as compared to the empirical electrochemical potentials obtained (Figure 4.4), the computational results appear to provide a good match with the LUMO trend, while it is more cumbersome for the HOMO. This mismatch for the relative order of the HOMOs might arise from the close proximity of the electrochemical potentials with the oxidation threshold that leads to the structural instability observed in the tpy-based derivatives. Since DFT calculations suggest that the HOMO involves mainly the ADPM ligand, this stability issue could be associated with increased reactivity toward hydrolysis on the pyrrolic carbon adjacent to the N-bridge that would break the π-conjugated system. This hypothesis is further supported by the loss of color observed upon long-term air exposition in a methanolic solution of photosensitizer **6**. Nevertheless, the DFT results efficiently depict that the least positive oxidation encountered would be for the tpy-based sensitizers **5** (-4.09 eV) and **6** (-4.07 eV) as compared to the N^N series **2** – **4** ranging between -4.20 and -4.13 eV. Theoretical calculations provide a perfect match of LUMO relative order within the N^N series as compared to first reduction potentials, with sensitizer **4** (-2.14 eV) in between the ^{t}-Bu-bpy adduct **3** (-1,97 eV) and bpy adduct **2** (-2.17 eV). Similarly, tpy-based photosensitizer **5** (-1.94 eV) and **6** (-1.97 eV) follow the order obtained by electrochemistry and are in good agreement with calculated values of the N^N series. Combined together, the calculated HOMO and LUMO energy levels provide theoretical band gaps (ΔE_{Theo}, red) that are consistent with the electrochemical values obtained (ΔE_{Echem}, black) within a series of related structures (Figure 4). In fact, photosensitizer **3** provides the largest band gap both experimentally (ΔE_{Echem} = 1.62 eV) and from calculations (ΔE_{Theo} = 2.15 eV) in the N^N series. The two other photosensitizers have identical experimental values (ΔE_{Echem} = 1.57 eV) supported by close theoretical values

of 2.03 and 2.05 eV for **2** and **4**, respectively. The widest band gap of tpy-based sensitizer **5** observed by electrochemistry (ΔE_{Echem} = 1.42 eV) as compared to **6** (ΔE_{Echem} = 1.33 eV) was also rationalized from calculations (ΔE_{Theo} = 2.15 and 2.08 eV, respectively). Overall, the DFT method used herein provides a satisfactory theoretical protocol to understand key parameters controlling the experimental energy levels, including ADPM cyclometalation effect and stability issues. This approach establishes a strong foundation to foster exploration of structural improvements achievable within this exciting new family of photosensitizers.

A systematic TD-DFT analysis is described herein using B3LYP / 6-31G* (C, H, O, N) and LanL2DZ (Ru) with the Polarizable Continuum Model (PCM) of dichloromethane for the series of neutral Ru(II) ADPM cyclometalated photosensitizers. Additional calculations for adduct **6** were done with the PCM of methanol in order to accurately mimic the experimental spectrum. This protocol is analogous to previously reported theoretical investigations of ruthenium complexes for DSSC applications,[44,45,50,104] Calculated optical absorption bands, associated oscillator strengths and natural transition orbitals (NTO) implied in the excitations are summarized in Tables III.S3 – III.S14† of ESI. Assignment of the origin of the transitions was made based on the analysis of this data so as to assess effects of the various structural modifications. A superposition of the calculated absorption bands and experimental spectrum is presented for representatives N^N derivative **2** (PCM = CH_2Cl_2) and tpy-based derivative **6** (PCM = MeOH) in Figure 6 and Figures III.S32 – III.S35† for other members of the series.

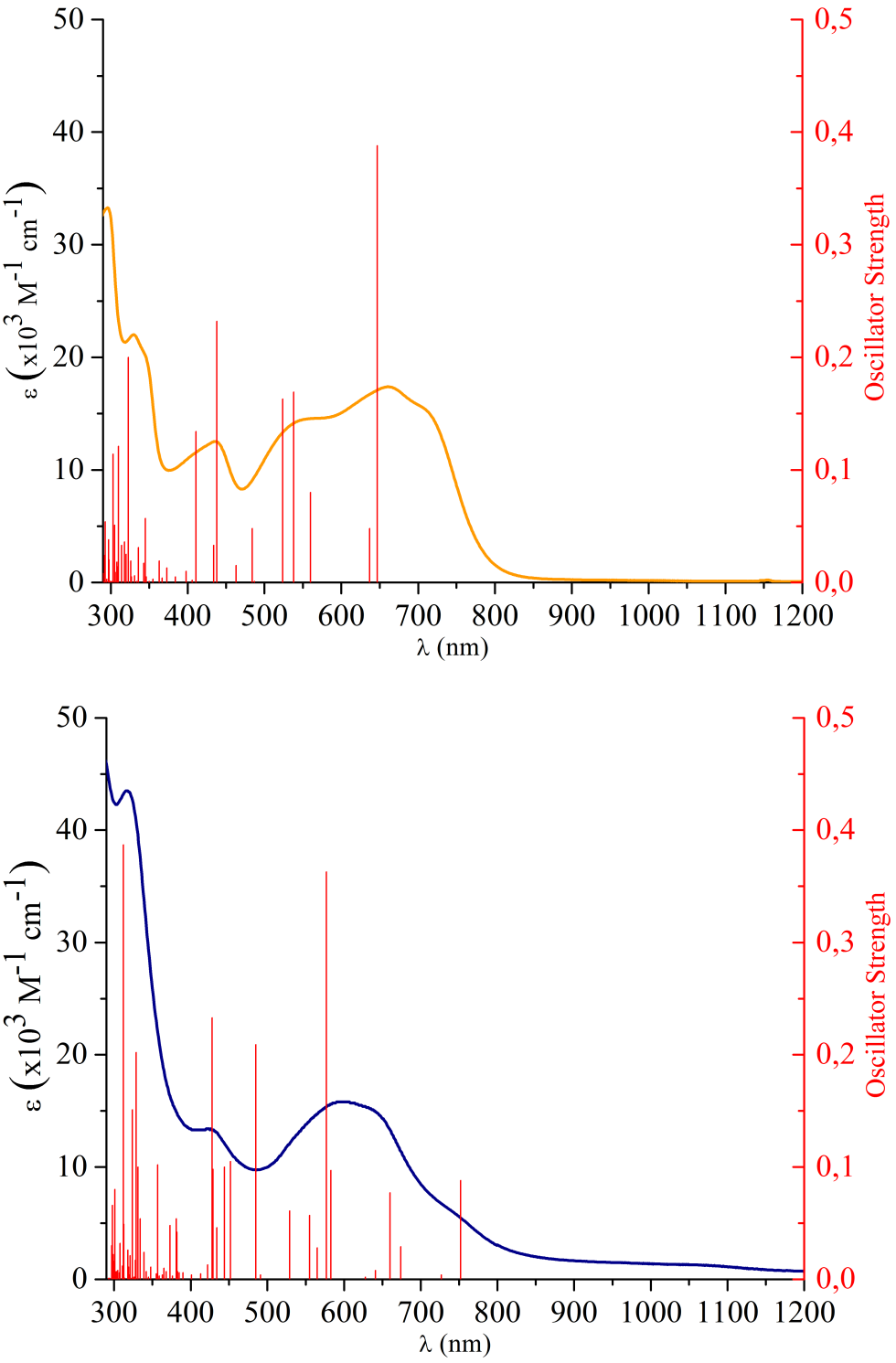

Figure 4.6 – Experimental absorption spectrum for ADPM photosensitizers **2** (top ; in CH_2Cl_2) and **6** (bottom ; in MeOH) along with corresponding calculated optical absorption bands (red lines ; TD-DFT B3LYP/6-31G*; Ru = LANL2DZ ; PCM = CH_2Cl_2 and MeOH, respectively)

The theoretical results are in close agreement with the empirical ones as their absorption bands correspond almost perfectly. It is noteworthy that slight shifts obtained for the transition energies calculated by TD-DFT can be attributed to the use of a simple solvent model, i.e. no corrections beyond linear-response, and the use of vertical transition that neglect vibronic effects.[105] The spin-orbit coupling of ruthenium that accounts for the tailing observed at low energy was not included in our modelization in view of the additional computational cost implied and its relatively weak effect compared to osmium derivatives.[106] In the case of tpy-based photosensitizers **5** and **6**, an almost perfect match of calculated absorption bands is observed throughout the whole UV, visible and NIR regions of the spectra. The N^N series also match perfectly in the UV and visible regions, but lack good overlap in the red region. A similar situation was observed in related DPM and ADPM complexes that can be rationalized by intrinsic inability of the TD-DFT method to accurately determine the exciton energy splitting between two transitions dipoles, only providing their relative orientation and magnitude.[30] This leads us to assign the T1 transition calculated in the N^N series **2** – **4** as the one associated with $\lambda_{shoulder\ red}$ (ESI, Tables III.S3 – III.S8)†, which imply a bathochromic shift of 50 – 65 nm.

In fact, careful analysis of NTOs and major contributions to the lowest energy excitation T1 reveals that the shoulder in the red part of the spectrum that tails up to about 850 nm in the NIR for the N^N series ($\lambda_{shoulder\ red}$ = 702 – 712 nm) is the result of a strong electronic transition (osc. strength ~ 0.3 – 0.4) from the cyclometalated moiety of the ADPM, the ruthenium and the carbonyl ligand toward the corresponding N^N ligand and ADPM core. The $\lambda_{max\ red}$ is properly depicted by transition T2 departing from the

core and cyclometalated moieties of the ADPM toward the N^N, carbonyl and metallic centers. Therefore, both T1 and T2 are of great interest for efficient photoinjection in DSSC application since they directly involve electronic transfer from the cyclometalated moiety towards the N^N counter ligand as was initially rationalized in our design (*vide supra*). The shoulder in the green part of the solar spectrum ($\lambda_{shoulder\ green}$ = 544 – 552 nm) is more complicated with multiples transitions involved, mainly arising from the ruthenium along with N^N and carbonyl ligands toward the ADPM and cyclometalated moieties. Further panchromaticity is achieved by a series of transitions providing $\lambda_{max\ purple}$ (436 – 439 nm). The main assignments regarding these maxima are either from core and cyclometalated ADPM moieties, ruthenium center and carbonyl ligand toward the corresponding N^N ligand or from metal-to-ligand charge transfer (MLCT) transitions where both the ADPM core and N^N ligand receive the electronic density. These last transitions are in the absorption range expected for Ru(II) polypyridine complexes.[107]

Tpy-based photosensitizers **5** and **6** exhibit NIR tailing beyond 1100 nm ($\lambda_{shoulder\ red}$) arising from transitions T1 and T2. The first transition calculated at 745 nm (osc. strength = 0.076) in derivative **5** is from the metallic center and the cyclometalated moiety toward the whole tpy scaffold (core + Ph-Br) and, in to lesser extent, the ADPM core. The second one at 736 nm (osc. strength = 0.030) implies the electronic transfer from the whole ADPM (core + cyclometalation) and the metallic center toward the tpy ligand (core + Ph-Br). For sensitizer **6** in methanol, the electronic density is taken upon photoexcitation in T1 (752 nm; osc. strength = 0.088) from the ruthenium center, the cyclometalated moiety and the tpy core toward the ADPM core and the Ph_2-COOH. The

second transition arises from the whole ADPM (core + cyclometalation) and metallic center toward the tpy ligand (core and Ph_2-COOH). Interestingly, when the PCM of dichloromethane is used instead as a direct comparison with other sensitizers, both transitions are from ruthenium and ADPM ligand (core + cyclometalation) toward the whole tpy ligand (core + Ph_2-COOH). Thus, T1 and T2 transitions of the tpy-based sensitizers are also of great interest for efficient photoinjection. The $\lambda_{max\ red}$ for adducts **5** (610 nm) and **6** (600 nm) is the result of a multitude of transitions mostly involving the electron transfer from the metallic center and the entire ADPM ligand toward the tpy ligand and its substituents. For $\lambda_{shoulder\ green}$, sensitizer **5** presents a sharp absorption peak at 536 nm also arising from the cyclometalated and core moieties of the ADPM ligand along with the ruthenium center toward the entire tpy scaffold. On the other hand, photosensitizer **6** has a more complex combination of six calculated transitions that account for the smooth shouldering observed at 538 nm. Their assignment is in close agreement with that found in **5** for this specific shouldering. Finally, $\lambda_{max\ purple}$ at 423 nm in **5** is mainly the result of T13 at 452 nm (osc. strength = 0.105), a MLCT transition toward the entire ADPM, and of T15 at 427 nm (osc. strength = 0.249) that involves the cyclometalated moiety and the ruthenium toward the ADPM and tpy cores. Complex **6** in methanol offers a similar behaviour with a MLCT toward the ADPM scaffold (T14; 452 nm; osc. strength = 0.105) and another transition taking electron density from the cyclometalated moiety and the ruthenium toward the ADPM and tpy cores (T18; 428 nm; osc. strength = 0.233). In addition, a series of transitions follow where the ruthenium and whole ADPM ligand transfer electron density toward the entire tpy scaffold upon photoexcitation.

The most interesting feature emerging from TD-DFT analysis of the series is the central impact of the ADPM ligand cyclometalation strategy on the electronic transitions at both low and high energies. The vectorial charge-transfer observed in the Ru(II) complexes of this highly absorbing ligand toward either N^N or tpy derivatives strongly supports further use of dipyrromethene derivatives as cyclometalating ligands for the development of new panchromatic photosensitizers with extended NIR absorption properties.

4.4.6 – Photoinjection Assay

In order to assess the viable of this class of compounds as photosensitizers, compound **6** was anchored to mesoporous thin films. The thin films of anatase TiO_2 nanocrystallites or ZrO_2 nanoparticles were deposited on glass substrates using a previously reported method.[108] Compound **6** was attached to the thin films by submersion in concentrated DMSO solutions (~mM range) for a minimum of 24 hours. After rinsing with neat acetonitrile, the sensitized thin films were placed in quartz cuvettes containing an argon-saturated electrolyte solution of 0.1 M $LiClO_4$ in acetonitrile.

Pulsed 532 nm excitation (~5 mJ / pulse) of sensitized TiO_2 thin films submerged in the acetonitrile electrolyte resulted in the appearance of visible absorption features that persisted for >80 μs (Figure 4.7). Pulsed light excitation of the sensitized ZrO_2 thin films under otherwise identical conditions did not result in the appearance of long-lived transients. The electron acceptor states in ZrO_2 are much higher in energy (toward the vacuum level) than those in TiO_2, which apparently inhibited electron transfer from

photo-excited **6**. The ZrO_2 studies also served as a control and showed that there were no long-lived triplet states created after light excitation of **6**, and indicated that the long-lived transient observed on TiO_2 was indeed a result of dye sensitization and the formation of a charge separated states comprised of an injected electron and oxidized **6**.

The appearance of the oxidized **6** could not be time resolved, consistent with fast excited state injection, $k_{inj} > 10^8$ s^{-1}. The subsequent charge recombination, of the injected electron with the oxidized sensitizer did not follow first-order kinetics, but was well described by the Kohlraush-Williams-Watts (KWW) stretched exponential function, **Equation 1**:

$$A(t) = A_0 e^{(-kt)^{\beta}} \qquad (1)$$

where A_0 is the initial amplitude, k is the rate constant and β is inversely proportional to the width of an underlying Lévy distribution.[109,110] A value of β = 0.20 was found to provide the best fits of the kinetic data with $k = 1.6 \times 10^6$ s^{-1}. An "average" rate constant, calculated as the first moment in the distribution, could be obtained from **Equation 2**, with $k_{KWW} = 1.3 \times 10^4$ s^{-1}

$$k_{KWW} = \frac{k\beta}{\Gamma\left(\frac{1}{\beta}\right)} \qquad (2)$$

The appearance of a long-lived transient for **6** on TiO_2 that was absent on ZrO_2 as well as the slow recombination rate constants abstracted from the kinetic data are fully consistent with excited state sensitization. This observation indicates that if the stability issues associated with **6** can be addressed, this class of sensitizers offers the real possibility for practical application in dye-sensitized solar cells with sensitization across the entire visible region.

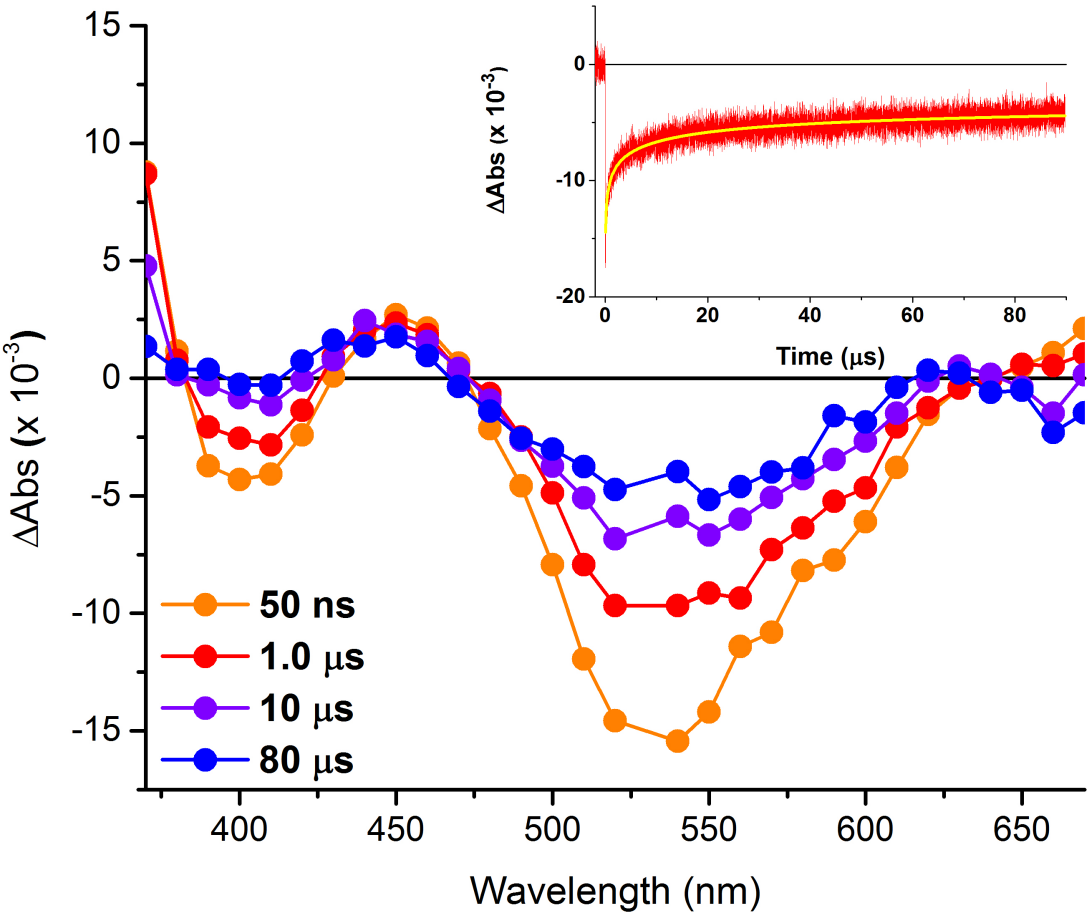

Figure 4.7 – Absorption change measured at the indicated delay times after pulsed 532 nm light excitation of **6** anchored to TiO_2. The inset is absorption change monitored at 540 nm with an overlaid fit to the KWW function.

4.5 – Conclusion

In summary, a novel family of neutral Ru^{II} complexes bearing a cyclometalated ADPM chromophore is reported. The resulting organometallic photosensitizers present an impressive panchromaticity, with light absorption beyond 1000 nm. Evaluation of the potential for DSSC and OPV applications was made possible through systematic evaluation of X-ray structures, and the spectroscopic, electrochemical and computational properties of the complexes. Spectroelectochemistry and photoinjection studies were further made on adduct **6** anchored on a titanium dioxide surface and indicate an efficient photoinjection into its conduction band. Hence, potential for integration in solar energy conversion applications of this series of photosensitizers appears highly appealing. Further studies are on-going in order to rationally develop a new generation of DPM-cyclometalated ruthenium chromophores with optimized energy levels, enhanced stability and efficient harvesting of NIR photons.

4.6 – Associated Content

Supporting Information

† Experimental section including materials, instrumentation and synthetic methods; NMR; HRMS; electrochemical and spectroscopic experimental details; computational methods and results; crystallographic data for **2**, **4** and **5** (CCDC 1419506-1419508, respectively).

4.7 – Acknowledgements

GSH thanks the Natural Sciences and Engineering Research Council of Canada, the Centre for Self-Assembled Chemical Structures (CSACS), the Centre in Green Chemistry and Catalysis (CGCC) and the Université de Montréal for financial support. GJM acknowledge support by a grant from the Division of Chemical Sciences, Office of Basic Energy Sciences, Office of Energy Research, U.S. Department of Energy (DE-FG02-96ER14662). AB is thankful of NSERC, FQRNT and PCAS Canada for a BMP-Innovation grant and to Hydro-Québec for an excellence grant. Acknowledgments go to Compute Canada for access to their national supercomputing platform and to Prof. Christian Reber for access to his UV/vis instrument. AB is grateful to Anne-Catherine Bédard and Daniel Chartrand for useful scientific discussions.

4.7 – Bibliography

1. M. Z. Jacobson and M. A. Delucchi, *Sci. Am.*, 2009, **301**, 58-65.
2. N. Armaroli and V. Balzani, *Energy Environ. Sci.*, 2011, **4**, 3193-3222.
3. G. D. Scholes, G. R. Fleming, A. Olaya-Castro and R. van Grondelle, *Nat. Chem.*, 2011, **3**, 763-774.
4. E. Collini, C. Y. Wong, K. E. Wilk, P. M. G. Curmi, P. Brumer and G. D. Scholes, *Nature*, 2010, **463**, 644-647.
5. A. Hagfeldt, G. Boschloo, L. Sun, L. Kloo and H. Pettersson, *Chem. Rev.*, 2010, **110**, 6595-6663.
6. D. G. Nocera, *Acc. Chem. Res.*, 2012, **45**, 767-776.
7. S. Mathew, A. Yella, P. Gao, R. Humphry-Baker, F. E. CurchodBasile, N. Ashari-Astani, I. Tavernelli, U. Rothlisberger, M. K. Nazeeruddin and M. Grätzel, *Nat. Chem.*, 2014, **6**, 242-247.
8. A. Yella, C.-L. Mai, S. M. Zakeeruddin, S.-N. Chang, C.-H. Hsieh, C.-Y. Yeh and M. Grätzel, *Angew. Chem., Int. Ed.*, 2014, **53**, 2973-2977.
9. A. Yella, H.-W. Lee, H. N. Tsao, C. Yi, A. K. Chandiran, M. K. Nazeeruddin, E. W.-G. Diau, C.-Y. Yeh, S. M. Zakeeruddin and M. Grätzel, *Science*, 2011, **334**, 629-634.
10. A. Mishra and P. Bäuerle, *Angew. Chem., Int. Ed.*, 2012, **51**, 2020-2067.
11. Z.-G. Zhang and J. Wang, *J. Mater. Chem.*, 2012, **22**, 4178-4187.
12. H. J. Son, B. Carsten, I. H. Jung and L. Yu, *Energy Environ. Sci.*, 2012, **5**, 8158-8170.
13. H. Xu, R. Chen, Q. Sun, W. Lai, Q. Su, W. Huang and X. Liu, *Chem. Soc. Rev.*, 2014.
14. Y. Wu, C. Cheng, L. Jiao, C. Yu, S. Wang, Y. Wei, X. Mu and E. Hao, *Org. Lett.*, 2014, **16**, 748-751.
15. H. Dau and I. Zaharieva, *Acc. Chem. Res.*, 2009, **42**, 1861-1870.
16. A. Bessette and G. S. Hanan, *Chem. Soc. Rev.*, 2014, **43**, 3342-3405.
17. T. K. Khan, P. Sheokand and N. Agarwal, *Eur. J. Org. Chem.*, 2014, 1416-1422.
18. W. Senevirathna, C. M. Daddario and G. Sauvé, *J. Phys. Chem. Lett.*, 2014, **5**, 935-941.
19. W. Senevirathna and G. Sauvé, *J. Mater. Chem. C*, 2013, **1**, 6684-6694.
20. W.-J. Shi, M. E. El-Khouly, K. Ohkubo, S. Fukuzumi and D. K. P. Ng, *Chem. Eur. J.*, 2013, **19**, 11332-11341.
21. T. Mueller, R. Gresser, K. Leo and M. Riede, *Sol. Energy Mater. Sol. Cells*, 2012, **99**, 176-181.
22. F. D'Souza, A. N. Amin, M. E. El-Khouly, N. K. Subbaiyan, M. E. Zandler and S. Fukuzumi, *J. Am. Chem. Soc.*, 2012, **134**, 654-664.
23. S. Y. Leblebici, L. Catane, D. E. Barclay, T. Olson, T. L. Chen and B. Ma, *ACS Appl. Mater. Interfaces*, 2011, **3**, 4469-4474.
24. A. Bessette, M. Cibian, F. Belanger, D. Desilets and G. S. Hanan, *Phys. Chem. Chem. Phys.*, 2014, **16**, 22207-22221.
25. A. Bessette, J. G. Ferreira, M. Giguère, F. Bélanger, D. Désilets and G. S. Hanan, *Inorg. Chem.*, 2012, **51**, 12132-12141.

26. M. Cibian, A. Bessette, A. O'Connor, J. G. Ferreira and G. S. Hanan, *Acta Crystallographica Section C*, 2015, **71**, 122-127.
27. S. A. Berhe, M. T. Rodriguez, E. Park, V. N. Nesterov, H. Pan and W. J. Youngblood, *Inorg. Chem.*, 2014, **53**, 2346-2348.
28. N. Deligonul, A. R. Browne, J. A. Golen, A. L. Rheingold and T. G. Gray, *Organometallics*, 2014, **33**, 637-643.
29. N. Deligonul and T. G. Gray, *Inorg. Chem.*, 2013, **52**, 13048-13057.
30. T. M. McLean, S. G. Telfer, A. B. S. Elliott, K. C. Gordon, M. Lein and M. R. Waterland, *Dalton Trans.*, 2014, **43**, 17746-17753.
31. L. Gao, S. Tang, L. Zhu and G. Sauvé, *Macromolecules*, 2012, **45**, 7404-7412.
32. Y. Kubo, D. Eguchi, A. Matsumoto, R. Nishiyabu, H. Yakushiji, K. Shigaki and M. Kaneko, *J. Mater. Chem. A*, 2014, **2**, 5204-5211.
33. Y. Ooyama, Y. Hagiwara, T. Mizumo, Y. Harima and J. Ohshita, *New J. Chem.*, 2013, **37**, 2479-2485.
34. S. Kolemen, O. A. Bozdemir, Y. Cakmak, G. Barin, S. Erten-Ela, M. Marszalek, J.-H. Yum, S. M. Zakeeruddin, M. K. Nazeeruddin, M. Grätzel and E. U. Akkaya, *Chem. Sci.*, 2011, **2**, 949-954.
35. J. Warnan, F. Buchet, Y. Pellegrin, E. Blart and F. Odobel, *Org. Lett.*, 2011, **13**, 3944-3947.
36. C. Y. Lee and J. T. Hupp, *Langmuir*, 2010, **26**, 3760-3765.
37. S. Erten-Ela, M. D. Yilmaz, B. Icli, Y. Dede, S. Icli and E. U. Akkaya, *Org. Lett.*, 2008, **10**, 3299-3302.
38. C.-C. Chou, F.-C. Hu, H.-H. Yeh, H.-P. Wu, Y. Chi, J. N. Clifford, E. Palomares, S.-H. Liu, P.-T. Chou and G.-H. Lee, *Angew. Chem., Int. Ed.*, 2014, **53**, 178-183.
39. Y. Numata, S. P. Singh, A. Islam, M. Iwamura, A. Imai, K. Nozaki and L. Han, *Adv. Funct. Mater.*, 2013, **23**, 1817-1823.
40. S. K. Balasingam, M. Lee, K. Man Gu and Y. Jun, *Chem. Commun.*, 2013, **49**, 1471-1487.
41. T. Funaki, H. Funakoshi, O. Kitao, N. Onozawa-Komatsuzaki, K. Kasuga, K. Sayama and H. Sugihara, *Angew. Chem., Int. Ed.*, 2012, **51**, 7528-7531.
42. P. G. Bomben, K. C. D. Robson, B. D. Koivisto and C. P. Berlinguette, *Coord. Chem. Rev.*, 2012, **256**, 1438-1450.
43. K. C. D. Robson, P. G. Bomben and C. P. Berlinguette, *Dalton Trans.*, 2012, **41**, 7814-7829.
44. S. Sinn, B. Schulze, C. Friebe, D. G. Brown, M. Jäger, J. Kübel, B. Dietzek, C. P. Berlinguette and U. S. Schubert, *Inorg. Chem.*, 2014, **53**, 1637-1645.
45. S. Sinn, B. Schulze, C. Friebe, D. G. Brown, M. Jäger, E. Altuntaş, J. Kübel, O. Guntner, C. P. Berlinguette, B. Dietzek and U. S. Schubert, *Inorg. Chem.*, 2014, **53**, 2083-2095.
46. Y.-S. Yen, H.-H. Chou, Y.-C. Chen, C.-Y. Hsu and J. T. Lin, *J. Mater. Chem.*, 2012, **22**, 8734-8747.
47. G. C. Vougioukalakis, A. I. Philippopoulos, T. Stergiopoulos and P. Falaras, *Coord. Chem. Rev.*, 2011, **255**, 2602-2621.
48. G. Li, K. Hu, K. C. D. Robson, S. I. Gorelsky, G. J. Meyer, C. P. Berlinguette and M. Shatruk, *Chem. Eur. J.*, 2015, **21**, 2173-2181.
49. T. Swetha, S. Niveditha, K. Bhanuprakash and S. P. Singh, *Electrochim. Acta*, 2015, **153**, 343-351.

50. G. Li, A. Yella, D. G. Brown, S. I. Gorelsky, M. K. Nazeeruddin, M. Grätzel, C. P. Berlinguette and M. Shatruk, *Inorg. Chem.*, 2014, **53**, 5417-5419.
51. G. Li, K. Hu, C. Yi, K. L. Knappenberger, G. J. Meyer, S. I. Gorelsky and M. Shatruk, *J. Phys. Chem. C*, 2013, **117**, 17399-17411.
52. G. Li, P. G. Bomben, K. C. D. Robson, S. I. Gorelsky, C. P. Berlinguette and M. Shatruk, *Chem. Commun.*, 2012, **48**, 8790-8792.
53. G. Li, L. Ray, E. N. Glass, K. Kovnir, A. Khoroshutin, S. I. Gorelsky and M. Shatruk, *Inorg. Chem.*, 2012, **51**, 1614-1624.
54. Y. Li, *Acc. Chem. Res.*, 2012, **45**, 723–733.
55. M. B. Dinger and J. C. Mol, *Organometallics*, 2003, **22**, 1089-1095.
56. B.-S. Chen, K. Chen, Y.-H. Hong, W.-H. Liu, T.-H. Li, C.-H. Lai, P.-T. Chou, Y. Chi and G.-H. Lee, *Chem. Commun.*, 2009, 5844-5846.
57. H. Ozawa, S. Honda, D. Katano, T. Sugiura and H. Arakawa, *Dalton Trans.*, 2014, **43**, 8026-8036.
58. Y. Chi and P.-T. Chou, *Chem. Soc. Rev.*, 2007, **36**, 1421-1431.
59. S.-W. Wang, C.-C. Chou, F.-C. Hu, K.-L. Wu, Y. Chi, J. N. Clifford, E. Palomares, S.-H. Liu, P.-T. Chou, T.-C. Wei and T.-Y. Hsiao, *J. Mater. Chem. A*, 2014, **2**, 17618-17627.
60. Y. Chi, K.-L. Wu and T.-C. Wei, *Chem. Asian J.*, 2015, **10**, 1098-1115.
61. R. Katoh and A. Furube, *J. Photochem. Photobiol. C*, 2014, **20**, 1-16.
62. K. A. McGee and K. R. Mann, *J. Am. Chem. Soc.*, 2009, **131**, 1896-1902.
63. M. Biner, H. B. Buergi, A. Ludi and C. Roehr, *J. Am. Chem. Soc.*, 1992, **114**, 5197-5203.
64. E. C. Constable, C. E. Housecroft, E. A. Medlycott, M. Neuburger, F. Reinders, S. Reymann and S. Schaffner, *Inorg. Chem. Commun.*, 2008, **11**, 805-808.
65. M. Brissard, M. Gruselle, B. Malézieux, R. Thouvenot, C. Guyard-Duhayon and O. Convert, *Eur. J. Inorg. Chem.*, 2001, **2001**, 1745-1751.
66. C. Mikel and P. G. Potvin, *Inorg. Chim. Acta*, 2001, **325**, 1-8.
67. C. R. Wade and F. P. Gabbaï, *Inorg. Chem.*, 2010, **49**, 714-720.
68. D. Ooyama, T. Tomon, K. Tsuge and K. Tanaka, *J. Organomet. Chem.*, 2001, **619**, 299-304.
69. C.-F. Chow, B. K. W. Chiu, M. H. W. Lam and W.-Y. Wong, *J. Am. Chem. Soc.*, 2003, **125**, 7802-7803.
70. C. E. Housecroft and A. G. Sharpe, *Inorganic Chemistry*, 4th edn., Pearson, 2012.
71. B. Serli, E. Zangrando, E. Iengo and E. Alessio, *Inorg. Chim. Acta*, 2002, **339**, 265-272.
72. A. Klose, E. Solari, J. Hesschenbrouck, C. Floriani, N. Re, S. Geremia and L. Randaccio, *Organometallics*, 1999, **18**, 360-372.
73. C.-C. Chou, K.-L. Wu, Y. Chi, W.-P. Hu, S. J. Yu, G.-H. Lee, C.-L. Lin and P.-T. Chou, *Angew. Chem., Int. Ed.*, 2011, **50**, 2054-2058.
74. L. Hammarström and O. Johansson, *Coord. Chem. Rev.*, 2010, **254**, 2546-2559.
75. D. V. Partyka, N. Deligonul, M. P. Washington and T. G. Gray, *Organometallics*, 2009, **28**, 5837-5840.
76. T. S. Teets, D. V. Partyka, A. J. Esswein, J. B. Updegraff, III, M. Zeller, A. D. Hunter and T. G. Gray, *Inorg. Chem.*, 2007, **46**, 6218-6220.

77. R. C. Jones, H. Muller-Bunz, P. Evans and D. F. O'Shea, *Acta Crystallogr., Sect. C*, 2014, **70**, 165-168.
78. Y. Kubo, K. Watanabe, R. Nishiyabu, R. Hata, A. Murakami, T. Shoda and H. Ota, *Org. Lett.*, 2011, **13**, 4574-4577.
79. B. Schulze , D. G. Brown, K. C. D. Robson, C. Friebe , M. Jäger , E. Birckner, C. P. Berlinguette and U. S. Schubert *Chem. Eur. J.*, 2013, **19**, 14171-14180.
80. The most common redox mediator use in DSSC, iodine, is generally considered to work as a 2-electron chemical transformation between I3- and I- in the cell at a potential of -5.0 eV (+0.3 V vs NHE). However, a 1-electron transfer process between I2°- and I- at ~ -5.5 eV (+0.8 +/- 0.1 V vs NHE) cannot be ruled out since the regeneration of the oxidized dye involve only one electron. Refer to: 1) Hagfeldt et al., Chem. Rev., 2010, 110, 6595-6663. 2) Robson et al., Dalton Trans., 2012, 41, 7814-7829.
81. L. E. Polander, A. Yella, B. F. E. Curchod, N. Ashari Astani, J. Teuscher, R. Scopelliti, P. Gao, S. Mathew, J.-E. Moser, I. Tavernelli, U. Rothlisberger, M. Grätzel, M. K. Nazeeruddin and J. Frey, *Angew. Chem., Int. Ed.*, 2013, **52**, 8731-8735.
82. J.-H. Yum, E. Baranoff, F. Kessler, T. Moehl, S. Ahmad, T. Bessho, A. Marchioro, E. Ghadiri, J.-E. Moser, C. Yi, M. K. Nazeeruddin and M. Grätzel, *Nat. Commun.*, 2012, **3**, 631.
83. N. Blouin, A. Michaud, D. Gendron, S. Wakim, E. Blair, R. Neagu-Plesu, M. Belletête, G. Durocher, Y. Tao and M. Leclerc, *J. Am. Chem. Soc.*, 2008, **130**, 732-742.
84. Various values are reported in literature regarding the exact LUMO level of the PCBM vs vacuum. The value of -3.91 eV is from: He et al., Phys. Chem. Chem. Phys., 2011, 13, 1970-1983. The value of -4.3 eV is from: Blouin et al., J. Am. Chem. Soc. 2008, 130, 732-742.
85. Although evaluated at -4.2 eV (-0.5 V vs NHE), the exact position of the TiO2 conduction band is known to depend on several factors including the local pH, the concentration of potential determining ions (e.g. Li+), the nature of the electrolyte solvent and on the dye molecular structure.
86. D. Rehm and A. Weller, *Israel Journal of Chemistry*, 1970, **8**, 259-271.
87. D. M. Schultz and T. P. Yoon, *Science*, 2014, **343**.
88. C. K. Prier, D. A. Rankic and D. W. C. MacMillan, *Chem. Rev.*, 2013, **113**, 5322-5363.
89. J. M. R. Narayanam and C. R. J. Stephenson, *Chem. Soc. Rev.*, 2011, **40**, 102-113.
90. E. Y. Li, Y.-M. Cheng, C.-C. Hsu, P.-T. Chou, G.-H. Lee, I. H. Lin, Y. Chi and C.-S. Liu, *Inorg. Chem.*, 2006, **45**, 8041-8051.
91. N. A. F. Al-Rawashdeh, S. Chatterjee, J. A. Krause and W. B. Connick, *Inorg. Chem.*, 2014, **53**, 294-307.
92. S. H. Wadman, M. Lutz, D. M. Tooke, A. L. Spek, F. e. Hartl, R. W. A. Havenith, G. P. M. van Klink and G. van Koten, *Inorg. Chem.*, 2009, **48**, 1887-1900.
93. It is noteworthy that two small reduction peaks at -0.54 and -0.70 V were also observed by DPV and tend to corroborate the decomposition observed during synthesis of this rather sensitive intermediate (refer to experimental section).

94. Stability issue was also observed for adduct 6 upon long-term exposition in hot methanol solution during a recrystallization attempt.
95. M. Falkenström, O. Johansson and L. Hammarström, *Inorganica Chimica Acta*, 2007, **360**, 741-750.
96. A. K. Pal, N. Zaccheroni, S. Campagna and G. S. Hanan, *Chem. Commun.*, 2014, **50**, 6846-6849.
97. A. K. Pal, S. Serroni, N. Zaccheroni, S. Campagna and G. S. Hanan, *Chem. Sci.*, 2014, **5**, 4800-4811.
98. F. De Angelis, *Acc. Chem. Res.*, 2014.
99. J. Hachmann, R. Olivares-Amaya, A. Jinich, A. L. Appleton, M. A. Blood-Forsythe, L. R. Seress, C. Roman-Salgado, K. Trepte, S. Atahan-Evrenk, S. Er, S. Shrestha, R. Mondal, A. Sokolov, Z. Bao and A. Aspuru-Guzik, *Energy Environ. Sci.*, 2014, **7**, 698-704.
100. D. Casanova, F. P. Rotzinger and M. Grätzel, *J. Chem. Theory Comput.*, 2010, **6**, 1219-1227.
101. J. Preat, D. Jacquemin and E. A. Perpete, *Energy Environ. Sci.*, 2010, **3**, 891-904.
102. Y. Zhao and D. G. Truhlar, *Acc. Chem. Res.*, 2008, **41**, 157-167.
103. D. D. Méndez-Hernández, P. Tarakeshwar, D. Gust, T. A. Moore, A. L. Moore and V. Mujica, *J. Mol. Model.*, 2013, **19**, 2845-2848.
104. C.-C. Chou, F.-C. Hu, K.-L. Wu, T. Duan, Y. Chi, S.-H. Liu, G.-H. Lee and P.-T. Chou, *Inorg. Chem.*, 2014, **53**, 8593-8599.
105. C. Adamo and D. Jacquemin, *Chem. Soc. Rev.*, 2013, **42**, 845-856.
106. E. Ronca, F. De Angelis and S. Fantacci, *J. Phys. Chem. C*, 2014, **118**, 17067-17078.
107. K. Kalyanasundaram, *Photochemistry of Polypyridine and Porphyrin Complexes*, Academic Press, London, 1992.
108. T. A. Heimer, S. T. D'Arcangelis, F. Farzad, J. M. Stipkala and G. J. Meyer, *Inorg. Chem.*, 1996, **35**, 5319-5324.
109. R. Kohlrausch, *Ann. Phys. Chem. (Poggendorf)*, 1854, **91**, 56-82.
110. G. Williams and D. C. Watts, *Transactions of the Faraday Society*, 1970, **66**, 80-85.

Chapitre 5 : Conclusions et Perspectives

5.1 – Conclusions

Dans le cadre de cette thèse, différentes stratégies ont été explorées pour moduler les propriétés optoélectroniques de dérivés DPM et favoriser leur intégration dans des dispositifs photovoltaïques de type OPV et / ou DSSC. En général, une combinaison d'effets a été investiguée de façon rationnelle afin de discerner les limites inhérentes à chaque stratégie et de tirer avantage des photons du proche-infrarouge. La relation structure-propriétés à l'intérieur des séries de dérivés ainsi qu'avec d'autres molécules d'intérêt a été déterminée en utilisant les données électrochimiques, photophysiques, structurales et computationnelles. La Figure 5.1 résume l'ensemble des stratégies explorées en collaboration industrielle avec SJPC, nommément l'utilisation du cœur ADPM *vs.* DPM, l'extension des systèmes électroniques π-conjugués, l'emploi de groupements fonctionnels à richesse électronique variable, la génération d'un effet *Push-Pull*, la coordination de divers métaux de transition ainsi que l'ajustement du mode de coordination des ligands.

Dans le Chapitre 2, un cœur ADPM a été la base pour le développement des nouveaux chromophores tétradentates symétriques et asymétriques **1** – **6** susceptibles d'être coordonnés à des centres métalliques de façon biomimétique aux porphyrinoïdes. L'effet *Push-Pull* a pu être intégré dans les dérivés asymétriques comportant en positions proximales un aryle riche en électron munit d'un groupement 2-hydroxyle ou 2-méthoxyle ainsi qu'une unité 2-pyridyle pauvre en électron. Les six combinaisons

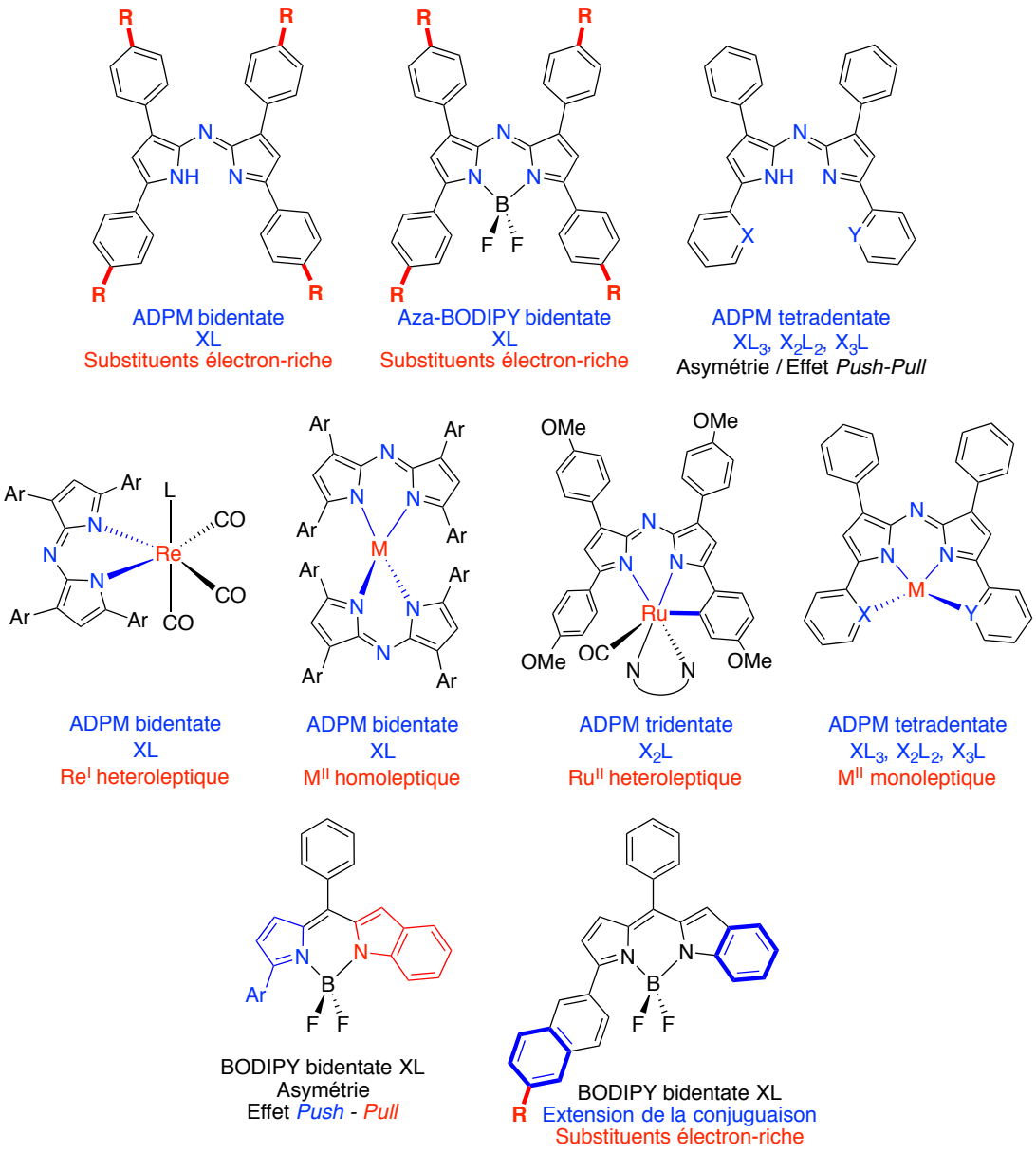

Figure 5.1 – Stratégies employées pour moduler les propriétés optoélectroniques des dérivés dipyrrométhène.

possibles utilisant ces trois unités ont été obtenues grâce à la nouvelle méthode synthétique développée pour l'obtention de dérivés ADPM asymétriques. Ainsi, le mode de coordination accessible a pu être étendu de XL_3 à X_3L. La comparaison directe a aussi été effectuée avec les dérivés bidentates tétraphényles ADPM **7** et tétra-*p*-méthoxy-phényles ADPM **8**. L'étude structure-propriété entreprise a montré qu'une modulation du maximum d'absorption dans le rouge pouvait être faite entre 598 et 619 nm. De même, la présence de groupements méthoxyle ou hydroxyle augmente l'absorption dans le violet (~410 nm). La caractérisation électrochimique a montré que les dérivés tétradentates étaient moins stables aux processus redox que leurs contre-parties bidentate, ce qui concorde avec l'observation de la décomposition en solution du dérivé symétrique comportant deux unités 2-pyridyle. Les études structurales et computationnelles ont facilité la compréhension des phénomènes électrochimique et photophysique. La méthode TD-DFT utilisée a permis de prédire adéquatement l'ordre relatif du maximum d'absorption dans le rouge pour l'ensemble de la série ainsi que l'absorption accrue de photons dans le violet pour les substituants riches en électrons. Le potentiel pour la coordination de centres métalliques sur ces ligands ADPM tétradentates apparaissait alors très intéressant afin de favoriser l'extension du système π-conjugué, stabiliser les processus redox et obtenir des propriétés d'absorption dans le NIR.

Des efforts subséquents pour coordonner deux des ligands ADPM tétradentate de type X_2L_2 sur les mêmes centres métalliques que dans l'étude des complexes homoleptiques (Co^{II}, Ni^{II} Cu^{II}et Zn^{II}) ainsi que sur le Pd^{II} ou le Pt^{II} n'ont pas été particulièrement fructueux (Figure 5.1).[1] Seul un complexe neutre de Cu^{II} basé sur l'ADPM **4** du Chapitre 2 (groupements 2-méthoxyle et 2-hydroxyle) a pu être isolé,

présentant un profil d'absorption très similaire à celui obtenu pour les complexes homoleptiques **1.11** – **1.18** (voir Chapitre 1). Cette observation supporte l'hypothèse initiale que l'utilisation d'un motif tétradentate permet d'étendre les propriétés optiques vers le NIR. Malheureusement, le composé n'offrait pas des propriétés électroniques souhaitables pour son intégration dans des applications en photovoltaïque et ce projet a donc été écarté. L'effet de la coordination bidentate du tétra-*p*-méthoxy-phényles ADPM a aussi été évalué sur deux complexes *fac*-tricarbonyl Re^{I} dont la structure octahédrique déformée est complétée par une molécule de solvant.[2] Les informations structurales obtenues par rayons-X ont montrées que l'arrangement atomique autour du centre métallique Re^{I} était dicté surtout par l'encombrement stérique et l'empilement cristallin. L'intégration dans des applications de photo-récoltage d'énergie a cependant été délaissé en raison de l'instabilité de ces deux complexes en solution.

Dans le Chapitre 3, l'hypothèse a été faite que les propriétés optoélectroniques d'un cœur BODIPY fusionné de façon asymétrique en position [*b*] pourraient être grandement affectées en utilisant sur l'aryle proximal du pyrrole différents groupements électron-riche et / ou en étendant le système π-conjugué. L'idée provenait du fait que le cœur fusionné de cette façon mène à un effet *Push-Pull* intrinsèque où le pyrrole agit comme donneur alors que le noyau indolique accepte la densité électronique pour rehausser son caractère azafulvène.[3] La comparaison des dix dérivés **1** – **10** nouvellement synthétisés avec une vaste série de BODIPYs a été faite pour mettre à l'épreuve cette hypothèse et mieux comprendre l'effet d'induire de l'asymétrie dans le système. Les résultats empiriques ont montré que les propriétés optoélectroniques de la plateforme étaient régies par le degré de communication entre l'aryle proximal, le

pyrrole sur lequel il est attaché et le noyau indolique adjacent à ce dernier. La modélisation moléculaire a permis de valider ces observations et d'assigner les transitions électroniques associées aux bandes d'absorptions. Les maximums d'absorption dans le rouge ont pu être modulés entre 547 et 628 nm et la plateforme de BODIPY asymétriques fusionnés en position [*b*] s'est révélée fluorescente dans le NIR. D'entre tous les dérivés synthétisés, le composé **8** portant un *p*-diméthylamine-phényle comme aryle proximal s'est révélé avoir le plus fort potentiel pour des applications en photovoltaïque et en tant que sonde à pH.

Dans le Chapitre 4, l'exploration de la réaction de cyclométalation d'un des aryles proximaux du ligand tétra-*p*-méthoxy-phényles ADPM pour former des complexes de Ru^{II} polypyridines neutres a été menée. Cette stratégie de coordination sans précédant pour les dérivés DPM a permis de rendre le ligand ADPM tridentate de type X_2L tout en renforçant la planéité de l'aryle proximal avec le cœur dipyrrolique. L'analyse des propriétés optoélectroniques de façon empirique et théorique a montré un impact significatif de la cyclométalation et ouvert la voie pour leur étude en tant que photosensibilisateurs en OPV et en DSSC. Les cinq complexes **2** – **6** obtenus ont présenté une LUMO dont le niveau énergétique était supérieur à celui du **PCBM** et de la bande de conduction du TiO_2. Le composé **6** portant un dérivé tpy substitué avec l'ancrage nécessaire a démontré une absorption au-delà de 1 000 nm et une capacité à photo-injecter dans la bande de conduction du TiO_2. Il est intéressant de noter qu'une stratégie de synthèse de type « chimie sur le complexe » a pu être utilisée pour convertir par couplage de Suzuki le précurseur **5** portant le ligand bromo-phényle-tpy en son analogue **6** disponible pour des tests en DSSC. Par contre, une instabilité structurale

observée en solution a empêché son emploi dans une cellule électrochimique complète. En fait, l'électrochimie a démontré que les deux dérivés tpy possédaient une HOMO oxydable au contact de l'air. Les trois complexes portant des ligands dérivés du motif bpy **2** – **4** étaient quant à eux plus stables et ont le potentiel d'être employés en OPV. Leur absorption s'étendant jusqu'à environ 850 nm dans le NIR en fait des candidats de choix en tant que donneur ou additif et des études en ce sens devraient être effectuées.

5.2 – Perspectives

Au fil de l'exploration des divers dérivés DPM discutés dans cette thèse, certaines stratégies pour la modulation des propriétés optoélectroniques se sont révélées plus robustes que d'autres face aux conditions environnementales auxquelles elles étaient soumises (exposition à la lumière, purification sur Si, stabilité en solution et face aux cycles redox, *etc.*). Les composés basés sur un cœur azadipyrrométhène se sont avérés beaucoup moins stables que leur contrepartie dipyrrométhène, vraisemblablement en raison d'une réactivité accrue sur le carbone pyrrolique adjacent à l'azote situé en position *meso*. Pourtant, le déplacement bathochrome intrinsèque des ADPM nous apparaissait initialement une plateforme de choix pour l'édification de chromophores atteignant le proche-infrarouge. Face a cette déconvenue et à la lumière des résultats probants obtenus avec les BODIPYs asymétriques fusionnés en position [*b*] (Chapitre 3) ainsi que la nouvelle réaction de cyclométalation développée (Chapitre 4), il appert que la modification du mode de coordination des DPM pourrait être une avenue intéressante

à explorer afin d'obtenir des niveaux électroniques adéquats pour le photovoltaïque et une absorption dans le NIR.

Une étude computationnelle préliminaire a donc été entreprise afin d'identifier les meilleurs candidats DPM qui pourraient posséder des propriétés optoélectroniques optimales une fois installés sur des complexes de ruthénium neutres.[4] Dans un premier temps, la même méthode DFT // TD-DFT que dans le Chapitre 2 a été utilisée pour mettre en relation une série de cinq familles de ligands DPM potentiels (**5.2** -**5.6**) avec le ligand tétra-*p*-méthoxyphényles ADPM **5.1** préalablement étudié (Figure 5.2). Le Tableau 5.I compile les résultats concernant les niveaux électroniques et le E_g associé calculés par DFT ainsi que les transitions électroniques de plus base énergie prédit par TD-DFT. L'analyse du tableau montre que deux familles de ligands ressortent du lot au point de vue électronique afin de remplacer les ADPM, soit les DPM asymétriques fusionnés en position [*b*] ainsi que ceux basés sur un motif triazole en position proximale. En effet, elles possèdent un niveau de la LUMO (-2,96 et -2,73 eV, respectivement) qui est supérieur à celui de l'ADPM (-2,81 eV). À l'opposé, le niveau de leur HOMO (-5,73 et -5,76 eV, respectivement) est inférieur à celui de l'ADPM (-5,23 eV) et devrait ainsi permettre une stabilité accrue face à l'oxydation de l'air. De ces deux familles, la première est particulièrement intéressante en raison de ces propriétés d'absorption qui devraient théoriquement être le plus déplacées vers le rouge. Tel que démontré dans le Chapitre 3, la plateforme DPM asymétrique fusionnée à la position [*b*] est grandement versatile et devrait donc permettre une modulation fine des propriétés en cas de besoin.

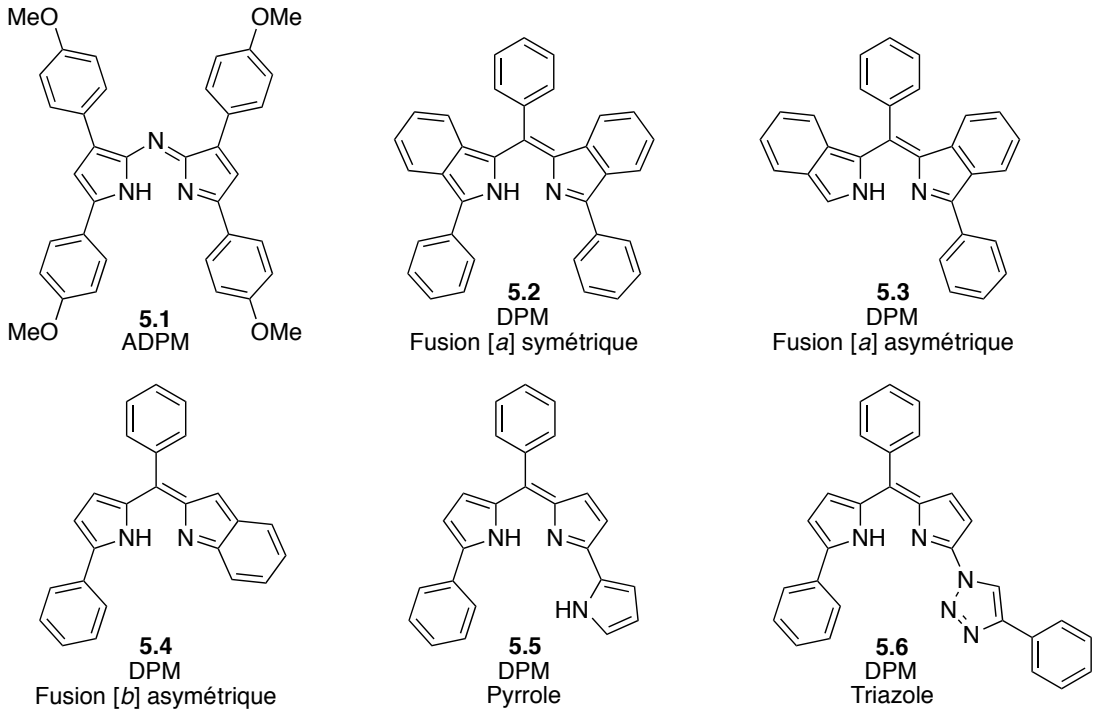

Figure 5.2 – Les cinq familles DPM et la référence ADPM étudiées par modélisation.

Table 5.I – Résultats de modélisation pour les cinq familles DPM et la référence ADPM.

Dérivé	Famille	HOMO (eV)	LUMO (eV)	E_g (eV)	Transition (nm; force oscillateur)
5.1	ADPM	-5,23	-2,81	2,41	587 (0,889)
5.2	fusion [*a*] symétrique	-5,14	-2,49	2,65	544 (0,906)
5.3	fusion [*a*] asymétrique	-5,23	-2,38	2,85	498 (1,02)
5.4	fusion [*b*] asymétrique	-5,73	-2,96	2,77	494 (0,929) / 538 (0,040)
5.5	Pyrrole	-5,34	-2,46	2,88	488 (0,777)
5.6	Triazole	-5,76	-2,73	3,03	471 (0,811)

Méthode DFT // TD-DFT utilisée : r-pbe0 / 6-311G (2d,p) (PCM = DCM) // BMK / 6-311+G (2d,p) (PCM = DCM)

À partir des résultats intéressants obtenus pour les ligands DPM de remplacement, les complexes neutres de ruthénium correspondants (**5.8** – **5.12**) ont été modélisés en utilisant la méthode du Chapitre 4 (Figure 5.3). Dans le cas des familles DPM fusionnées permettant la cyclométalation ainsi que celle contenant un pyrrole supplémentaire, une coordination de type X_2L est attendue et pourrait être utilisée avec un contre-ligand dérivé des terpyridines. À l'opposé, la famille contenant un noyau triazole devrait se coordonner au ruthénium de façon XL_2 et, dans ce cas, la neutralité du complexe serait préservée en utilisant un contre-ligand capable de cyclométaler. Un dérivé de type NNC a donc été utilisé comme contre-ligand. Dans tous les cas, un ancrage acide carboxylique a été ajouté pour déterminer si le complexe pourrait agir comme photosensibilisateur en DSSC. Dans le cadre de cette comparaison, les niveaux énergétiques du complexe **5.7** (**2**, Chapitre 4) ont été considérés comme la référence. En effet, les résultats empiriques avaient démontré que ce dérivé possède une LUMO suffisamment haute pour la photo-injection, tout en ayant la HOMO la plus stable de la série.

Les résultats de la modélisation compilés à la Table 5.II montrent une fois de plus que les complexes basés sur les familles asymétriques fusionnées en position [*b*] (**5.10**) ainsi que portant un noyau triazole (**5.12**) constitueraient des options sérieuses à explorer de façon empirique. En effet, ces deux complexes sont les seuls à présenter une LUMO supérieure (-2,13 et -1,96 eV, respectivement) et une HOMO en-deçà (-4,39 et -4,37 eV) de ce qui est obtenu pour le composé de référence **5.7** (LUMO = -2,17 eV; HOMO = -4,20 eV). De même, leur maximum d'absorption calculé (769 et 748 nm, respectivement) s'établit plus de 100 nm au-delà de celui qui a été obtenue pour cette

même référence (647 nm). Une absorption dans le NIR accompagnée d'une stabilité améliorée est donc attendue pour ces complexes.

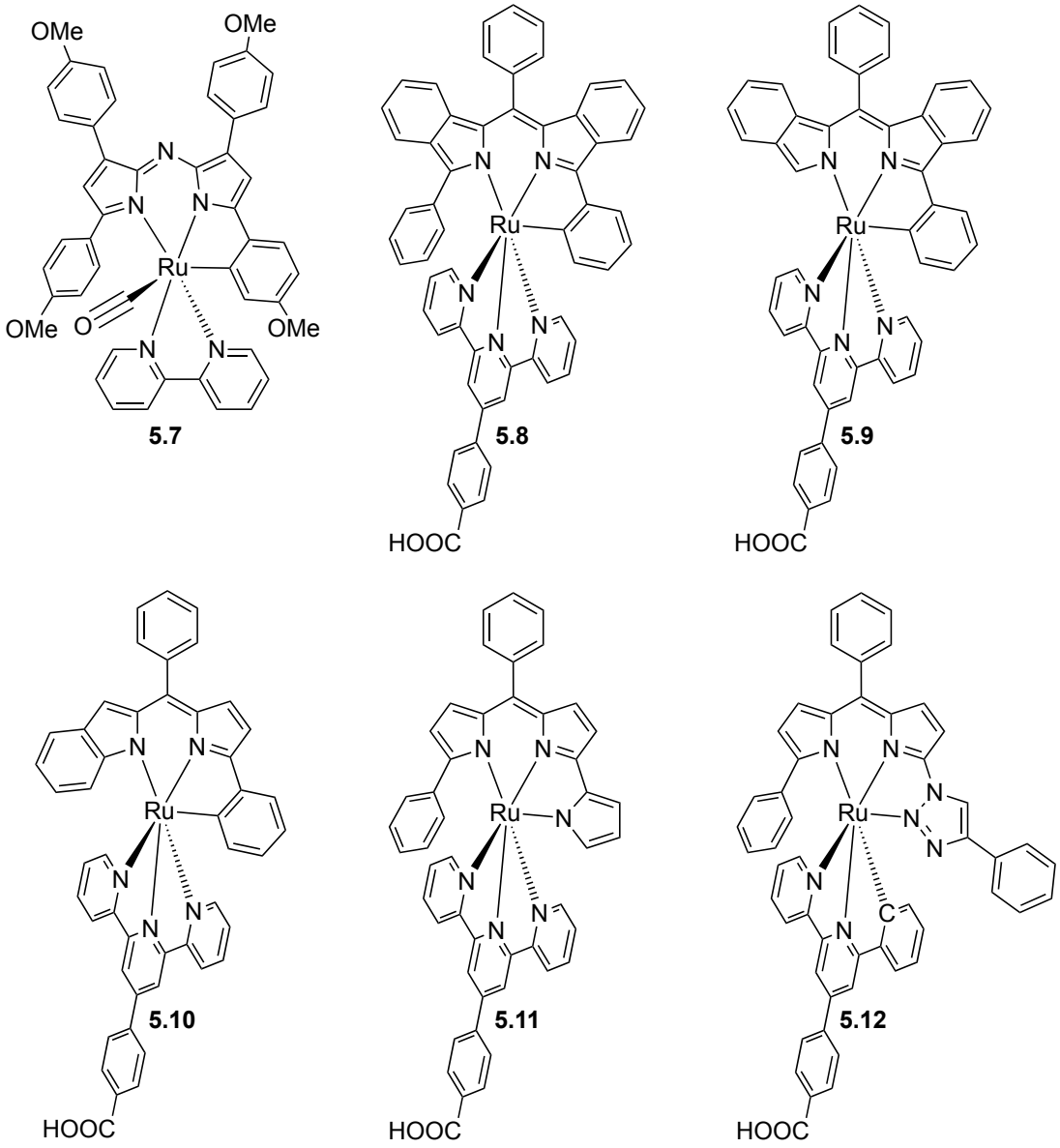

Figure 5.3 – Les cinq complexes neutres de ruthénium et de la référence étudiés par modélisation.

Table 5.II – Résultats de modélisation pour les complexes neutres de Ru^{II} basés sur les cinq familles DPM et la référence ADPM.

Dérivé	Famille	HOMO (eV)	LUMO (eV)	E_g (eV)	Transitions (nm; force oscillateur)
5.7	ADPM	-4,20	-2,17	2,02	647 (0,388)
5.8	fusion [*a*] symétrique	-3,95	-2,17	1,78	812 (0,004)
5.9	fusion [*a*] asymétrique	-3,98	-2,23	1,74	814 (0,003)
5.10	fusion [*b*] asymétrique	-4,39	-2,13	2,26	769 (0,005)
5.11	Pyrrole	-3,85	-2,25	1,61	751 (0,001)
5.12	Triazole	-4,37	-1,96	2,41	748 (0,005)

Méthode DFT // TD-DFT utilisée : B3LYP / 6-31G* (Ru = LANL2DZ; Sans PCM) // B3LYP / 6-31G* (Ru = LANL2DZ; PCM = DCM)

En conclusion, les diverses stratégies de modulation optoélectronique des dérivés dipyrrométhènes explorées dans cette thèse ont permis de mieux comprendre le potentiel énorme de cette famille de chromophores pour des applications dans le photovoltaïque. La versatilité synthétique qui leur est associée permet d'entrevoir une infinité de combinaisons des effets afin d'ajuster les propriétés de façon optimale pour une application donnée, que cela soit en chimie des matériaux ou en sciences de la vie. De même, l'étude systématique de la relation structure-propriétés de ces dérivés DPM effectuée en conjoncture avec des méthodes de modélisation computationnelle de pointe permettent d'avoir confiance que les deux familles de complexes neutres de ruthénium proposées dans la section *Perspectives* de ce chapitre méritent d'être investiguées. Elles constituent un condensé des connaissances acquises sur le sujet dans le cadre de cette thèse et, espérons-le, une chance d'améliorer les performances photovoltaïques pour un avenir carburant aux énergies renouvelables.

5.3 – Notes et références de la conclusion

1. Résultats non-publiés. Travaux de André Yvon-Bessette et Mihaela Cibian (cristallographie aux rayons-X).
2. Cibian, M.; Bessette, A.; O'Connor, A.; Ferreira, J. G.; Hanan, G. S. *Acta Crystallogr., Sect. C* **2015**, *71*, 122.
3. Wakamiya, A.; Murakami, T.; Yamaguchi, S. *Chem. Sci.* **2013**, *4*, 1002.
4. Résultats non-publiés. Travaux de André Yvon-Bessette.

Annexe I : Informations supplémentaires du Chapitre 2

"Introducing Asymmetry in Tetradentate Azadipyrromethene Chromophores:

A Systematic Study of the Impact on Electronic and Photophysical Properties"

Physical Chemistry Chemical Physics, **2014**, *16*, 22207-22221.

Lien permanent vers l'article (DOI) : 10.1039/C4CP02629B

NMR Characterization

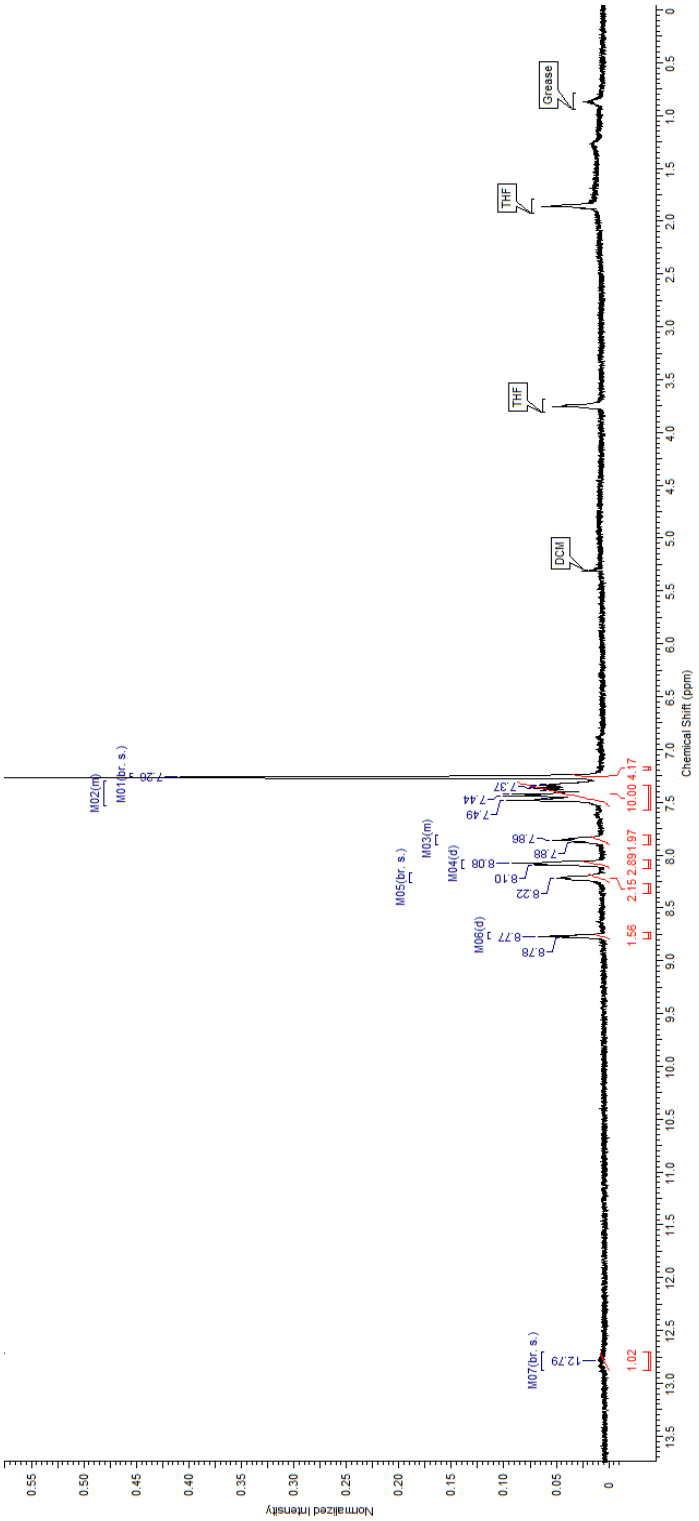

Figure I.S1 – ^{1}H of *Azadipyrromethene* **3** ($CDCl_3$; poorly soluble)

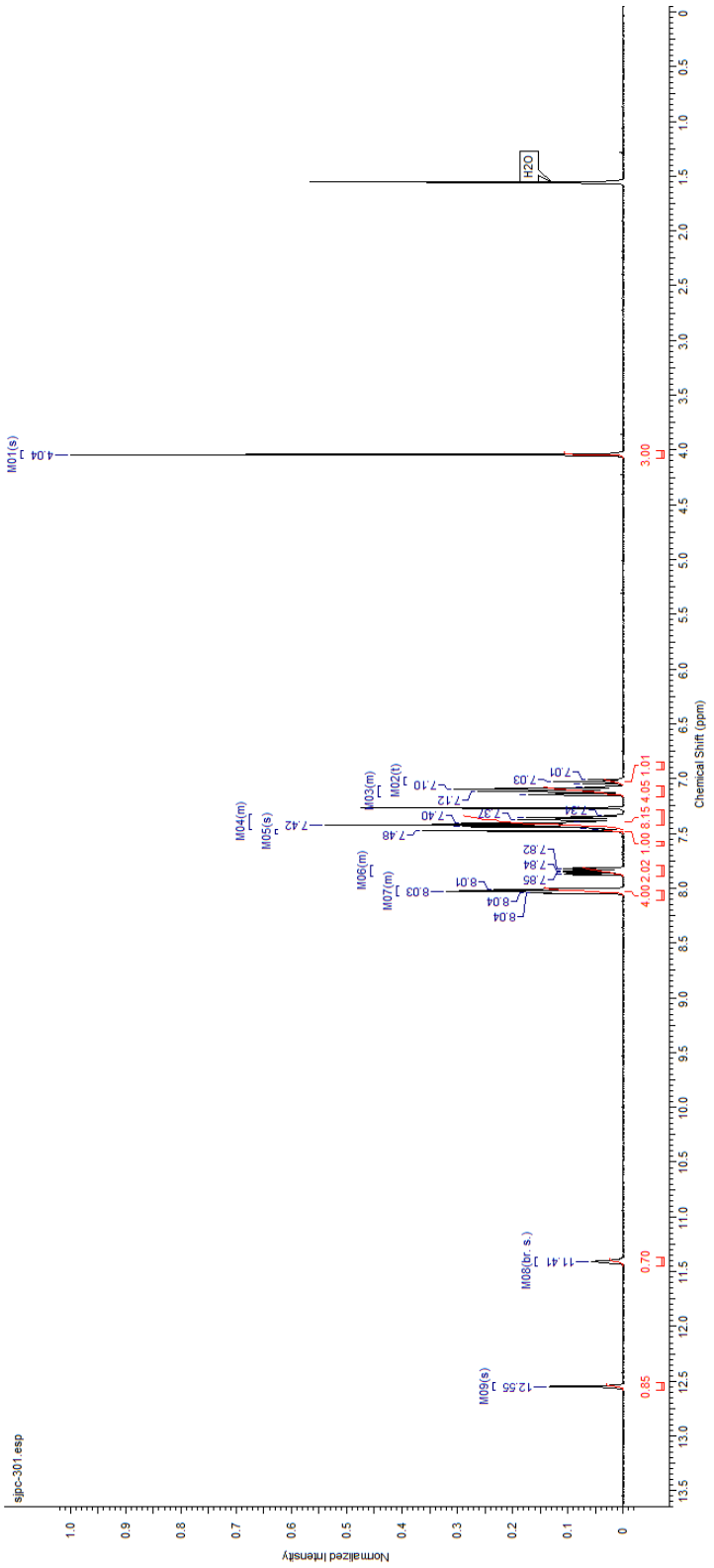

Figure I.S2 – ^{1}H of *Azadipyrromethene* **4** ($CDCl_3$)

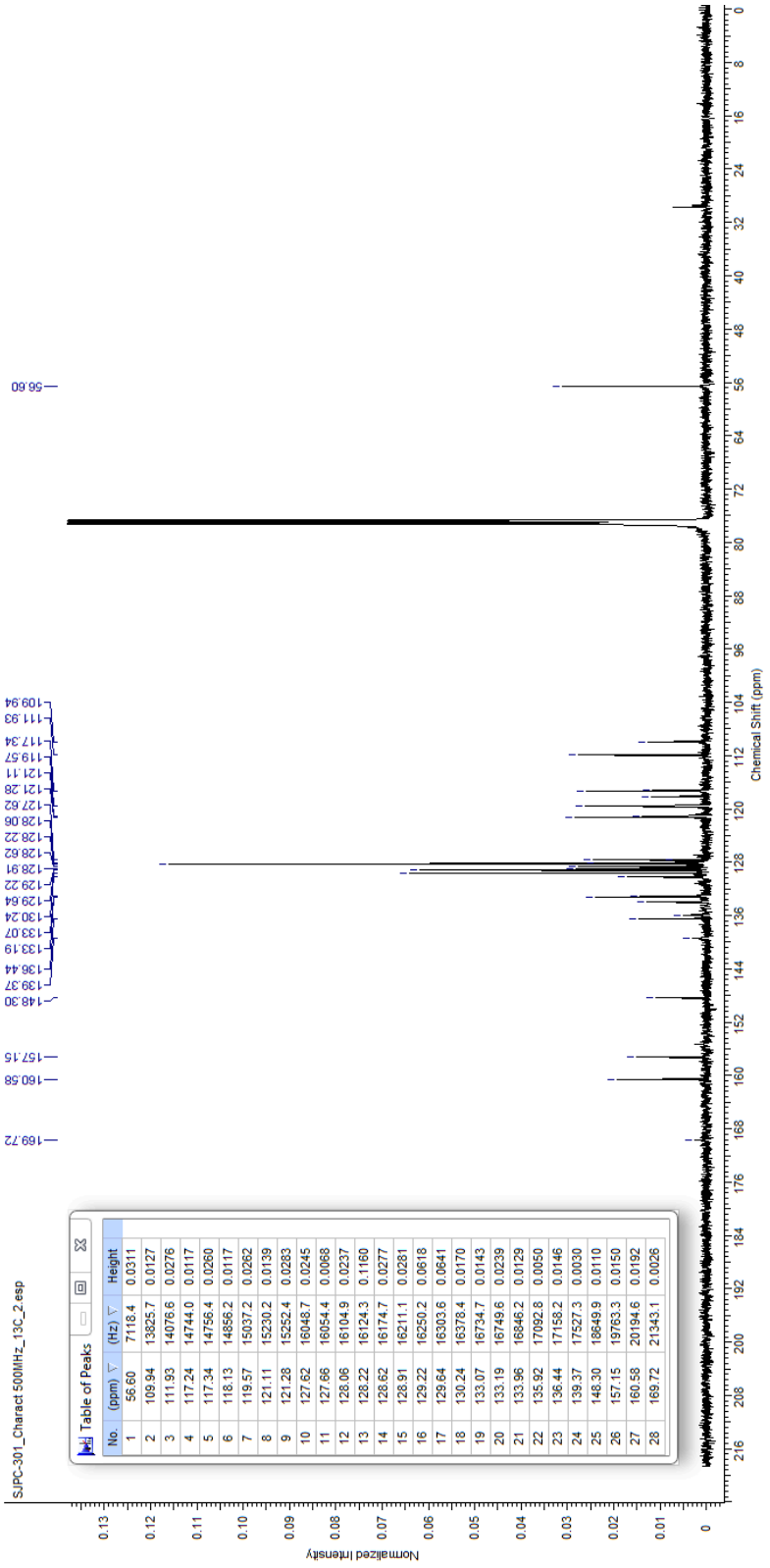

Figure I.S3 – ^{13}C of *Azadipyrromethene* **4** ($CDCl_3$)

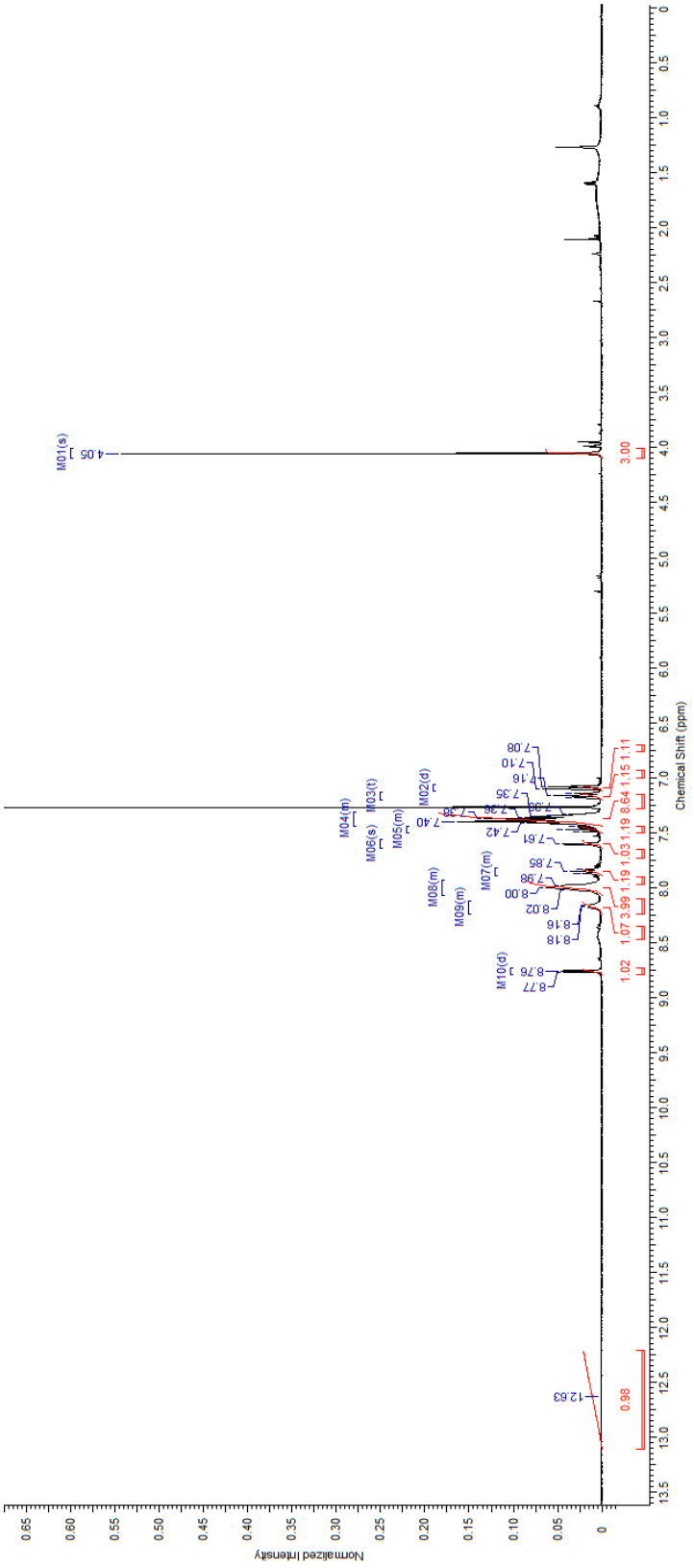

Figure I.S4 – ^{1}H of *Azadipyrromethene* **5** ($CDCl_3$)

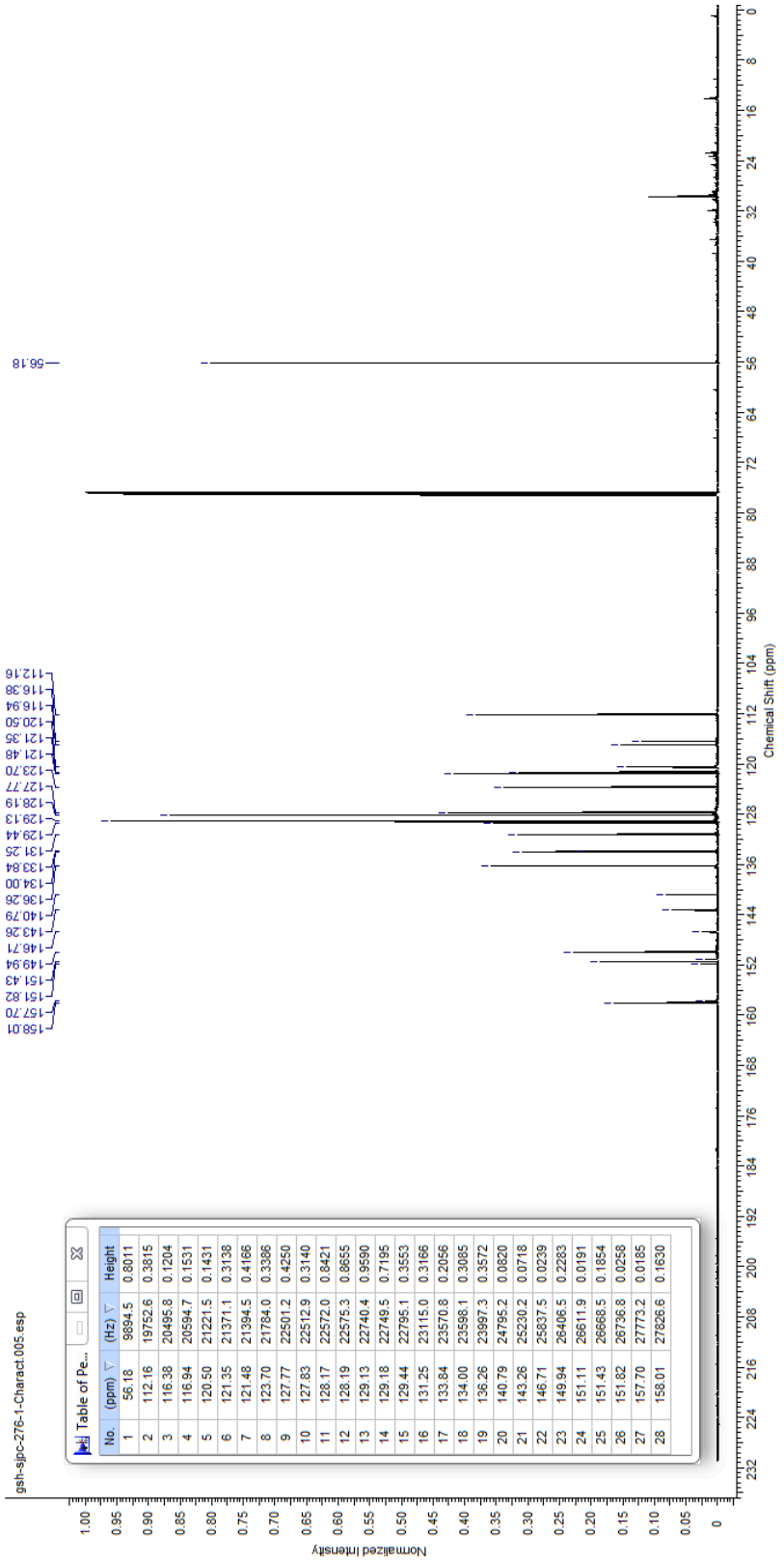

No.	(ppm)	(Hz)	Height
1	56.18	9894.5	0.8011
2	112.16	19752.6	0.3815
3	116.38	20495.8	0.1204
4	116.94	20594.7	0.1531
5	120.50	21221.5	0.1431
6	121.35	21371.1	0.3138
7	121.48	21394.5	0.4166
8	123.70	21784.0	0.3386
9	127.77	22501.2	0.4250
10	127.83	22512.9	0.3140
11	128.17	22572.0	0.8421
12	128.19	22575.3	0.8655
13	129.13	22740.4	0.9590
14	129.18	22749.5	0.7195
15	129.44	22795.1	0.3553
16	131.25	23115.0	0.3166
17	133.84	23570.8	0.2056
18	134.00	23598.1	0.3085
19	136.26	23997.3	0.3572
20	140.79	24795.2	0.0820
21	143.26	25230.2	0.0718
22	146.71	25837.5	0.0239
23	149.94	26406.5	0.2283
24	151.11	26611.9	0.0191
25	151.43	26668.5	0.1854
26	151.82	26736.8	0.0258
27	157.70	27773.2	0.0185
28	158.01	27826.6	0.1630

Figure I.S5 – ^{13}C of *Azadipyrromethene* **5** ($CDCl_3$)

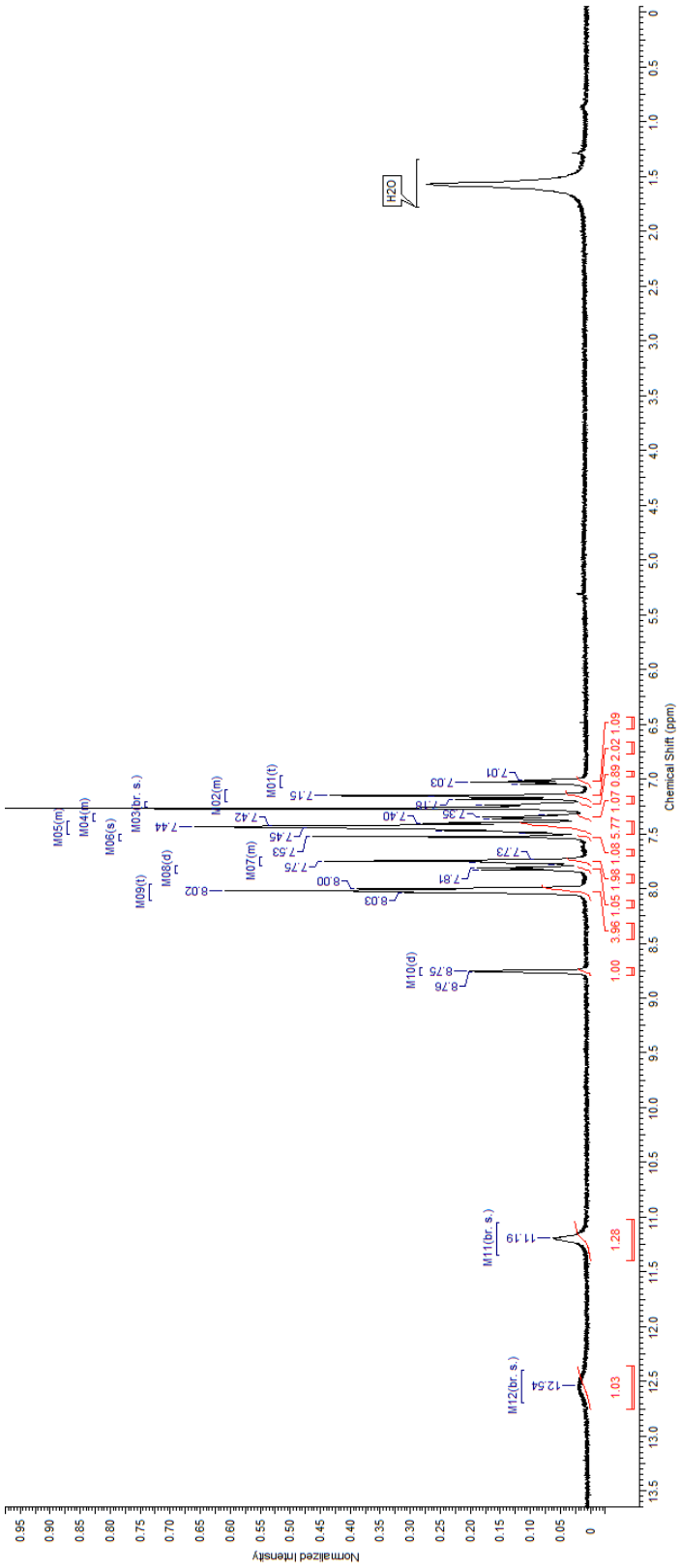

Figure I.S6 – ^{1}H of *Azadipyrromethene* **6** ($CDCl_3$)

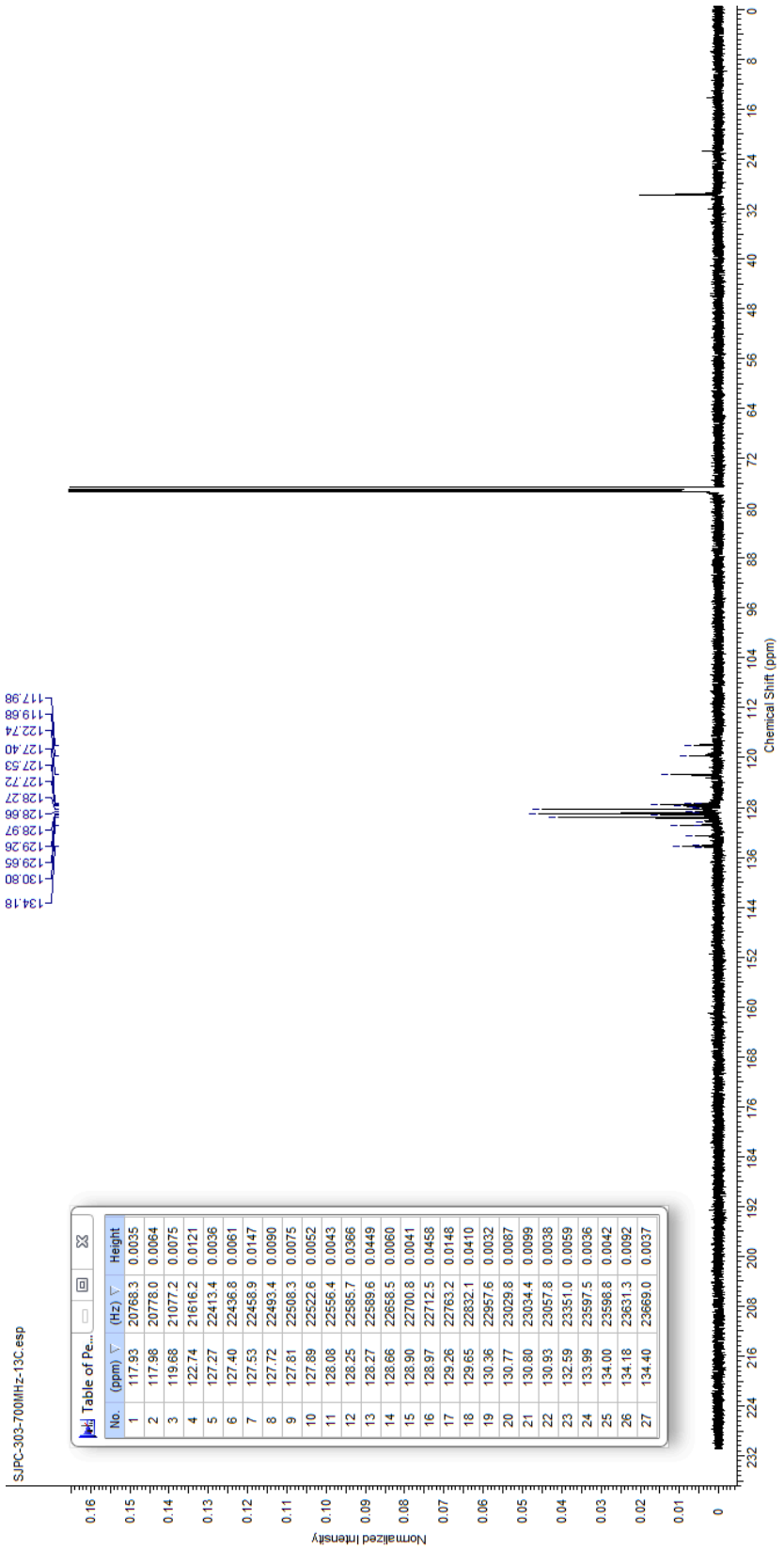

No.	(ppm)	(Hz)	Height
1	117.93	20768.3	0.0035
2	117.98	20778.0	0.0064
3	119.68	21077.2	0.0075
4	122.74	21616.2	0.0121
5	127.27	22413.4	0.0036
6	127.40	22436.8	0.0061
7	127.53	22458.9	0.0147
8	127.72	22493.4	0.0090
9	127.81	22508.3	0.0075
10	127.89	22522.6	0.0052
11	128.08	22556.4	0.0043
12	128.25	22585.7	0.0366
13	128.27	22589.6	0.0449
14	128.66	22658.5	0.0060
15	128.90	22700.8	0.0041
16	128.97	22712.5	0.0458
17	129.26	22763.2	0.0148
18	129.65	22832.1	0.0410
19	130.36	22957.6	0.0032
20	130.77	23029.8	0.0087
21	130.80	23034.4	0.0099
22	130.93	23057.8	0.0038
23	132.59	23351.0	0.0059
24	133.99	23597.5	0.0036
25	134.00	23598.8	0.0042
26	134.18	23631.3	0.0092
27	134.40	23669.0	0.0037

Figure I.S7 – ^{13}C of *Azadipyrromethene* **6** ($CDCl_3$)

HRMS Characterization

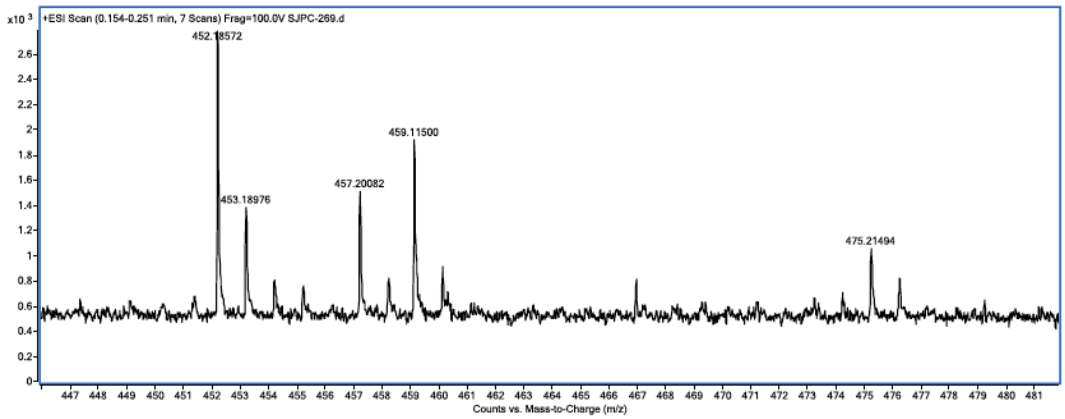

MS Spectrum Peak List

Ion	Ion Formula	Abund	*Expe. m/z*	*Calc. m/z*	Diff(ppm)
(M+H)+	C30H21N5		452.18572	452.18697	2.77

Figure I.S8 – HRMS of *Azadipyrromethene* **3**

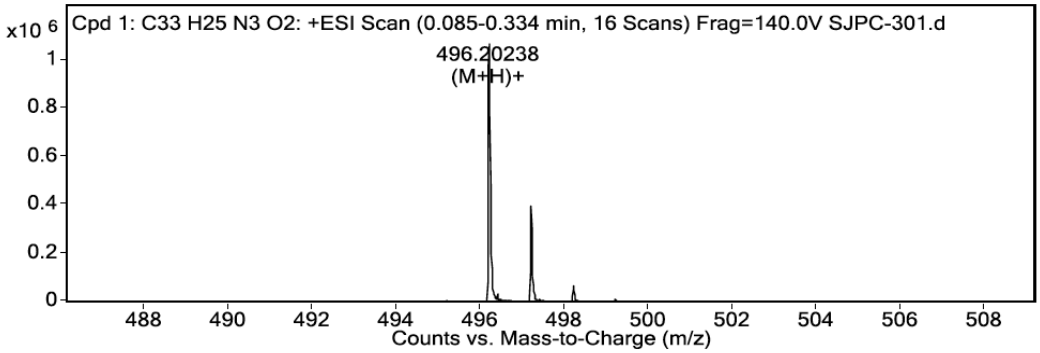

MS Spectrum Peak List

Ion	Formula	Abund	Observed m/z	Calc m/z	Diff (ppm)
(M+H)+	C33H25N3O2	1075282.31	496.20238	496.20195	-0.87

Figure I.S9 – HRMS of *Azadipyrromethene* **4**

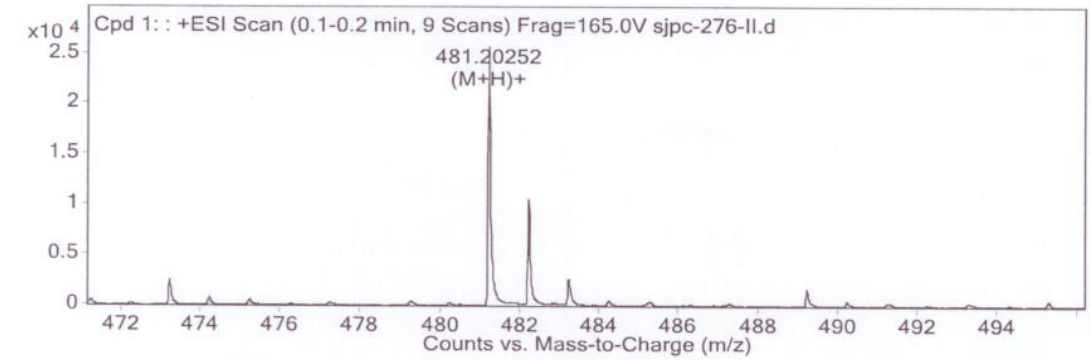

MS Spectrum Peak List

Ion	Ion Formula	Abund	*Expe. m/z*	*Calc. m/z*	Diff(ppm)
(M+H)+	C32H25N4O	25811.2	481.20252	481.20229	0.49

Figure I.S10 – HRMS of *Azadipyrromethene* **5**

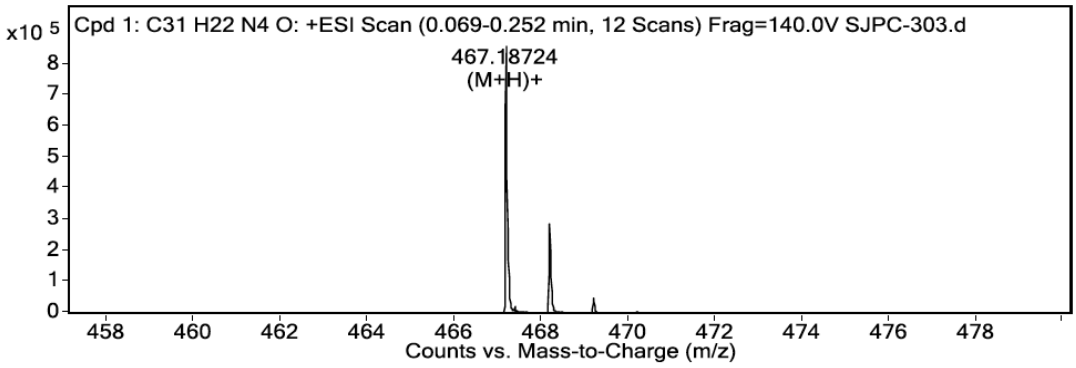

MS Spectrum Peak List

Ion	Formula	Abund	Observed m/z	Calc m/z	Diff (ppm)
(M+H)+	C31H22N4O	856545.24	467.18724	467.18664	-1.29

Figure I.S11 – HRMS of *Azadipyrromethene* **6**

Electrochemistry

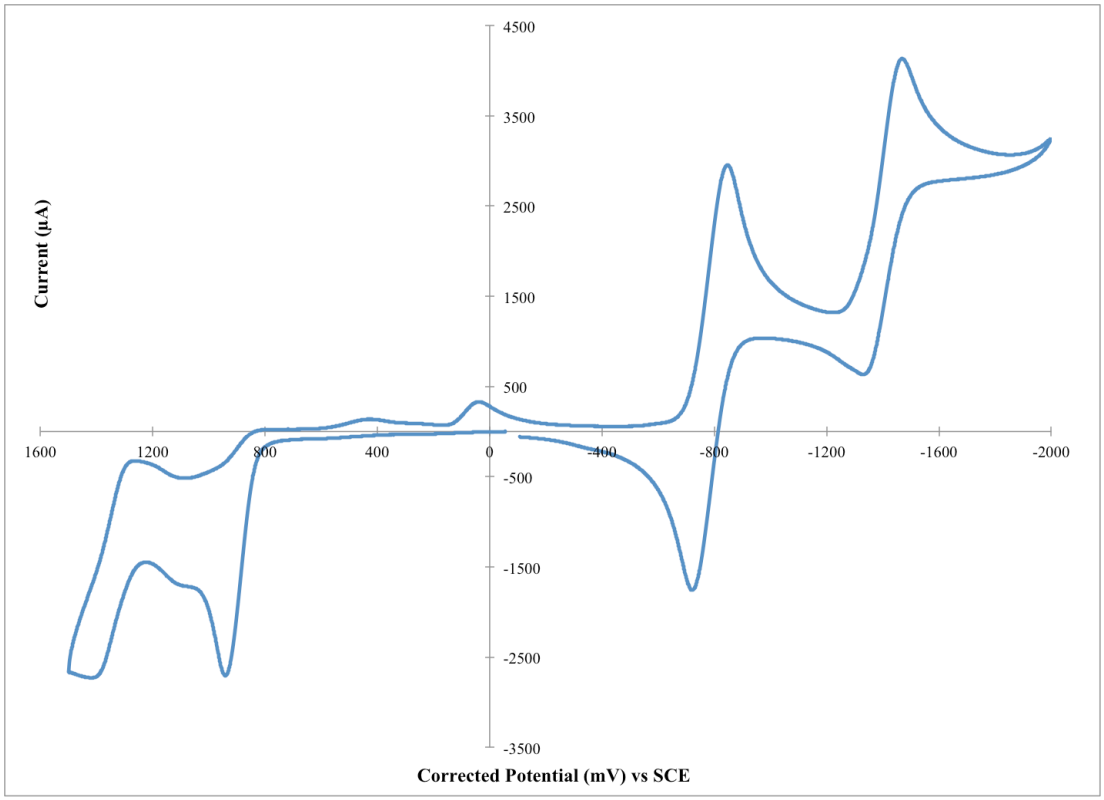

Figure I.S12 – CV of ADPM **1** with ferrocene reference measured before and after due to interaction with the compound.
(0.46V vs SCE in DCM) (Scan rate of 50 mV/s at R.T.)

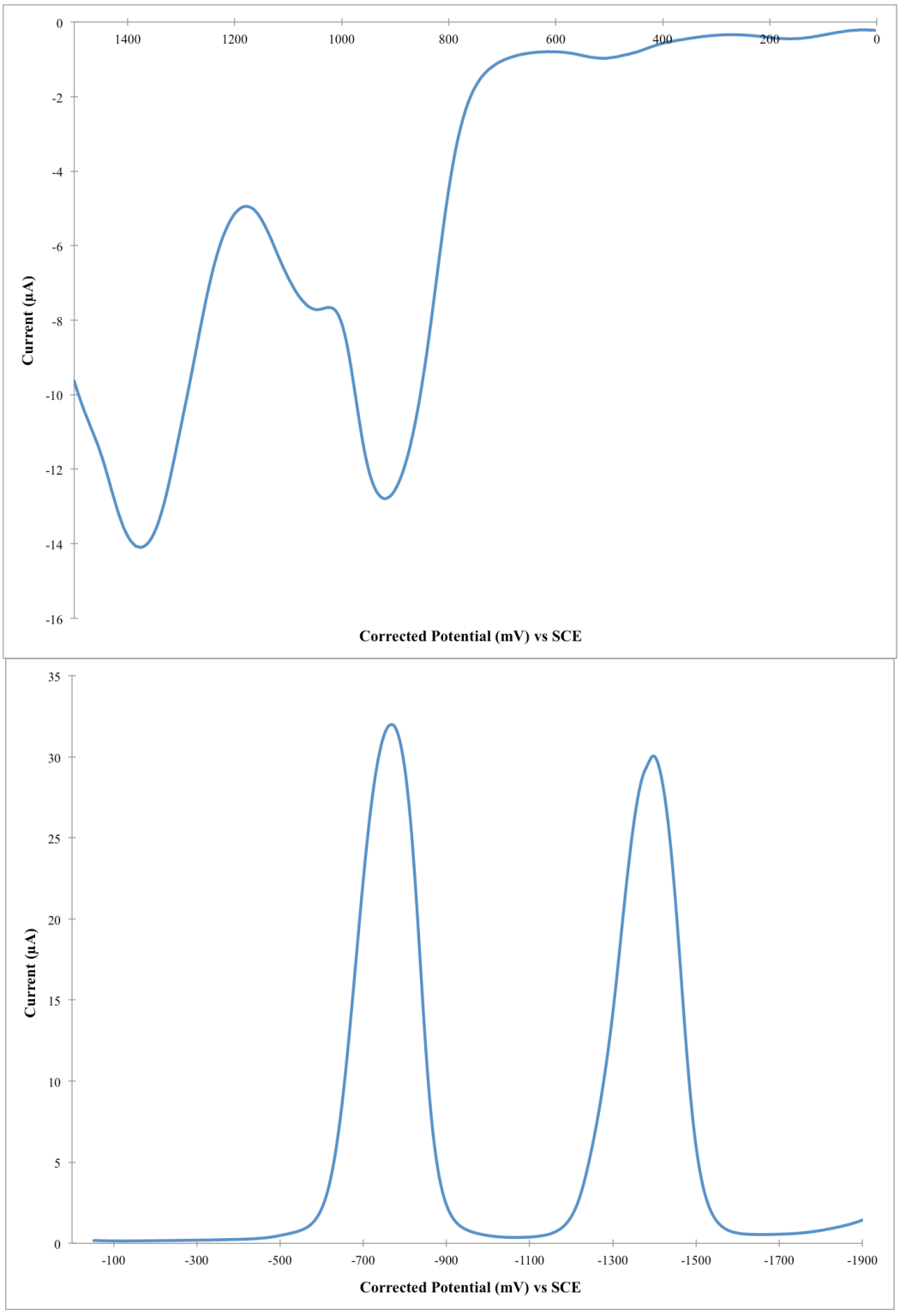

Figure I.S13 – DPV of ADPM **1** with ferrocene reference measured before and after due to interaction with the compound.

(0.46V vs SCE in DCM) (Scan rate of 50 mV/s at R.T.)

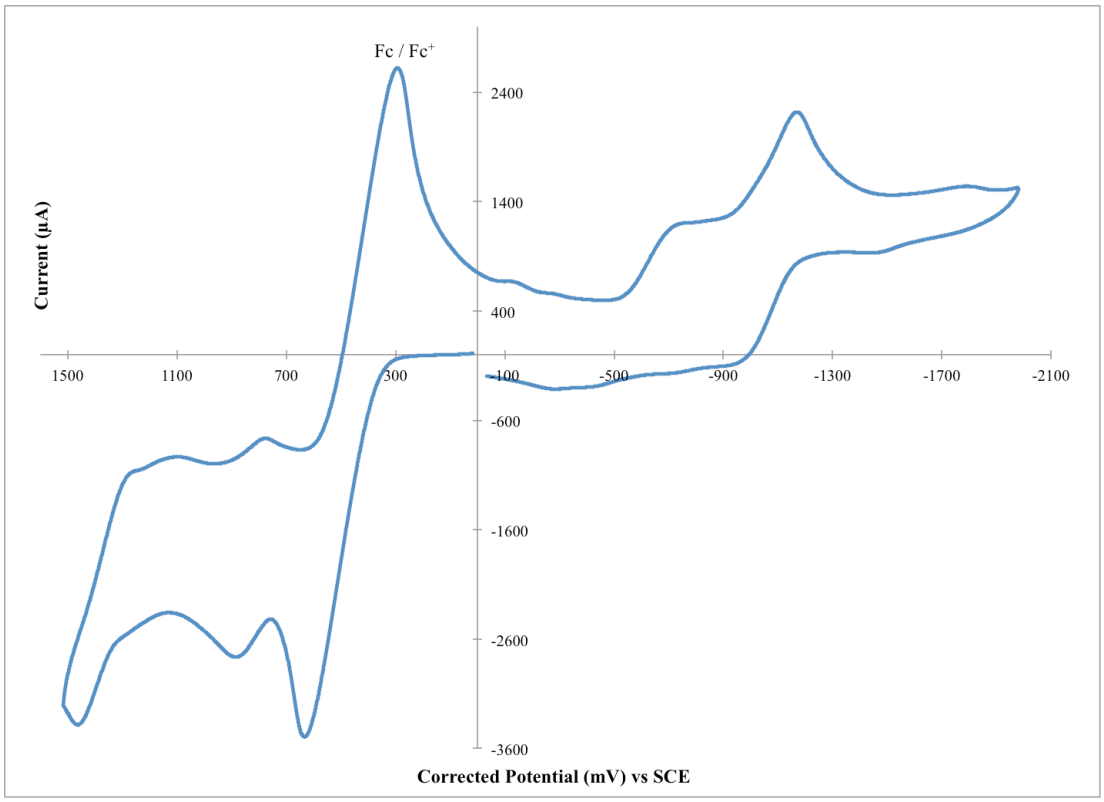

Figure I.S14 – CV of ADPM **2** with ferrocene as internal reference.
(0.46V vs SCE in DCM) (Scan rate of 50 mV/s at R.T.)

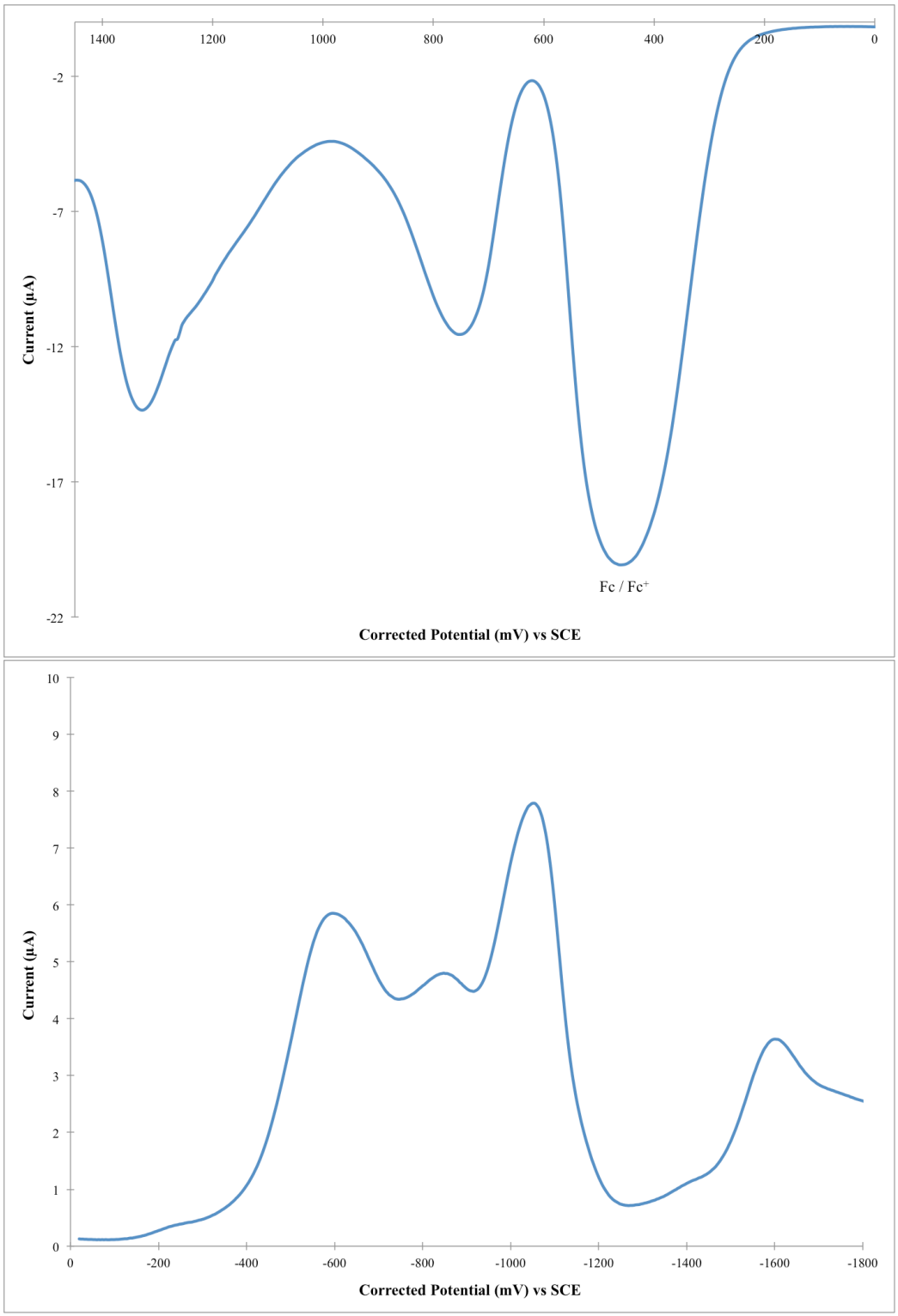

Figure I.S15 – DPV of ADPM **2** with ferrocene as internal reference. (0.46V vs SCE in DCM) (Scan rate of 50 mV/s at R.T.)

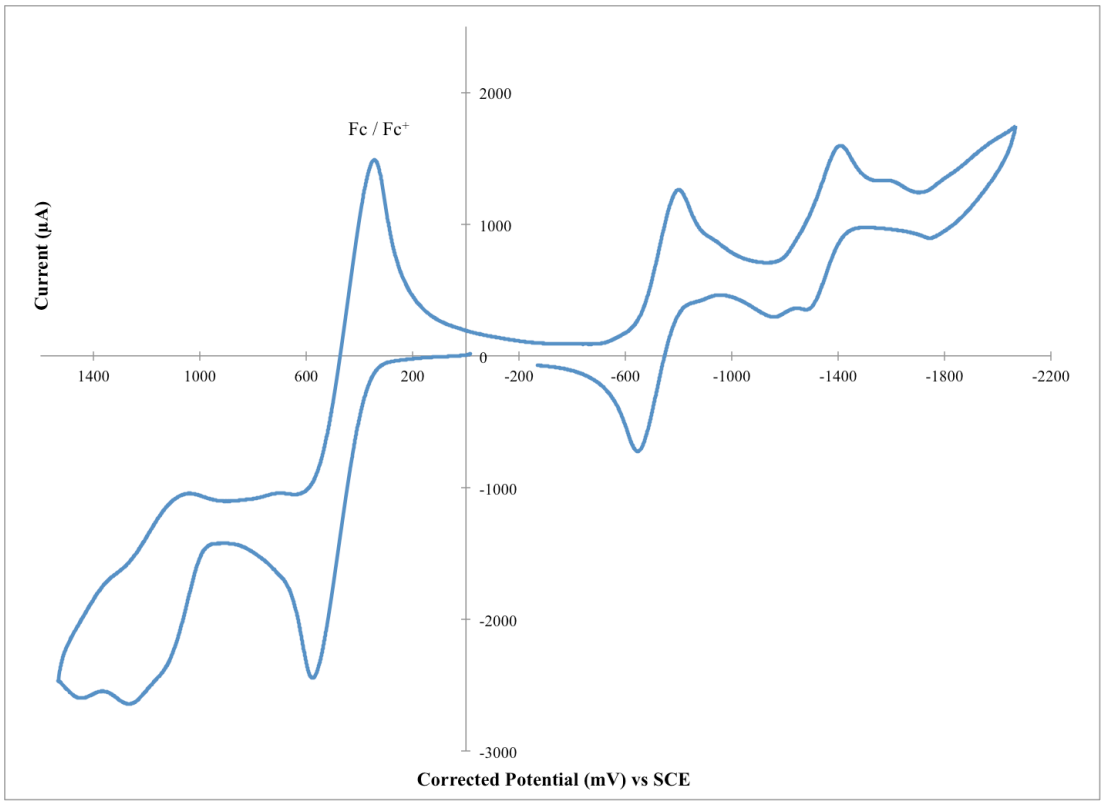

Figure I.S16 – CV of ADPM **3** with ferrocene as internal reference.
(0.46V vs SCE in DCM) (Scan rate of 50 mV/s at R.T.)

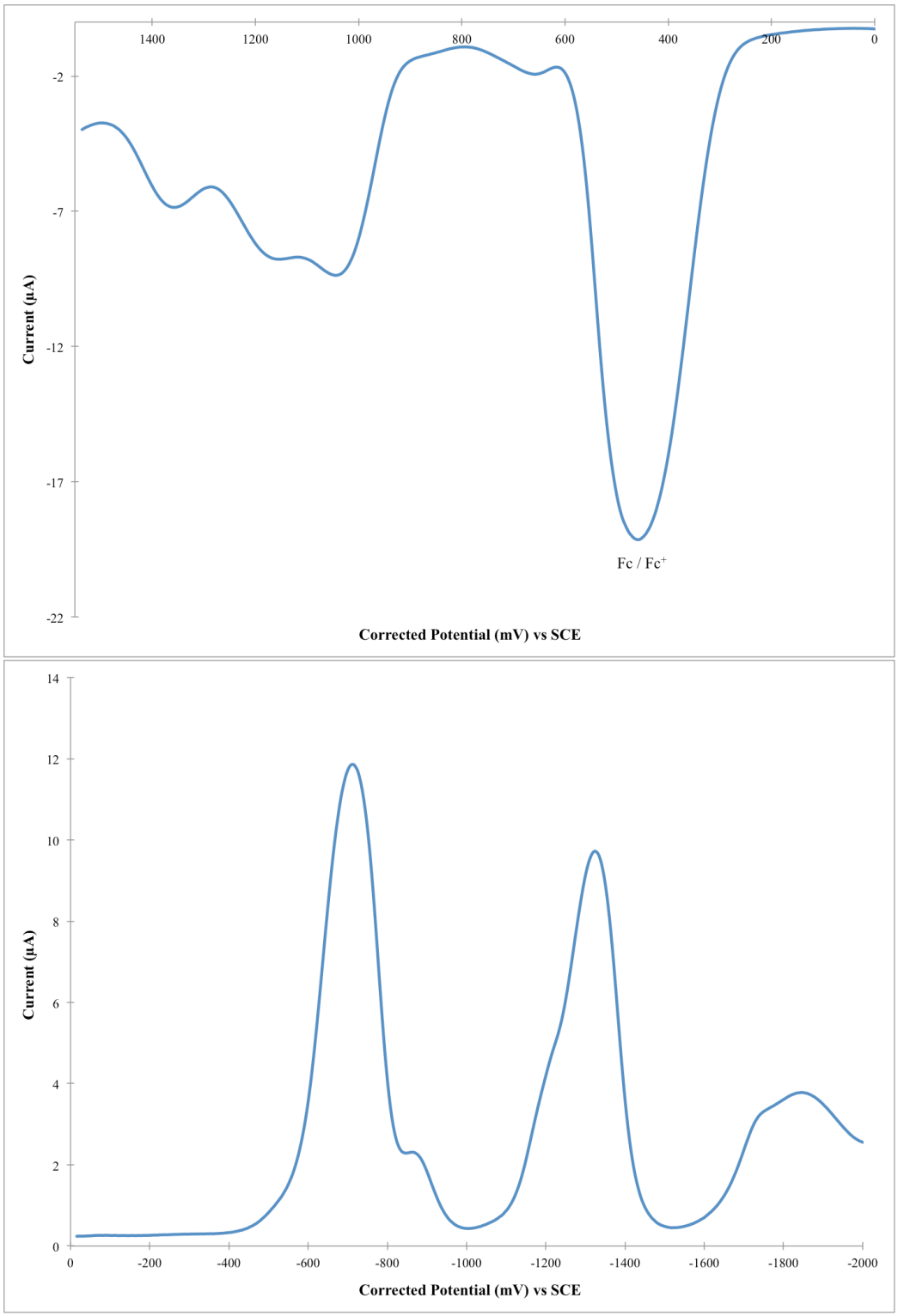

Figure I.S17 – DPV of ADPM **3** with ferrocene as internal reference. (0.46V vs SCE in DCM) (Scan rate of 50 mV/s at R.T.)

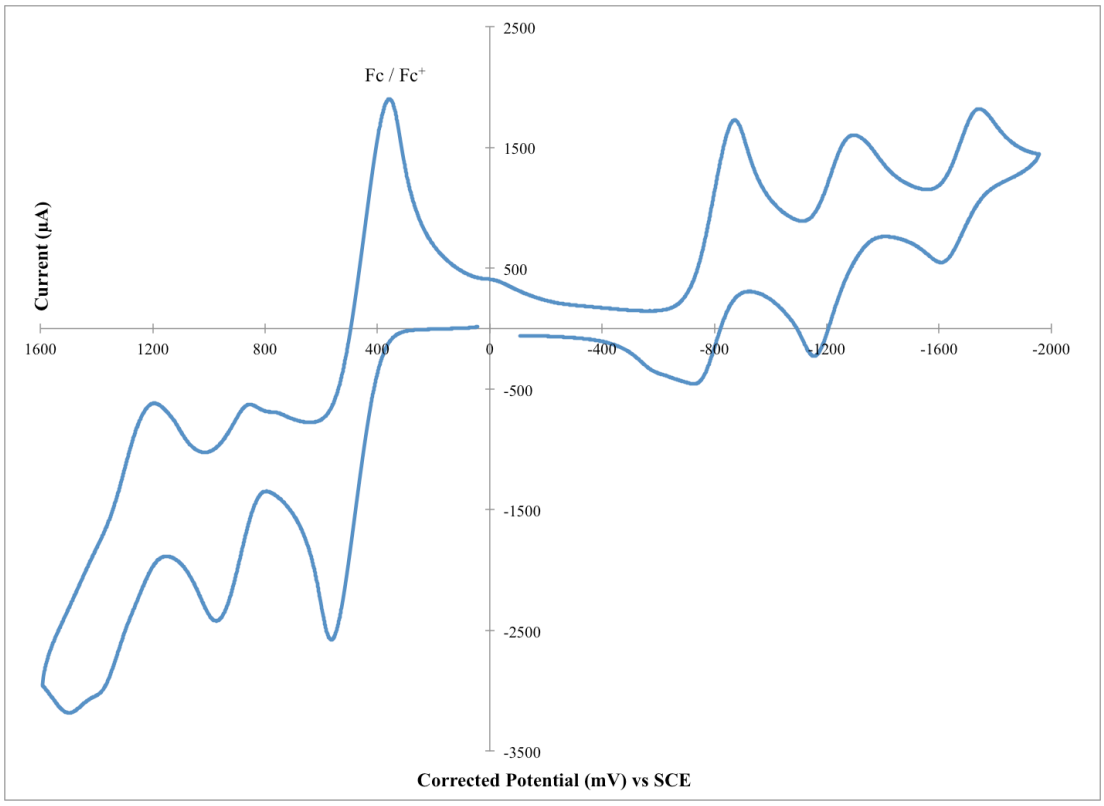

Figure I.S18 – CV of ADPM **4** with ferrocene as internal reference.

(0.46V vs SCE in DCM) (Scan rate of 50 mV/s at R.T.)

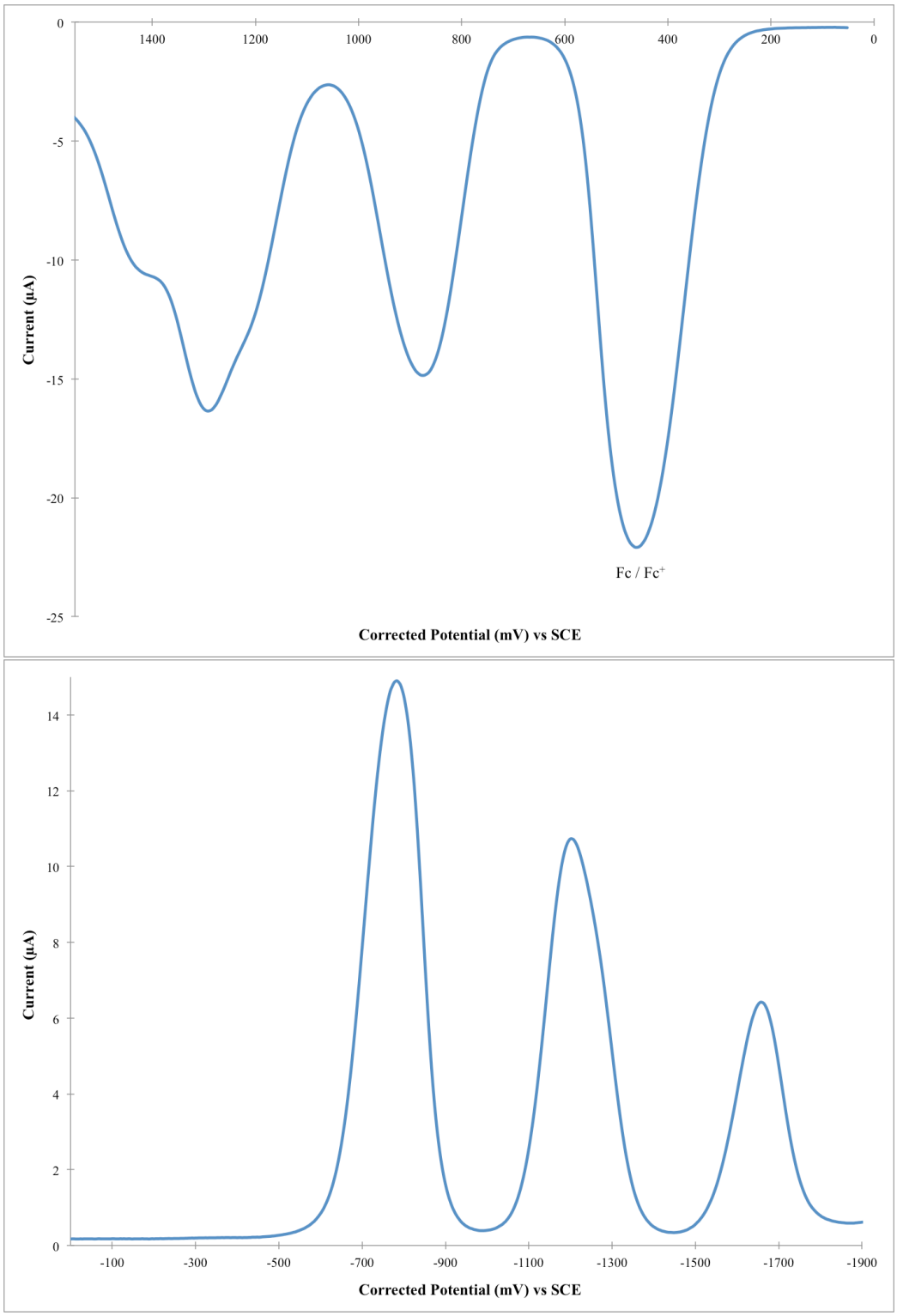

Figure I.S19 – DPV of ADPM **4** with ferrocene as internal reference. (0.46V vs SCE in DCM) (Scan rate of 50 mV/s at R.T.)

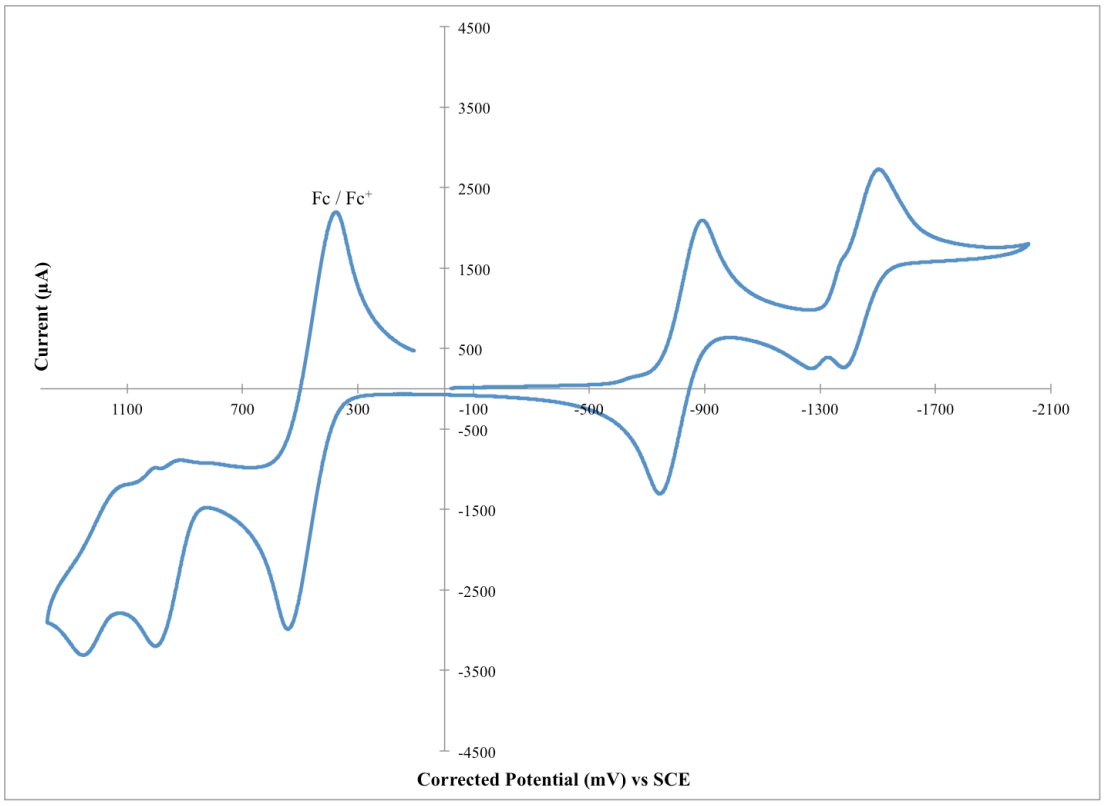

Figure I.S20 – CV of ADPM **5** with ferrocene as internal reference.
(0.46V vs SCE in DCM) (Scan rate of 50 mV/s at R.T.)

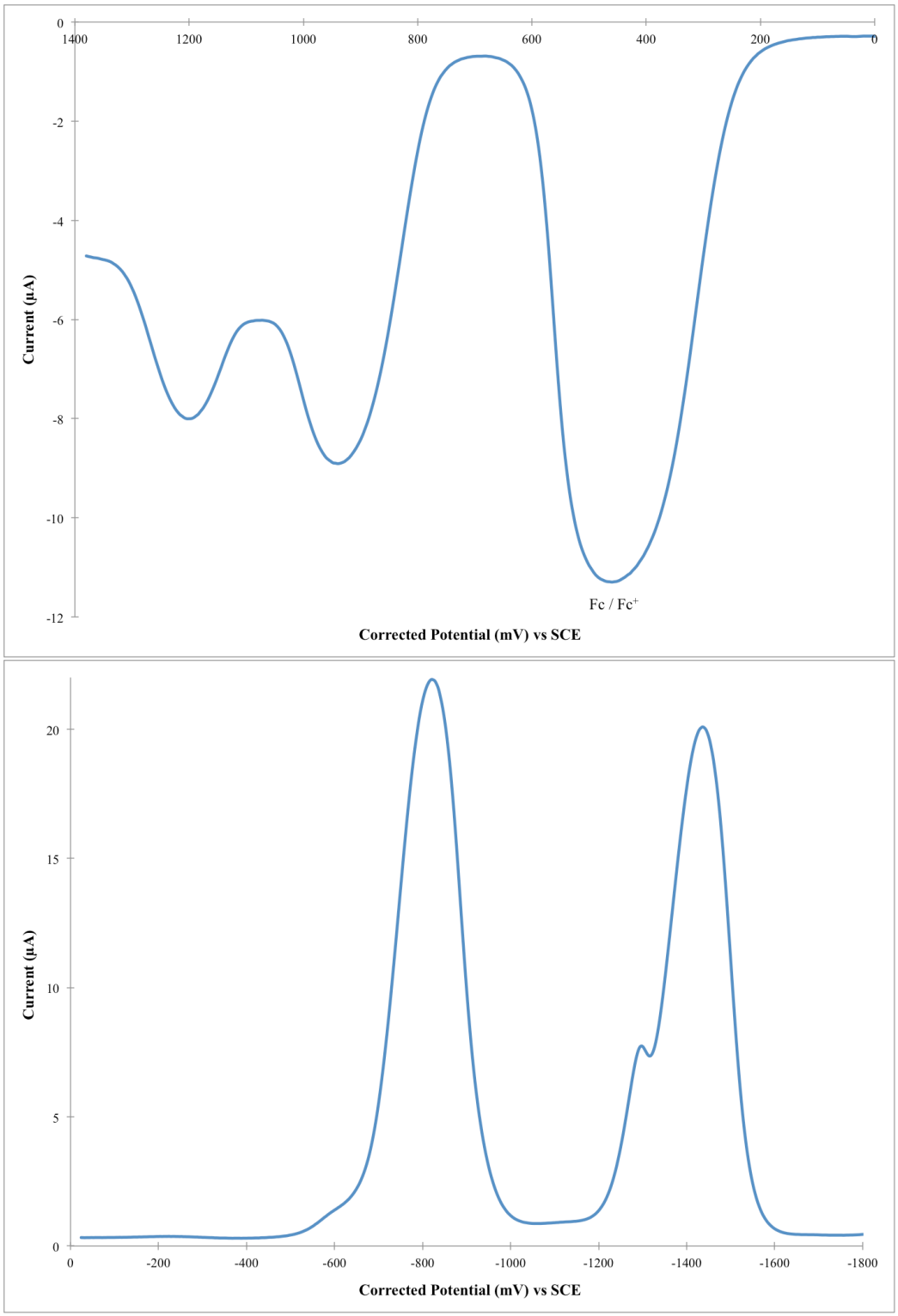

Figure I.S21 – DPV of ADPM **5** with ferrocene as internal reference. (0.46V vs SCE in DCM) (Scan rate of 50 mV/s at R.T.)

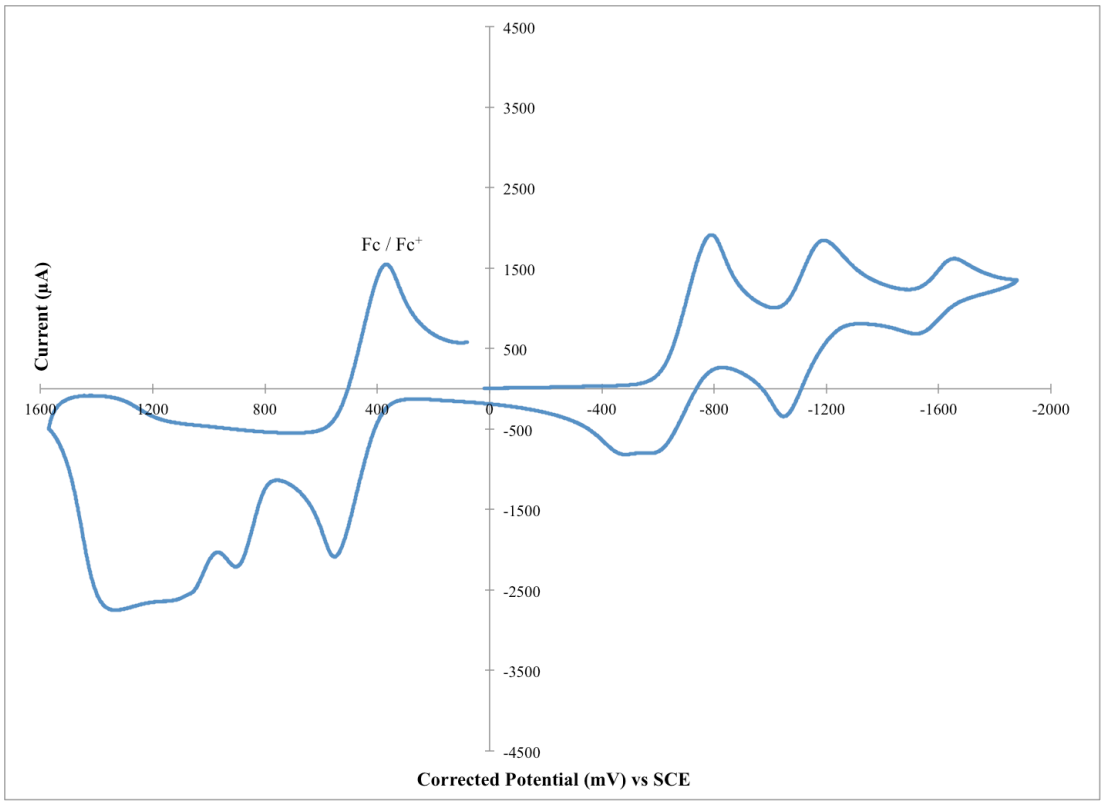

Figure I.S22 – CV of ADPM **6** with ferrocene as internal reference.
(0.46V vs SCE in DCM) (Scan rate of 50 mV/s at R.T.)

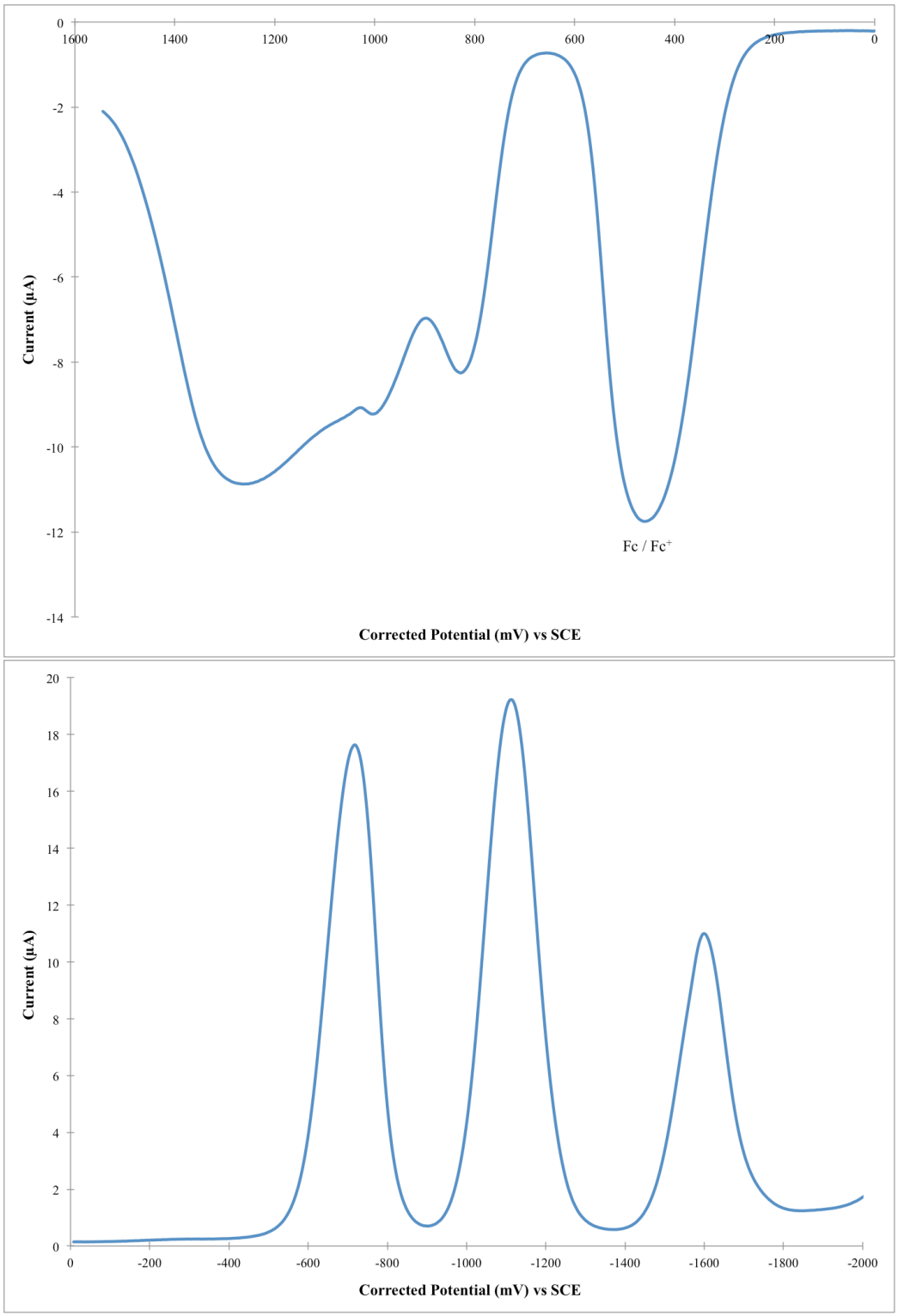

Figure I.S23 – DPV of ADPM **6** with ferrocene as internal reference. (0.46V vs SCE in DCM) (Scan rate of 50 mV/s at R.T.)

Computational Modelization

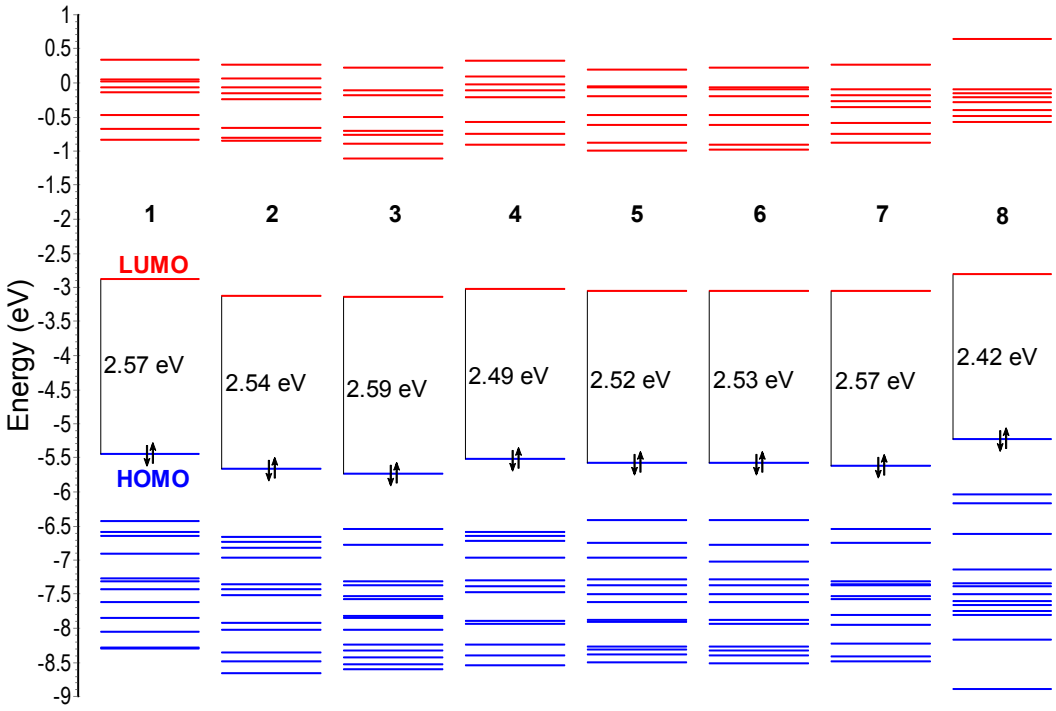

Figure I.S24 – Representation of molecular orbital's energy levels (in eV) of ADPM derivatives **1** – **8** as obtained by DFT computational modelization and the corresponding band gap (occupied orbitals = blue; virtual orbitals = red).

Table I.S1 - Electronic distribution (%) on HOMO and LUMO for ADPM derivatives **1** – **8** as obtained by DFT computational modelization

(r-pbe0 / 6-311g(2d,p); CPCM = CH_2Cl_2). [a), b)]

(Refer to Figure 5 for division of ADPM chromophore in computational modelization analysis)

	Molecular Orbital	**ADPM**	**Proximal Ar_1**	**Proximal Ar_2**	**Distal Ar_1'**	**Distal Ar_2'**
1	HOMO	62	17	11	6	4
	LUMO	66	8	14	6	5
2	HOMO	59	15	16	6	3
	LUMO	65	9	16	6	5
3	HOMO	68	12	8	8	4
	LUMO	70	7	11	7	5
4	HOMO	60	17	14	5	4
	LUMO	66	8	15	6	5
5	HOMO	66	18	7	5	4
	LUMO	67	8	11	4	10
6	HOMO	66	17	8	5	4
	LUMO	67	8	11	4	10
7	HOMO	66	13	9	7	4
	LUMO	63	12	14	6	5
8	HOMO	54	17	12	11	6
	LUMO	61	12	14	6	6

a) Ar1 is the aryl on the pyrrole side of the ADPM.

b) Distal Ar = Ph, otherwise stated. The prime number (#') in subscript corresponds to the distal aryl on the same side as the proximal one.

Table I.S2 - Assignment of optical absorption bands of ADPM **1** in CH_2Cl_2 based on TD-DFT calculations (TD-BMK/6-311+G(2d,p); CPCM = CH_2Cl_2).

λ, nm		**Excitation**	**Assignation**
Observed (ε, x10^3 $M^{-1}cm^{-1}$)	**Calculated** (Osc. Strength)		
605 (47)	553 (0.834)	H -> L (99%)	Prox_1 -> ADPM
407 (6.8)	422 (0.040)	H-1 -> L (94%)	Dist_2 -> ADPM
	368 (0.252)	H-2 (77%), H-3 (16%) -> L	Periphery (except Dist_2) -> ADPM
	356 (0.168)	H-3 (79%), H-2 (16%) -> L	Prox_2 + Dist_1 -> ADPM
	349 (0.005)	H-8 (59%), H-9 (17%), H-6 (14%) -> L	Prox_1 + Dist_2 -> ADPM
299 (34)	320 (0.062)	H-4 -> L (92%)	Prox 1+2 -> Dist 1+2 + ADPM
	305 (0.004)	H-10 (38%), H-12 (32%), H-6 (12%), H-8 (10%) -> L	Dist 1+2 --> Prox 1+2 + ADPM
	297 (0.264)	H -> L+1 (80%)	ADPM + Side 2 --> Side 1
	296 (0.015)	H-5 -> L (78%)	Dist 1+2 --> Prox 1+2 + ADPM
	288 (0.433)	H-7 -> L (72%); H -> L+1 (10%)	Prox_2 --> ADPM

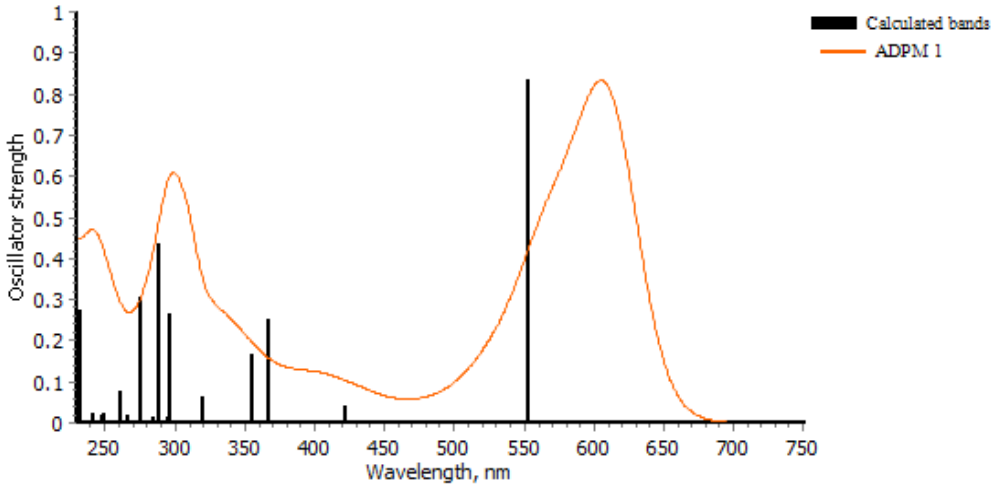

Figure I.S25 – Experimental absorption spectrum in CH_2Cl_2 vs calculated optical absorption bands of ADPM **1** based on TD-DFT calculations (TD-BMK/6-311+G(2d,p); CPCM = CH_2Cl_2).

Table I.S3 - Assignment of optical absorption bands of ADPM **2** in CH_2Cl_2 based on TD-DFT calculations

(TD-BMK/6-311+G(2d,p); CPCM = CH_2Cl_2)

λ, nm		**Excitation**	**Assignation**
Observed (ε, x10^3 $M^{-1}cm^{-1}$)	**Calculated** (Osc. Strength)		
615 (39) and 577 (21)	560 (0.834)	H -> L (99%)	Side 1 -> ADPM
415 (6.0)	413 (0.093)	H-2 (70%), H-1 (22%) -> L	Periphery (except Dist_1) -> ADPM
	378 (0.130)	H-1 (73%), H-2 (17%) -> L	Periphery (except Dist_1) -> ADPM
	368 (0.233)	H-3 -> L (85%)	Side 1 -> ADPM
307 (26)	339 (0.008)	H-9 (53%), H-4 (20%), H-6 (14%) -> L	Periphery (except Prox_2) -> ADPM
	332 (0.092)	H-4 (70%), H-9 (15%) -> L	Prox_1 -> ADPM
	309 (0.003)	H-5 -> L (86%)	Dist 1+2 + Prox_1 -> ADPM + Prox_2
	303 (0.026)	H-7 (58%), H-6 (17%) -> L	Periphery -> ADPM
	297 (0.026)	H-6 (48%), H-7 (24%), H-9 (13%), H-5 (11%) -> L	Periphery -> ADPM
	283 (0.023)	H-12 (34%), H-10 (28%), H-8 (12%) -> L; H -> L+1 (10%)	Periphery -> ADPM

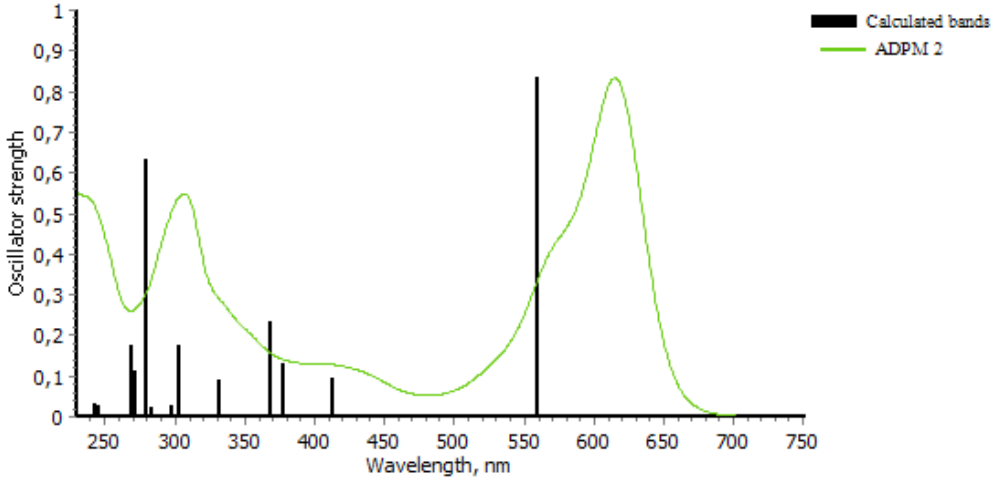

Figure I.S26 – Experimental absorption spectrum in CH_2Cl_2 vs calculated optical absorption bands of ADPM **2** based on TD-DFT calculations (TD-BMK/6-311+G(2d,p); CPCM = CH_2Cl_2).

Table I.S4 - Assignment of optical absorption bands of ADPM **3** in CH_2Cl_2 based on TD-DFT calculations

(TD-BMK/6-311+G(2d,p); CPCM = CH_2Cl_2)

λ, nm			
Observed (ε, x10^3 $M^{-1}cm^{-1}$)	**Calculated** (Osc. Strength)	**Excitation**	**Assignation**
590 (39) and 558 (28)	547 (0.877)	H -> L (99%)	Side 1 -> Side 2 + ADPM
--	441 (0.064)	H-1 -> L (95%)	Dist_2 -> Periphery + ADPM
--	381 (0.164)	H-2 -> L (94%)	Dist_1 -> Periphery + ADPM
307 (30)	357 (0.006)	H-9 (37%), H-7 (20%), H-6 (18%), H-4 (12%) -> L	Periphery -> ADPM
	328 (0.003)	H-6 -> L (56%)	Periphery (except Dist_1) -> ADPM
	311 (0.000)	H-3 -> L (86%)	Dist 1+2 -> ADPM + Prox 1+2
	305 (0.076)	H-5 (35%), H-4 (20%), H-7 (13%) -> L	Periphery -> ADPM
	299 (0.026)	H-4 (34%), H-5 (33%), H-9 (10%) -> L; H -> L+1 (11%)	Periphery (except Prox_1) -> Prox_1 + ADPM
	293 (0.266)	H -> L+1 (37%); H-14 (15%), H-4 (10%) -> L	Periphery (except Prox_1) -> Prox_1 + ADPM
	289 (0.826)	H -> L+1 (37%); H-5 (21%), H-14 (15%) -> L	Periphery (except Prox_1) -> Prox_1 + ADPM

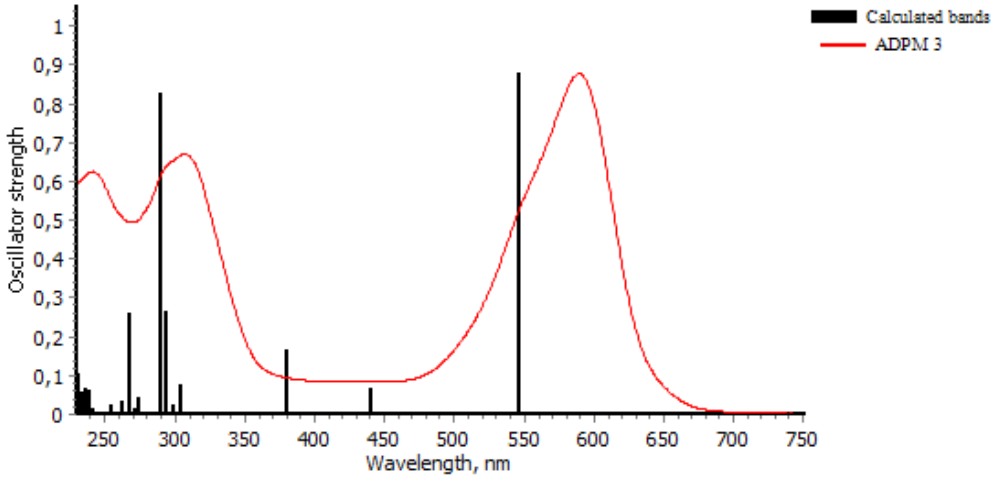

Figure I.S27 – Experimental absorption spectrum in CH_2Cl_2 vs calculated optical absorption bands of ADPM **3** based on TD-DFT calculations (TD-BMK/6-311+G(2d,p); CPCM = CH_2Cl_2)

Table I.S5 - Assignment of optical absorption bands of ADPM **4** in CH_2Cl_2 based on TD-DFT calculations

(TD-BMK/6-311+G(2d,p); CPCM = CH_2Cl_2)

λ, nm		**Excitation**	**Assignation**
Observed (ε, x10^3 $M^{-1}cm^{-1}$)	**Calculated** (Osc. Strength)		
602 (33) and 567 (24)	571 (0.861)	H -> L (99%)	Prox_1 + Prox_2 + Dist_1 -> Dist_2 + ADPM
417 (8.3)	409 (0.070)	H-2 -> L (87%)	Dist 1+2 -> Prox_2 + ADPM
	374 (0.380)	H-1 -> L (88%)	Periphery -> ADPM
	370 (0.019)	H-3 -> L (86%)	Prox_2 + Dist 1+2 -> Prox_1 + ADPM
298 (30)	340 (0.009)	H-9 (64%), H-6 (15%) -> L	Dist 1+2 -> Prox_2 + ADPM
	328 (0.089)	H-4 -> L (84%)	Prox_1 -> Dist_2 + ADPM
	304 (0.002)	H-5 -> L (89%)	Dist 1+2 -> Prox 1+2 + ADPM
	301 (0.024)	H-7 (50%), H-6 (12%) -> L; H -> L+1 (23%)	Prox_2 + Dist 1+2 -> Prox_1 + ADPM
	294 (0.374)	H -> L+1 (48%); H-6 (29%), H-9 (10%) -> L	Prox_2 + Dist 1+2 -> Prox_1 + ADPM
	292 (0.347)	H-7 (32%), H-6 (27%) -> L; H -> L+1 (22%)	Prox_2 + Dist 1+2 -> Prox_1 + ADPM

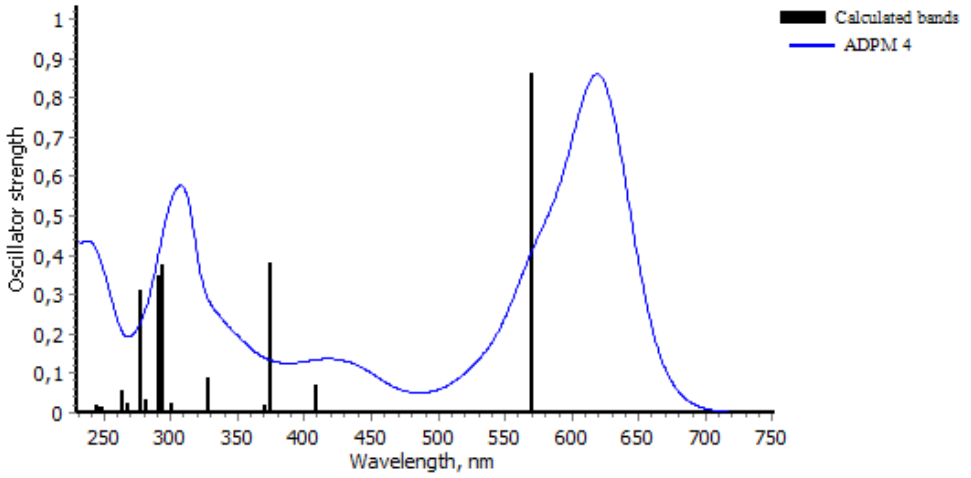

Figure I.S28 – Experimental absorption spectrum in CH_2Cl_2 vs calculated optical absorption bands of ADPM **4** based on TD-DFT calculations (TD-BMK/6-311+G(2d,p); CPCM = CH_2Cl_2)

Table I.S6 - Assignment of optical absorption bands of ADPM **5** in CH_2Cl_2 based on TD-DFT calculations (TD-BMK/6-311+G(2d,p); CPCM = CH_2Cl_2).

λ, nm		**Excitation**	**Assignation**
Observed (ε, x10^3 $M^{-1}cm^{-1}$)	**Calculated** (Osc. Strength)		
619 (52) and 576 (28)	566 (0.830)	H -> L (99%)	Prox_1 -> Prox_2 + Dist_2 + ADPM
417 (3.9)	445 (0.051)	H-1 -> L (96%)	Dist_2 -> Periphery + ADPM
	373 (0.228)	H-2 -> L (89%)	Side 1 -> Side 2 + ADPM
307 (35)	348 (0.021)	H-9 (43%), H-7 (32%) -> L	Prox_2 + Dist 1+2 -> Prox_1 + ADPM
	332 (0.085)	H-3 -> L (87%)	Side 1 -> Side 2 + ADPM
	308 (0.030)	H-7 (26%), H-13 (20%), H-4 (19%), H-5 (11%), H-6 (10%) -> L	Prox_2 + Dist 1+2 -> Prox_1 + ADPM
	306 (0.009)	H-4 -> L (74%)	Dist 1+2 -> Periphery + ADPM
	298 (0.060)	H-6 -> L (58%); H -> L+2 (17%)	Periphery (except Prox_1) -> ADPM
	294 (0.004)	H-5 (57%), H-9 (26%) -> L	Dist_1 + Prox_2 -> Prox_1 + Dist_2 + ADPM
	289 (0.749)	H -> L+1 (41%); H -> L+2 (35%)	ADPM -> Periphery (except Dist_1)

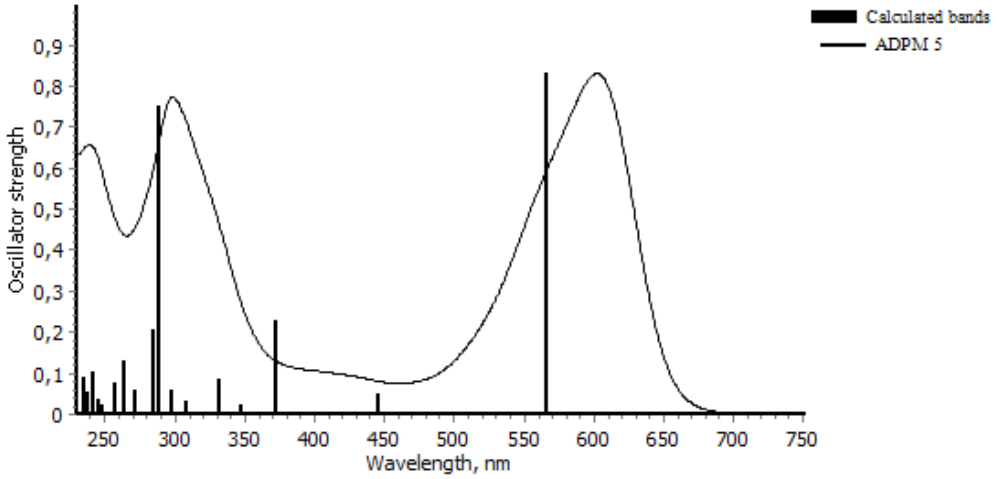

Figure I.S29 – Experimental absorption spectrum in CH_2Cl_2 vs calculated optical absorption bands of ADPM **5** based on TD-DFT calculations (TD-BMK/6-311+G(2d,p); CPCM = CH_2Cl_2).

Table I.S7 - Assignment of optical absorption bands of ADPM **6** in CH_2Cl_2 based on TD-DFT calculations (TD-BMK/6-311+G(2d,p); CPCM = CH_2Cl_2).

λ, nm			
Observed (ε, x10^3 $M^{-1}cm^{-1}$)	**Calculated** (Osc. Strength)	**Excitation**	**Assignation**
598 (43) and 561 (28)	564 (0.850)	H -> L (99%)	Prox_1 -> Side 2 + ADPM
418 (6.9)	446 (0.054)	H-1 -> L (96%)	Dist_2 -> Periphery + ADPM
	371 (0.203)	H-2 -> L (91%)	Side 1 -> Side 2 + ADPM
308 (36)	348 (0.018)	H-9 (45%), H-7 (33%) -> L	Prox_2 + Dist 1+2 -> Prox_1 + ADPM
	325 (0.091)	H-3 -> L (92%)	Prox_1 -> Side 2 + ADPM
	309 (0.034)	H-7 (26%), H-13 (20%), H-4 (15%), H-6 (12%), H-5 (11%) -> L	Prox_2 + Dist 1+2 -> Prox_1 + ADPM
	306 (0.009)	H-4->L (78%)	Dist 1+2 -> Prox 1+2 + ADPM
	299 (0.042)	H-6 -> L (55%); H -> L+2 (20%)	Prox_2 + Dist 1+2 -> Prox_1 + ADPM
	294 (0.003)	H-5 (57%), H-9 (26%) ->L	Dist_1 + Prox_2 -> Prox_1 + Dist_2 + ADPM
	290 (0.736)	H-6 -> L (10%); H -> L+1 (16%); H -> L+2 (53%)	ADPM -> Periphery (exept Prox_2)

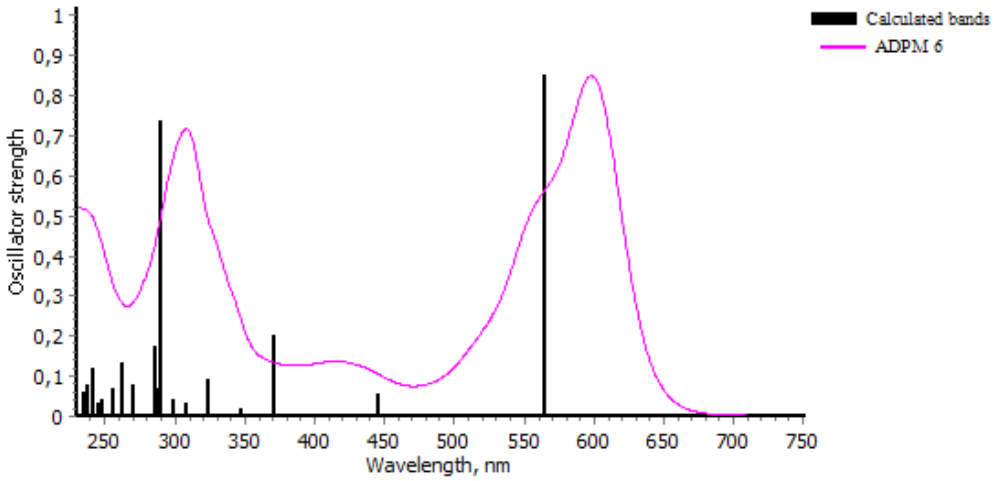

Figure I.S30 – Experimental absorption spectrum in CH_2Cl_2 vs calculated optical absorption bands of ADPM **6** based on TD-DFT calculations (TD-BMK/6-311+G(2d,p); CPCM = CH_2Cl_2).

Table I.S8 - Assignment of optical absorption bands of ADPM **7** in CH_2Cl_2 based on TD-DFT calculations (TD-BMK/6-311+G(2d,p); CPCM = CH_2Cl_2).

λ, nm		**Excitation**	**Assignation**
Observed (ε, x10^3 $M^{-1}cm^{-1}$)	**Calculated** (Osc. Strength)		
590 (40)	551 (0.885)	H -> L (99%)	Side 1 -> Side 2 + ADPM
--	428 (0.059)	H-1 -> L (96%)	Dist_2 -> Periphery + ADPM
--	372 (0.190)	H-2 -> L (97%)	Dist_1 -> Side 2 + ADPM
297 (43)	346 (0.003)	H-9 (61%), H-5 (16%), H-8 (13%) -> L	Prox_1 + Dist 1+2 -> Prox_2 + ADPM
	311 (0.261)	H-4 -> L (66%)	Periphery -> ADPM
	305 (0.000)	H-3 -> L (80%)	Dist 1+2 -> Prox 1+2 + ADPM
	299 (0.084)	H-5 (24%), H-12 (21%), H-4 (19%), H-10 (10%) -> L	Prox_2 + Dist 1+2 -> Prox_1 + ADPM
	293 (0.023)	H-6 (68%), H-5 (16%) ->L	Prox_2 + Dist 1+2 -> Prox_1 + ADPM
	291 (0.017)	H-5 (27%), H-10 (21%), H-12 (20%), H-6 (13%) -> L	Prox_2 + Dist 1+2 -> Prox_1 + ADPM
	286 (0.714)	H -> L+1 (79%)	ADPM + Side 2 -> Side 1

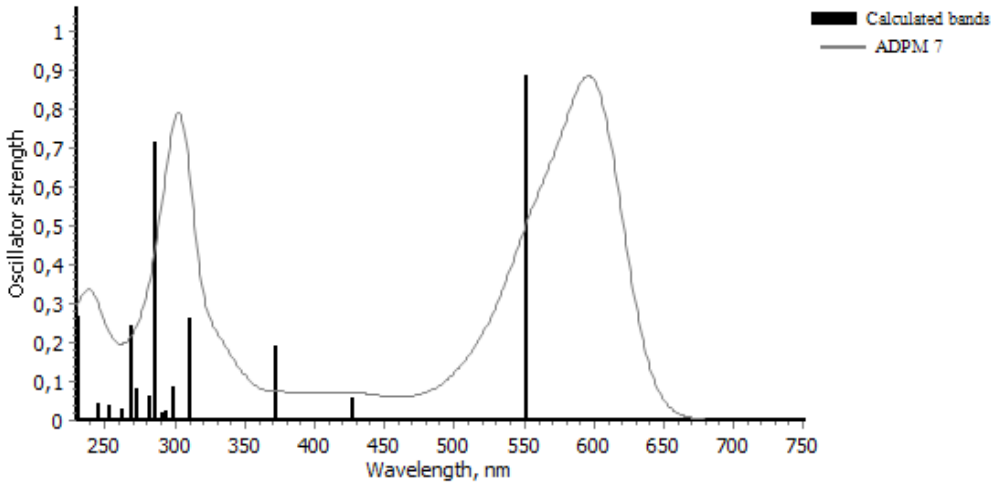

Figure I.S31 – Experimental absorption spectrum in CH_2Cl_2 vs calculated optical absorption bands of ADPM **7** based on TD-DFT calculations (TD-BMK/6-311+G(2d,p); CPCM = CH_2Cl_2).

Table I.S9 - Assignment of optical absorption bands of ADPM **8** in CH_2Cl_2 based on TD-DFT calculations

(TD-BMK/6-311+G(2d,p); CPCM = CH_2Cl_2)

λ, nm		**Excitation**	**Assignation**
Observed (ε, x10^3 $M^{-1}cm^{-1}$)	**Calculated** (Osc. Strength)		
627 (52)	587 (0.889)	H -> L (99%)	Periphery -> Dist_2 + ADPM
414 (10)	452 (0.147)	H-1 -> L (93%)	Dist_2 -> Periphery + ADPM
	400 (0.283)	H-2 -> L (96%)	Side 1 -> Side 2 + ADPM
322 (40)	345 (0.505)	H-3 -> L (88%)	Prox 1+2 -> Dist 1+2 + ADPM
	337 (0.022)	H-11 (51%), H-10 (16%), H-6 (14%) -> L	Dist 1+2 -> Prox 1+2 + ADPM
	303 (0.050)	H-4 -> L (66%)	Periphery -> Dist_1 + ADPM
	292 (0.098)	H-12 -> L (47%); H -> L+1 (15%)	Periphery -> Prox_1 + ADPM
	290 (0.450)	H -> L+1 (67%); H-5 -> L (16%)	ADPM + Periphery -> Prox_1
	287 (0.063)	H-5 (64%), H-6 (10%) -> L (47%); H -> L+1 (10%)	Dist 1+2 -> Prox 1+2 + ADPM
	283 (0.169)	H -> L+2 (42%); H-7 -> L (30%)	Periphery -> Dist_2 + ADPM

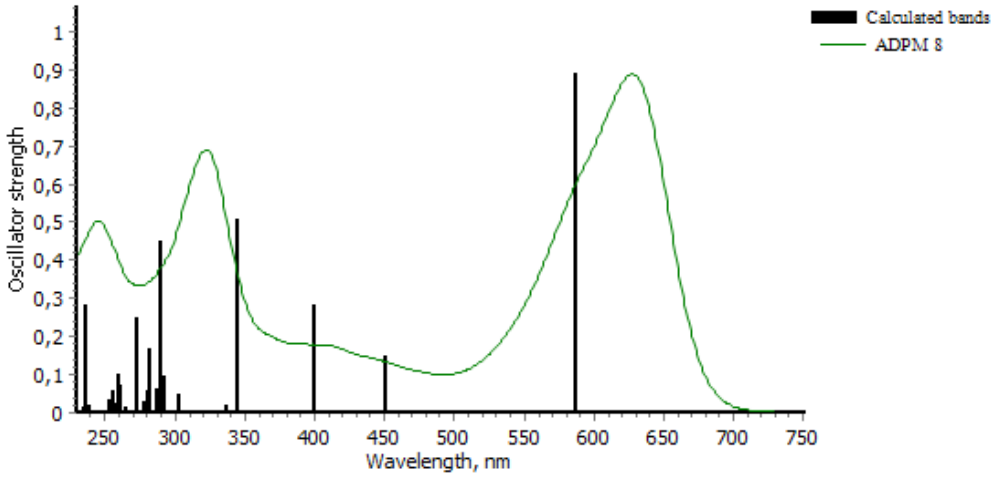

Figure I.S32 – Experimental absorption spectrum in CH_2Cl_2 vs calculated optical absorption bands of ADPM **8** based on TD-DFT calculations (TD-BMK/6-311+G(2d,p); CPCM = CH_2Cl_2)

X-ray diffraction measurements and structure determination

Crystallographic data for **3** and **5** were collected at 150 K, from single crystal samples, which were mounted on a loop fiber. Data were collected using a Bruker Microstar diffractometer equipped with a Platinum 135 CCD Detector, a Helios optics and a Kappa goniometer. The crystal-to-detector distance was 3.8 cm, and the data collection was carried out in 512 x 512 pixel mode. The initial unit cell parameters were determined by a least-squares fit of the angular setting of strong reflections, collected by a 110.0 degree scan in 110 frames over three different parts of the reciprocal space. Crystallographic data for **1** and **4** were collected at 100 K, using a Bruker smart diffractometer equipped with an APEX II CCD Detector, a Incoatec IMuS source and a Quazar MX mirror. The crystal-to-detector distance was 4.0 cm, and the data collection was carried out in 512 x 512 pixel mode. The initial unit cell parameters were determined by a least-squares fit of the angular setting of strong reflections, collected by a 180.0 degree scan in 180 frames over three different parts of the reciprocal space. For determination of cell parameters, cell refinement and data reduction APEX2 was used.[1] Absorption corrections were applied using SADABS.[2] Structure solution was performed using direct methods with SHELXS97 and refined on F^2 by full-matrix least squares using SHELXL97.[3]

For **1**, **4** and **5**, all non-H atoms were refined by full-matrix least-squares with anisotropic displacement parameters. The H-atoms were included in calculated positions and treated as riding atoms: aromatic C—H 0.95 Å, methyl C—H 0.98 Å, with $U_{iso}(H)$ =

$k \times U_{eq}$ (parent C-atom), where k = 1.2 for the aromatic H-atoms and 1.5 for the methyl H-atoms. The H-atoms connected to heteroatoms (N and O) were in all cases located from the difference Fourier map. For **1** and **5**, they were freely refined. For **4**, in order to better model the disorder, the H-atoms on N and O atoms were refined using the riding model, with appropriate thermal displacement coefficient: $U_{iso}(H) = 1.2 \times U_{eq}$(heteroatom).

The structure of the compound **3** was obtained from the best available crystal, which unfortunately was very poor quality, resulting in poor data quality. In addition, the whole molecule presents a very high degree of disorder. Therefore, only the isotropic refinement of the atoms was possible. All the H-atoms were located using the riding model. Under these circumstances, only the connectivity of the atoms can be discussed in this structure. The position of the pyridyl groups can be either *endo*- or *exo*-, but a final conclusion can't be derived from the analysis due to a so highly disordered model. The identity of the compound was confirmed by mass spectrometry performed on the same crystal sample (see experimental section).

For compound **4**, a very good data set was obtained, but nevertheless high residual electron density peaks were located during the refinement. They were considered to be highly disordered solvent molecules. All the attempts to model the solvent molecules were unsuccessful, and they were removed using the SQUEEZE routine from PLATON.[4] As a result, an improvement of the R_1 factor with ~ 2.3% was obtained. Solvent accessible voids of 56 $Å^3$ were found, containing 12 electrons. Water didn't fit. The structure of **4** contains 4 molecules in the asymmetric unit, and two of these display disorder at the level of the ADPM moiety and of the proximal phenyl

groups, over two positions. The disorder was modelled as two components using PART instructions. The occupation factor was first refined, and then fixed at the values obtained after refinement [0.63:0.37]. The model was refined anisotropically. SIMU restraints were used.

The following software were used to prepare material for publication: PLATON, UdMX and Mercury.[4, 5, 6]. Figures were generated using ORTEP3 and POV-Ray.[7,8] Data were deposited in CCDC under the deposit numbers: CCDC 1005388-1005391.[9] The alerts given by the checkCIF/ PLATON routine are commented in the crystallographic information files (cifs) of the corresponding compounds.

Table I.S10 - Solid-state structure and refinement data for compounds **1**, **3**, **4** and **5**.

		1	**3**[a]	**4**[b]	**5**
Formula		$C_{34}H_{27}N_3O_2$	$C_{30}H_{21}N_5$	$C_{33}H_{25}N_3O_2$	$C_{32}H_{24}N_4O$
M_w(g/mol)		509.58	451.52	495.56	480.55
T (K)		100	150	100	100
Wavelength (Å)		1.54178	1.54178	1.54178	1.54178
Crystal System		Monoclinic	Monoclinic	Monoclinic	Monoclinic
Space Group		$P2_1/n$	$P2_1$	Pc	$P2_1/c$
Unit Cell:	a (Å)	14.2562(1)	5.6755(2)	20.1555(2)	11.3385(6)
	b (Å)	14.1356(1)	11.9628(4)	9.6757(1)	13.9762(7)
	c (Å)	14.3787(1)	16.5633(6)	25.4600(3)	15.3735(8)
	α (°)	90	90	90	90
	β (°)	117.825(1)	91.632(2)	100.668(1)	97.732(2)
	γ (°)	90	90	90	90
	V (Å^3)	2562.57(3)	1124.11(7)	4879.35(9)	2414.1(2)
Z		4	2	8	4
$d_{calcd.}$ (g/cm^3)		1.321	1.334	1.349	1.322
μ (mm^{-1})		0.656	0.636	0.674	0.644
F(000)		1072	472	2080	1008
θ range (°)		3.61 to 71.04	2.67 to 69.58	2.23 to 71.12	3.93 to 69.67
Reflections collected		100228	22472	94028	64766
Independent reflections		4923	4153	18292	4534
GoF		1.057	1.034	1.034	1.019
R1(F); wR(F^2) [I > 2σ(I)]		0.0360; 0.0883	0.1790; 0.3067	0.0461; 0.1183	0.0360; 0.0955
R1(F); wR(F^2) (all data)		0.0362; 0.0884	0.1853; 0.3091	0.0531; 0.1241	0.0390; 0.0984
Largest diff. peak and hole (e/Å^3)		0.256 and 0.154	1.400 and 0.653	0.306 and -0.232	0.212 and -0.191

[a] only isotropic refinement of the structure was possible due to a whole molecule disorder situation and poor quality of the crystal; we only aim to highlight the connectivity of the atoms in this structure.
[b] the SQUEEZE routine from PLATON was applied in the case of this structure (see text).

Table I.S11 - Selected bond lengths (Å) and angles (°) for compounds **1**, **4** and **5**.

	1	**4**[a]	**5**
Bond length (Å)/ Angle (°)			
N1-C1	1.380(1)	1.392(8)[a]	1.384(1)
C1-N2	1.339(1)	1.332(8)[a]	1.342(1)
N2-C17	1.317(2)	1.320(7)[a]	1.318(2)
C17-N3	1.390(1)	1.400(7)[a]	1.391(2)
N1-C1-N2	125.6(1)	129.6(7)[a]	126.4(1)
C1-N2-C17	124.2(1)	129.2(7)[a]	123.0(1)
N2-C17-N3	126.6(1)	128.3(7)[a]	125.0(1)
Tilt angles (°) between the planes of the two central pyrrolic rings			
	10.9(1)	8.0(1)[b]	9.8(1)
Tilt angles (°) between ADPM moiety and the aryl rings[c]			
Ar_1 (proximal)	13.6(1)	1.2(1) - 2.4(1)[b]	17.5(1)
Ar_2 (distal)	9.5(1)	28.7(1) - 38.1(1)[b]	35.7(1)
Ar_3 (distal)	45.3(1)	24.8(1) - 38.2(1)[b]	27.5(1)
Ar_4 (proximal)	26.4(1)	1.2(1) - 4.2(1)[b]	19.8(1)

[a] average values on the four molecules in the asymmetric unit; the error was calculated using the formula for propagation of error in calculations.
[b] values are shown as range for the four molecules in the asymmetric unit.
[c] see Figure 1 in the article for the numbering of the aryl rings.

Table I.S12 - Intramolecular H-bonding for compounds **1**, **4** and **5**.

Distances are in Å and angles in degree (°)

3-center bifurcated H-bonds are displayed in *italic*.

D*—H···*A	***D*—H**	**H···*A***	***D*···*A***	***D*—H···*A***
1				
N1—H1···N3	*0.88(1)*	*2.16(1)*	*2.76(1)*	*125(1)*
N1—H1···O1	*0.88(1)*	*2.12(1)*	*2.64(1)*	*117(1)*
C10—H10···N2	0.95(1)	2.31(1)	2.99(1)	129(1)
C19—H19···O2	0.95(1)	2.41(1)	2.87(1)	109(1)
C32—H32···N3	0.95(1)	2.46(1)	2.80(1)	101(1)
4 (values are shown for one of the 4 molecules in the asymmetric unit; similar intramolecular H-bonding pattern is observed for the other three molecules)				
N1—H1A···O1	*0.86(1)*	*2.20(1)*	*2.73(1)*	*120(1)*
N1—H1···N3	*0.86(1)*	*2.59(1)*	*3.06(1)*	*116(1)*
O2—H2B···N3	0.82(1)	1.88(1)	2.60(1)	146(1)
C6—H6···N2	0.93(1)	2.53(1)	3.05(1)	116(1)
C26—H26···N2	0.93(1)	2.46(1)	3.03(1)	119(1)
5				
N1—H1···N3	*0.88(1)*	*2.19(1)*	*2.70(1)*	*124(1)*
N1—H1···O1	*0.88(1)*	*2.15(1)*	*2.65(1)*	*116(1)*
C6—H6···N2	0.95(1)	2.62(1)	3.10 (1)	112(1)
C22—H22···N2	0.95(1)	2.48(1)	3.05(1)	118(1)

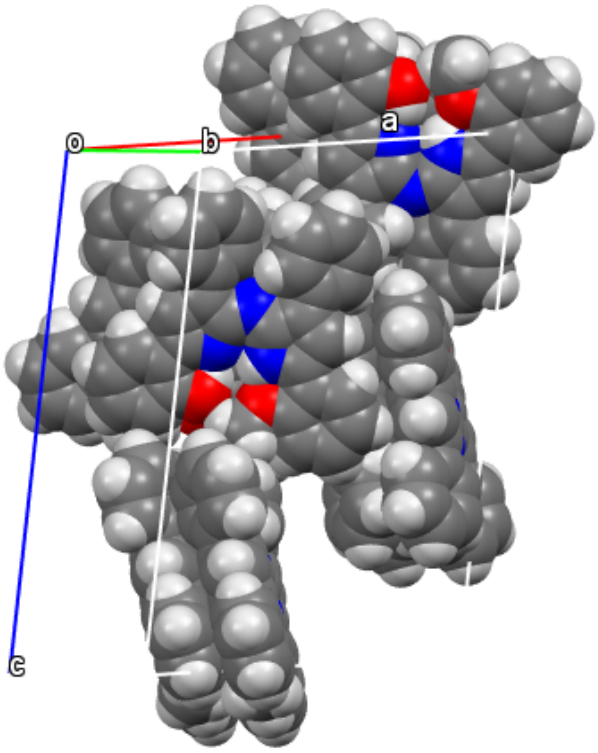

Figure I.S33 – Packing diagram for compound **4**

(space-filling model showing the π – π and π – H-C(sp^2) intermolecular interactions)

References

1. Madison, WI 53719-1173, 2009-2011.
2. Sheldrick, G. M. 1996.
3. Madison, WI 53719-1173., 2001.
4. Spek, A. L. 2003.
5. Maris, T. 2004-2013.
6. CCDC 2001-2012.
7. Farrugia, L. J. *J. Appl. Crystallogr.* **1997**, *30*, 565.
8. POV-Ray; Persistence of Vision Pty. Ltd., retrieved from http://www.povray.org/download/: 2004.
9. CCDC 1005388-1005391 contains the supplementary crystallographic data for this paper. These data can be obtained free of charge via http://www.ccdc.cam.ac.uk/data_request/cif, or by emailing data_request@ccdc.cam.ac.uk, or by contacting The Cambridge Crystallographic Data Centre, 12, Union Road, Cambridge CB2 1EZ, UK; fax: +44 1223 336033.

Annexe II : Informations supplémentaires du Chapitre 3

" Non-symmetric benzo[b]-fused BODIPYs as a versatile fluorophore platform reaching the NIR: A systematic study of the underlying structure–property relationship "

Accepté avec révisions mineures le 29 novembre 2015 par *Dalton Transactions*
Identification du manuscrit : DT-ART-11-2015-004444

Materials and Instrumentation

Asymmetric benzo[b]-fused BODIPYs (BbF) **1** – **10** were obtained by adaptation of the synthetic procedure first reported by Wakamiya *et al.* for a similar derivative.[1] The synthesis of aryl-pyrrole derivatives **11** – **20** was done by palladium-catalyzed cross-coupling of pyrrole anions with aryl halides following an adapted procedure from Sadighi *et al*.[2, 3] and all characterizations matched previously reported literature for compounds **11** – **18**.[2, 4-6] The compound (1*H*-indol-2-yl)(phenyl)methanone **21** was synthetized following the procedure from Zhang *et al*.[7] Reagents and solvents were obtained commercially and used without further purification. Reactions were carried out under ambient atmosphere unless otherwise stated. Solvents were removed under reduced pressure using a rotary evaporator unless otherwise stated.

Nuclear magnetic resonance (NMR) spectra were recorded in $CDCl_3$ at room temperature (r.t.). 300 MHz ^{1}H and 75 MHz ^{13}C NMR of BbF **1** – **4** and **7** – **10** along with aryl-pyrrole **19** and **20** were recorded on a Bruker Avance 300 spectrometer. 400 MHz ^{1}H and 100 MHz ^{13}C NMR of BbF **5** and **6** were recorded on a Bruker Avance 400 spectrometer. Chemical shifts are reported in part per million (ppm) relative to residual solvent protons (7.27 ppm) and carbon resonance (77.00 ppm) of the solvent.

High-Resolution Electro Spray Ionization Mass Spectrometry (HR-ESIMS) was performed on a Bruker micrOTOF II for BbF **1** – **10**. Low resolution Electronic Ionization (EI) mass spectrometry for compounds **19** and **20** was performed on a Agilent 6890 Series GC equipped with a 5973 Network Mass Selective Detector module.

Absorption spectra were measured in CH_2Cl_2 (DCM) at concentrations obeying Beer-Lambert's law at r.t. on a Cary 6000i UV-vis-NIR Spectrophotometer. Luminescence measurements were done on a Perkin LS 55 Fluorescence Spectrometer.

Full details on crystal structure determination and refinement data for compounds **1**, **5**, **8** and **9** are reported in corresponding section and on the Cambridge Crystallographic Data Centre (CCDC numbers 1418610 – 1418613).

Electrochemical measurements were carried out in argon-purged CH_2Cl_2 at room temperature with a BAS CV50W multipurpose potentiostat. The working electrode used was a glassy carbon electrode for every compound. The counter electrode was a Pt wire, and the pseudo-reference electrode was a silver wire. The reference was set using an internal 1 mM ferrocene/ferrocenium sample at 0.46 V vs SCE in CH_2Cl_2.[8] The concentration of the compounds was about 1 mM. Tetrabutylammonium hexafluorophosphate (TBAP) was used as supporting electrolyte and its concentration was 0.10 M. Cyclic voltammograms (CV) were obtained at scan rates of 50, 100, 200, and 500 mV/s. For reversible processes, half-wave potentials (vs. SCE) from CV were used. To establish the potential of irreversible processes, differential pulse voltammetry (DPV) experiments were performed with a step rate of 4 mV, a pulse height of 50 mV, and a frequency of 5 Hz. Criteria for reversibility were the separation of 60 mV between cathodic and anodic peaks, the close to unity ratio of the intensities of the cathodic and anodic currents, and the constancy of the peak potential on changing scan rate.

Experimental uncertainties are as follows: absorption maxima, ±2 nm; molar absorption coefficient, 10%; redox potentials, ± 10 mV.

Computational Methods

Computational modelization of BbF **1** – **10** was achieved following the general procedure depicted by Jacquemin and coworkers for Aza-BODIPYs.[9] All calculations were performed with the Gaussian 09 software (G09).[10] Crystallographic coordinates of **1** were used as starting points for construction of the various derivatives before geometry optimizations. Geometry optimizations, frequency calculations and molecular orbital (MO) calculations were performed by DFT method using the PBE0[11-13] / 6-311G(2d,p) basis set using the Polarization Continuum Model (PCM)[14] of dichloromethane. Tight convergence criteria and no symmetry constraints were imposed during the optimization process. Only positive frequencies were found for the optimized structures. The 40 firsts absorption bands were calculated by TD-DFT using the BMK[15] / 6-311+G(2d,p) level of theory with the PCM of dichloromethane. MOs were visualized (isovalue = 0.02) with GaussView 3 software.[16] GaussSum 3.0 was employed to extract from TD-DFT results the absorption energies and oscillator strengths, while molecular orbital energies were obtained from DFT.[17] Chemissian 4.23 program was used to represent MO's energy levels (Figure S.62) and determine the electronic distribution (in %) of the various parts of the fluorophores from DFT results and calculate the natural transition orbitals (NTO) (isovalue = 0.02) associated with absorption bands in the visible (> 400 nm) range obtained from TD-DFT results.[18]

Synthetic Methods

General procedure for asymmetric benzo[b]-fused BODIPYs **1** – **7**, **9** and **10**.

(1*H*-indol-2-yl)(phenyl)methanone **21** (1 equiv.) and the corresponding aryl-pyrrole (1 equiv.) were dissolved in CH_2Cl_2 under magnetic stirring. The reaction mixture was cooled to 0°C under an inert atmosphere and phosphoryl chloride ($POCl_3$; 2.1 equiv.) was added dropwise. After 0.5 hours, the cooling bath was removed and the reaction stirred at r.t. overnight. Water was added and the organic phase washed, dried over anhydrous MgSO4 and the solvent removed under reduced pressure. The crude intermediate obtained was dried *in vacuo* at 45°C overnight. A portion of the solid was than dissolved in dry CH_2Cl_2 in a flamed dried flask, triethylamine (TEA; 6.5 equiv.) was added under inert atmosphere, followed by boron trifluoride diethyl etherate **(**$BF_3{\cdot}OEt_2$; 9 equiv.), and the reaction mixture was stirred at r.t. for 4 hours or upon completion by TLC analysis. Water was added and the organic phase washed, dried over anhydrous MgSO4 and the solvent removed under reduced pressure. Purification by silica gel chromatography, isolation by solvent evaporation and *in vacuo* drying afforded the entitled product as a deeply coloured solid.

BbF **1** (Ar_{Prox} = Ph)

21 (886 mg; 4.00 mmol), 2-phenyl-1*H*-pyrrole **11** (573 mg; 4.00 mmol) and $POCl_3$ (0.79 mL; 8.41 mmol) in 25 mL of CH_2Cl_2. 1.56 g of a dark red solid was recovered as the crude intermediate; 96 mg used for next step with TEA (0.25 mL; 1.80 mmol) and $BF_3 \cdot OEt_2$ (0.31 mL; 2.49 mmol) in 5 mL of dry CH_2Cl_2. Yield = 28.4 mg of dark red powder (29 % over 2 steps). Dark red needles suitable for X-ray structural analysis crystallized from slow diffusion of heptane in a concentrated $CDCl_3$ solution. ^{1}H NMR ($CDCl_3$, 400 MHz) δ/ppm: 8.15 - 8.09 (m, 2 H), 7.81 (d, *J* = 8.6 Hz, 1 H), 7.69 - 7.51 (m, 9 H), 7.34 (m, 1 H), 7.14 (d, *J* = 4.6 Hz, 1 H), 7.09 - 7.00 (m, 2 H), 6.89 (d, *J* = 4.6 Hz, 1 H). ^{13}C NMR ($CDCl_3$, 100 MHz) δ/ppm: 164.5, 147.5, 146.3, 140.6, 136.9, 134.6, 134.16, 131.4, 131.0, 130.9, 130.5, 129.9, 129.9, 129.6, 128.5, 128.4, 124.4, 123.4, 122.3, 121.8, 115.7. Mass Spec (*m/z*); HRMS calcd for $C_{25}H_{17}BF_2N_2$: [$(M + Na)^+$] 417.1349, found: 417.1347 (-0.48 ppm).

BbF **2** (Ar_{Prox} = *p*-Me-Ph)

21 (1.23 g; 5.55 mmol), 2-(*p*-tolyl)-1*H*-pyrrole **12** (873 mg; 5.55 mmol) and $POCl_3$ (0.79 mL; 8.41 mmol) in 50 mL of CH_2Cl_2. 2.70 g of a dark red solid was recovered as the crude intermediate; 200 mg used for next step with TEA (0.50 mL; 3.61 mmol) and $BF_3 \cdot OEt_2$ (0.62 mL; 4.99 mmol) in 10 mL of dry CH_2Cl_2. Yield = 79.6 mg of dark purple crystals (47 % over 2 steps). ^{1}H NMR ($CDCl_3$, 400 MHz) δ/ppm: 8.05 (d, *J* = 8.3 Hz, 2 H), 7.84 (d, *J* = 8.6 Hz, 1 H), 7.67 - 7.50 (m, 6 H), 7.41 - 7.31 (m, 3 H), 7.11 (d, *J* = 4.6 Hz, 1 H), 7.08 - 7.00 (m, 2 H), 6.89 (d, *J* = 4.6 Hz, 1 H), 2.48 (s, 3 H). ^{13}C NMR ($CDCl_3$, 100 MHz) δ/ppm: 164.7, 147.2, 145.4, 141.9, 140.8, 136.9, 134.7, 134.2,

130.9, 130.4, 130.1, 130.0, 129.9, 129.4, 129.3, 128.5, 128.3, 124.5, 123.2, 121.6, 115.6, 21.7. Mass Spec (*m/z*); HRMS calcd for $C_{26}H_{19}BF_2N_2$: [(M + Na)$^+$] 431.1506, found: 431.1502 (-0.93 ppm).

BbF **3** (Ar_{Prox} = *p*-^{i}Pr-Ph)

21 (896 mg; 4.05 mmol), 2-(4-isopropylphenyl)-1*H*-pyrrole **13** (750 mg; 4.05 mmol) and $POCl_3$ (0.80 mL; 8.50 mmol) in 50 mL of CH_2Cl_2. 1.75 g of a dark red solid was recovered as the crude intermediate; 200 mg used for next step with TEA (0.47 mL; 3.35 mmol) and $BF_3{\cdot}OEt_2$ (0.57 mL; 4.63 mmol) in 10 mL of dry CH_2Cl_2. Yield = 136 mg of gold-red powder (67 % over 2 steps). ^{1}H NMR ($CDCl_3$, 400 MHz) δ/ppm: 8.13 - 8.07 (m, 2 H), 7.84 (d, *J* = 8.6 Hz, 1 H), 7.67 - 7.51 (m, 6 H), 7.43 (d, *J* = 8.3 Hz, 2 H), 7.34 (m, 1 H), 7.12 (d, *J* = 4.6 Hz, 1 H), 7.08 - 7.00 (m, 2 H), 6.91 (d, *J* = 4.6 Hz, 1 H), 3.03 (quin, *J* = 6.9 Hz, 1 H), 1.34 (d, *J* = 6.9 Hz, 6 H). ^{13}C NMR ($CDCl_3$, 100 MHz) δ/ppm: 164.8, 152.5, 147.2, 145.3, 140.8, 136.9, 134.6, 134.2, 130.9, 130.8, 130.4, 130.2 (t, *J* = 6 Hz), 129.2, 128.8, 128.3, 126.8, 124.6, 123.2, 121.6, 121.5, 115.6, 34.2, 23.7. Mass Spec (*m/z*); HRMS calcd for $C_{28}H_{23}BF_2N_2$: [(M + Na)$^+$] 459.1819, found: 459.1837 (3.92 ppm).

BbF **4** (Ar_{Prox} = *p*-^{t}Bu-Ph)

21 (833 mg; 3.76 mmol), 2-(4-(*tert*-butyl)phenyl)-1*H*-pyrrole **14** (750 mg; 3.76 mmol) and $POCl_3$ (0.74 mL; 7.90 mmol) in 50 mL of CH_2Cl_2. 1.79 g of a dark red solid was recovered as the crude intermediate; 200 mg used for next step with TEA (0.45 mL;

3.23 mmol) and $BF_3 \cdot OEt_2$ (0.55 mL; 4.47 mmol) in 10 mL of dry CH_2Cl_2. Yield = 103 mg of gold-red powder (54 % over 2 steps). ^{1}H NMR ($CDCl_3$, 400 MHz) δ/ppm: 8.14 - 8.08 (m, 2 H), 7.84 (d, *J* = 8.8 Hz, 1 H), 7.68 - 7.51 (m, 8 H), 7.34 (m, 1 H), 7.13 (d, *J* = 4.6 Hz, 1 H), 7.07 - 7.00 (m, 2 H), 6.92 (d, *J* = 4.6 Hz, 1 H), 1.41 (s, 9 H). ^{13}C NMR ($CDCl_3$, 100 MHz) δ/ppm: 164.7, 154.8, 147.2, 145.3, 140.9, 136.9, 134.6, 134.3, 130.9, 130.8, 130.0 (t, *J* = 6 Hz), 129.9, 129.2, 128.4, 128.4, 125.7, 124.7, 123.2, 121.6, 121.5, 115.6, 35.1, 31.1. Mass Spec (*m/z*); HRMS calcd for $C_{29}H_{25}BF_2N_2$: $[(M + Na)^+]$ 473.1976, found: 473.1954 (-4.65 ppm).

BbF **5** (Ar_{Prox} = *p*-OMe-Ph)

21 (2.32 g; 10.5 mmol), 2-(4-methoxyphenyl)-1*H*-pyrrole **15** (1.50 g; 10.5 mmol) and $POCl_3$ (2.07 mL; 22.0 mmol) in 60 mL of CH_2Cl_2. 4.14 g of a dark red solid was recovered as the crude intermediate; 135 mg used for next step with TEA (0.32 mL; 2.33 mmol) and $BF_3 \cdot OEt_2$ (0.40 mL; 3.23 mmol) in 5 mL of dry CH_2Cl_2. Yield = 52.1 mg dark purple powder (36 % over 2 steps). Dark red needles suitable for X-ray structural analysis crystallized from slow diffusion of heptane in a concentrated CH_2Cl_2 solution. ^{1}H NMR ($CDCl_3$, 400 MHz) δ/ppm: 8.22 - 8.16 (m, 2 H), 7.85 (d, *J* = 8.5 Hz, 1 H), 7.65 - 7.51 (m, 6 H), 7.34 (m, 1 H), 7.13 - 7.07 (m, 3 H), 7.04 (m, 1 H), 7.00 (s, 1 H), 6.91 (d, *J* = 4.8 Hz, 1 H), 3.93 (s, 3 H). ^{13}C NMR ($CDCl_3$, 100 MHz) δ/ppm: 164.4, 162.3, 146.9, 144.3, 141.0, 136.9, 134.6, 134.3, 132.2 (t, *J* = 6 Hz), 130.9, 130.8, 130.3, 128.9, 128.3, 124.5, 123.6, 123.1, 121.5, 120.8, 115.5, 114.2, 55.4. Mass Spec (*m/z*); HRMS calcd for $C_{26}H_{19}BF_2N_2O$: $[(M + Na)^+]$ 447.1455, found: 447.1453 (-0.45 ppm).

BbF **6** (Ar_{Prox} = *m*-OMe-Ph)

21 (825 mg; 3.73 mmol), 2-(3-methoxyphenyl)-1*H*-pyrrole **16** (646 mg; 3.73 mmol) and $POCl_3$ (0.74 mL; 7.83 mmol) in 50 mL of CH_2Cl_2. 1.71 g of a dark red solid was recovered as the crude intermediate; 250 mg used for next step with TEA (0.60 mL; 4.32 mmol) and $BF_3 \cdot OEt_2$ (0.74 mL; 5.98 mmol) in 10 mL of dry CH_2Cl_2. Yield = 132 mg of dark red powder (57% over 2 steps). ^{1}H NMR ($CDCl_3$, 500 MHz) δ/ppm: 7.82 (d, *J* = 8.7 Hz, 1 H), 7.81 - 7.78 (m, 1 H), 7.66 - 7.61 (m, 4 H), 7.60 - 7.51 (m, 3 H), 7.46 (t, *J* = 7.9 Hz, 1 H), 7.35 (m, 1 H), 7.14 - 7.09 (m, 2 H), 7.08 - 7.01 (m, 2 H), 6.88 (d, *J* = 4.6 Hz, 1 H), 3.95 (s, 3 H). ^{13}C NMR ($CDCl_3$, 125 MHz) δ/ppm: 164.3, 159.52, 159.47, 146.2, 140.6, 136.9, 134.6, 134.1, 132.6, 130.9, 130.49 (d, *J* = 2 Hz), 129.6, 129.5, 128.4, 124.4, 123.4, 122.4 (t, *J* = 4 Hz), 122.3, 121.8, 117.4, 115.7, 114.9 (t, *J* = 5 Hz), 114.8, 55.5. Mass Spec (*m/z*); HRMS calcd for $C_{26}H_{19}BF_2N_2O$: [$(M + Na)^+$] 447.1455, found: 447.1460 (1.12 ppm).

BbF **7** (Ar_{Prox} = di-*m*-OMe-Ph)

21 (1.09 g; 4.92 mmol), 2-(3,5-dimethoxyphenyl)-1*H*-pyrrole **17** (999 mg; 4.92 mmol) and $POCl_3$ (0.97 mL; 10.3 mmol) in 50 mL of CH_2Cl_2. 2.13 g of a dark red solid was recovered as the crude intermediate; 254 mg used for next step with TEA (0.57 mL; 4.06 mmol) and $BF_3 \cdot OEt_2$ (0.69 mL; 5.62 mmol) in 10 mL of dry CH_2Cl_2. Yield = 134 mg (50 % over 2 steps). ^{1}H NMR ($CDCl_3$, 400 MHz) δ/ppm: 7.82 (d, *J* = 8.8 Hz, 1 H), 7.67 - 7.49 (m, 6 H), 7.35 (m, 1 H), 7.31 (d, *J* = 2.4 Hz, 2 H), 7.11 (d, *J* = 4.6 Hz, 1 H), 7.08 - 6.99 (m, 2 H), 6.87 (d, *J* = 4.6 Hz, 1 H), 6.67 (t, *J* = 2.2 Hz, 1 H), 3.91 (s, 6 H). ^{13}C NMR ($CDCl_3$, 100 MHz) δ/ppm: 164.3, 160.6, 147.6, 146.3, 140.6, 136.9, 134.6,

134.2, 133.0, 130.9 (2C), 130.5, 129.7, 128.4, 124.4, 123.4, 122.4, 121.8, 115.7, 108.0 (t, J = 6 Hz), 103.7, 55.6. Mass Spec (*m/z*); HRMS calcd for $C_{27}H_{21}BF_2N_2O_2$: [(M + Na)$^+$] 477.1561, found: 477.1544 (-3.56 ppm).

BbF **8** (Ar_{Prox} = *p*-NMe_2-Ph)

21 (245 mg; 1.07 mmol; 1 equiv.) and *N*,*N*-dimethyl-4-(1*H*-pyrrol-2-yl)aniline **18** (200 mg; 1.07 mmol; 1 equiv.) were dissolved in CH_2Cl_2 (50 mL) under magnetic stirring. The reaction mixture put under an inert atmosphere and triethylamine (0.17 mL; 1.18 mmol; 1.1 equiv.) followed by phosphoryl chloride ($POCl_3$; 0.21 mL; 2.25 mmol; 2.1 equiv.) were added dropwise. After 0.5 hours at r.t., the reaction was heated at reflux overnight. The reaction mixture was than exposed to air for 36 hours under reflux were a colour change from brown to deep purple was observed. Water was added and the organic phase washed, dried over anhydrous MgSO4 and the solvent removed under reduced pressure. The crude intermediate obtained as a dark blue solid was dried *in vacuo* at 45°C overnight, than dissolved in dry CH_2Cl_2 in a flamed dried flask. Triethylamine (0.85 mL; 6.11 mmol; 6.5 equiv.) was added under inert atmosphere, followed by boron trifluoride diethyl etherate (1.04 mL; 8.46 mmol; 9 equiv.), and the reaction mixture was stirred at r.t. for 3 hours. Water was added and the organic phase washed, dried over anhydrous MgSO4 and the solvent removed under reduced pressure. Purification by silica gel chromatography, isolation by solvent evaporation and *in vacuo* drying afforded the entitled product as a deep blue solid. Gold blue needles suitable for X-ray structural crystallized from diffusion of heptane in a concentrated CH_2Cl_2 solution. Yield = 337 mg (72 %). ^{1}H NMR ($CDCl_3$, 300 MHz) δ/ppm: 8.27 (d, J = 9.3

Hz, 2 H), 7.88 (d, *J* = 8.3 Hz, 1 H), 7.65 - 7.48 (m, 6 H), 7.31 (m, 1 H), 7.09 - 6.99 (m, 3 H), 6.89 - 6.79 (m, 3 H), 3.15 (s, 6 H). ^{13}C NMR ($CDCl_3$, 75 MHz) δ/ppm: 164.8, 152.6, 145.6, 141.8, 140.0, 137.0, 134.8, 134.2, 132.9 (t, *J* = 6 Hz), 130.8, 130.6, 129.7, 128.2, 127.4, 124.7, 122.5, 121.0, 117.7, 117.5, 115.3, 111.6, 40.0. Mass Spec (*m/z*); HRMS calcd for $C_{27}H_{22}BF_2N_3$: [$(M + Na)^+$] 460.1772, found: 460.1773 (0.22 ppm).

BbF **9** (Ar_{Prox} = *p*-OMe-Naphtyl)

21 (843 mg; 4.92 mmol), 2-(6-methoxynaphthalen-2-yl)-1H-pyrrole **19** (850 mg; 3.81 mmol) and $POCl_3$ (0.75 mL; 7.99 mmol) in 50 mL of CH_2Cl_2. 1.82 g of a dark purple solid was recovered as the crude intermediate; 200 mg used for next step with TEA (0.42 mL; 3.05 mmol) and $BF_3{\cdot}OEt_2$ (0.52 mL; 4.22 mmol) in 10 mL of dry CH_2Cl_2. Yield = 35 mg of dark green powder (18 % over 2 steps). Dark purple needles suitable for X-ray structural analysis crystallized from slow diffusion of heptane in a concentrated CH_2Cl_2 solution. ^{1}H NMR ($CDCl_3$, 500 MHz) δ/ppm: 8.64 (s, 1 H), 8.22 (dd, *J* = 8.7, 1.8 Hz, 1 H), 7.98 - 7.81 (m, 3 H), 7.69 - 7.49 (m, 6 H), 7.41 - 7.30 (m, 1 H), 7.26 - 7.14 (m, 3 H), 7.08 - 7.00 (m, 3 H), 3.98 (s, 3 H). ^{13}C NMR ($CDCl_3$, 125 MHz) δ/ppm: 164.7, 159.6, 147.2, 145.0, 141.1, 137.0, 136.1, 134.6, 134.3, 131.1, 131.03, 131.91, 130.4, 129.2, 128.40, 128.37, 127.1 (t, *J* = 6 Hz), 127.0, 126.4, 124.8, 123.2, 121.6, 121.4, 119.6, 115.6, 105.8, 55.5. Mass Spec (*m/z*); HRMS calcd for $C_{30}H_{21}BF_2N_2O$: [$(M + Na)^+$] 497.1612, found: 497.1626 (2.82 ppm).

BbF **10** (Ar_{Prox} = Phen)

21 (227 mg; 1.03 mmol), 2-(phenanthren-9-yl)-1H-pyrrole **20** (250 mg; 1.03 mmol) and $POCl_3$ (0.20 mL; 2.16 mmol) in 25 mL of CH_2Cl_2. 459 mg of a dark red solid was recovered as the crude intermediate and used for the next step with TEA (0.93 mL; 6.68 mmol) and $BF_3{\cdot}OEt_2$ (1.14 mL; 9.25 mmol) in 40 mL of dry CH_2Cl_2. Yield = 127 mg of dark purple powder (25 % over 2 steps). ^{1}H NMR ($CDCl_3$, 400 MHz) δ/ppm: 8.79 (dd, *J* = 14.2, 8.3 Hz, 2 H), 8.37 (s, 1 H), 8.07 (dd, *J* = 7.9, 1.1 Hz, 1 H), 7.88 (d, *J* = 8.1 Hz, 1 H), 7.82 - 7.48 (m, 11 H), 7.32 - 7.21 (m, 2 H), 7.13 (s, 1 H), 7.00 (t, *J* = 7.5 Hz, 1 H), 6.86 (d, *J* = 4.6 Hz, 1 H). ^{13}C NMR ($CDCl_3$, 100 MHz) δ/ppm: 163.4, 147.7, 146.9, 139.4, 137.1, 134.1, 133.4, 131.1, 130.9, 130.8, 130.63, 130.58, 130.4, 130.3 (t, *J* = 5 Hz), 130.2, 130.0, 129.9, 128.4, 128.03, 127.98, 127.1, 126.93, 126.87, 126.6, 126.0, 123.4, 123.13, 123.09, 122.6, 121.8, 115.6. Mass Spec (*m/z*); HRMS calcd for $C_{33}H_{21}BF_2N_2$: $[(M + Na)^+]$ 517.1664, found: 517.1663 (-0.19 ppm).

*General procedure for aryl-pyrroles **19** and **20**.*

Pyrrole (1.6 equiv.) was slowly added under an inert atmosphere to a cooled (0°C) suspension of sodium hydride (NaH 60 % dispersion in mineral oil; 1.6 equiv.) in anhydrous THF (20 mL) and stirring was continued for 0.5 h at r.t. After cooling to 0°C, a solution of zinc chloride ($ZnCl_2$; 1.6 equiv.) in anhydrous THF (80 mL) was syringed. After stirring for 10 min at r.t., di-*tert*-butyl-*o*-biphenylphosphine (JohnPhos; 1.5 - 2 mol %) and $Pd(OAc)_2$ (1.5 -2 mol %) were added in one portion and the resulting mixture was degassed with N_2. The corresponding aryl halide (1 equiv.) was subsequently quickly added to the reaction mixture and the resulting brown solution was refluxed for 72 hours. After cooling to r.t., a saturated solution of sodium thiosulfate ($Na_2S_2O_3$, 100 mL) was added, stirring was continued for 15 min, followed by concentration of the reaction mixture under reduced pressure and filtration. The filter cake was repeatedly washed with ethyl acetate (5 x 50 mL) and the filtrate was transferred to a separatory funnel. After separation of both phases, the aqueous layer was extracted with ethyl acetate (2 x 50 mL) and the combined organic phase was washed with water (100 mL). Drying over anhydrous $MgSO_4$, followed by filtration and removal of the solvent under reduced pressure afforded a yellow-brown solid which was purified by column chromatography giving the entitle compound.

2-(6-methoxynaphthalen-2-yl)-1H-pyrrole **19**

Pyrrole (2.34 mL; 33.1 mmol), NaH (1.32 g; 33.1 mmol), $ZnCl_2$ (4.55 g; 33.1 mmol), JohnPhos (127 mg; 0.413 mmol), $Pd(OAc)_2$ (94.7 mg; 0.413 mmol) and 2-bromo-6-methoxynaphtalene (5.00 g; 20.7 mmol). Yield = 1.09 g of dark yellow cristals (24 %). ^{1}H NMR ($CDCl_3$, 300 MHz) δ/ppm: 8.55 (br. s., 1 H), 7.83 - 7.57 (m, 4 H), 7.20 - 7.06 (m, 2 H), 6.96 - 6.85 (m, 1 H), 6.63 - 6.60 (m, 1 H), 6.39 - 6.30 (m, 1 H), 3.94 (s, 3 H). ^{13}C NMR ($CDCl_3$, 75 MHz) δ/ppm: 157.4, 133.2, 132.3, 129.2, 128.2 (2C), 127.4, 123.7, 121.2, 119.2, 118.8, 110.2, 106.0, 105.8, 55.3. Mass Spec (*m/z*); MS calcd for $C_{15}H_{13}NO$: [M^+] 223.1, found: 223.1.

2-(phenanthren-9-yl)-1H-pyrrole **20**

Pyrrole (2.16 mL; 30.5 mmol), NaH (1.22 g; 30.5 mmol), $ZnCl_2$ (4.20 g; 30.5 mmol), JohnPhos (87.9 mg; 0.286 mmol), $Pd(OAc)_2$ (65.5 mg; 0.286 mmol) and 9-bromo-phenanthrene (5.00 g; 19.1 mmol). Yield = 0.37 g of an off-white solid (8 %). ^{1}H NMR ($CDCl_3$, 300 MHz) δ/ppm: 8.78 (d, J = 8.3 Hz, 1 H), 8.71 (d, J = 8.1 Hz, 1 H), 8.47 (br. s., 1 H), 8.36 (dd, J = 8.2, 1.1, 1 H), 7.92 - 7.84 (m, 1 H), 7.82 - 7.57 (m, 5 H), 7.04 - 6.97 (m, 1 H), 6.63 - 6.56 (m, 1 H), 6.47 (m, 1 H). ^{13}C NMR ($CDCl_3$, 75 MHz) δ/ppm: 131.5, 130.8, 130.7, 130.4, 130.2, 129.8, 128.5, 126.9, 126.9, 126.8, 126.6 (2C), 126.5, 123.0, 122.5, 118.3, 109.7, 109.4. Mass Spec (*m/z*); MS calcd for $C_{18}H_{13}N$: [M^+] 243.1, found: 243.1.

NMR Characterization

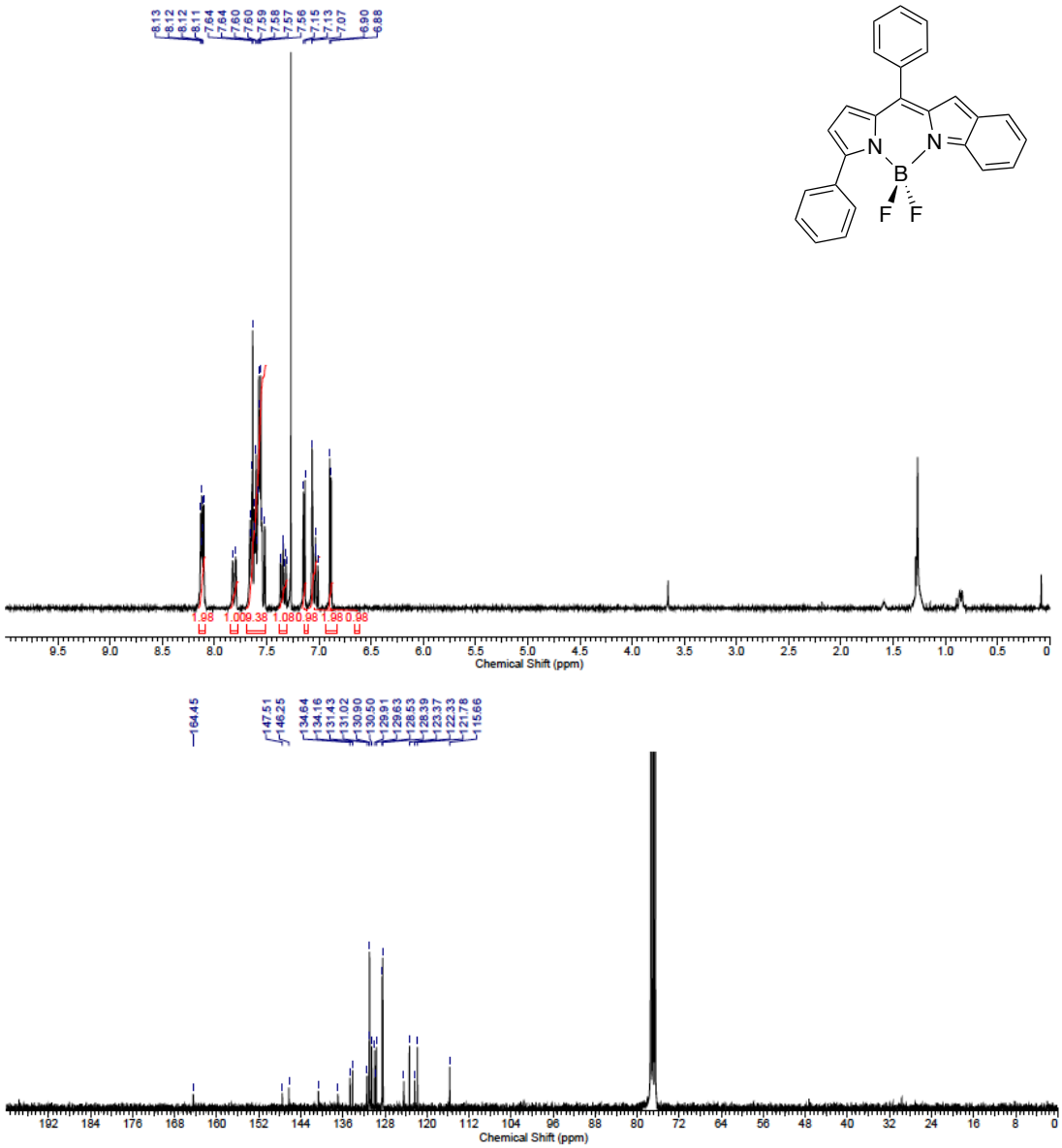

Figure II.S1 – ^{1}H (top) and ^{13}C (bottom) of BbF **1** ($CDCl_3$; 400 MHz and 100 MHz, respectively)

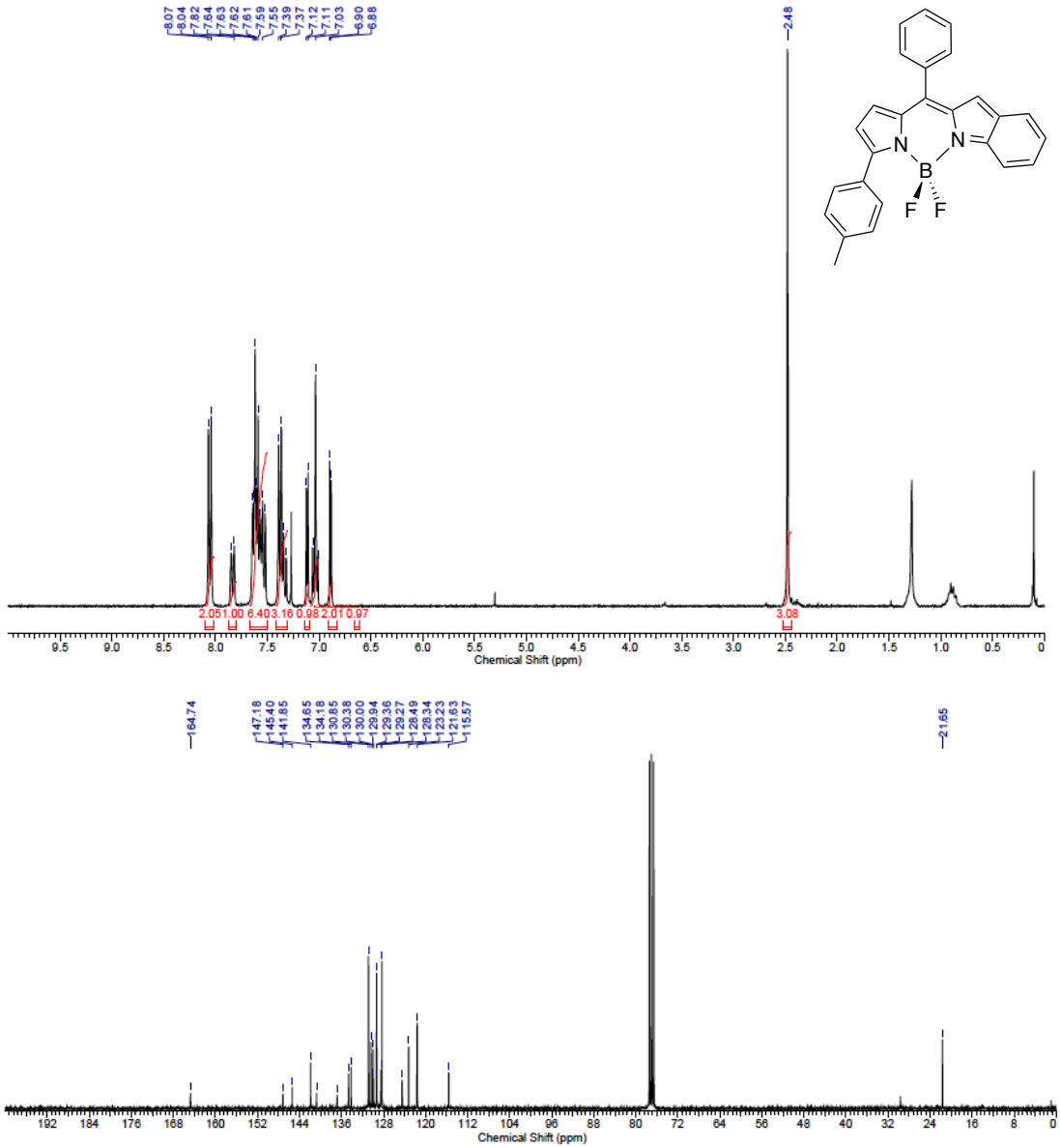

Figure II.S2 – ^{1}H (top) and ^{13}C (bottom) of BbF **2** ($CDCl_3$; 400 MHz and 100 MHz, respectively)

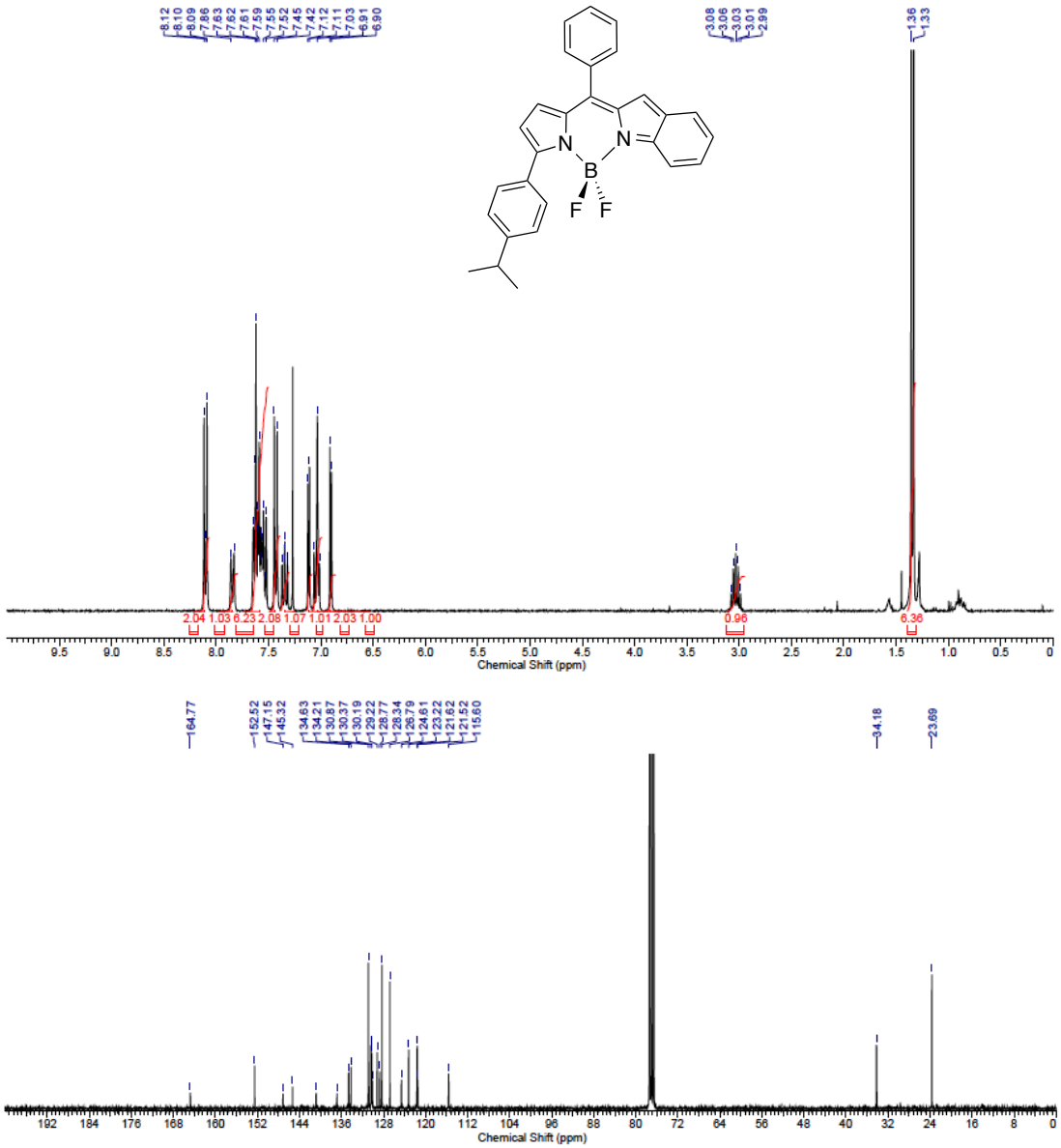

Figure II.S3 – ^{1}H (top) and ^{13}C (bottom) of BbF **3** ($CDCl_3$; 400 MHz and 100 MHz, respectively)

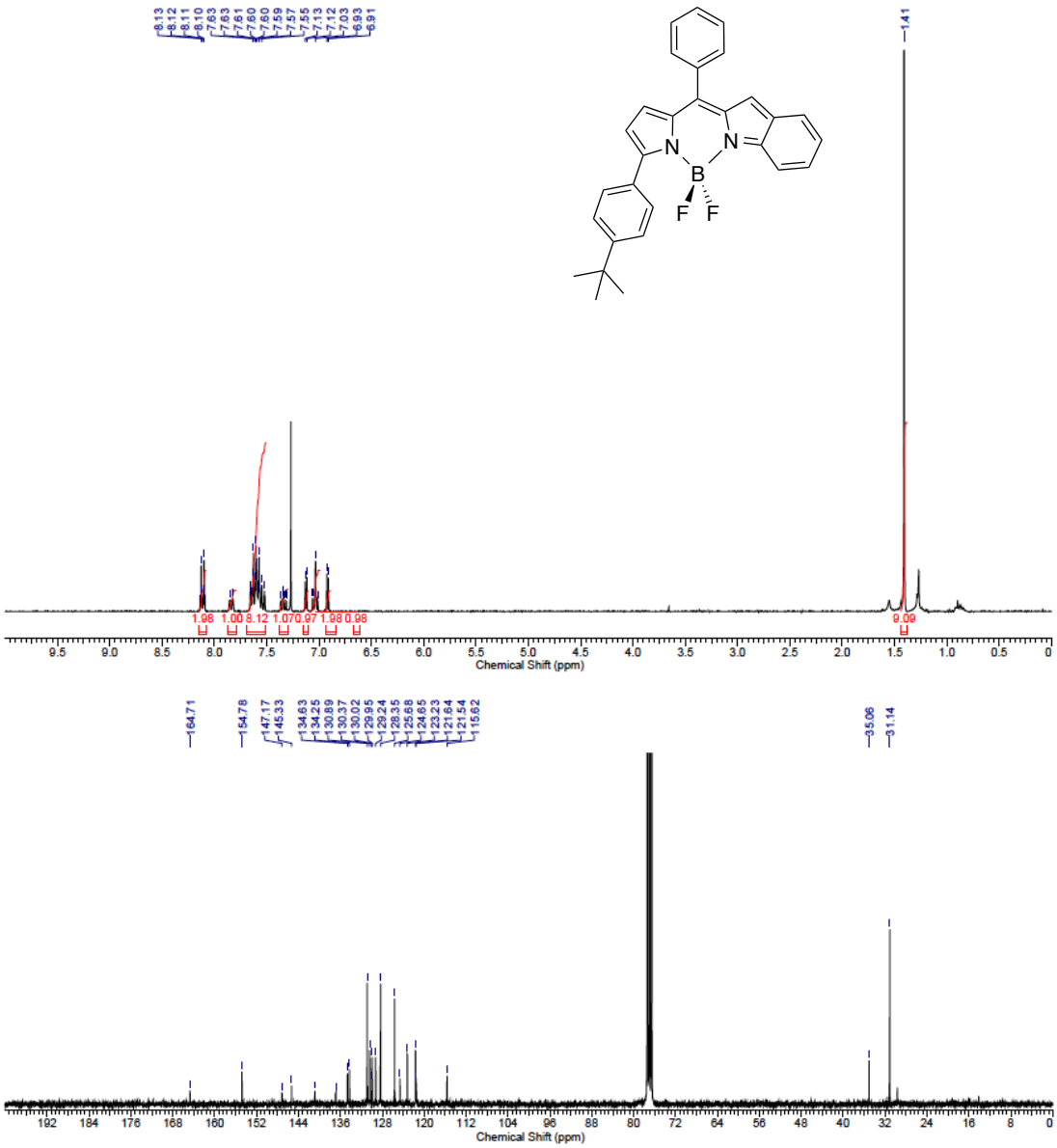

Figure II.S4 – ^{1}H (top) and ^{13}C (bottom) of BbF **4** ($CDCl_3$; 400 MHz and 100 MHz, respectively)

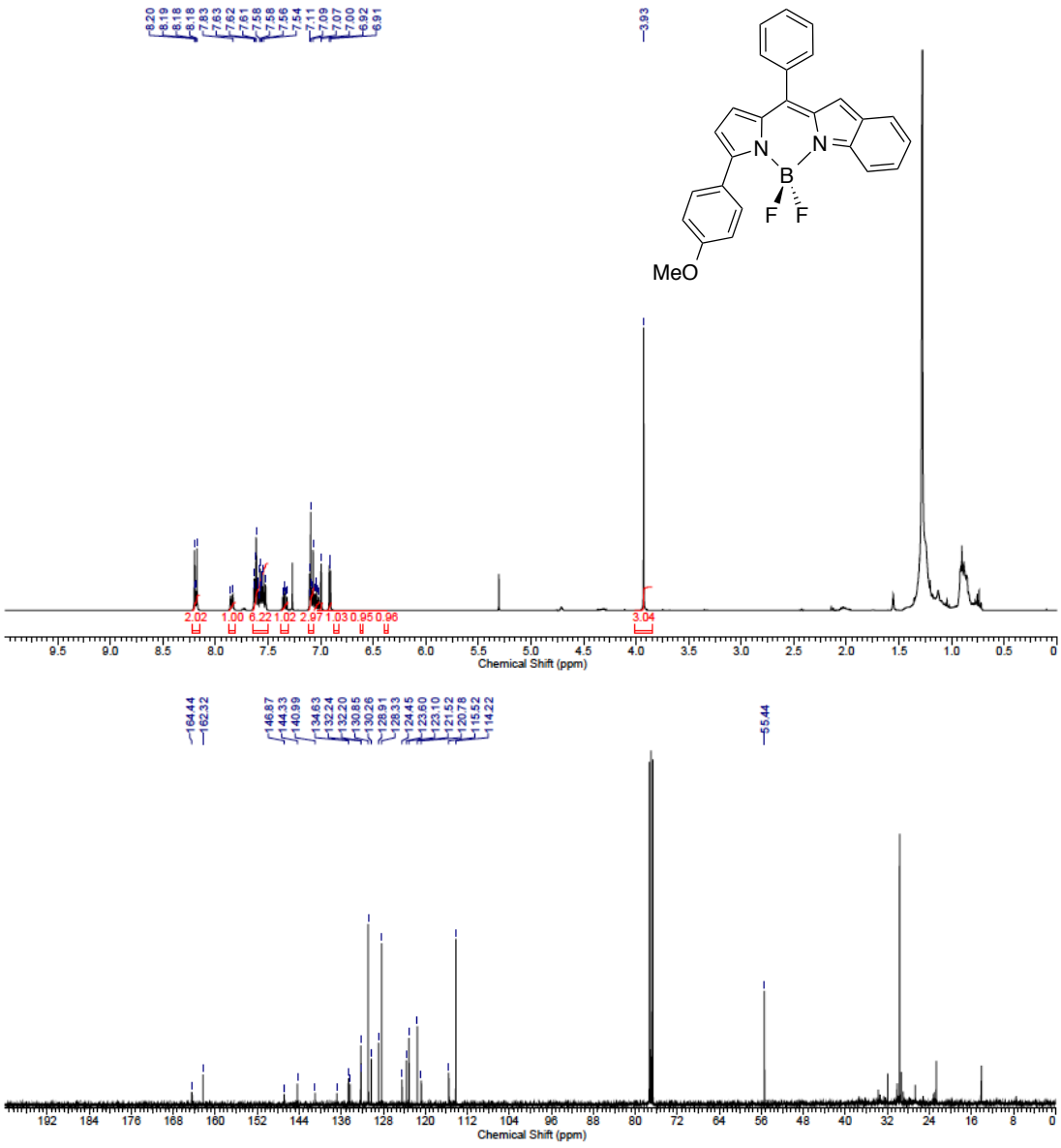

Figure II.S5 – ^{1}H (top) and ^{13}C (bottom) of BbF **5** ($CDCl_3$; 500 MHz and 125 MHz, respectively)

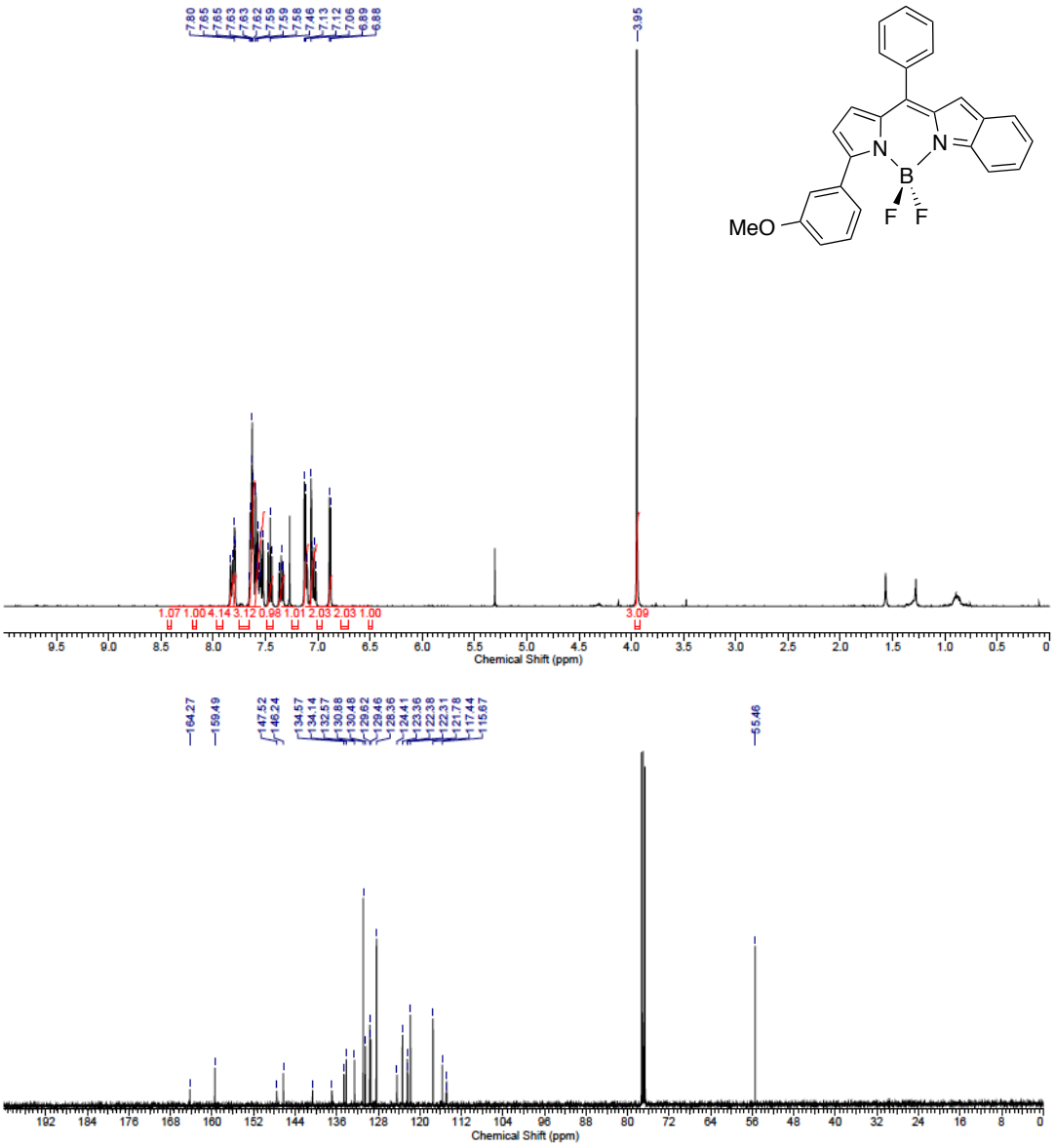

Figure II.S6 – ^{1}H (top) and ^{13}C (bottom) of BbF **6** ($CDCl_3$; 500 MHz and 125 MHz, respectively)

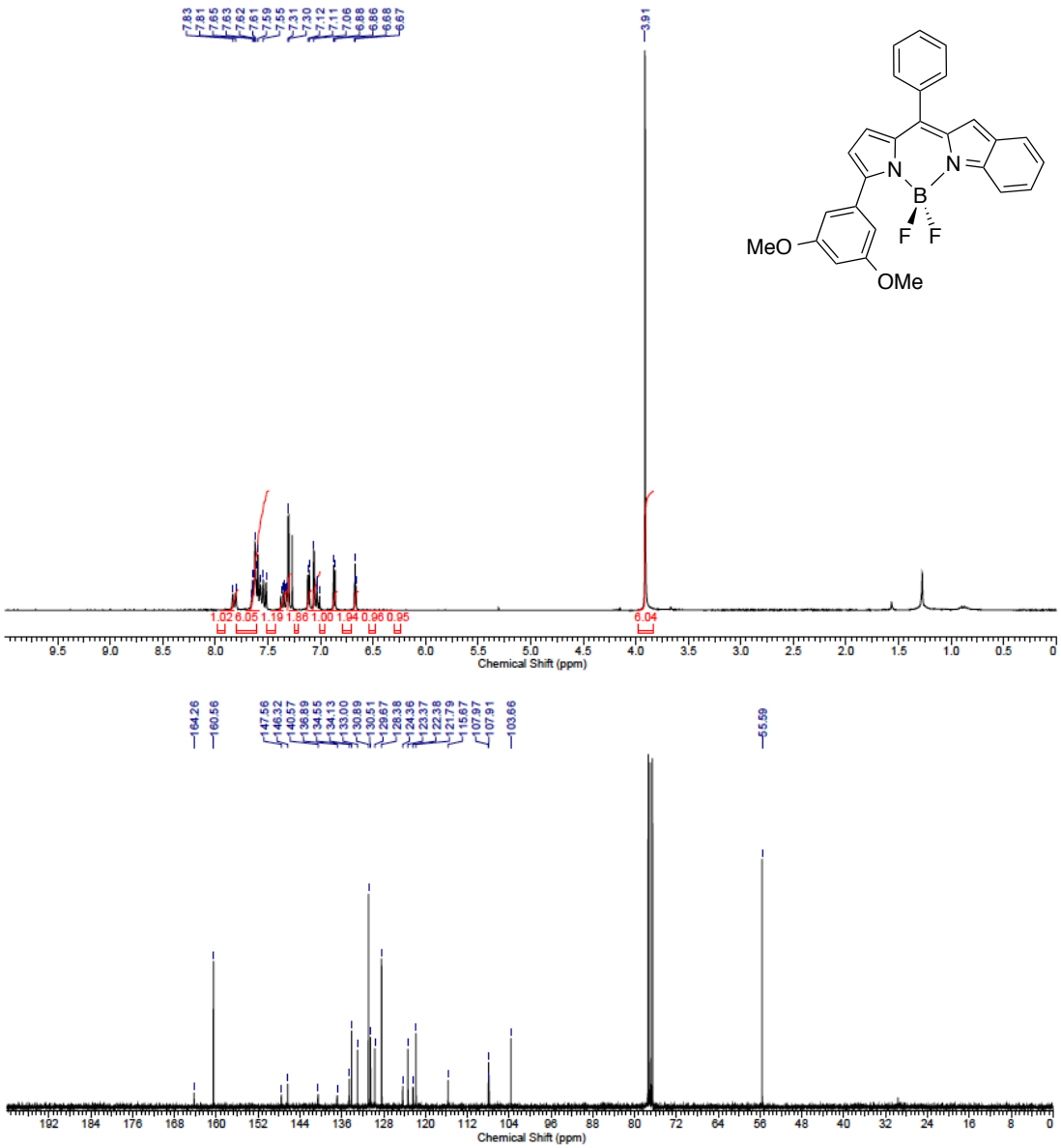

Figure II.S7 – ^{1}H (top) and ^{13}C (bottom) of BbF **7** ($CDCl_3$; 400 MHz and 100 MHz, respectively)

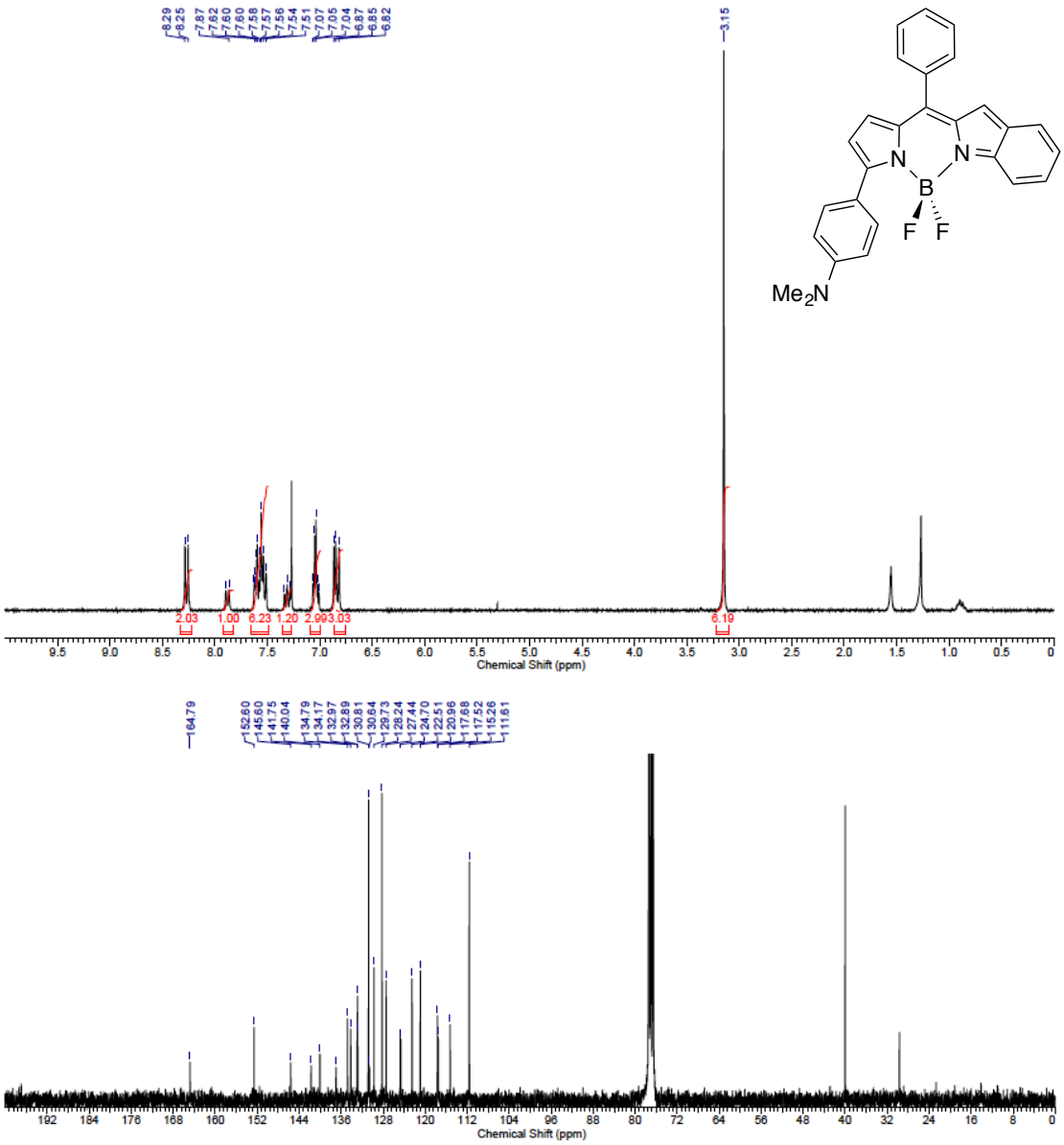

Figure II.S8 – ^{1}H (top) and ^{13}C (bottom) of BbF **8** ($CDCl_3$; 300 MHz and 75 MHz, respectively)

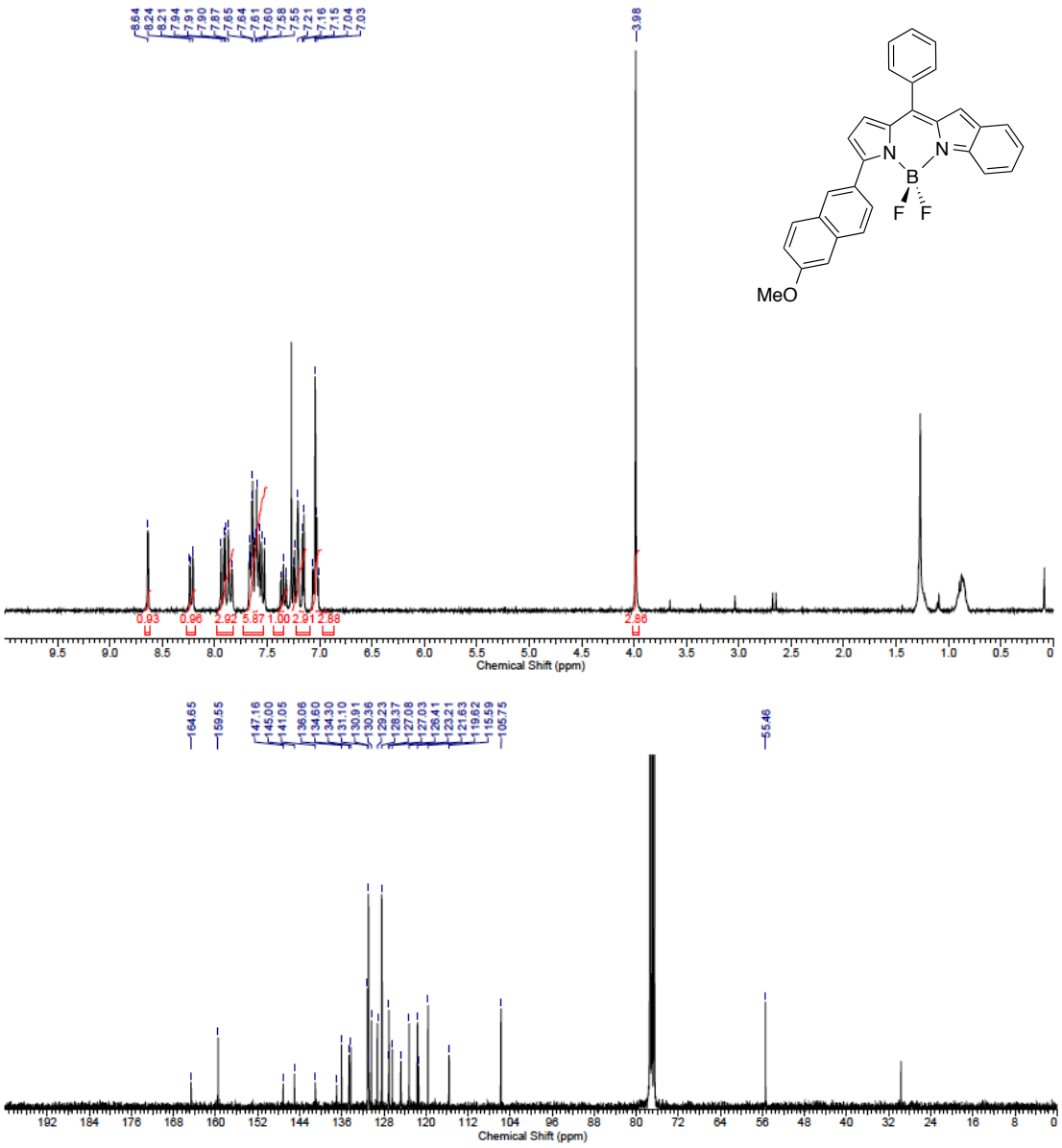

Figure II.S9 – ^{1}H (top) and ^{13}C (bottom) of BbF **9** ($CDCl_3$; 500 MHz and 125 MHz, respectively)

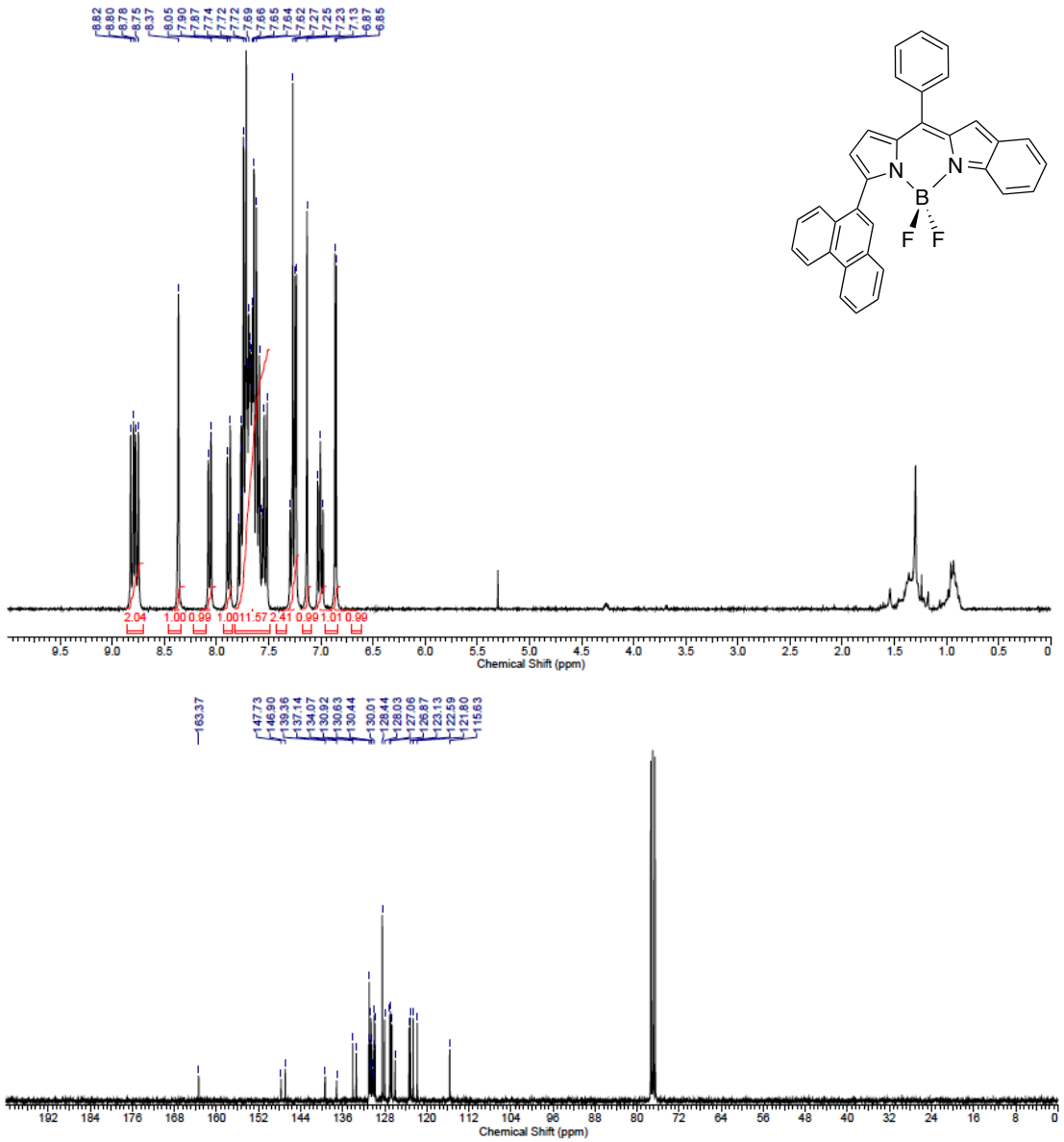

Figure II.S10 – ^{1}H (top) and ^{13}C (bottom) of BbF **10** ($CDCl_3$; 400 MHz and 100 MHz, respectively)

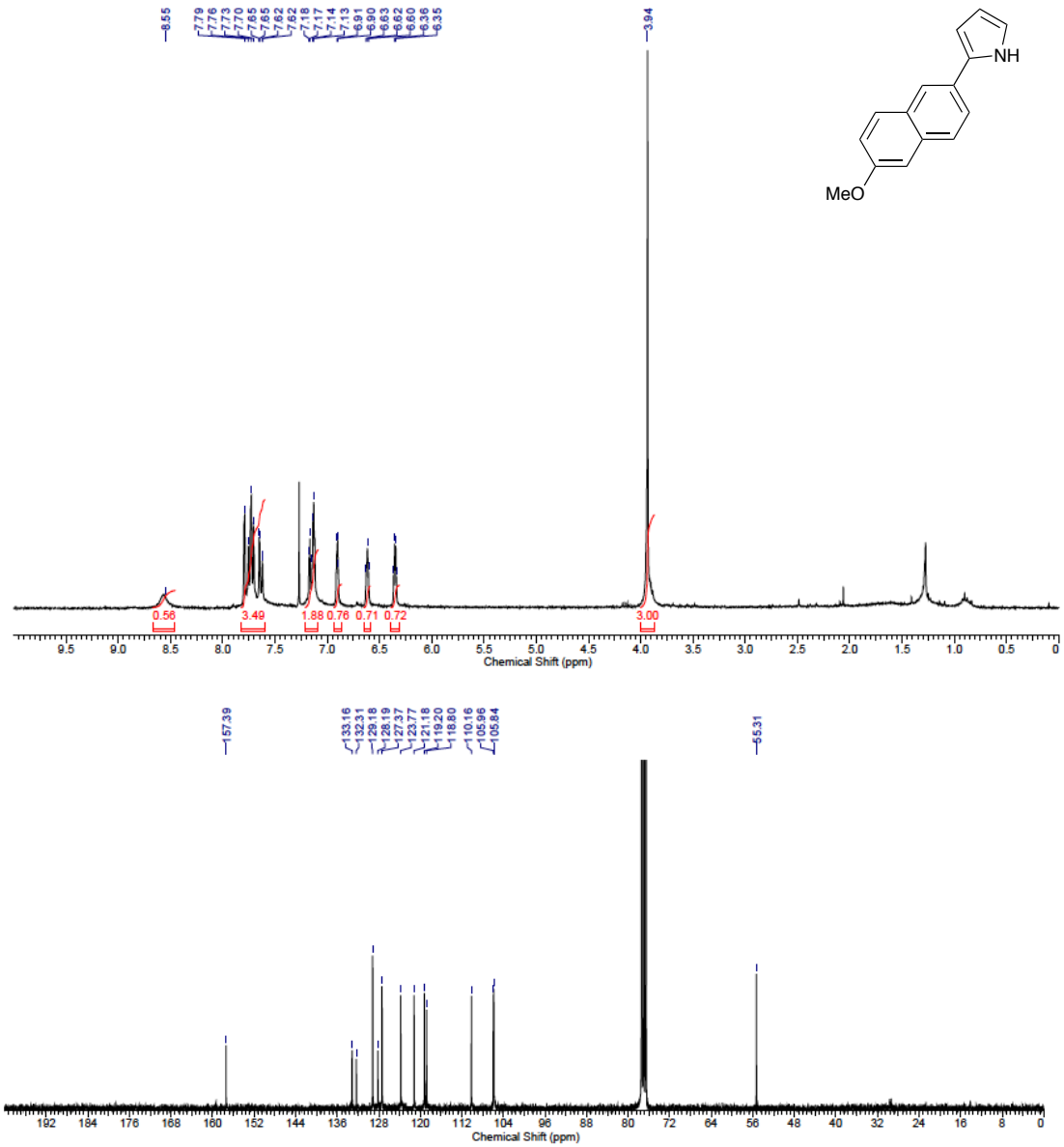

Figure II.S11 – ^{1}H (top) and ^{13}C (bottom) of 2-(6-methoxynaphthalen-2-yl)-1H-pyrrole **19** ($CDCl_3$; 300 MHz and 75 MHz, respectively)

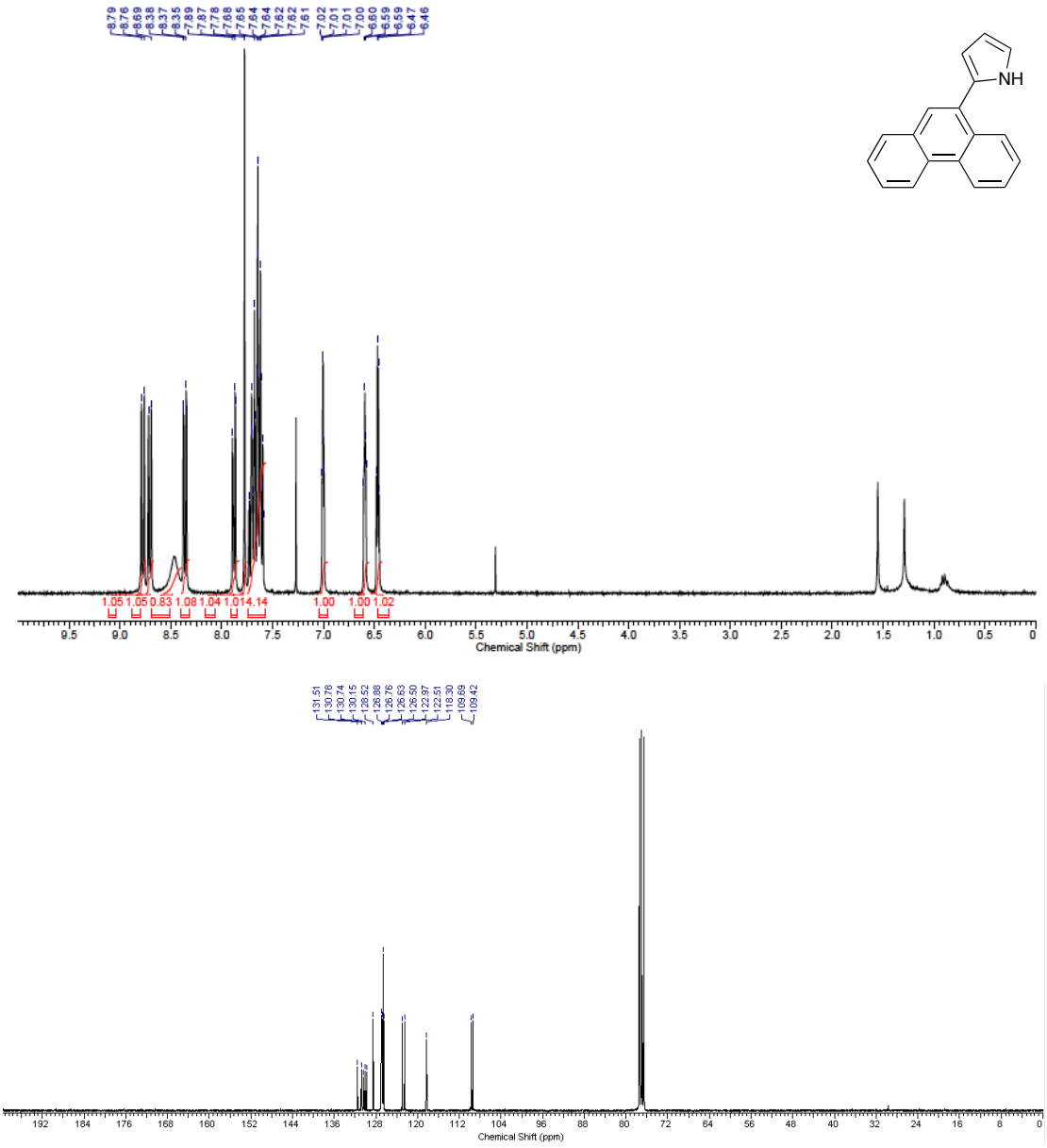

Figure II.S12 – ^{1}H (top) and ^{13}C (bottom) of 2-(phenanthren-9-yl)-1H-pyrrole **20** ($CDCl_3$; 300 MHz and 75 MHz, respectively)

Mass Spectrometry

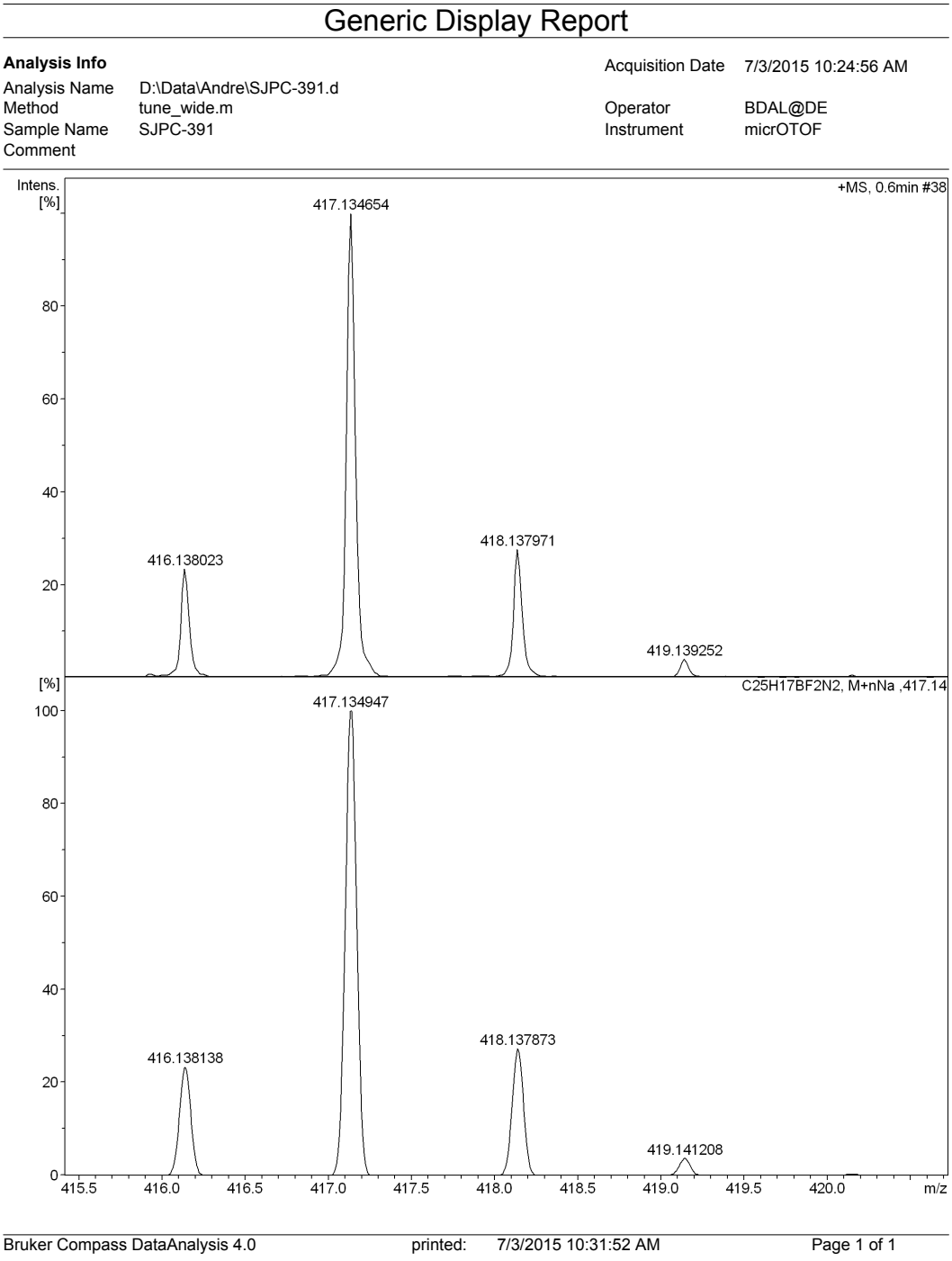

Figure II.S13 – HRMS of BbF **1**

Generic Display Report

Analysis Info

Analysis Name	D:\Data\Andre\SJPC-432.d	Acquisition Date	6/1/2015 1:43:30 PM
Method	tune_wide.m	Operator	BDAL@DE
Sample Name	SJPC-432	Instrument	micrOTOF
Comment	Utiliser calibration de SJPC-441		

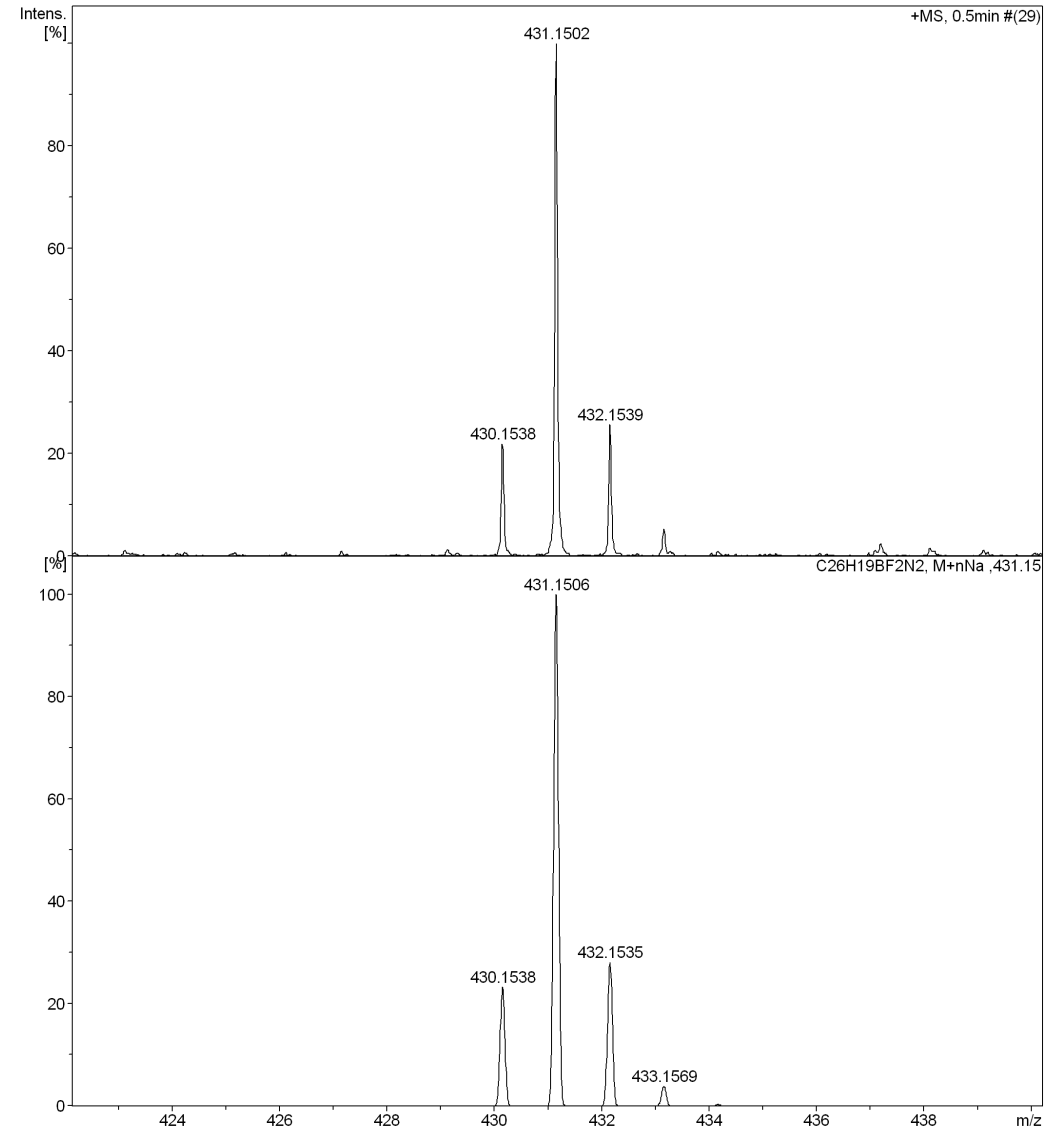

Figure II.S14 – HRMS of BbF **2**

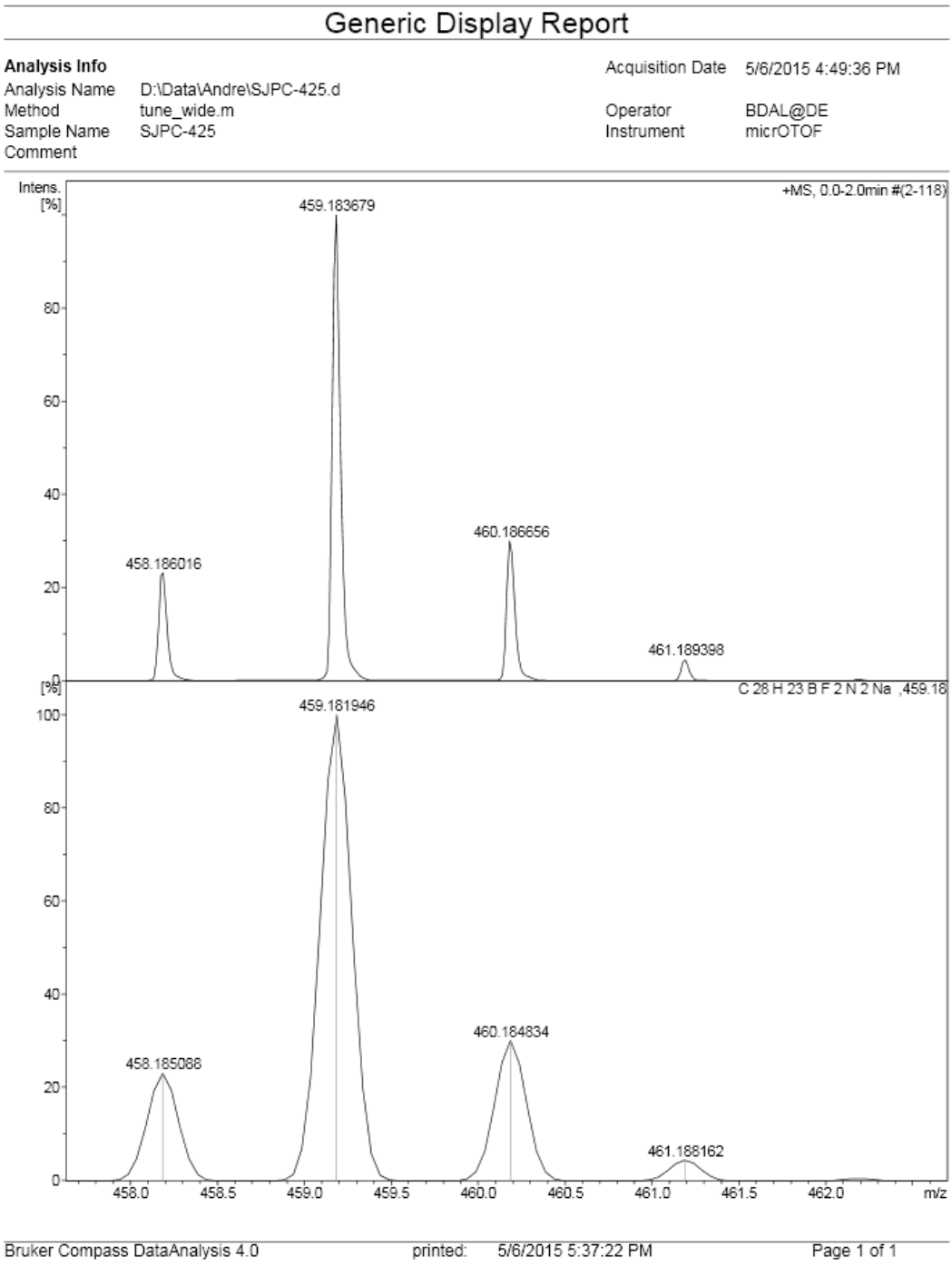

Figure II.S15 – HRMS of BbF **3**

Generic Display Report

Analysis Info

Analysis Name	D:\Data\Andre\SJPC-429.d	Acquisition Date	6/1/2015 12:08:58 PM
Method	tune_wide.m	Operator	BDAL@DE
Sample Name	SJPC-429	Instrument	micrOTOF
Comment	Utiliser calibration de SJPC-441		

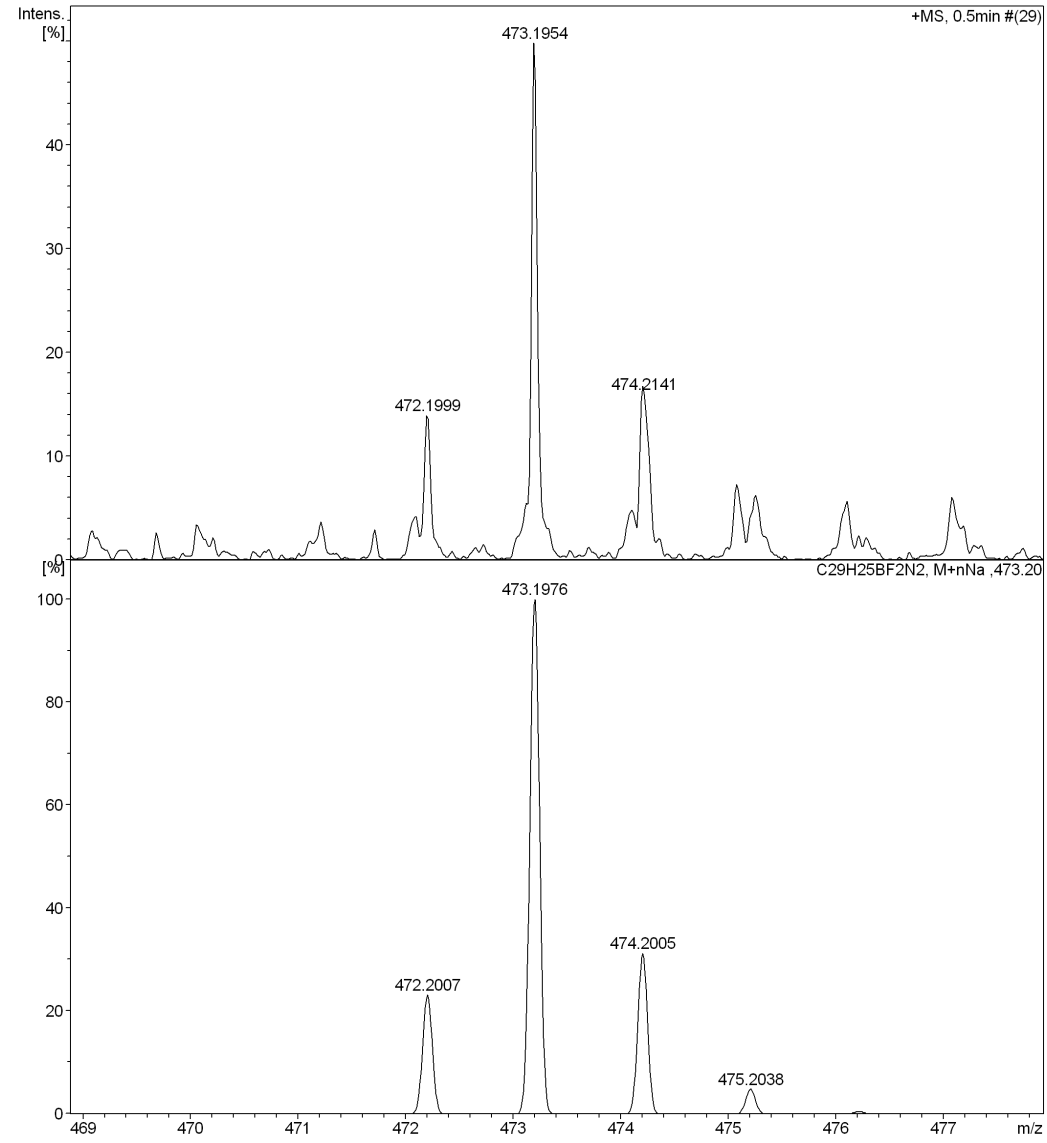

Bruker Compass DataAnalysis 4.0 printed: 6/1/2015 12:33:49 PM Page 1 of 1

Figure II.S16 – HRMS of BbF **4**

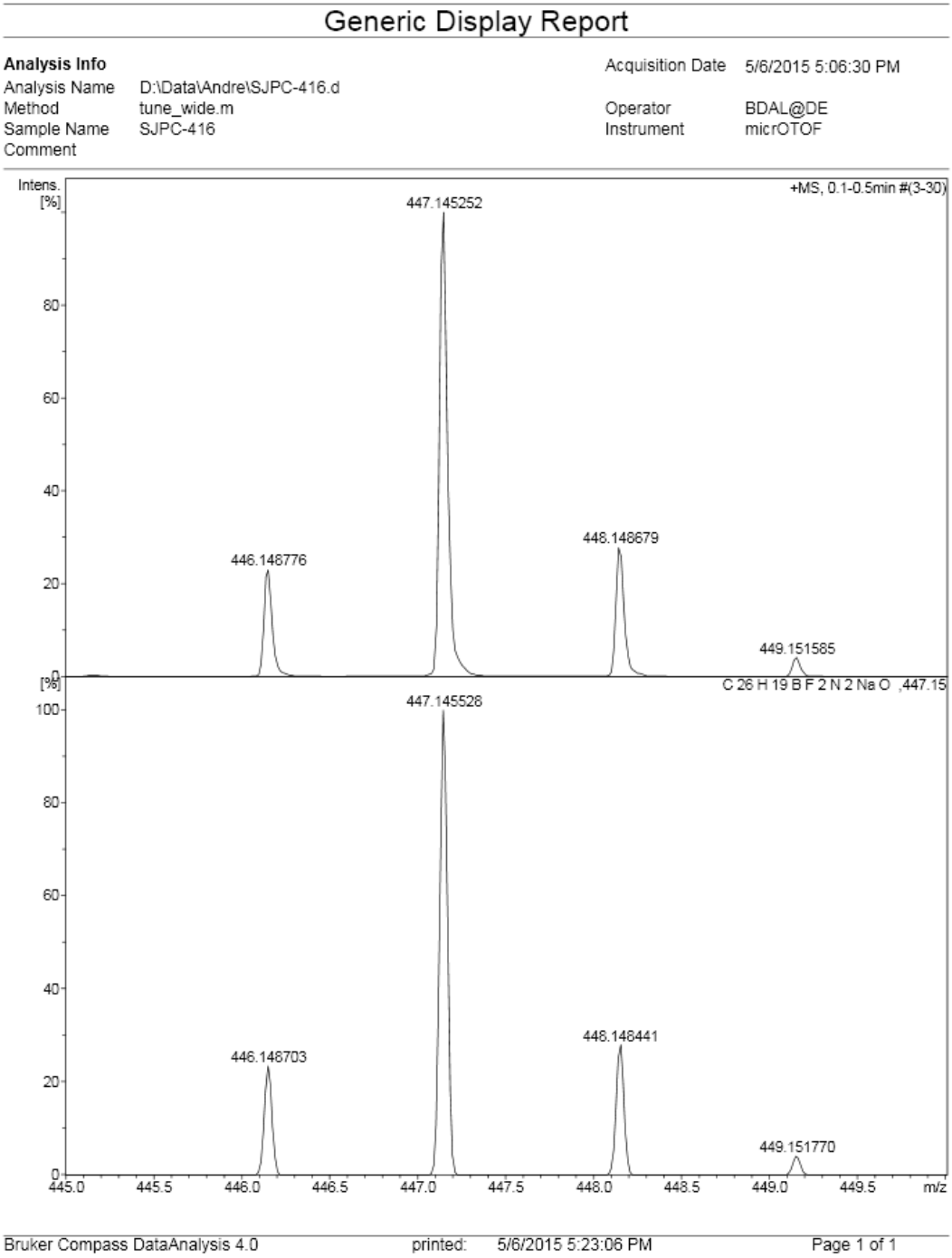

Figure II.S17 – HRMS of BbF **5**

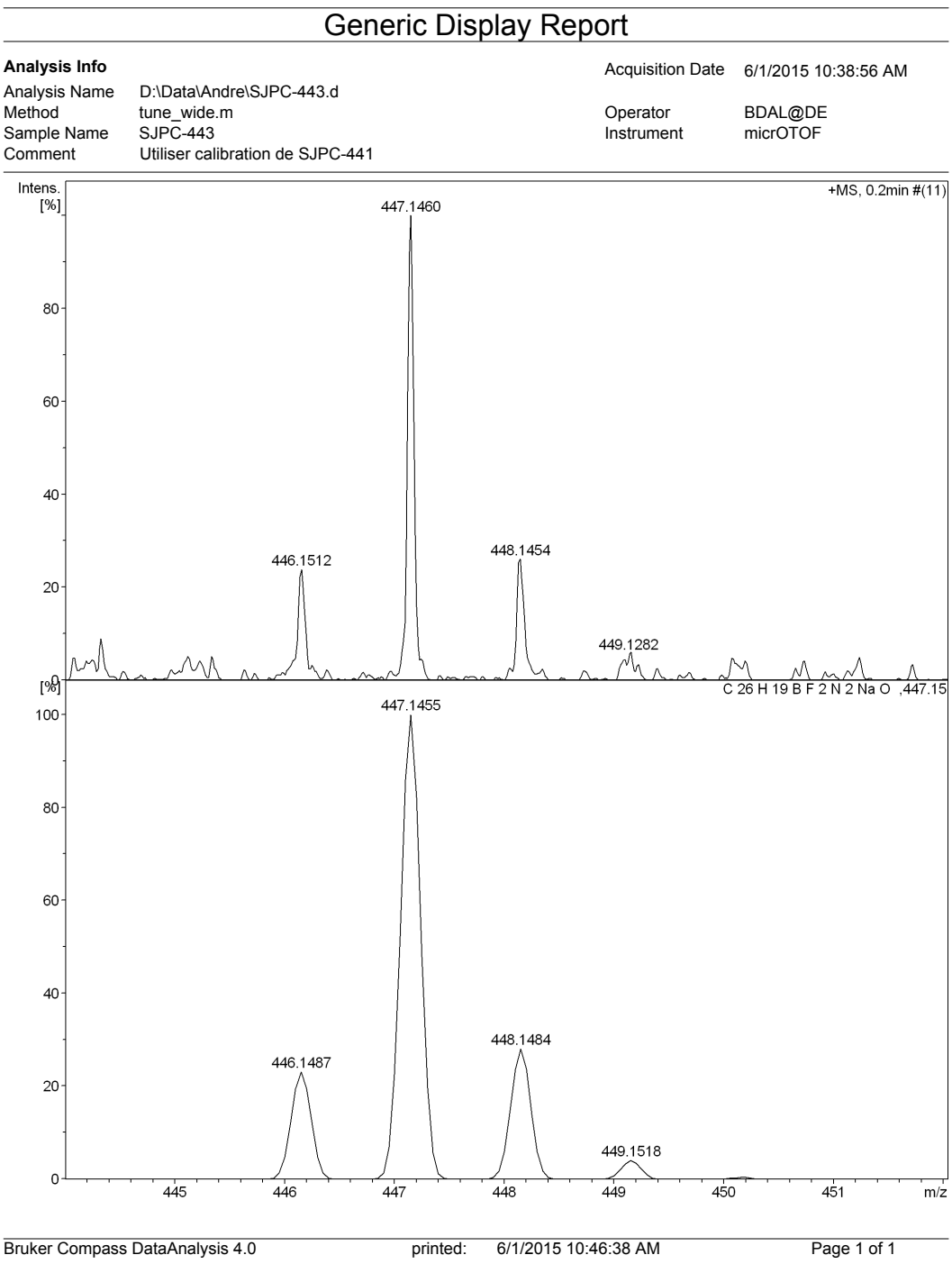

Figure II.S18 – HRMS of BbF **6**

Generic Display Report

Analysis Info

Analysis Name	D:\Data\Andre\SJPC-441.d	Acquisition Date	6/1/2015 9:36:05 AM
Method	tune_wide.m	Operator	BDAL@DE
Sample Name	SJPC-441	Instrument	micrOTOF
Comment			

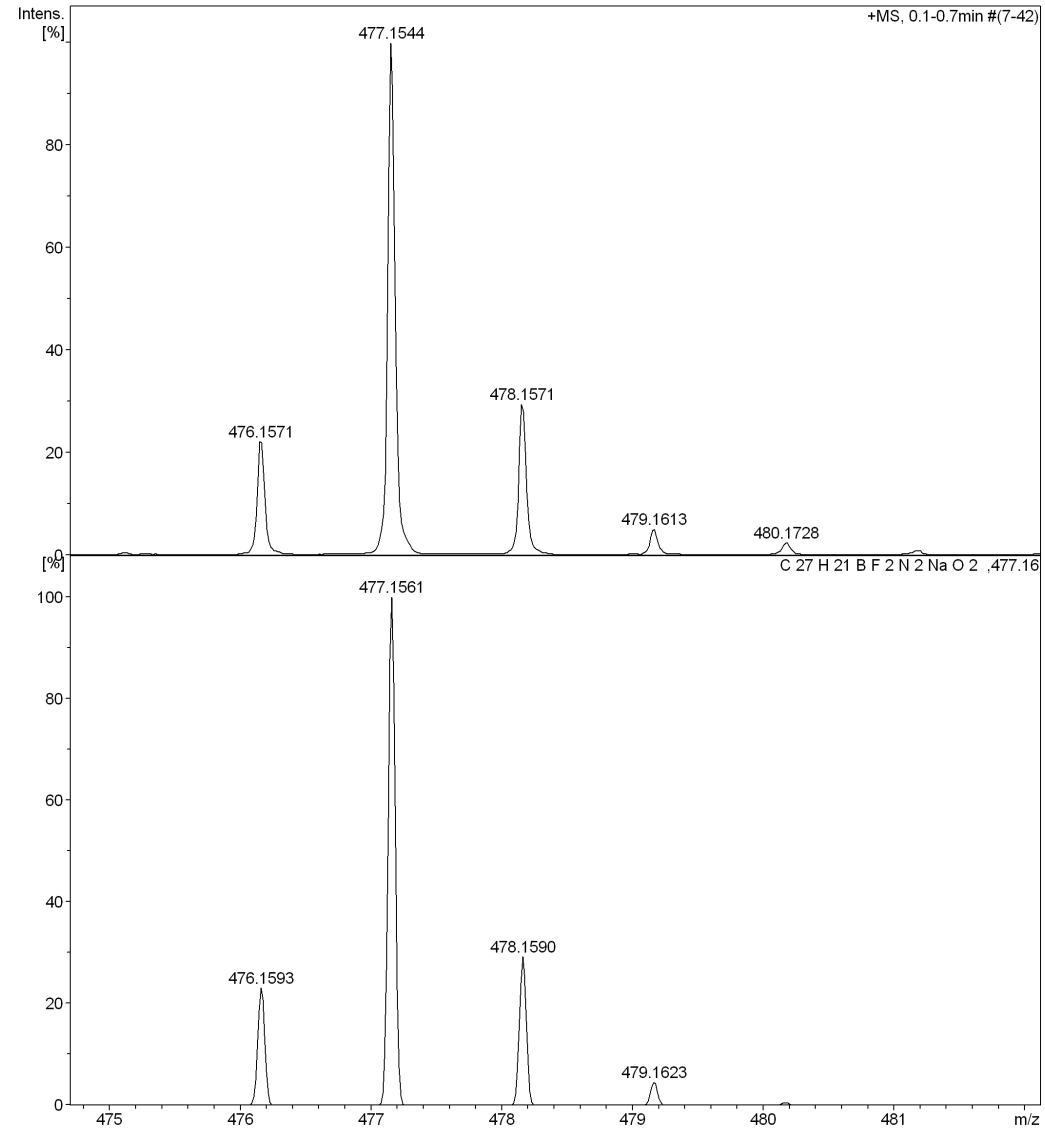

Bruker Compass DataAnalysis 4.0 printed: 6/1/2015 9:48:53 AM Page 1 of 1

Figure II.S19 – HRMS of BbF **7**

Generic Display Report

Analysis Info

Analysis Name	D:\Data\Andre\SJPC-437.d	Acquisition Date	6/1/2015 2:30:06 PM
Method	tune_wide.m	Operator	BDAL@DE
Sample Name	SJPC-437	Instrument	micrOTOF
Comment	Utiliser calibration de SJPC-432		

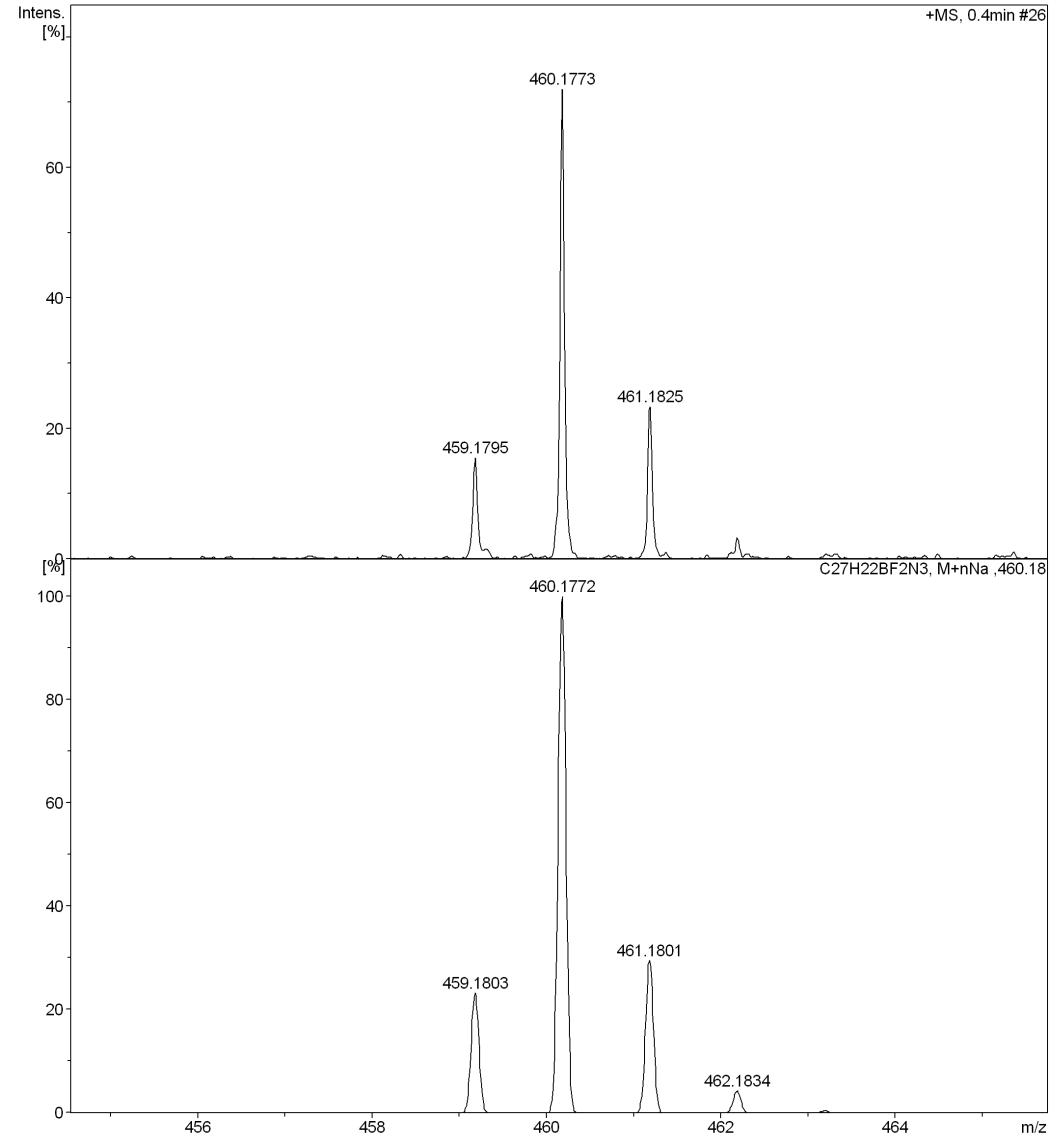

Bruker Compass DataAnalysis 4.0 printed: 6/1/2015 3:09:09 PM Page 1 of 1

Figure II.S20 – HRMS of BbF **8**

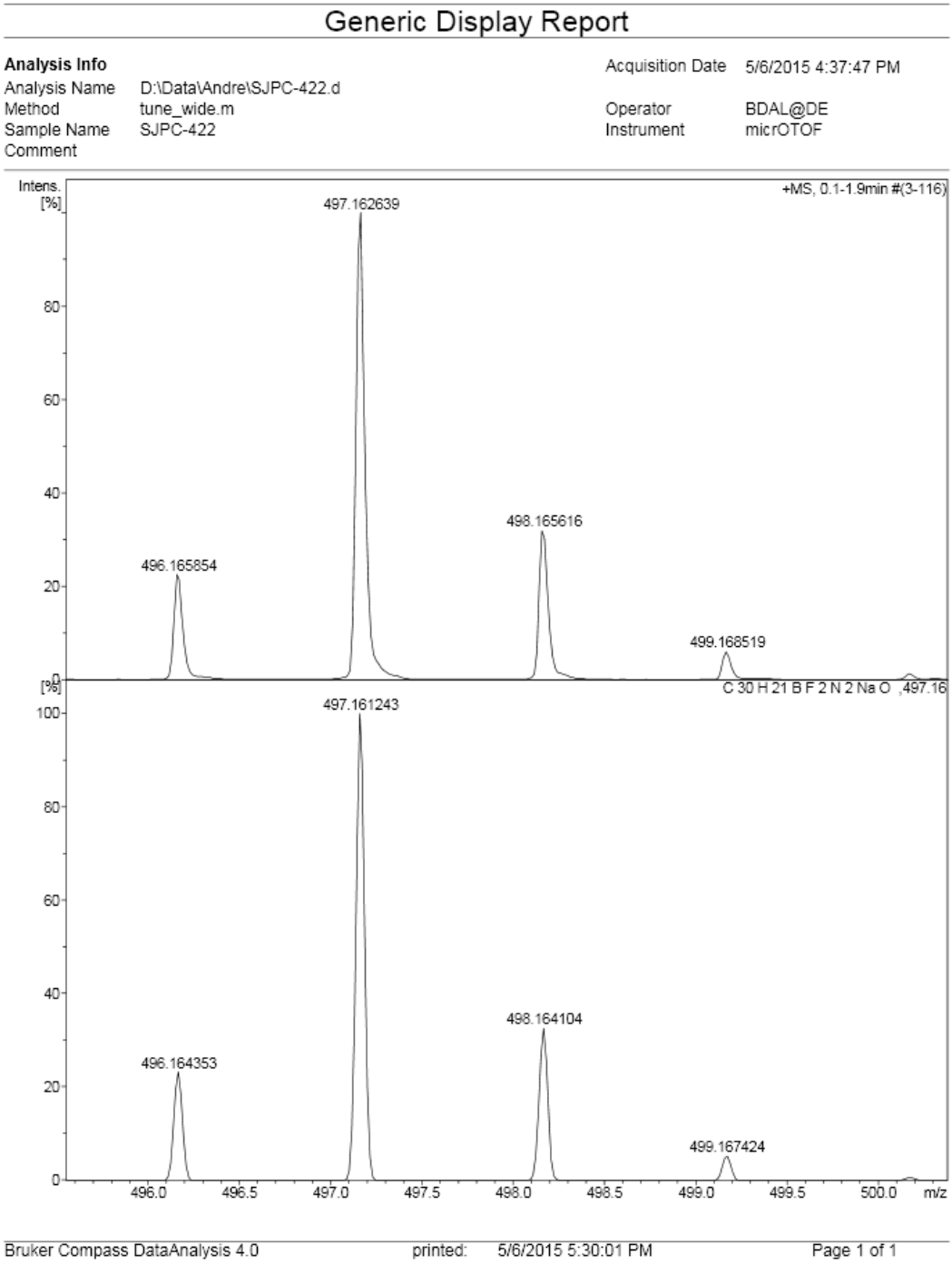

Figure II.S21 – HRMS of BbF **9**

Generic Display Report

Analysis Info

Analysis Name	D:\Data\Andre\SJPC-442.d	Acquisition Date	6/1/2015 2:14:09 PM
Method	tune_wide.m	Operator	BDAL@DE
Sample Name	SJPC-442	Instrument	micrOTOF
Comment	Utiliser calibration de SJPC-432		

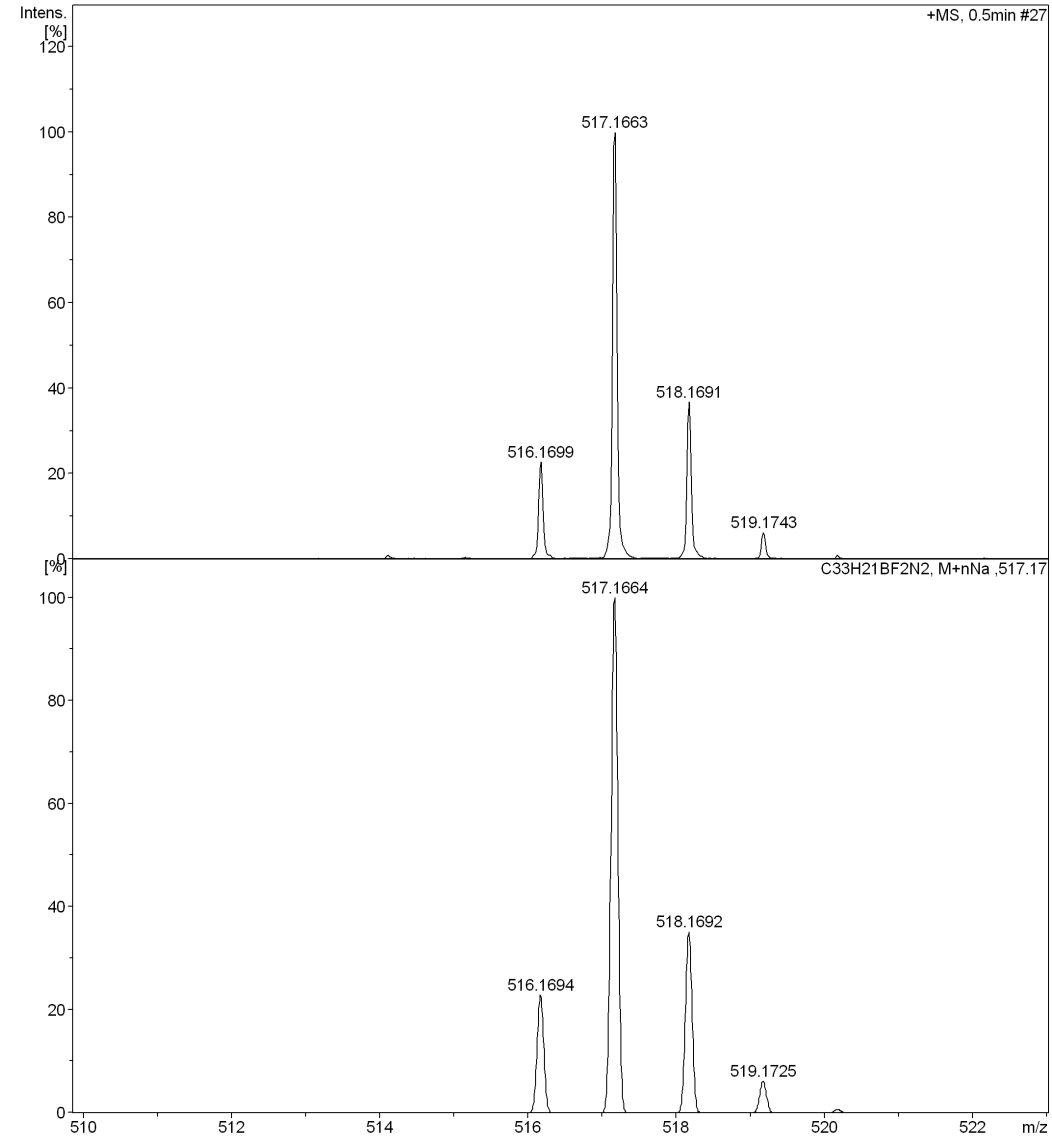

Bruker Compass DataAnalysis 4.0 printed: 6/1/2015 2:20:24 PM Page 1 of 1

Figure II.S22 – HRMS of BbF **10**

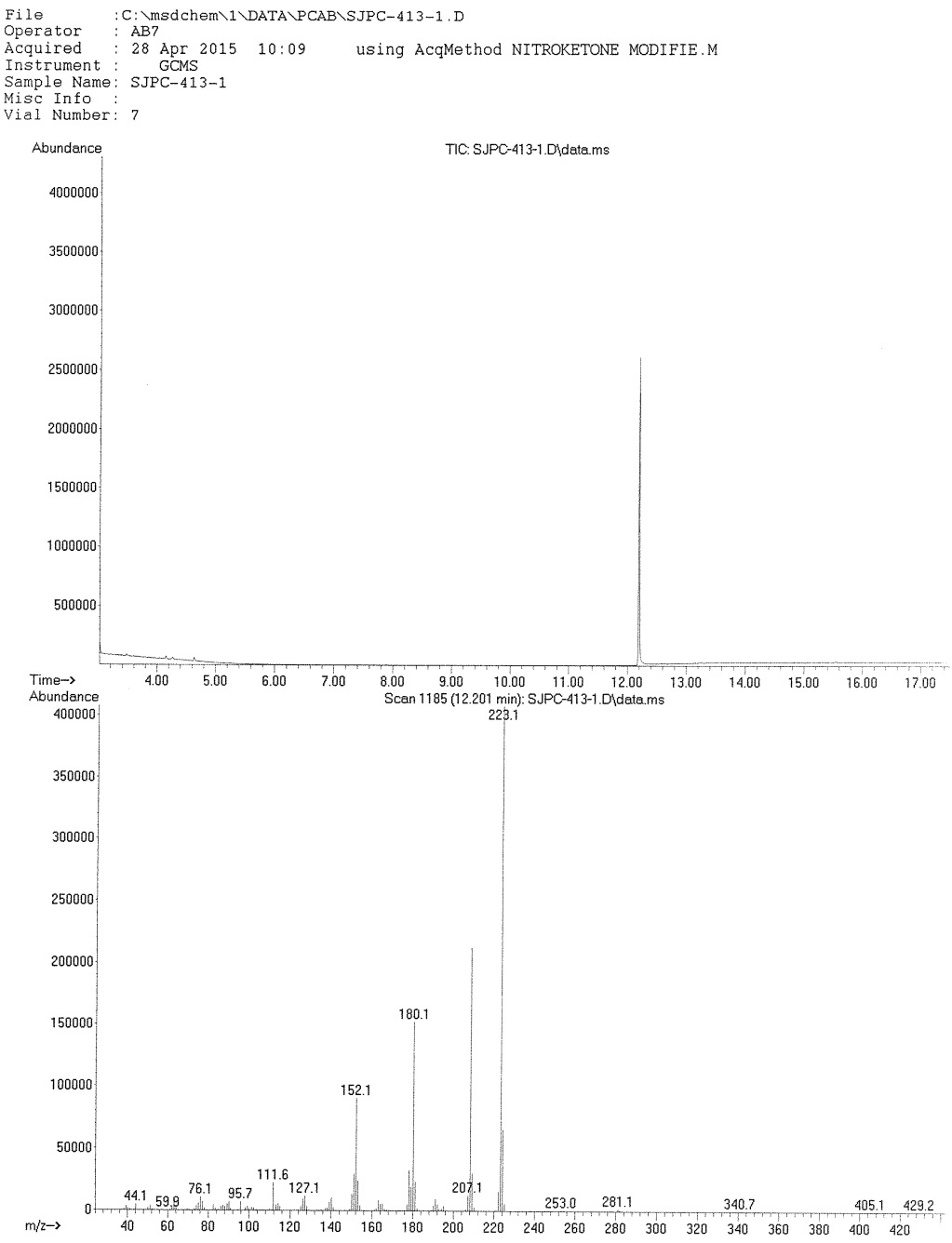

Figure II.S23 – GC-MS of 2-(6-methoxynaphthalen-2-yl)-1H-pyrrole **19**

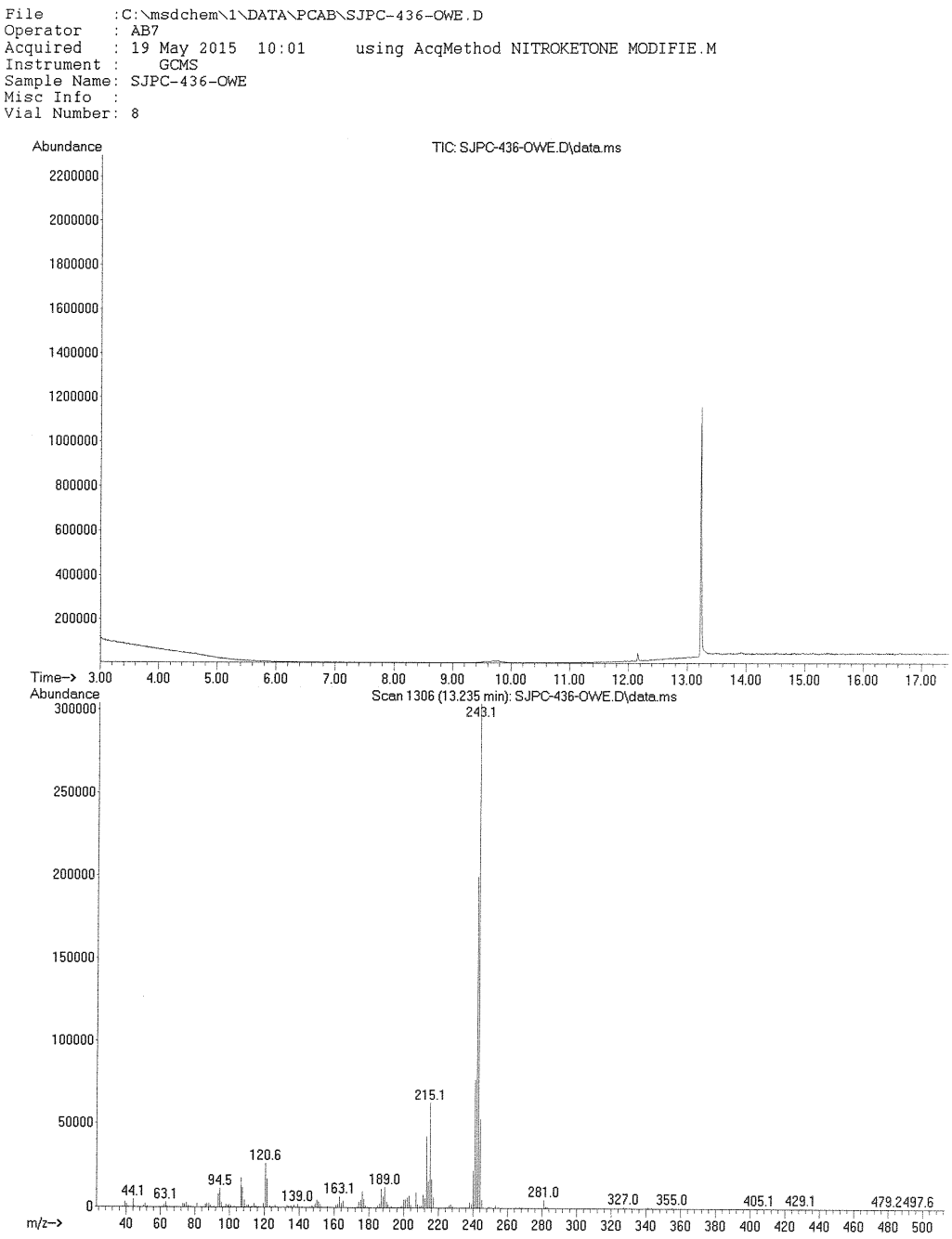

Figure II.S24 – GC-MS of 2-(phenanthren-9-yl)-1H-pyrrole **20**

Spectroscopy

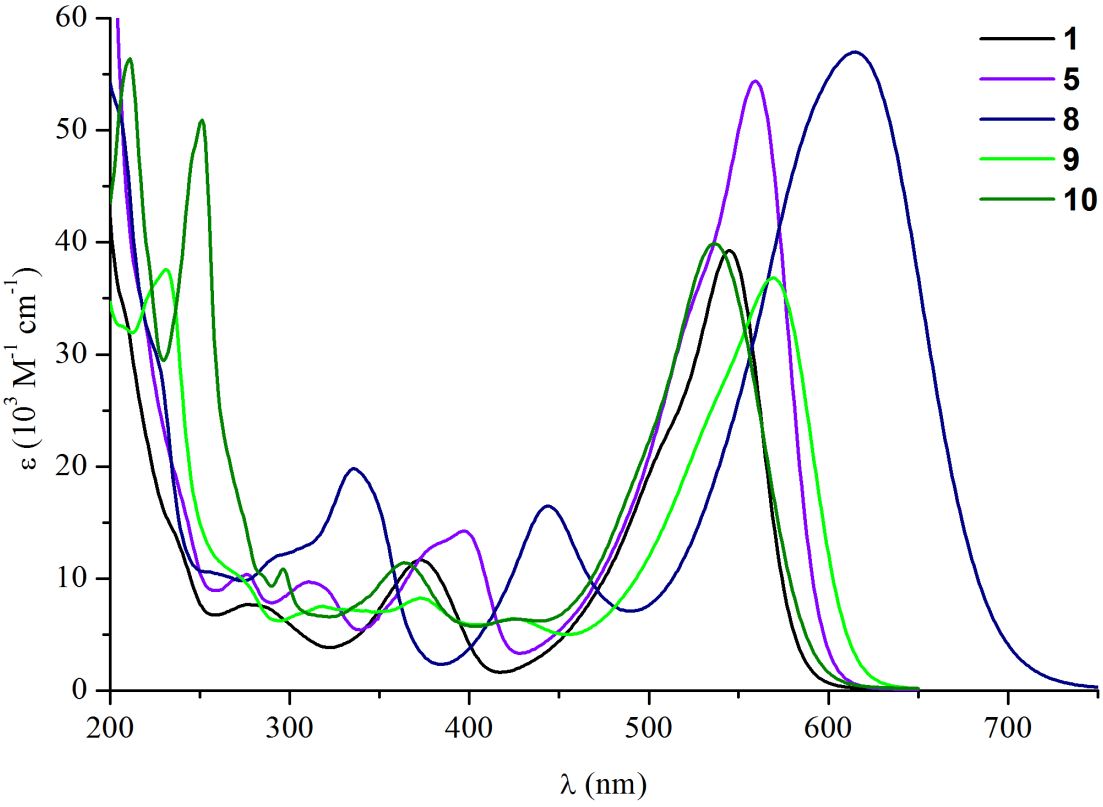

Figure II.S25 – UV/vis absorption spectrum of BbF **1**, **5** and **8** – **10** in ACN solution.

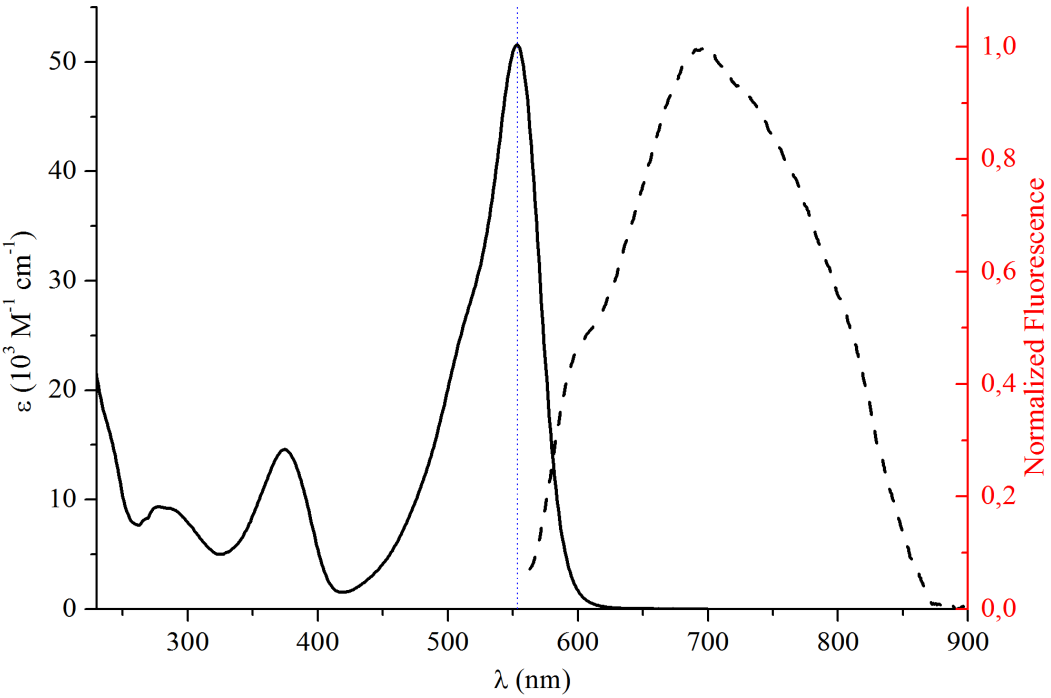

Figure II.S26 – Absorption (solid) and emission spectrum (dash; excitation = 553 nm) of BbF **1** in DCM solution.

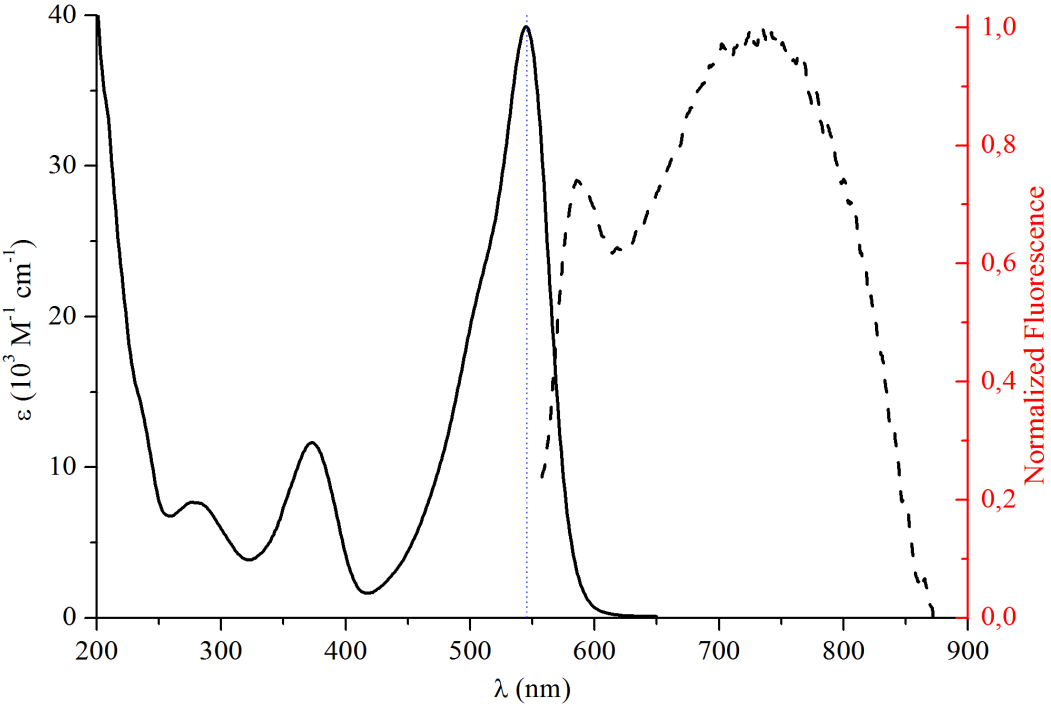

Figure II.S27 – Absorption (solid) and emission spectrum (dash; excitation = 545 nm) of BbF **1** in ACN solution.

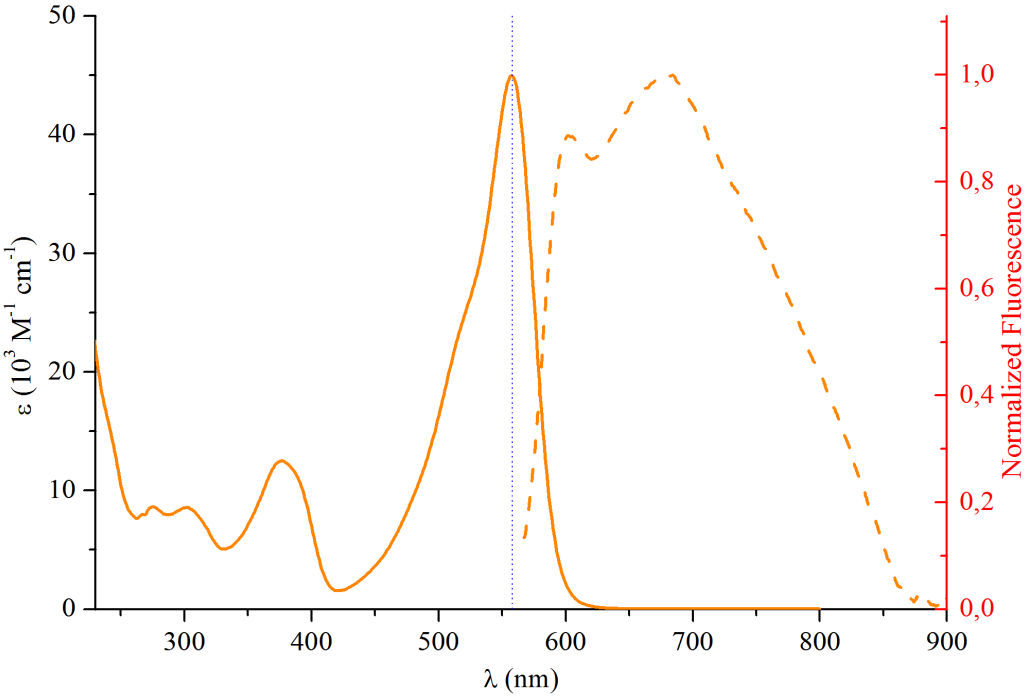

Figure II.S28 – Absorption (solid) and emission spectrum (dash; excitation = 557 nm) of BbF **2** in DCM solution.

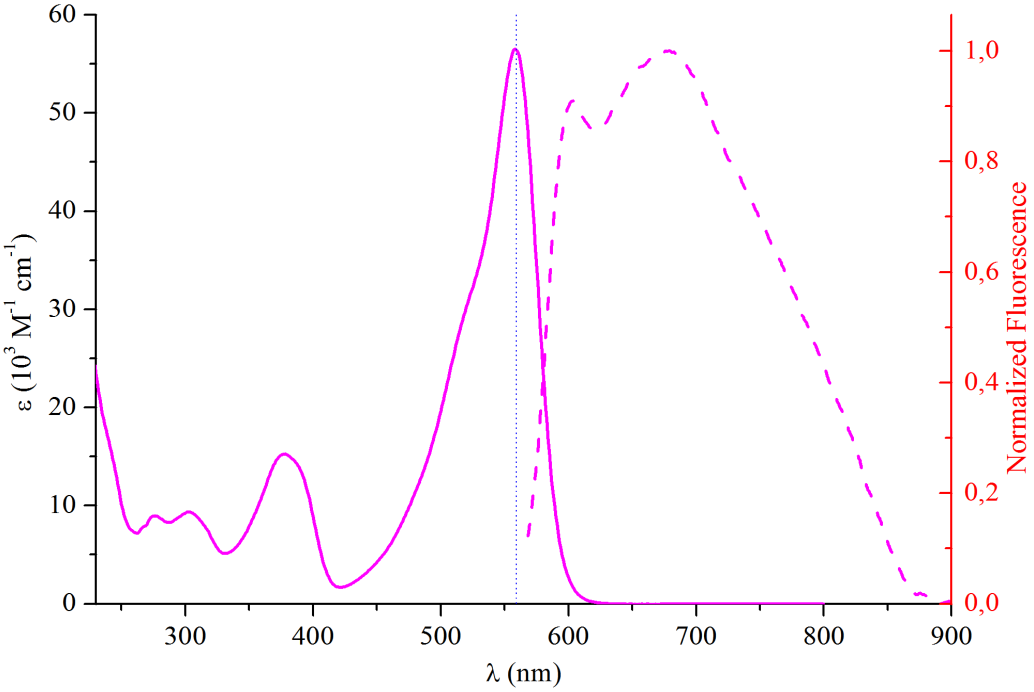

Figure II.S29 – Absorption (solid) and emission spectrum (dash; excitation = 558 nm) of BbF **3** in DCM solution.

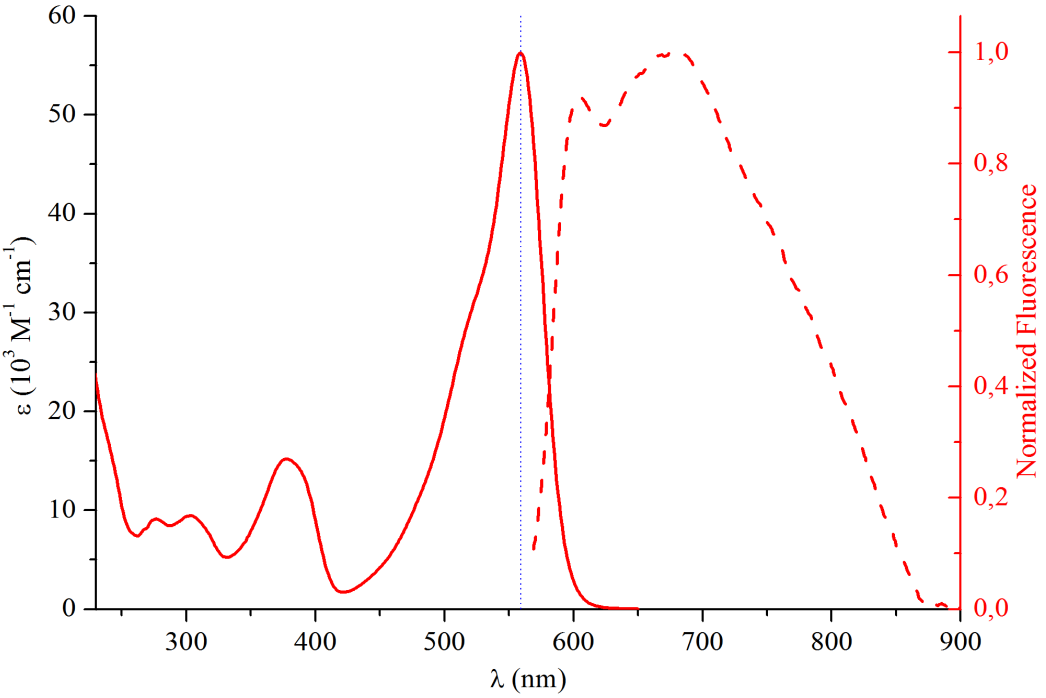

Figure II.S30 – Absorption (solid) and emission spectrum (dash; excitation = 559 nm) of BbF **4** in DCM solution.

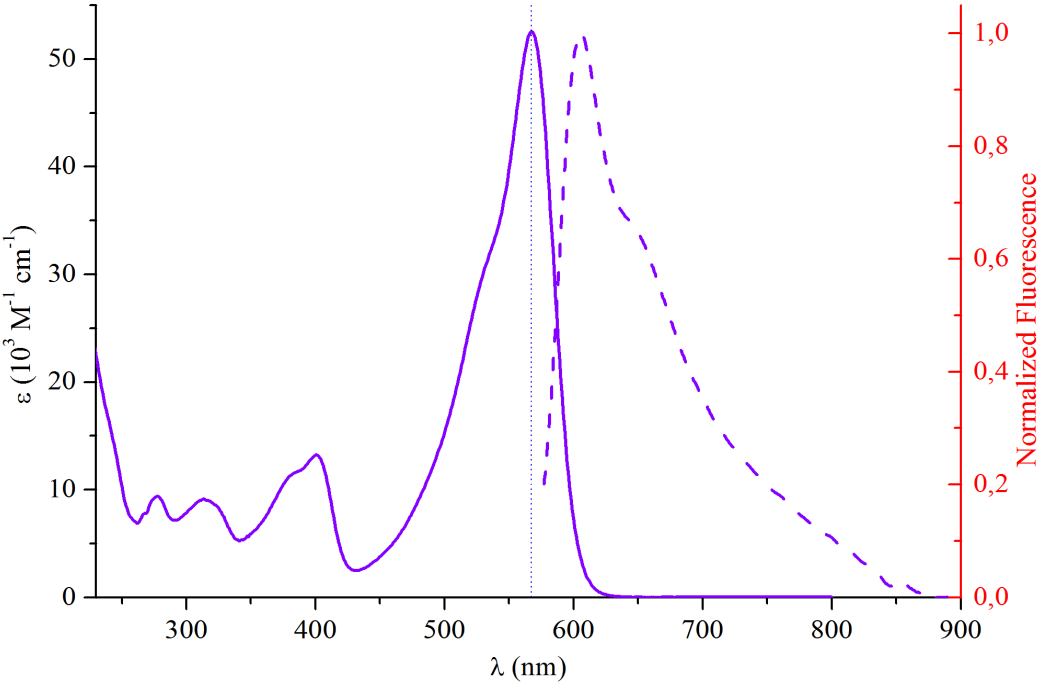

Figure II.S31 – Absorption (solid) and emission spectrum (dash; excitation = 567 nm) of BbF **5** in DCM solution.

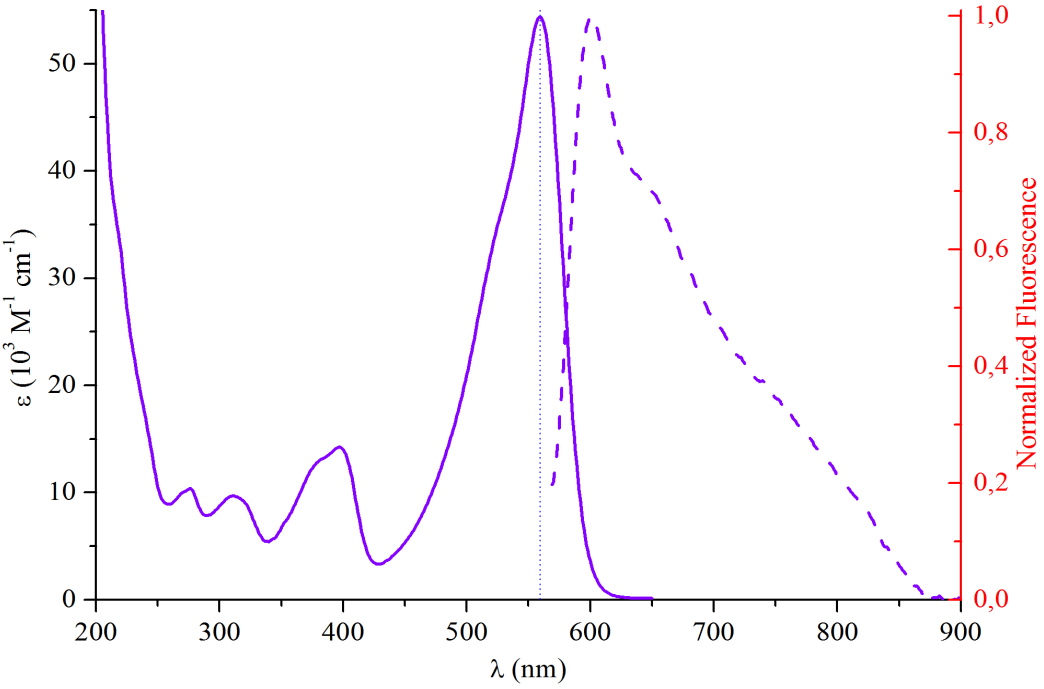

Figure II.S32 – Absorption (solid) and emission spectrum (dash; excitation = 559 nm) of BbF **5** in ACN solution.

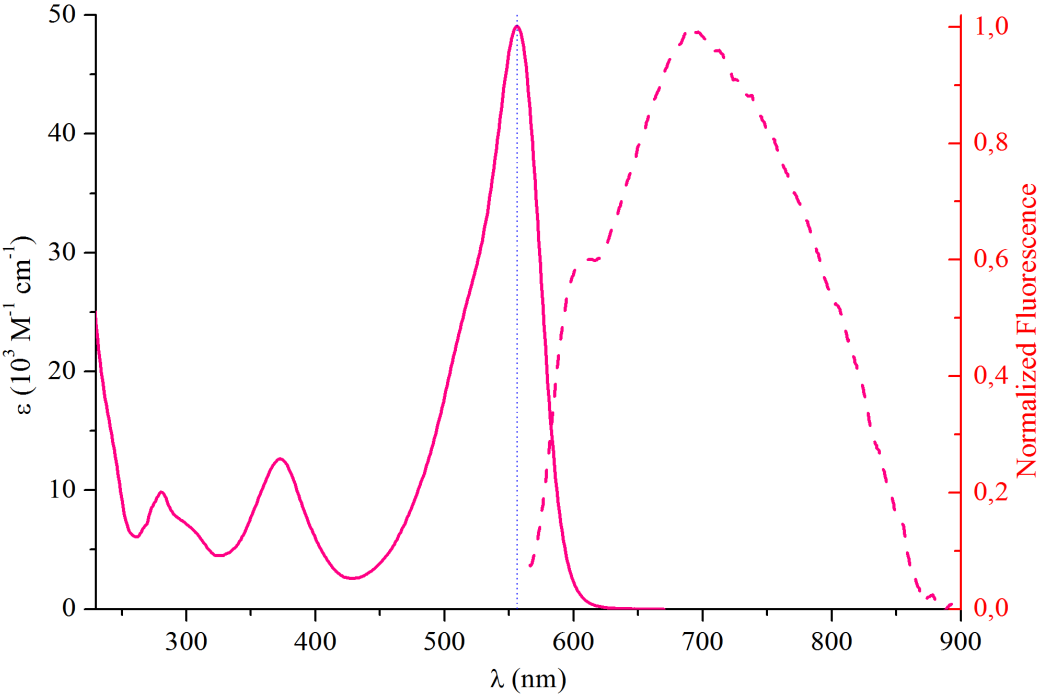

Figure II.S33 – Absorption (solid) and emission spectrum (dash; excitation = 556 nm) of BbF **6** in DCM solution.

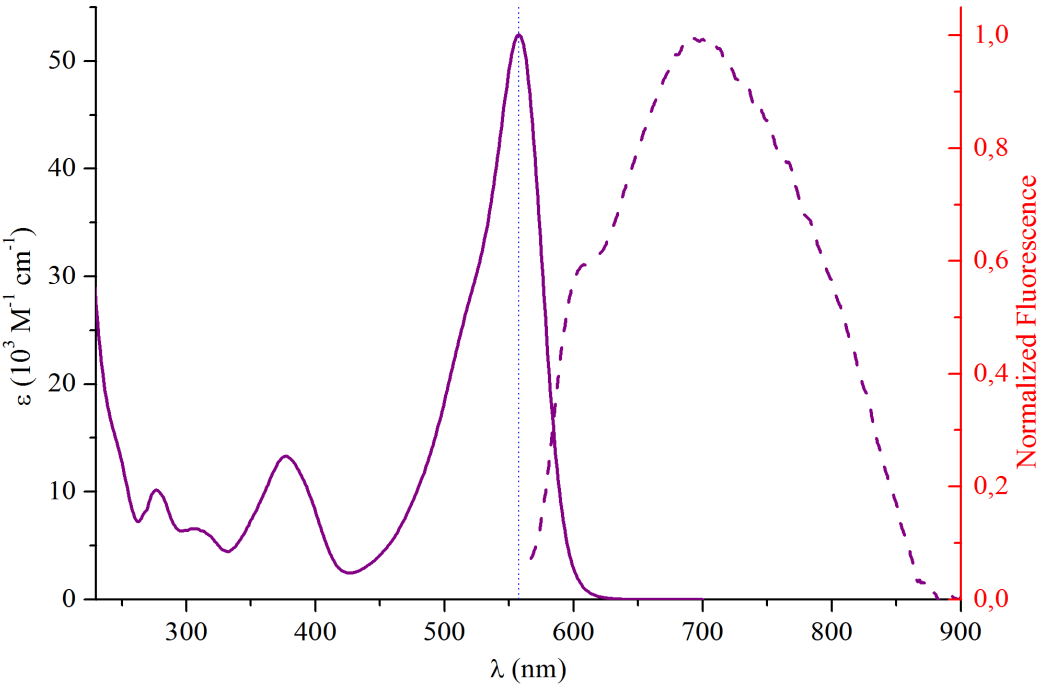

Figure II.S34 – Absorption (solid) and emission spectrum (dash; excitation = 557 nm) of BbF **7** in DCM solution.

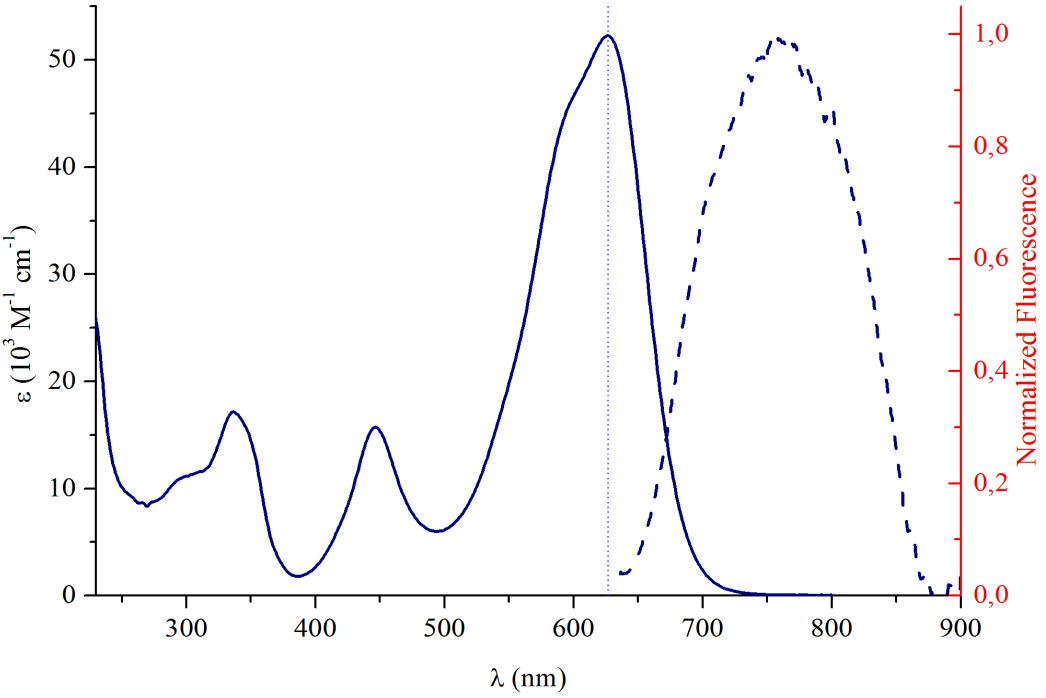

Figure II.S35 – Absorption (solid) and emission spectrum (dash; excitation = 626 nm) of BbF **8** in DCM solution.

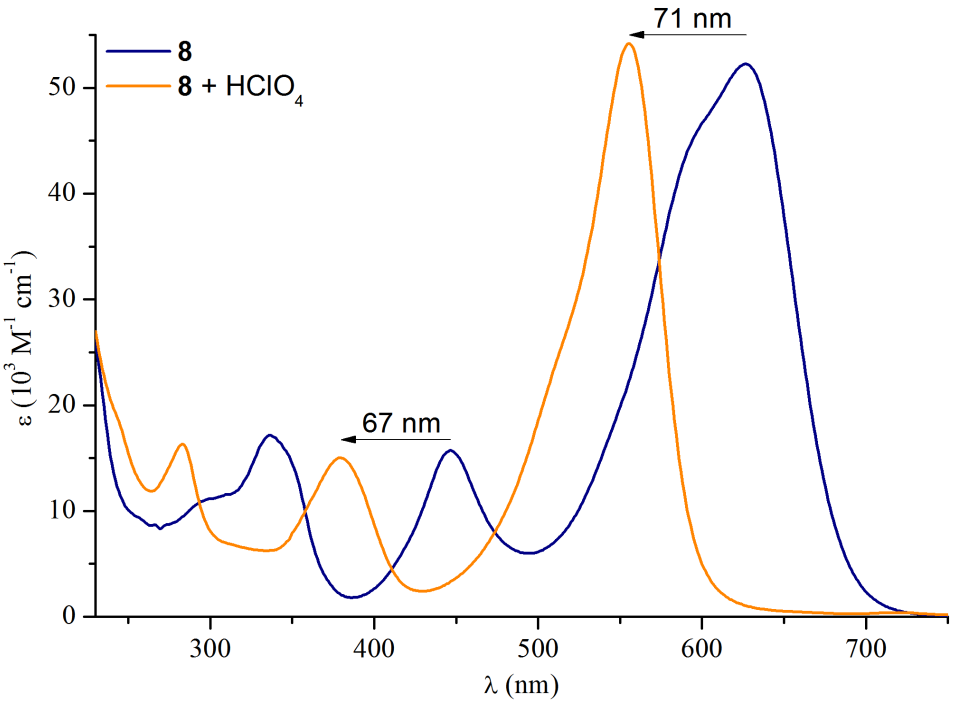

Figure II.S36 – UV/vis absorption spectrum of BbF **8** before (blue) and after (orange) addition of an excess of $HClO_4$ in DCM solution.

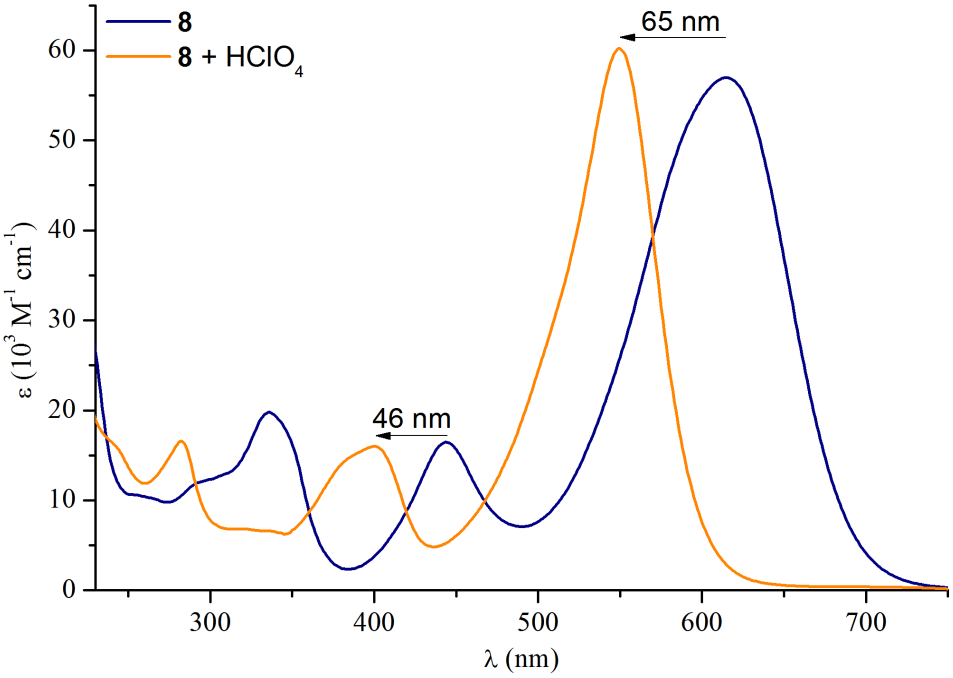

Figure II.S37 – UV/vis absorption spectrum of BbF **8** before (blue) and after (orange) addition of an excess of $HClO_4$ in ACN solution.

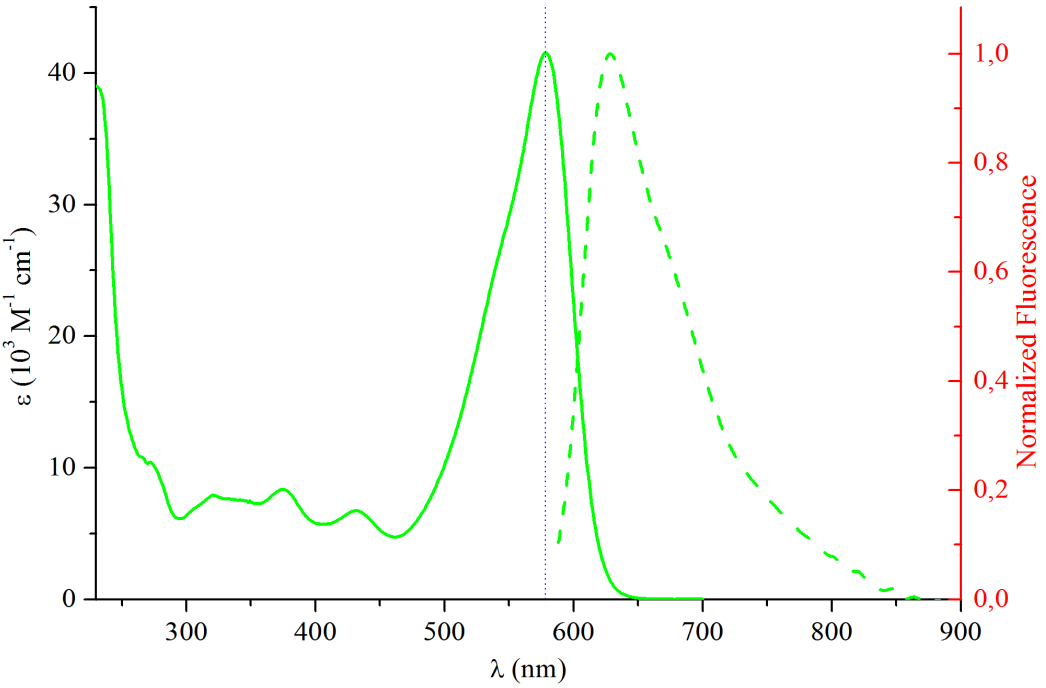

Figure II.S38 – Absorption (solid) and emission spectrum (dash; excitation = 578 nm) of BbF **9** in DCM solution.

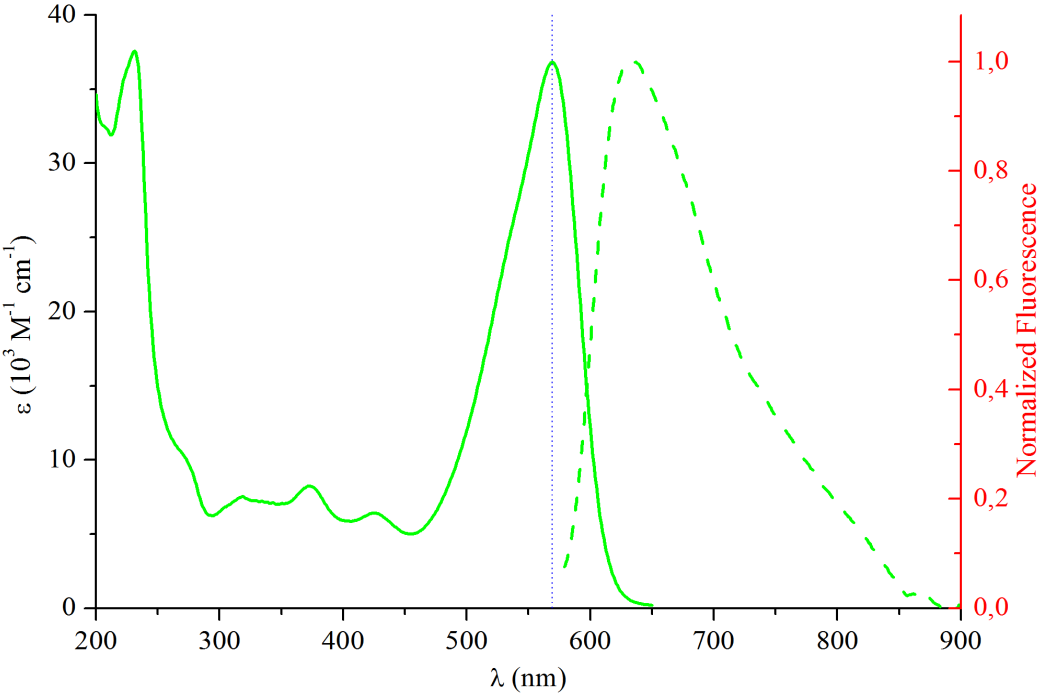

Figure II.S39 – Absorption (solid) and emission spectrum (dash; excitation = 569 nm) of BbF **9** in ACN solution.

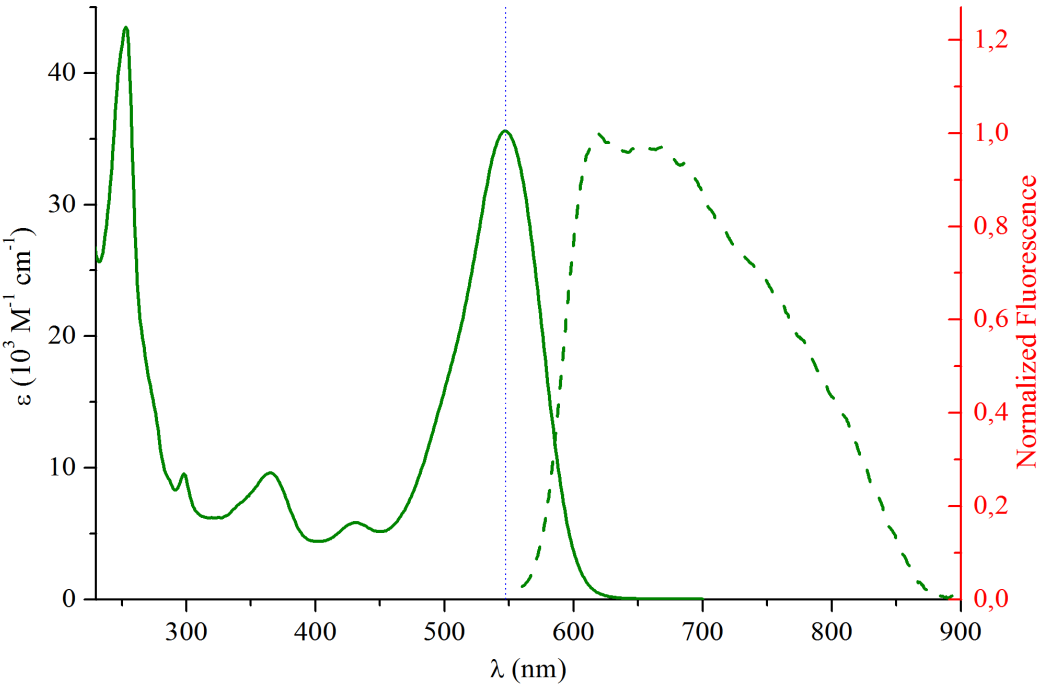

Figure II.S40 – Absorption (solid) and emission spectrum (dash; excitation = 547 nm) of BbF **10** in DCM solution.

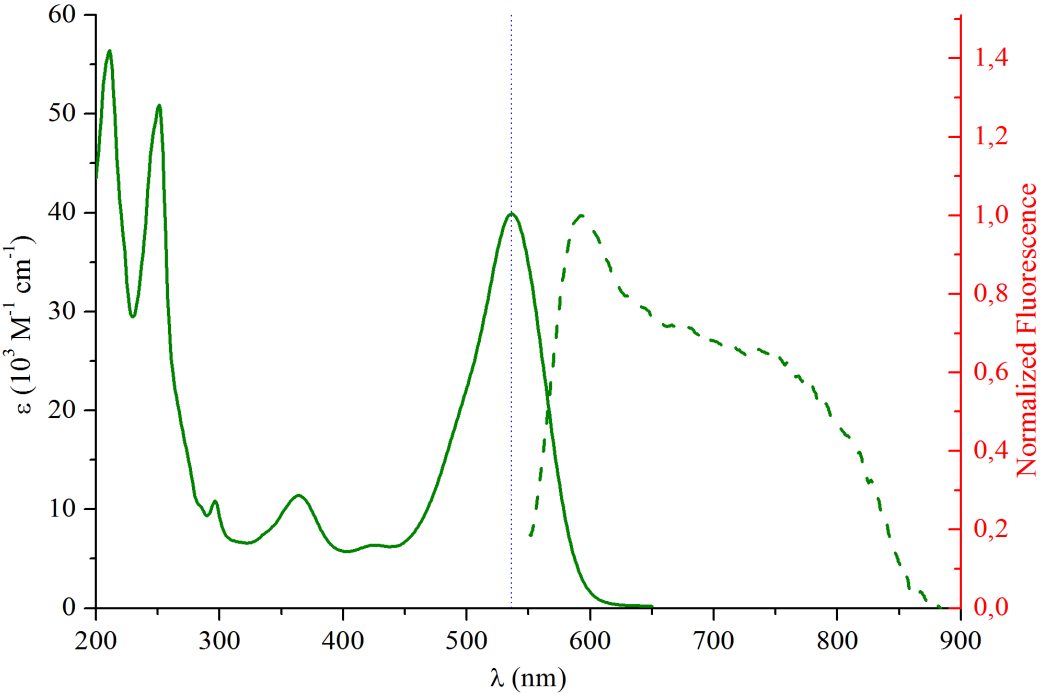

Figure II.S41 – Absorption (solid) and emission spectrum (dash; excitation = 536 nm) of BbF **10** in ACN solution.

Table II.S1 - Compilation of the optoelectronic properties for related BODIPYs of interest previously reported in literature.

	Spectroscopy [a]							Electrochemistry [b]						
	Solvent	**$\lambda_{Abs\ max}$**	**λ_{Em}**	**Δ_{Stoke} (cm^{-1})**	**Φ_F**	**τ (ns)**	**Ref**	**Solvent**	**E_{Ox}**	**E_{Red}**	**HOMO redox**	**LUMO redox**	**ΔE_{Ox}**	**Ref**
22	$CHCl_3$	504 (14)	512	311	0.70	5.0	19	DCM	1.61*	-0.73*	-6.56	-4.22	2.34	19
23	$CHCl_3$	504 (58)	521	620	0.06	0.45	19	DCM	1.65*	-0.73; -1.71*	-6.60	-4.22	2.38	20
	DCM	500 (33)	527	1025	0.03	NA	21							
24	DCM	501 (87)	513	467	0.67	3.51	22	DCM	1.51	-1.22*	-6.46	-3.73	2.73	23
	ACN	497 (48)	511	520	0.52	3.21	24	ACN	1.17	-1.19	-6.12	-3.76	2.36	25
25	ACN	523	547	839	0.015	NA	26							
26	ACN	536	556	671	0.884	NA	27							
27	ACN	552	577	785	0.854	NA	27							
28	ACN	608	NF	---	---	---	27							
	MeOH	608	NF	---	---	---	27							
	MeOH + $HClO_4$	535	554	641	0.54	NA	27							
29	ACN	547	572	799	0.77	NA	27							
30	DCM	512 (42)	655	4264	~0.10	NA	23	DCM	1.57*	-0.78	-6.52	-4.17	2.35	23
31	THF	539 (54)	690	4060	<0.01	NA	1	DCM	1.51*	-0.59; -1.63	-6.46	-4.36	2.10	1
32	DCM	568 (~34)	NF	---	---	---	23	DCM	1.66*	-0.24	-6.61	-4.71	1.90	23
33	DCM	570	599	849	0.80	NA	28							
34	DCM	631 (102)	664	788	0.93	5.2	29	DCM	0.83; 1.68*	-1.08	-5.78	-3.87	1.91	29
35	DCM	617 (108)	652	870	0.91	5.8	29	DCM	0.78; 1.63*	-1.17	-5.73	-3.78	1.95	29
36	$CHCl_3$	542 (140)	549	235	0.96	NA	30							
37	$CHCl_3$	579 (202)	583	118	0.96	NA	31							
38	$CHCl_3$	652 (314)	661	447	0.90	NA	30							
39	$CHCl_3$	673 (288)	683	218	0.86	NA	31							
40	$CHCl_3$	671 (313)	680	197	0.91	NA	30							
41	$CHCl_3$	662 (316)	671	203	0.97	NA	30							

42	DCM	518 (56) / 770 (br)	NF	---	---	---	23	DCM	1.24	-0.39; -1.15	-6.19	-4.56	1.63	23
43	DCM	482 (~55)	528	1810	Very Low	NA	32	DCM	0.95; 1.12	-1.39	-5.90	-3.56	2.34	32
44	DCM	516 (36)	546	1065	0.66	NA	33							
45	DCM	578 (105)	603	1083	0.97	NA	34							

[a] NF = Non-Fluorescent / NA = Non-Available. For compound **43**, only the mention "very low" can be found in the reference regarding the quantum yields.

[b] Reported *vs* SCE. * = Irreversible process. The values reported herein for compounds **23**, **24**, **30**-**32**, **34**, **35**, **42** and **43** were corrected *vs* SCE using Fc^{+}/Fc = 0.46V in DCM.

Electrochemistry

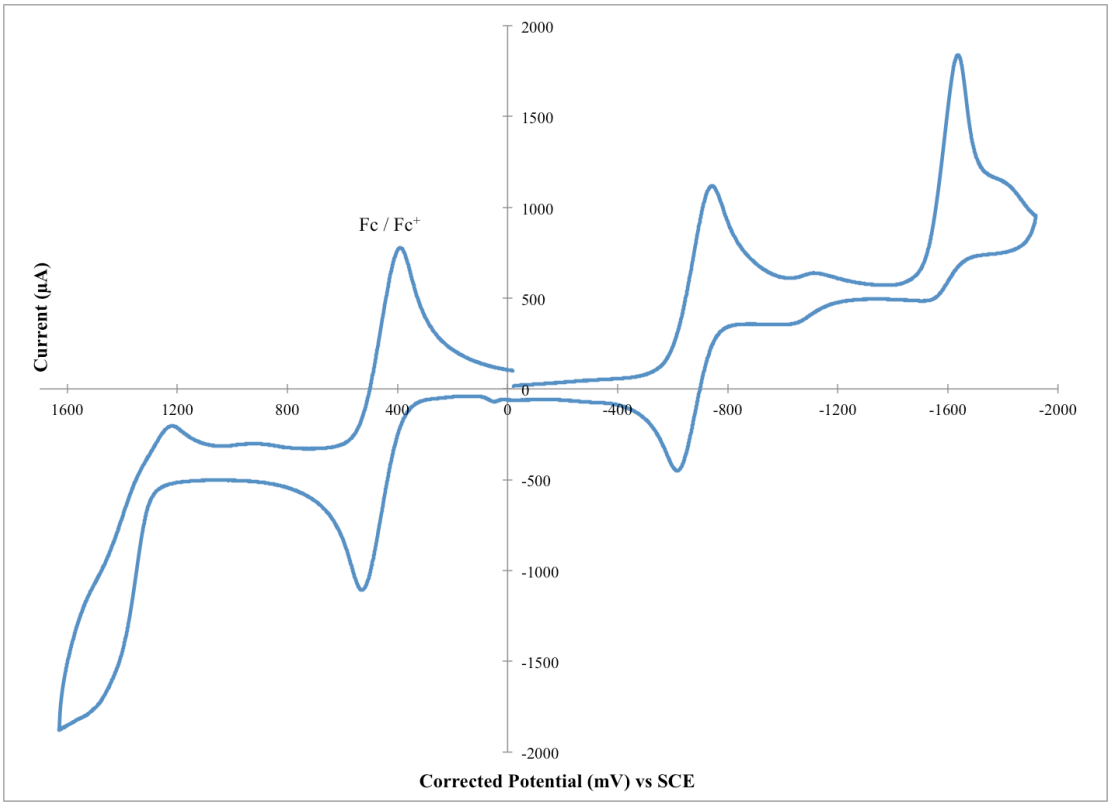

Figure II.S42 – CV of BbF **1** with ferrocene internal reference. (Fc = 0.46 V vs SCE in DCM; Scan rate of 50 mV/s at R.T.)

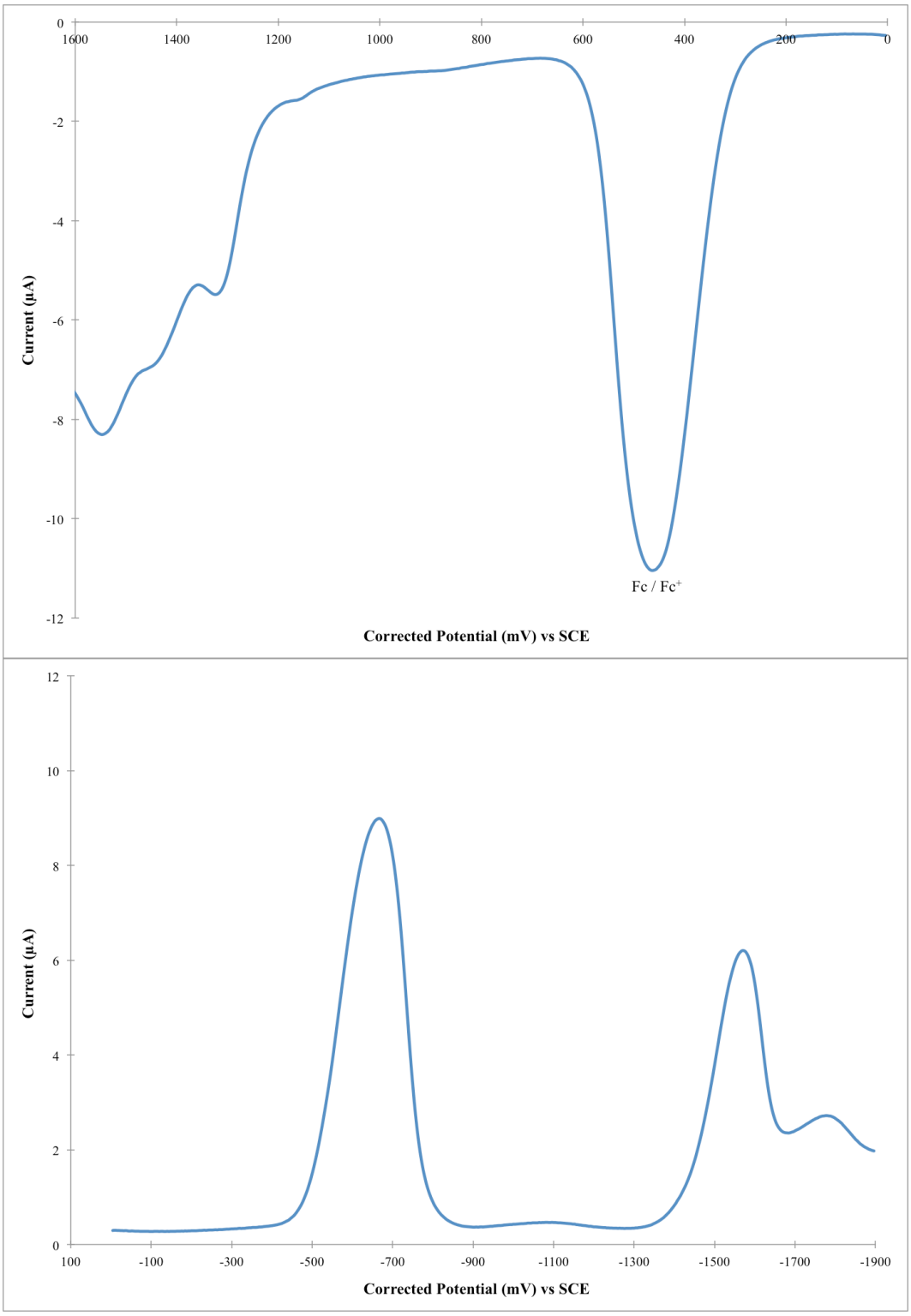

Figure II.S43 – DPV of oxidation (top) and reduction (bottom) potentials for BbF **1** with ferrocene internal reference. (0.46 V vs SCE in DCM) (Scan rate of 50 mV/s at R.T.)

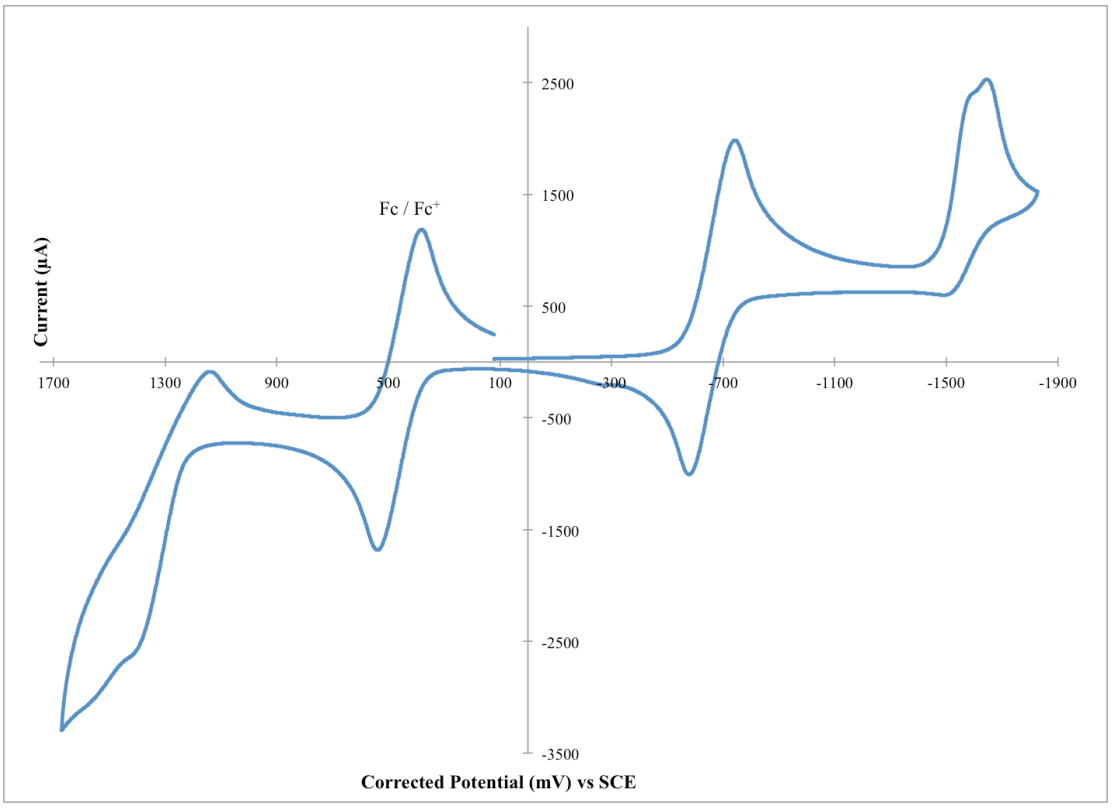

Figure II.S44 – CV of BbF **2** with ferrocene internal reference. (Fc = 0.46 V vs SCE in DCM; Scan rate of 50 mV/s at R.T.)

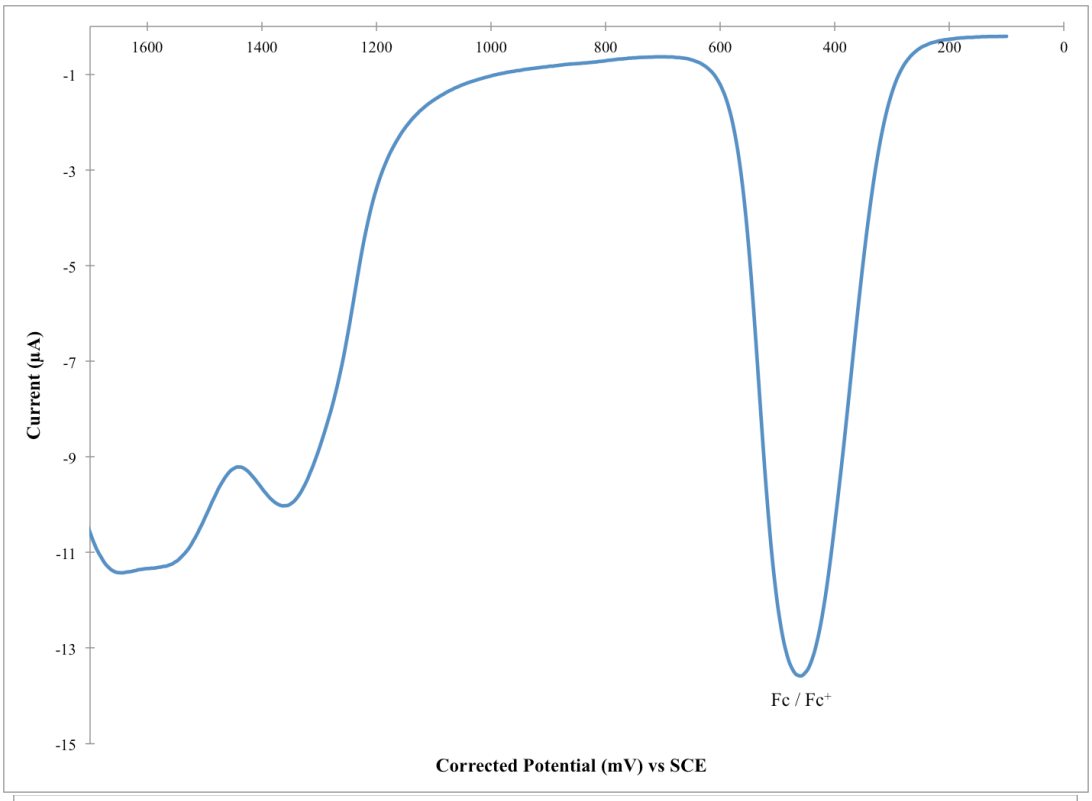

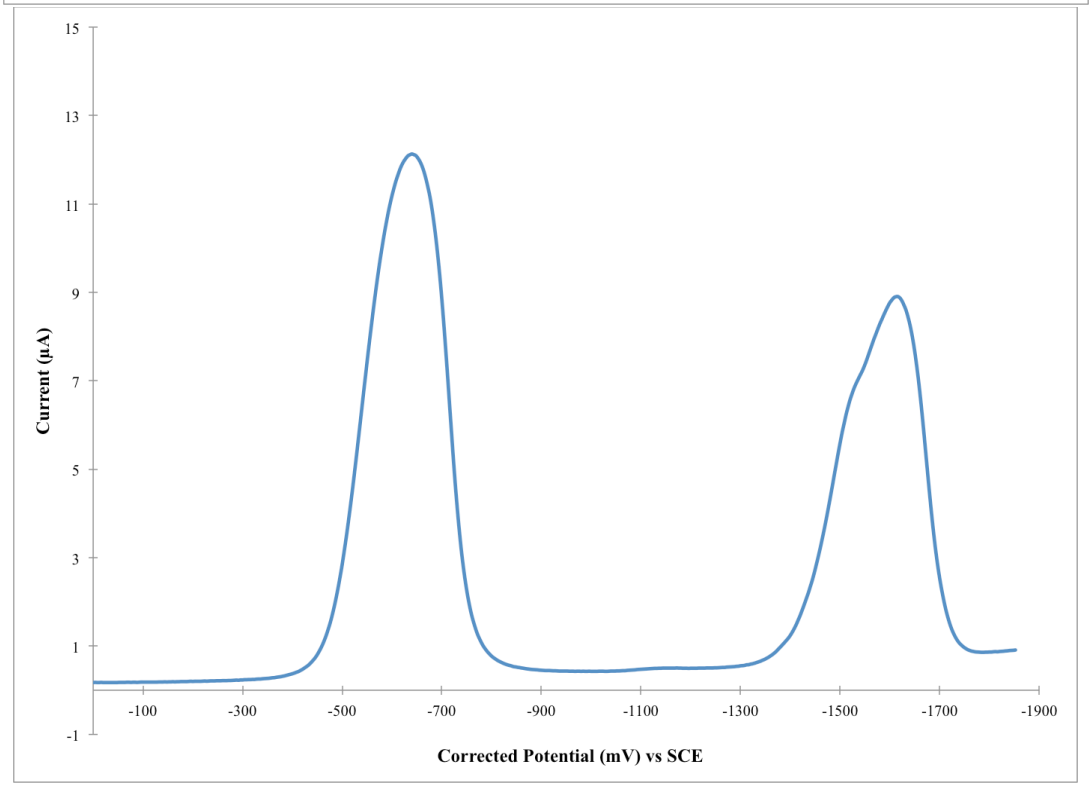

Figure II.S45 – DPV of oxidation (top) and reduction (bottom) potentials for BbF **2** with ferrocene internal reference. (0.46 V vs SCE in DCM) (Scan rate of 50 mV/s at R.T.)

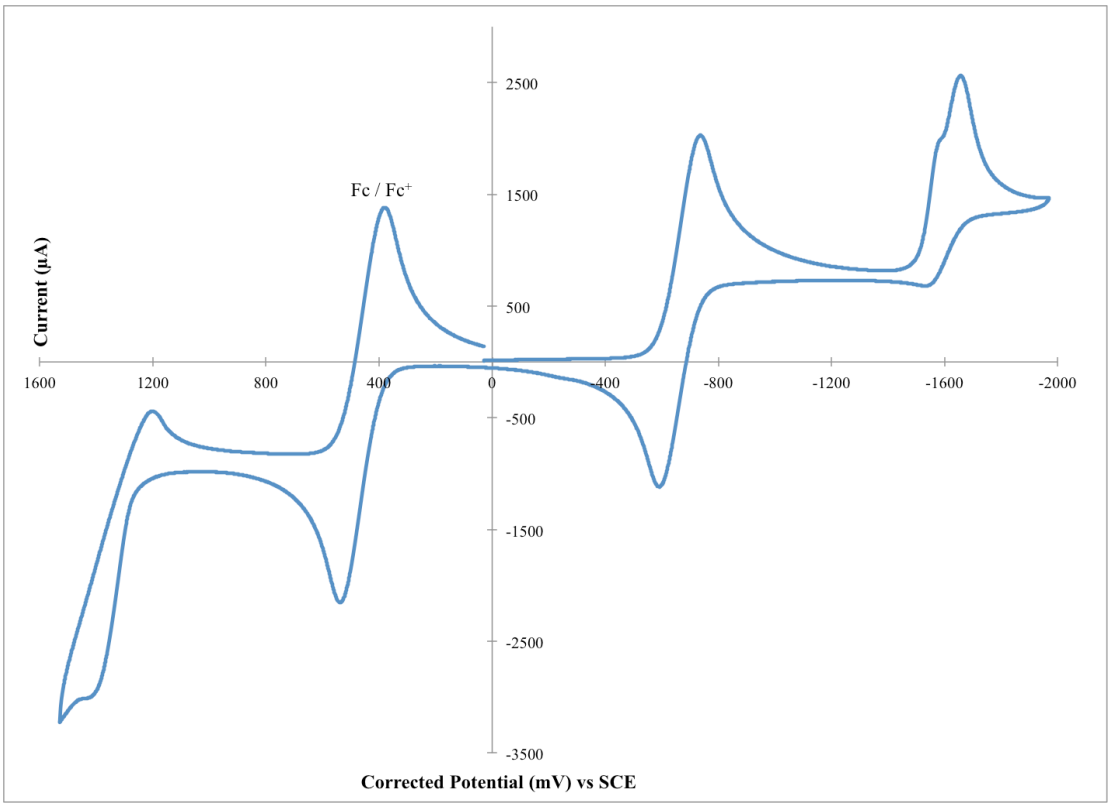

Figure II.S46 – CV of BbF **3** with ferrocene internal reference. (Fc = 0.46 V vs SCE in DCM; Scan rate of 50 mV/s at R.T.)

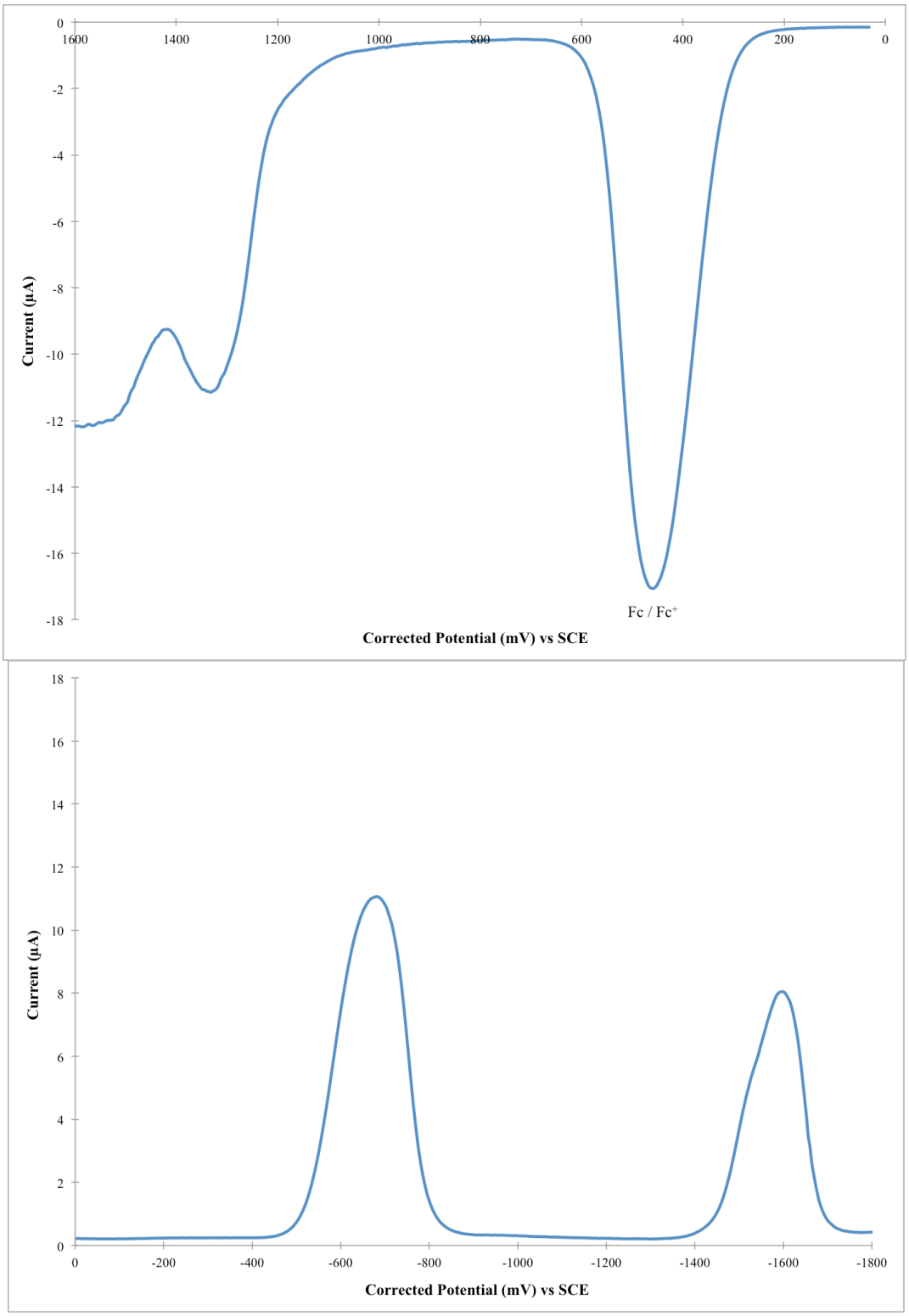

Figure II.S47 – DPV of oxidation (top) and reduction (bottom) potentials for BbF **3** with ferrocene internal reference. (0.46 V vs SCE in DCM) (Scan rate of 50 mV/s at R.T.)

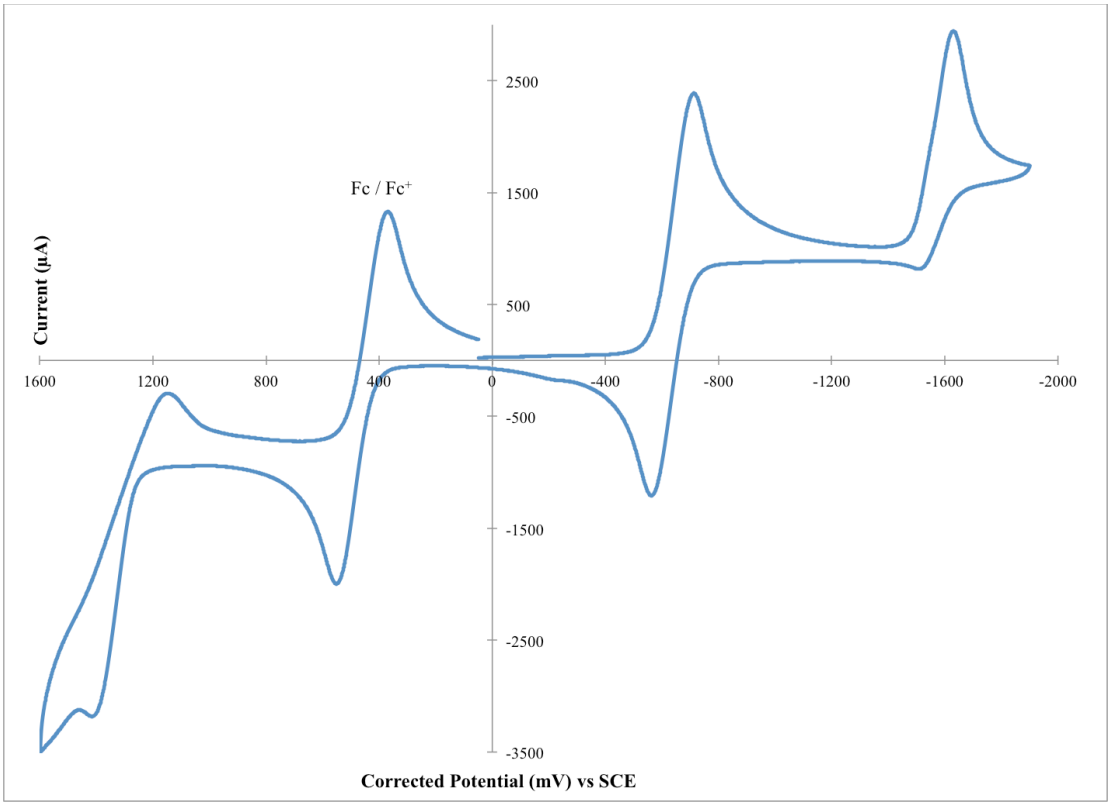

Figure II.S48 – CV of BbF **4** with ferrocene internal reference. (Fc = 0.46 V vs SCE in DCM; Scan rate of 50 mV/s at R.T.)

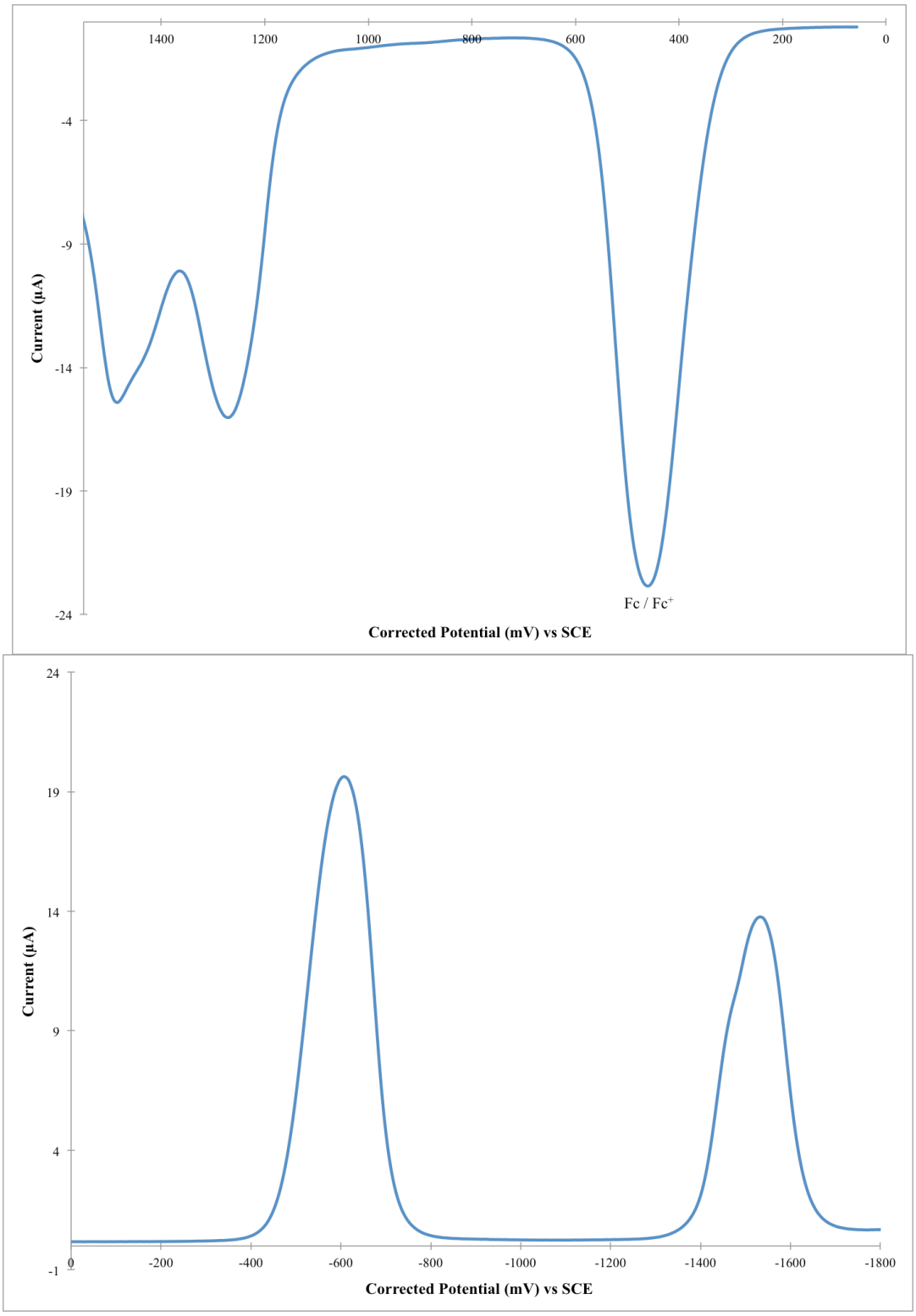

Figure II.S49 – DPV of oxidation (top) and reduction (bottom) potentials for BbF **4** with ferrocene internal reference. (0.46 V vs SCE in DCM) (Scan rate of 50 mV/s at R.T.)

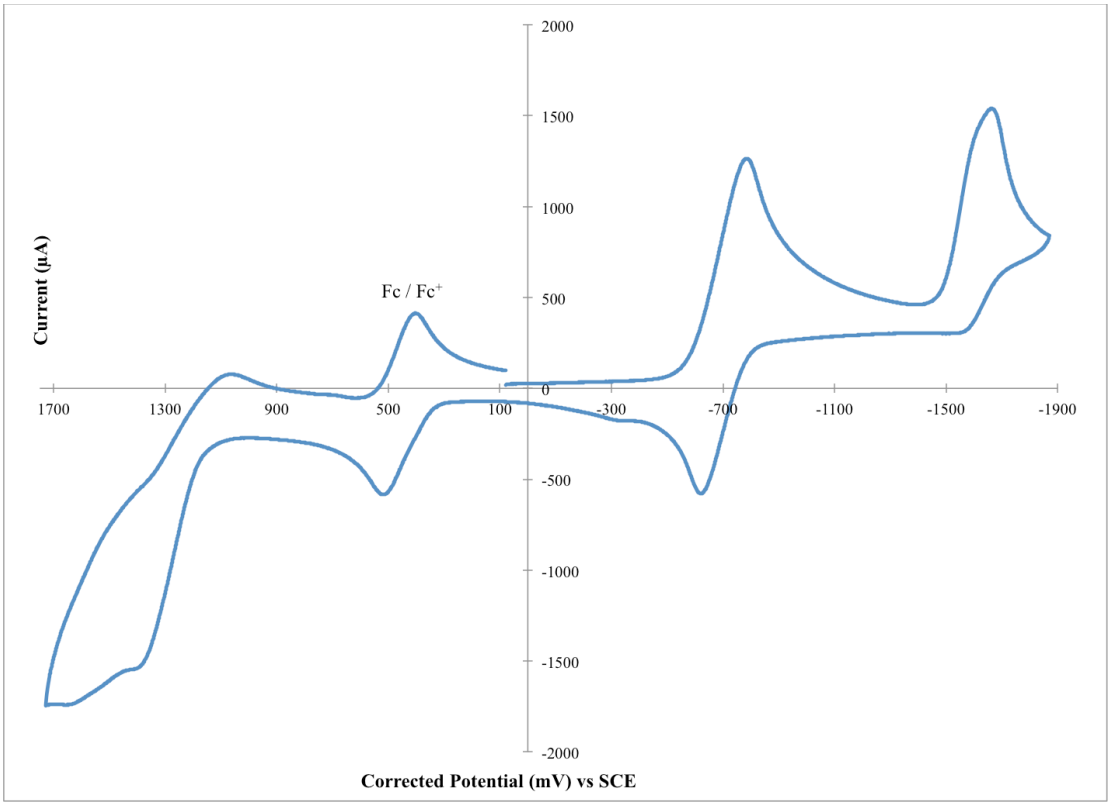

Figure II.S50 – CV of BbF **5** with ferrocene internal reference. (Fc = 0.46 V vs SCE in DCM; Scan rate of 50 mV/s at R.T.)

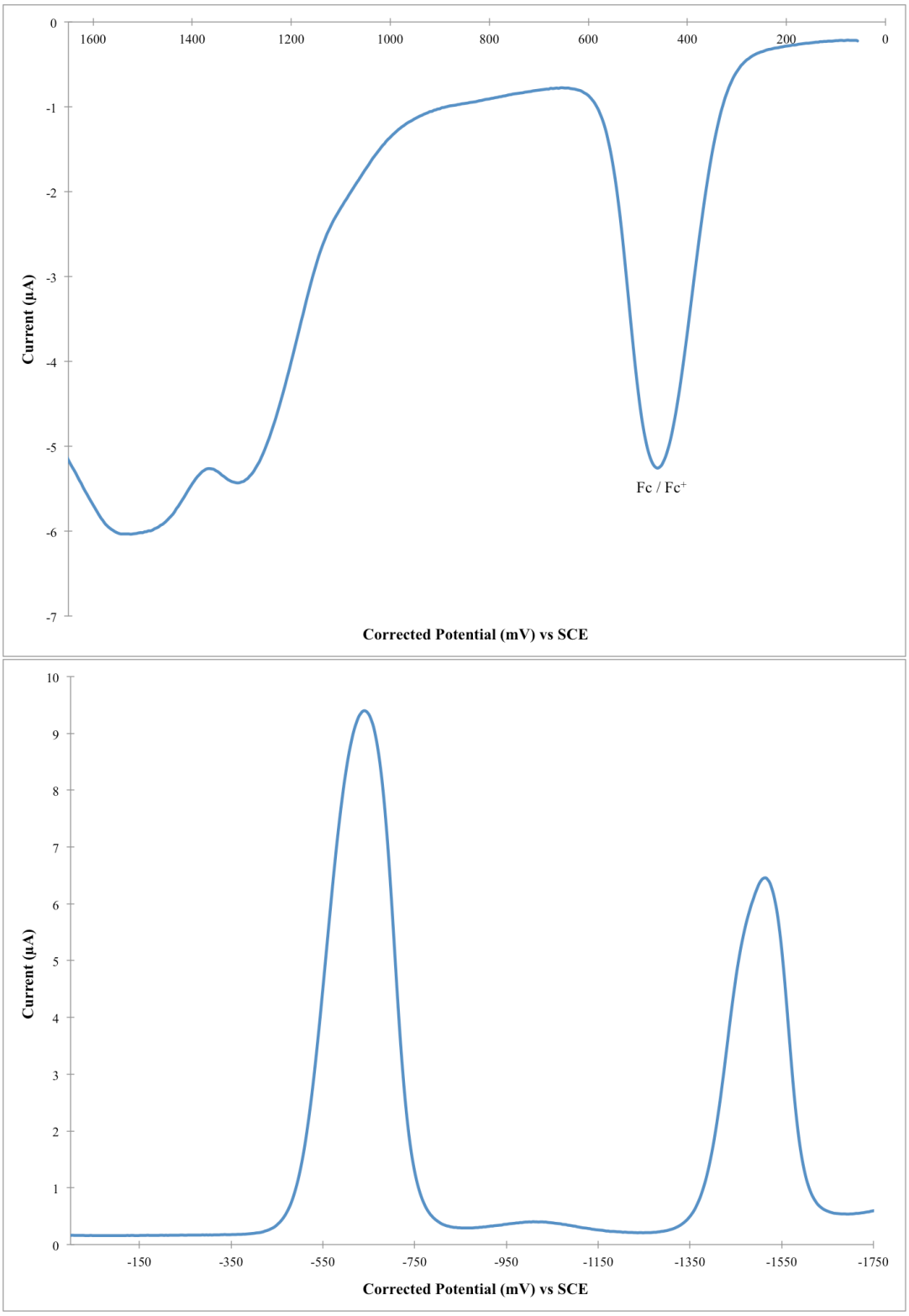

Figure II.S51 – DPV of oxidation (top) and reduction (bottom) potentials for BbF **5** with ferrocene internal reference. (0.46 V vs SCE in DCM) (Scan rate of 50 mV/s at R.T.)

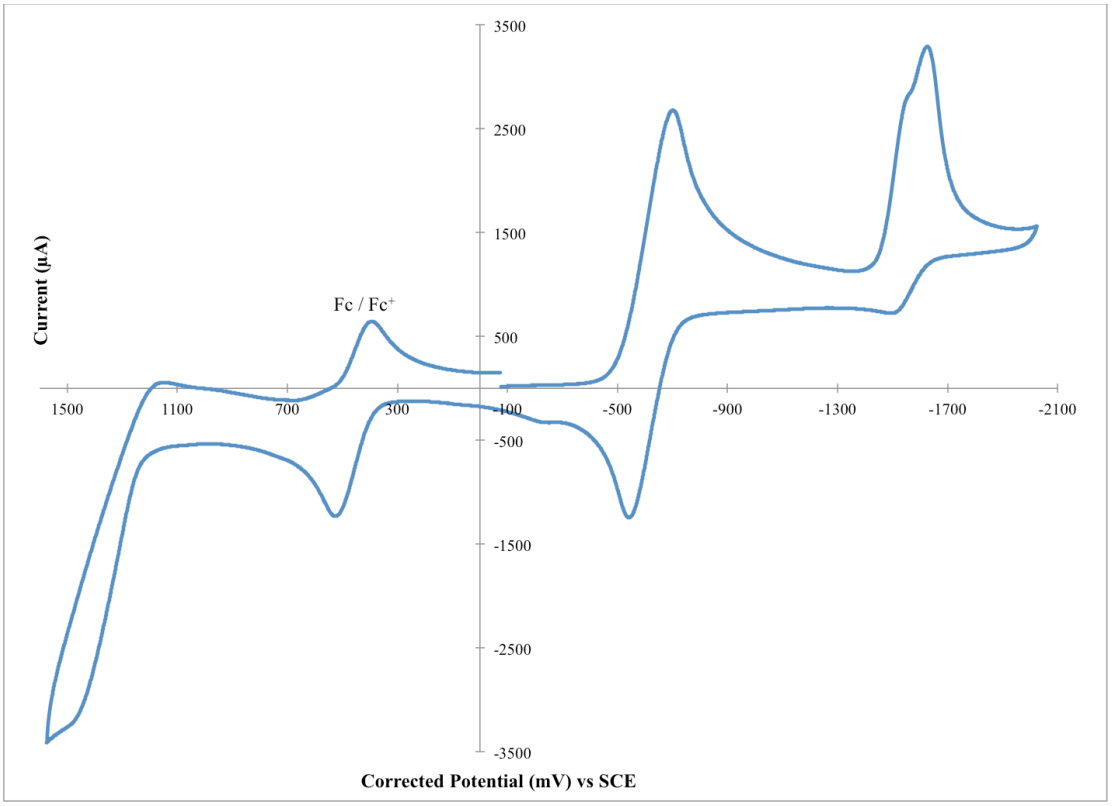

Figure II.S52 – CV of BbF **6** with ferrocene internal reference. (Fc = 0.46 V vs SCE in DCM; Scan rate of 50 mV/s at R.T.)

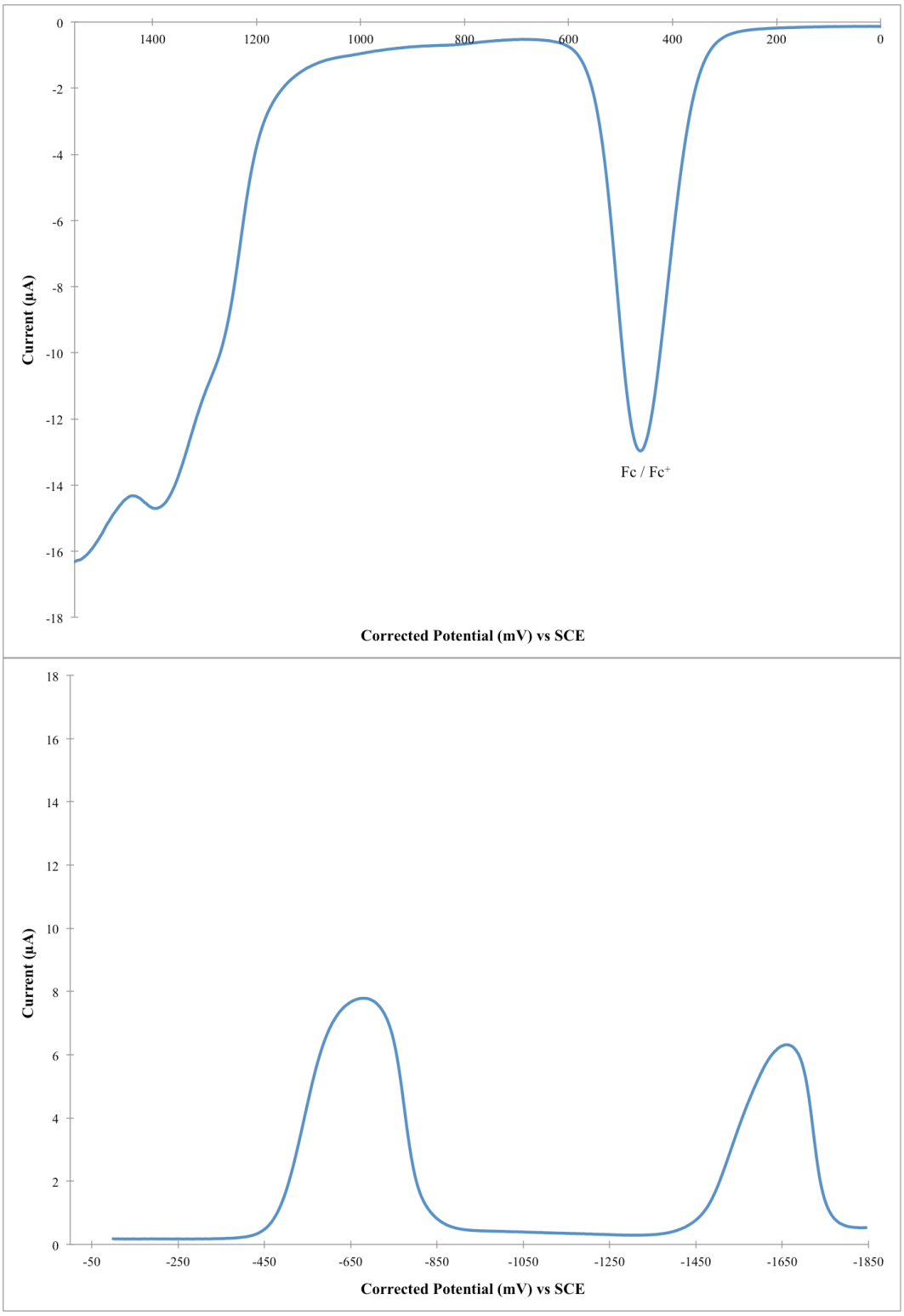

Figure II.S53 – DPV of oxidation (top) and reduction (bottom) potentials for BbF **6** with ferrocene internal reference. (0.46 V vs SCE in DCM) (Scan rate of 50 mV/s at R.T.)

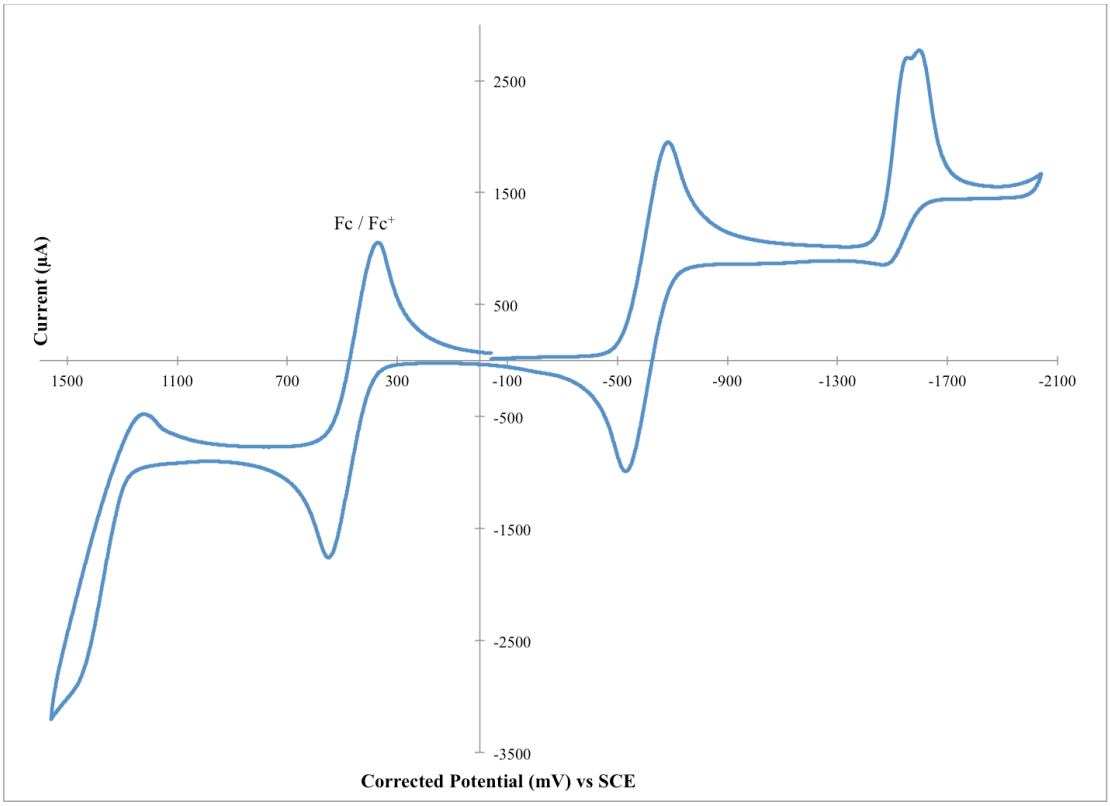

Figure II.S54 – CV of BbF **7** with ferrocene internal reference. (Fc = 0.46 V vs SCE in DCM; Scan rate of 50 mV/s at R.T.)

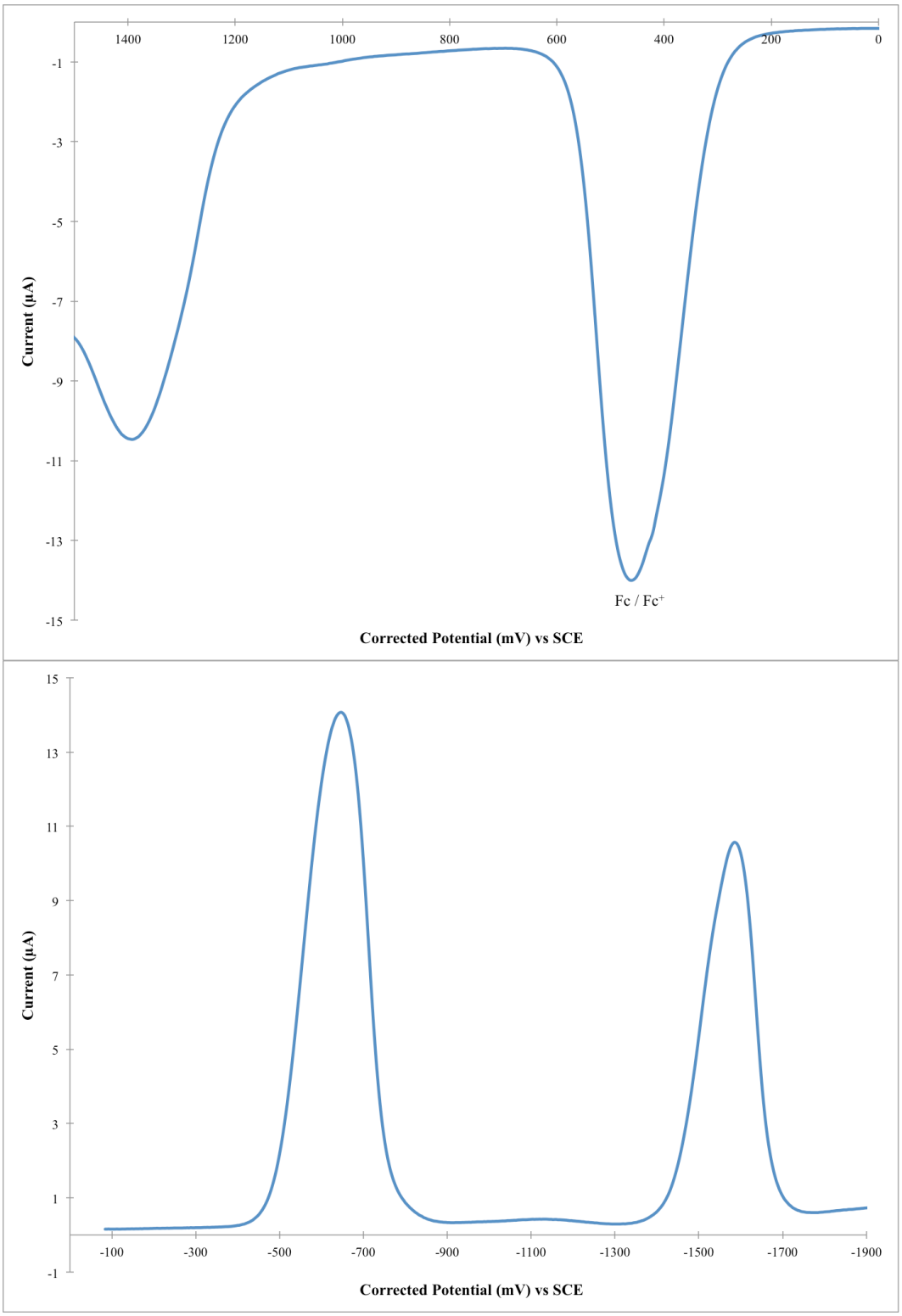

Figure II.S55 – DPV of oxidation (top) and reduction (bottom) potentials for BbF **7** with ferrocene internal reference. (0.46 V vs SCE in DCM) (Scan rate of 50 mV/s at R.T.)

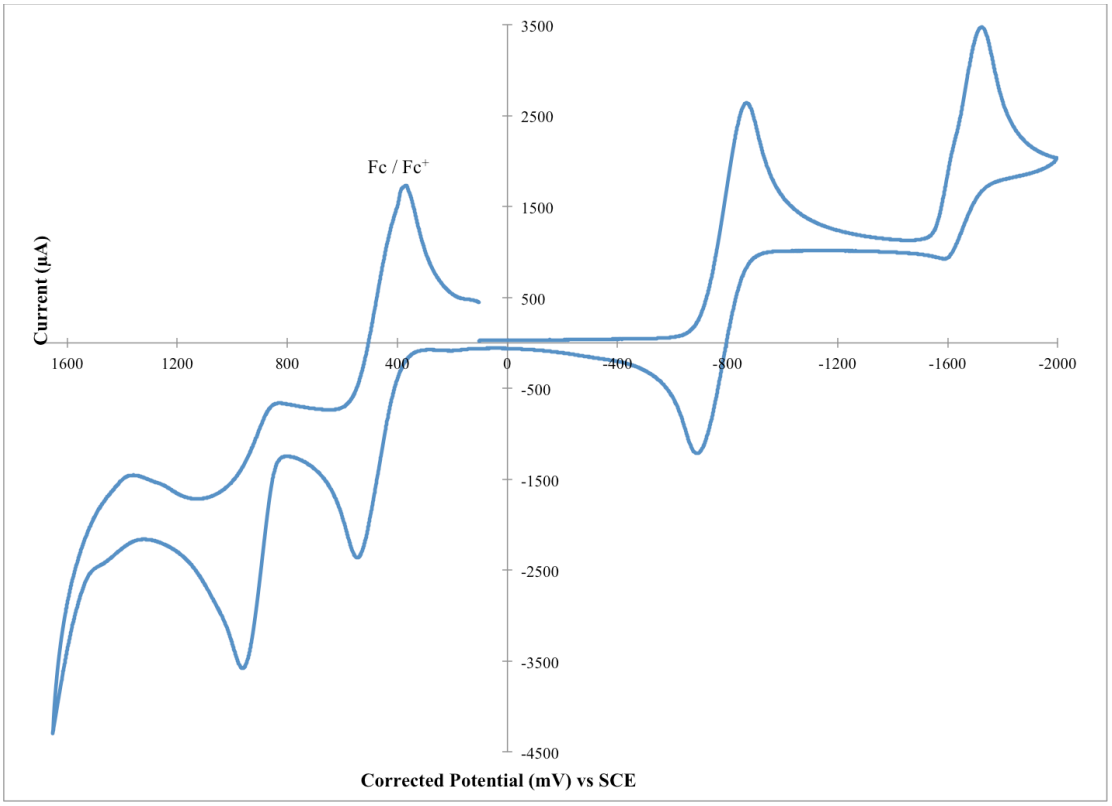

Figure II.S56 – CV of BbF **8** with ferrocene internal reference. (Fc = 0.46 V vs SCE in DCM; Scan rate of 50 mV/s at R.T.)

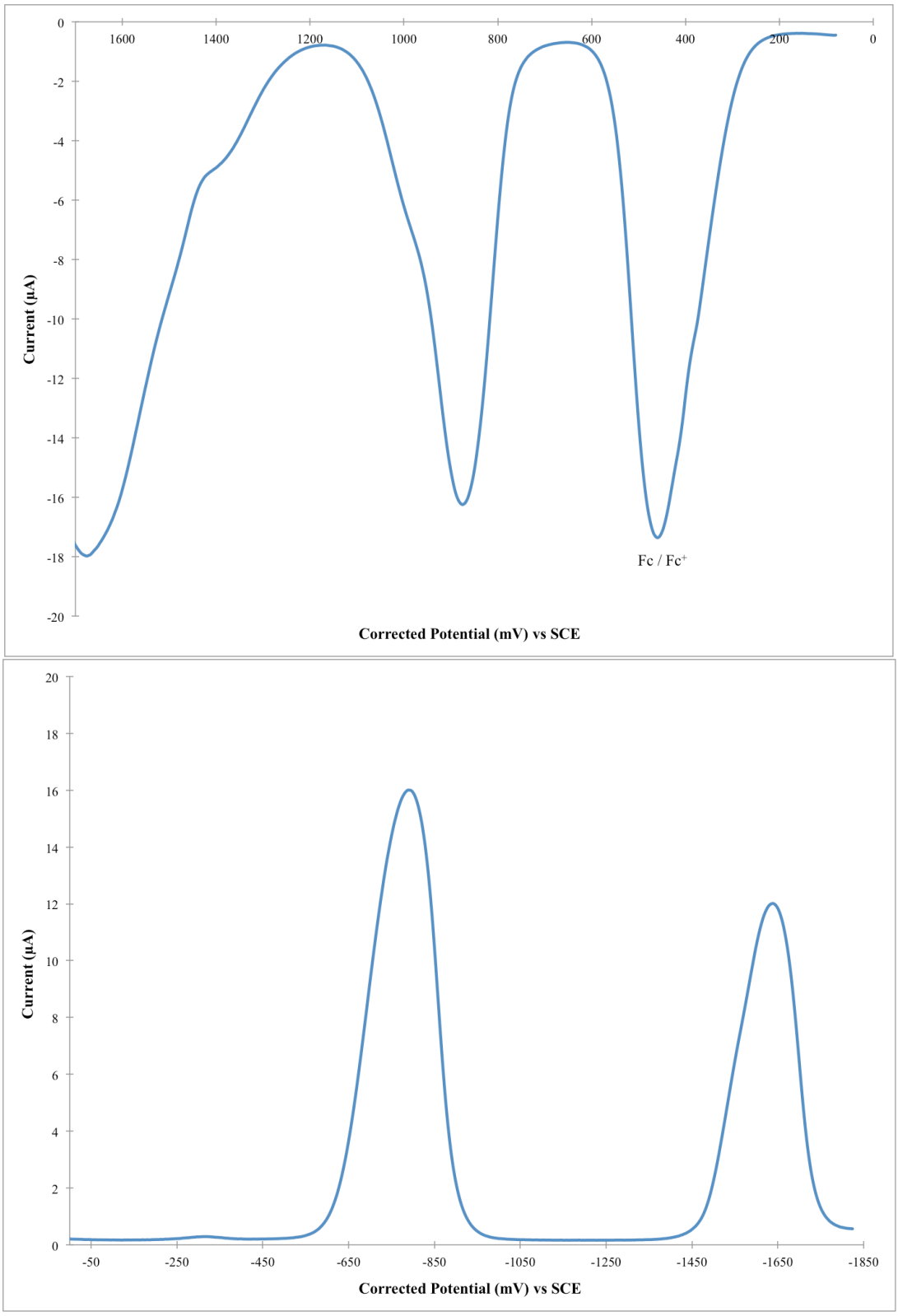

Figure II.S57 – DPV of oxidation (top) and reduction (bottom) potentials for BbF **8** with ferrocene internal reference. (0.46 V vs SCE in DCM) (Scan rate of 50 mV/s at R.T.)

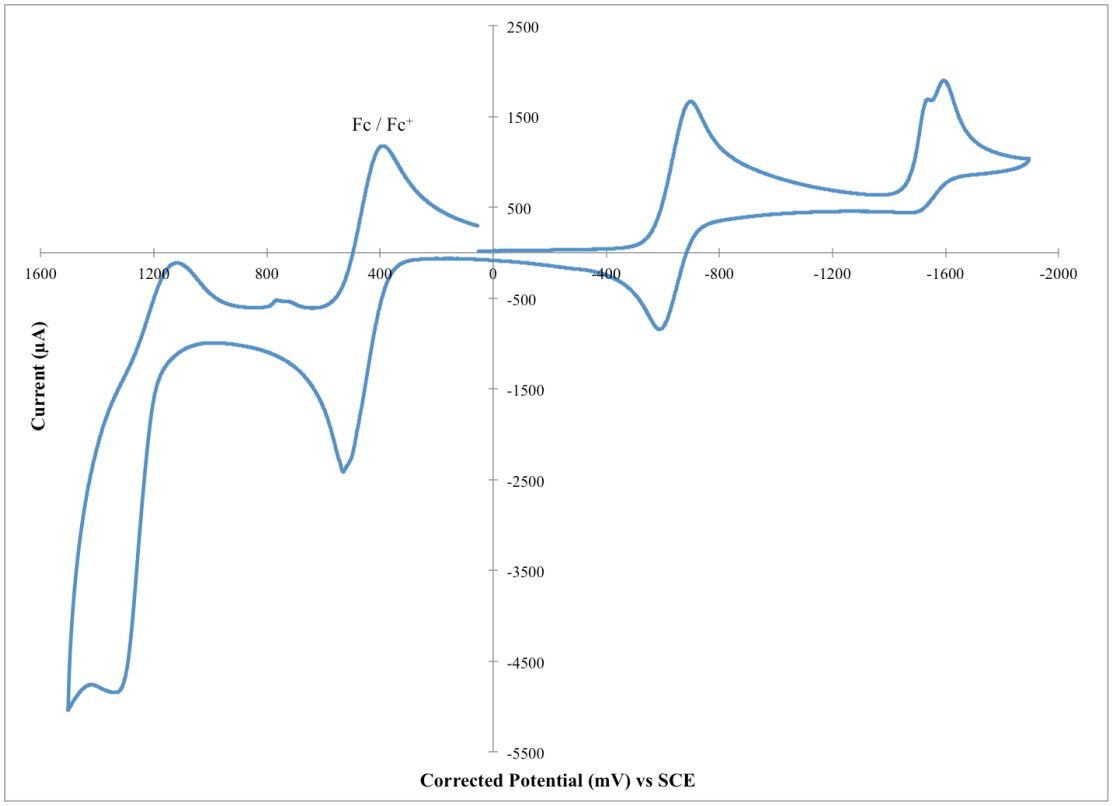

Figure II.S58 – CV of BbF **9** with ferrocene internal reference. (Fc = 0.46 V vs SCE in DCM; Scan rate of 50 mV/s at R.T.)

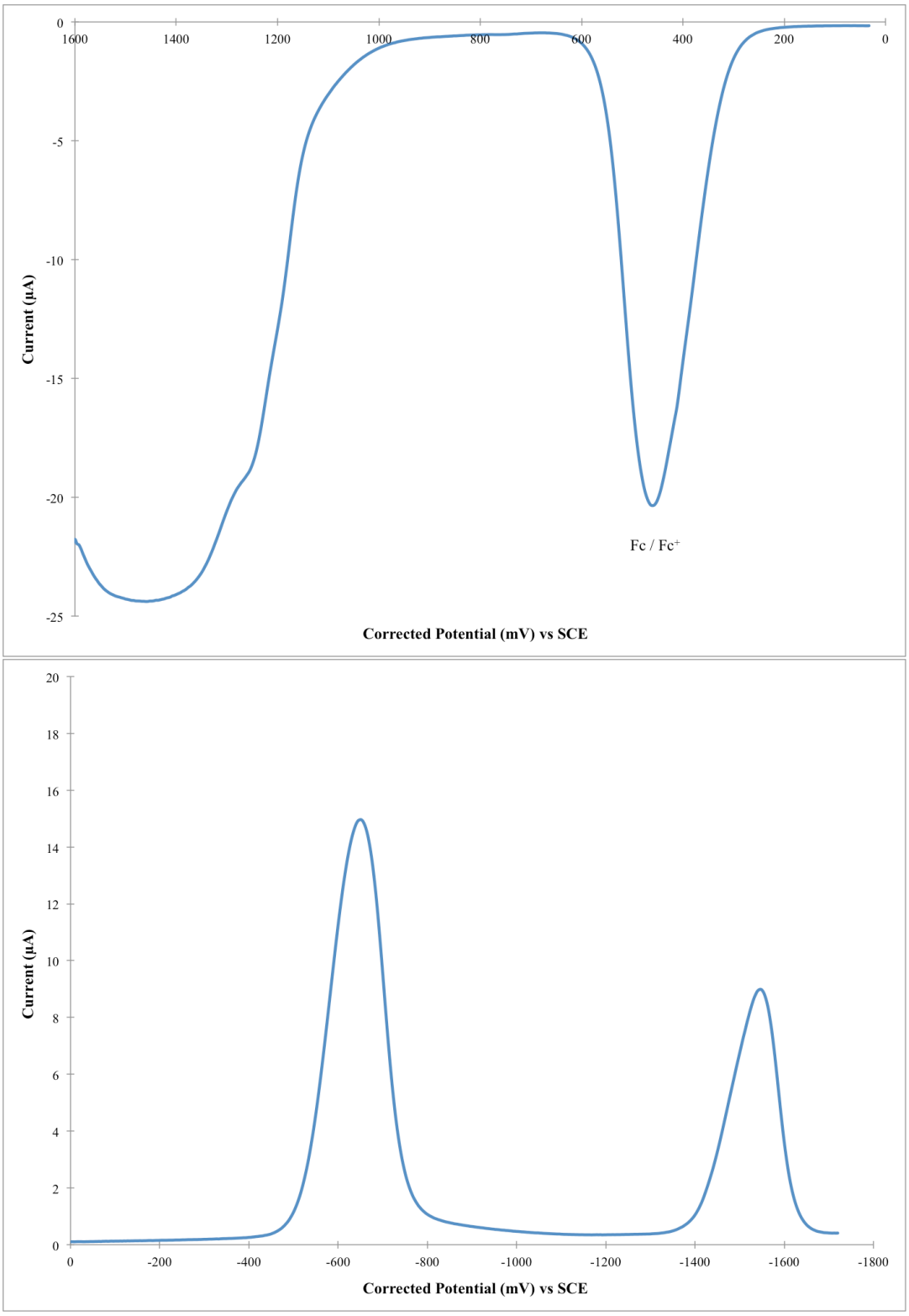

Figure II.S59 – DPV of oxidation (top) and reduction (bottom) potentials for BbF **9** with ferrocene internal reference. (0.46 V vs SCE in DCM) (Scan rate of 50 mV/s at R.T.)

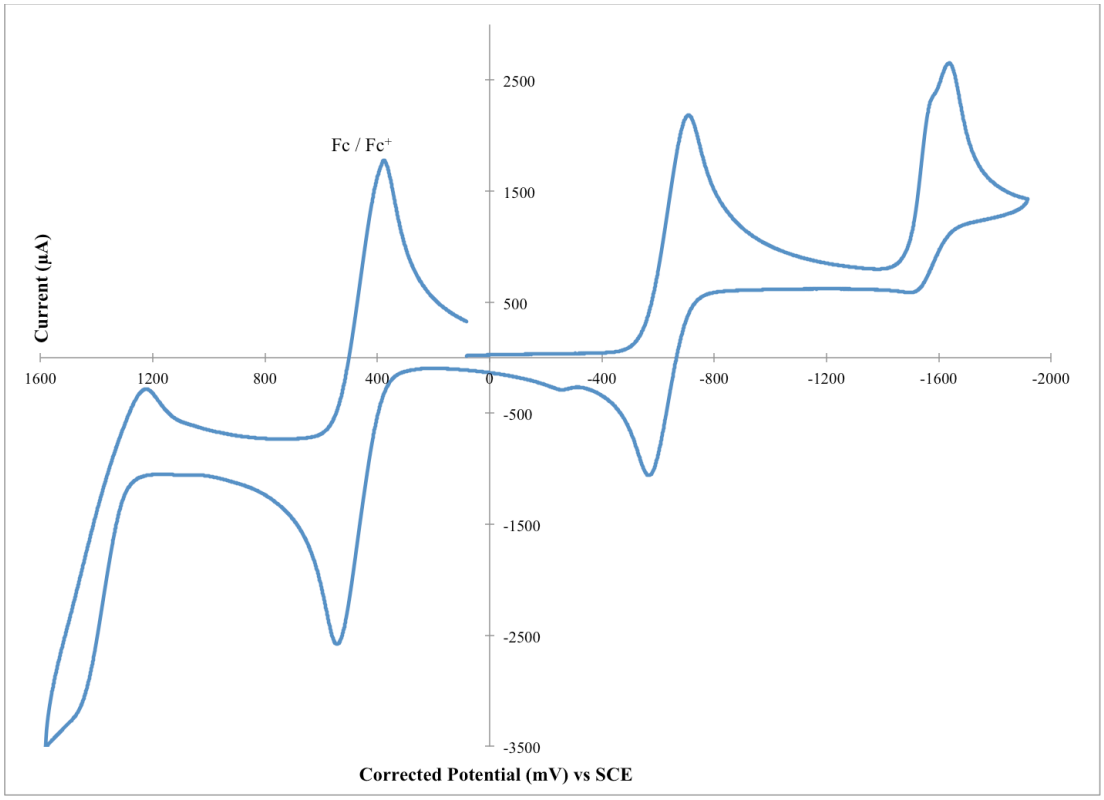

Figure II.S60 – CV of BbF **10** with ferrocene internal reference. (Fc = 0.46 V vs SCE in DCM; Scan rate of 50 mV/s at R.T.)

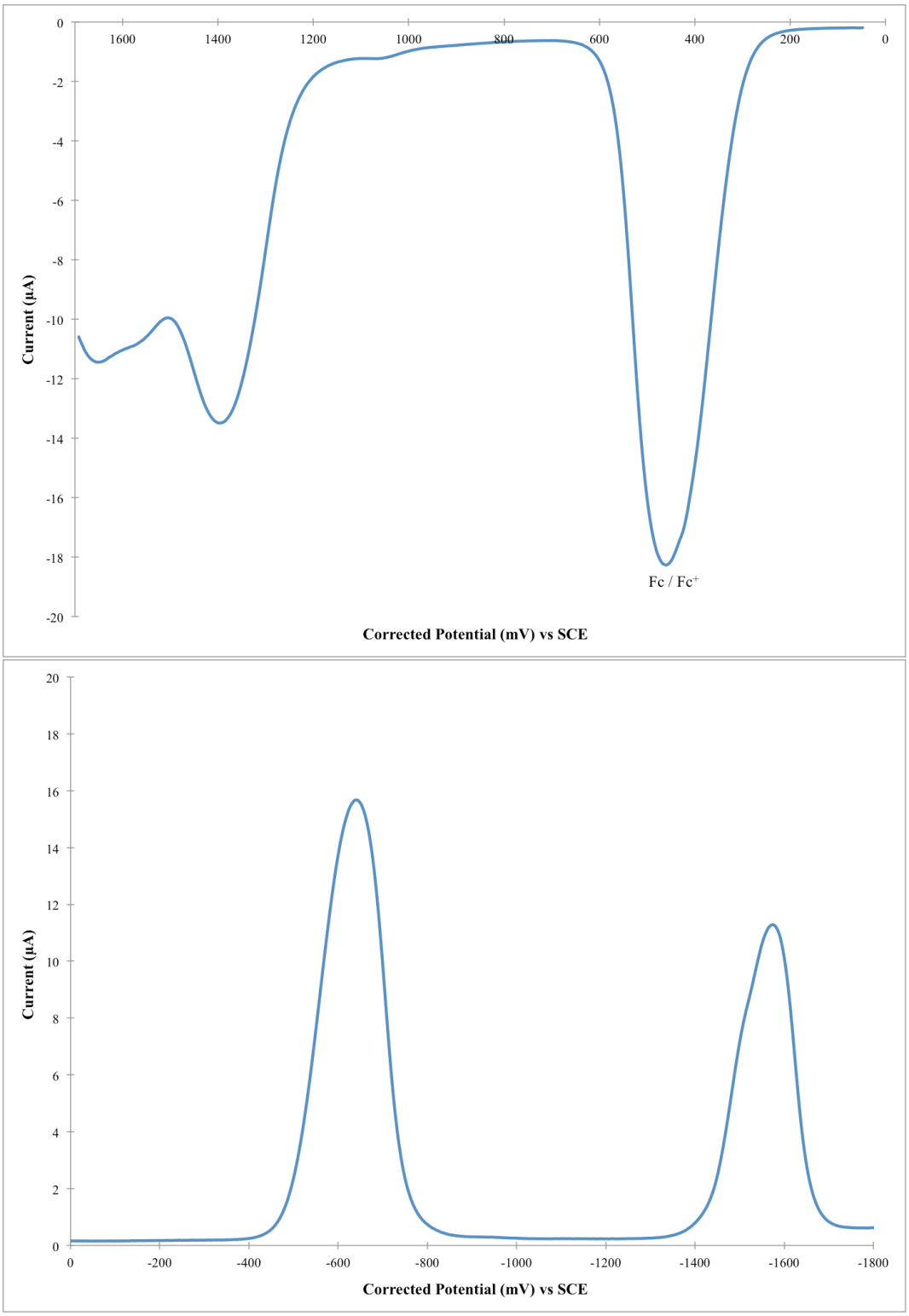

Figure II.S61 – DPV of oxidation (top) and reduction (bottom) potentials for BbF **10** with ferrocene internal reference. (0.46 V vs SCE in DCM) (Scan rate of 50 mV/s at R.T.)

Computational Modelization

Table II.S2 - Electronic distribution (%) of frontier molecular orbitals for BbF **1** – **10** as obtained by DFT.

	MO	DPM	Subst	meso	BF2
1	L + 1	48	48	4	1
	LUMO	81	10	8	1
	HOMO	86	11	2	1
	H -1	92	4	1	2
2	L + 1	48	47	4	1
	LUMO	81	11	7	1
	HOMO	82	15	2	0
	H -1	91	5	2	2
3	L + 1	48	46	4	1
	LUMO	81	11	7	1
	HOMO	82	15	2	0
	H -1	91	5	2	2
4	L + 1	48	47	4	1
	LUMO	80	11	7	1
	HOMO	82	15	2	0
	H -1	91	5	2	2
5	L + 1	51	41	8	1
	LUMO	80	12	7	1
	HOMO	70	28	2	0
	H -1	88	7	2	3
6	L + 1	46	49	4	1
	LUMO	82	9	8	1
	HOMO	84	13	2	1
	H -1	82	14	2	2
7	L + 1	54	37	9	1
	LUMO	82	10	8	1
	HOMO	85	12	2	1
	H -1	4	95	0	0
8	L + 1	52	36	11	1
	LUMO	76	16	7	1
	HOMO	40	58	2	0
	H -1	83	12	3	3
9	L + 1	17	82	0	0
	LUMO	79	12	7	1
	HOMO	49	50	2	0
	H -1	76	19	3	2
10	L + 1	13	87	0	0
	LUMO	82	10	8	1
	HOMO	63	34	2	1
	H -1	75	20	2	3

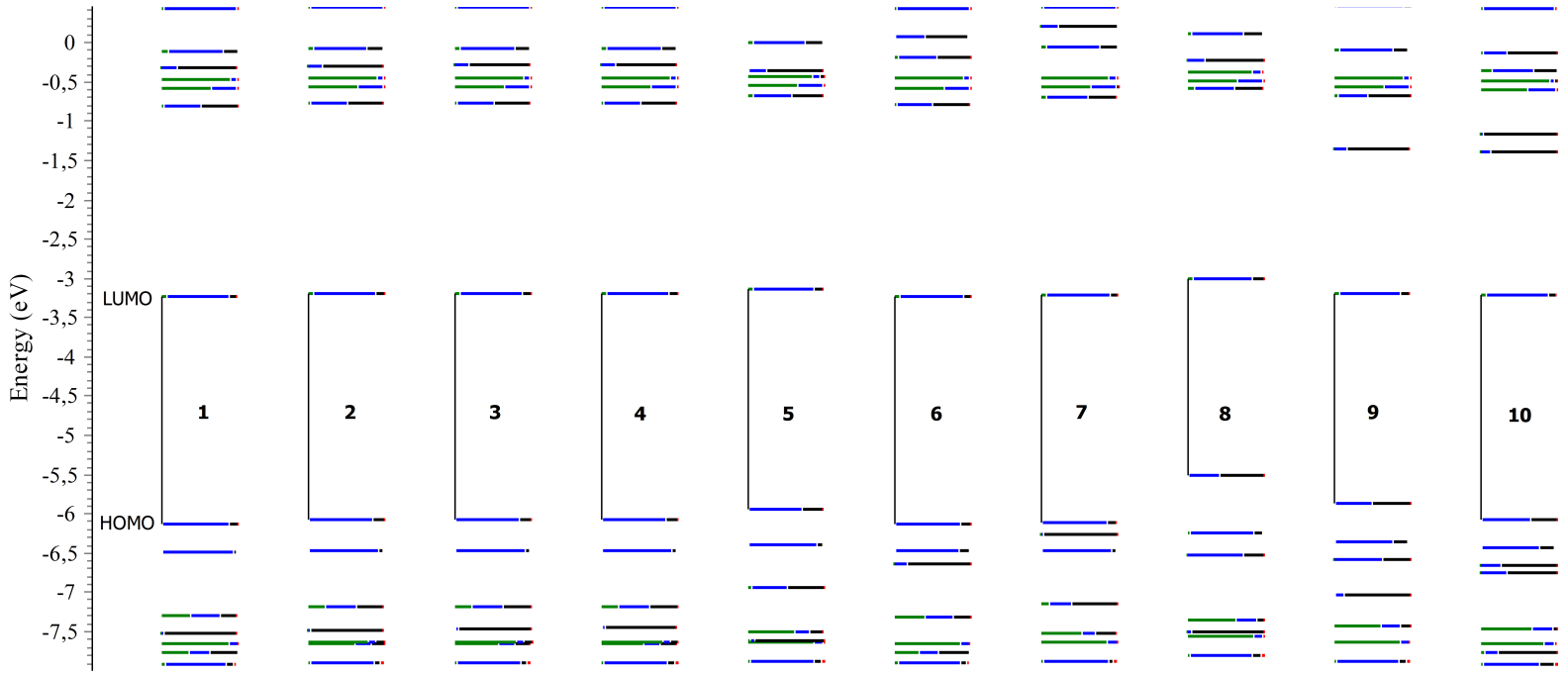

Figure II.S62 – Representation of frontier molecular orbital's energy levels (in eV) of BbF **1** – **10** and electronic distribution as obtained by DFT (refer to Scheme 1 for color legend)

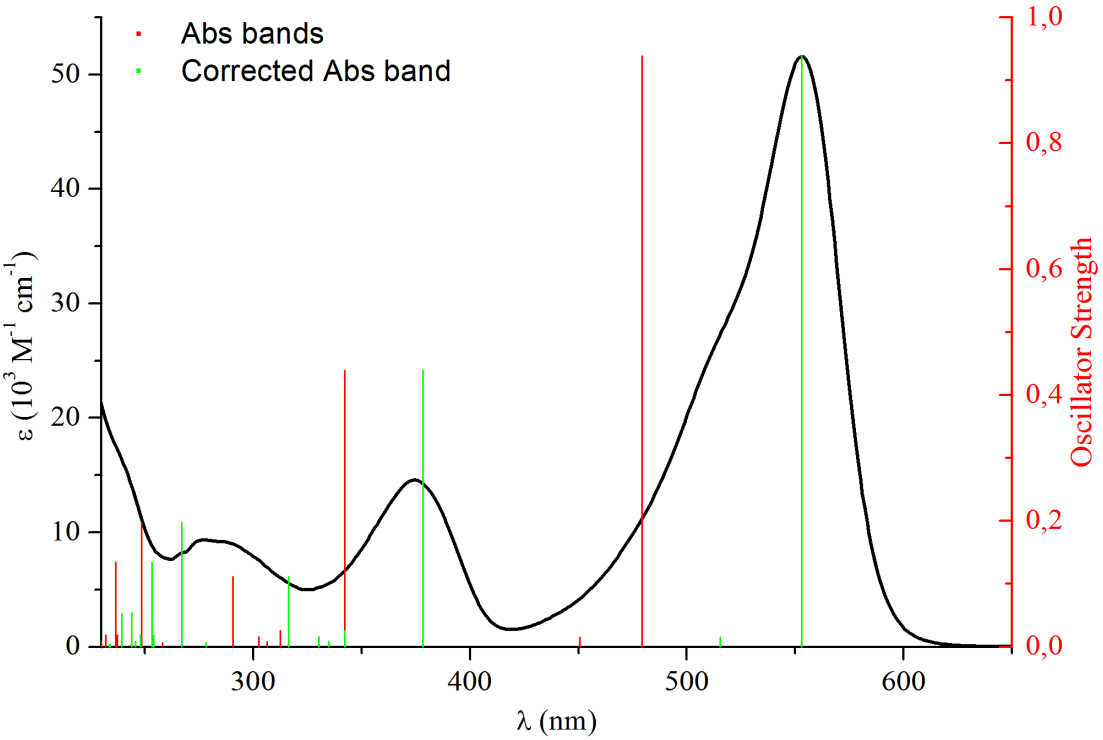

Figure II.S63 – BbF **1** experimental absorption spectrum in CH_2Cl_2 vs TD-DFT calculated optical absorption bands (Red = uncorrected; Green = corrected; PCM = CH_2Cl_2).

Table II.S3 - Assignation of optical absorption bands for BbF **1** based on TD-DFT calculations

λ, nm				
Observed (ε, x10^3 $M^{-1}cm^{-1}$)	**Calculated** (Osc. Strength)	**Corr.**	**Trans. No.**	**Major contributions to excitation**
553 (52)	479 (0.939)	553	T1	H (99%) -> L
517 (28)	451 (0.015)	515	T2	H-1 (98%) -> L
374 (15)	342 (0.439)	378	T3	H-2 (91%) -> L
	312 (0.026)	342	T4	H-6 (38%), H-5 (15%), H-4 (42%) -> L
	306 (0.008)	335	T5	H-6 (25%), H-5 (10%), H-4 (55%) -> L
	302 (0.016)	330	T6	H-3 (85%) -> L
287 (9.2)	291 (0.111)	316	T7	H-6 (25%), H-5 (65%) -> L
	258 (0.006)	278	T8	H-7 (94%) -> L
277 (9.3)	249 (0.198)	267	T9	H (86%) -> L+1
	237 (0.019)	254	T10	H (86%) -> L+2

Table II.S4 - NTO analysis for BbF **1** absorption bands T1 to T10 obtained by TD-DFT

(Isovalue = 0.02; PCM = CH_2Cl_2)

Transition / Eigenvalue	**NTO Hole "From"**	**NTO Particle "To"**
T1 / 0.99	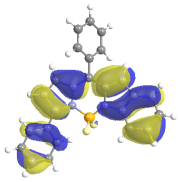	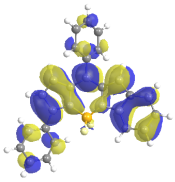
T2 / 0.99	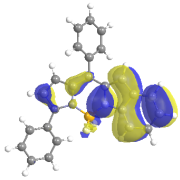	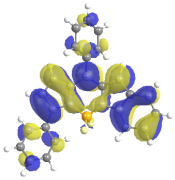
T3 / 0.99	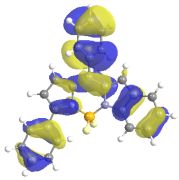	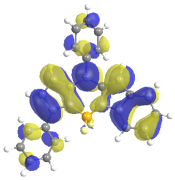
T4 / 0.99	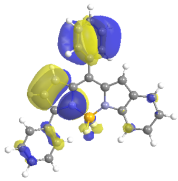	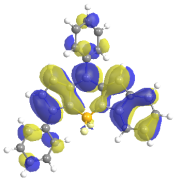
T5 / 0.99	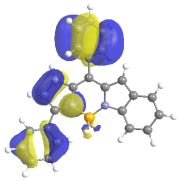	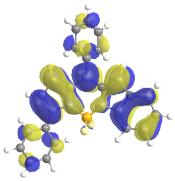
T6 / 0.98	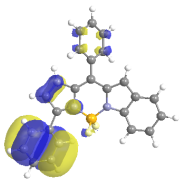	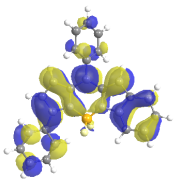

T7 / 0.98	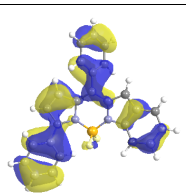	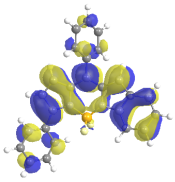
T8 / 0.98	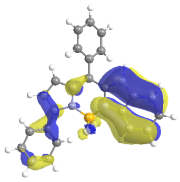	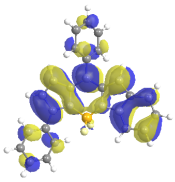
T9 / 0.93	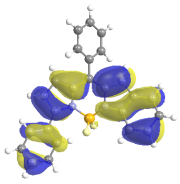	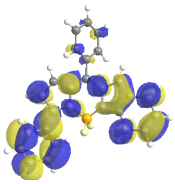
T10 / 0.93	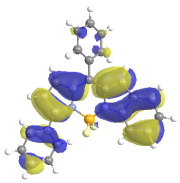	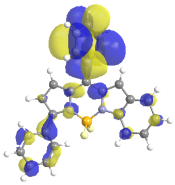

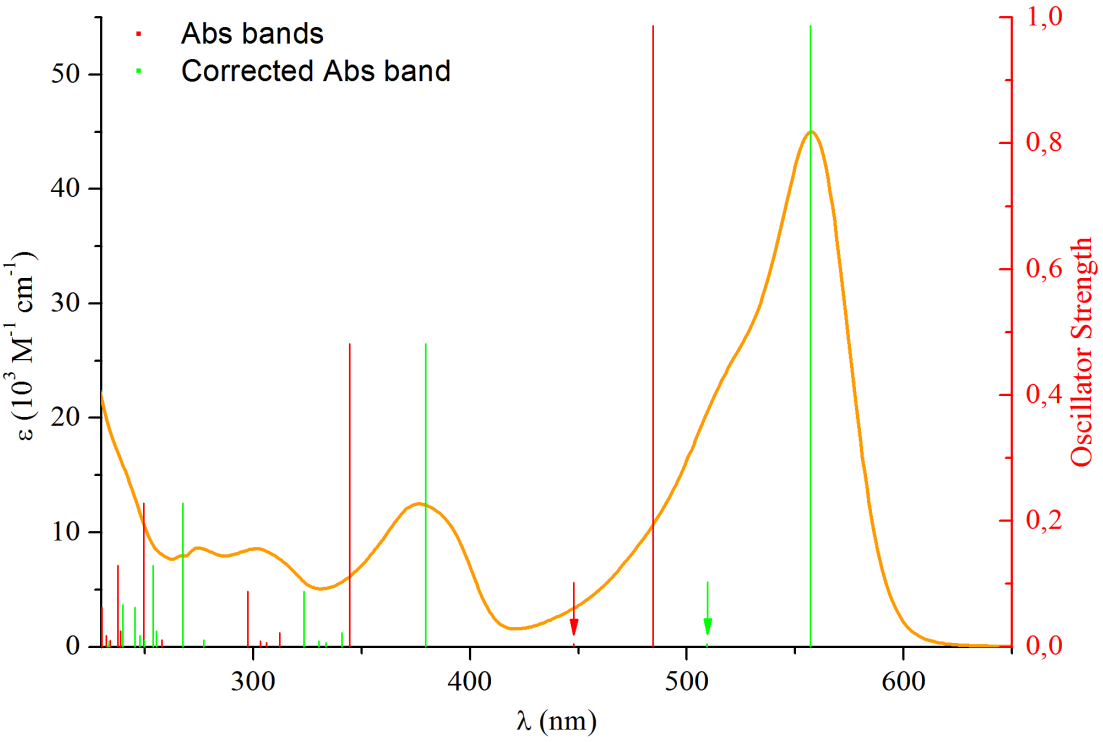

Figure II.S64 – BbF **2** experimental absorption spectrum in CH_2Cl_2 vs TD-DFT calculated optical absorption bands

(Red = uncorrected; Green = corrected; PCM = CH_2Cl_2).

Table II.S5 - Assignation of optical absorption bands for BbF **2** based on TD-DFT calculations

λ, nm				
Observed (ε, x10^3 $M^{-1}cm^{-1}$)	**Calculated** (Osc. Strength)	**Corr.**	**Trans. No.**	**Major contributions to excitation**
557 (45)	484 (0.987)	557	T1	H (98%) -> L
521 (25)	448 (0.005)	509	T2	H-1 (97%) -> L
377 (12)	344 (0.482)	380	T3	H-2 (88%) -> L
	312 (0.023)	341	T4	H-6 (39%), H-5 (46%) -> L
	306 (0.007)	334	T5	H-5 (27%), H-4 (58%), H-3 (10%) -> L
302 (8.6)	303 (0.010)	330	T6	H-4 (12%), H-3 (80%) -> L
	297 (0.088)	323	T7	H-6 (51%), H-5 (24%), H-4 (16%) -> L
275 (8.6)	258 (0.011)	277	T8	H-7 (93%) -> L
	250 (0.229)	268	T9	H (87%) -> L+1
	239 (0.025)	255	T10	H (89%) -> L+2

Table II.S6 - NTO analysis for BbF **2** absorption bands T1 to T10 obtained by TD-DFT

(Isovalue = 0.02; PCM = CH_2Cl_2)

Transition / Eigenvalue	**NTO Hole "From"**	**NTO Particle "To"**
T1 / 0.99	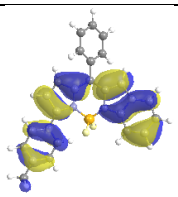	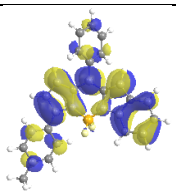
T2 / >0.99	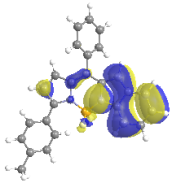	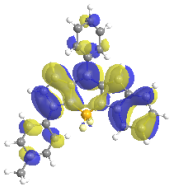
T3 / 0.99	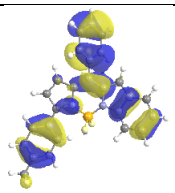	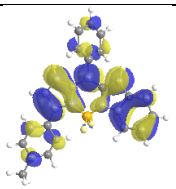
T4 / 0.99	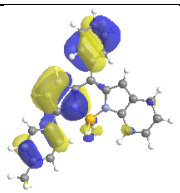	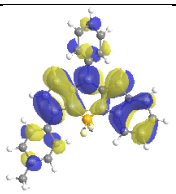
T5 / 0.99	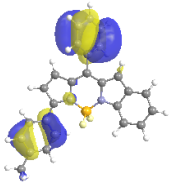	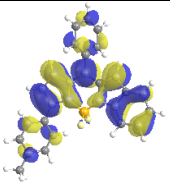
T6 / 0.98	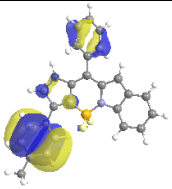	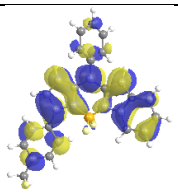

T7 / 0.99	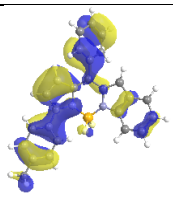	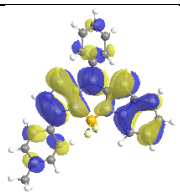
T8 / 0.97	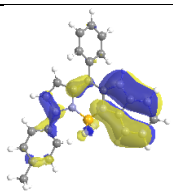	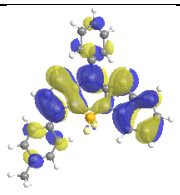
T9 / 0.93	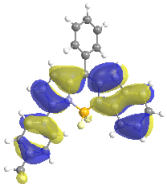	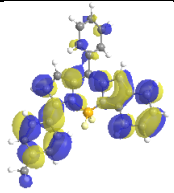
T10 / 0.95	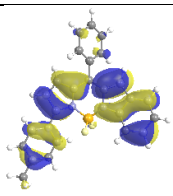	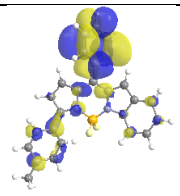

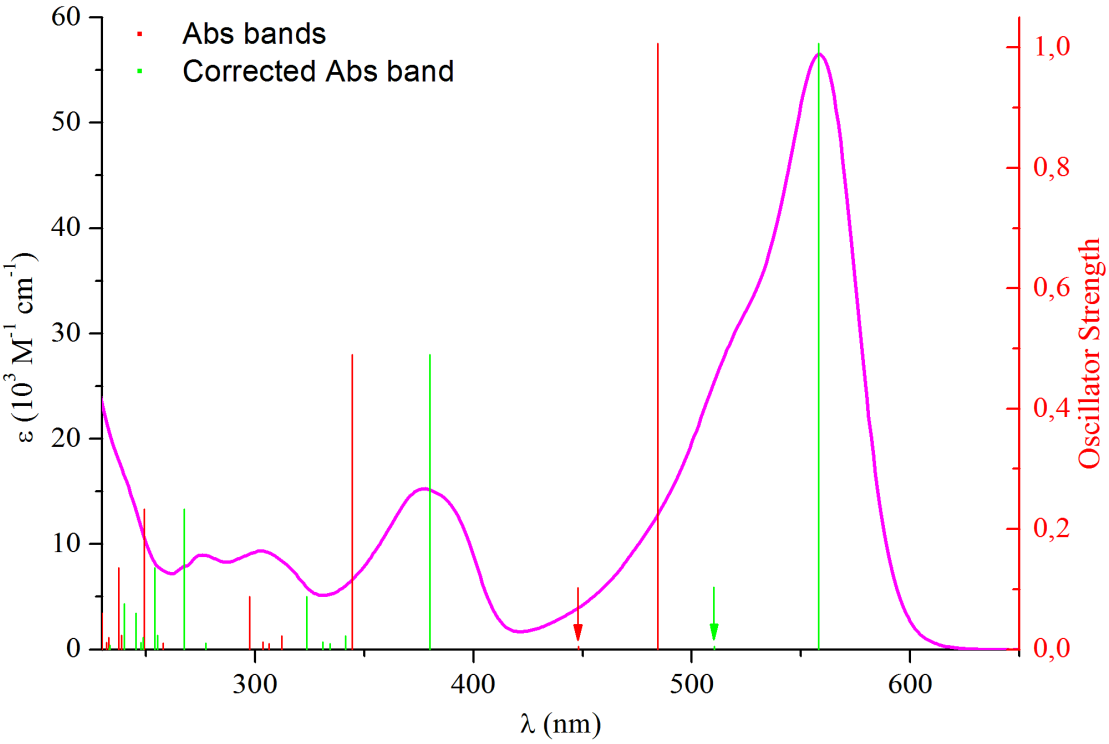

Figure II.S65 – BbF **3** experimental absorption spectrum in CH_2Cl_2 vs TD-DFT calculated optical absorption bands

(Red = uncorrected; Green = corrected; PCM = CH_2Cl_2).

Table II.S7 - Assignation of optical absorption bands for BbF **3** based on TD-DFT calculations

λ, nm				
Observed (ε, x10^3 $M^{-1}cm^{-1}$)	**Calculated** (Osc. Strength)	**Corr.**	**Trans. No.**	**Major contributions to excitation**
558 (57)	484 (1.007)	558	T1	H (98%) -> L
523 (31)	448 (0.005)	510	T2	H-1 (97%) -> L
378 (15)	344 (0.490)	380	T3	H-2 (88%) -> L
	312 (0.022)	341	T4	H-6 (39%), H-5 (41%), H-3 (11%) -> L
	306 (0.009)	334	T5	H-5 (31%), H-4 (43%), H-3 (22%) -> L
303 (9.3)	304 (0.012)	331	T6	H-6 (11%), H-4 (23%), H-3 (62%) -> L
	298 (0.088)	324	T7	H-6 (47%), H-5 (24%), H-4 (19%) -> L
276 (9.0)	258 (0.011)	277	T8	H-7 (93%) -> L
	249 (0.233)	268	T9	H (86%) -> L+1
	239 (0.024)	255	T10	H (88%) -> L+2

Table II.S8 - NTO analysis for BbF **3** absorption bands T1 to T10 obtained by TD-DFT

(Isovalue = 0.02; PCM = CH_2Cl_2)

Transition / Eigenvalue	**NTO Hole "From"**	**NTO Particle "To"**
T1 / 0.99	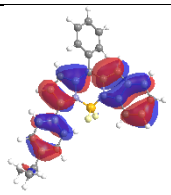	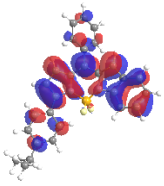
T2 / >0.99	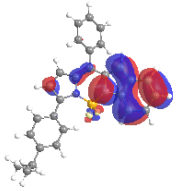	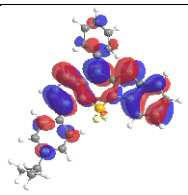
T3 / 0.99	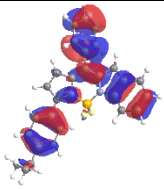	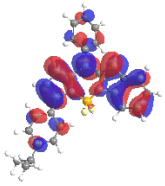
T4 / 0.99	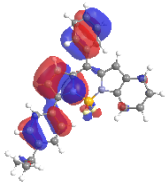	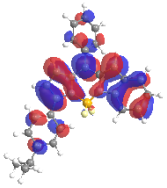
T5 / 0.98	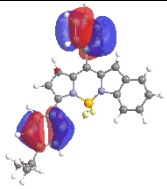	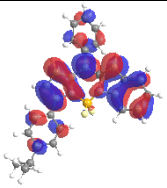
T6 / 0.98	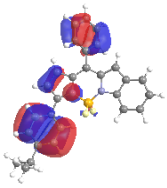	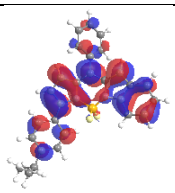

T7 / 0.99	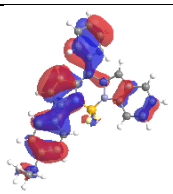	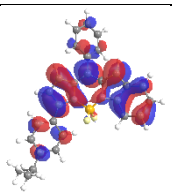
T8 / 0.97	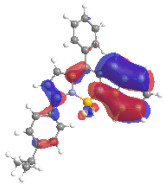	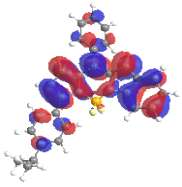
T9 / 0.92	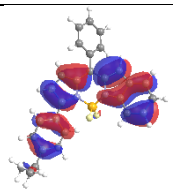	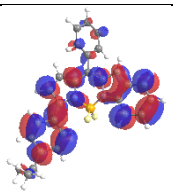
T10 / 0.94	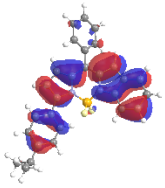	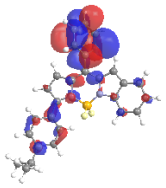

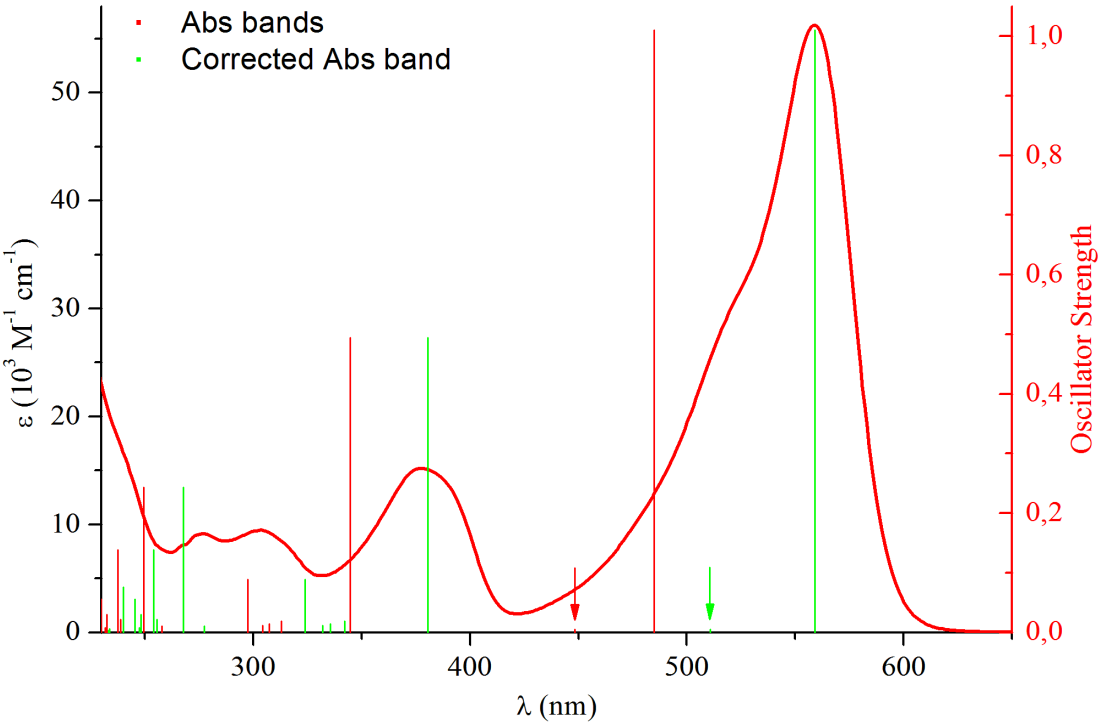

Figure II.S66 – BbF **4** experimental absorption spectrum in CH_2Cl_2 vs TD-DFT calculated optical absorption bands

(Red = uncorrected; Green = corrected; PCM = CH_2Cl_2)

Table II.S9 - Assignation of optical absorption bands for BbF **4** based on TD-DFT calculations

λ, nm				
Observed (ε, x10^3 $M^{-1}cm^{-1}$)	**Calculated** (Osc. Strength)	**Corr.**	**Trans. No.**	**Major contributions to excitation**
559 (56)	485 (1.011)	559	T1	H (98%) -> L
525 (32)	448 (0.005)	511	T2	H-1 (97%) -> L
378 (15)	345 (0.494)	380	T3	H-2 (87%) -> L
	313 (0.019)	342	T4	H-6 (33%), H-5 (36%), H-3 (22%) -> L
	307 (0.014)	336	T5	H-5 (32%), H-4 (25%), H-3 (38%) -> L
303 (9.5)	304 (0.012)	332	T6	H-6 (17%), H-4 (42%), H-3 (35%) -> L
	297 (0.089)	324	T7	H-6 (44%), H-5 (26%), H-4 (19%) -> L
277 (9.1)	258 (0.011)	278	T8	H-7 (93%) -> L
	250 (0.243)	268	T9	H (87%) -> L+1
	239 (0.021)	256	T10	H (87%) -> L+2

Table II.S10 - NTO analysis for BbF **4** absorption bands T1 to T10 obtained by TD-DFT (Isovalue = 0.02; PCM = CH_2Cl_2)

Transition / Eigenvalue	**NTO Hole "From"**	**NTO Particle "To"**
T1 / 0.99	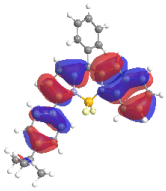	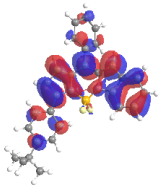
T2 / >0.99	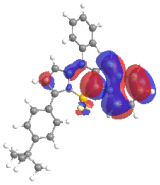	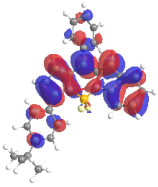
T3 / 0.99	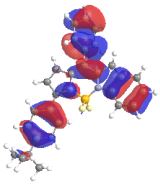	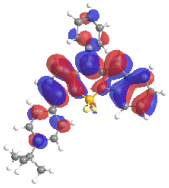
T4 / 0.99	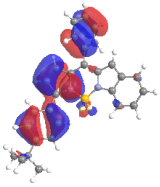	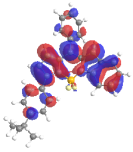
T5 / 0.98	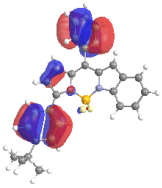	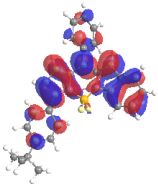
T6 / 0.98	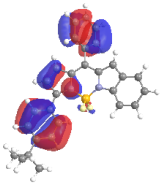	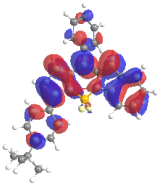

T7 / 0.98	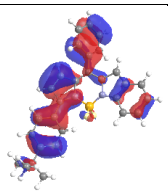	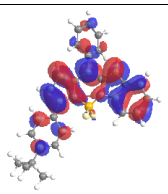
T8 / 0.97	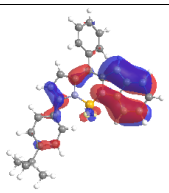	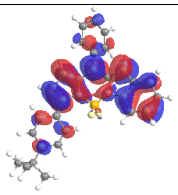
T9 / 0.93	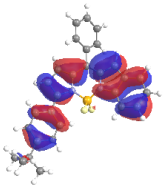	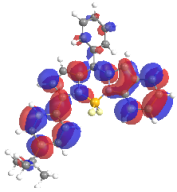
T10 / 0.93	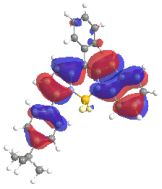	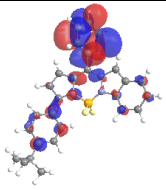

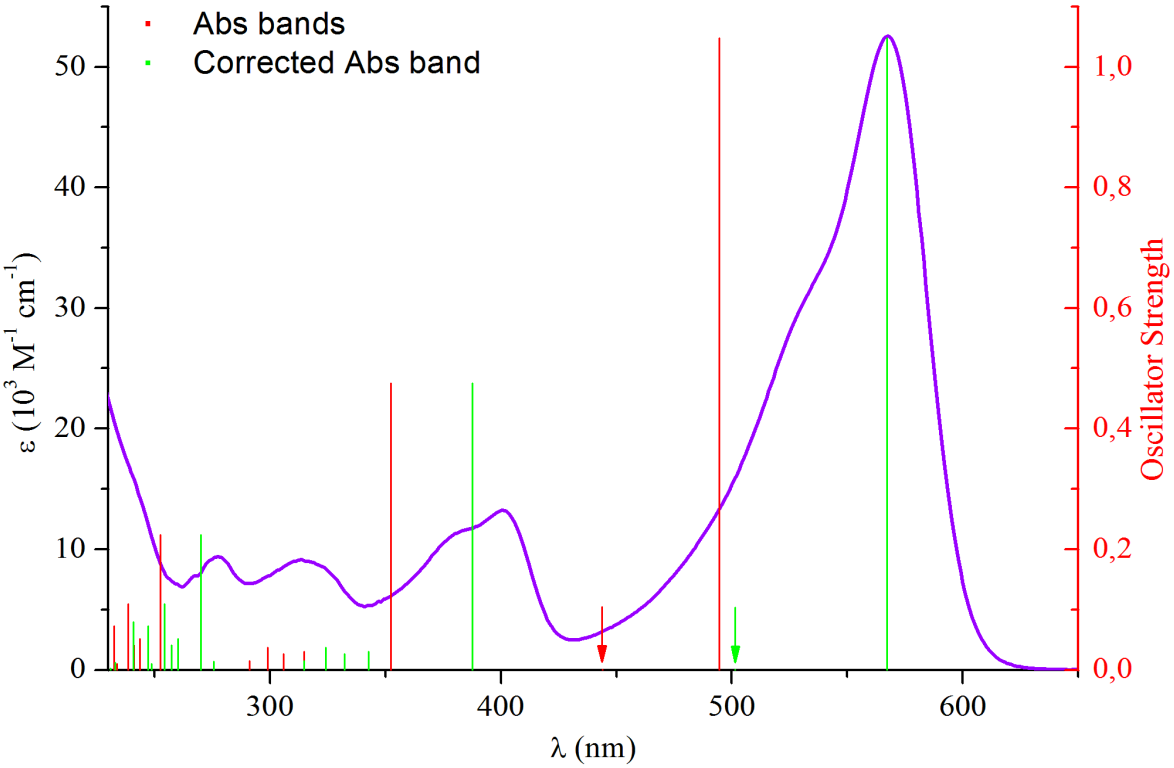

Figure II.S67 – BbF **5** experimental absorption spectrum in CH_2Cl_2 vs TD-DFT calculated optical absorption bands

(Red = uncorrected; Green = corrected; PCM = CH_2Cl_2).

Table II.S11 - Assignation of optical absorption bands for BbF **5** based on TD-DFT calculations

λ, nm				
Observed (ε, x10³ $M^{-1}cm^{-1}$)	**Calculated** (Osc. Strength)	**Corr.**	**Trans. No.**	**Major contributions to excitation**
567 (53)	495 (1.048)	567	T1	H (98%) -> L
537 (33)	444 (0.001)	501	T2	H-1 (96%) -> L
401 (13)	352 (0.475)	388	T3	H-2 (88%) -> L
	315 (0.031)	343	T4	H-3 (78%) -> L
314 (9.1)	306 (0.027)	332	T5	H-6 (23%), H-4 (63%) -> L
	299 (0.037)	324	T6	H-6 (55%), H-5 (13%), H-4 (26%) -> L
	291 (0.015)	315	T7	H-5 (79%) -> L
278 (9.4)	257 (0.014)	276	T8	H-7 (92%) -> L
	253 (0.224)	270	T9	H (88%) -> L+1
	244 (0.052)	260	T10	H (24%) -> L+2; H -> L+4 (51%)

Table II.S12 - NTO analysis for BbF **5** absorption bands T1 to T10 obtained by TD-DFT (Isovalue = 0.02; PCM = CH_2Cl_2)

Transition / Eigenvalue	**NTO Hole "From"**	**NTO Particle "To"**
T1 / 0.99	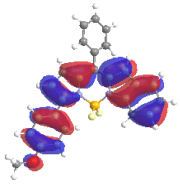	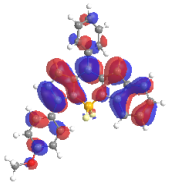
T2 / >0.99	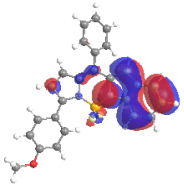	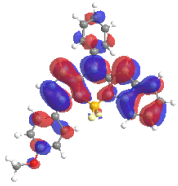
T3 / 0.99	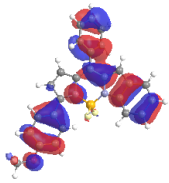	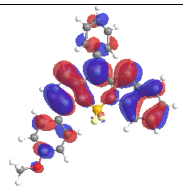
T4 / 0.99	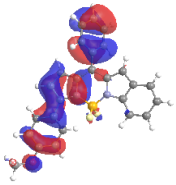	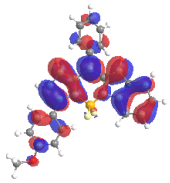
T5 / 0.99	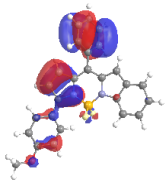	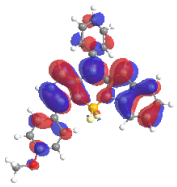
T6 / 0.99	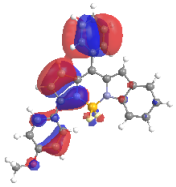	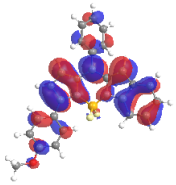

T7 / 0.96	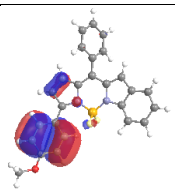	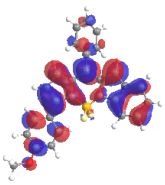
T8 / 0.97	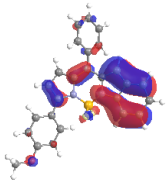	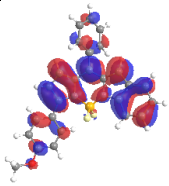
T9 / 0.91	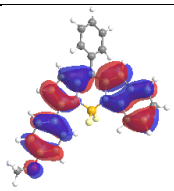	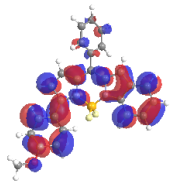
T10 / 0.80	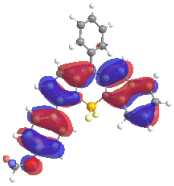	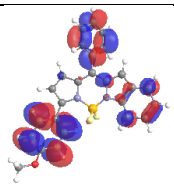

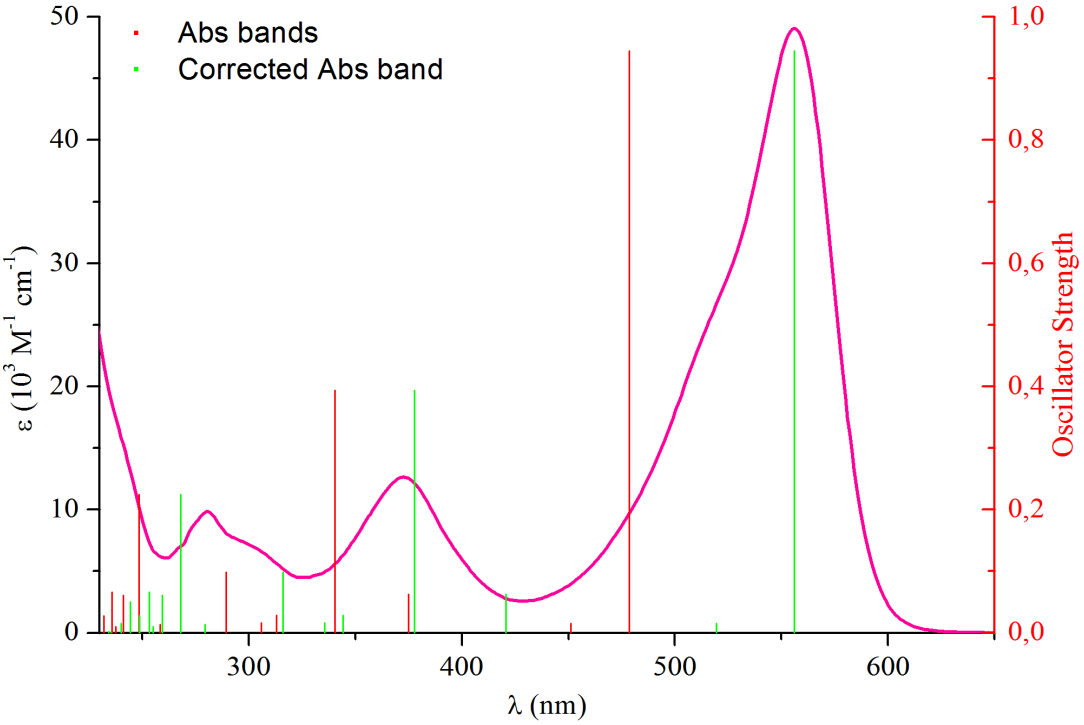

Figure II.S68 – BbF **6** experimental absorption spectrum in CH_2Cl_2 vs TD-DFT calculated optical absorption bands

(Red = uncorrected; Green = corrected; PCM = CH_2Cl_2)

Table II.S13 - Assignation of optical absorption bands for BbF **6** based on TD-DFT calculations

λ, nm				
Observed (ε, x10^3 $M^{-1}cm^{-1}$)	**Calculated** (Osc. Strength)	**Corr.**	**Trans. No.**	**Major contributions to excitation**
556 (49)	479 (0.946)	556	T1	H (99%) -> L
520 (27)	451 (0.016)	519	T2	H-1 (96%) -> L
373 (13)	375 (0.063)	421	T3	H-2 (96%) -> L
	340 (0.394)	378	T4	H-3 (91%) -> L
	313 (0.028)	344	T5	H-6 (36%), H-5 (11%), H-4 (51%) -> L
	306 (0.016)	336	T6	H-6 (39%), H-5 (12%), H-4 (47%) -> L
303 (6.9)	289 (0.099)	316	T7	H-6 (21%), H-5 (69%) -> L
281 (9.8)	259 (0.014)	280	T8	H-7 (92%) -> L
	249 (0.225)	268	T9	H (82%) -> L+1
	241 (0.061)	259	T10	H-8 (15%) -> L; H-2 (36%) -> L+1; H (12%) -> L+4

Table II.S14 - NTO analysis for BbF **6** absorption bands T1 to T10 obtained by TD-DFT

(Isovalue = 0.02; PCM = CH_2Cl_2)

Transition / Eigenvalue	**NTO Hole "From"**	**NTO Particle "To"**
T1 / 0.99	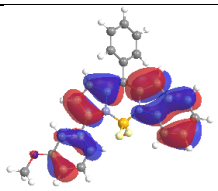	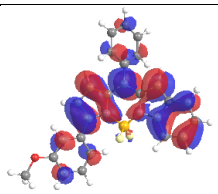
T2 / 0.99	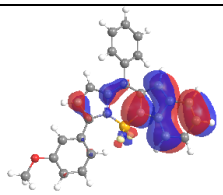	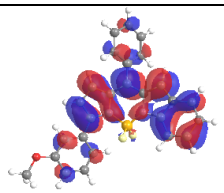
T3 / 0.99	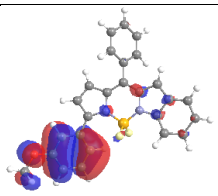	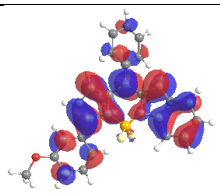
T4 / 0.99	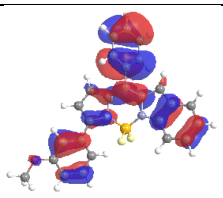	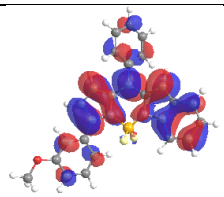
T5 / 0.99	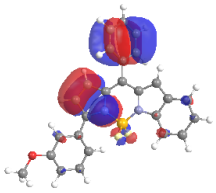	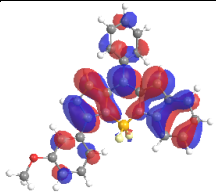
T6 / 0.99	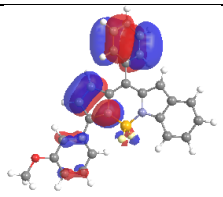	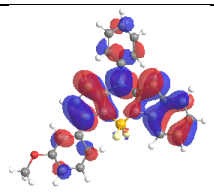
T7 / 0.98	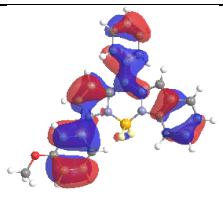	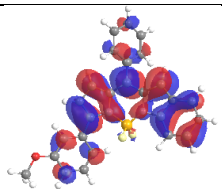

T8 / 0.97	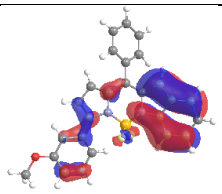	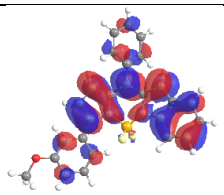
T9 / 0.90	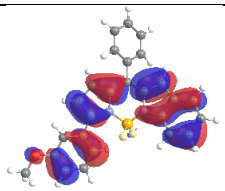	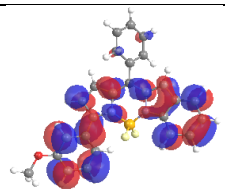
T10 / 0.52	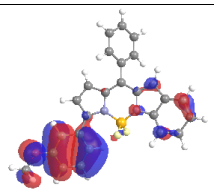	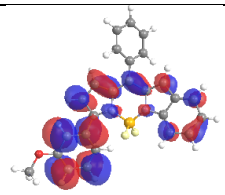

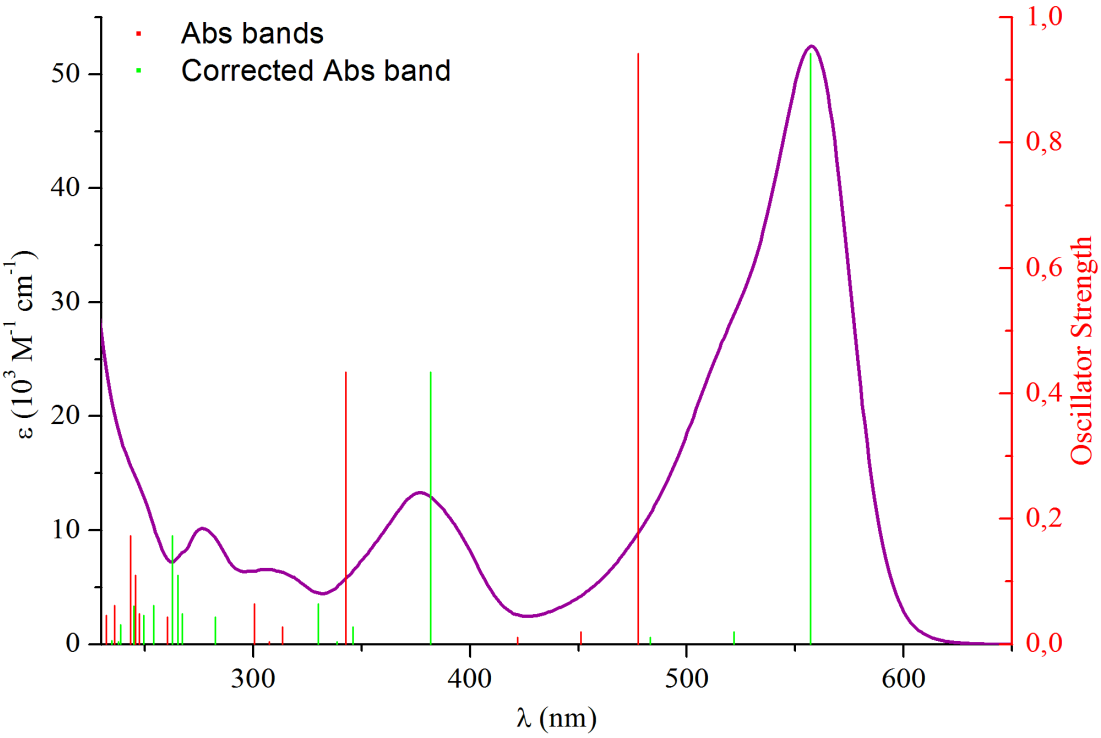

Figure II.S69 – BbF **7** experimental absorption spectrum in CH_2Cl_2 vs TD-DFT calculated optical absorption bands

(Red = uncorrected; Green = corrected; PCM = CH_2Cl_2).

Table II.S15 - Assignation of optical absorption bands for BbF **7** based on TD-DFT calculations

λ, nm				
Observed (ε, x10^3 $M^{-1}cm^{-1}$)	**Calculated** (Osc. Strength)	**Corr.**	**Trans. No.**	**Major contributions to excitation**
557 (52)	477 (0.942)	557	T1	H (99%) -> L
522 (29)	451 (0.020)	522	T2	H-2 (97%) -> L
	422 (0.011)	483	T3	H-1 (98%) -> L
377 (13)	343 (0.434)	382	T4	H-4 (19%), H-3 (77%) -> L
	314 (0.027)	346	T5	H-6 (44%), H-5 (36%), H-4 (16%) -> L
	308 (0.004)	339	T6	H-5 (54%), H-4 (31%) -> L
307 (6.5)	300 (0.065)	330	T7	H-6 (46%), H-4 (29%), H-3 (14%) -> L
	260 (0.044)	282	T8	H-7 (87%) -> L
277 (10)	248 (0.049)	267	T9	H-1 (64%) -> L+1; H-1 (12%) -> L+4
	246 (0.110)	265	T10	H (80%) -> L+1

Table II.S16 - NTO analysis for BbF **7** absorption bands T1 to T10 obtained by TD-DFT

(Isovalue = 0.02; PCM = CH_2Cl_2)

Transition / Eigenvalue	**NTO Hole "From"**	**NTO Particle "To"**
T1 / 0.99	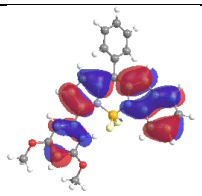	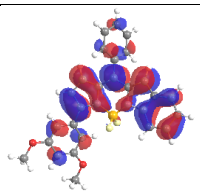
T2 / >0.99	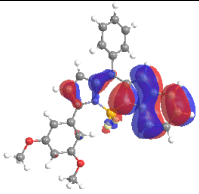	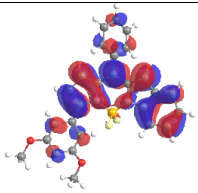
T3 / 0.99	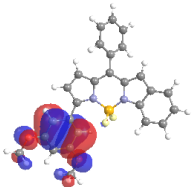	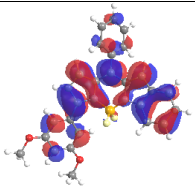
T4 / 0.99	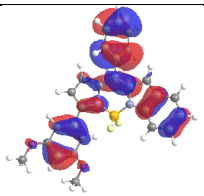	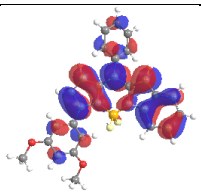
T5 / 0.99	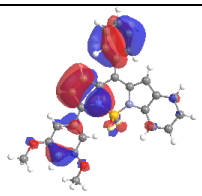	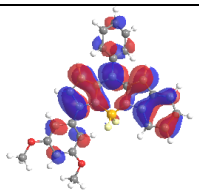
T6 / 0.94	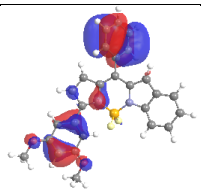	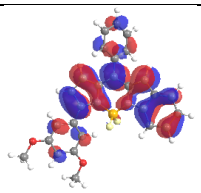

T7 / 0.93	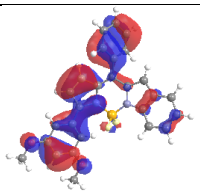	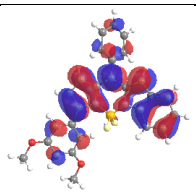
T8 / 0.90	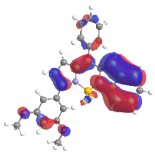	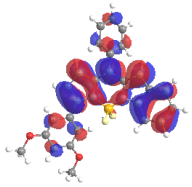
T9 / 0.86	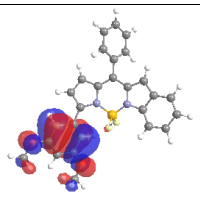	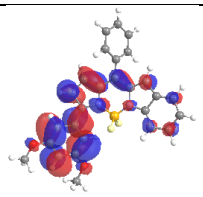
T10 / 0.95	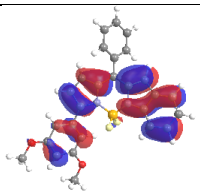	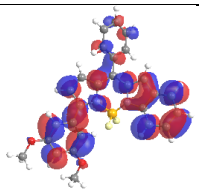

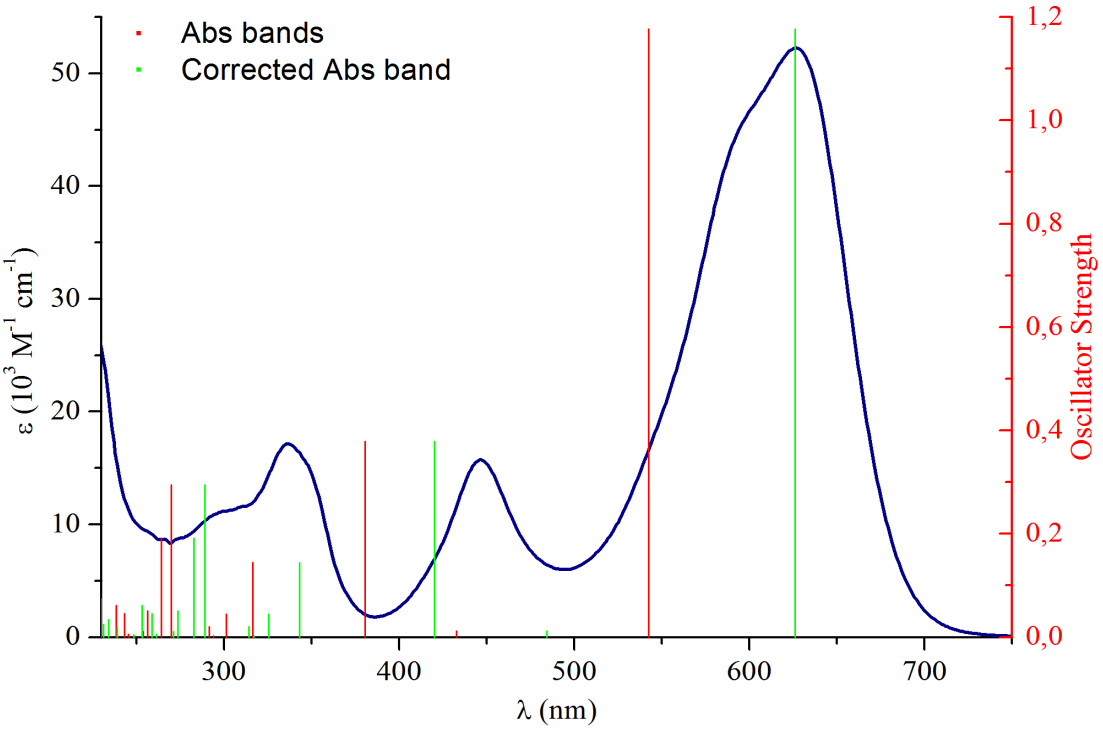

Figure II.S70 – BbF **8** experimental absorption spectrum in CH_2Cl_2 vs TD-DFT calculated optical absorption bands

(Red = uncorrected; Green = corrected; PCM = CH_2Cl_2).

Table II.S17 - Assignation of optical absorption bands for BbF **8** based on TD-DFT calculations

λ, nm				
Observed (ε, x10³ $M^{-1}cm^{-1}$)	**Calculated** (Osc. Strength)	**Corr.**	**Trans. No.**	**Major contributions to excitation**
626 (52)	542 (1.177)	626	T1	H (98%) -> L
597 (46)	---	---	---	
446 (16)	433 (0.013)	484	T2	H-2 (18%), H-1 (81%) -> L
	381 (0.379)	420	T3	H-2 (77%), H-1 (18%) -> L
336 (17)	317 (0.145)	343	T4	H-3 (94%) -> L
	301 (0.045)	325	T5	H-6 (52%), H-5 (28%), H-4 (17%) -> L
	294 (0.003)	317	T6	H-5 (58%), H-4 (31%) -> L
301 (11)	292 (0.021)	314	T7	H-6 (40%), H-5 (12%), H-4 (40%) -> L
	270 (0.295)	289	T8	H (72%) -> L+1; H (15%) -> L+4
	264 (0.191)	283	T9	H (17%) -> L+1; H (61%) -> L+4
	256 (0.051)	274	T10	H-7 (88%) -> L

Table II.S18 - NTO analysis for BbF **8** absorption bands T1 to T10 obtained by TD-DFT

(Isovalue = 0.02; PCM = CH_2Cl_2)

Transition / Eigenvalue	**NTO Hole "From"**	**NTO Particle "To"**
T1 / 0.99	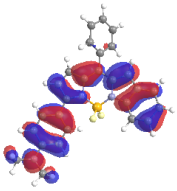	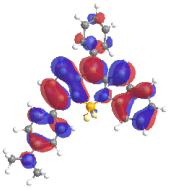
T2 / >0.99	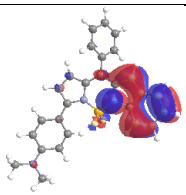	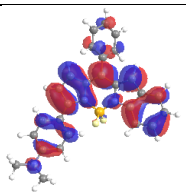
T3 / 0.99	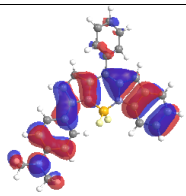	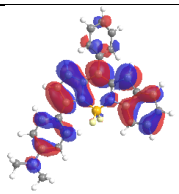
T4 / 0.99	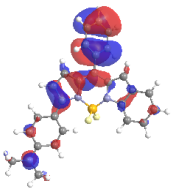	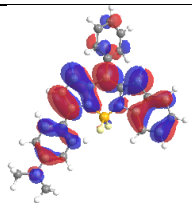
T5 / 0.99	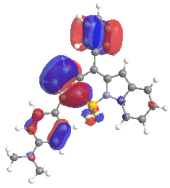	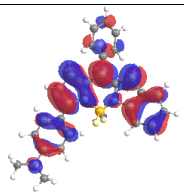
T6 / 0.94	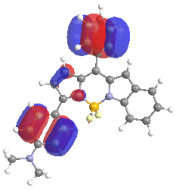	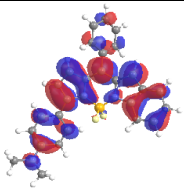

T7 / 0.93	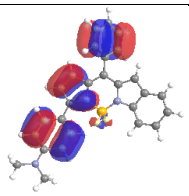	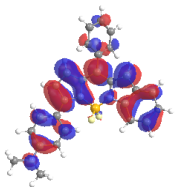
T8 / 0.90	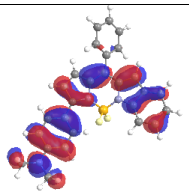	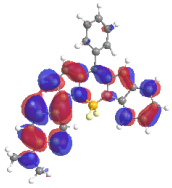
T9 / 0.86	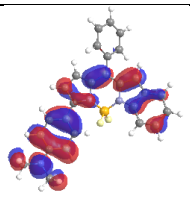	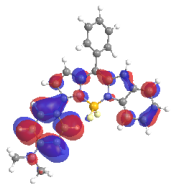
T10 / 0.95	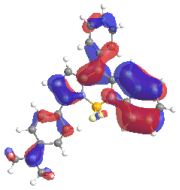	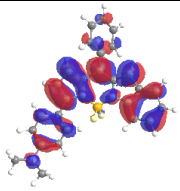

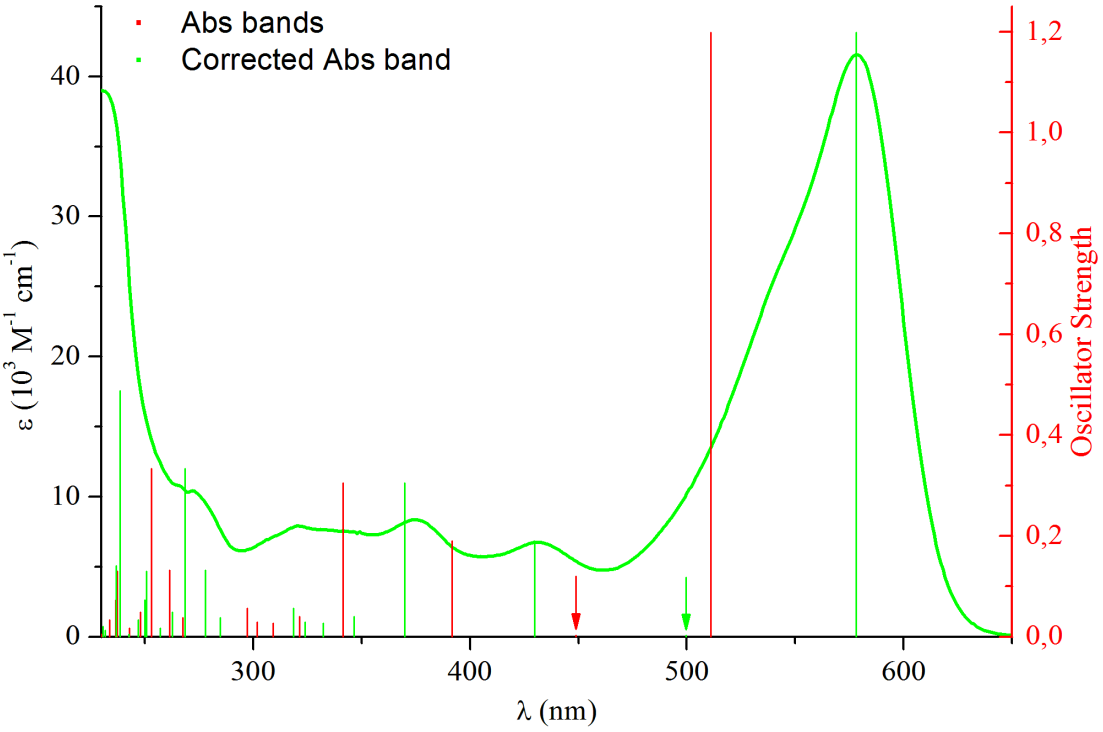

Figure II.S71 – BbF **9** experimental absorption spectrum in CH_2Cl_2 vs TD-DFT calculated optical absorption bands

(Red = uncorrected; Green = corrected; PCM = CH_2Cl_2).

Table II.S19 - Assignation of optical absorption bands for BbF **9** based on TD-DFT calculations

λ, nm				
Observed (ε, x10^3 $M^{-1}cm^{-1}$)	**Calculated** (Osc. Strength)	**Corr.**	**Trans. No.**	**Major contributions to excitation**
578 (42)	511 (1.198)	578	T1	H (97%) -> L
548 (28)	449 (0.002)	500	T2	H-2 (27%), H-1 (71%) -> L
431 (6.7)	392 (0.191)	430	T3	H-2 (67%), H-1 (27%) -> L
375 (8.3)	341 (0.305)	370	T4	H-4 (20%), H-3 (73%) -> L
321 (7.9)	321 (0.040)	347	T5	H-4 (71%), H-3 (15%) -> L
	309 (0.027)	332	T6	H-6 (31%), H-5 (63%) -> L
	302 (0.029)	324	T7	H-6 (57%), H-5 (34%) -> L
	297 (0.056)	319	T8	H (72%) -> L+1
272 (10)	268 (0.038)	285	T9	H-3 (25%) -> L+1; H (47%) -> L+2
	262 (0.132)	278	T10	H-8 (12%), H-7 (80%) -> L

Table II.S20 - NTO analysis for BbF **9** absorption bands T1 to T10 obtained by TD-DFT (Isovalue = 0.02; PCM = CH_2Cl_2)

Transition / Eigenvalue	**NTO Hole "From"**	**NTO Particle "To"**
T1 / 0.99	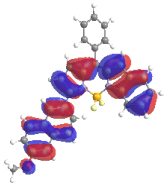	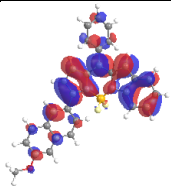
T2 / >0.99	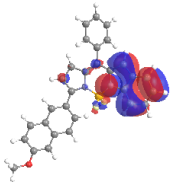	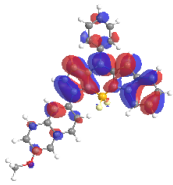
T3 / 0.99	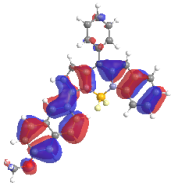	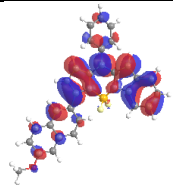
T4 / 0.96	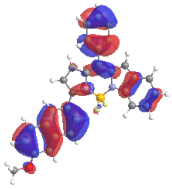	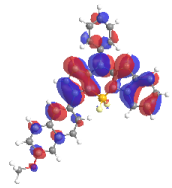
T5 / 0.93	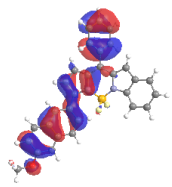	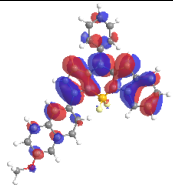
T6 / 0.97	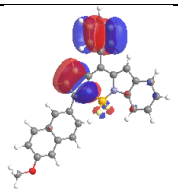	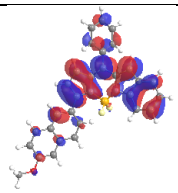

T7 / 0.92	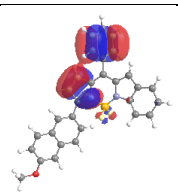	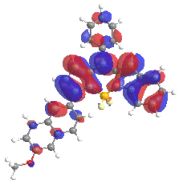
T8 / 0.81	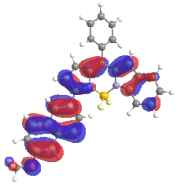	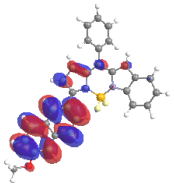
T9 / 0.65	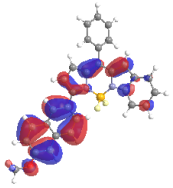	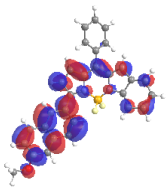
T10 / 0.95	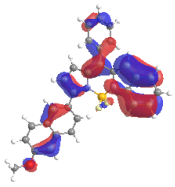	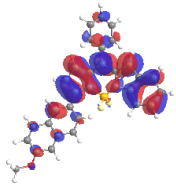

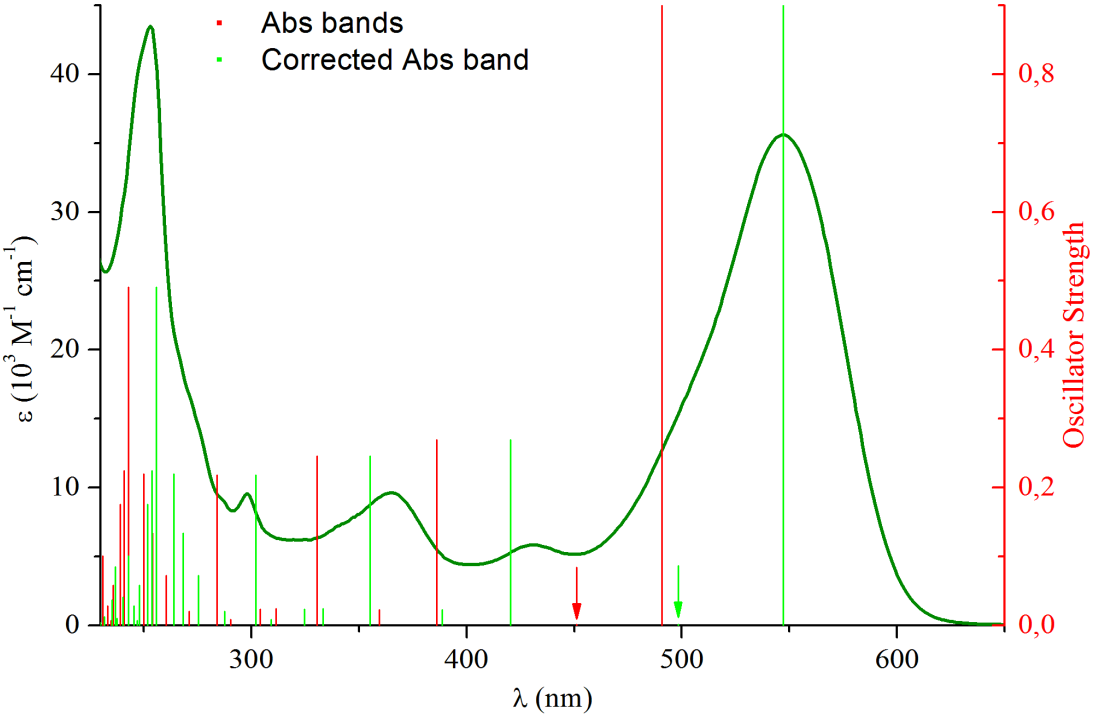

Figure II.S72 – BbF **10** experimental absorption spectrum in CH_2Cl_2 vs TD-DFT calculated optical absorption bands

(Red = uncorrected; Green = corrected; PCM = CH_2Cl_2).

Table II.S21 - Assignation of optical absorption bands for BbF **10** based on TD-DFT calculations

λ, nm				
Observed (ε, x10^3 $M^{-1}cm^{-1}$)	**Calculated** (Osc. Strength)	**Corr.**	**Trans. No.**	**Major contributions to excitation**
547 (36)	491 (0.901)	547	T1	H (97%) -> L
511 (20)	451 (0.001)	498	T2	H-1 (83%) -> L
431 (5.8)	386 (0.269)	420	T3	H-3 (32%), H-2 (49%), H-1 (16%) -> L
365 (9.6)	359 (0.022)	389	T4	H-3 (58%), H-2 (38%) -> L
	330 (0.246)	355	T5	H-4 (95%) -> L
	312 (0.024)	333	T6	H-7 (33%), H-5 (62%) -> L
	304 (0.023)	325	T7	H-7 (49%), H-6 (13%), H-5 (36%) -> L
298 (9.5)	290 (0.008)	309	T8	H-3 (15%), H-2 (17%) -> L+1
				H-1 (11%), H (38%) -> L+2
	284 (0.218)	302	T9	H (73%) -> L+1
273 (16)	271 (0.020)	287	T10	H-7 (14%), H-6 (77%) -> L

Table II.S22 - NTO analysis for BbF **10** absorption bands T1 to T10 obtained by TD-DFT

(Isovalue = 0.02; PCM = CH_2Cl_2)

Transition / Eigenvalue	**NTO Hole "From"**	**NTO Particle "To"**
T1 / 0.99	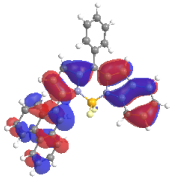	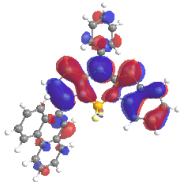
T2 / >0.99	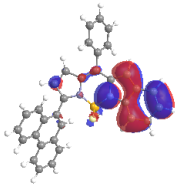	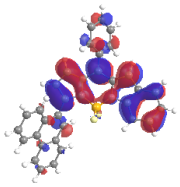
T3 / 0.99	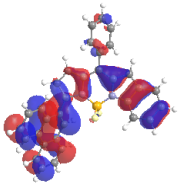	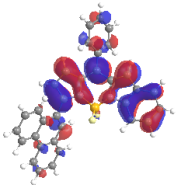
T4 / 0.99	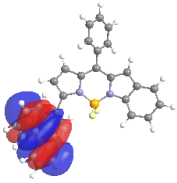	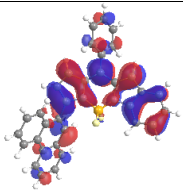
T5 / 0.99	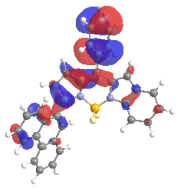	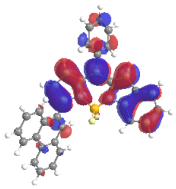
T6 / 0.99	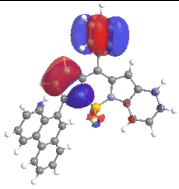	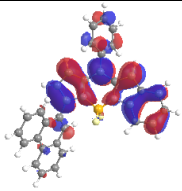

T7 / 0.99	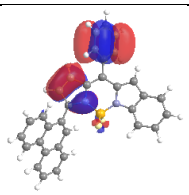	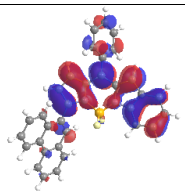
T8 / 0.63	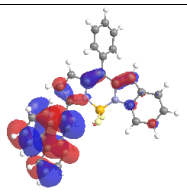	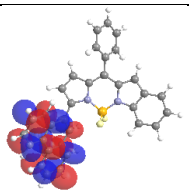
T9 / 0.88	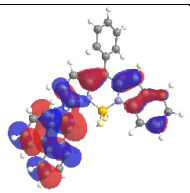	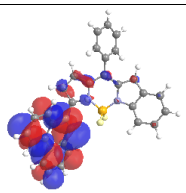
T10 / 0.96	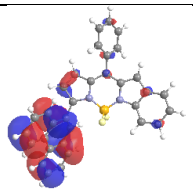	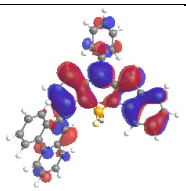

Table II.S23 - Selected bond lengths (Å) and angles (°) for BbF **1**, **5**, **8** and **9** calculated by DFT.[a]

	1	**5**	**8**	**9** [b]
Bond lengths				
F1-B1	1.396 (-0.001)	1.397 (+0.004)	1.399 (-0.004)	1.397 (+0.016)
F2-B1	1.383 (+0.005)	1.384 (=)	1.386 (=)	1.384 (-0.018)
N1-B1	1.532 (-0.005)	1.531 (-0.003)	1.530 (+0.001)	1.532 (+0.010)
N2-B1	1.566 (-0.002)	1.565 (-0.002)	1.562 (-0.009)	1.565 (-0.007)
N1-C1	1.361 (-0.011)	1.362 (-0.014)	1.364 (-0.014)	1.361 (-0.014)
N1-C8	1.377 (-0.010)	1.377 (-0.004)	1.376 (-0.007)	1.377 (-0.014)
N2-C10	1.393 (-0.013)	1.394 (-0.021)	1.396 (-0.012)	1.394 (-0.010)
N2-C13	1.345 (-0.002)	1.346 (-0.013)	1.351 (-0.008)	1.346 (-0.001)
C8-C9	1.412 (-0.014)	1.414 (-0.011)	1.418 (-0.014)	1.413 (-0.016)
C9-C10	1.385 (+0.003)	1.382 (=)	1.378 (-0.003)	1.384 (=)
C13-C14	1.462 (-0.008)	1.454 (-0.012)	1.444 (-0.008)	1.457 (-0.010)
C_{Subst}-O1/N3	---	1.344 (-0.064)	1.355 (-0.003)	1.349 (-0.015)
Angles				
C1-N1-B1	126.6 (-0.1)	126.5 (+0.1)	126.2 (+0.6)	126.4 (-0.2)
C13-N2-B1	129.4 (+0.5)	129.5 (-0.6)	129.6 (+0.1)	129.4 (+0.5)
F1-B1-F2	110.1 (-0.4)	109.9 (+0.4)	109.6 (-0.3)	110.0 (-0.2)
F1-B1-N1	109.3 (-0.9)	109.3 (-0.2)	109.1 (-0.4)	109.3 (-2.0)
F1-B1-N2	109.4 (+1.1)	109.5 (-0.9)	109.8 (=)	109.5 (-1.5)
F2-B1-N1	110.6 (+0.1)	110.6 (+1.5)	110.4 (-0.3)	110.6 (+1.2)
F2-B1-N2	110.5 (-0.3)	110.5 (-0.9)	110.5 (+0.7)	110.4 (+2.2)
N1-B1-N2	106.9 (+0.5)	107.0 (-0.3)	107.4 (+0.3)	107.0 (+0.3)
Tilt angles between planes of the pyrrole and the benzo[b]-fused pyrrolic rings				
	8.9 (-6.4)	8.8 (-1.5)	7.5 (+3.3)	8.9 (-1.0)
Tilt angle between planes of the pyrrole ring and proximal aryl				
	36.3 (-0.7)	32.3	25.9 (-3.3)	33.3 (+9.6)
Tilt angles between the DPM moiety and the aryl rings				
meso-Ph	57.6 (+9.3)	58.0 (+6.9)	58.4 (+6.2)	57.4 (+10)
Ar proximal	40.5 (-2.8)	36.6 (+8.9)	29.6 (-2.7)	37.5 (-10.3)

[a] Atom numbering following the one used for X-ray crystallography (Refer to Figure 6). Difference with corresponding X-ray structure given in parenthesis. [b] Atom numbering following the one used for X-ray crystallography, except for F1 assigned to the fluoride doing an H-bond with H19 in order to be consistent with other calculated structures.

Table II.S24 - Selected bond lengths (Å) and angles (°) for BbF **2-4**, **6**, **7** and **10** calculated by DFT.

	2	**3**	**4**	**6**	**7**	**10**
Bond lengths						
F1-B1	1.396	1.396	1.396	1.396	1.395	1.394
F2-B1	1.383	1.383	1.383	1.382	1.382	1.382
N1-B1	1.532	1.532	1.532	1.533	1.534	1.535
N2-B1	1.565	1.566	1.566	1.566	1.567	1.565
N1-C1	1.361	1.361	1.361	1.361	1.360	1.360
N1-C8	1.377	1.377	1.377	1.377	1.377	1.378
N2-C10	1.394	1.394	1.394	1.393	1.393	1.392
N2-C13	1.345	1.345	1.345	1.345	1.344	1.341
C8-C9	1.412	1.413	1.413	1.412	1.412	1.412
C9-C10	1.385	1.384	1.384	1.385	1.385	1.386
C13-C14	1.459	1.459	1.459	1.463	1.464	1.467
C_{Subst}-O1/N3	1.498	1.510	1.525	1.352	1.351/2	---
Angles						
C1-N1-B1	126.5	126.6	126.5	126.4	126.4	126.5
C13-N2-B1	129.4	129.4	129.4	129.3	129.4	128.4
F1-B1-F2	110.1	110.1	110.1	110.2	110.3	110.2
F1-B1-N1	109.3	109.3	109.3	109.2	109.2	109.4
F1-B1-N2	109.4	109.4	109.4	109.5	109.5	109.6
F2-B1-N1	110.6	110.6	110.6	110.5	110.5	110.9
F2-B1-N2	110.5	110.5	110.5	110.5	110.5	110.3
N1-B1-N2	106.9	106.9	106.9	106.9	106.8	106.4
Tilt angles between planes of the pyrrole and the benzo[b]-fused pyrrolic rings						
	8.8	8.9	8.8	8.6	8.8	8.7
Tilt angle between planes of the pyrrole ring and proximal aryl						
	34.7	35.0	34.7	37.0	37.8	57.8
Tilt angles between the DPM moiety and the aryl rings						
meso-Ph	57.7	57.7	57.7	57.5	58.1	57.0
Ar proximal	38.9	39.3	38.9	41.0	42.0	61.6

Table II.S25 - Intramolecular H-bonding for BbF **1**, **5**, **8** and **9** calculated by DFT.[a]

D-H···A	**D-H**	**H···A**	**D···A**	**< D-H···A**
1				
C19-H19···F1	1.081	2.124	3.219	143.2
2				
C19-H19···F1	1.081	2.119	3.058	143.6
3				
C19A-H19A···F1	1.081	2.121	3.216	143.7
4				
C19-H19···F1	1.081	2.120	3.059	143.7
5				
C19A-H19A···F1	1.081	2.102	3.050	144.8
6				
C19-H19···F2	1.080	2.123	3.049	142.1
7				
C19-H19···F2	1.080	2.126	3.042	141.0
8				
C19-H19···F1	1.080	2.082	3.041	146.3
9				
C19-H19···F2	1.081	2.102	3.051	145.0
10				
C19-H19···F2	1.083	2.259	3.025	126.0

[a] Distances in Å and angles in °.

X-ray Diffraction Measurements and Structure Determination

Crystallographic data were collected at 100 K for **1** and at 105K for **5**, **8** and **9** from single crystal samples that were mounted on a loop fiber (refer to Synthetic Methods section for specific crystallization conditions). Data were collected using a Bruker D8 Venture diffractometer configured with a Metal Jet liquid-metal source (Ga Kα λ=1.34Å), a Helios MX Mirror optics and a Photon 100 CMOS-based area detector. The crystal-to-detector distance was 4.0 cm and the data collection was carried out in 1024 x 1024 pixel mode. The initial unit cell parameters were determined by a least-squares fit of the angular setting of strong reflections, collected by a 52.0 degree scan in 104 frames over three different parts of the reciprocal space.

For data collection, determination of cell parameters, cell refinement, and data reduction *APEX2* and *SAINT* were used.[35] Absorption corrections were applied using *SADABS*.[36] Structure solution was performed using direct methods with *SHELXT* and refined on F^2 by full-matrix least squares using *SHELXL2014*.[37, 38] The absence of twinning was investigated using TWINRotMat from PLATON.[39] The material was prepared for publication using Mercury and *OLEX2*.[40, 41] Figures were generated using ORTEP3 and POV-Ray.[42, 43]

For all the structures, all non-H atoms were refined by full-matrix least-squares with anisotropic displacement parameters. The H-atoms were included in calculated positions and treated as riding atoms: aromatic C—H 0.95 Å, methyl C—H 0.98 Å, with

$U_{iso}(H) = k \times U_{eq}$ (parent C-atom), where k = 1.2 for the aromatic H-atoms and 1.5 for the methyl H-atoms.

Excellent sets of data were obtained for the four compounds. The use of the SIMU restraint was necessary for BbF **5** in order to model the disordered *para*-methoxyphenyl pointing toward each of the two fluoride atoms as two components and the occupancy of each part was determined to be in a 53:47 ratio using a least-square refined free variable.

Data were deposited in CCDC under the deposit numbers: CCDC 1418610 – 1418613. The alerts given by the checkCIF/ PLATON routine are commented in the crystallographic information files (cifs) of the corresponding compounds.

Table II.S26 - Solid-state structure and refinement data for BbF **1**, **5**, **8** and **9**.

	1	**5**	**8**	**9**
Empirical formula	$C_{25}H_{17}BN_2F_2$	$C_{26}H_{19}BF_2N_2O$	$C_{27}H_{22}BF_2N_3$	$C_{30}H_{21}BF_2N_2O$
Formula weight	394.21	424.24	437.28	474.30
Temperature (K)	100	105	105	105
Crystal system	orthorhombic	monoclinic	orthorhombic	orthorhombic
Space group	Pbca	$P2_1/c$	$P2_12_12_1$	$Pna2_1$
Unit Cell: *a* (Å)	12.2509(7)	20.5702(9)	7.5580(2)	7.6330(2)
b (Å)	7.8383(4)	12.2670(5)	10.8156(3)	18.6828(4)
c (Å)	39.829(2)	7.9969(4)	25.7212(8)	15.7103(4)
a (°)	90	90	90	90
β (°)	90	99.415(3)	90	90
g (°)	90	90	90	90
V (Å^3)	3824.6(4)	1990.7(2)	2102.6(1)	2240.4(1)
Z	8	4	4	4
d_{calc} (g/cm^3)	1.369	1.416	1.381	1.406
μ (mm^{-1})	0.489	0.521	0.488	0.504
F(000)	1632.0	880.0	912.0	984.0
2θ range (°)	3.86 to 121.356	7.326 to 121.666	5.978 to 121.31	6.396 to 121.202
Reflections collected	38065	30340	33147	34104
Independent reflections	4375	4579	4803	5130
GoF	1.043	1.025	1.047	1.073
Final R indexes [I>=2σ (I)]	R_1 = 0.0488, wR_2 = 0.1122	R_1 = 0.0504, wR_2 = 0.1160	R_1 = 0.0277, wR_2 = 0.0721	R_1 = 0.0304, wR_2 = 0.0644
Final R indexes [all data]	R_1 = 0.0685, wR_2 = 0.1215	R_1 = 0.0717, wR_2 = 0.1287	R_1 = 0.0278, wR_2 = 0.0723	R_1 = 0.0360, wR_2 = 0.0664
Largest diff. peak and hole (e/Å^3)	0.39 and -0.19	0.36 and -0.48	0.25 and -0.16	0.20 and -0.12
Flack parameter	---	---	0.025(17)	0.03(6)

Table II.S27 - Selected bond lengths (Å) and angles (°) for BbF **1**, **5**, **8** and **9**.

	1	**5**	**8**	**9**
Bond lengths (Å)				
F1-B1	1.397(2)	1.393(2)	1.403(2)	1.381(3)
F2-B1	1.378(2)	1.384(2)	1.386(2)	1.402(2)
N1-B1	1.537(2)	1.534(2)	1.529(2)	1.522(3)
N2-B1	1.568(2)	1.567(2)	1.571(2)	1.572(3)
N1-C1	1.372(2)	1.376(2)	1.378(2)	1.375(2)
N1-C8	1.387(2)	1.381(2)	1.383(2)	1.391(2)
N2-C10	1.406(2)	1.415(2)	1.408(2)	1.404(2)
N2-C13	1.347(2)	1.359(2)	1.359(2)	1.347(3)
C8-C9	1.426(2)	1.425(2)	1.432(2)	1.429(2)
C9-C10	1.382(2)	1.382(2)	1.381(2)	1.384(3)
C13-C14	1.470(2)	1.466(2)	1.452(2)	1.467(3)
C-X in proximal Ar	---	1.408(2) (C17-01)	1.358(2) (C17-N3)	1.364(3) (C22-O1)
Angles (°)				
C1-N1-B1	126.7(1)	126.4(1)	125.6(1)	126.6(2)
C13-N2-B1	128.9(1)	130.1(1)	129.5(1)	128.9(2)
F1-B1-F2	110.5(1)	109.5(1)	109.9(1)	110.2(2)
F1-B1-N1	110.2(1)	110.6(1)	109.5(1)	111.3(2)
F1-B1-N2	108.3(1)	109.0(1)	109.8(1)	111.0(2)
F2-B1-N1	110.5(1)	109.1(1)	110.7(1)	109.4(2)
F2-B1-N2	110.8(1)	111.4(1)	109.8(1)	108.2(2)
N1-B1-N2	106.4(1)	107.3(1)	107.1(1)	106.7(2)
Dihedral angles (°)				
C12-C13-C14-C15	-34.6(2)	-18.9(4) / 11.6(3) [a]	-27.7(2)	39.5(3)
C8-C9-C_i-C_j	49.3(2) (C20-C21)	49.6(2) (C21-C22)	53.3(2) (C22-C23)	-49.0(2) (C25-C26)
Tilt angles (°) between planes of the pyrrole and the benzo[b]-fused pyrrolic rings	15.3(1)	10.3(1)	4.2(1)	9.9(1)
Tilt angle (°) between planes of the pyrrole ring and proximal aryl	37.0(1)	23.0(2) / 18.4(1) [a]	29.2(1)	42.9(1)
Tilt angles (°) between the DPM moiety and aryl rings				
meso-Ph	48.3(1)	51.1(1)	52.2(1)	47.4(1)
Ar proximal	43.3(1)	27.7(2) / 14.1(1) [a]	32.3(1)	47.8(1)

[a] Two angles given, corresponding to the two disordered positions of the *para*-methoxyphenyl.

Table II.S28 - Intramolecular H-bonding for BbF **1**, **5**, **8** and **9**.

D-H···A	**D-H**	**H···A**	**D···A**	**< D-H···A**
1				
C19-H19···F1	0.950	2.352(1)	3.166(2)	143.5(1)
5				
C19A-H19A···F1	0.950	2.080(1)	2.948(4)	150.7(2)
C19B-H19B···F2	0.950	1.933(1)	2.788(5)	148.5(2)
8				
C19-H19···F1	0.950	2.227(1)	3.077(2)	148.4(1)
9				
C19-H19···F2	0.950	2.351(1)	3.137(2)	139.8(1)

[a] Distances in Å and angles in °.

References

1. Wakamiya, A.; Murakami, T.; Yamaguchi, S., *Chem. Sci.* **2013,** *4*, 1002-1007.
2. Rieth, R. D.; Mankad, N. P.; Calimano, E.; Sadighi, J. P., *Org. Lett.* **2004,** *6*, 3981-3983.
3. Verdoes, M.; Hillaert, U.; Florea, B. I.; Sae-Heng, M.; Risseeuw, M. D. P.; Filippov, D. V.; van der Marel, G. A.; Overkleeft, H. S., *Bioorg. Med. Chem. Lett.* **2007,** *17*, 6169-6171.
4. Wen, J.; Qin, S.; Ma, L.-F.; Dong, L.; Zhang, J.; Liu, S.-S.; Duan, Y.-S.; Chen, S.-Y.; Hu, C.-W.; Yu, X.-Q., *Org. Lett.* **2010,** *12*, 2694-2697.
5. Aliev, I. A.; Almamedova, D. T.; Gasanov, B. R.; Mikhaleva, A. I., *Chem. Heterocycl. Compd.* **1984,** *20*, 1117-1119.
6. Ohri, R. V.; Radosevich, A. T.; Hrovat, K. J.; Musich, C.; Huang, D.; Holman, T. R.; Toste, F. D., *Org. Lett.* **2005,** *7*, 2501-2504.
7. Gao, W.-C.; Jiang, S.; Wang, R.-L.; Zhang, C., *Chem. Commun.* **2013,** *49*, 4890-4892.
8. Connelly, N. G.; Geiger, W. E., *Chem. Rev.* **1996,** *96*, 877-910.
9. Le Guennic, B.; Maury, O.; Jacquemin, D., *Phys. Chem. Chem. Phys.* **2012,** *14*, 157-164.
10. Frisch, M. J.; Trucks, G. W.; Schlegel, H. B.; Scuseria, G. E.; Robb, M. A.; Cheeseman, J. R.; Scalmani, G.; Barone, V.; Mennucci, B.; Petersson, G. A.; Nakatsuji, H.; Caricato, M.; Li, X.; Hratchian, H. P.; Izmaylov, A. F.; Bloino, J.; Zheng, G.; Sonnenberg, J. L.; Hada, M.; Ehara, M.; Toyota, K.; Fukuda, R.; Hasegawa, J.; Ishida, M.; Nakajima, T.; Honda, Y.; Kitao, O.; Nakai, H.; Vreven, T.; J. A. Montgomery, J.; Peralta, J. E.; Ogliaro, F.; Bearpark, M.; Heyd, J. J.; Brothers, E.; Kudin, K. N.; Staroverov, V. N.; Kobayashi, R.; Normand, J.; Raghavachari, K.; Rendell, A.; Burant, J. C.; Iyengar, S. S.; Tomasi, J.; Cossi, M.; Rega, N.; Millam, J. M.; Klene, M.; Knox, J. E.; Cross, J. B.; Bakken, V.; Adamo, C.; Jaramillo, J.; Gomperts, R.; Stratmann, R. E.; Yazyev, O.; Austin, A. J.; Cammi, R.; Pomelli, C.; Ochterski, J. W.; Martin, R. L.; Morokuma, K.; Zakrzewski, V. G.; Voth, G. A.; Salvador, P.; Dannenberg, J. J.; Dapprich, S.; Daniels, A. D.; Farkas, Ö.; Foresman, J. B.; Ortiz, J. V.; Cioslowski, J.; Fox, D. J. *Gaussian 09 Revision D.01*, Gaussian Inc.: Wallingford CT 2009.
11. Perdew, J. P.; Burke, K.; Ernzerhof, M., *Phys. Rev. Lett.* **1996,** *77*, 3865-3868.
12. Perdew, J. P.; Burke, K.; Ernzerhof, M., *Phys. Rev. Lett.* **1997,** *78*, 1396.
13. Adamo, C.; Barone, V., *J. Chem. Phys.* **1999,** *110*, 6158-6169.
14. Tomasi, J.; Mennucci, B.; Cammi, R., *Chem. Rev.* **2005,** *105*, 2999-3093.
15. Boese, A. D.; Martin, J. M. L., *J. Chem. Phys.* **2004,** *121*, 3405-3416.
16. Dennington, R.; Keith, T.; Millam, J.; Eppinnett, K.; Hovell, W. L.; Gilliland, R. *GaussView Version 3.09*, Semichem Inc.: Shawnee Mission KS, 2003.
17. O'Boyle, N. M.; Tenderholt, A. L.; Langner, K. M., *J. Comp. Chem.* **2008,** *29*, 839-845.
18. Chemissian, a computer program to analyze and visualize quantum-chemical calculations, by L. Skripnikov. For the current version, see http://www.chemissian.com
19. Lakshmi, V.; Shaikh, M.; Ravikanth, M., *J. Fluoresc.* **2013,** *23*, 519-525.

20. Richards, V. J.; Gower, A. L.; Smith, J. E. H. B.; Davies, E. S.; Lahaye, D.; Slater, A. G.; Lewis, W.; Blake, A. J.; Champness, N. R.; Kays, D. L., *Chem. Commun.* **2012,** *48*, 1751-1753.
21. Yu, C.; Jiao, L.; Yin, H.; Zhou, J.; Pang, W.; Wu, Y.; Wang, Z.; Yang, G.; Hao, E., *Eur. J. Org. Chem.* **2011,** *2011*, 5460-5468.
22. Wang, L.; Zhang, Y.; Xiao, Y., *RSC Adv.* **2013,** *3*, 2203-2206.
23. Ni, Y.; Zeng, W.; Huang, K.-W.; Wu, J., *Chem. Commun.* **2013,** *49*, 1217-1219.
24. Guzow, K.; Kornowska, K.; Wiczk, W., *Tetrahedron Lett.* **2009,** *50*, 2908-2910.
25. Gabe, Y.; Ueno, T.; Urano, Y.; Kojima, H.; Nagano, T., *Anal. Bioanal. Chem.* **2006,** *386*, 621-626.
26. Wang, L.; Verbelen, B.; Tonnele, C.; Beljonne, D.; Lazzaroni, R.; Leen, V.; Dehaen, W.; Boens, N., *Photochem. Photobiol. Sci.* **2013,** *12*, 835-847.
27. Verbelen, B.; Boodts, S.; Hofkens, J.; Boens, N.; Dehaen, W., *Angew. Chem., Int. Ed.* **2015,** *54*, 4612-4616.
28. Yu, C.; Xu, Y.; Jiao, L.; Zhou, J.; Wang, Z.; Hao, E., *Chem. Eur. J.* **2012,** *18*, 6437-6442.
29. Tomimori, Y.; Okujima, T.; Yano, T.; Mori, S.; Ono, N.; Yamada, H.; Uno, H., *Tetrahedron* **2011,** *67*, 3187-3193.
30. Umezawa, K.; Matsui, A.; Nakamura, Y.; Citterio, D.; Suzuki, K., *Chem. Eur. J.* **2009,** *15*, 1096-1106.
31. Umezawa, K.; Nakamura, Y.; Makino, H.; Citterio, D.; Suzuki, K., *J. Am. Chem. Soc.* **2008,** *130*, 1550-1551.
32. Maeda, C.; Todaka, T.; Ema, T., *Org. Lett.* **2015,** *17*, 3090-3093.
33. Bochkov, A. Y.; Akchurin, I. O.; Dyachenko, O. A.; Traven, V. F., *Chem. Commun.* **2013,** *49*, 11653-11655.
34. Zatsikha, Y. V.; Yakubovskyi, V. P.; Shandura, M. P.; Dubey, I. Y.; Kovtun, Y. P., *Tetrahedron* **2013,** *69*, 2233-2238.
35. Bruker *APEX2 and SAINT*, Bruker AXS Inc.: Madison, Wisconsin, USA., 2007.
36. Bruker *SADABS and TWINABS*, Bruker AXS Inc.: Madison, Wisconsin, USA., 2001.
37. Sheldrick, G. M., *Acta Crystallogr., Sect. A* **2008,** *64*, 112-122.
38. Sheldrick, G. M., *Acta Crystallogr., Sect. A* **2015,** *71*, 3-8.
39. Spek, A. L., *Acta Crystallogr., Sect. D* **2009,** *65*, 148-155.
40. CCDC *Mercury 3.1 - 3.3*, 2001-2013.
41. Dolomanov, O. V., Bourhis, L. J., Gildea, R. J., Howard, J. A. K., Puschmann, H., *J. Appl. Cryst.* **2009,** *42*, 339-341.
42. Farrugia, L. J., *J. Appl. Crystallogr.* **1997,** *30*, 565.
43. *POV-Ray* Persistence of Vision Pty. Ltd., retrieved from http://www.povray.org/download/: 2004.

Annexe III : Informations supplémentaires du Chapitre 4

“ Azadipyrromethene Cyclometallation on Neutral RuII Complexes: Sensitizers with Extended NIR Absorption for Solar Energy Conversion Applications”

Soumis le 30 septembre 2015 à *Chemical Science.*

Materials and Instrumentation

ADPM **1** was obtained from Saint-Jean Photochemicals Inc. (sjpc.com) and used as received. Literature procedures were used for the synthesis of complexes $Ru(N^N)(MeOH)Cl_3$ and $Ru(tpy\text{-}Ph\text{-}Br)Cl_3$.[10,11] Reagents and solvents were obtained commercially and used without further purification. Reactions were carried out under ambient atmosphere. Solvents were removed under reduced pressure using a rotary evaporator unless otherwise stated.

Nuclear magnetic resonance (NMR) spectra were recorded in $CDCl_3$ at room temperature (r.t.). 700 MHz ^1H and 175 MHz ^{13}C NMR of sensitizer **2** were obtained on a Bruker Avance 700. 500 MHz ^1H and 125 MHz ^{13}C NMR of sensitizers **3** and **4** were recorded on a Bruker Avance 500 spectrometer. 400 MHz ^1H of sensitizers **5** and **6** were recorded on a Bruker AV400 spectrometer, while the ^{13}C of the later was recorded on the Bruker Avance 700. Chemical shifts are reported in part per million (ppm) relative to residual solvent protons (7.27 ppm for chloroform-d and 2.50 ppm for DMSO-d_6) and the carbon resonance of the solvent (77.00 ppm for chloroform-d and 39.51 ppm for DMSO-d_6).

High-Resolution Electro Spray Ionization Mass Spectrometry (HR-ESIMS) was performed on a Liquid Chromatography / Mass Spectrometry with a Time of Flight detector (LC/MS TOF) from Agilent for sensitizer **2**. Compounds 3-6 were performed on a Bruker micrOTOF II.

Absorption spectra were measured in CH_2Cl_2 (DCM) at concentrations obeying Beer-Lambert's law at r.t. on a Cary 6000i UV-vis-NIR Spectrophotometer. The absence of fluorescence for the series of sensitizers investigated herein was assessed on a Cary Eclipse Fluorescence Spectrophotometer.

Full details on crystal structure determination and refinement data for compounds **2**, **4** and **5** are reported in corresponding section of the ESI and on the Cambridge Crystallographic Data Centre (CCDC 1419506-1419508, respectively).

Electrochemical measurements were carried out in argon-purged CH_2Cl_2 at room temperature with a BAS CV50W multipurpose potentiostat. The working electrode used was a glassy carbon electrode for every compound. The counter electrode was a Pt wire, and the pseudo-reference electrode was a silver wire. The reference was set using an internal 1 mM ferrocene/ferrocenium sample at 0.46 V vs SCE in CH_2Cl_2. and 0.45 V vs SCE in DMF.[12] The concentration of the compounds was about 1 mM. Tetrabutylammonium hexafluorophosphate (TBAP) was used as supporting electrolyte and its concentration was 0.10 M. Cyclic voltammograms (CV) were obtained at scan rates of 50, 100, 200, and 500 mV/s. For reversible processes, half-wave potentials (vs. SCE) from CV were used. To establish the potential of irreversible processes, differential pulse voltammetry (DPV) experiments were performed with a step rate of 4 mV, a pulse height of 50 mV, and a frequency of 5 Hz. Criteria for reversibility were the separation of 60 mV between cathodic and anodic peaks, the close to unity ratio of the intensities of the cathodic and anodic currents, and the constancy of the peak potential on changing scan rate. Experimental uncertainties are as follows: absorption maxima, ±2 nm; molar absorption coefficient, 10%; redox potentials, ± 10 mV.

Computational Methods

Computational modelization of sensitizers **2** – **6** was performed with the Gaussian 09 software (G09).[13] Geometry optimizations, frequency calculations and molecular orbital (MO) calculations were performed by DFT method under vacuum using the B3LYP[14-17] hybrid functional and 6-31G* as the basis set for all atoms except ruthenium, for which LanL2DZ was used. Crystallographic coordinates were used as starting points for geometry optimizations when available. When no crystallographic data were available for a given compound, modification of a similar derivative was used. Tight convergence criteria and no symmetry constraints were imposed during the optimization process. Only positive frequencies were found for the optimized structures. The 80 firsts absorption bands were calculated by TD-DFT (B3LYP / 6-31G* and LanL2DZ for Ru) from optimized structures with the PCM[18] of dichloromethane for sensitizers **2** – **6** and also of methanol for **6**. MOs were visualized (isovalue = 0.02) with GaussView 3 software.[19] GaussSum 6.5 was employed to extract from TD-DFT results the absorption energies and oscillator strengths, while molecular orbital energies were obtained from DFT.[20] Chemissian 4.23 program was used to represent MO's energy levels (Figure S.30) and determine the electronic distribution (in %) of the various parts of the sensitizers from DFT results and calculate the natural transition orbitals (NTO) (isovalue = 0.02) associated with absorption bands in the visible (> 400 nm) and NIR ranges obtained from TD-DFT results.[21]

Synthetic Methods

General procedure for sensitizers **2** – **4**

A suspension of ADPM **1** (1 equiv.), the corresponding Ru(N^N)(MeOH)Cl_3·MeOH (1 equiv.), and triethylamine (TEA) (6 equiv.) in a 9:1 *n*-butanol (13.5 mL) / MeOH (1.5 mL) solvent mixture was reacted in a microwave reactor at 150°C for 2 hours under magnetic stirring. The reaction mixture was evaporated to dryness, dissolved in CH_2Cl_2 and impregnated on silica. The crude product was purified by silica gel chromatography, isolated by evaporation and *in vacuo* drying to afford a black powder.

Sensitizer **2** *[Ru^{II}(ADPM)(2,2'-bpy)CO]*

ADPM **1** (100 mg; 0.175 mmol), Ru(2,2'-bpy)(MeOH)Cl_3·MeOH (75.0 mg; 0.175 mmol) and TEA (0.142 mL; 1.05 mmol). Black needles suitable for X-ray structural crystallized from slow evaporation of a concentrated solution in chlorobenzene. Yield = 87.5 mg (59 %). ^{1}H NMR ($CDCl_3$, 700 MHz) δ/ppm: 3.51 (s, 3 H), 3.76 (s, 3 H), 3.86 (s, 3 H), 3.91 (s, 3 H), 5.51 (d, J = 2.69 Hz, 1 H), 6.28 (s, 1 H), 6.31 (dd, J = 8.29, 2.46 Hz, 1 H), 6.48 (d, J = 8.29 Hz, 2 H), 6.86 - 6.94 (m, 4 H), 6.97 - 7.02 (m, 3 H), 7.06 (s, 1 H), 7.19 - 7.23 (m, 1 H), 7.41 (d, J = 8.29 Hz, 1 H), 7.53 (td, J = 7.73, 1.34 Hz, 1 H), 7.70 - 7.76 (m, 2 H), 7.87 (d, J = 8.73 Hz, 2 H), 7.89 (d, J = 8.06 Hz, 1 H), 8.09 (d, J = 5.82 Hz, 1 H), 8.16 (d, J = 8.73 Hz, 2 H), 8.82 (d, J = 5.15 Hz, 1 H). ^{13}C NMR ($CDCl_3$, 175 MHz) δ/ppm: 54.5, 55.2, 55.3, 55.4, 106.5 (2C), 111.5, 112.7

(2C), 113.3 (2C), 113.6 (2C), 117.4, 120.6, 120.8, 121.6, 125.2, 125.4, 125.6, 127.7, 128.2, 129.5, 130.0 (2C), 130.6 (2C), 130.7, 132.0, 136.3, 136.4, 142.6, 142.9, 144.3, 144.8, 149.3, 153.3, 153.9, 154.2, 158.5, 158.7, 158.9, 159.1, 163.9, 168.0, 179.1, 200.9. Mass Spec (*m/z*); MS calcd for $C_{47}H_{37}N_5O_5Ru$: [M^+] 853.18327, found: 853.18673.

Sensitizer **3** *[Ru^{II}(ADPM)(4,4'-di-^{t}Bu-2,2'-bpy)CO]*

ADPM **1** (79.1 mg; 0.139 mmol), Ru(4,4'-di-^{t}Bu-2,2'-bpy)(MeOH)Cl_3·MeOH (75.0 mg; 0.139 mmol) and TEA (0.113 mL; 0.833 mmol). Yield = 34.6 mg (26 %). ^{1}H NMR ($CDCl_3$, 500 MHz) δ/ppm: 1.31 (s, 9 H), 1.42 (s, 9 H), 3.49 (s, 3 H), 3.78 (s, 3 H), 3.86 (s, 3 H), 3.91 (s, 3 H), 5.57 (d, J = 2.57 Hz, 1 H), 6.24 - 6.33 (m, 2 H), 6.51 (d, J = 8.80 Hz, 2 H), 6.88 - 7.02 (m, 7 H), 7.06 (s, 1 H), 7.20 (dd, J = 5.96, 1.93 Hz, 1 H), 7.40 (d, J = 8.25 Hz, 1 H), 7.68 (s, 1 H), 7.81 (s, 1 H), 7.85 - 7.95 (m, 3 H), 8.16 (d, J = 8.80 Hz, 2 H), 8.67 (d, J = 5.87 Hz, 1 H). ^{13}C NMR ($CDCl_3$, 125 MHz) δ/ppm: 30.4 (6C), 34.8, 35.1, 54.4, 55.1, 55.3, 55.4, 106.8 (2C), 111.5, 112.7 (2C), 113.3 (2C), 113.6 (2C), 117.1, 117.4, 118.0, 120.5, 122.4, 123.2, 125.3, 127.8, 128.3, 129.6, 130.0 (2C), 130.6 (2C), 131.0, 136.5, 142.7, 142.9, 144.0, 145.0, 148.7, 153.4, 153.5, 154.2, 156.9, 158.5, 158.7, 158.8, 159.1, 160.6, 163.8, 168.2, 180.0, 200.9. Mass Spec (*m/z*); MS calcd for $C_{55}H_{53}N_5O_5Ru$: [M^+] 965.3100, found: 965.3083.

Sensitizer **4** *[Ru^{II}(ADPM)(1,10-phen)CO]*

ADPM **1** (94.6 mg; 0.166 mmol), Ru(1,10-phen)(MeOH)Cl_3·MeOH (75.0 mg; 0.166 mmol) and TEA (0.135 mL; 0.996 mmol). Yield = 50.1 mg (34 %). ^{1}H NMR

($CDCl_3$, 500 MHz) δ/ppm: 3.41 (s, 3 H), 3.76 (s, 3 H), 3.86 (s, 3 H), 3.87 (s, 3 H), 5.46 (d, J = 2.57 Hz, 1 H), 6.17 (s, 1 H), 6.23-6.29 (m, 3 H), 6.59 (d, J = 7.70 Hz, 2 H), 6.89 - 6.93 (m, 2 H), 6.93 - 6.98 (m, 2 H), 7.08 (s, 1 H), 7.31 (dd, J = 8.16, 5.23 Hz, 1 H), 7.40 (d, J = 8.44 Hz, 1 H), 7.44 (dd, J = 8.07, 5.14 Hz, 1 H), 7.77 (d, J = 1.83 Hz, 2 H), 7.83 - 7.88 (m, 2 H), 7.99 (dd, J = 8.25, 1.28 Hz, 1 H), 8.06 (dd, J = 8.07, 1.47 Hz, 1 H), 8.12 - 8.17 (m, 2 H), 8.32 (dd, J = 5.14, 1.47 Hz, 1 H), 9.11 (dd, J = 5.32, 1.10 Hz, 1 H). ^{13}C NMR ($CDCl_3$, 125 MHz) δ/ppm: 54.4, 55.1, 55.28, 55.33, 106.3 (2C), 111.6, 112.4 (2C), 113.3 (2C), 113.6 (2C), 117.5, 121.0, 124.4, 124.5, 125.5, 126.5, 126.9, 127.7, 128.2, 129.0, 129.2, 129.7, 130.1 (2C), 130.6 (2C), 130.7, 131.0, 135.2, 136.4, 142.9, 143.1, 144.2, 144.4, 145.0, 146.2, 149.1, 153.0, 158.3, 158.7, 158.8, 159.2, 164.0, 168.1, 178.9, 201.4. Mass Spec (*m/z*); MS calcd for $C_{49}H_{37}N_5O_5Ru$: [M^+] 877.1846, found: 877.1876.

Sensitizer **5** *[Ru^{II}(ADPM)(Br-Ph-tpy)]*

ADPM **1** (0.956 g; 1.68 mmol), Ru(Br-Ph-tpy)Cl_3 (1.00 g; 1.68 mmol) and KO^{t}Bu (0.198 g; 1.68 mmol) were suspended in 75 mL of *n*-butanol. TEA (1.36 mL; 10.1 mmol) was added and the reaction mixture was refluxed for 72 hours under inert atmosphere and protected from light. The reaction mixture was evaporated to dryness, dissolved in CH_2Cl_2, washed with water (x3) and the organic layer was dried over anhydrous Na_2SO_4 and evaporated. Recrystallization in hot CH_2Cl_2 / heptane, filtration, heptane washes and *in vacuo* drying afforded the product as a black solid that was quickly took to the next step due to instability in solution. A X-ray quality crystal was isolated from the brown residue obtained after slow diffusion of heptane in a concentrated solution in CH_2Cl_2. Yield = 1.19 g (76 %). ^1H NMR ($CDCl_3$, 400 MHz)

δ/ppm: 3.45 (s, 3 H), 3.81 (s, 3 H), 3.88 (s, 3 H), 4.31 (s, 3 H), 6.15 (s, 4 H), 6.77 (d, J = 8.30 Hz, 2 H), 7.13-7.22 (m, 2 H), 7.55-7.67 (m, 5 H), 7.70 (d, J = 8.30 Hz, 3 H), 7.77-7.88 (m, 5 H), 7.89-7.99 (m, 2 H), 8.07 (d, J = 8.48 Hz, 2 H), 8.61 (s, 2 H), 8.96 (br.s., 2 H), 9.24 (br. s., 1 H), 9.34 (br. s., 1 H). Mass Spec (*m/z*); MS calcd for $C_{57}H_{43}N_6O_4RuBr$: [M^+] 1056.1577, found: 1056.1537.

Sensitizer **6** *[Ru^{II}(ADPM)(tpy-Ph_2-COOH)]*

Sensitizer **5** (100 mg; 0.095 mmol) and 4-carboxyphenylboronic acid (23.5 mg; 0.142 mmol) were dissolved in 5 mL of THF. A 2M aqueous solution of K_2CO_3 (0.12 mL; 0.240 mmol) was added and the reaction mixture was degassed. $Pd(PPh_3)_4$ (11 mg; 0.009 mmol) was added and the reaction mixture was refluxed for 12 hours. The reaction mixture was allowed to cool down, filtered and the precipitate obtained was washed with cool THF followed by heptane. The isolated dark solid was further suspended in water, stirred, filtered and washed with isopropanol and methyl *t*-butyl ether (MTBE). Vacuum drying afforded the product as a black solid. Yield = 63.5 mg (61 %). ^{1}H NMR (DMSO-d_6, 400 MHz) (Poorly soluble) δ/ppm: 3.37 (br.s., 3 H), 3.43 (s, 3 H), 3.79 (s, 3 H), 4.03 (s, 3 H), 5.88 (d, J = 7.95 Hz, 2 H), 6.26 (d, J = 7.42 Hz, 2 H), 6.89 (d, J = 8.48 Hz, 3 H), 7.28 (d, J = 4.24 Hz, 3 H), 7.68 (s, 2H), 7.77-7.92 (m, 9 H), 7.95-8.11 (m, 8 H), 8.37 (d, J = 8.48 Hz, 2 H), 8.61 (d, J = 7.59 Hz, 2 H), 9.08 (s, 2 H). ^{13}C NMR (DMSO-d_6, 175 MHz) δ/ppm: 53.6, 54.5, 55.1, 55.2, 104.8 (2C), 112.3 (2C), 113.2 (2C), 113.4 (2C), 118.3, 122.3, 124.8, 125.9, 126.0 (2C), 126.1, 126.8, 127.1 (2C), 127.3 (2C), 127.5, 127.8, 127.9 (2C), 128.0, 128.7, 128.79, 128.84, 129.0, 129.1, 129.75, 129.78, 129.81, 129.83, 129.88 (2C), 129.93 (2C), 131.2, 131.45, 131.50, 132.6,

134.4, 137.3, 139.1, 142.4 (2C), 154.74, 154.75, 157.4, 157.8 (2C), 157.9 (2C), 158.1 (2C), 158.8, 167.7 (2C), 172.1. Mass Spec (*m/z*); MS calcd for $C_{64}H_{48}N_6O_6Ru$: [M^+] 1098.2691, found: 1098.2658.

NMR Characterization

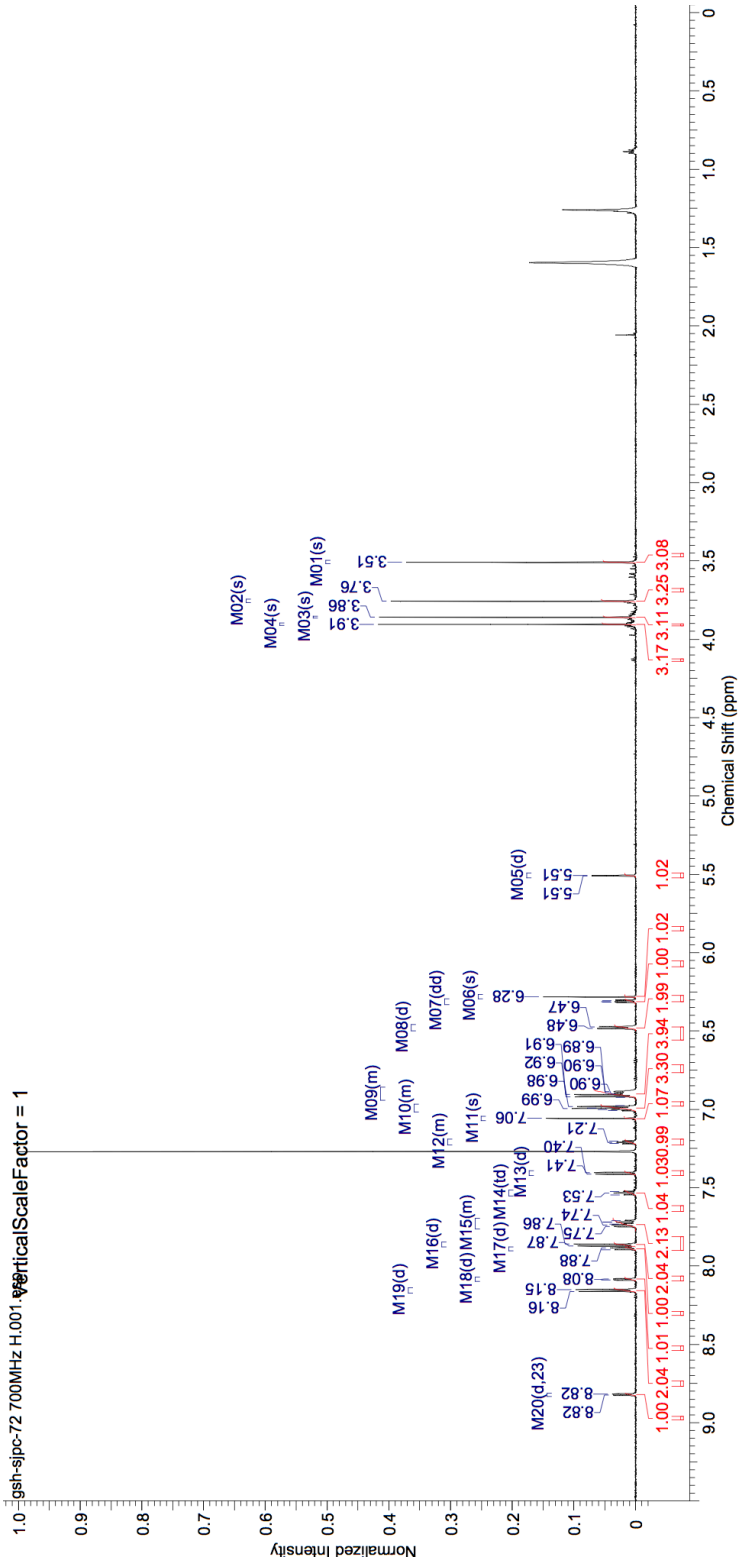

Figure III.S1 – ^{1}H of ADPM sensitizer **2** ($CDCl_3$; 700 MHz)

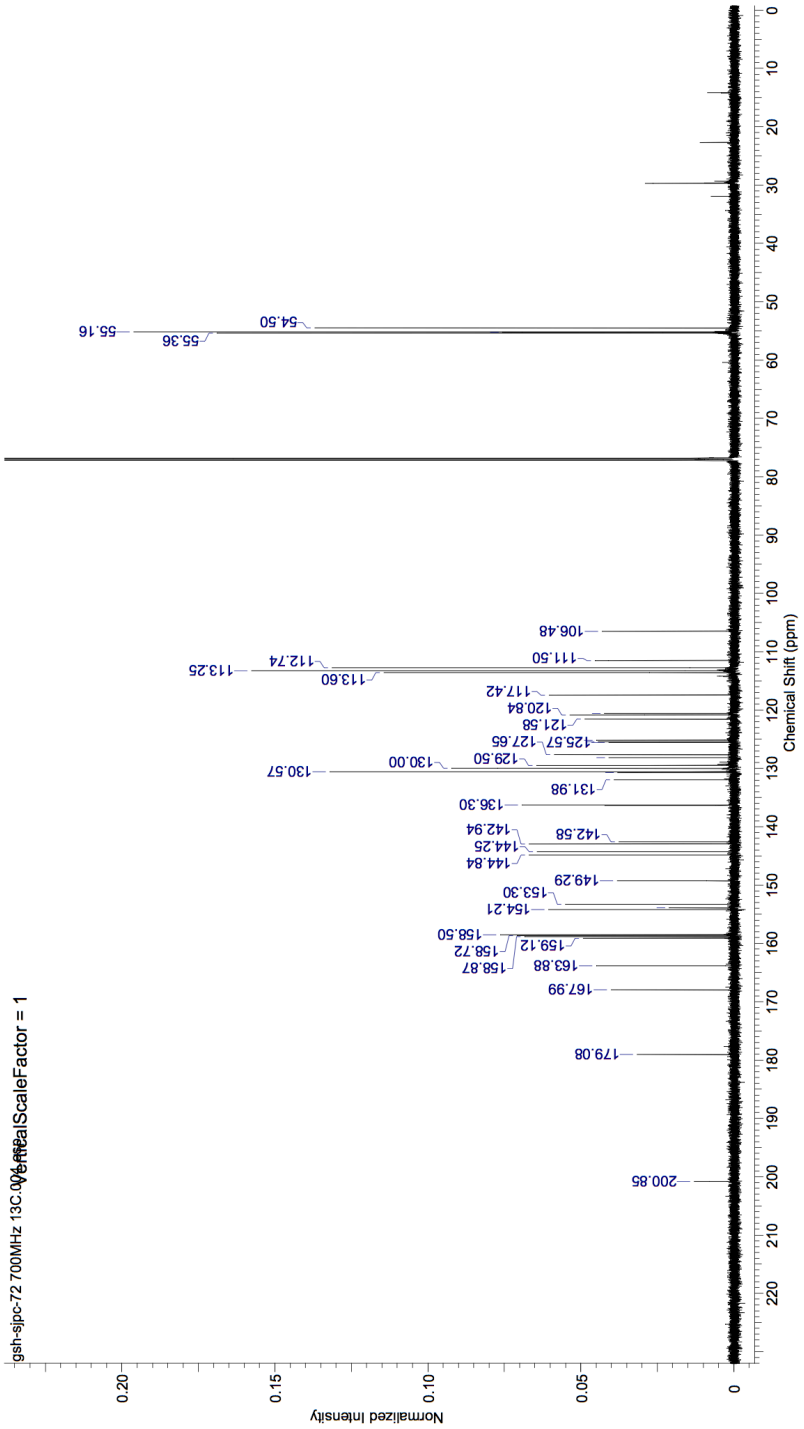

Figure III.S2 – ^{13}C of ADPM sensitizer **2** ($CDCl_3$; 175 MHz)

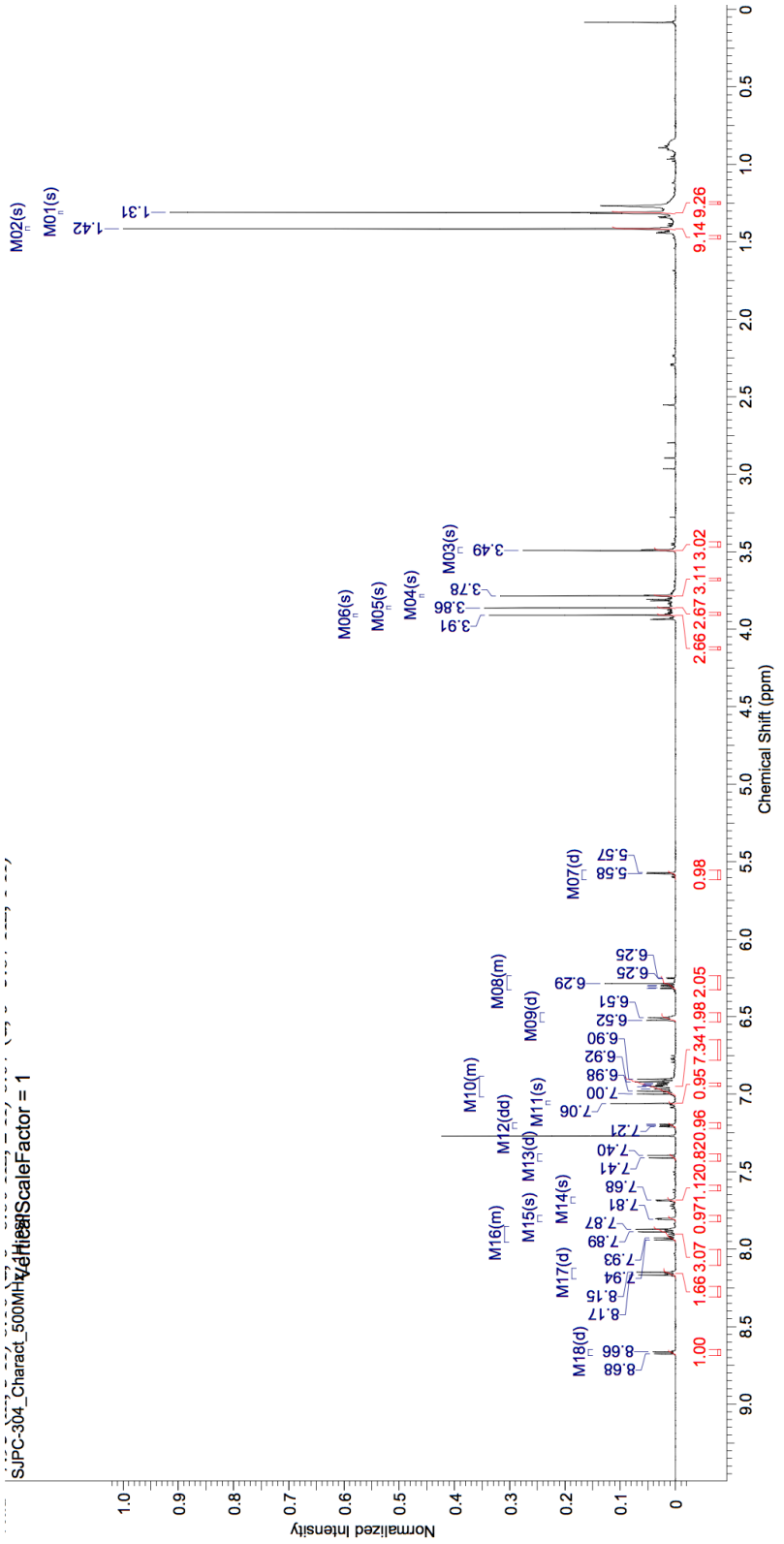

Figure III.S3 – ^{1}H of ADPM sensitizer **3** ($CDCl_3$; 500 MHz)

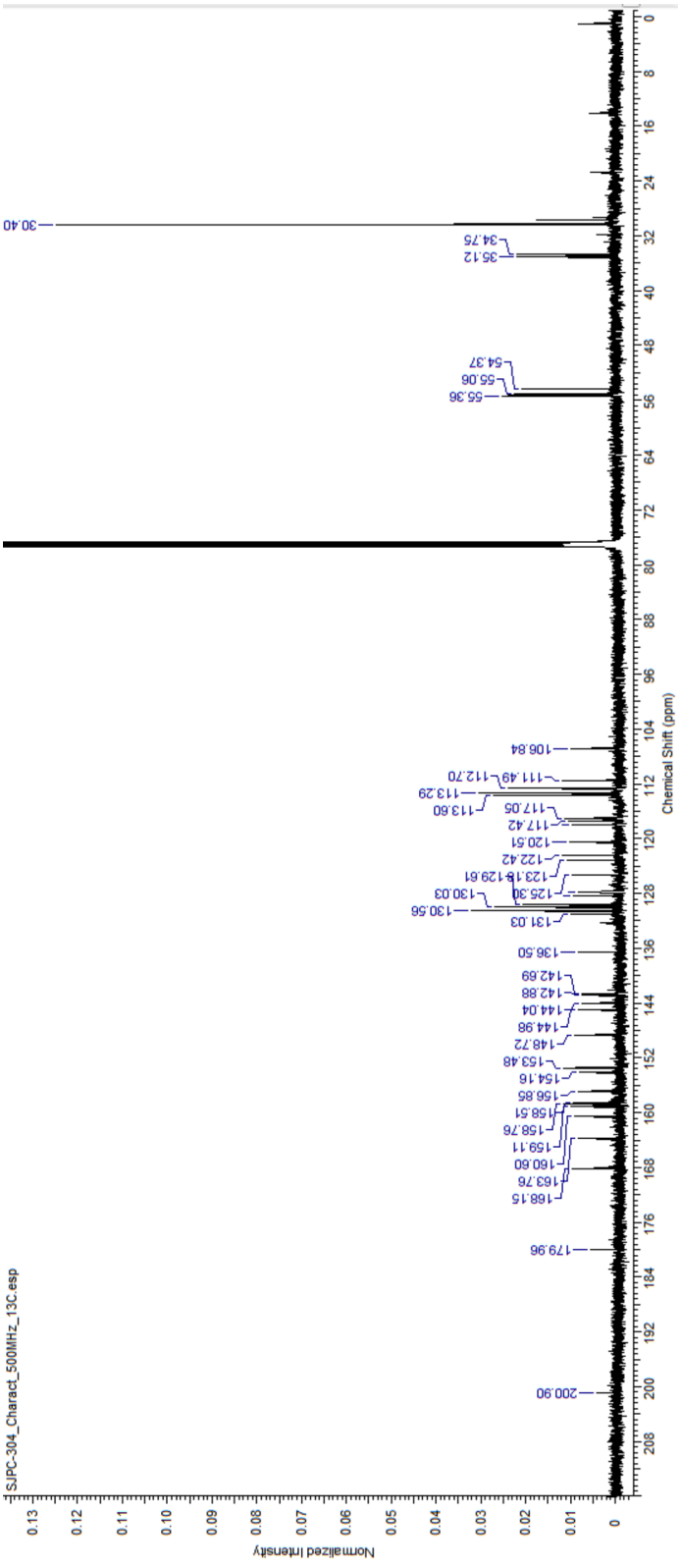

Figure III.S4 – ^{13}C of ADPM sensitizer **3** ($CDCl_3$; 125 MHz)

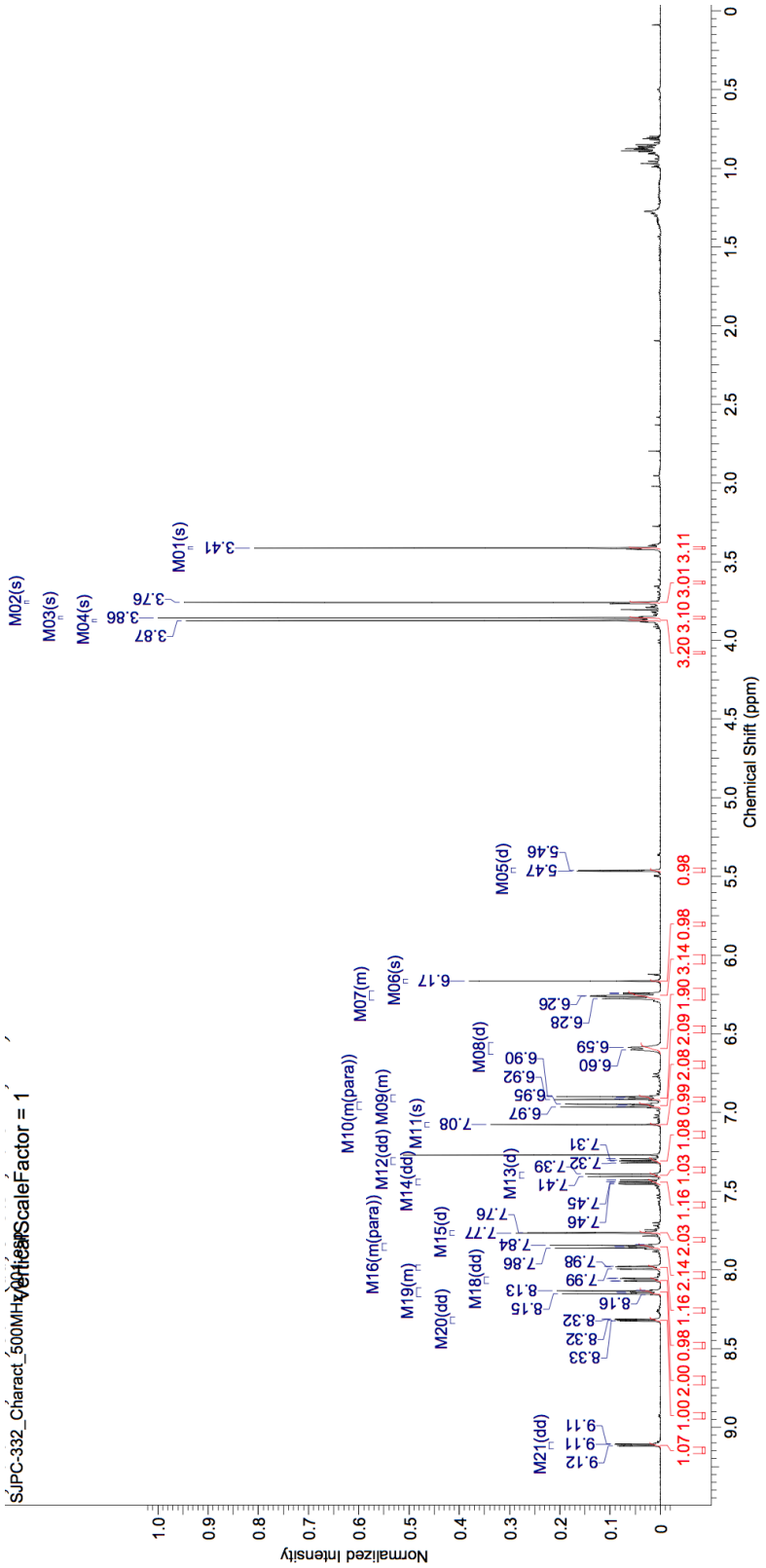

Figure III.S5 – ^{1}H of ADPM sensitizer **4** ($CDCl_3$; 500 MHz)

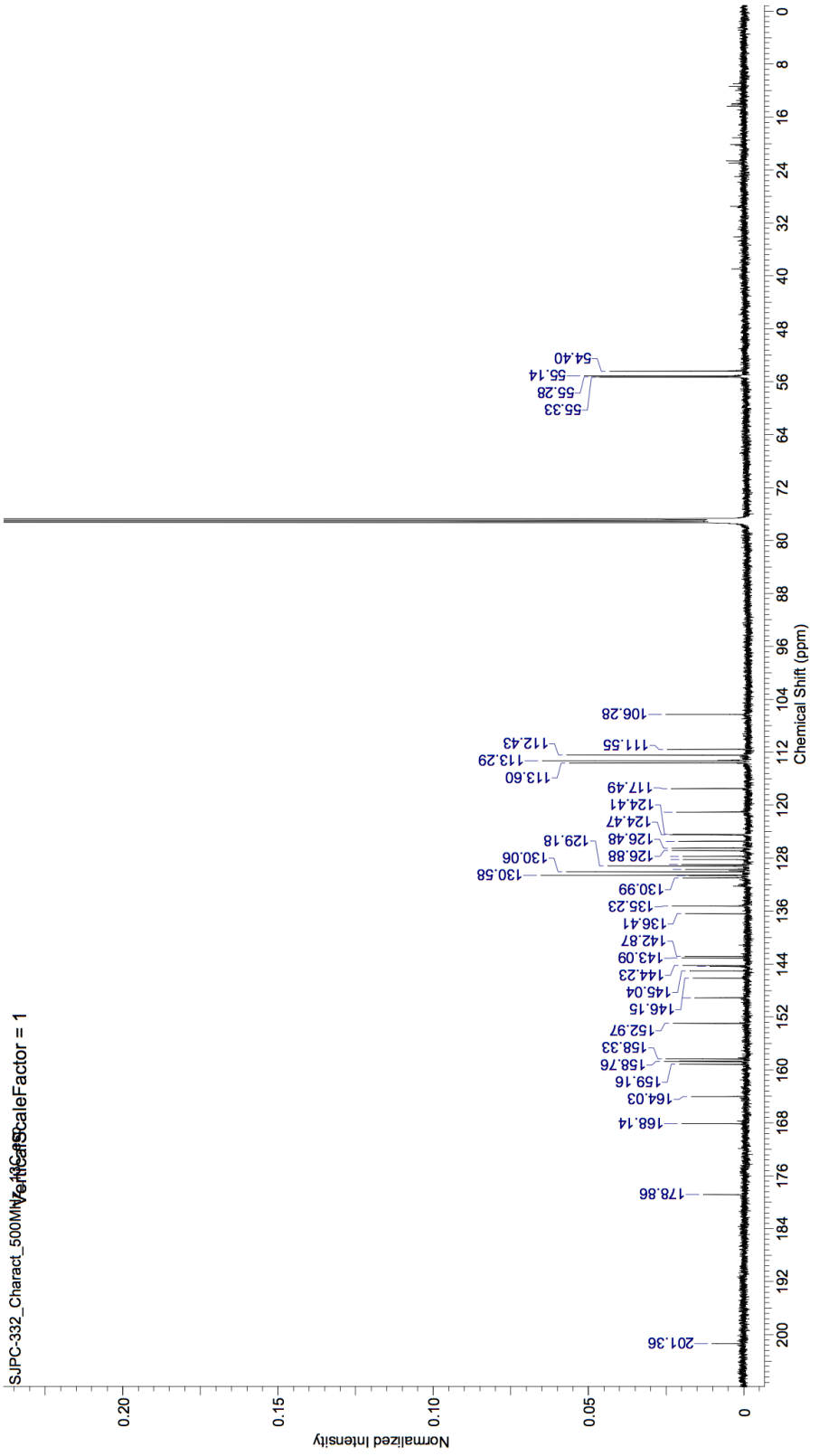

Figure III.S6 – ^{13}C of ADPM sensitizer **4** ($CDCl_3$; 125 MHz)

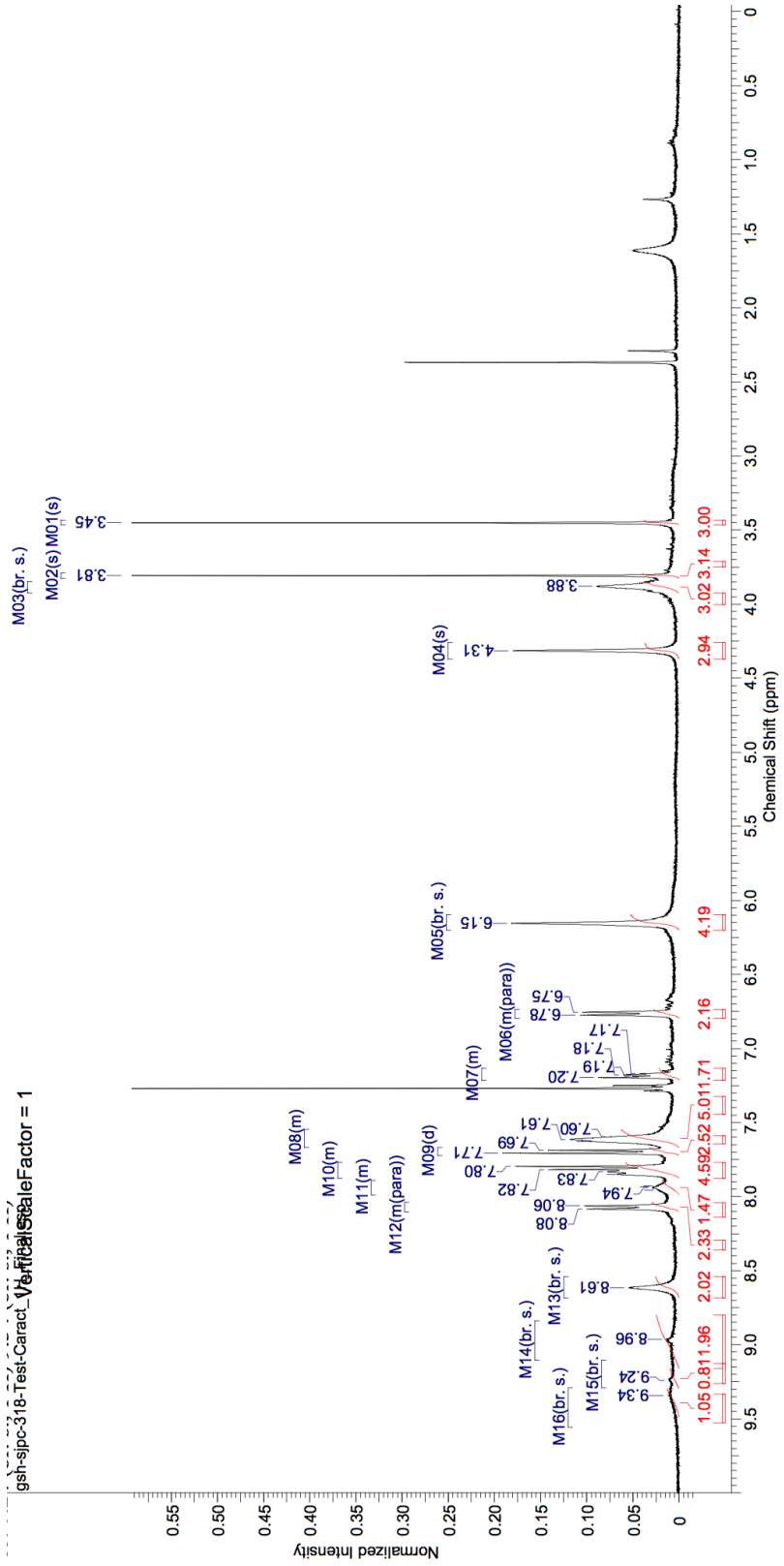

Figure III.S7 – ^{1}H of ADPM sensitizer **5** ($CDCl_3$; 400 MHz)

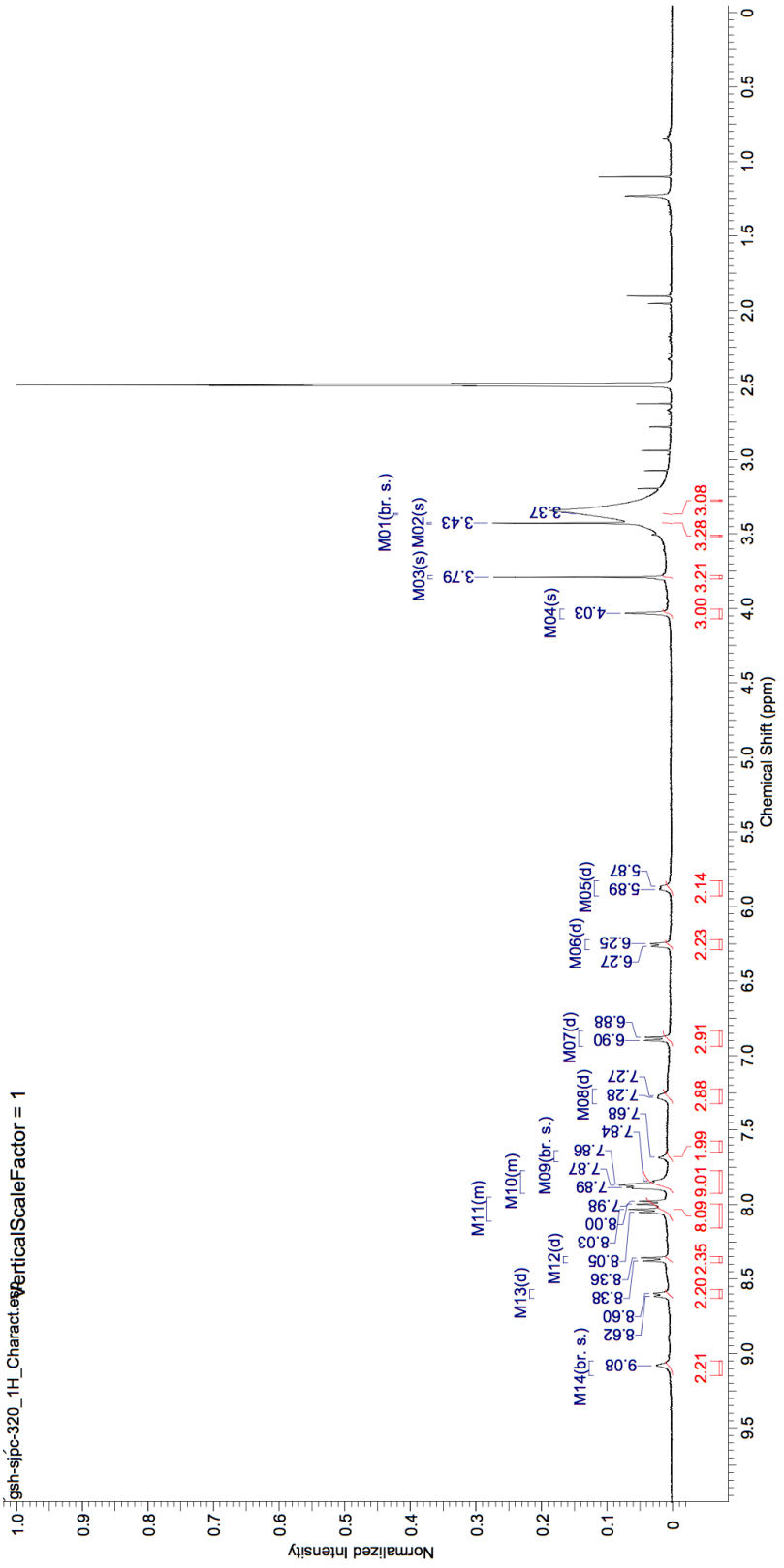

Figure III.S8 – ^{1}H of ADPM sensitizer **6** (DMSO-d_6; 400 MHz)

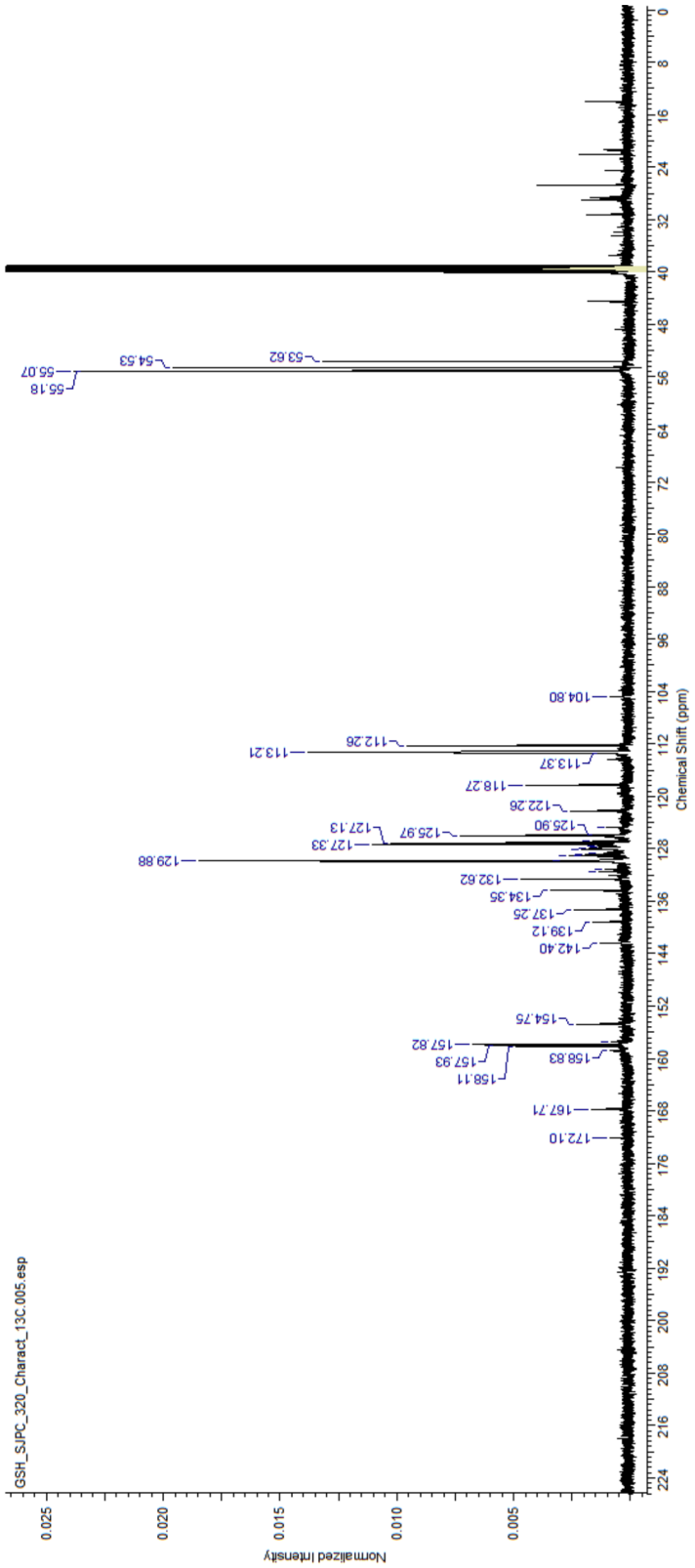

Figure III.S9 – ^{13}C of ADPM sensitizer **6** (DMSO-d_6; 175 MHz)

High-Resolution Mass Spectrometry Characterization

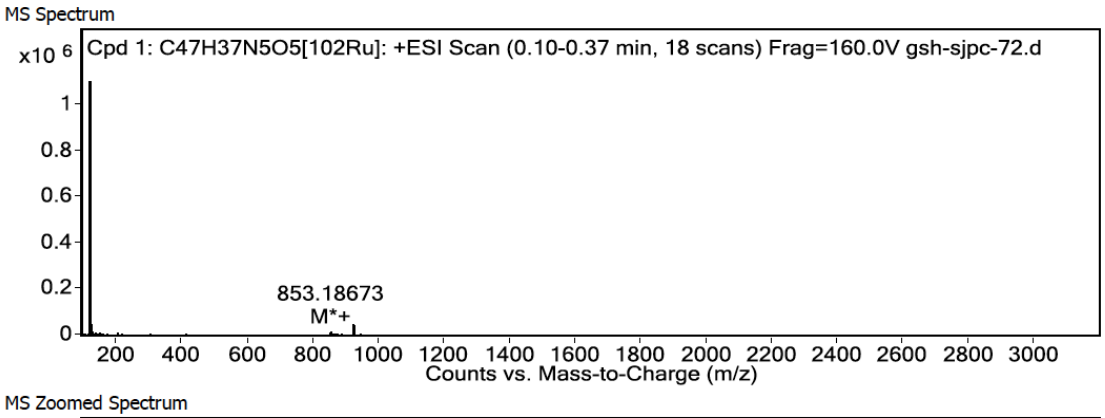

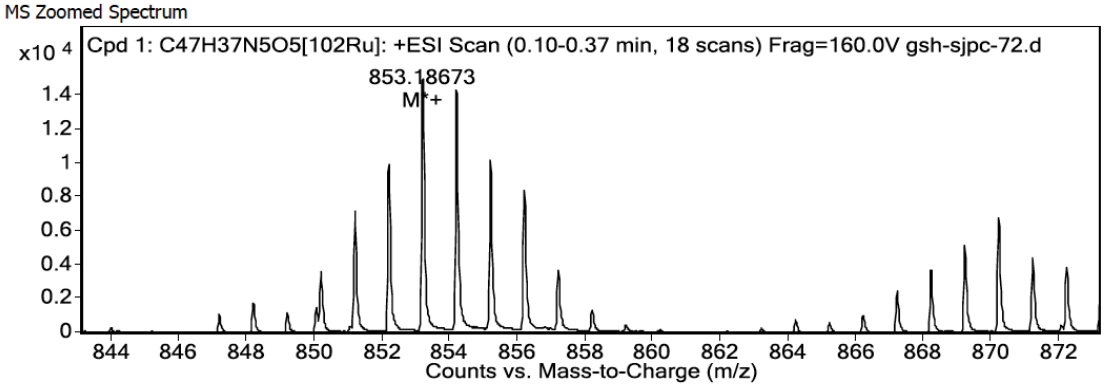

MS Spectrum Peak List

Ion	Ion Formula	Abund	*Expe. m/z*	*Calc. m/z*	Diff(ppm)
		1100181	118.12249		
M*+	C47 H37 N5 O5 [102Ru]	15270	853.18673	853.18327	4.05

Figure III.S10 – HRMS of ADPM sensitizer **2**

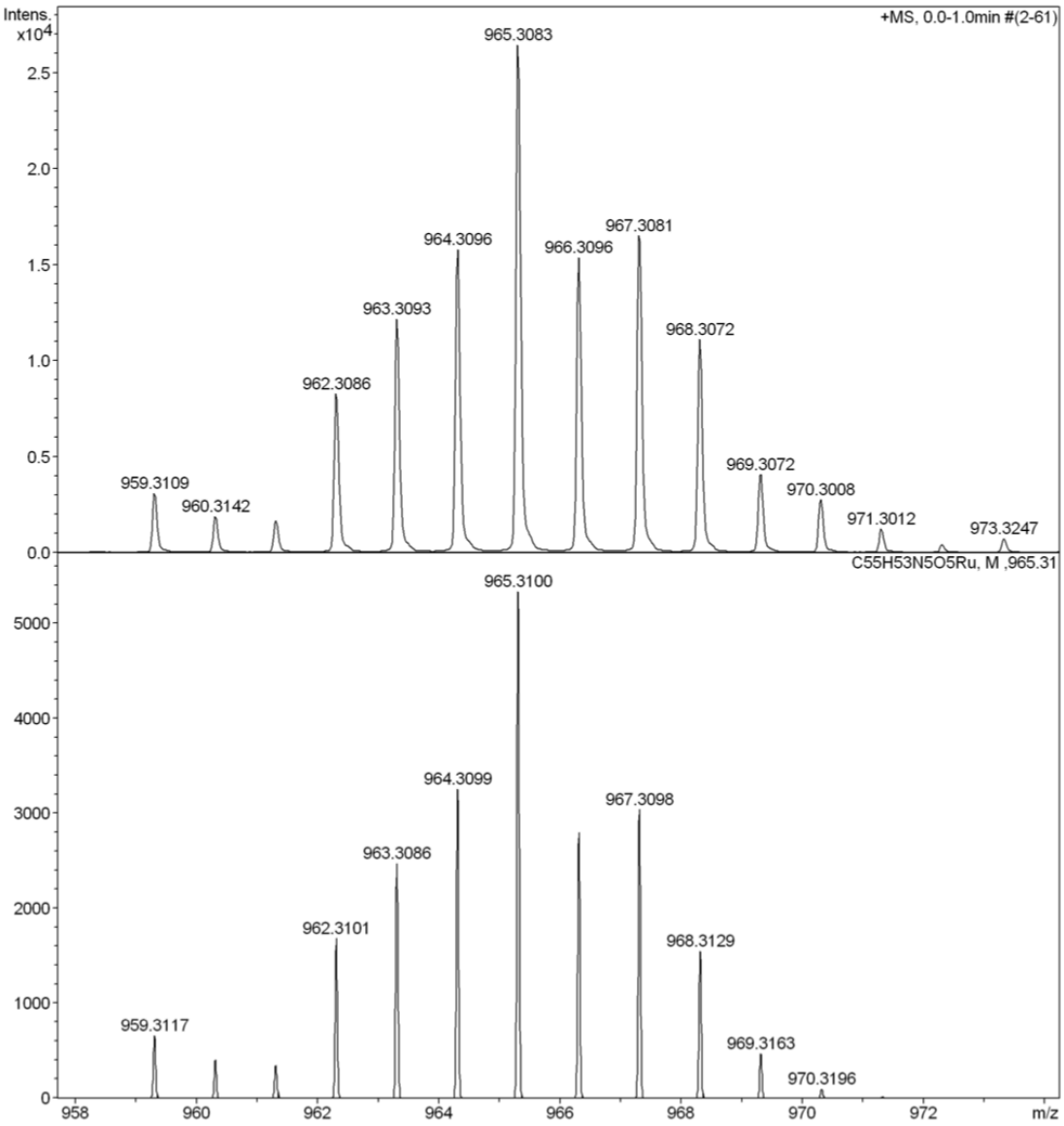

Figure III.S11 – HRMS of ADPM sensitizer **3**

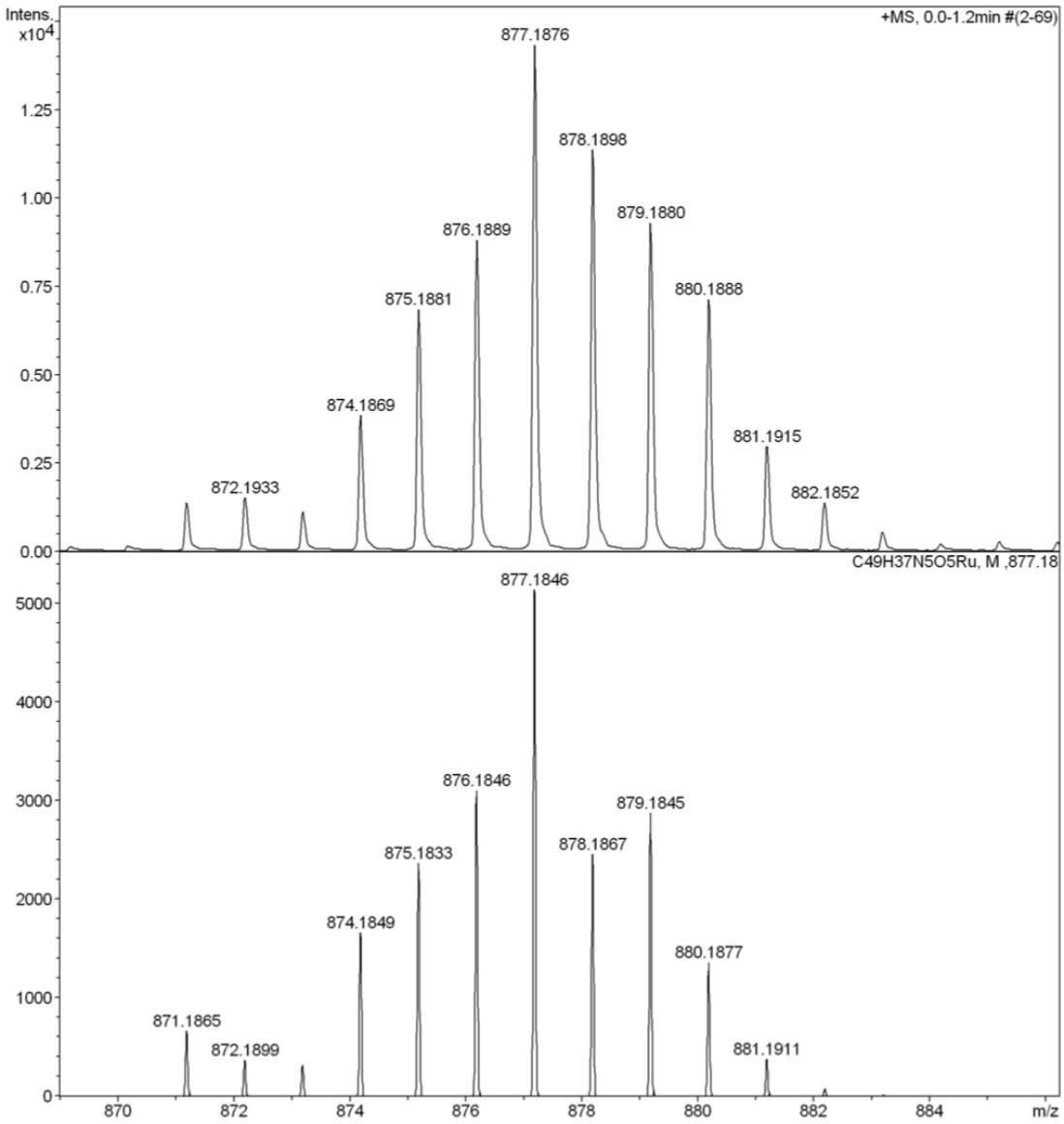

Figure III.S12 – HRMS of ADPM sensitizer **4**

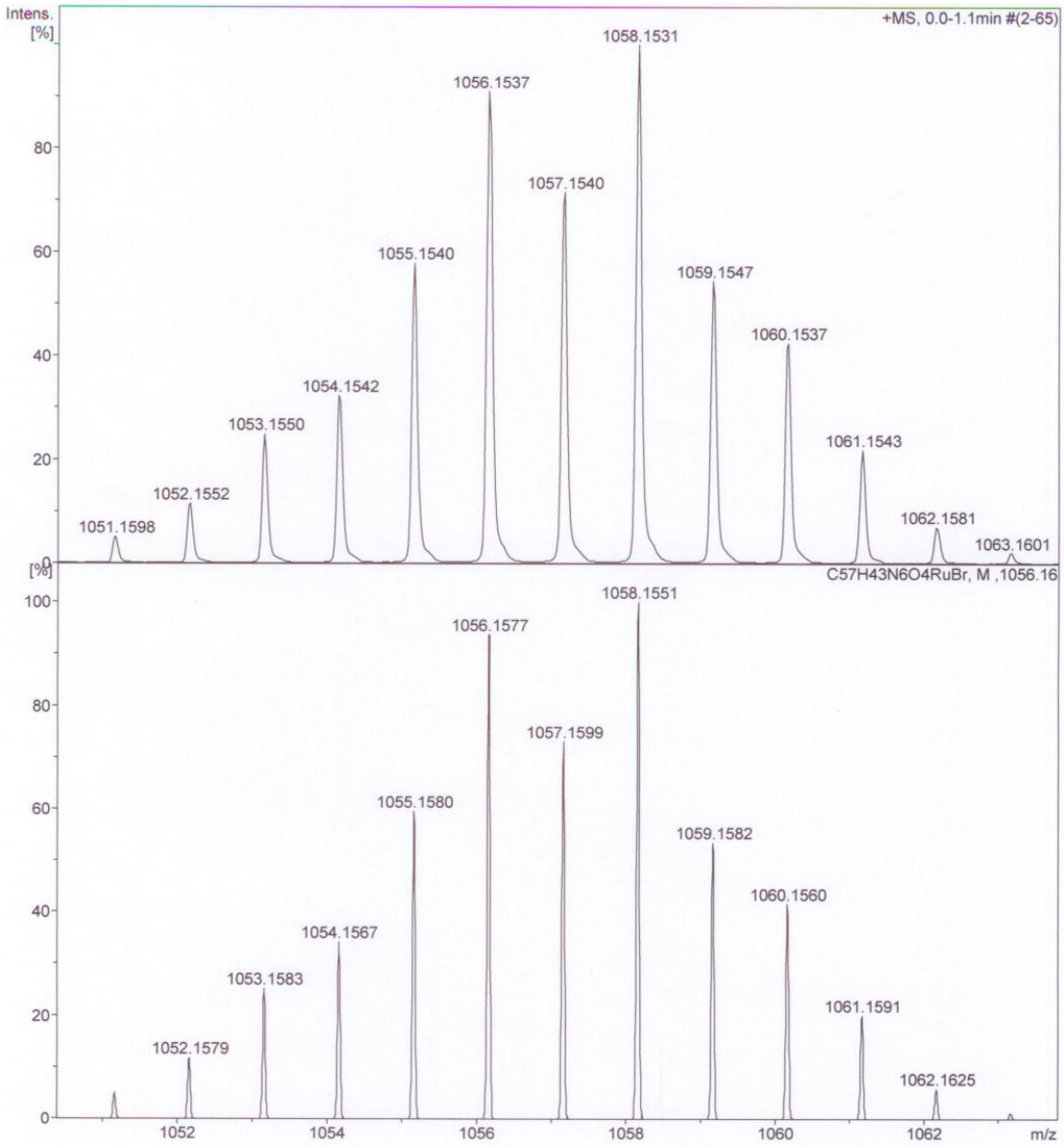

Figure III.S13 – HRMS of ADPM sensitizer **5**

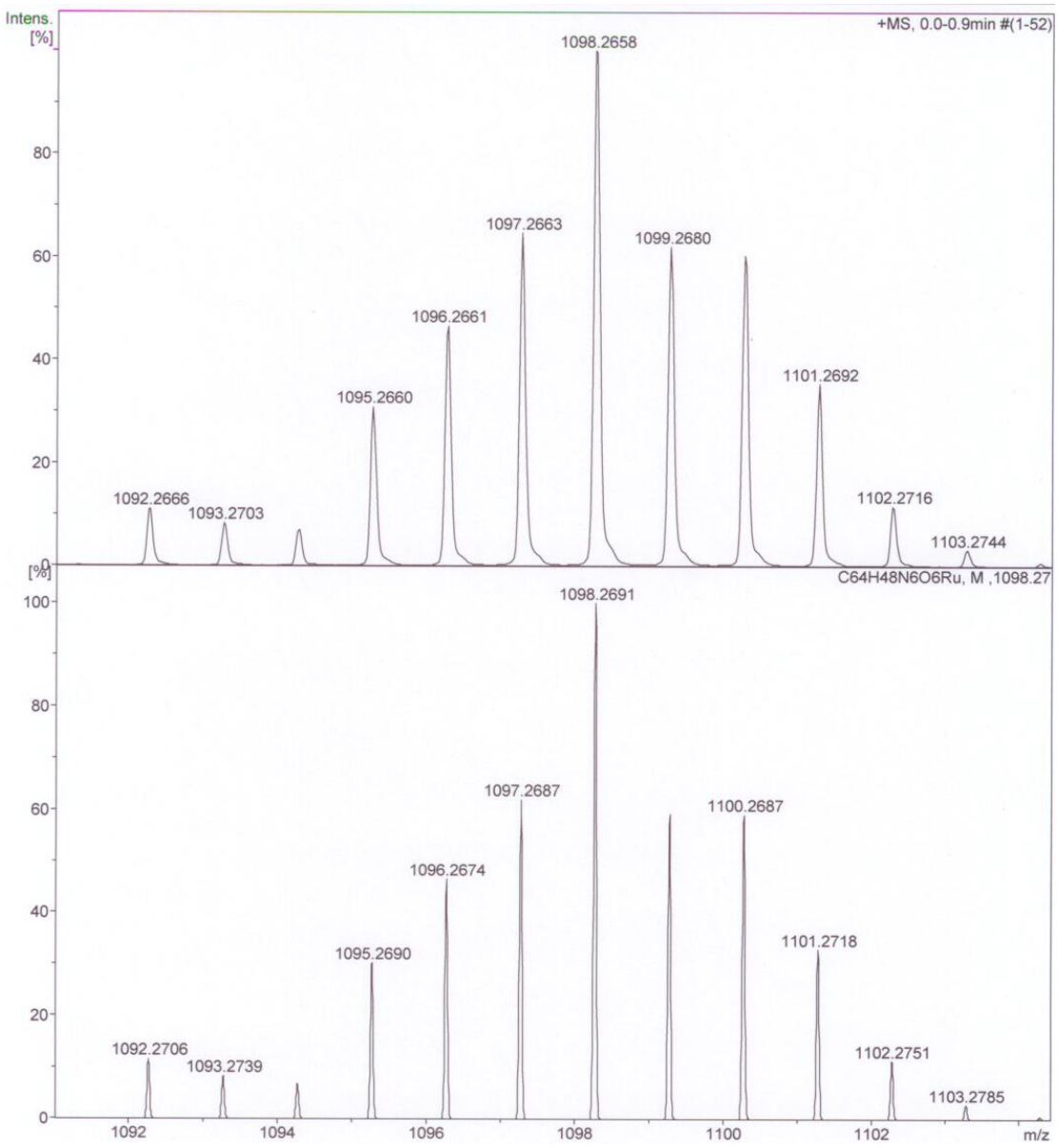

Figure III.S14 – HRMS of ADPM sensitizer **6**

Electrochemistry

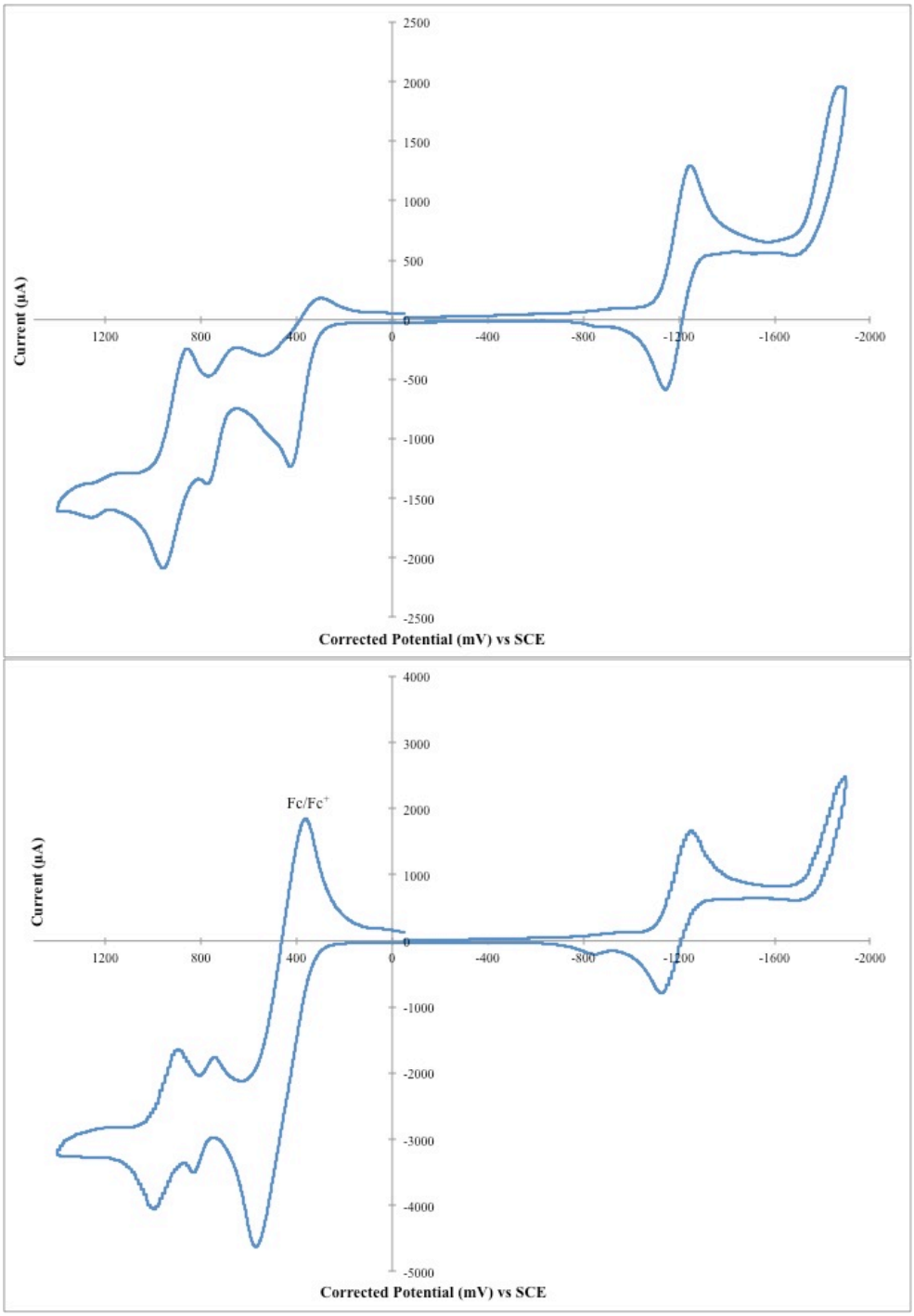

Figure III.S15 – CV of ADPM sensitizer **2** before (top) and after addition of ferrocene internal reference (bottom).

(Fc = 0.46 V vs SCE in DCM) (Scan rate of 50 mV/s at R.T.)

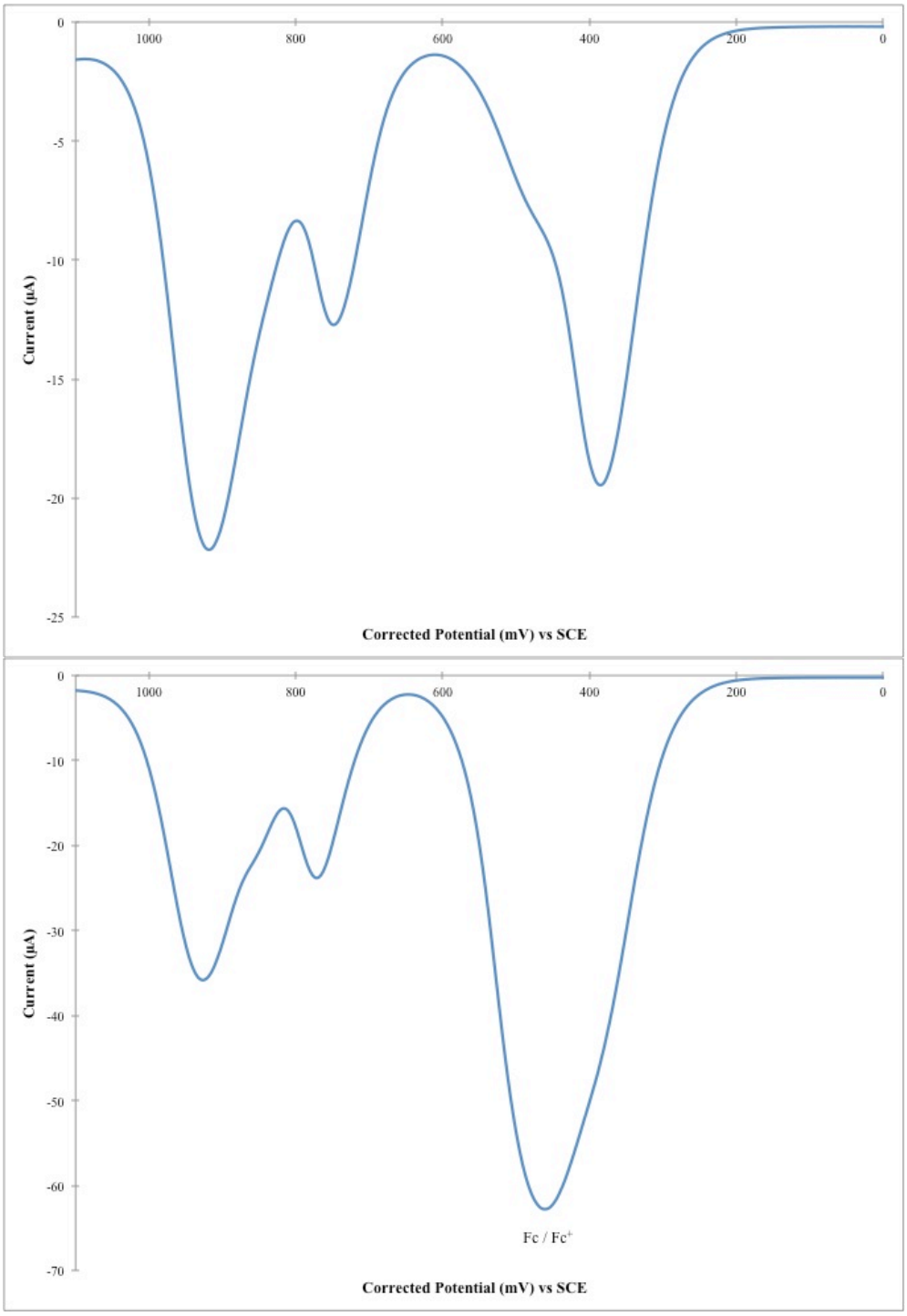

Figure III.S16 – DPV of oxidation potentials for ADPM sensitizer **2** before (top) and after addition of ferrocene internal reference (bottom).
(0.46 V vs SCE in DCM) (Scan rate of 50 mV/s at R.T.)

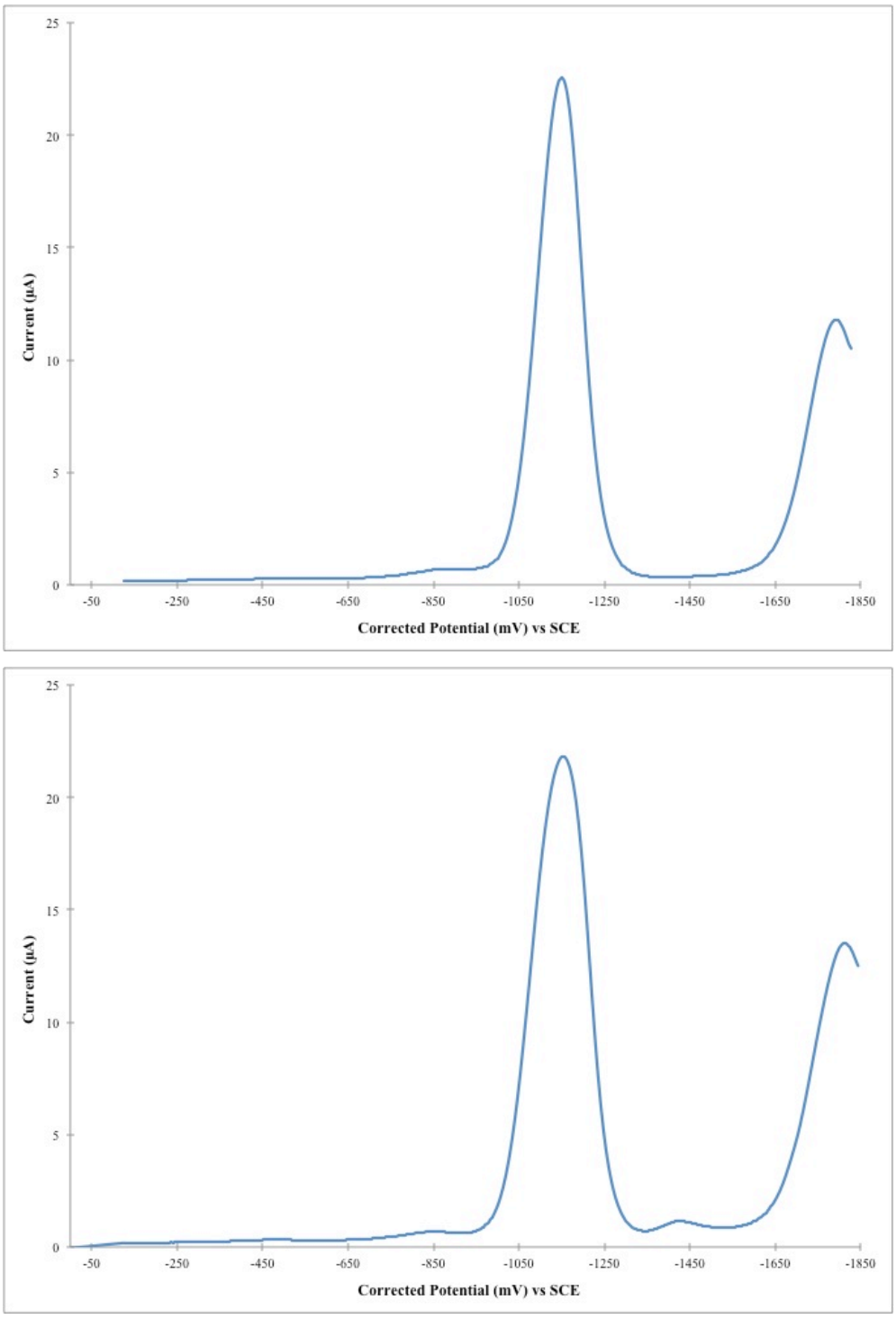

Figure III.S17 – DPV of reduction potentials for ADPM sensitizer **2** before (top) and after addition of ferrocene internal reference (bottom).
(0.46 V vs SCE in DCM) (Scan rate of 50 mV/s at R.T.)

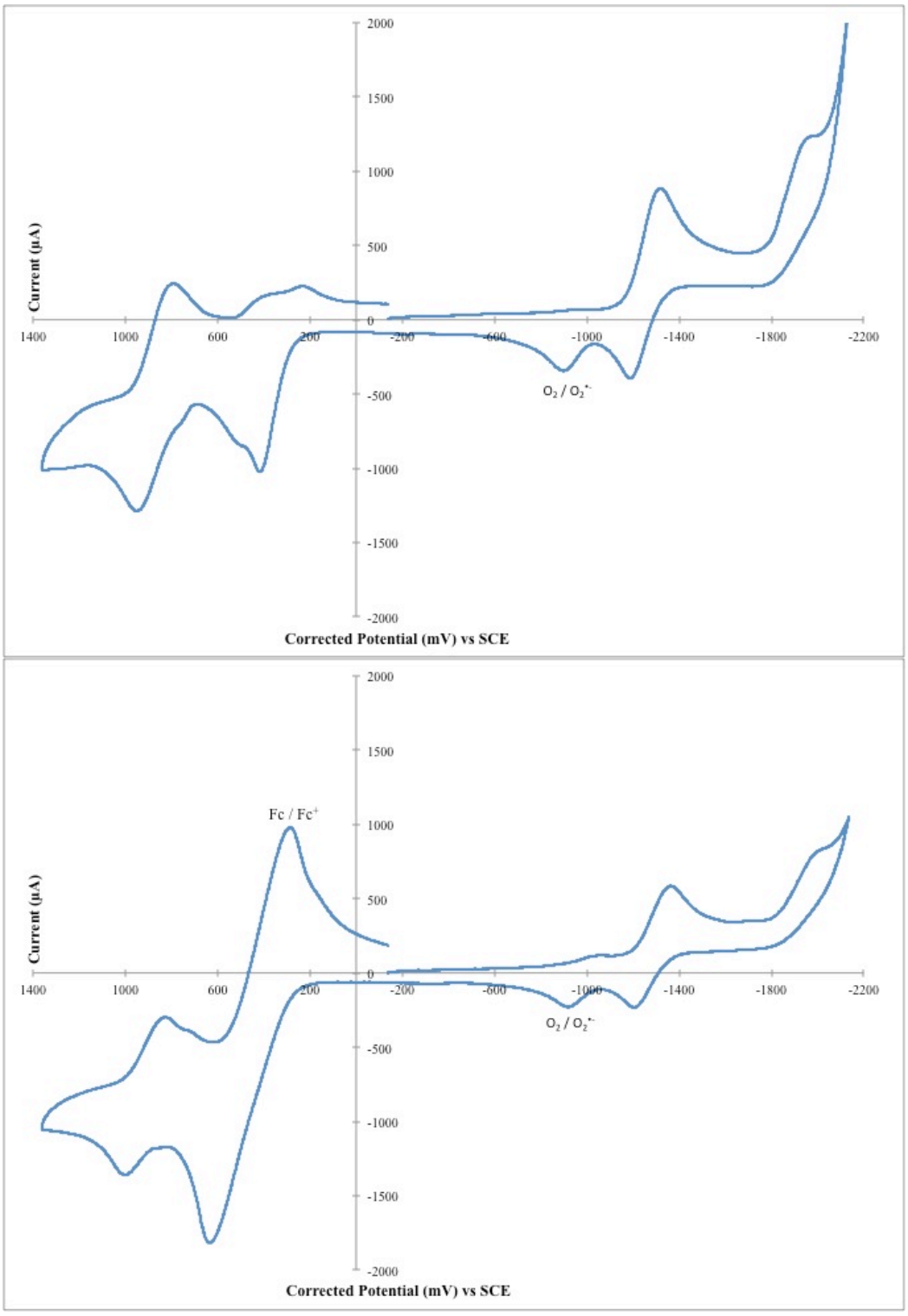

Figure III.S18 – CV of ADPM sensitizer **3** before (top) and after addition of ferrocene internal reference (bottom).

(0.46 V vs SCE in DCM) (Scan rate of 50 mV/s at R.T.)

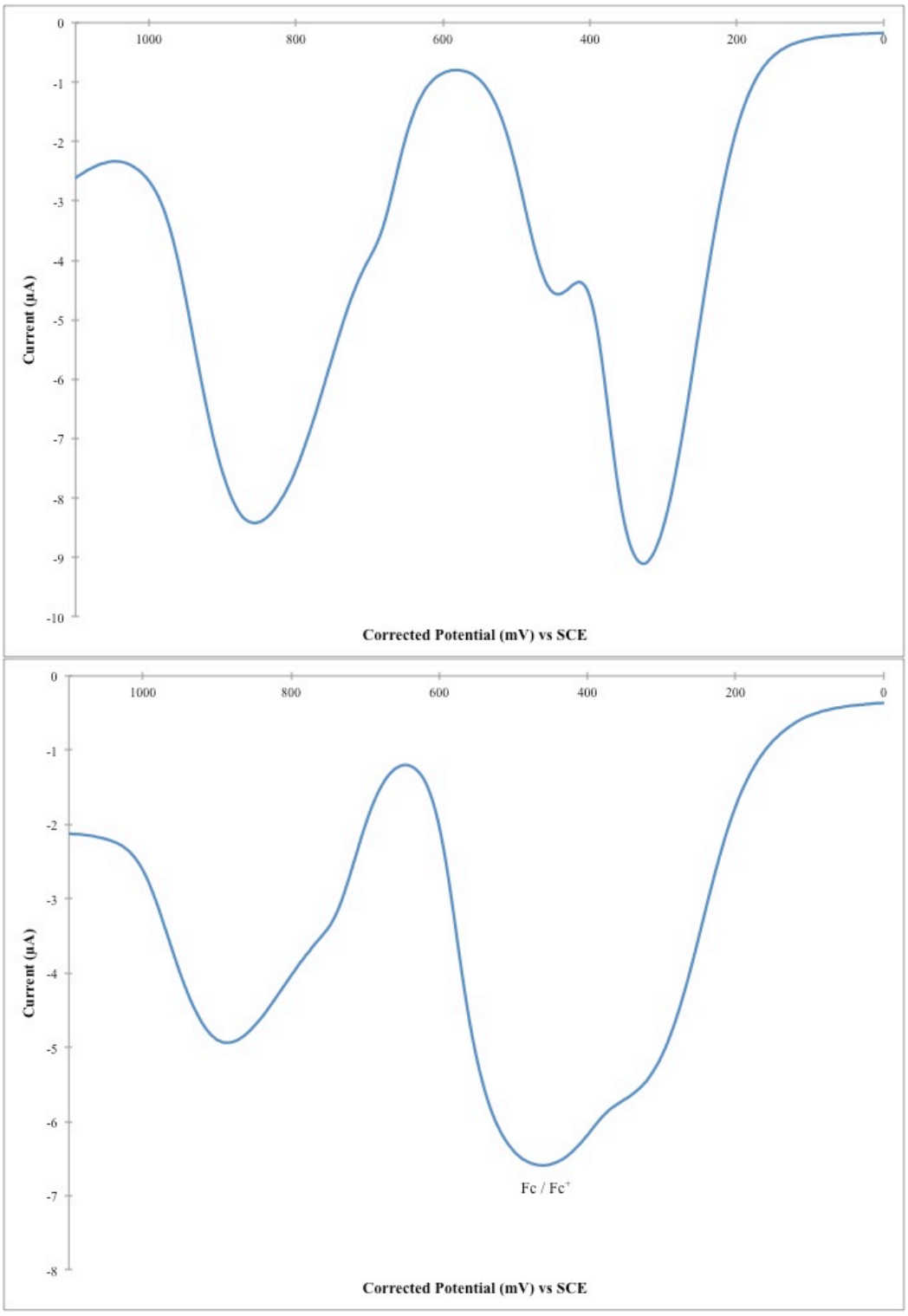

Figure III.S19 – DPV of oxidation potentials for ADPM sensitizer **3** before (top) and after addition of ferrocene internal reference (bottom).
(0.46 V vs SCE in DCM) (Scan rate of 50 mV/s at R.T.)

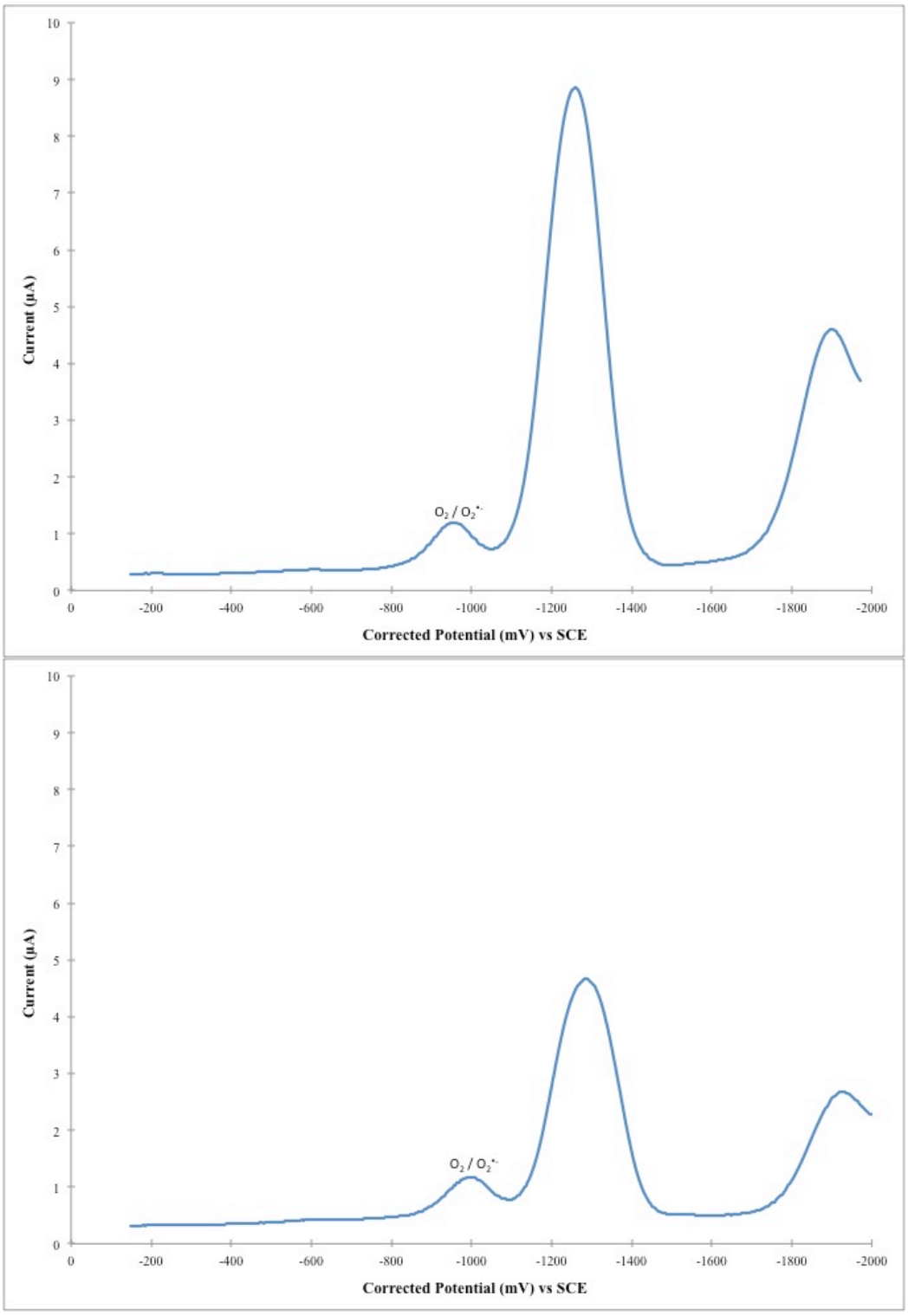

Figure III.S20 – DPV of reduction potentials for ADPM sensitizer **3** before (top) and after addition of ferrocene internal reference (bottom).
(0.46 V vs SCE in DCM) (Scan rate of 50 mV/s at R.T.)

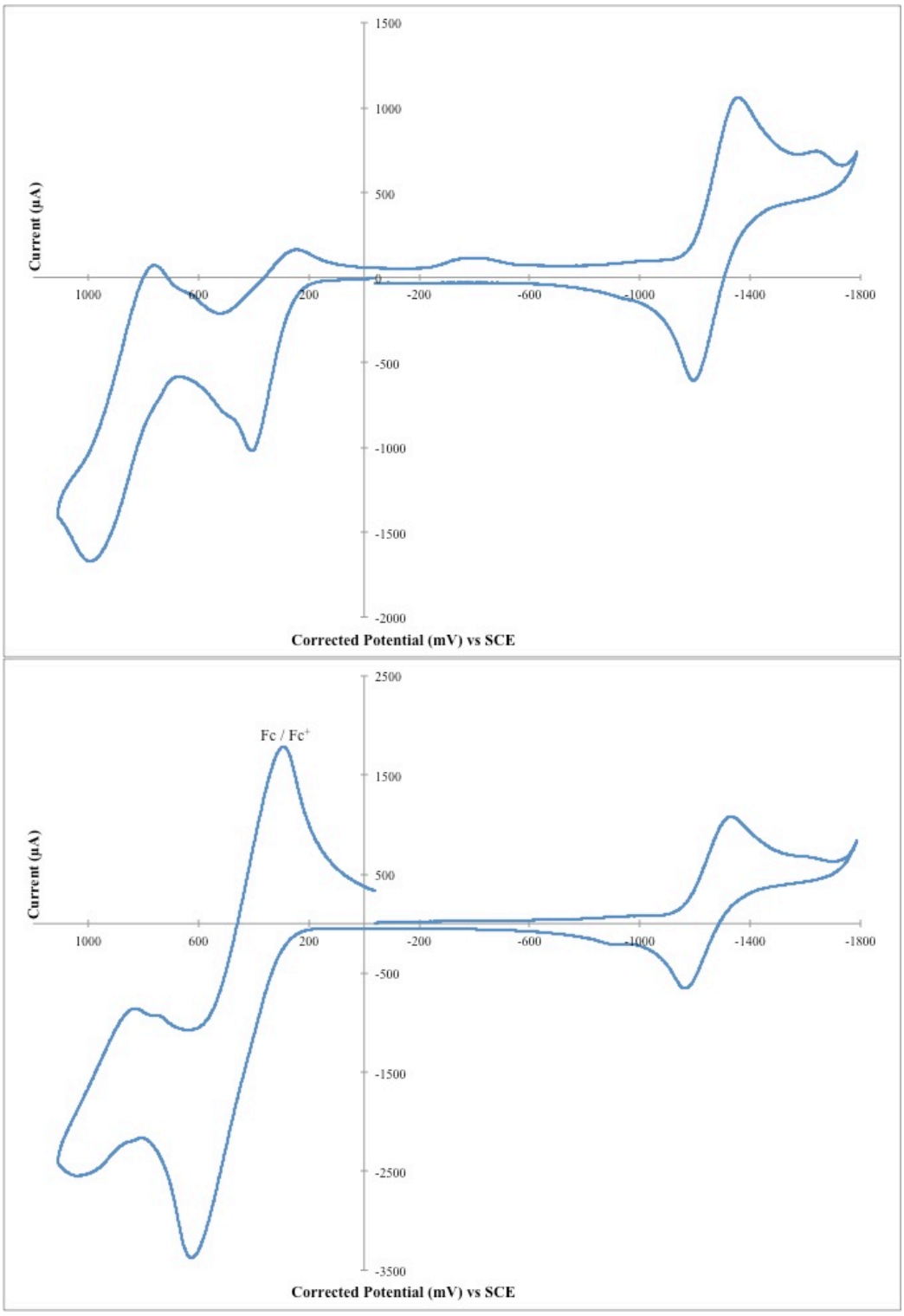

Figure III.S21 – CV of ADPM sensitizer **4** before (top) and after addition of ferrocene internal reference (bottom).

(0.46 V vs SCE in DCM) (Scan rate of 50 mV/s at R.T.)

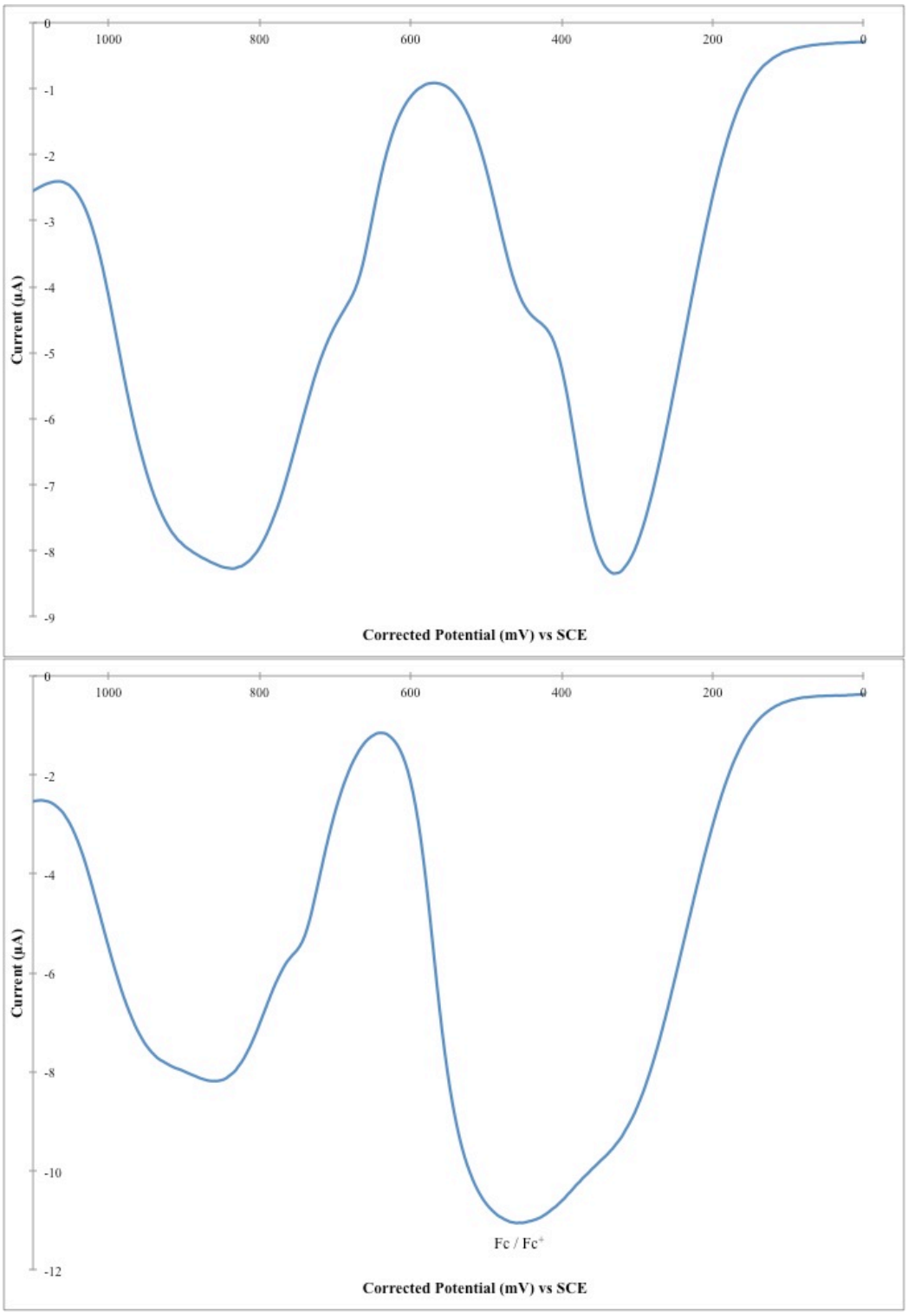

Figure III.S22 – DPV of oxidation potentials for ADPM sensitizer **4** before (top) and after addition of ferrocene internal reference (bottom).
(0.46 V vs SCE in DCM) (Scan rate of 50 mV/s at R.T.)

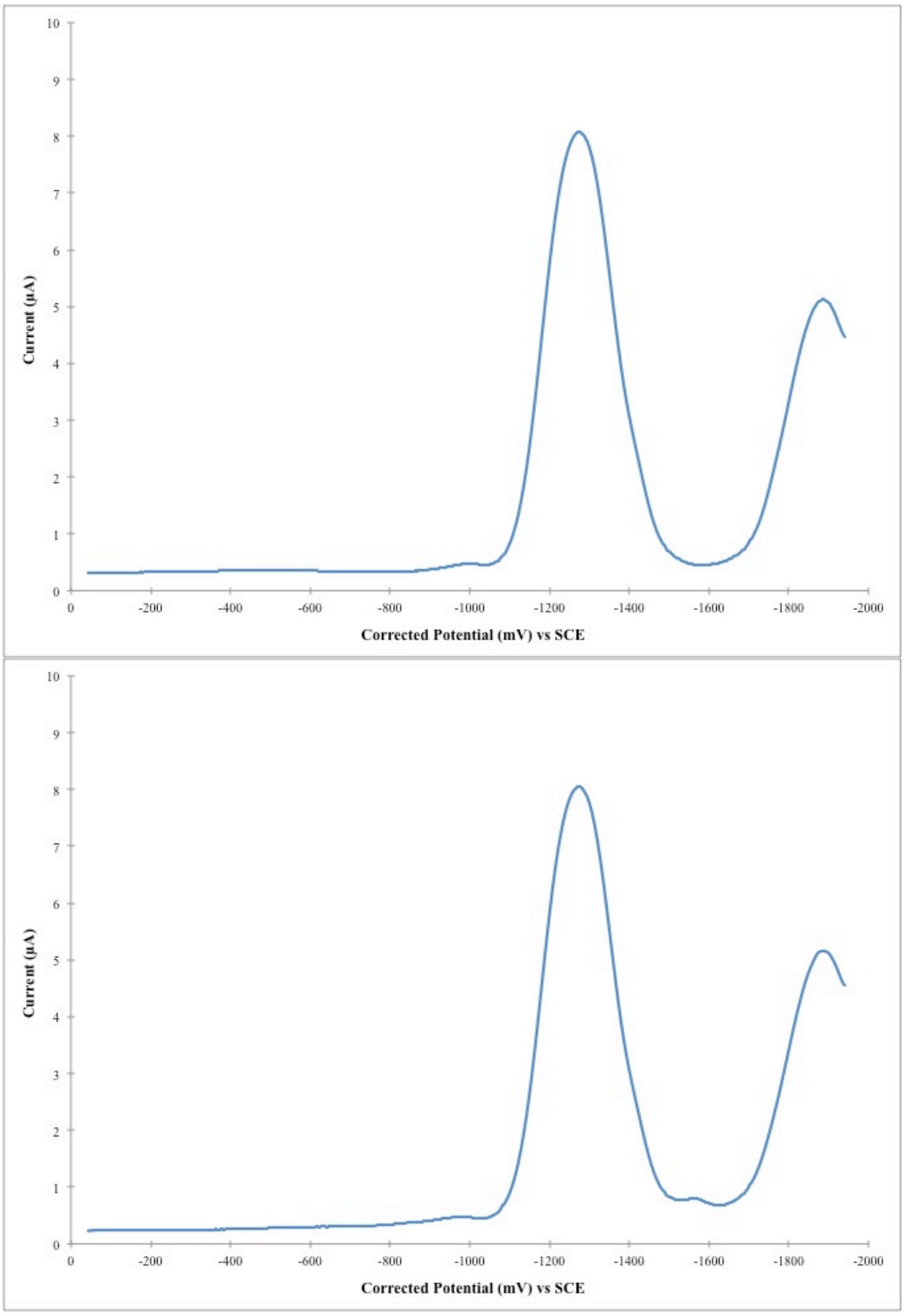

Figure III.S23 – DPV of reduction potentials for ADPM sensitizer **4** before (top) and after addition of ferrocene internal reference (bottom).
(0.46 V vs SCE in DCM) (Scan rate of 50 mV/s at R.T.)

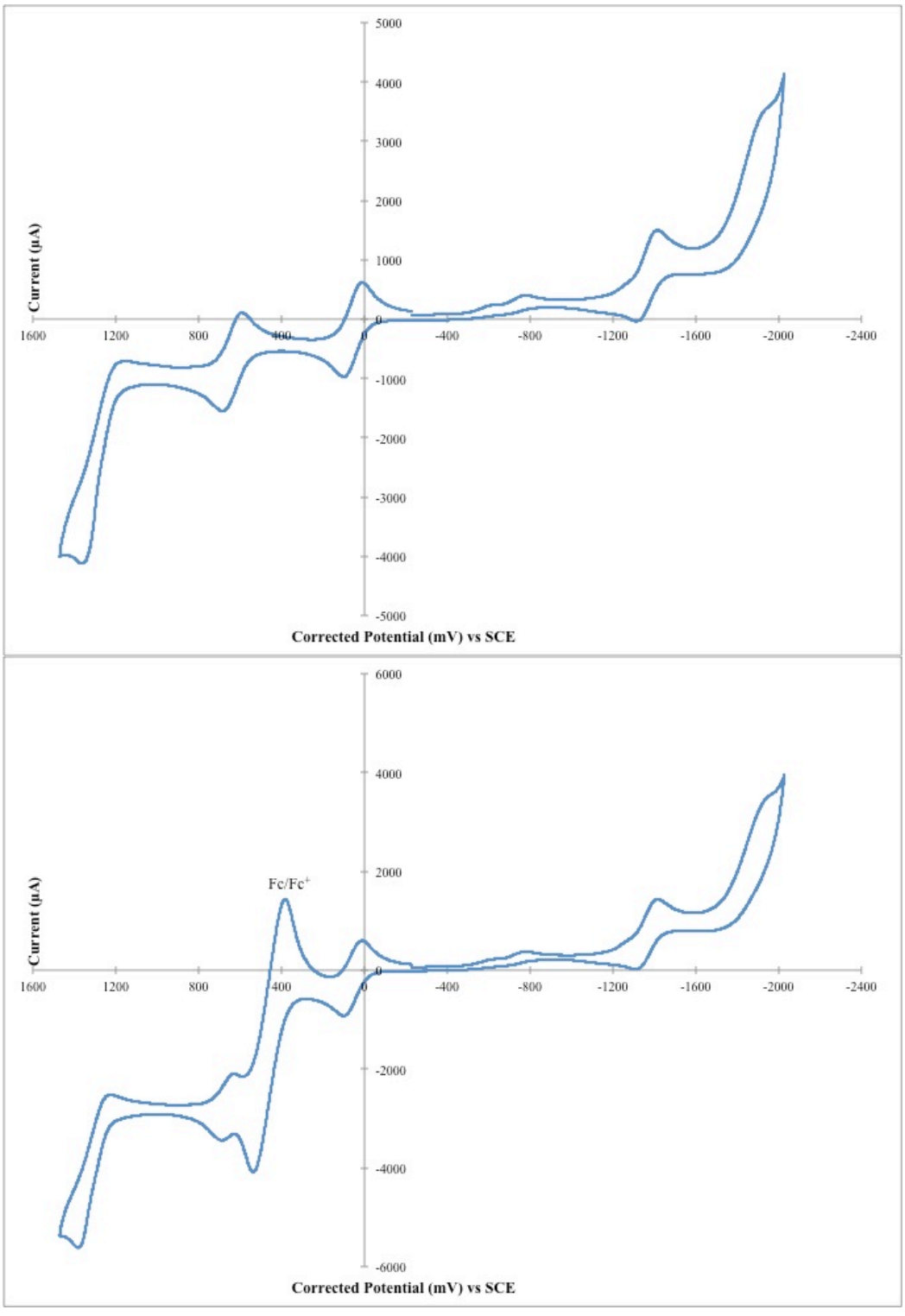

Figure III.S24 – CV of ADPM sensitizer **5** before (top) and after addition of ferrocene internal reference (bottom).

(0.46 V vs SCE in DCM) (Scan rate of 50 mV/s at R.T.)

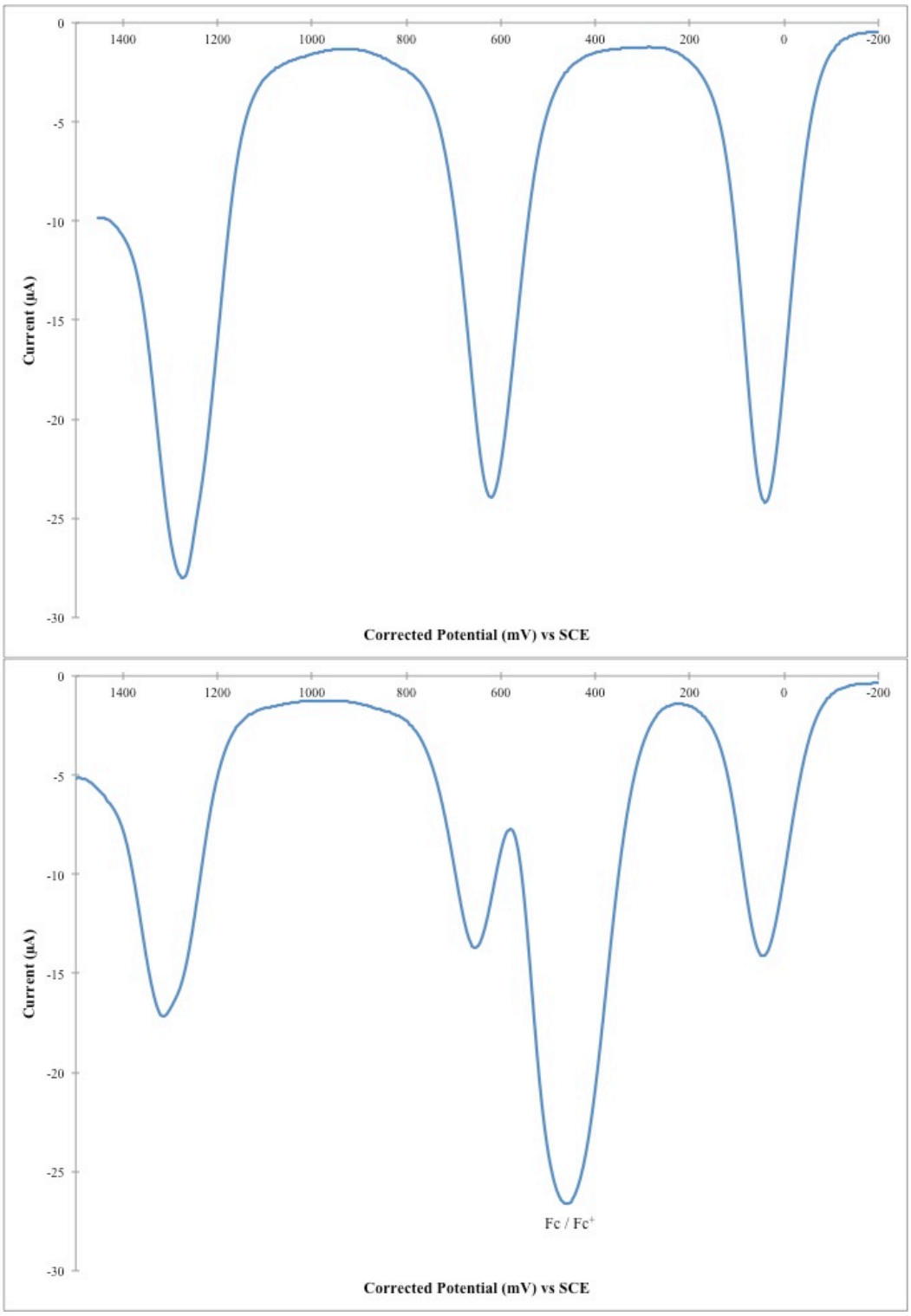

Figure III.S25 – DPV of oxidation potentials for ADPM sensitizer **5** before (top) and after addition of ferrocene internal reference (bottom).
(0.46 V vs SCE in DCM) (Scan rate of 50 mV/s at R.T.)

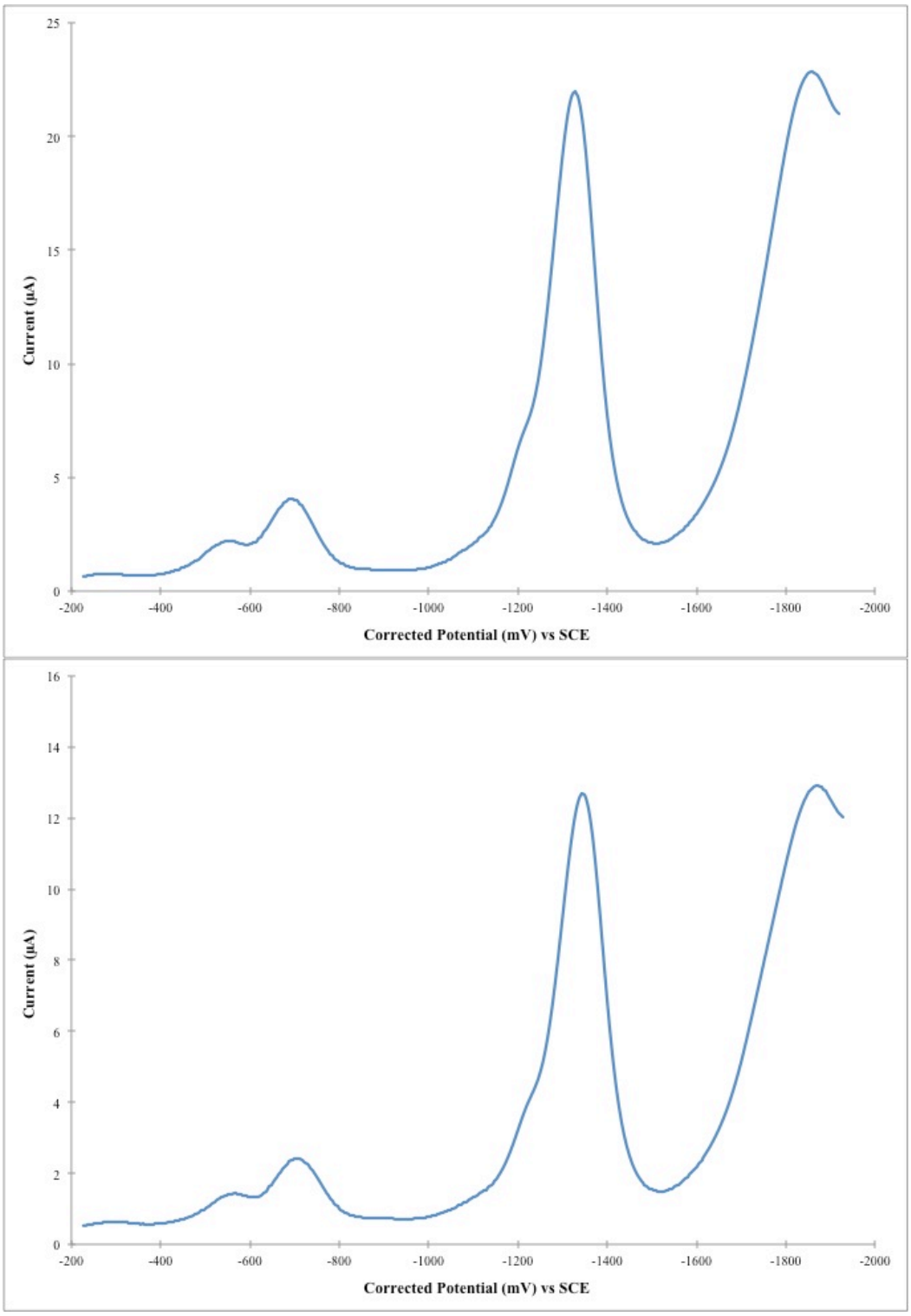

Figure III.S26 – DPV of reduction potentials for ADPM sensitizer **5** before (top) and after addition of ferrocene internal reference (bottom).
(0.46 V vs SCE in DCM) (Scan rate of 50 mV/s at R.T.)

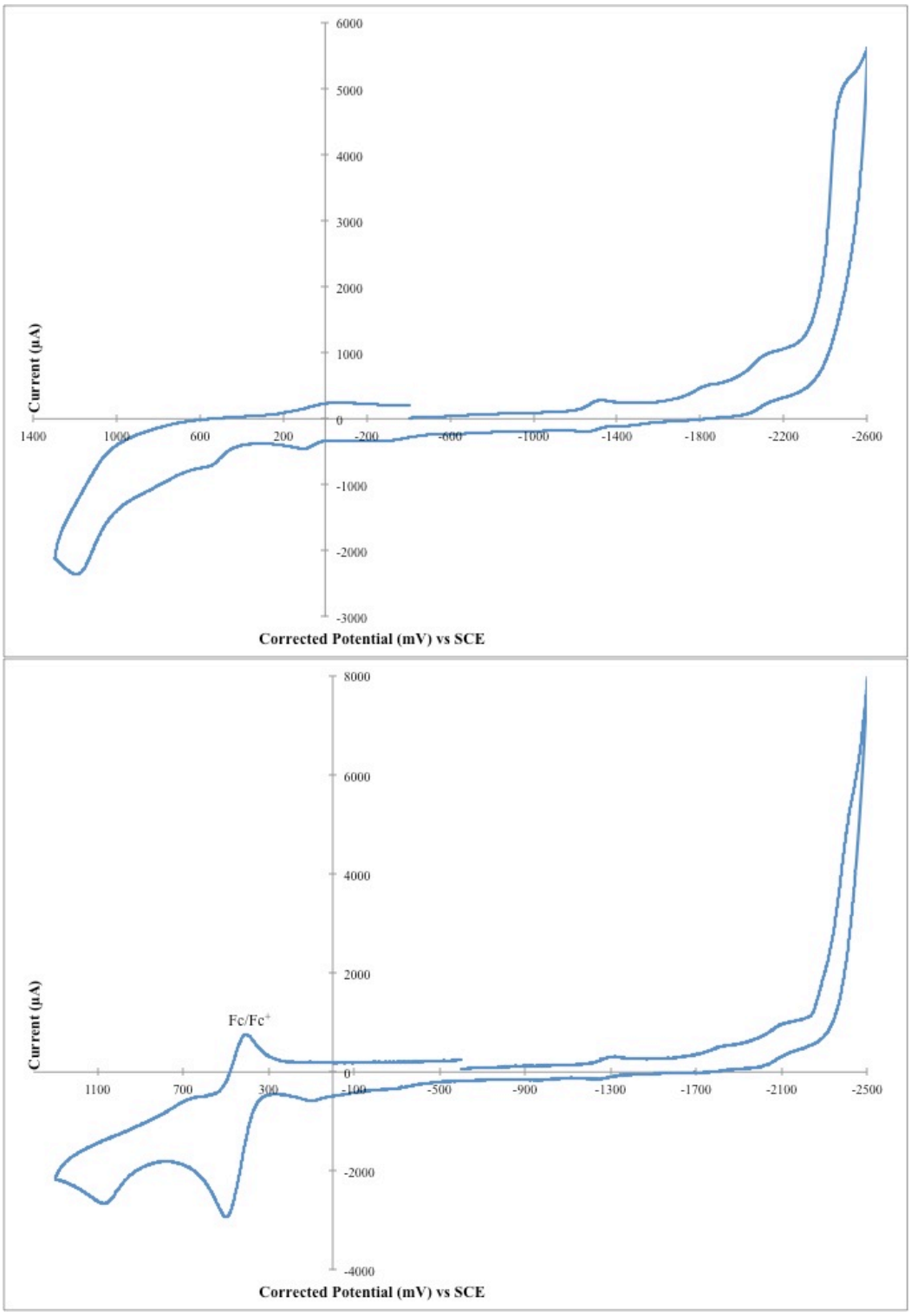

Figure III.S27 – CV of ADPM sensitizer **6** before (top) and after addition of ferrocene internal reference (bottom).

(Fc = 0.45 V vs SCE in DMF) (Scan rate of 50 mV/s at R.T.)

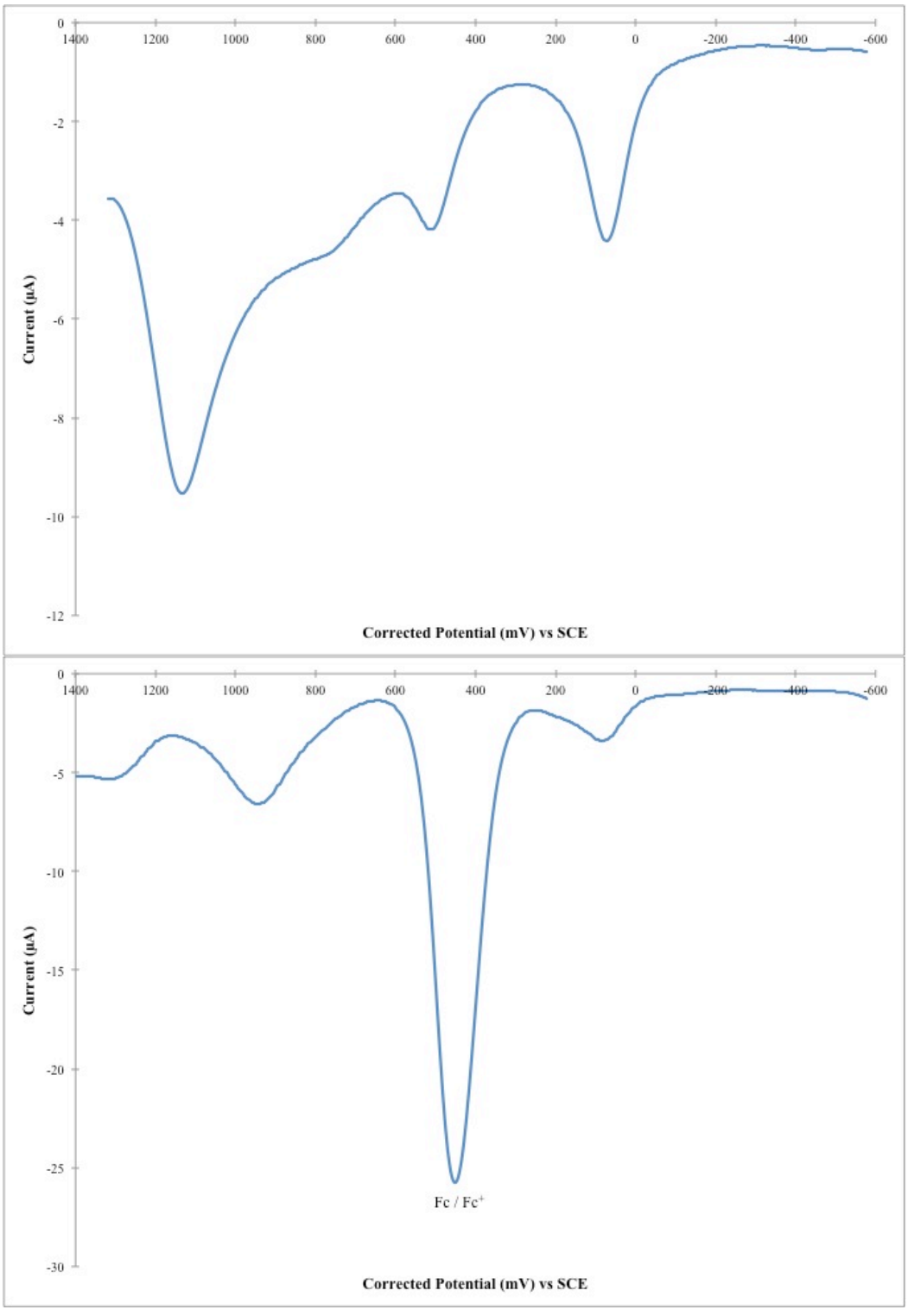

Figure III.S28 – DPV of oxidation potentials for ADPM sensitizer **6** before (top) and after addition of ferrocene internal reference (bottom).
(0.45 V vs SCE in DMF) (Scan rate of 50 mV/s at R.T.)

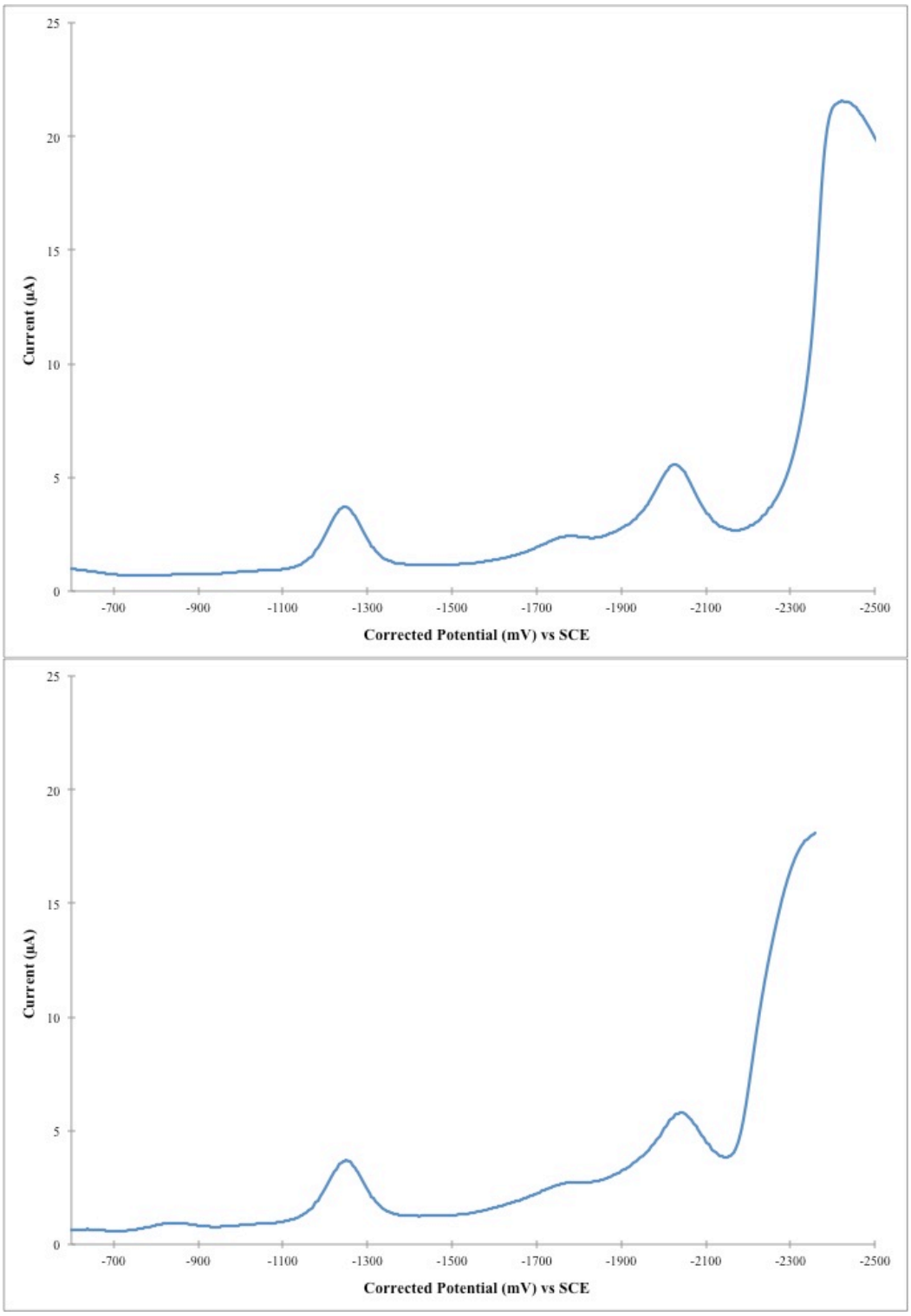

Figure III.S29 – DPV of reduction potentials for ADPM sensitizer **6** before (top) and after addition of ferrocene internal reference (bottom).
(0.45 V vs SCE in DMF) (Scan rate of 50 mV/s at R.T.)

Table III.S1 - HOMO/LUMO levels (in eV) determined by electrochemistry and theoretical calculation in CH_2Cl_2 along with corresponding ΔE for ADPM derivatives **1** – **6** and **8**.

	HOMO	LUMO	ΔE [a]	E_{Ox}*	HOMO Theo [b]	LUMO Theo [b]	ΔE Theo [b]	Dipole Moment [b]
1 [d]	-5.66	-4.03	1.63	---	---	---	---	---
2	-5.30	-3.76	1.54	-3.93	-4.20	-2.17	2.03	8.41
3	-5.28	-3.66	1.62	-3.89	-4.13	-1.97	2.15	9.95
4	-5.27	-3.70	1.57	-3.86	-4.19	-2.14	2.05	8.76
5	-5.00	-3.58	1.42	-3.90	-4.09	-1.94	2.15	4.88
6	-5.03 c)	-3.70 c)	1.33 c)	-3.97	-4.07	-1.99	2.08	4.94
8 [d]	-5.90	-4.36	1.54	---	---	---	---	---

[a] Energetic difference between the HOMO and the LUMO obtained by electrochemistry. [b] Theoretical calculations (B3LYP / 6-31g*; Ru : LANL2DZ) / Dipole moment in Debye. [c] In DMF solution. [d] Values from literature.[22]

Computational Modelization

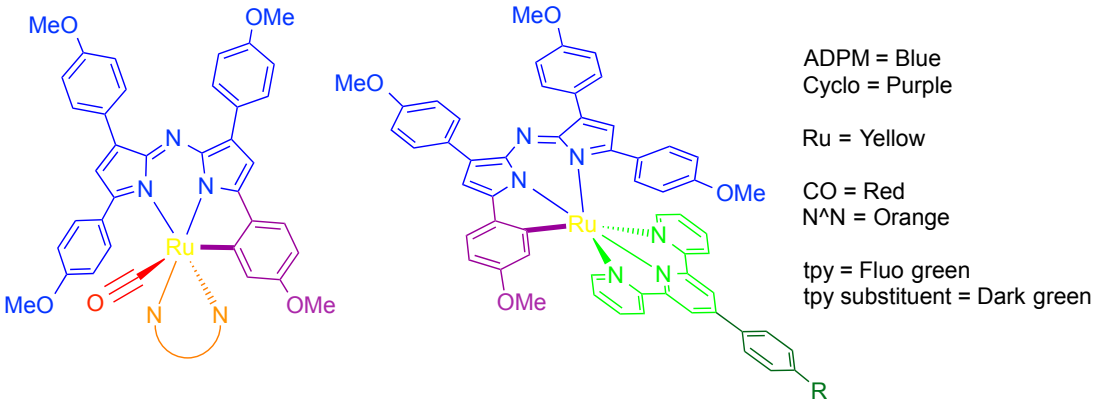

Figure III.S30 – Color legend for computational modelization analysis of ADPM photosentizers

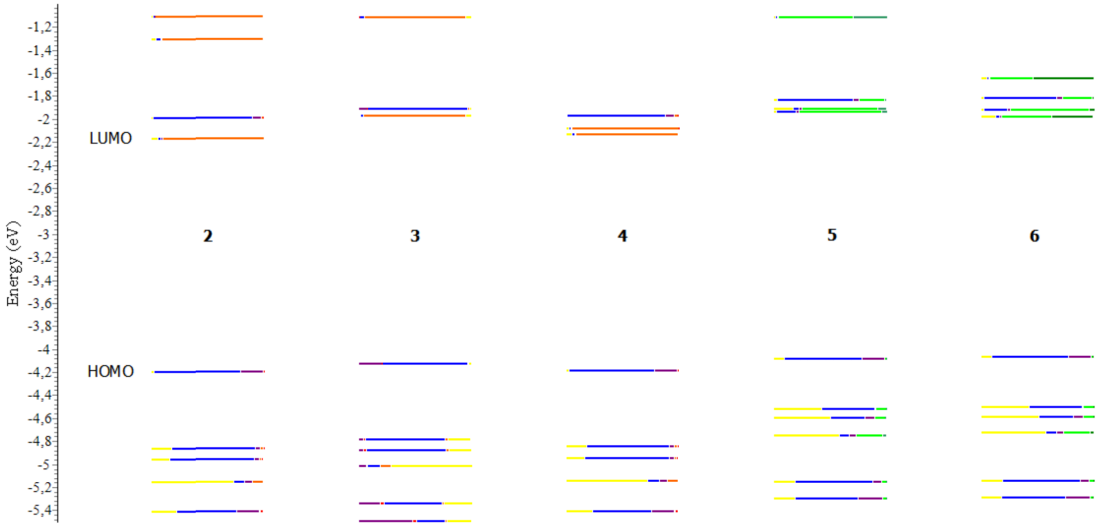

Figure III.S31 – Representation of frontier molecular orbital's energy levels (in eV) of ADPM photosensitizers **2** – **6** and electronic distribution as obtained by DFT calculations

(refer to Figure S.30 for color legend)

Table III.S2 - Electronic distribution (%) of frontier molecular orbitals for ADPM photosensitizers **2** – **6** as obtained by DFT

(B3LYP/6-31G*; Ru = LANL2DZ)

	MO	ADPM	Cyclo	Ru	N^N	CO	tpy	tpy subst
2	L + 1	88	8	1	2	0	---	---
	LUMO	3	2	6	89	0	---	---
	HOMO	76	20	3	1	0	---	---
	H -1	73	4	18	2	2	---	---
3	L + 1	88	8	1	2	0	---	---
	LUMO	2	1	5	91	0	---	---
	HOMO	76	20	3	1	0	---	---
	H -1	70	5	20	3	2	---	---
4	L + 1	3	2	8	87	1	---	---
	LUMO	1	0	0	99	0	---	---
	HOMO	76	20	3	1	0	---	---
	H -1	73	4	18	2	2	---	---
5	L + 1	5	3	18	---	---	67	8
	LUMO	17	2	2	---	---	73	5
	HOMO	68	20	10	---	---	2	0
	H -1	47	1	42	---	---	9	0
6	L + 1	21	3	2	---	---	68	6
	LUMO	3	2	13	---	---	43	38
	HOMO	68	20	10	---	---	2	0
	H -1	47	1	42	---	---	10	0

Table III.S3 - Natural transition orbitals (NTO) associated with absorption bands **T1** to **T12** of complex **2** obtained by TD-DFT

(Isovalue = 0.02) (PCM = CH_2Cl_2)

	λ_{Calc}, nm (Osc. Strenght) / Eigenvalue	**NTO Hole**	**NTO Particle**
T1	647 (0.388) / >0.99	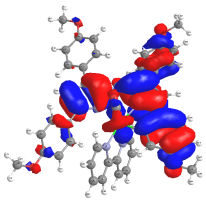	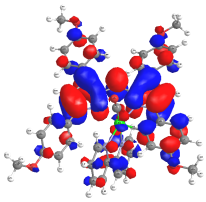
T2	637 (0.048) / 0.99	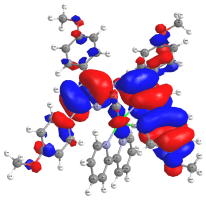	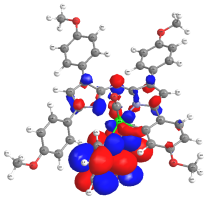
T3	560 (0.080) / >0.99	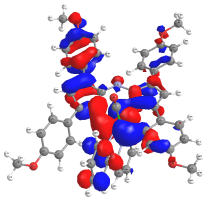	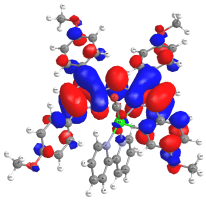
T4	538 (0.169) / 0.98	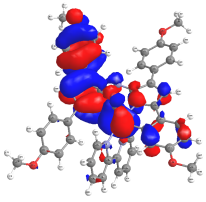	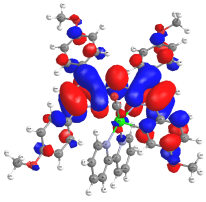
T5	524 (0.163) / 0.96	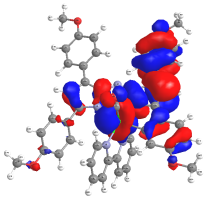	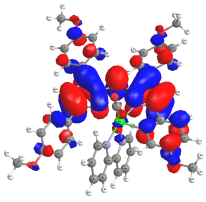

T6	487 (0.001) / >0.99	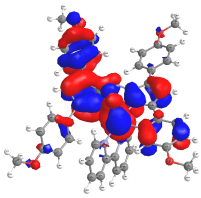	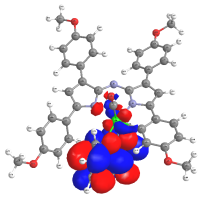
T7	484 (0.048) / 0.95	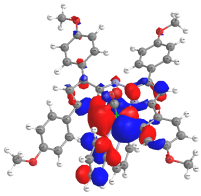	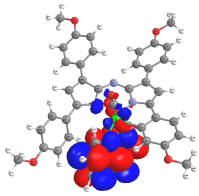
T8	463 (0.015) / 0.99	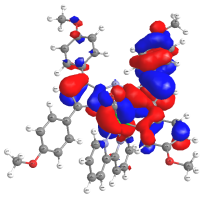	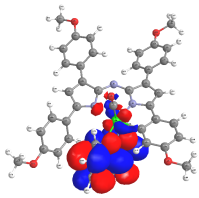
T9	438 (0.232) / 0.92	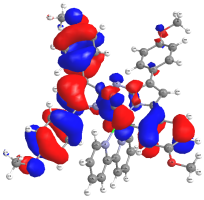	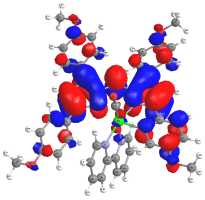
T10	434 (0.033) / 0.93	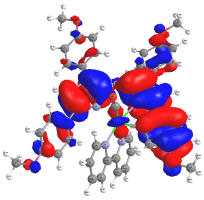	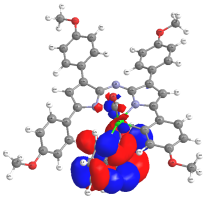
T11	411 (0.134) / 0.98	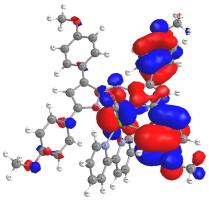	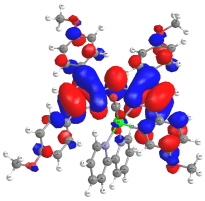
T12	406 (0.002) / 0.99	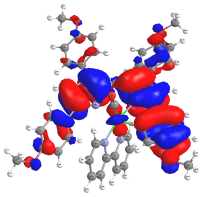	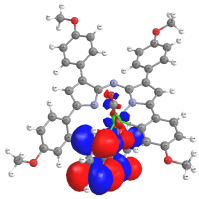

Table III.S4 - Assignation of optical absorption bands of ADPM photosensitizer **2** based on TD-DFT calculations

(B3LYP/6-31G*; Ru = LANL2DZ; PCM = CH_2Cl_2)

λ, nm				
Observed (ε, x10^3 $M^{-1}cm^{-1}$)	**Calculated** (Osc. Strength)	**Trans. No.**	**Major contributions to excitation**	**Assignation**
712 (15)	647 (0.388)	T1	H -> L (81%)	Cyclo + Ru + CO --> N^N + ADPM
660 (17)	637 (0.048)	T2	H -> L+1 (90%)	ADPM + Cyclo --> N^N + CO + Ru
550 (15)	560 (0.080)	T3	H-3 (30%), H-2 (36%), H-1 (29%) -> L	Ru + N^N + CO --> ADPM + Cyclo
	538 (0.169)	T4	H-3 (39%), H-1 (53%) -> L	Ru + N^N + CO --> ADPM + Cyclo
	524 (0.163)	T5	H-3 (28%), H-2 (57%) -> L	Ru + N^N + CO --> ADPM + Cyclo
	487 (0.001)	T6	H-3 (19%), H-1 (63%) -> L+1	ADPM + Cyclo + Ru + CO --> N^N
	484 (0.048)	T7	H-3 (62%), H-1 (26%) -> L+1	Ru + ADPM + Cyclo + CO --> N^N
436 (13)	463 (0.015)	T8	H-2 -> L+1 (81%)	ADPM + Cyclo + Ru + CO --> N^N
	438 (0.232)	T9	H-4 -> L (86%)	Ru + Cyclo + CO --> ADPM + N^N
	434 (0.033)	T10	H -> L+2 (91%)	ADPM + Cyclo --> N^N + CO
	411 (0.134)	T11	H-5 -> L (90%)	Cyclo + Ru + CO + N^N --> ADPM
	406 (0.002)	T12	H -> L+3 (97%)	ADPM + Cyclo + Ru + CO --> N^N

Figure III.S32 – Experimental absorption spectrum in CH_2Cl_2 vs calculated optical absorption bands of ADPM photosensitizer **3** based on TD-DFT calculations (B3LYP/6-31G*; Ru = LANL2DZ; PCM = CH_2Cl_2)

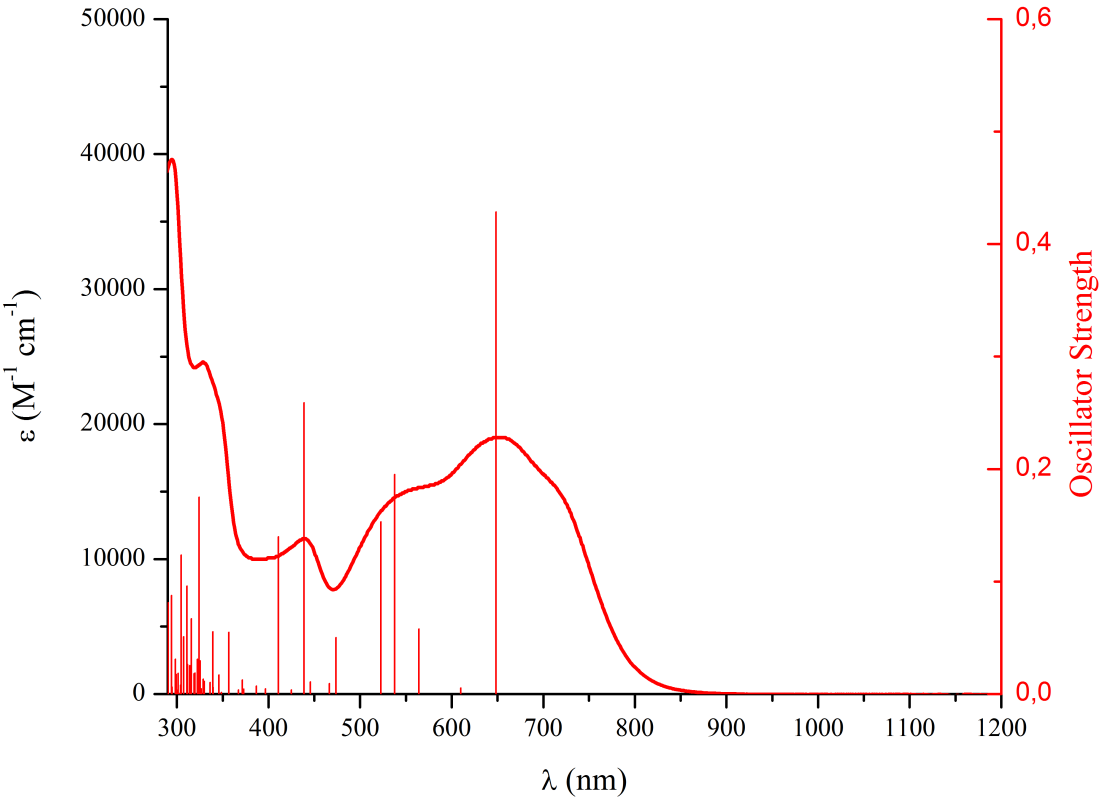

Table III.S5 - Natural transition orbitals (NTO) associated with absorption bands **T1** to **T12** of complex **3** obtained by TD-DFT

(Isovalue = 0.02) (PCM = CH_2Cl_2)

	λ_{Calc}, nm (Osc. Strenght) / Eigenvalue	**NTO Hole**	**NTO Particle**
T1	648 (0.429) / >0.99	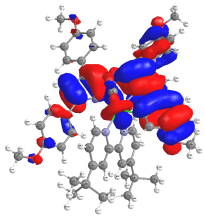	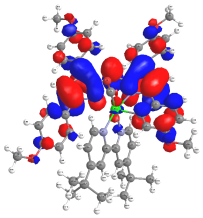
T2	610 (0.005) / >0.99	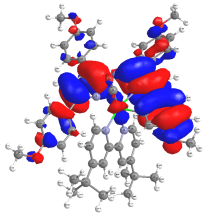	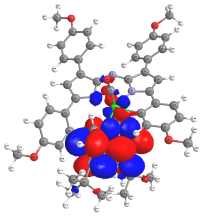
T3	564 (0.058) / >0.99	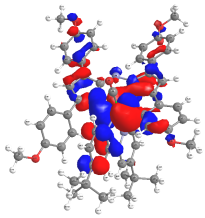	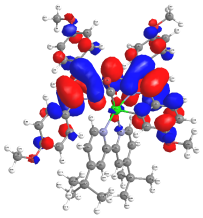
T4	538 (0.195) / 0.99	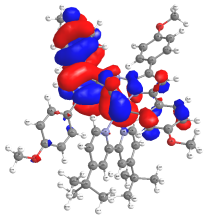	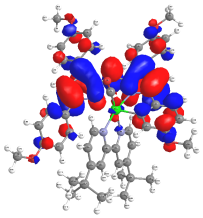
T5	523 (0.153) / 0.97	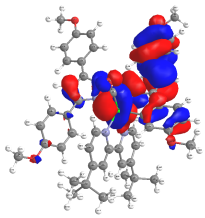	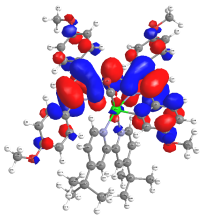

T6	474 (0.050) / 0.96	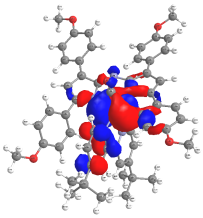	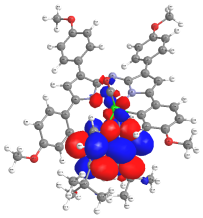
T7	467 (0.009) / 0.99	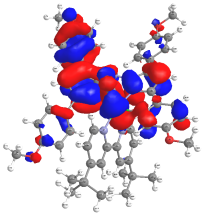	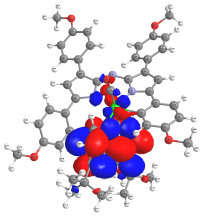
T8	446 (0.011) / 0.99	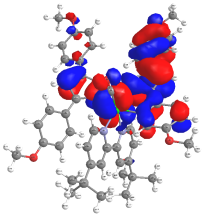	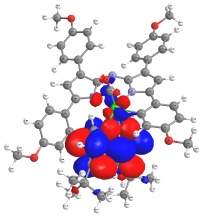
T9	439 (0.259) / 0.99	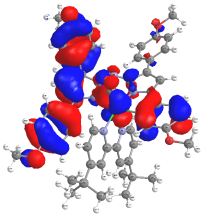	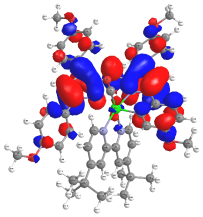
T10	425 (0.004) / 0.99	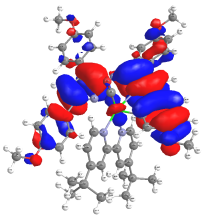	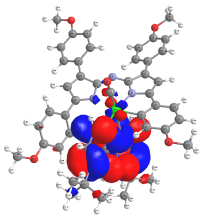
T11	411 (0.140) / 0.98	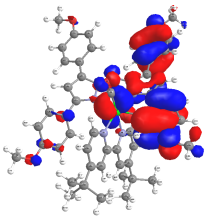	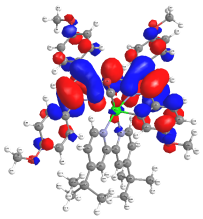
T12	397 (0.005) / 0.99	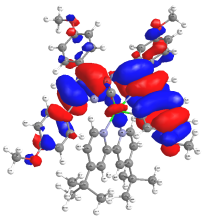	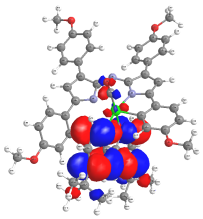

Table III.S6 - Assignation of optical absorption bands of ADPM photosensitizer **3** based on TD-DFT calculations

(B3LYP/6-31G*; Ru = LANL2DZ; PCM = CH_2Cl_2)

λ, nm				
Observed (ε, x10^3 $M^{-1}cm^{-1}$)	**Calculated** (Osc. Strength)	**Trans. No.**	**Major contributions to excitation**	**Assignation**
712 (16)	648 (0.429)	T1	H -> L (89%)	Cyclo + Ru + CO --> N^N + ADPM
654 (19)	610 (0.005)	T2	H -> L+1 (99%)	ADPM + Cyclo --> N^N + CO + Ru
552 (15)	564 (0.058)	T3	H-3 (23%), H-2 (51%), H-1 (23%) -> L	Ru + N^N + CO --> ADPM + Cyclo
	538 (0.195)	T4	H-3 (28%), H-1 (61%) -> L	Ru + N^N + CO --> ADPM + Cyclo
	523 (0.153)	T5	H-3 (46%), H-2 (42%) -> L	Ru + N^N + CO --> ADPM + Cyclo
	474 (0.050)	T6	H-3 (56%), H-2 (32%) -> L+1	ADPM + Cyclo + Ru + CO --> N^N
439 (12)	467 (0.009)	T7	H-1 -> L+1 (84%)	ADPM + Cyclo + Ru + CO --> N^N
	446 (0.011)	T8	H-3 (35%), H-2 (54%) -> L+1	ADPM + Cyclo + Ru + CO --> N^N
	439 (0.259)	T9	H-4 -> L (92%)	Ru + Cyclo + CO --> ADPM
	425 (0.004)	T10	H -> L+2 (97%)	ADPM + Cyclo --> N^N + Ru
	411 (0.140)	T11	H-5 -> L (90%)	Cyclo + Ru + CO + N^N --> ADPM
	397 (0.005)	T12	H -> L+3 (97%)	ADPM + Cyclo + Ru --> N^N + CO

Figure III.S33 – Experimental absorption spectrum in CH_2Cl_2 vs calculated optical absorption bands of ADPM photosensitizer **4** based on TD-DFT calculations (B3LYP/6-31G*; Ru = LANL2DZ; PCM = CH_2Cl_2)

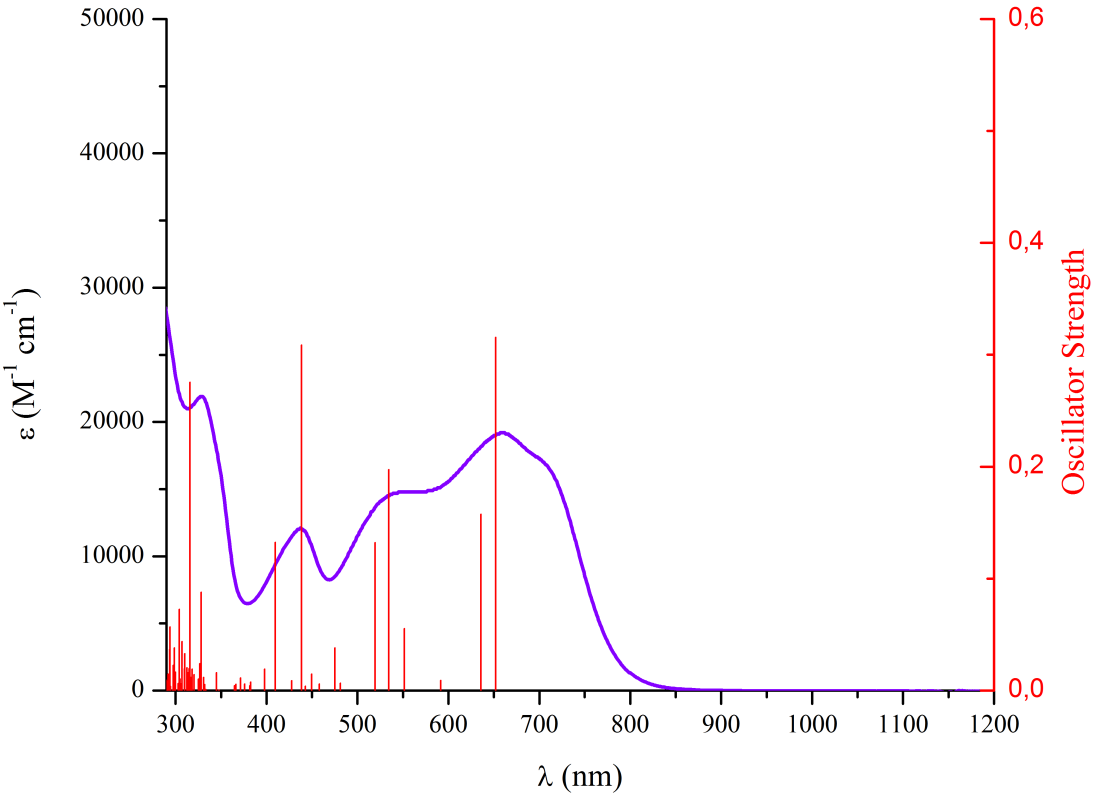

Table III.S7 – Natural transition orbitals (NTO) associated with absorption bands **T1** to **T14** of complex **4** obtained by TD-DFT

(Isovalue = 0.02) (PCM = CH_2Cl_2)

	λ_{Calc}, nm (Osc. Strenght) / Eigenvalue	**NTO Hole**	**NTO Particle**
T1	652 (0.316) / 0.99	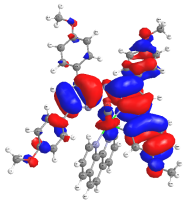	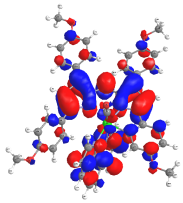
T2	636 (0.158) / 0.99	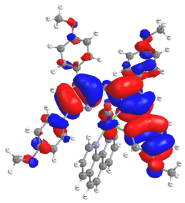	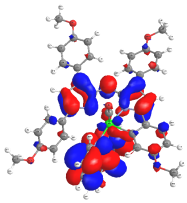
T3	591 (0.009) / >0.99	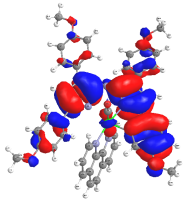	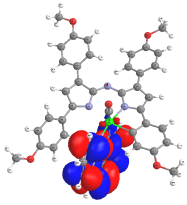
T4	552 (0.055) / >0.99	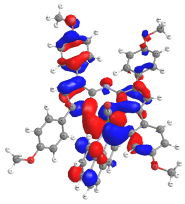	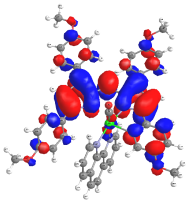
T5	534 (0.197) / 0.98	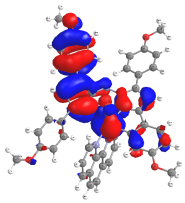	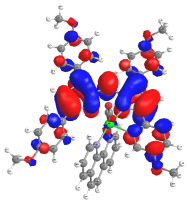

T6	520 (0.132) / 0.97	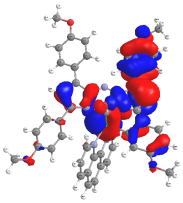	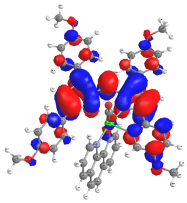
T7	481 (0.007) / 0.98	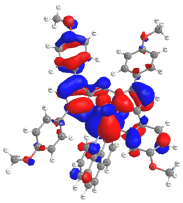	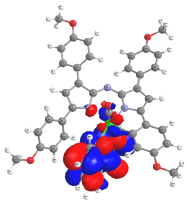
T8	475 (0.038) / 0.93	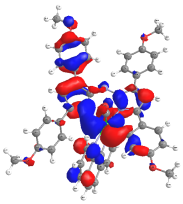	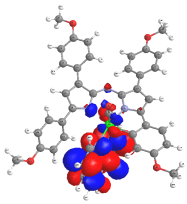
T9	458 (0.006) / 0.92	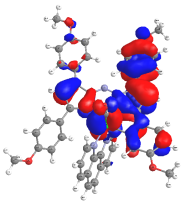	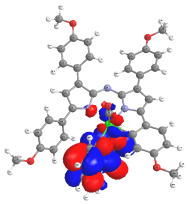
T10	450 (0.015) / 0.96	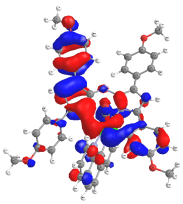	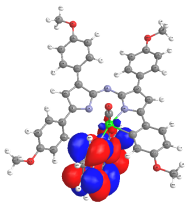
T11	443 (0.004) / 0.84	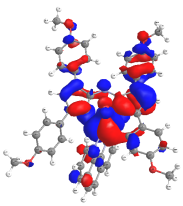	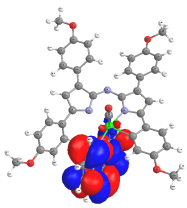
T12	439 (0.309) / 0.92	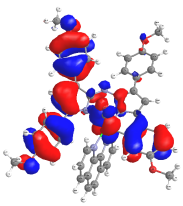	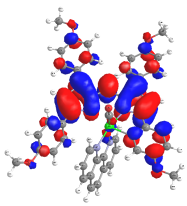

T13	428 (0.009) / 0.84	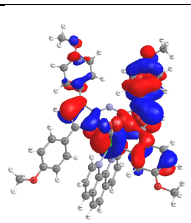	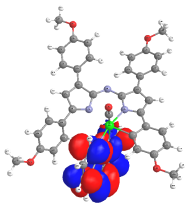
T14	410 (0.132) / 0.97	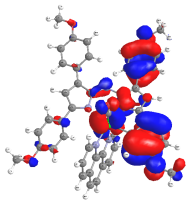	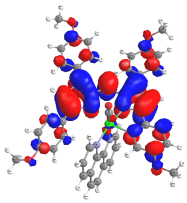

Table III.S8 - Assignation of optical absorption bands of ADPM photosensitizer **4** based on TD-DFT calculations

(B3LYP/6-31G*; Ru = LANL2DZ; PCM = CH_2Cl_2)

λ, nm				
Observed (ε, x10^3 $M^{-1}cm^{-1}$)	**Calculated** (Osc. Strength)	**Trans. No.**	**Major contributions to excitation**	**Assignation**
702 (17)	652 (0.316)	T1	H -> L (68%), H -> L+1 (26%)	Cyclo + ADPM + Ru --> N^N
659 (19)	636 (0.158)	T2	H -> L (24%), H -> L+1 (73%)	ADPM + Cyclo --> N^N + CO + Ru
544 (15)	591 (0.009)	T3	H -> L+2 (99%)	ADPM + Cyclo + Ru --> N^N
	552 (0.055)	T4	H-3 (35%), H-2 (45%), H-1 (17%) -> L	Ru + N^N + CO --> ADPM + Cyclo
	534 (0.197)	T5	H-3 (25%), H-1 (68%)->L	Ru + N^N + CO --> ADPM + Cyclo
	520 (0.132)	T6	H-3 (37%), H-2 (51%) -> L	Ru + N^N + CO --> ADPM + Cyclo
437 (12)	481 (0.007)	T7	H-3 (37%), H-2 (13%), H-1 (41%) -> L+1	ADPM + Cyclo + Ru + CO --> N^N
	475 (0.038)	T8	H-3 (37%), H-1 (47%) -> L+1	ADPM + Cyclo + Ru + CO --> N^N
	458 (0.006)	T9	H-3 (17%), H-2 (66%) -> L+1	ADPM + Cyclo + Ru + CO --> N^N
	450 (0.015)	T10	H-3 (15%), H-1 (67%) -> L+2	ADPM + Cyclo + Ru + CO --> N^N
	443 (0.004)	T11	H-3 (27%), H-2 (29%), H-1 (25%) -> L+2	ADPM + Cyclo + Ru + CO --> N^N
	439 (0.309)	T12	H-4 -> L (84%)	Ru + Cyclo + CO --> ADPM + N^N
	428 (0.009)	T13	H-3 (40%), H-2 (53%) -> L+2	ADPM + Cyclo + Ru + CO --> N^N
	410 (0.132)	T14	H-5 -> L (88%)	Ru + Cyclo + CO --> ADPM + N^N

Figure III.S34 – Experimental absorption spectrum in CH_2Cl_2 vs calculated optical absorption bands of ADPM photosensitizer **5** based on TD-DFT calculations (B3LYP/6-31G*; Ru = LANL2DZ; PCM = CH_2Cl_2)

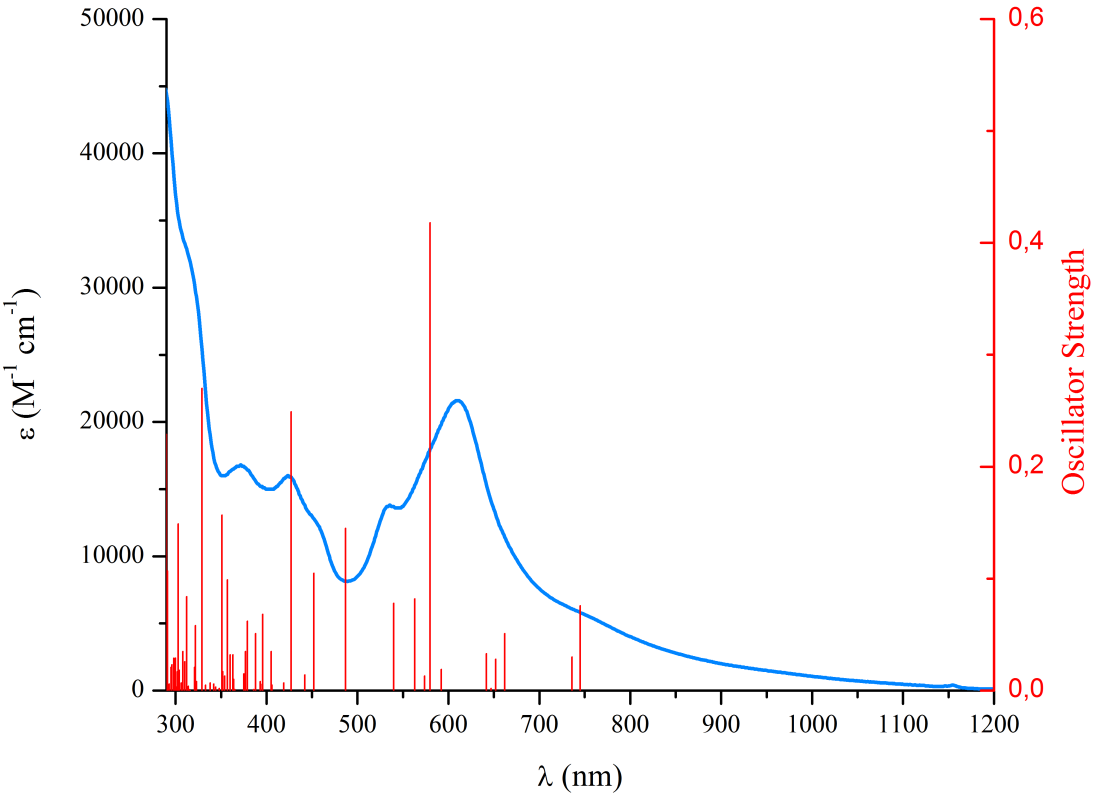

Table III.S9 – Natural transition orbitals (NTO) associated with absorption bands **T1** to **T18** of complex **5** obtained by TD-DFT

(Isovalue = 0.02) (PCM = CH_2Cl_2)

	λ_{Calc}, nm (Osc. Strenght) / Eigenvalue	**NTO Hole**	**NTO Particle**
T1	745 (0.076) / 0.99	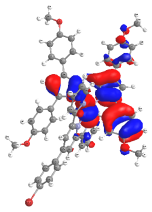	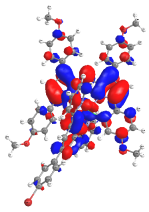
T2	736 (0.030) / 0.98	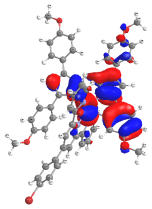	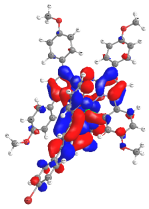
T3	662 (0.051) / 0.98	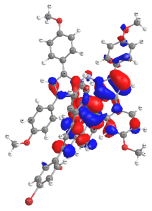	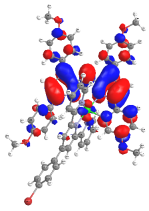
T4	652 (0.028) / 0.81	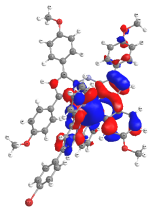	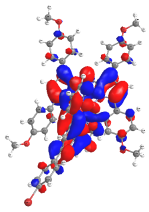
T5	647 (0.002) / 0.70	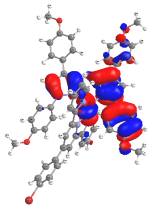	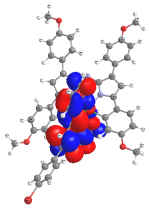

T6	642 (0.033) / 0.63	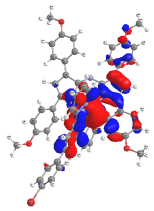	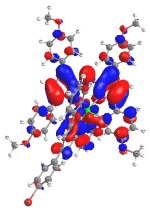
T7	592 (0.019) / 0.91	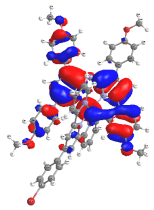	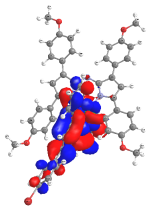
T8	580 (0.418) / 0.93	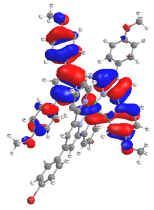	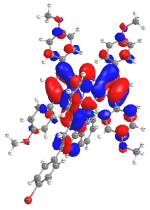
T9	574 (0.013) / 0.81	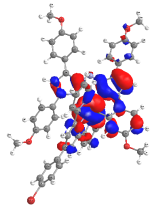	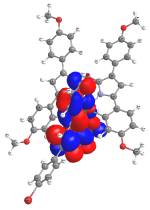
T10	563 (0.082) / 0.82	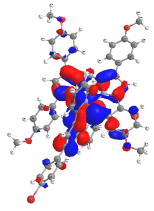	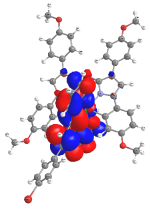
T11	540 (0.078) / 0.96	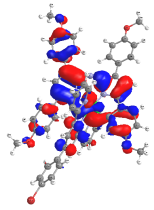	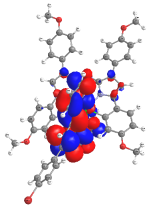
T12	487 (0.145) / 0.56	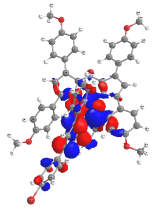	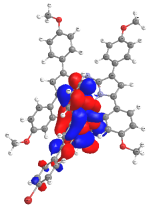

T13	452 (0.105)	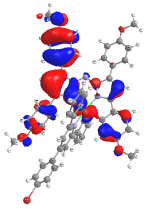	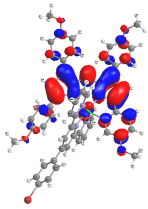
T14	442 (0.014)	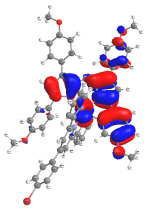	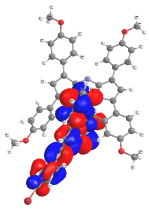
T15	427 (0.249)	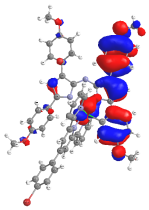	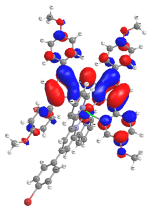
T16	419 (0.007)	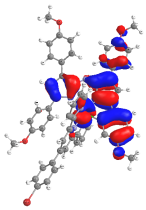	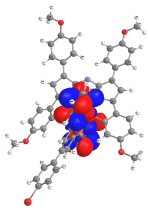
T17	406 (0.005)	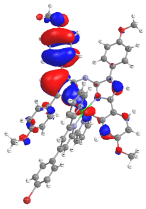	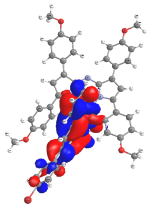
T18	405 (0.035)	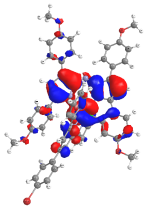	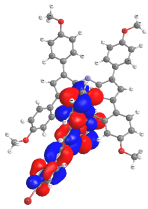

Table S.10 - Assignation of optical absorption bands of ADPM photosensitizer **5** based on TD-DFT calculations

(B3LYP/6-31G*; Ru = LANL2DZ; PCM = CH_2Cl_2)

λ, nm				
Observed (ε, x10^3 $M^{-1}cm^{-1}$)	**Calculated** (Osc. Strength)	**Trans. No.**	**Major contributions to excitation**	**Assignation**
752 (5.6)	745 (0.076)	T1	H-1 (10%), H (53%) -> L; H -> L+1 (18%)	Ru + Cyclo --> TPY + PhBr + ADPM
	736 (0.030)	T2	H-1 (18%), H (50%) -> L+1; H -> L (16%)	ADPM + Cyclo + Ru --> TPY + PhBr
610 (22)	662 (0.051)	T3	H-3 (16%), H-2 (34%), H-1 (45%) -> L	Ru + TPY + PhBr --> ADPM + Cyclo
	652 (0.028)	T4	H-3 (21%), H-2 (22%) -> L; H-2 -> L+1 (38%)	Ru + Cyclo --> TPY + PhBr + ADPM
	647 (0.002)	T5	H-2 -> L+1 (15%), H -> L+2 (62%)	ADPM + Cyclo + Ru --> TPY + PhBr
	642 (0.033)	T6	H-3 (32%), H-2 (15%) -> L; H-2 -> L+1 (20%); H -> L+2 (19%)	Ru + Cyclo --> TPY + PhBr + ADPM
	592 (0.019)	T7	H-2 (14%), H-1 (48%), H (25%) -> L+1	ADPM + Cyclo + Ru --> TPY + PhBr
	580 (0.418)	T8	H-3 (19%), H-2 (12%), H-1 (26%), H (22%) -> L; H-3 -> L+1 (10%)	Ru + Cyclo --> TPY + ADPM
	574 (0.013)	T9	H-3 -> L+1 (15%); H-2 (39%), H-1 (38%) -> L+2	ADPM + Cyclo + Ru --> TPY + PhBr
536 (14)	563 (0.082)	T10	H-3 (27%), H-2 (20%), H-1 (29%) -> L+2	ADPM + Cyclo + Ru --> TPY
	540 (0.078)	T11	H-3 (65%), H-1 (16%) -> L+2	ADPM + Cyclo + Ru + PhBr --> TPY
	487 (0.145)	T12	H-3 -> L+1 (48%); H-2 -> L+2 (27%)	ADPM + Cyclo + Ru --> TPY + PhBr
423 (16)	452 (0.105)	T13	H-4 -> L (96%)	Ru --> ADPM + Cyclo
	442 (0.014)	T14	H -> L+3 (86%)	ADPM + Cyclo + Ru --> TPY + PhBr
	427 (0.249)	T15	H-5 -> L (96%)	Cyclo + Ru --> ADPM + TPY
	419 (0.007)	T16	H-1 (11%), H (79%) -> L+4	ADPM + Cyclo + Ru --> TPY + PhBr
	406 (0.005)	T17	H-4 -> L+1 (87%)	ADPM + Cyclo --> TPY + PhBr + Ru
	405 (0.035)	T18	H-1 -> L+3 (71%)	ADPM + Ru + Cyclo --> TPY + PhBr

Figure III.S35 – Experimental absorption spectrum in CH_2Cl_2 vs calculated optical absorption bands of ADPM photosensitizer **6** based on TD-DFT calculations (B3LYP/6-31G*; Ru = LANL2DZ; PCM = CH_2Cl_2)

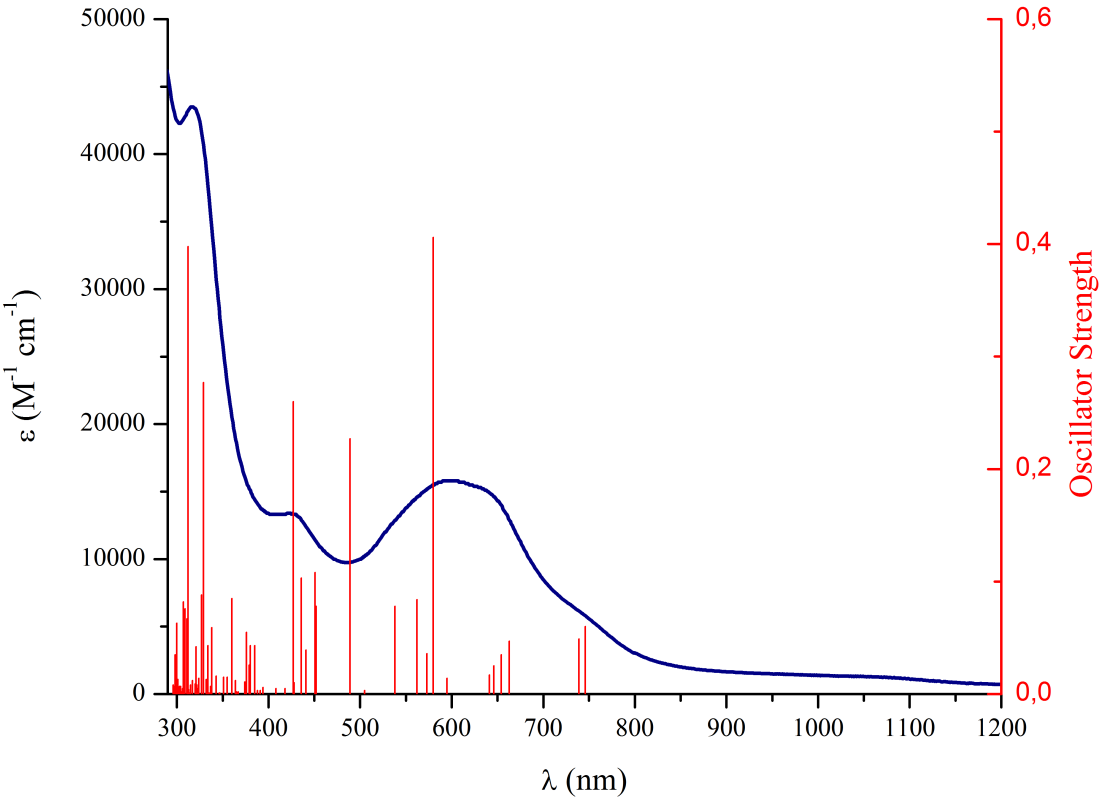

Table III.S11 – Natural transition orbitals (NTO) associated with absorption bands **T1** to **T21** of complex **6** obtained by TD-DFT

(Isovalue = 0.02) (PCM = CH_2Cl_2)

	λ_{Calc}, nm (Osc. Strenght) / Eigenvalue	**NTO Hole**	**NTO Particle**
T1	746 (0.060) / 0.98	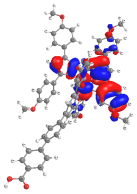	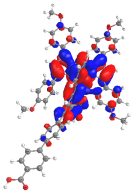
T2	739 (0.049) / 0.98	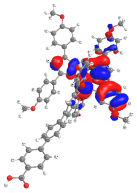	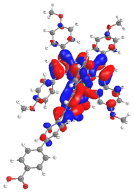
T3	663 (0.047) / 0.98	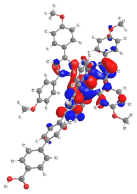	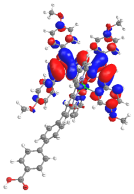
T4	654 (0.035) / 0.89	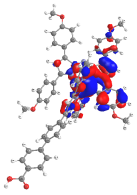	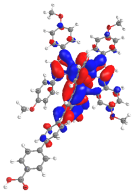
T5	646 (0.025) / 0.55	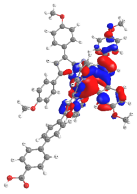	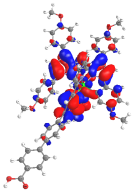

T6	641 (0.017) / 0.75	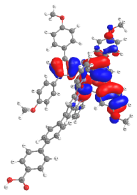	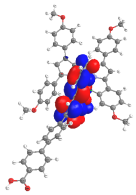
T7	595 (0.014) / 0.92	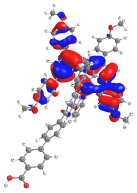	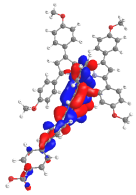
T8	580 (0.406) / 0.89	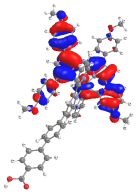	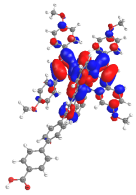
T9	573 (0.036) / 0.80	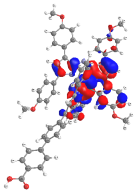	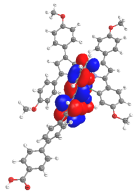
T10	562 (0.084) / 0.83	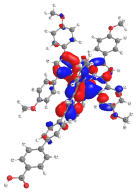	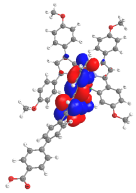
T11	538 (0.078) / 0.95	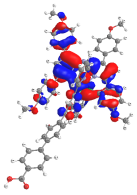	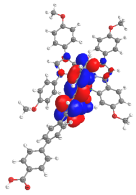
T12	505 (0.003) / 0.99	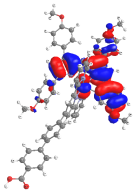	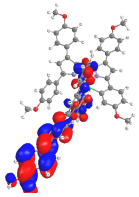

T13	489 (0.227) / 0.53	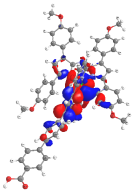	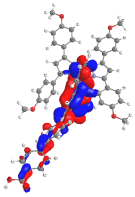
T14	452 (0.078) / 0.98	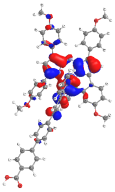	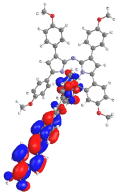
T15	451 (0.108) / 0.99	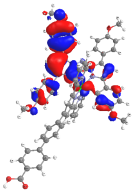	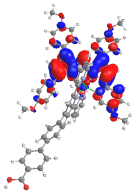
T16	441 (0.039) / 0.98	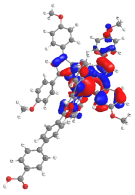	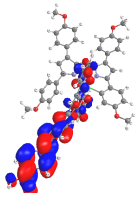
T17	436 (0.103) / 0.94	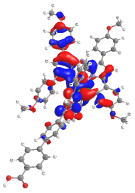	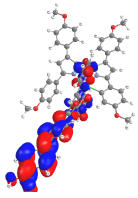
T18	428 (0.010) / 0.93	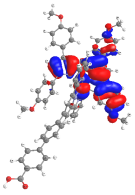	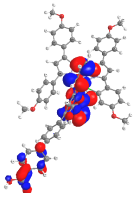
T19	427 (0.260) / 0.98	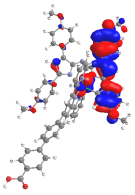	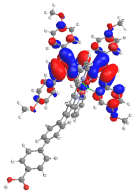

T20	418 (0.005) / 0.95	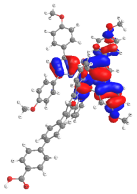	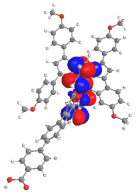
T21	408 (0.005) / 0.97	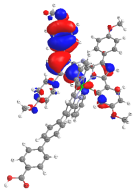	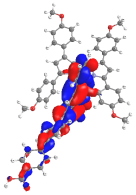

Table III.S12 - Assignation of optical absorption bands of ADPM photosensitizer **6** based on TD-DFT calculations (B3LYP/6-31G*; Ru = LANL2DZ; PCM = CH_2Cl_2)

λ, nm				
Observed (ε, x10^3 $M^{-1}cm^{-1}$)	**Calculated** (Osc. Strength)	**Trans. No.**	**Major contributions to excitation**	**Assignation**
753 (5.4)	746 (0.060)	T1	H->L (42%), H->L+1 (26%)	Ru + Cyclo + ADPM --> TPY + Ph2COOH
	739 (0.049)	T2	H-1 (12%), H (36%) -> L+1; H -> L (27%)	Ru + Cyclo + ADPM --> TPY + Ph2COOH
600 (16)	663 (0.047)	T3	H-3 (22%), H-2 (25%), H-1 (47%) -> L	Ru + TPY --> ADPM + Cyclo + Ph2COOH
	654 (0.035)	T4	H-3 (14%), H-2 (28%) -> L; H-2 -> L+1 (37%)	Ru + Cyclo --> TPY + Ph2COOH + ADPM
	646 (0.025)	T5	H-3 (20%), H-2 (16%) ->L; H-2 (23%), H-1 (10%) -> L+1; H -> L+2 (19%)	Ru + Cyclo --> TPY + Ph2COOH + ADPM
	641 (0.017)	T6	H-3 -> L (12%), H -> L+2 (64%)	ADPM + Cyclo + Ru --> TPY + Ph2COOH
	595 (0.014)	T7	H-2 (13%), H-1 (44%), H (24%) -> L+1	ADPM + Cyclo + Ru --> TPY + Ph2COOH
538 (13)	580 (0.406)	T8	H-3 (20%), H-2 (11%), H-1 (23%), H (22%) -> L; H-3 -> L+1 (14%)	Ru + Cyclo --> ADPM + TPY + Ph2COOH
	573 (0.036)	T9	H-3 -> L+1 (12%); H-2 (37%), H-1 (40%) -> L+2	Ru + ADPM + Cyclo --> TPY + Ph2COOH
	562 (0.084)	T10	H-3 (27%), H-2 (19%), H-1 (31%) -> L+2	Ru + ADPM + Cyclo --> TPY + Ph2COOH
	538 (0.078)	T11	H-3 (64%), H-1 (16%) -> L+2	Ru + ADPM + Cyclo --> TPY
	505 (0.003)	T12	H -> L+3 (88%)	ADPM + Cyclo + Ru --> Ph2COOH + TPY
	489 (0.227)	T13	H-3 -> L+1 (42%), H-2 -> L+2 (30%)	Ru + ADPM + Cyclo --> TPY + Ph2COOH
422 (13)	452 (0.078)	T14	H-1 -> L+1 (10%), H-1 -> L+3 (78%)	Ru + ADPM + Cyclo --> Ph2COOH + TPY
	451 (0.108)	T15	H-4 -> L (97%)	Ru --> ADPM + Cyclo
	441 (0.039)	T16	H-2 -> L+1 (10%), H-2 -> L+3 (77%)	Ru + ADPM + Cyclo --> Ph2COOH + TPY
	436 (0.103)	T17	H-3 -> L+3 (70%)	Ru + ADPM + Cyclo --> Ph2COOH + TPY
	428 (0.010)	T18	H -> L+4 (82%)	ADPM + Cyclo + Ru --> TPY + Ph2COOH
	427 (0.260)	T19	H-5 -> L (96%)	Cyclo + Ru --> ADPM + TPY
	418 (0.005)	T20	H-1 (11%), H (79%) -> L+5	ADPM + Cyclo + Ru --> TPY + Ph2COOH
	408 (0.005)	T21	H-4 -> L+1 (88%)	ADPM + Cyclo --> TPY + PhBr + Ru

Table III.S13 – Natural transition orbitals (NTO) associated with absorption bands **T1** to **T21** of complex **6** obtained by TD-DFT

(Isovalue = 0.02) (PCM = MeOH)

	λ_{Calc}, nm (Osc. Strenght) / Eigenvalue	**NTO Hole**	**NTO Particle**
T1	752 (0.088) / 0.99	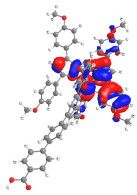	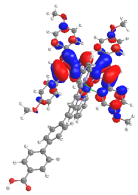
T2	727 (0.004) / 0.96	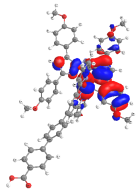	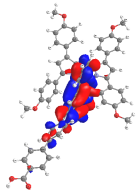
T3	674 (0.029) / 0.97	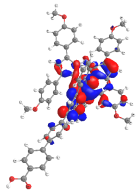	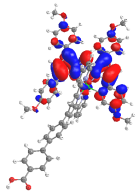
T4	660 (0.077) / 0.97	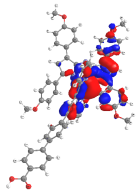	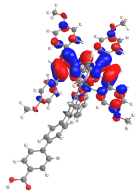
T5	641 (0.008) / 0.93	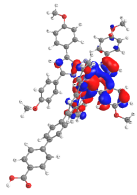	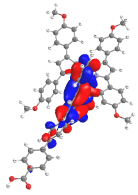

T6	628 (0.002) / 0.95	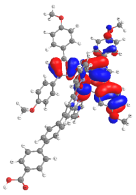	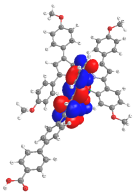
T7	583 (0.097) / 0.87	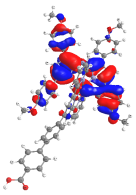	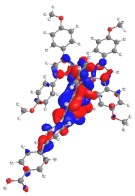
T8	577 (0.363) / 0.96	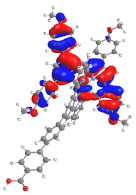	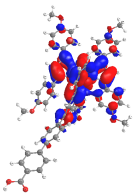
T9	565 (0.028) / 0.76	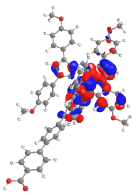	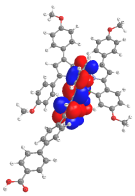
T10	555 (0.057) / 0.85	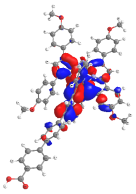	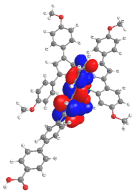
T11	529 (0.061) / 0.95	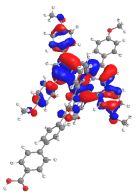	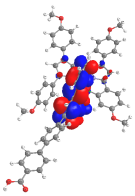
T12	491 (0.004) / 0.98	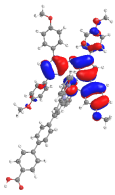	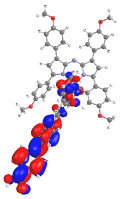

T13	485 (0.209) / 0.52	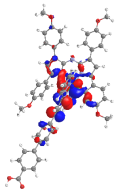	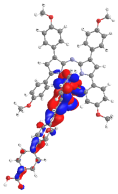
T14	452 (0.105) / 0.99	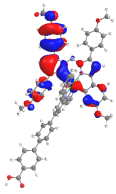	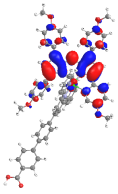
T15	444 (0.100) / 0.98	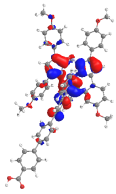	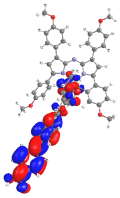
T16	434 (0.046) / 0.97	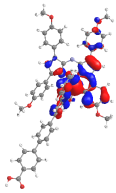	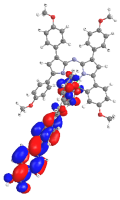
T17	429 (0.098) / 0.91	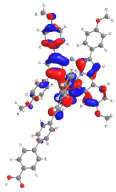	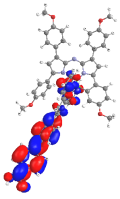
T18	428 (0.233) / 0.98	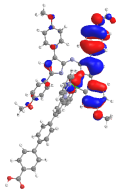	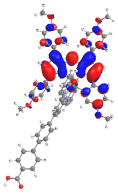
T19	422 (0.013) / 0.89	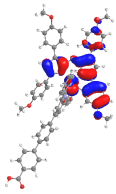	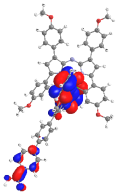

T20	413 (0.005) / 0.95	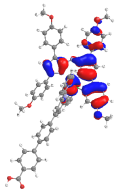	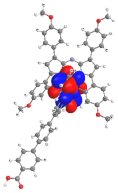
T21	401 (0.004) / 0.98	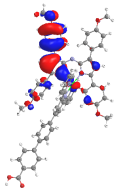	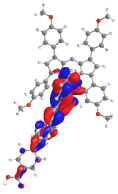

Table III.S14 - Assignation of optical absorption bands of ADPM photosensitizer **6** based on TD-DFT calculations

(B3LYP/6-31G*; Ru = LANL2DZ; PCM = MeOH)

λ, nm			**Major contributions to excitation**	**Assignation**
Observed (ε, x10^3 $M^{-1}cm^{-1}$)	**Calculated** (Osc. Strength)	**Trans. No.**		
753 (5.4)	752 (0.088)	T1	H-2 (12%), H-1 (12%), H (68%) -> L	Ru + Cyclo + TPY --> ADPM + Ph2COOH
	727 (0.004)	T2	H-1 (16%), H (61%) -> L+1	ADPM + Cyclo + Ru --> TPY +Ph2COOH
600 (16)	674 (0.029)	T3	H-3 (28%), H-2 (14%), H-1 (53%) -> L	Ru + TPY + Ph2COOH --> ADPM + Cyclo
	660 (0.077)	T4	H-3 (30%), H-2 (60%) -> L	Ru + TPY + Cyclo --> ADPM + Ph2COOH
	641 (0.008)	T5	H-2 (63%), H-1 (17%) -> L+1	Ru + ADPM + Cyclo --> TPY + Ph2COOH
	628 (0.002)	T6	H -> L+2 (82%)	ADPM + Cyclo + Ru --> TPY +Ph2COOH
	583 (0.097)	T7	H-2 (11%), H-1 (39%), H (18%) -> L+1	Ru + ADPM + Cyclo --> TPY +Ph2COOH
538 (13)	577 (0.363)	T8	H-3 (21%), H-1 (20%), H (19%) -> L; H-3 -> L+1 (13%)	Ru + Cyclo --> ADPM + Ph2COOH + TPY
	565 (0.028)	T9	H-3 -> L+1 (17%); H-2 (36%), H-1 (37%) -> L+2	Ru + ADPM + Cyclo --> TPY + Ph2COOH
	555 (0.057)	T10	H-3 (26%), H-2 (20%), H-1 (34%) -> L+2	Ru + ADPM + Cyclo --> TPY + Ph2COOH
	529 (0.061)	T11	H-3 (63%), H-1 (16%), H (10%) -> L+2	Ru + ADPM + Cyclo --> TPY
	491 (0.004)	T12	H -> L+3 (88%)	ADPM + Cyclo + Ru --> Ph2COOH + TPY
	485 (0.209)	T13	H-3 -> L+1 (38%), H-2 -> L+2 (31%)	Ru + ADPM + Cyclo --> TPY + Ph2COOH
422 (13)	452 (0.105)	T14	H-4 -> L (97%)	Ru --> ADPM + Cyclo
	444 (0.100)	T15	H-1 -> L+3 (79%)	Ru + ADPM + Cyclo --> Ph2COOH + TPY
	434 (0.046)	T16	H-3 (10%), H-2 (74%) -> L+3	Ru + ADPM + Cyclo --> Ph2COOH + TPY
	429 (0.098)	T17	H-3 (64%), H-2 (12%) -> L+3	Ru + ADPM + Cyclo --> Ph2COOH + TPY
	428 (0.233)	T18	H-5 -> L (96%)	Cyclo + Ru --> ADPM + TPY
	422 (0.013)	T19	H -> L+4 (79%)	ADPM + Ru + Cyclo --> TPY + Ph2COOH
	413 (0.005)	T20	H-1 (12%), H (78%) -> L+5	ADPM + Ru + Cyclo --> TPY + Ph2COOH
	401 (0.004)	T21	H-4 -> L+1 (89%)	ADPM + Cyclo --> TPY + Ph2COOH + Ru

X-ray diffraction measurements and structure determination

Crystallographic data for **2** were collected at 150 K, from single crystal samples, which were mounted on a loop fiber. Data were collected using a Bruker Microstar diffractometer equipped with a Platinum 135 CCD Detector, a Helios optics and a Kappa goniometer. The crystal-to-detector distance was 3.8 cm, and the data collection was carried out in 512 x 512 pixel mode. The initial unit cell parameters were determined by a least-squares fit of the angular setting of strong reflections, collected by a 110.0 degree scan in 110 frames over three different parts of the reciprocal space. Crystallographic data for **4** and **5** were collected at 100 K, using a Bruker D8 Venture diffractometer configured with a Metal Jet liquid-metal source, and a Photon 100 CMOS-based area detector. For data collection, determination of cell parameters, cell refinement, and data reduction *APEX2* and *SAINT* (Bruker, 2007) were used.[1] Absorption corrections were applied using *SADABS* and *TWINABS* (Bruker 2001).[2] Structure solution was performed using direct methods with *SHELXS* or *SHELXT* (Sheldrick, 2008 and 2015)[3,4] and refined on F^2 by full-matrix least squares using *SHELXL2014* (Sheldrick, 2008 and 2015).[3,4] *OLEX2* (Dolomanov *et al.*, 2009),[5] *ORTEP-3 for Windows* (Farrugia, 2012),[6] and POV-ray (2013)[7] were used for molecular graphics. The material was prepared for publication using *PLATON* (Spek, 2009),[8] Mercury,[9] and *publCIF* (Westrip, 2010).[10]

Crystal data, data collection and structure refinement details are summarized in Table S15. For **2**, **4** and **5**, all non-H atoms were refined by full-matrix least-squares

with anisotropic displacement parameters. The H-atoms were included in calculated positions and treated as riding atoms: aromatic C—H 0.95 Å, methyl C—H 0.98 Å, with $U_{iso}(H) = k \times U_{eq}$ (parent C-atom), where k = 1.2 for the aromatic H-atoms and 1.5 for the methyl H-atoms.

Compound **2** contains a co-crystallized 4-chlorobenzene molecule. In addition, solvent accessible voids of 41 $Å^3$ were found, with an electron count of 2. The void is too small to accommodate molecules bigger than water; water didn't fit. The structures of the compounds **4** and **5** were obtained from the best available crystals, which unfortunately were very poor quality, resulting in overall poor data quality. In addition, both structures present high degree of disorder. The structure of **4** contains two molecules in the asymmetric unit. One molecule displays disorder at the level of one proximal 4-methoxy-phenyl group. The disorder was modelled as two components using PART instructions. The disordered benzene groups were constrained to an ideal hexagon, with C—C distances equal to 1.39 Å. The occupation factors were first freely refined, and then fixed at the values obtained after refinement (50:50). Bond distance and mild displacement parameter (U^{ij}) restraints were also applied.). In order to improve the model, the reflections (hkl: 7 3 1; -6 7 2; 9 3 4) with $|F_o - F_c| > 5\sigma(F_o)$ were omitted from the refinement. The weight second parameter is unusually large for **4** (22.96), which can indicate twinning. No twin law was detected with TwinRotMat routine from *PLATON* (Spek, 2009);[8] treatment for non-merohedrally twinned crystal data was also performed using *CELL_NOW* (2 and 3 domains)/ *TWINABS*/ *BASF* / *HKLF5* (Bruker 2001),[2] but the models obtained were worse than the present model. Therefore the twinning treatment was not retained. The structure of compound **5** is highly disordered

at the level of the ADPM moiety and of three of the four *p*-methoxy-phenyl groups. The disorder was modeled as described above, using in addition hard displacement parameter (U^{ij}) restraints. The occupation factors were first freely refined, and then fixed at the values obtained after refinement (60:40 and 55:45 for the distal 4-methoxy-phenyl groups, and 70:30 for the proximal one). The structure of **5** contains a co-crystallized disordered toluene molecule on a symmetry position, which was modelled using PART -1 instruction, together with bond distance and angle constraints. A calculated residual density of 1.52 e/Å^3 is present in **5**, at 0.95 Å from the Ru atom. As the presence of a Ru-H bond is chemically not possible, this remaining electron density is most likely a Fourier truncation error.

Compound **4** crystallized with two molecules in the asymmetric unit showing similar conformations. The only notable difference between the two molecules is observed at the level of distal and proximal aryl rings, which present different orientations maximizing the π–π and π–H–C(sp^2) intermolecular interactions: the phen ligand does not participate in intramolecular π–π interactions with the non-cyclometallated proximal aryl ring of the ADPM moiety, but in intermolecular π –π interactions with one of the distal aryl rings of an adjacent molecule. (Figure S.37). The π-delocalized nature of the ADPM unit is retained after complexation, as confirmed by the analysis of bond lengths in this moiety (Table S.16), and in accordance with what was found for similar compounds.[11-13] Nevertheless, the synclinical angles between the planes of the pyrrole rings upon complexation are 13.5(1)° for **2**, 16.4(1)° and 18.0(1)° for **4**, and 8.9(1)° for **5** (Table S.16) *vs.* 1.3(1)° in the free ligand,[11] indicating the flexible nature of the coordinated ADPM ligands. The H-bonding pattern analysis (Table

S.18) reveals conventional and weak (intramolecular and intermolecular) H-bonds.[14] The intramolecular H-bonding patterns for the three compounds are shown in Figure 1. A 3-centre-bifurcated H-bond is observed in **2** and **4** (formed by one intramolecular H-bond and one intermolecular H-bond) (Table S.18).[† 15] In addition, intermolecular π–π and π–H–C(sp^2) interactions are present in the crystal packing (Figures S.36 – S.40).

Crystallographic data for **2**, **4**, and **5** were deposited in CCDC[16] under the deposit numbers: CCDC 1419506 – 1419508. The alerts given by the checkCIF/ PLATON routine are commented in the crystallographic information files (cifs) of the corresponding compounds.

Selected bond lengths and angles for **2**, **4**, and **5** are presented in Table S.16, whereas Table S.17 shows selected parameters reported in relevant ruthenium(II) complexes. The hydrogen bonding geometry for **2**, **4**, and **5** is highlighted in Table S.18.

Table III.S15 – Solid-state structure and refinement data for compounds **2**, **4** and **5**.

	2	**4**	**5**
Formula	$C_{47}H_{37}N_5O_5Ru \bullet C_6H_5Cl$	$C_{49}H_{37}N_5O_5Ru$	$C_{57}H_{43}BrN_6O_4Ru \bullet 0.5(C_7H_8)$
M_w(g/mol)	965.43	876.90	1103.02
T (K)	150	100	100
Wavelength (Å)	1.54178	1.3418	1.3418
Crystal System	Tetragonal	Monoclinic	Triclinic
Space Group	I-4	$P2_1/c$	P-1
Unit Cell: a (Å)	22.3944(5)	15.6633(7)	12.207(2)
b (Å)	22.3944(5)	24.0100(10)	13.408(3)
c (Å)	17.6264(4)	21.6141(10)	16.302(3)
a (°)	90	90	73.36(3)
β (°)	90	104.679(2)	70.90(3)
g (°)	90	90	73.29(3)
V (Å^3)	8839.8(4)	7863.2(6)	2359.8(10)
Z	8	8	2
$d_{calcd.}$ (g/cm^3)	1.451	1.481	1.552
m (mm^{-1})	3.884	2.453	2.789
F(000)	3968	3600	1126
θ range (°)	3.19 to 70.50	2.43 to 54.30	2.55 to 61.29
Reflections collected	93738	83129	42720
Independent reflections	8397	14471	10177
GoF	1.051	1.058	1.020
R1(F) [I > 2σ(I)]	0.0270	0.0745	0.0768
wR(F^2) [I > 2σ(I)]	0.0689	0.1959	0.1666
R1(F) (all data)	0.0275	0.1045	0.1233
wR(F^2) (all data)	0.0694	0.2150	0.1911
Largest diff. peak and hole (e/Å^3)	0.57 and -0.41	1.33 and -1.02	1.61 and -1.02

Table III.S16 – Selected bond lengths (Å) and angles (°) for compounds **2**, **4** and **5**

	2	**4**	**5**
Bond length (Å)/ Angle (°)			
Ru1-N1	2.032(3)	2.022(8)[a]	2.055(5)
Ru1-N3	2.222(3)	2.197(8)[a]	2.192(6)
Ru1-N4	2.138(3)	2.141(8)[a]	2.043(4)
Ru1-N5	2.087(3)	2.082(8)[a]	1.938(5)
Ru1-X	X=C47(carbonyl)	X=C49(carbonyl)	X=N6(N"-tpy)
	1.831(4)	1.814(11)[a]	2.035(4)
Ru1-C12	2.071(3)	2.069(10)[a]	2.102(3)
C-O(carbonyl)	1.157(4)	1.159(12)[a]	-
N1-C1	1.372(4)	1.375(13)[a]	1.389(9)
C1-N2	1.320(4)	1.322(13)[a]	1.312(10)
N2-C17	1.341(4)	1.345(13)[a]	1.339(9)
C17-N3	1.400(4)	1.391(13)[a]	1.408(8)
N1-Ru1-N5	164.9(1)	163.8(4)[a]	168.7(2)
N3-Ru1-C12	161.6(1)	164.1(4)[a]	160.2(2)
N4-Ru1-X	X=C47(carbonyl)	X=C49(carbonyl)	X=N6(N"-tpy)
	171.8(1)	175.7(4)[a]	158.2(2)
N1-Ru1-N3	82.1(1)	85.1(3)[a]	82.3(2)
N1-Ru1-C12	79.6(1)	79.5(4)[a]	78.0(2)
N1-Ru1-X	X=C47(carbonyl)	X=C49(carbonyl)	X=N6(N"-tpy)
	94.8(1)	94.9(4)[a]	96.8(1)
N1-Ru1-N4	92.6(1)	89.0(3)[a]	105.0(1)
N3-Ru1-N4	90.0(1)	84.5(3)[a]	89.9(2)
N3-Ru1-N5	108.4(1)	104.3(3)[a]	108.5(1)
N3-Ru1-X	X=C47(carbonyl)	X=C49(carbonyl)	X=N6(N"-tpy)
	94.5(1)	96.0(4)[a]	93.9(1)
N4-Ru1-N5	76.9(1)	79.1(3)[a]	79.0(1)
N4-Ru1-C12	88.7(1)	91.8(4)[a]	94.5(1)
N5-Ru1-C12	89.2(1)	90.1(4)[a]	91.2(1)
N5-Ru1-X	X=C47(carbonyl)	X=C49(carbonyl)	X=N6(N"-tpy)
	95.1(1)	97.2(4)[a]	79.5(1)
C12-Ru1-X	X=C47(carbonyl)	X=C49(carbonyl)	X=N6(N"-tpy)
	89.2(1)	88.8(4)[a]	89.2(1)
N1-C1-N2	125.6(3)	129.0(9)[a]	125.1(7)
C1-N2-C17	124.2(3)	124.9(8)[a]	124.4(6)
N2-C17-N3	127.8(3)	129.5(9)[a]	128.5(6)
Tilt angles (°) between the planes of the two central pyrrolic rings			
	13.5(1)	16.4(1); 18.0(1)[b]	8.9(1)
Tilt angles (°) between ADPM moiety and the aryl rings[c]			
Ar_1 (proximal)	23.5(1)	7.1(1); 10.3(1)[b]	3.4(1)
Ar_2 (distal)	19.7(1)	44.8(1); 41.0(1)[b]	3.4(1)
Ar_3 (distal)	35.1(1)	53.4(1); 45.5(1)[b]	32.0(1)
Ar_4 (proximal)	67.8(1)	52.2(1); 61.1(1)[b]	79.0(1)

[a] average values on the two molecules in the asymmetric unit; the error was calculated using the formula for propagation of error in calculations. [b] values are shown for the two molecules in the asymmetric unit. [c] Ar_1 is associated with the cyclometallated aryl moiety in proximal position, whereas the following aryls are numbered in a counter-clockwise fashion.

Table III.S17 – Selected parameters for relevant reported ruthenium(II) complexes.

CSD Code	QUBZAO[17]	acetyl-carbonyl-bis(2,2'-bipyridyl)-ruthenium(II) hexafluorophosphate
Bond length (Å)		
Ru-N_{bpy} (*trans* to carbonyl)		2.137(5)
Ru- N_{bpy} (*trans* to N)		2.070(5)
Ru-$C_{carbonyl}$		1.837(6)
C-O		1.152(7)
Ru-C_{acetyl}		2.038(6)
CSD Code	EJOHUG[18]	$Ru(phen)_2(CN)_2$
Bond length (Å)		
Ru-N_{phen} (*trans* to C)		2.124(8) and 2.107(9)
Ru-N_{phen}		2.073(7) and 2.081(8)

Table III.S18 – H-bonding geometry for compounds **2**, **4** and **5**. Distances are in (Å) and angles in (°); 3-center bifurcated H-bonds are displayed in italic.

***D*—H⋯*A* (type*)**	***D*—H**	**H⋯*A***	***D*⋯*A***	***D*—H⋯*A***
		2		
C10—H10⋯N2 (intra)	0.95(1)	2.51(1)	3.13(1)	123(1)
C10—H10⋯O4^{i} (inter)	0.95(1)	2.50(1)	3.18(1)	129(1)
C22—H22⋯N2 (intra)	0.95(1)	2.57(1)	3.09(1)	115(1)
C7—H7⋯O2^{ii} (inter)	0.95(1)	2.67(1)	3.29(1)	123(1)
		4		
		(for each of the 2 molecules in the asymmetric unit)		
C10—H10⋯N2 (intra)	0.95(1)	2.70(1)	3.13 (1)	108(1)
C22—H22⋯N2 (intra)	0.95(1)	2.72(1)	3.09(1)	104(1)
C37—H37⋯N1 (intra)	0.95(1)	2.64(1)	3.13(1)	113(1)
C9—H9⋯O10^{iii} (inter)	0.95(1)	2.60(1)	3.41(1)	144(1)
C23—H23⋯O10^{iii} (inter)	0.95(1)	2.38(1)	3.18(1)	142(1)
C42—H42⋯O3^{iv} (inter)	0.95(1)	2.38(1)	3.32(1)	171(1)
C86—H86⋯N6 (intra)	0.95(1)	2.61(1)	3.12(1)	114(1)
C71A—H71A⋯N7 (intra)	0.95(1)	2.55(1)	3.00(2)	109(1)
C59—H59⋯N7 (intra)	0.95(1)	2.64(1)	3.13(1)	113(1)
C59—H59⋯O5^{v} (inter)	0.95(1)	2.71(1)	3.26(1)	118(1)
C58—H58⋯O5^{v} (inter)	0.95(1)	2.66(1)	3.25(1)	121(1)
C72A—H72A⋯O5^{v} (inter)	0.95(1)	2.53(1)	3.28(1)	135(1)
C93—H93⋯O5^{v} (inter)	0.95(1)	2.51(1)	3.31(1)	141(1)
C75A—H75A⋯O4^{vi} (inter)	0.95(1)	2.57(1)	3.30(2)	134(1)
		5		
C10A—H10A⋯N2 (intra)	0.95(1)	2.56(1)	3.29(1)	134(1)
C22A—H22A⋯N2 (intra)	0.95(1)	2.46(1)	2.96(1)	113(1)
C32A—H32A⋯Br1^{vii} (inter)	0.95(1)	2.94(1)	3.84(1)	159(1)
C48—H48⋯O2^{viii} (inter)	0.95(1)	2.44(1)	3.19(1)	135(1)

*intra = intramolecular; inter = intermolecular

Symmetry codes: (i) ½-x, ½-y, -½+z; (ii) x, 1-y; 1-z (iii) x, ½+y, ½-z; (iiv) 1+x, y, z; (v) -x, -½+y, ½-z; (vi) 1-x, 1-y; 1-z; (vii) -1+x, y, z; (viii) 2-x, 2-y, 1-z.

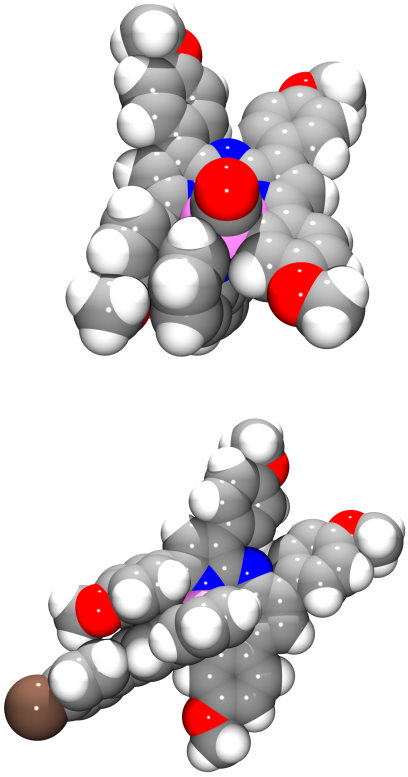

Figure III.S36 – The solid-state structure of **2** (left) and **5** (right) – space-fill models showing the π – π and π – H-C(sp^2) intramolecular interactions.
Co-crystallized solvent and the minor-disorder components have been omitted for clarity.

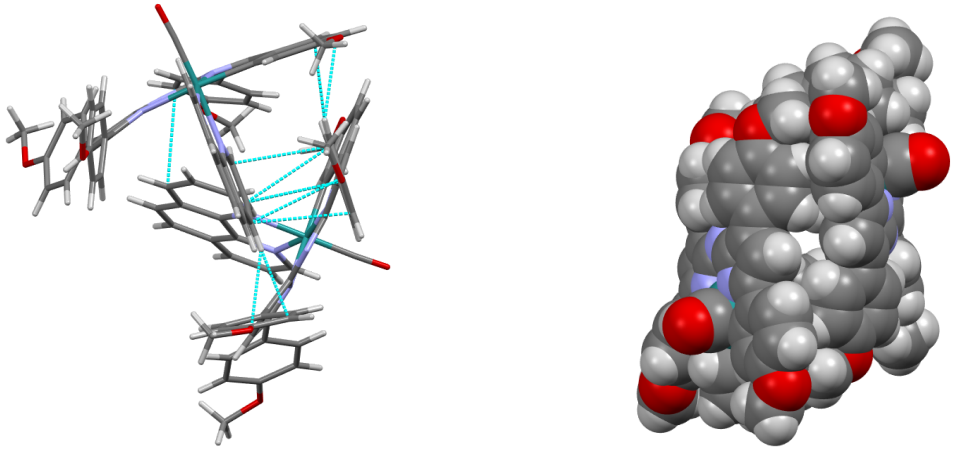

Figure III.S37 – The solid-state structure of **4** (asymmetric unit) – capped stick model (left) and space-fill model (right) showing the π – π and π – H-C(sp^2) intermolecular interactions.

The minor-disorder components have been omitted for clarity.

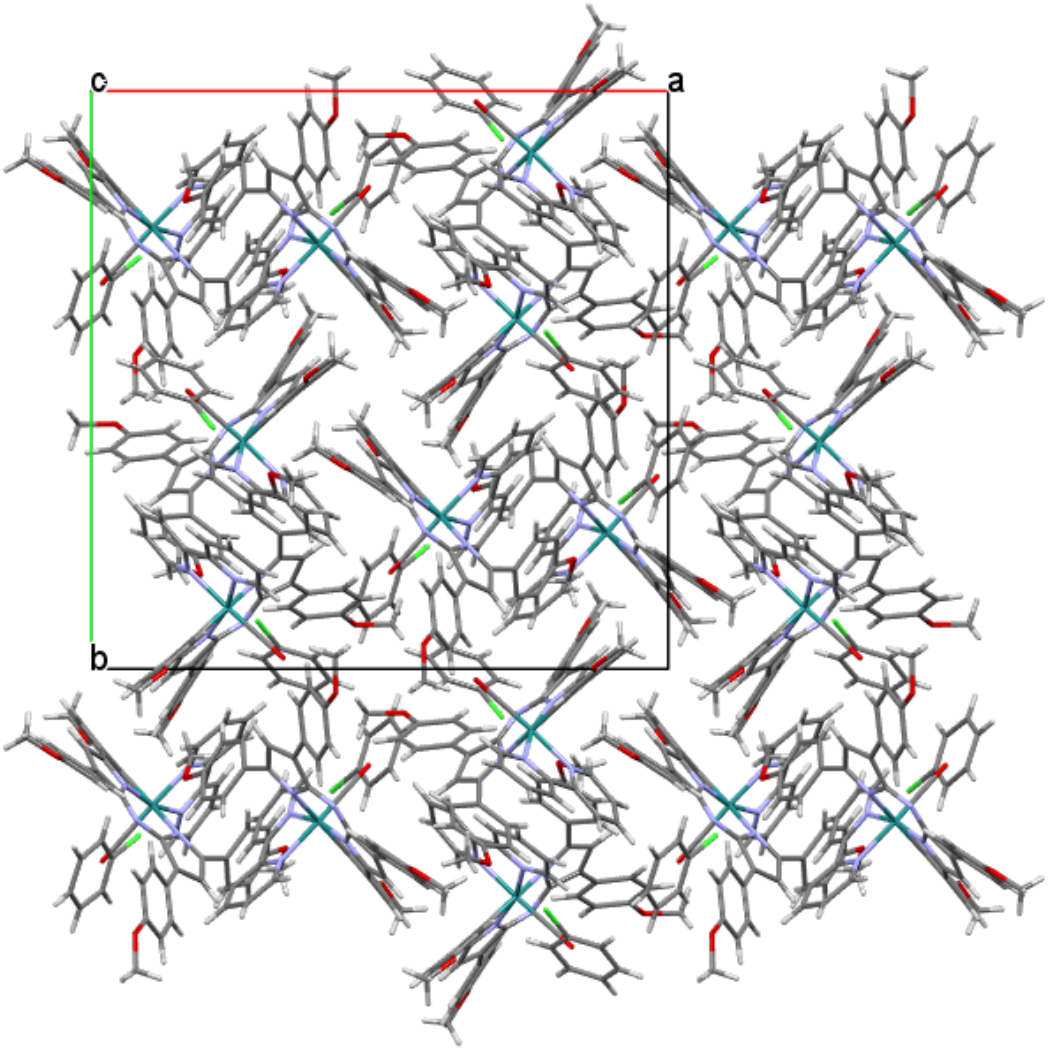

Figure III.S38 – A packing diagram for compound **2** – view along *c* axis.

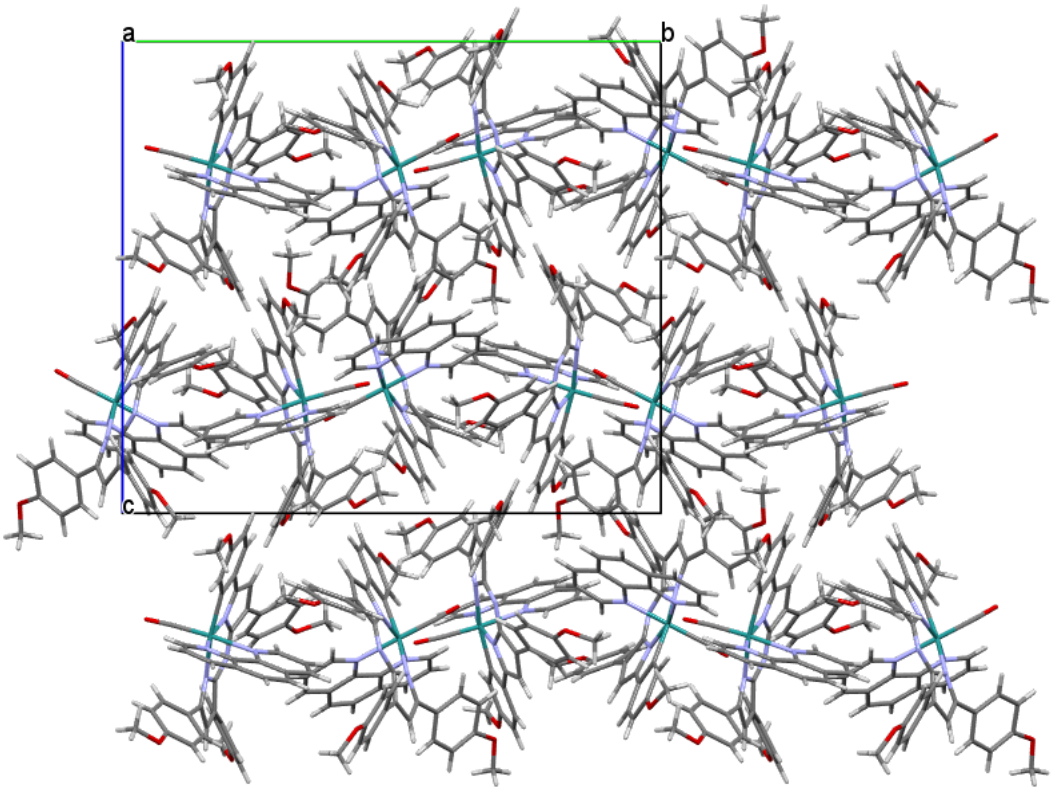

Figure III.S39 – A packing diagram for compound **4** – view along *a* axis.
The minor-disorder components have been omitted for clarity.

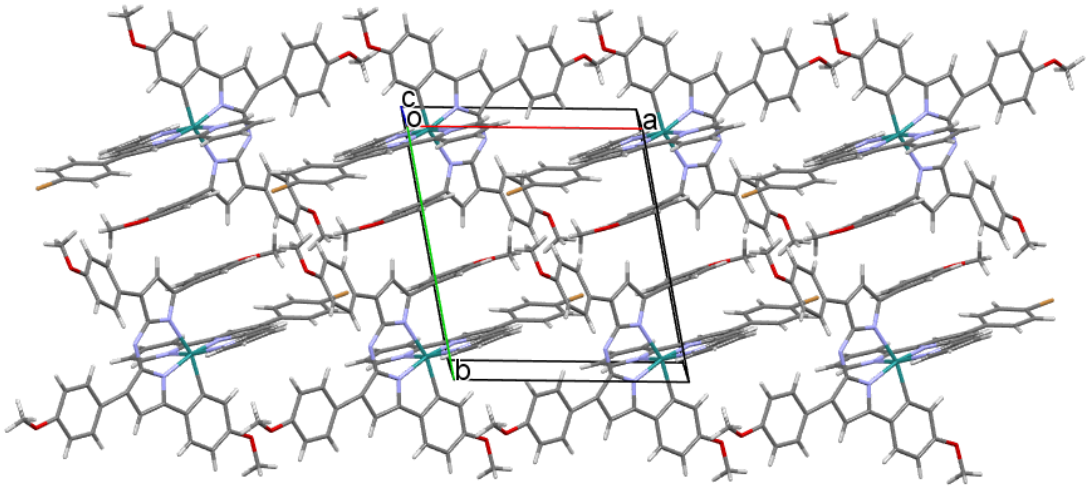

Figure III.S40 – A packing diagram for compound **5** – view along *c* axis showing the intramolecular and intermolecular π – π interactions.

Co-crystallized solvent and the minor-disorder components have been omitted for clarity.

References

1. E. Eskelinen, P. Da Costa and M. Haukka, *J. Electroanal. Chem.*, 2005, **579**, 257-265.
2. M.-P. Santoni, A. K. Pal, G. S. Hanan, A. Proust and B. Hasenknopf, *Inorg. Chem. Commun.*, 2011, **14**, 399-402.
3. N. G. Connelly and W. E. Geiger, *Chem. Rev.*, 1996, **96**, 877-910.
4. M. J. Frisch, G. W. Trucks, H. B. Schlegel, G. E. Scuseria, M. A. Robb, J. R. Cheeseman, G. Scalmani, V. Barone, B. Mennucci, G. A. Petersson, H. Nakatsuji, M. Caricato, X. Li, H. P. Hratchian, A. F. Izmaylov, J. Bloino, G. Zheng, J. L. Sonnenberg, M. Hada, M. Ehara, K. Toyota, R. Fukuda, J. Hasegawa, M. Ishida, T. Nakajima, Y. Honda, O. Kitao, H. Nakai, T. Vreven, J. J. A. Montgomery, J. E. Peralta, F. Ogliaro, M. Bearpark, J. J. Heyd, E. Brothers, K. N. Kudin, V. N. Staroverov, R. Kobayashi, J. Normand, K. Raghavachari, A. Rendell, J. C. Burant, S. S. Iyengar, J. Tomasi, M. Cossi, N. Rega, J. M. Millam, M. Klene, J. E. Knox, J. B. Cross, V. Bakken, C. Adamo, J. Jaramillo, R. Gomperts, R. E. Stratmann, O. Yazyev, A. J. Austin, R. Cammi, C. Pomelli, J. W. Ochterski, R. L. Martin, K. Morokuma, V. G. Zakrzewski, G. A. Voth, P. Salvador, J. J. Dannenberg, S. Dapprich, A. D. Daniels, Ö. Farkas, J. B. Foresman, J. V. Ortiz, J. Cioslowski and D. J. Fox, *Gaussian 09 Revision D.01*, (2009) Gaussian Inc., Wallingford CT
5. A. D. Becke, *J. Chem. Phys.*, 1993, **98**, 5648-5652.
6. C. Lee, W. Yang and R. Parr, *Phys. Rev. B*, 1988, **37**, 785-789.
7. S. H. Vosko, L. Wilk and M. Nusair, *Can. J. Phys.*, 1980, **58**, 1200-1211.
8. P. J. Stephens, F. J. Devlin, C. F. Chabalowski and M. J. Frisch, *J. Phys. Chem.*, 1994, **98**, 11623-11627.
9. J. Tomasi, B. Mennucci and R. Cammi, *Chem. Rev.*, 2005, **105**, 2999-3093.
10. R. Dennington, T. Keith, J. Millam, K. Eppinnett, W. L. Hovell and R. Gilliland, *GaussView Version 3.09*, (2003) Semichem Inc., Shawnee Mission KS.
11. N. M. O'Boyle, A. L. Tenderholt and K. M. Langner, *J. Comp. Chem.*, 2008, **29**, 839-845.
12. Chemissian, a computer program to analyze and visualize quantum-chemical calculations, by L. Skripnikov. For the current version, see http://www.chemissian.com
13. A. Bessette, J. G. Ferreira, M. Giguère, F. Bélanger, D. Désilets and G. S. Hanan, *Inorg. Chem.*, 2012, **51**, 12132-12141.
14. Bruker, *APEX2 and SAINT*, (2007) Bruker AXS Inc., Madison, Wisconsin, USA.
15. Bruker, *SADABS and TWINABS*, (2001) Bruker AXS Inc., Madison, Wisconsin, USA.
16. G. M. Sheldrick, *Acta Crystallogr., Sect. A*, 2008, **64**, 112-122.
17. G. M. Sheldrick, *Acta Crystallogr., Sect. A*, 2015, **71**, 3-8.
18. O. V. Dolomanov, Bourhis, L. J., Gildea, R. J., Howard, J. A. K., Puschmann, H., *J. Appl. Cryst.*, 2009, **42**, 339-341.
19. L. J. Farrugia, *J. Appl. Crystallogr.*, 1997, **30**, 565.

20. POV-Ray, *POV-Ray 3.7.0*, (2013) Persistence of Vision Pty. Ltd., Persistence of Vision Raytracer, retrieved from http://www.povray.org/download/.
21. A. L. Spek, *Acta Crystallogr., Sect. D*, 2009, **65**, 148-155.
22. CCDC, *Mercury 3.1 - 3.3*, (2001-2013).
23. S. P. Westrip, *J. Appl. Crystallogr.*, 2010, **43**, 920-925.
24. A. Loudet, R. Bandichhor, K. Burgess, A. Palma, S. O. McDonnell, M. J. Hall and D. F. O'Shea, *Org. Lett.*, 2008, **10**, 4771-4774.
25. M. Cibian, A. Bessette, A. O'Connor, J. G. Ferreira and G. S. Hanan, *Acta Crystallographica Section C*, 2015, **71**, 122-127.
26. G. R. Desiraju and T. Steiner, *The Weak Hydrogen Bond: In Structural Chemistry and Biology*, Oxford University Press, New York, 2001.
27. G. A. Jeffrey and W. Saenger, *Hydrogen bonding in biological structures*, Springer-Verlag, Berlin, 1991.
28. F. Allen, *Acta Crystallogr., Sect. B: Struct. Sci.*, 2002, **58**, 380-388.
29. D. Ooyama, T. Tomon, K. Tsuge and K. Tanaka, *J. Organomet. Chem.*, 2001, **619**, 299-304.
30. C.-F. Chow, B. K. W. Chiu, M. H. W. Lam and W.-Y. Wong, *J. Am. Chem. Soc.*, 2003, **125**, 7802-7803.